Synchrotron X-ray Diffraction Studies of Proton Transfer in Hydrogen Bonded Molecular Complexes

Saunders, Lucy

Award date:
2016

Awarding institution:
University of Bath

Synchrotron X-ray Diffraction Studies of Proton Transfer in Hydrogen Bonded Molecular Complexes

Lucy Katherine Saunders

A thesis submitted for the degree of Doctor of Philosophy

University of Bath

Department of Chemistry

July 2016

Supervisors: Prof. Chick Wilson, Dr. Harriott Nowell and Prof. Paul Raithby

Table of Contents

List of figures

Figure 8.20 The aggregation of the $DMANH^+$ cation and $ACID^-$ anion unit in (a) DMAN5-NIP, (b) DMAN2-NBA, (c) DMAN3-OMBA, (d) DMAN3-ABA and (e) DMAN4-ABA hydrate i DMAN A, ii DMAN B and iii DMAN C.

Figure 8.21 The aggregation of the $DMANH^+$ cation and $ACID^-$ anion unit in (a) DMAN2-CBA, (b) DMU4-CBA and (c) DMAN4-NBA II i DMAN A, ii DMAN B and iii DMAN C.

Figure 8.22 Weak interactions to the naphthalene C—H groups on the protonated side of the $DMANH^+$ cation in (a) DMAN4-ABA hydrate DMAN A (b) DMAN4-ABA hydrate DMAN C and (c) DMAN2-CBA and (d) DMAN4-CBA.

Figure 8.23 Weak interactions to the naphthalene C—H groups on both sides of the $DMANH^+$ cation in (a) DMAN5-NIP, (b) DMAN2-NBA, (c) DMAN3-ABA, (d) DMAN 4-NBA II DMAN A, (e) DMAN 4-NBA II DMAN B and (f) DMAN 4-NBA II DMAN C.

Figure 8.24 Weak interactions to the naphthalene C—H groups on the non-protonated side of the $DMANH^+$ cation in (a) DMAN4-ABA DMAN B and (b) DMAN3-OMBA.

Figure 8.25 Fourier difference electron density maps showing the electron density associated with the H-atom in the $[N—H\cdots N]^+$ IHB in (a) DMAN5-NIP, (b) DMAN2-NBA, (c) DMAN3-OMBA, (d) DMAN3-ABA, (e) DMAN4-ABA hydrate (i) DMAN A, (ii) DMAN B and (iii) DMAN C, (f) DMAN2-CBA, (g) DMAN4-CBA and (h) DMAN4-NBA II i DMAN A, ii DMAN B and iii DMAN C.

Figure 8.26 Fourier difference electron density maps showing the electron density associated with the H-atom in the $ACID^-$ anion unit O—H···O hydrogen bonds in (a) DMAN5-NIP, (b) DMAN3-OMBA, (c) DMAN3-ABA, (d) DMAN4-ABA hydrate i A, ii B, iii O10—H91···O12 and iv O8—H98···O8', (e) DMAN2-CBA i O3—H27···O1 and ii O5—H28···O4, (f) DMAN4-CBA i O1—H29···O3 and ii O6—H28···O4, (g) DMAN4-NBA II i A O2G—H5G···O3F, ii A O1H—H1H···O4F, iii B O4I—H1I···O2E, iv B O2D—H1D···O1E, v C O3J—H1J···O1K, vi C O3L—H1L···O2K.

Figure 8.27 Thermal parameters of the IHB proton and X^- in the $[Me_2N—H\cdots NMe_2]^+\cdots X^-$ fragment in (a) DMAN5-NIP, (b) DMAN2-NBA, (c) DMAN3-OMBA, (d) DMAN3-ABA, (e) DMAN4-ABA hydrate i DMAN A, ii DMAN B, iii DMAN C, (f) DMAN2-CBA, (g) DMAN4-CBA and (h) DMAN4-NBA II i DMAN A, ii DMAN B, iii DMAN C.

Figure 8.28 Torsions between carboxyl and carboxylate groups in the $ACID^-$ anion units in (a) DMAN5-NIP, (b) DMAN3-OMBA, (c) DMAN3-ABA, (d) DMAN4-ABA hydrate, (e) DMAN2-CBA, (f) DMAN4-CBA and (g) DMAN4-NBA II.

Figure 8.29 Fourier difference electron density maps showing the electron density associated with the H-atom in the $[N—H\cdots N]^+$ IHB in (a) DMAN2-FBA and (b) DMAN2-IBA generated from the (i) the laboratory X-ray structure [128] and the (ii) synchrotron X-ray structure.

Figure 9.1 The possible hydrogen bond synthons on molecular recognition of substituted ureas and 5-nitroisophthalic acid: (a) carboxylic acid $\boldsymbol{R22}(8)$ homo dimers, (b) carboxylic acid:amide $\boldsymbol{R22}(8)$ and (c) $\boldsymbol{R21}(6)$ hydrogen bond synthons, (d) amide:amide $\boldsymbol{R22}(8)$ homo dimers, (e) nitro:amide $\boldsymbol{R12}(4)$ and (f) $\boldsymbol{R22}(8)$ and (g) $\boldsymbol{R21}(6)$ hydrogen bonded synthons.

Figure 9.2 Top: Molecular building (a) urea, (b) *N*-methylurea, (c) *N*,*N*-dimethylurea, (d) *N*-phenylurea, (e) 5-nitroisophthalic acid, (f) methanol, (g) ethanol, (h) acetonitrile, (i) acetone, (j) tetrahydrofuran (THF), (k) ethyl acetate, (l) diethyl ether and (m) water.

Figure 9.3 Hydrogen bonded ring networks in (a)i and ii IM1, (b) IM2, (c) IM3, (d) IM4, (e) IM5, (f) IM6, (g) IM7, (h) CIM1 and (i) CIM2.

Figure 9.4 The different orientations of the *N*-phenylurea molecular building blocks in structurally similar (a) IM1, IM2 and IM4, (b) IM3, (c) IM5.

Figure 9.5 The size of the hydrogen bond ring in (a) IM1 – IM5, (b) IM6 and (c) IM7 in terms of a ring cross section; ellipsoid axis lengths are given in Table 9.8.

Figure 9.6 Pockets occupied by the guest molecules in the *N*-phenylurea and 5-nitroisophthalic acid host framework in (a) IM1, (b) IM3, (b) IM4, (c) IM5, (d) IM5, (e) CIM1 and (f) CIM2.

Figure 9.7 Channels occupied by the guest molecules in the *N*-phenylurea and 5-nitroisophthalic acid host framework in (a) IM2, (b) IM6 and (c) IM7.

Figure 9.8 Hydrogen bonding networks in non-solvated *N*-phenylurea 5-nitroisophthalic acid (a) NS1 and (b) NS2.

Figure 9.9 Layered structures of the *N*-phenylurea 5-nitroisophthalic acid non-solvated forms (a) NS1 and (b) NS2.

Figure 9.10 Hydrogen bonded networks formed in (a) U5-NIP, (b) MU5-NIP and (c) DMU5-NIP.

Figure 9.11 The crystal packing in (a) U5-NIP, (b) MU5-NIP and (c) DMU5-NIP.

Figure 9.12 The TGA-MS for (a) IM1: methanol peaks MS1 = 31 m/z, MS2 = 32 m/z, MS3 = 29 m/z, MS4 = 15 m/z, (b) IM2: ethanol peaks MS1 = 31 m/z, MS2 = 45 m/z, MS3 = 27 m/z, MS4 = 29 m/z, water peak MS5 = 18 m/z and (c) IM3: acetonitrile peaks MS1 = 41 m/z, MS2 = 39 m/z, MS3 = 28 m/z, MS4 = 14 m/z.

Figure 9.13 The TGA-MS for (a) IM4: acetone peaks MS1 = 43 m/z, MS2 = 58 m/z, MS3 = 15 m/z, MS4 = 42 m/z, water peaks MS5 = 18 m/z, (b) IM5: THF peaks MS1 = 42 m/z, MS2 = 41 m/z, MS3 = 71 m/z, MS4 = 43 m/z, water peak MS5 18 m/z and (c) IM6: ethyl acetate peaks MS1 = 43 m/z, MS2 = 61 m/z, MS3 = 45 m/z, MS4 = 70 m/z.

Figure 9.14 The TGA-MS for (a) IM7: THF peaks MS1 = 42, MS2 = 41, MS3 = 71, MS4 = 43, methanol peaks and MS5 = 31, MS6 = 32, MS7 = 29, MS8 = 15, (b) CIM1: water peaks MS1 = 18 m/z, MS2 = 17 m/z, MS3 = 16 m/z, (c) CIM2: acetone peaks MS1 = 43 m/z, MS2 = 58 m/z, MS3 = 15 m/z, MS4 = 42 m/z, water peaks MS5 = 18 m/z.

Figure 9.15 DSC traces of IM1 – IM7, CIM1, CIM2, NS1 and NS2, recorded at a 5 °C min^{-1} heating rate.

Figure 9.16 PXRD patterns for (a) IM1, (b) IM2 and (c) IM3 on samples at 25 °C and after preheating to 145 °C.

Figure 9.17 PXRD patterns for (a) IM4, (b) IM5 and (c) IM6 on samples at 25 °C and after preheating to 145 °C.

Figure A7.7 A comparison of TLS tensors from TLS refinement model of heavy atom thermal parameters in Topas-Academic V5.0 [168] and in Jana2006 [223] in molecules (a) benzimidazole1 and (b) benzimidazole2 and (c) benzimidazole3 in the molecular complex BZN4-OHBA STEP at 300 K.

Figure A7.8 A comparison of TLS tensors from TLS refinement model of heavy atom thermal parameters in Topas-Academic V5.0 [168] and in Jana2006 [223] in molecules (a) benzimidazole4 and (b) 4-hydroxybenzoic acid1 and (c) 4-hydroxybenzoic acid2 in the molecular complex BZN4-OHBA STEP at 300 K.

Figure A7.9 A comparison of TLS tensors from TLS refinement model of heavy atom thermal parameters in Topas-Academic V5.0 [168] and in Jana2006 [223] in molecules (a) benzimidazole1 and (b) benzimidazole2 and (c) benzimidazole3 in the molecular complex BZN4-OHBA CONT. at 300 K.

Figure A7.10 A comparison of TLS tensors from TLS refinement model of heavy atom thermal parameters in Topas-Academic V5.0 [168] and in Jana2006 [223] in molecules (a) benzimidazole4 and (b) 4-hydroxybenzoic acid1 and (c) 4-hydroxybenzoic acid2 in the molecular complex BZN4-OHBA CONT. at 300 K.

Figure A7.11 R_{wp} as a function of temperature for a surface refinement, employing model H_{para} and (a) normal ADPs 100 K rigid only, (b) normal ADPs all rigid and (c) TLS ADPs 100 K rigid only for DMU2,4-DNBA.

Figure A7.12 R_{wp} as a function of temperature for (a) independent and (b) surface refinements employing a H_{free} model with TLS refined ADPs and 100 K rigid only for DMU2,4-DNBA.

Figure A7.13 R_{wp} as a function of temperature for a surface refinement employing model H_{free} and (a) normal ADPs with 100 K rigid only, (b) normal ADPs with all rigid and (c) TLS ADPs with 100 K rigid only for BZN4-OHBA STEP.

Figure A7.14 R_{wp} as a function of temperature for a surface refinement employing model H_{para} and (a) normal ADPs with 100 K rigid only, (b) normal ADPs with all rigid and (c) TLS ADPs with 100 K rigid only for BZN4-OHBA STEP.

Figure A7.15 R_{wp} as a function of temperature for (a) independent and (b) surface refinements employing a H_{free} model with TLS refined ADPs and 100 K rigid only for BZN4-OHBA STEP.

Figure A7.16 R_{wp} as a function of temperature for (a) independent and (b) surface refinements employing a H_{para} model with TLS refined ADPs and 100 K rigid only for BZN4-OHBA STEP.

Figure A7.17 R_{wp} as a function of temperature for a surface refinement employing model H_{free} and (a) normal ADPs with 100 K rigid only, (b) normal ADPs with all rigid and (c) TLS ADPs with 100 K rigid only for BZN4-OHBA CONT.

Figure A7.18 R_{wp} as a function of temperature for a surface refinement employing model H_{para} and (a) normal ADPs with 100 K rigid only, (b) normal ADPs with all rigid and (c) TLS ADPs with 100 K rigid only for BZN4-OHBA CONT.

Figure A7.19 Tensor T_{11} as a function of temperature for molecules in DMU2,4-DNBA: (a) DMU and (b) 2,4-DNBA, in BZN4-OHBA STEP: (c) BZN1, (d) BZN2, (e) BZN3, (f) BZN4, (g) 4-

OHBA1 and (h) 4-OHBA2 and in BZN4-OHBA CONT: (i) BZN1, (j) BZN2, (k) BZN3, (l) BZN4, (m) 4-OHBA1 and (n) 4-OHBA2.

Figure A7.20 Tensor T_{12} as a function of temperature for molecules in DMU2,4-DNBA: (a) DMU and (b) 2,4-DNBA, in BZN4-OHBA STEP: (c) BZN1, (d) BZN2, (e) BZN3, (f) BZN4, (g) 4-OHBA1 and (h) 4-OHBA2 and in BZN4-OHBA CONT. (i) BZN1, (j) BZN2, (k) BZN3, (l) BZN4, (m) 4-OHBA1 and (n) 4-OHBA2.

Figure A7.21 Tensor T_{13} as a function of temperature for molecules in DMU2,4-DNBA: (a) DMU and (b) 2,4-DNBA, in BZN4-OHBA STEP (c) BZN1, (d) BZN2, (e) BZN3, (f) BZN4, (g) 4-OHBA1 and (h) 4-OHBA2 and in BZN4-OHBA CONT. (i) BZN1, (j) BZN2, (k) BZN3, (l) BZN4, (m) 4-OHBA1 and (n) 4-OHBA2.

Figure A7.22 Tensor T_{22} as a function of temperature for molecules in DMU2,4-DNBA: (a) DMU and (b) 2,4-DNBA, in BZN4-OHBA STEP: (c) BZN1, (d) BZN2, (e) BZN3, (f) BZN4, (g) 4-OHBA1 and (h) 4-OHBA2 and in BZN4-OHBA CONT. (i) BZN1, (j) BZN2, (k) BZN3, (l) BZN4, (m) 4-OHBA1 and (n) 4-OHBA2.

Figure A7.23 Tensor T_{23} as a function of temperature for molecules in DMU2,4-DNBA: (a) DMU and (b) 2,4-DNBA, in BZN4-OHBA STEP: (c) BZN1, (d) BZN2, (e) BZN3, (f) BZN4, (g) 4-OHBA1 and (h) 4-OHBA2 and in BZN4-OHBA CONT: (i) BZN1, (j) BZN2, (k) BZN3, (l) BZN4, (m) 4-OHBA1 and (n) 4-OHBA2.

Figure A7.24 Tensor T_{33} as a function of temperature for molecules in DMU2,4-DNBA: (a) DMU and (b) 2,4-DNBA, in BZN4-OHBA STEP: (c) BZN1, (d) BZN2, (e) BZN3, (f) BZN4, (g) 4-OHBA1 and (h) 4-OHBA2 and in BZN4-OHBA CONT. (i) BZN1, (j) BZN2, (k) BZN3, (l) BZN4, (m) 4-OHBA1 and (n) 4-OHBA2.

Figure A7.25 Tensor L_{11} as a function of temperature for molecules in DMU2,4-DNBA: (a) DMU and (b) 2,4-DNBA, in BZN4-OHBA STEP: (c) BZN1, (d) BZN2, (e) BZN3, (f) BZN4, (g) 4-OHBA1 and (h) 4-OHBA2 and in BZN4-OHBA CONT: (i) BZN1, (j) BZN2, (k) BZN3, (l) BZN4, (m) 4-OHBA1 and (n) 4-OHBA2.

Figure A7.26 Tensor L_{12} as a function of temperature for molecules in DMU2,4-DNBA: (a) DMU and (b) 2,4-DNBA, in BZN4-OHBA STEP: (c) BZN1, (d) BZN2, (e) BZN3, (f) BZN4, (g) 4-OHBA1 and (h) 4-OHBA2 and in BZN4-OHBA CONT. (i) BZN1, (j) BZN2, (k) BZN3, (l) BZN4, (m) 4-OHBA1 and (n) 4-OHBA2.

Figure A7.27 Tensor L_{13} as a function of temperature for molecules in DMU2,4-DNBA: (a) DMU and (b) 2,4-DNBA, in BZN4-OHBA STEP: (c) BZN1, (d) BZN2, (e) BZN3, (f) BZN4, (g) 4-OHBA1 and (h) 4-OHBA2 and in BZN4-OHBA CONT.: (i) BZN1, (j) BZN2, (k) BZN3, (l) BZN4, (m) 4-OHBA1 and (n) 4-OHBA2.

Figure A7.28 Tensor L_{22} as a function of temperature for molecules in DMU2,4-DNBA: (a) DMU and (b) 2,4-DNBA, in BZN4-OHBA STEP: (c) BZN1, (d) BZN2, (e) BZN3, (f) BZN4, (g) 4-OHBA1 and (h) 4-OHBA2 and in BZN4-OHBA CONT.: (i) BZN1, (j) BZN2, (k) BZN3, (l) BZN4, (m) 4-OHBA1 and (n) 4-OHBA2.

Figure A7.29 Tensor L_{23} as a function of temperature for molecules in DMU2,4-DNBA: (a) DMU and (b) 2,4-DNBA, in BZN4-OHBA STEP: (c) BZN1, (d) BZN2, (e) BZN3, (f) BZN4, (g) 4-

List of tables

$^{-}$OCCC where O^{-} is X^{-}), the torsion angle between carboxyl group and benzene ring in the protonated acid (angle 3 OCCC) and the co-planarity of the benzene rings of each acid (angle 4).

Table 8.12 The torsion angle between DMAN amino groups in each molecular complex.

Table 8.13 The C—C (Å) bond lengths in the neutral DMAN [124] and in the $DMANH^{+}$ cations of the molecular complexes (see Figure 1.20 for atom labelling scheme).

Table 8.14 The C—N *peri*-amino bond lengths and angles in the neutral DMAN [124] and in the $DMANH^{+}$ cations of the molecular complexes (see Figure 1.20 for atom labelling scheme).

Table 8.15 The bond lengths of the carboxylate and carboxyl groups in the $ACID^{-}$ dimer across the molecular complexes.

Table 8.16 The parameters of the minor component (C—H···X^{-}) of the $[Me_2N_1—H···N_2Me_2]^{+}···X^{-}$ fragment across the molecular complexes. $N(CH_3)_2$ group 1 is the most 'protonated' forming the IHB.

Table 8.17 The parameters of the minor component (C—H···X^{-}) of the $[Me_2N_1—H···N_2Me_2]^{+}···X^{-}$ fragment (continued) across the molecular complexes. $N(CH_3)_2$ group 1 is the most 'protonated' forming the IHB.

Table 8.18 The parameters of the minor component (C—H···X^{-}) of the $[Me_2N_1—H···N_2Me_2]^{+}···X^{-}$ fragment (continued) across the molecular complexes. $N(CH_3)_2$ group 1 is the most 'protonated' forming the IHB.

Table 8.19 The bifurcated hydrogen bond parameters within the $[Me_2N_1—H···N_2Me_2]^{+}···X^{-}$ fragment across the molecular complexes.

Table 8.20 The parameters of the IHB in the $[Me_2N—H···NMe_2]^{+}···X^{-}$ fragment across the molecular complexes.

Table 8.21 The parameters of the O—H···O^{-} CAHB in the $ACID^{-}$ anion units across the molecular complexes.

Table 8.22 Angles within the $ACID^{-}$ hydrogen bonded motif in each DMAN molecular complex including the torsion angle of the carboxyl and carboxylate groups forming the SSHBs (angle 1 COOC), the torsion angle between carboxylate group and benzene ring in the deprotonated acid (angle 2 $^{-}$OCCC where O is on X^{-}), the torsion angle between carboxyl group and benzene ring in the protonated acid (angle 3 OCCC) and the co-planarity of the benzene rings of each acid (angle 4).

Table 8.23 The torsion angle between DMAN amino groups in each molecular complex.

Table 8.24 The C—C bond lengths (Å) in the neutral DMAN [124] and in the $DMANH^{+}$ cations of the molecular complexes (see Figure 1.20 for atom labelling scheme).

Table 8.25 The C—N *peri*-amino bond lengths and angles in the neutral DMAN [124] and in the $DMANH^{+}$ cations of the molecular complexes (see Figure 1.20 for atom labelling scheme).

Table 8.26 The bond lengths of the carboxylic acid groups in the $ACID^{-}$ anion unit.

Table 9.1 Crystallographic data for the inclusion materials IM1 to IM7.

Table A6.2 Crystallographic data for *N*,*N*-dimethylurea 4-cyanobenzoic acid (DMU4-CBA) (1:1), urea isophthalic acid (UIP) (1:1) and urea 5-aminoisophthalic acid (U5-AIP) (1:1).

Table A6.3 Crystallographic data for urea 5-nitroisophthalic acid (U5NIP), *N*-methylurea phthalic acid (MUP) (1:1), *N*-methylurea isophthalic acid (MUIP) (1:1), *N*-methylurea 5-nitrosiophthalic acid (MU5-NIP) (2:1) and *N*-methylurea 5-aminosiophthalic acid (MU5-AIP) (1:1).

Table A6.4 Crystallographic data for *N*,*N*-dimethylurea isophthalic acid (DMUIP) (2:1), *N*,*N*-dimethylurea 5-aminoisophthalic acid (DMU5-AIP) (2:1), *N*,*N*-dimethylurea 3-nitrophthalic acid (DMU3-NP) (1:1) and *N*,*N*-dimethylurea 5-nitroisophthalic acid (DMU5-NIP) (2:1).

Table A6.5 Crystallographic data for *N*,*N*-dimethylurea 5-nitroisophthalic acid (DMU5-NIP) (2:1), *N*-phenylurea 2,4-dinitrobenzoic acid (PhU2,4-DNBA) (1:1), *N*-phenylurea 3-nitroisophthalic acid (PhU3-NP) (1:1), *N*-phenylurea 5-nitroisophthalic acid form I (PhU5-NIP I) (2:1) and *N*-phenylurea 5-nitroisophthalic acid form II (PhU5-NIP II) (1:1).

Table A6.6 Crystallographic data for *N.N'*-dimethylurea 5-aminoisophthalic acid (DM'U-5-AIP) (1:1), 3-deazauracil 3-nitrophthalic acid (3-DAZA3-NP) (2:1), 3-deazauracil 2,4-dinitrobenzoic acid (3-DAZA2,4-DNBA) (1:1) and 3-deazauracil chloranilic acid (3-DAZAClA) (1:1).

Table A6.7 Crystallographic data for isoniazid phthalic acid (INZP) (1:1), isoniazid 2,4-dinitrobenzoic acid (INZ2,4-DNBA) (1:1), isoniazid 5-nitroisophthalic acid (INZ5-NIP) (1:1) and isonicotinamide 2,4-dinitrobenzoic acid I (IN2,4-DNBA I) (1:1).

Table A6.8 Crystallographic data for isonicotinamide 2,4-dinitrobenzoic acid I (IN2,4-DNBA I) (1:1), isonicotinamide 2,4-dinitrobenzoic acid III (IN2,4-DNBA III) (1:1), pyrazole bromanilic acid (PYBrA) (1:1), pyrazole chloranilic acid hydrate (PYClA hydrate) (1:1:1), 4(5)-methylimidazole bromanilic acid (4(5)-MIBrA) (1:1) and 4(5)-methylimidazole chloranilic acid hydrate (4(5)-MIClA hydrate) (2:1:1:2).

Table A6.9 Crystallographic data for 4-acetylpyridine bromanilic acid (4-APBrA) (1:1), 4-acetylpyridine chloranilic acid (4-APClA) (1:1) and 1,2,4-*1H*-triazole chloranilic acid hydrate (1,2,4-TZClA hydrate) (2:1:1), 3,5-dimethylpyrazole bromanilic acid hydrate (3,5-DMPYBrA hydrate) (2:1:2), 3,5-dimethylpyrazole chloranilic acid hydrate (3,5-DMPYClA hydrate) (2:1:2) and 3,5-dimethylpyrazole chloranilic acid (3,5-DMPYClA) (1:1).

Table A6.10 The ΔpKa values of each literature molecular complex in Figure 6.19 calculated using the ACD-I Lab (ACD pKa). [270]

Table A7.1 The O1—H1···O5 SSHB hydrogen bond parameters in DMU2,4-DNBA over the 100 to 350 K temperature range for refinement model 2.

Table A7.2 The N^{+}—H···O^{-} SSHB hydrogen bond parameters in INP over the 100 to 350 K temperature range for refinement model 2.

Table A7.3 Refinement details from the structural refinement of each molecular complex in Jana2006 [223] employing the normal and TLS refinement of the anisotropic thermal parameters.

Acknowledgements

There are a number of people I would like to acknowledge for their contributions, both academic and personal, during the undertaking of this work. First and foremost, Chick and Paul, thank you for the opportunity of this PhD, especially forming the link with Diamond, allowing me to realise my dream of working at a synchrotron facility. It has provided endless fun, learning and adventure and I really have loved every minute. Thank you both for your endless support, always being available when needed and there to share the excitement and ideas along the way. Thank you to my Diamond supervisor, Harriott, for taking me on and making me feel so welcome. Thank you for always listening, for the cups of tea and for giving me endless time and help. Thank you to the I19 team, for the experimental help over the years, for the team breakfasts and pub lunches. I have loved coming to Diamond and I will definitely miss it!

Thank you to the Wilson and Raithby groups and all the members over the years. Thanks for being such great people to work with and friends to have. Thank you to my project student Helen, for all her hard work and enthusiasm. A special thank you goes to Lynne, for all your knowledge, your realistic approach, for taking my endless questions and for all the fun (I know you like me really). Thank you to my beam time buddies, for passing the hours with me in new and inventive ways; Lauren for the trips to Triple Rock, Lynne for cheering me up with her three o'clock in the morning look and especially Char, for the songs, the internet shopping, the food conversations, naps and late night tea trips.

I have had the opportunity to carry out experiments at a number of facilities during my PhD including at the Diamond Light Source, on Beamlines I19, and at the Advanced Light Source on Beamline 11.3.1, and I would like to thank all of the beamline scientists for their help in the studies. I have also been lucky enough to work with John Evans (University of Durham) during this PhD research project and I would like to thank him for his contribution, I have learnt so much and could not have achieved what I did without it.

I would like to thank my parents, Dad for letting me borrow the Astra every week to make the trip to Diamond (and for fixing it when it breaks!) and Mum for the many sandwiches and early morning lifts. Thank you for your continued love and encouragement. Thanks to Ed, for all the adventures over the years, for listening to all my stories about crystals and my programme, for handling the boring Sundays because I need to work, and for always being ready to cheer me up. And a last thank you to Sarah, for the fun Bristol times, keeping me sane until the end.

Abstract

The technique of single crystal synchrotron X-ray diffraction is applied in the study of solid state proton transfer processes in hydrogen bonded molecular complexes. Proton transfer processes are of interest where they are responsible for a number of physical and chemical properties within solid state functional materials; their study gives insight into the occurrence of such properties and where they may be targeted and tuned in future materials. The synchrotron X-ray diffraction technique has been trialled with respect to the potential it offers for high throughput capability for studying proton transfer processes as a function of an external stimulus or across a number of molecular systems.

Chapter 1 contains a review of the literature of the hydrogen bond, including its role in crystal engineering and proton transfer effects. In Chapter 2, the theory behind the analytical techniques used in the study of hydrogen bonded molecular complexes, in which crystallographic methods are fundamental, are described. In Chapter 3 the research project aims and objectives are presented; these objectives are targeted at the use of single crystal synchrotron X-ray diffraction in the study and rationalisation of solid state proton transfer processes. In Chapter 4, the experimental methods implemented in this research project to achieve these research goals are reported.

Chapter 5 is the first of the result chapters and applies the synchrotron single crystal X-ray diffraction technique in the study of variable temperature proton disorder in centrosymmetric hydrogen bonded carboxylic acid dimers. Chapter 6 focuses on the design of proton transfer systems implementing a number of crystal engineering strategies in the design of short strong hydrogen bonds (SSHBs) for potential proton migration studies. Chapter 7 applies a combination of diffraction methods (synchrotron and laboratory X-ray diffraction) and refinement strategies in the study of temperature dependent proton migration across SSHBs, allowing the potential of these methods in the study of proton migration to be assessed. Chapter 8 is the final application of the synchrotron technique in studies of proton transfer behaviour investigating static proton transfer behaviour in molecular complexes of the proton sponge 1,8-bis(dimethylamino)naphthalene with organic acids. The urea-acid inclusion materials presented in Chapter 9 additionally allow the investigation of the hydrogen bond as a crystal engineering tool in the design of hydrogen bonded solvent-inclusion networks.

In the last chapter, Chapter 10, conclusions from the findings in Chapters 5 to 9 are pulled together and patterns explored. Drawing on these overall findings, some suggestions for future work are also made.

Abbreviations

PES	Potential energy surface
HSAB	Hardness and softness of (Lewis) acids and bases
CAHB	Charge assisted hydrogen bond
RAHB	Resonance assisted hydrogen bond
SSHB	Short strong hydrogen bond
DMAN	1,8-bis(dimethylamino)naphthalene
IHB	Intramolecular hydrogen bond
ADP	Anisotropic displacement parameter
TLS	Translation libration screw
DLS	Diamond Light Source, U.K. [1]
ALS	Advanced Light Source, U.S.A. [2]
PXRD	Powder X-ray diffraction
DSC	Differential scanning calorimetry
TGA	Thermogravimetric analysis
MS	Mass spectrometry
CSD	The Cambridge Structural Database [3]
CCD	Charge coupled device
CMOS	Complementary metal-oxide semiconductor
EH	Experimental hutch
BA	Benzoic acid
U	Urea
Ac	Organic acid
D	Hydrogen bond donor
A	Hydrogen bond acceptor
H	Hydrogen atom
CONT.	Continuous
ACID$^-$	Organic acid anion unit
IM	Inclusion material
CIM	Condensed inclusion material
NS	Non-solvated
Ho	Host
G	Guest

List of publications

Crystal engineering urea organic acid hydrogen bonded networks with solvent inclusion properties

L. K. Saunders, H. Nowell, P. R. Raithby and C. C. Wilson, *CrystEngComm*, 2016, **18**, 5916-5929.

Chapter 1.

Introduction

In the research project upon which this thesis reports, the hydrogen bond is explored as both a crystal engineering tool and as a means to study interesting proton transfer effects in the solid state. The molecular complexes studied have been prepared by evaporative crystallisation. Single crystal X-ray diffraction has been used as the main technique for the characterisation of the materials studied whilst synchrotron X-ray diffraction has been investigated as a rapid throughput tool in studying proton transfer effects.

This Introductory Chapter gives an account of the principles underlying the molecular complexes studied: the hydrogen bond which is the principal intermolecular interaction by which the components are assembled; crystal engineering, the design tool which seeks to predict which intermolecular interactions will form between given components, which also informs the choice of components in attempting to form complexes with a designed structure or property; and proton transfer, an important phenomenon within hydrogen bonds in solid state materials and which is manifest in its different facets in various aspects of the complexes studied.

1.1 The hydrogen bond

The concept of the hydrogen bond was first introduced by Latimer and Rodebush to explain the structure and properties of water; the oxygen atoms can be considered to show tendencies partially to both add and give up hydrogen such that two water molecules may be bound together by a weak 'bond'. [4] Subsequently, Pimental and McClellan described the situation of hydrogen bond formation occurring when a hydrogen atom is bonded to an atom, called a hydrogen bond donor (D), that is more electronegative than itself such that the hydrogen atom is deshielded and may interact with a neighbouring atom in the same or a different molecule, called a hydrogen bond acceptor (A), which is electron rich or itself electronegative. [5] A hydrogen bond then exists if there is evidence of bond formation between D—H and A, specifically involving H (Figure 1.1). [6] The acceptor A must have lone-pair electrons or polarisable π-electrons. [7] The hydrogen bond can be distinguished from weaker van der Waals interactions by its tendency for linearity between the D—H and A groups. [8]

$$D^{\delta-} — H^{\delta+} \cdots A^{\delta-}$$

Figure 1.1 The description of a hydrogen bond formed between a hydrogen bond donor group, D—H, and a hydrogen bond acceptor group, A.

Hydrogen bonds form in solution or within a solid material and are important in both biological and chemical systems having structural or dynamic implications [9, 10] and leading to certain physical properties of materials. [11] Evidence of hydrogen bonding is observable in Nuclear Magnetic Resonance (NMR) spectra where the D—H proton signals are shifted significantly downfield and in Infrared spectroscopy (IR) where D—H stretch bands are shifted to lower stretching frequencies. [12]

1.1.1 The hydrogen potential energy surface (PES)

The formation of a hydrogen bonding interaction has consequences for both the position and vibrational motion of the hydrogen atom in the D—H bond which is governed by the potential energy surface (PES); in an isolated D—H bond, the PES has the shape of a single well. [7]

On forming a hydrogen bond, the vibrational motion of the hydrogen atom is restricted; due to the hydrogen atom now being restrained by two bonds (D—H and H···A). This restriction is reflected in the PES which broadens with smaller energy gaps between the D—H vibrational levels (representing a slight weakening of this bond as a bond to the acceptor is formed) and a second well is developed; the PES has the shape of an asymmetric double well (Figure 1.2). [13]

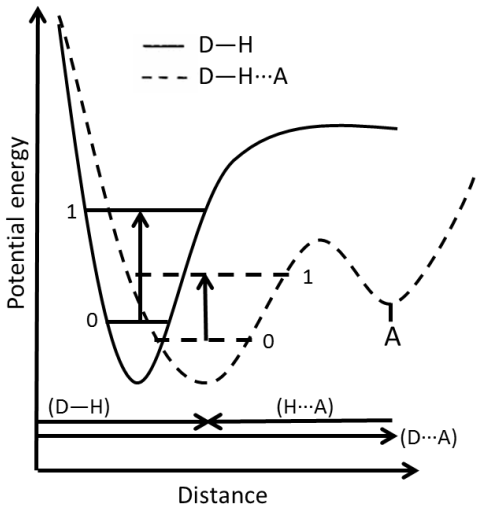

Figure 1.2 The potential energy surface (PES) for a free D—H (solid line) and D—H in a hydrogen bond (dashed line). [13]

All types of hydrogen bonds exist within two classes; those formed between donor and acceptor groups in different molecules are intermolecular hydrogen bonds whilst those formed between

donor and acceptor groups in the same molecule are intramolecular. [7] Within the two classes, three sub categories of hydrogen bonding interactions can be defined depending on bond energies, geometries and nature of the interaction (Table 1.1).

Table 1.1 Properties of strong, moderate and weak hydrogen bonds. [8]

Interaction	Strong	Moderate	Weak
	Mostly covalent	Mostly electrostatic	electrostatic
Bond lengths	D—H ≈ H···A	D—H < H···A	D—H << H···A
d(D···A) (Å)	2.2 – 2.5	2.5 – 3.2	3.2 – 4.0
d(H···A) (Å)	1.2 – 1.5	1.5 – 2.2	2.2 – 3.2
<(DHA) (°)	175 – 180	130 – 180	90 – 150
Energy (kcal mol^{-1})	14 – 40	4 – 15	< 4

The strength of a hydrogen bond may also be affected by donor acidity and acceptor basicity. Donor properties improve on increasing the acidity of the D—H proton; an increase in electron density on the donor will strengthen its donor ability, for example N>O>S, whilst a better hydrogen bond acceptor is one that is more basic. The hardness and softness of the acid (the donor, D) and the base (the acceptor, A) (HSAB) will also affect the hydrogen bond strength, defined as the ability of the hydrogen bond donor to polarise and the acceptor to become polarised; hard donors and acceptors have a lower ability to polarise or be polarised, respectively, whilst the opposite is true for soft donors and acceptors. Typically, hard acid donors prefer to form hydrogen bonds with hard base acceptors whilst soft acid donors prefer to form hydrogen bonds with soft base acceptors; this interaction of like with like creates extra stability in the hydrogen bonded adduct. [14, 15]

Different shapes of the PES are observed for D—H when involved in different strength hydrogen bonding interactions with A (Figure 1.3). Moderate strength hydrogen bonding interactions have a PES with the shape of an asymmetric double well potential. If the interaction of the proton with D becomes increasingly equivalent in energy to its interaction with A, the energy difference between the two wells reduces and the asymmetric potential becomes increasingly symmetric. For strong hydrogen bonds, the double wells in the PES become increasingly symmetric and the energy barrier between them is reduced; the PES has the shape of a symmetric double well potential. In some cases, where the donor-acceptor distance is increasingly short, the barrier between the two wells is sufficiently reduced such that the PES has the shape of a symmetrical single well potential. [7]

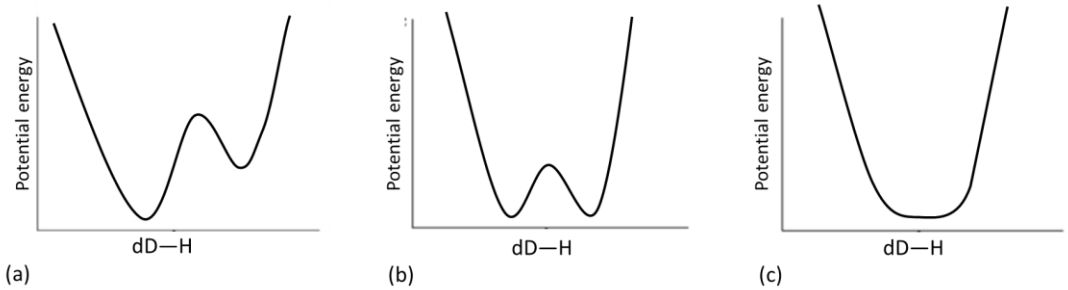

Figure 1.3 The potential energy surfaces for the motion of a hydrogen atom in (a) an asymmetric double well, (b) a symmetric double well and (c) a symmetric single well PES. [16]

1.1.2 Strong hydrogen bonds

Strong hydrogen bonds are the shortest, with donor-acceptor distances in the range of 2.2 to 2.5 Å, and are the most directional of the hydrogen bonding interactions with hydrogen bond angles approaching 180 °. Linearity provides strength in these interactions due to being the optimised geometry for electrostatic interaction of atoms. [17] Strong hydrogen bonds most commonly occur where there is an electron deficiency in the D—H donor group or where there is an excess of electron density in the acceptor group. An electron deficiency in D increases the partial positive charge on H whilst an increased electron density on A leads to an increased interaction with the deshielded proton; the result is a strengthening of the formed hydrogen bonding interaction. [7] Where either the donor or acceptor or both are charged, these are termed charge assisted hydrogen bonds (CAHB). [18, 19] Stronger hydrogen bonds have also been found to be formed for increasingly delocalised conjugated systems, such as in β-diketone moieties or in amide groups; the amide N—H group becomes a stronger donor if the amide C=O accepts a hydrogen bond. The D—H groups are polarised by charge flow through π-bonds. [8] This is the effect of resonance assisted hydrogen bonds (RAHB) and may be inter or intra molecular (Figure 1.4). [20]

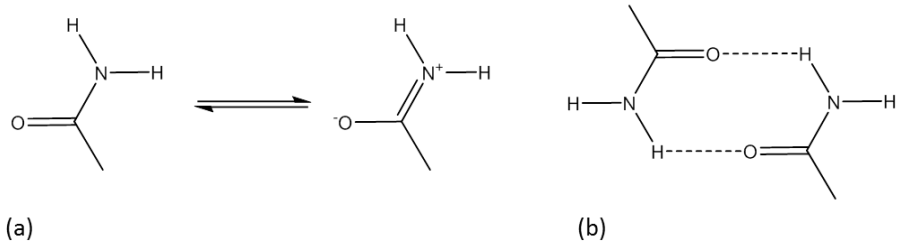

Figure 1.4 Resonance assisted hydrogen bonds (RAHBs) (a) resonance forms of an amide group and (b) RAHB rings.

Strong hydrogen bonds may also occur due to geometrical conformation, when donor and acceptor atoms are brought into closer contact than the sum of the van der Waals radii such as in 4,4'-dimethyl-2,2'-bipyridin-1-ium 2,4,5-tricarboxybenzoate (Figure 1.5); deprotonated and protonated carboxylic acid groups are in close proximity. [21]

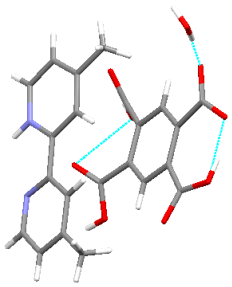

Figure 1.5 The intramolecular O—H···O in 4,4'-dimethyl-2,2'-bipyridin-1-ium 2,4,5-tricarboxybenzoate. [21]

Common types of strong hydrogen bonds include O^+—H···O, N^+—H···O^- or N^+—H···N hydrogen bonds. Strong hydrogen bonds may have bond energies in excess of 12 kcal mol^{-1}, comparable to some covalent interactions. Very short hydrogen bonds with donor-acceptor distances of less than 2.5 Å for O—H···O and less than 2.6 Å for N—H···O are considered short strong hydrogen bonds (SSHBs). These interactions may be described as three-centre four-electron bonding where the proton is involved in two partial covalent bonds to the donor and acceptor and, as such, are characterised by elongated D—H and shorter H···A distances. [22] The shortest SSHBs may exhibit interesting proton migration behaviour related to the symmetric shape of the PES of D—H in this short hydrogen bond (§1.3.2). [23]

1.1.3 Moderate hydrogen bonds

Moderate strength hydrogen bonds have donor-acceptor distances that are less than the sum of the van der Waals radii of the two atoms, typically in the range of 2.5 to 3.2 Å, and are the most commonly formed hydrogen bonds, often called 'normal' hydrogen bonds. They form between neutral donor and acceptor groups where D is electronegative relative to H and the acceptor atom has a lone pair; these are regarded as mostly electrostatic in nature. Moderate strength hydrogen bonds include O—H···O, N—H···O or N—H···N interactions. They are softer interactions able to exhibit a wider range of hydrogen bond angles, typically 130 to 180 °. [7] If the moderate strength hydrogen bond has an increasingly symmetric double well PES, split occupation of the two proton sites at either end of the hydrogen bond may be observed; this behaviour is proton disorder (§1.3.1). [24]

1.1.4 Weak hydrogen bonds

Weak hydrogen bonds are formed when the hydrogen atom is bonded to a slightly more electroneutral atom than itself or when the acceptor atom does not have lone pairs but π-electrons. The donor-acceptor distances in such cases are typically on the edge of the van der Waals limit (3.2 to 4.0 Å) and the hydrogen bond angles are highly non-directional (90 to 150 °). They are entirely electrostatic in nature and have strengths of less than 4 kcal mol^{-1}; the weakest of the weak

hydrogen bonds are barely distinguishable from van der Waals interactions. [7] Weak hydrogen bonds may be divided into subsets including those that are formed from a weak donor and strong acceptor, including C—H donors with oxygen and nitrogen acceptors, those that are formed from a strong donor and weak acceptor, including N—H and O—H donors with π and fluorine acceptors, and those that are formed from weak donor and weak acceptors, including alkyne and C—H donors and π and fluorine acceptors. C—H donor strength tends to depend on the carbon hybridisation C(sp)>C(sp^2)>C(sp^3) and whether the donor atom is bonded to electron withdrawing groups. [15]

Weak C—H···O hydrogen bonds

C—H···O hydrogen bonds are particularly important weak interactions in the solid state playing a role in crystal structure stabilisation and their existence has been confirmed by charge density studies. [25] They tend to form for C—H groups with oxygen acceptors in preference to interaction with other hydrogen bond acceptors. [26] Their formation usually occurs as a result of the hydrogen atom in the C—H bond pointing towards oxygen atom lone pairs, forming an electrostatic interaction. [27] They are suggested to have a significant role in crystal packing, stabilising structures due to this electrostatic nature, [28] particularly in a lateral manner such as those in quinoid compounds. [29] The geometrical parameters of these hydrogen bonds are of interest (Figure 1.6). Varied linearity of these interactions has been observed. For those formed between a C—H group with a carbonyl as the hydrogen bond acceptor, the C—H···O contacts tend to lie in the plane of the oxygen sp^2 lobes (the trigonal plane of R_1, R_2, C and O) and the hydrogen bond angle <CHO tends to be close to 120 °. Those formed between a C—H donor and oxygen atoms, in general, may vary significantly in their <CHO angle (Θ), with an average of 153 ° reported. [26]

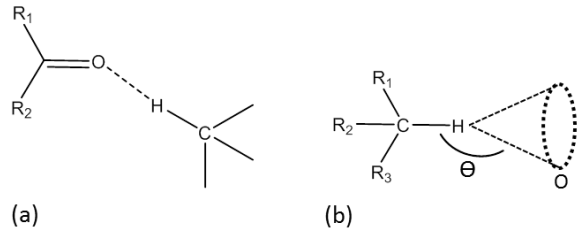

Figure 1.6 Types of C—H···O hydrogen bonding interactions: (a) formed between a C—H group and a carbonyl acceptor and (b) between a C—H group and an oxygen atom acceptor. Variation in the <CHO occurs.

A weak hydrogen bond is defined as having a donor-acceptor distance of 3.2 to 4.0 Å. However, for weak C—H···O hydrogen bonds the situation is more complicated as they may be distorted by other crystal forces or where the hydrogen atom is highly acidic; this leads to shorter C···O distances. In assessing a weak C—H···O hydrogen bond, both distance and angular characteristics should therefore be considered. [15]

1.1.5 Bifurcated hydrogen bonds

Hydrogen bonds are long range interactions and as such D—H may interact with more than one acceptor at once. The interaction of D—H with a second acceptor or the interaction of one acceptor with two donor D—H groups generates a bifurcated hydrogen bond (Figure 1.7). Hydrogen bonding interactions of the type D—H···A are two centre interactions whilst bifurcated hydrogen bonds are three centre interactions. The bifurcated hydrogen bonds are characterised by the distances *r*, d_1, d_2 and angles Θ_1, Θ_2 and Θ_3 with varying symmetries in *d* and Θ. [8, 15, 30] Related to the molecular geometry, certain components are prone to forming bifurcated hydrogen bonds. [31, 32]

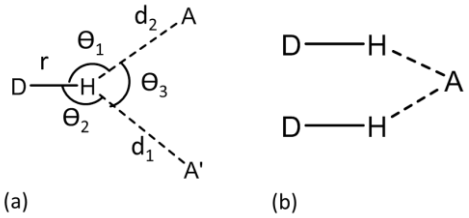

Figure 1.7 Three centre bifurcated hydrogen bonds (a) bifurcated donor DHAA and (b) bifurcated acceptor DHADH.

1.2 Crystal engineering

Hydrogen bonds are frequently exploited in the field of crystal engineering. Crystal engineering is defined as the controlled design of organic solids, employing a strategy which uses the understanding of intermolecular interactions in the context of crystal packing, with desired structure-related functions. [26] It is a bottom up construction approach starting from molecular building blocks, called molecular components, which assemble *via* a process of crystallisation to give a single or multi-component crystalline functional material (Figure 1.8). [33]

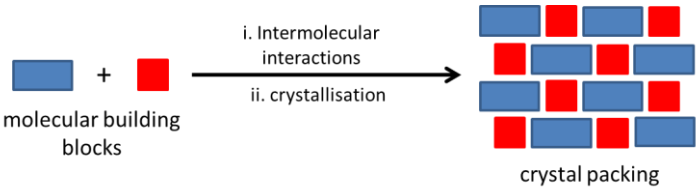

Figure 1.8 The assembly of molecular building blocks to form a multi-component material *via* crystallisation.

1.2.1 Crystal packing

The arrangement of the molecular building blocks in a crystalline material is called the crystal packing; the crystal packing is governed by intermolecular interactions between molecular building blocks. [26] The primary mode of assembly of the molecular building blocks is through hydrogen bonding interactions. Hydrogen bond donor and acceptor groups on different molecular

building blocks link to form primary hydrogen bonded structural motifs called 'synthons' (Figure 1.9). [34] The process of linking hydrogen bond donor and acceptor groups to form a hydrogen bond synthon is called molecular recognition [35] and occurs in a complementary or self-complementary fashion; the hydrogen donor and acceptors on each side of the synthon are from different functional groups for the former or are from the same functional group for the latter.

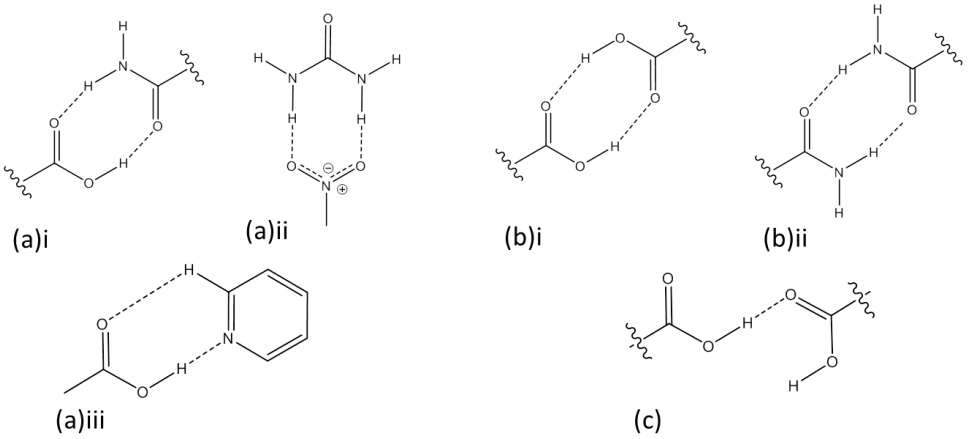

Figure 1.9 Common hydrogen bonded synthons: complementary (a)i carboxylic acid:amide $\boldsymbol{R_2^2(8)}$ synthon, (a)ii nitro:amide $\boldsymbol{R_2^2(8)}$ synthon, (a)iii carboxylic acid:pyridine $\boldsymbol{R_2^2(7)}$ and self-complementary (b)i carboxylic acid dimer $\boldsymbol{R_2^2(8)}$ synthon, (b)ii amide dimer $\boldsymbol{R_2^2(8)}$ synthon and (c) a single carboxylic acid link $\boldsymbol{D_1^1(3)}$.

Molecular building blocks may arrange themselves into extended networks including hydrogen bonded chains or rings by repetition or combination of different hydrogen bond synthons. Etter defined a set of rules for molecular arrangmemt *via* molecular recognition; all good proton donors and acceptors will be used in hydrogen bonding, six membered ring intramolecular hydrogen bonds form in preference to intermolecular hydrogen bonds and the best proton donors and acceptors that remain post intramolecular hydrogen bond formation then form intermolecular hydrogen bonds. [36] So-called graphset notation is used to describe the morphology of these networks; this notation includes the type of network, such as a ring (R), chain (C), finite (D) or intramolecular hydrogen bond (S), the number of hydrogen bond donors (subscript) and acceptors (superscript) and the size of the motif (in brackets), corresponding to the number of atoms in the repeat unit. [36, 37] As exemplars, the synthon in Figure 1.9(a)i is a ring network with graphset notation $R_2^2(8)$ whilst that in Figure 1.9(b)iii is a chain network with graphset notation $C_1^1(4)$.

Urea is a component commonly used in crystal engineering design strategies. The large number and arrangement of hydrogen bond donor and acceptor groups on the molecular building block offer the potential for a range of hydrogen bond synthons and networks to form; the nature of the network that is favoured is altered depending on the substitution of the urea. [38] These include head to tail one dimensional hydrogen bonded chains formed in urea, [39] *N,N'*-diphenylurea, [40] *N,N'*-

dimethylurea [41] and *N*-methylurea, [42] and isolated hydrogen bonded dimers formed in *N,N*-dimethyl urea [43] (Figure 1.10).

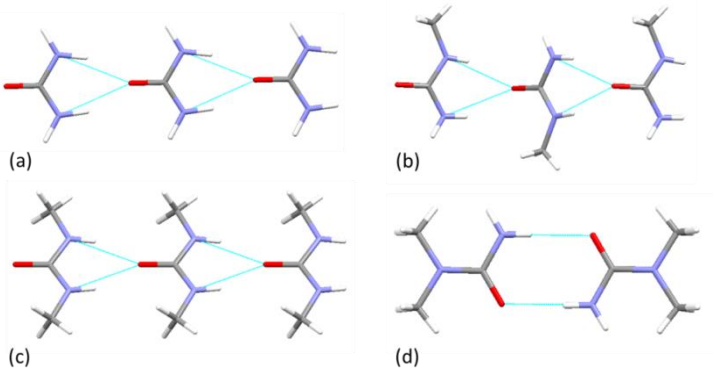

Figure 1.10 Hydrogen bonding networks in substituted ureas: head totail one-dimensional chains in (a) urea, (b) *N*-methylurea, (c) *N,N'*-dimethylurea and isolated dimers in (d) *N,N*-dimethylurea.

The combination of substituted ureas with molecular building blocks containing complementary but different hydrogen bond donor-acceptor groups to the ureas can either disrupt or work in combination with the head to tail one-dimensional hydrogen bonded urea chains and urea dimers to give further hydrogen bonded networks. Carboxylic acid molecular building blocks are commonly combined with urea and link *via* a carboxylic acid:amide $R_2^2(8)$ hydrogen bond synthon. For dicarboxylic acids, this synthon may form singly or on either side of the urea, depending on its substitution and crystallisation ratio of the molecular building blocks. Alhalaweh *et al* (2010) [44] defined the resulting hydrogen bonded motifs of urea (U) and carboxylic acid (Ac) as U:Ac, if crystallised in a 1:1 ratio, as U:Ac:U, if crystallised in a 2:1 ratio of U to Ac, or as Ac:U:Ac, if crystallised in a 1:2 ratio of U to Ac (Figure 1.11).

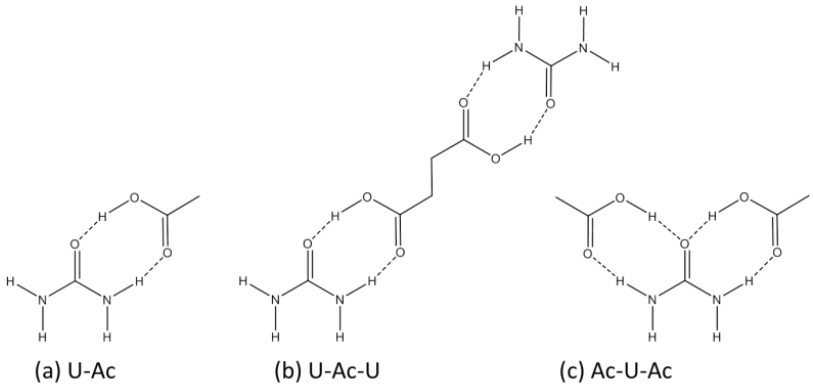

Figure 1.11 The resulting hydrogen bonding motifs in urea (U) carboxylic acid (Ac) molecular complexes when in ratios (a) 1:1, (b) 2:1 or (c) 1:2. **[44]**

The amine functionality on the urea, when substituted on one side only, has the potential to interact with nitro groups forming NH(O)O bifurcated $R_2^1(6)$ and $R_2^2(8)$ hydrogen bond

synthons such as in co-crystals of 3,5-dinitrobenzoic acid and 4-aminobenzoic acid where the nitro groups link to an amine group in the next molecule *via* these synthons. [36, 45]

Weaker interactions

Hydrogen bonding controls the primary linking of the molecular buildings blocks. However, weaker interactions in the crystal packing also exist which may dramatically alter the three-dimensional arrangement of the primary motifs as well as the nature of the hydrogen bonding within the motifs. [34]

Halogen bonding interactions have been shown to be comparable in strength to hydrogen bonding interactions in terms of their role in molecular assembly; [46] their location at the periphery of molecules means they are ideally positioned to be involved in intermolecular interactions. [47] A halogen atom (X) in an R—X bond has an electropositive area on its outer side, called a σ-hole, which can interact with a negative site (Y) such as a lone pair of a Lewis base or π-electron density. The result is a R—X···Y halogen bond formed along the extension of the R—X bond. [48-50] Halogen bond strength decreases in order of halogen Cl<Br<I and increases as the electronegativity of the R substituent increases. [47] Halogen···halogen contacts, characterised by an X···X' distance less than the sum of van der Waals radii, have also been recognised with a view to application in crystal engineering design strategies. [51] Two preferred geometries have been identified for the interaction of halogen atoms (Figure 1.12). [52]

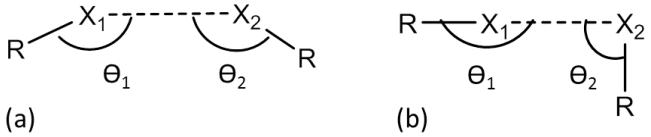

Figure 1.12 The two preferred geometries for halogen···halogen contacts: (a) $\Theta_1 = \Theta_2$ and (b) $\Theta_1 = 180^{\circ}$ and $\Theta_2 = 90^{\circ}$. R = organic group and X = Cl, Br and I.

Weak π···π interactions between aromatic moieties have been shown to exist [53] and have an influence on crystal packing and control of molecular orientation [54] in crystalline materials. Weak electrostatic interactions between aromatic rings mean that these moieties tend to organise themselves in two ways (Figure 1.13). Aromatic rings may be packed in a face-to-face manner, stacked parallel or offset or in a herringbone arrangement, or packed in an edge to face arrangement; these are more akin to weak hydrogen bonds, of the type C—H···π. [55] These arrangements occur as a result of the quadrupole moment created by the π-electron density which results in a negative charge in the centre of the ring and positive charges at the edges of the ring; [56] the parallel eclipsed packing (Figure 1.13(a)i) is therefore less favourable due to repulsive forces

occurring. The attractive interactions in a face-to-face stack may be enhanced by adding substituents to the aromatic rings, regardless of electron withdrawing or donating nature. [57]

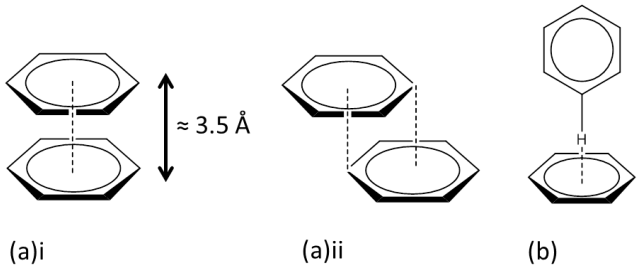

Figure 1.13 Types of π···π interactions: (a) face to face (i) eclipsed and (ii) offset and (b) edge-to-face.

Carbonyl-carbonyl pseudo π-stacking interactions have also been identified in the three-dimensional packing of crystalline materials including anti-parallel stacked carbonyl-carbonyl, parallel offset carbonyl-carbonyl and a 90 ° approach between carbonyl groups (Figure 1.14). [58]

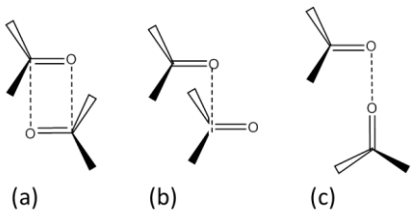

Figure 1.14 Weak carbonyl-carbonyl interactions: (a) anti-parallel, (b) offset parallel and (c) a 90 ° approach. **[58]**

Weaker hydrogen bonds such as C—H···X, C—X···π and C—H···π have also been suggested to play a significant role in the stabilisation of molecular assemblies. [59, 60]

1.2.2 Crystal forms

A crystalline material can exhibit a number of different crystal forms. Polymorphs are those that vary in the crystal packing of the molecular components; if multi-component, the stoichiometric ratio of components will be unchanged. Solvates contain solvent molecules in addition to the main components. Components within a crystal may be neutral, termed a co-crystal if multi-component, or charged, if proton transfer has occurred between components; this is a salt (Figure 1.15). [61-63] In some cases, neutral and charged components may be present in the same crystalline material.

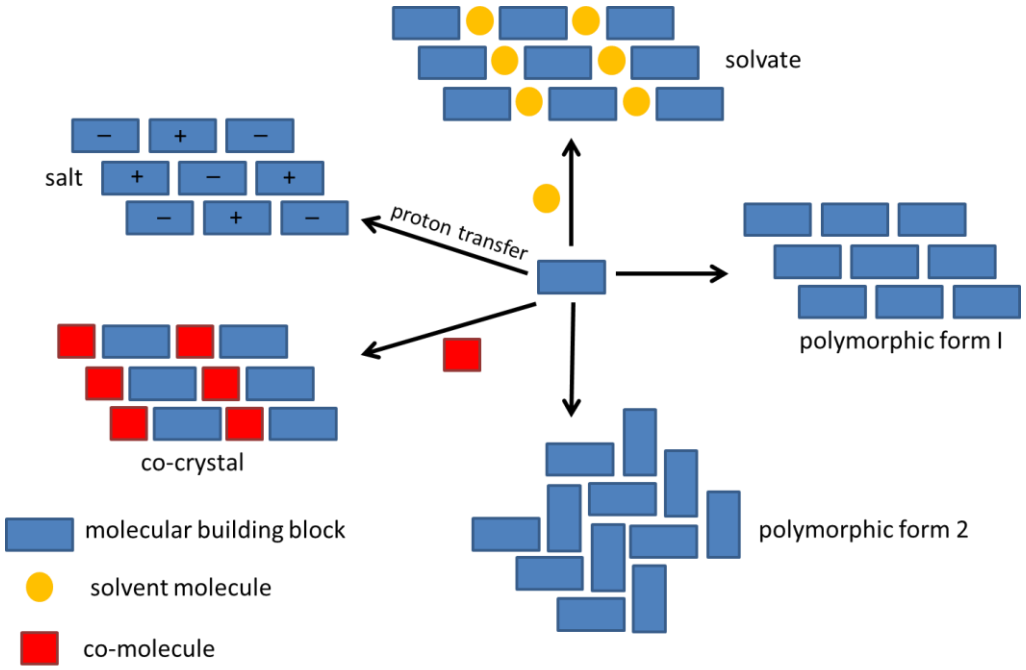

Figure 1.15 Differing crystal forms for a molecular building block including polymorphs, a salt, a solvate and a co-crystal.

The changes to the crystal packing in different crystal forms of a material may lead to different properties. These include differing physical properties such as colour, where changes in molecular packing can lead to changes in colour as observed in 5-methyl-2-[(2-nitrophenyl)amino]-3-thiophenecarbonitrile (ROY) as a result of the change in the angle rotation between two parts of the structure; [64] mechanical properties such as hardness, for example diamond and graphite are made from the same carbon building block however the tetrahedral arrangement of carbon atoms in diamond give it a hard, rigid structure whilst the layered arrangement of carbon atoms in graphite result in a softer material with sliding layers; [14] surface properties such as habit, for example the anti-malarial drug arteether exhibits a number of crystal morphologies as a result of changes in crystal packing [65] and different thermodynamic and physical properties such as solubility, an example of which is the introduction of isonicatinamide into the crystal structure of the active pharmaceutical ingredient (API) dexlansoprazole, which improved its solubility relative to the API alone. [66] Changes to the properties of a material on obtaining a different form are therefore of particular importance in the pharmaceutical industry.

Different crystal forms also have differing stabilities and may convert with time or be induced by temperature to the most thermodynamically stable form; this less stable form is termed metastable. [67] Crystal forms may also interconvert between anhydrous and solvated materials under atmospheric conditions or from exposure to solvent vapours (Figure 1.16). The addition of solvent to a material has been reported to improving tableting properties of an API. [68]

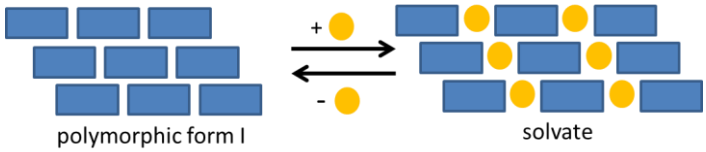

Figure 1.16 The interconversion between an anhydrous crystal form and a solvate.

1.2.3 Inclusion materials

Inclusion materials are chemical crystalline compounds in which a 'host' framework is formed around a 'guest' species. The host components are typically linked by hydrogen bonding or weak intermolecular interactions into an extended network which contains cavities of molecular size. [37] The guests can satisfy both inefficiencies in the crystal packing of the host, filling open framework spaces, and the hydrogen bond donor or acceptor abilities of the host. [69, 70] Guests may be included in the host lattice in channels, forming inclusion compounds, or in enclosed molecular pockets, termed inclusion clathrates. [71]

The formation of inclusion complexes may be targeted in crystal engineering design strategies by careful selection of host components and guest species. The large number of hydrogen bond donor and acceptor groups aid assembly into the hexagonal channel host structure in urea inclusion compounds [72] whilst their arrangement favours a honeycomb structure for the inclusion clathrate of trimesic acid. [73] Some host networks have been formed as a result of host component molecular symmetry, such as for the tris(*o*-phenylenedioxy)cyclophosphazene which packs into open hexagonal channels, [74] and host component molecular size, including xanthenol which is bulky and rigid and leads to packing inefficiencies in the structure. [75] Guests may also induce inclusion behaviour often controlled by guest size, solvents are frequently included into host networks due to their ability to fill empty space, or controlled by guest ability to accept or donate electron density for hydrogen bond formation to the host network or to bridge polar regions of the crystal. [69] Guest shape may also induce inclusion behaviour, for example the hexagonal host network in urea inclusion compounds only forms in the presence of linear guests. [76]

Inclusion complexes exhibit a range of interesting properties including guest release and uptake; [77] if guest release leads to structural collapse then the material has virtual porosity only. [78, 79] Some host networks may also exhibit selectivity for certain guests [80] and it may be possible to exchange one guest for another whilst the host framework remains intact. [81] Related to their properties, inclusion complexes are targeted in crystal engineering due to their potential applications in pharmaceutics, [82] chemical sensing, [83] in the separation of alkanes [84] and in the capture of volatile organic compound (VOCs). [85] In Chapter 9, hydrogen bonded inclusion networks are targeted using crystal engineering strategies.

1.3 Proton transfer

Within a hydrogen bonded synthon, various proton transfer processes are possible. Proton transfer is facilitated or limited by the hydrogen bond; in many situations this is considered as the most important property of the hydrogen bond, with proton transfer processes constituting a significant component of important areas such as enzyme catalysis and acid-base chemistry. [7] Proton transfer involves the transfer of charge, in the form of a proton, from one molecular component to another, usually between an acidic and basic species. Where proton transfer occurs across a hydrogen bonded synthon in a crystalline material, a salt is formed. If proton transfer occurs such that the proton occupies a mid-point between the acid and the base, this species is termed an 'intermediate'. [86]

The occurrence of salt formation *via* proton transfer between molecular components has been suggested to be related to the pK_a values of the interacting components. The pK_a is the acid dissociation constant, linked to the pH and concentrations of the dissociated [Ac^-] and non-dissociated acid [HAc] (Equation 1.1) in a particular solution. [87]

Equation 1.1 $$pH = pK_a + log\frac{[Ac^-]}{[HAc]}$$

A general rule frequently followed in crystal engineering is that if the value of ΔpK_a between two components (pK_a(base) – pK_a(acid)) is greater than 2 or 3, a salt will be formed and if it is less than 0, a neutral complex is observed. Between ΔpK_a values of 0 to 3, however, the ΔpK_a parameter is unable to reliably predict salt formation. One consideration for using ΔpK_a values is that they are only valid under the solution equilibrium conditions at which they were determined and are temperature dependent; [88] however, in crystal engineering, once a material has formed, it is in the solid state. Crystal engineering design strategies therefore often use values of ΔpK_a only as a guide.

Proton transfer, once it has occurred between molecular components may either be dynamic, where the proton position can be tuned upon varying the external environment such as by changes in temperature or static, where no further change in proton position is observed post transfer. Interesting dynamic proton transfer behaviour has been observed across hydrogen bonds in the form of proton disorder (§1.3.1) and proton migration (§1.3.2) whilst interesting static proton transfer behaviour has been observed in molecular complexes of proton sponges (§1.3.3). Materials exhibiting these proton transfer properties have been targeted by crystal engineering design strategies.

1.3.1 Proton disorder

The proton transfer process of proton disorder may occur across hydrogen bonds in the solid state. It involves the partial switch in function of the hydrogen bond donor and acceptor groups such that the hydrogen atom occupies two sites simultaneously (in different unit cells within the crystal packing). Two proton disorder mechanisms exist including conformational disorder, involving bond reorientation, and configurational disorder, involving bond making and breaking due to reorganisation of adjacent single and double covalent bonds; [7] configurational disorder is of interest in this thesis (Chapter 5). Proton disorder commonly occurs across moderate strength hydrogen bonds where the shape of the PES approaches that of a symmetric double well such that the energy difference between the two proton sites in the hydrogen bond is small. [16] Typically, the proton disorder may be temperature dependent, where a single proton site in the hydrogen bond is occupied at low temperature whilst a second proton site becomes increasingly occupied as the temperature of the system increases. [89]

Proton disorder is often present in systems containing cyclic hydrogen bonded $R_2^2(8)$ carboxylic acid dimers (Figure 1.17). [90, 91] These dimers commonly form between carboxylic acid groups, the $R_2^2(8)$ carboxylic acid hydrogen bonding synthon is insensitive to carboxylic acid group substituents, and, if formed between the same molecular species (homo dimer), permits the adoption of a centre of symmetry in the dimer; the symmetry of the dimer may lead to symmetry in the shape of the PES double wells and proton disorder. [26] The presence of proton disorder in these systems is suggested by shortened C—O and lengthened C=O carboxylic acid bond lengths [26] [92] from the average C—O (1.305 Å) and C=O (1.226 Å) lengths for an aromatic carboxylic acid group [93] and by elongated O—H distances. If the proton is modelled initially as a single site, proton disorder may be indicated by a substantially elongated anisotropic thermal ellipsoid for the proton along the hydrogen bond, as the proton seems to spread over the two simultaneously occupied sites. [94] In this case, the proton should be modelled as having two partly occupied sites. The presence of split hydrogen atom density along the hydrogen bond donor-acceptor line when imaged directly in Fourier difference maps (§2.4.1) also indicates the presence of proton disorder. [90]

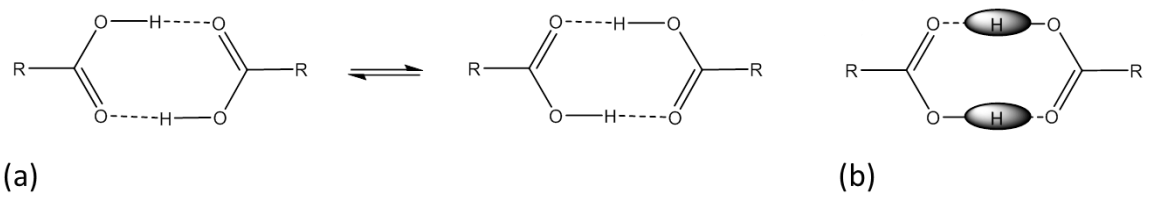

Figure 1.17 (a) The configuration disorder of carbonyl-hydroxyl groups in a carboxylic acid $\boldsymbol{R_2^2(8)}$ hydrogen bonded dimer and (b) the shape of the anisotropic hydrogen atom thermal ellipsoid when disorder is present.

Proton disorder has been observed in a number of substituted benzoic acids containing centrosymmetric homo hydrogen bonded $R_2^2(8)$ carboxylic acid dimers including benzoic acid, identified in the solid [95] and liquid phases, [96] 4-dimethylamino benzoic acid (4-DABA) in its native crystal structure, in a binary complex with 3,5-dinitrobenzoic acid (3,5-DNBA) [89, 97] and in a ternary complex with 3,5-dinitrobenzoic acid and 4,4-bipyridine [98] and in crystal polymorphs of 3,5-dinitrobenzoic acid. [97] The proton disorder in these systems was found to be temperature dependent from diffraction studies including split occupancies of the dimer proton of 86:13 at 20 K compared to 62:37 at 175 K in benzoic acid dimers, [92] 90:10 at 100 K compared to 62:38 at 300 K in 4-DABA hydrogen bonded homo dimers in the native crystal structure of 4-DABA, 66:34 at 100 K compared to 46:53 at 300 K in 3,5-DNBA hydrogen bonded homo dimers in the 4-DABA 3,5-DNBA binary complex, [89] 75:25 at 100 K compared to an approximate 50:50 disorder in 4-DABA hydrogen bonded homo dimers in the ternary complex with 3,5-dinitrobenzoic acid and 4,4-bipyridine. [98] The dynamics of temperature dependent proton disorder in benzoic acid have been followed by NMR [24, 99] and neutron diffraction methods [92] and were found to occur by the classical Arrhenius jump model at high temperatures; this model is based on the simplest assumptions of the collision and transition-state theories for reactions which must surmount an energy barrier and where the reaction probability jumps from 0 to 1 at a particular energy. [100] However, at low temperature below 50 K, the proton dynamics switch to phonon-assisted quantum tunnelling; where a particle may appear on the other side of a barrier it does not have the energy to classically overcome. [101] An energy difference between the two proton sites has been calculated, in terms of $\Delta H°$, at 0.12 kcal mol^{-1} for the 50 to 175 K temperature range. [102]

The proton disorder in these substituted benzoic acid systems is suggested to be tuneable by crystal packing. For example, in an isolated benzoic acid hydrogen bonded $R_2^2(8)$ homo dimer, the simultaneous transfer of the dimer proton results in a configuration equivalent in energy to the original [103] and 50:50 occupancy of each proton site is expected. However, on placing the hydrogen bonded dimer in a crystallographic lattice environment in the solid phase of benzoic acid, the geometry and energy of the two proton configurations differs from the situation in isolated dimers. This is related to the change in shape of the potential energy surface of hydrogen bonds forming the $R_2^2(8)$ homo dimer when in a crystal. An isolated dimer has a "symmetric double well potential"; the two wells are equivalent in energy and the barrier between them is small. However, in a dimer in a crystal, anisotropic crystal field effects in the local environment lead to an "asymmetric double well potential" where there is a significant difference in energy between the two wells and thermal activation is required to switch between the two proton configurations.

Crystal packing effects on proton disorder are observed in the binary complex of 4-DABA 3,5-DNBA; a carboxylic acid hydrogen bonded $R_2^2(8)$ homo dimer of 3,5-DNBA exhibits proton disorder with temperature, in one packing environment, whilst a carboxylic acid hydrogen bonded $R_2^2(8)$ homo dimer of 4-DABA, in another crystal packing environment, does not. [89] Jones *et al.* (2013) [97] suggested the lack of proton disorder in the 4-DABA homo $R_2^2(8)$ hydrogen bonded dimer could be attributed to the asymmetric arrangement of weak interactions to the 4-DABA acid groups; one acid oxygen interacts with a nitro group ($d_{O\cdots O}$ 2.988(2) Å) and the other with a methyl group forming a weak C—H···O hydrogen bond ($d_{C\cdots O}$ 3.214(3) Å). These interactions create an asymmetry in the dimer hydrogen bond such that one proton site is favoured over the other. In contrast, only very weak π-interactions, not strong enough to perturb the symmetry of the dimer hydrogen bond, formed to the acid groups in the 3,5-DNBA dimer ($d_{\pi\cdots\pi}$ 3.088(3) to 3.313(3) Å). [97] A similar effect is observed between polymorphs of 3,5-DNBA. [97] Both polymorphs contain carboxylic acid hydrogen bonded $R_2^2(8)$ homo dimers however, on changing the crystal packing environment of the dimer between the polymorphs, the proton disorder differs at 300 K; in polymorph I ($P2_1/c$) it is 64:36 whilst in polymorph II it is 72:28. The crystal packing environment of the dimer in polymorph I includes interactions between one of the dimer acid oxygen atoms with a nitro group ($d_{N\cdots O}$ 3.021(3) Å) and with an aromatic C—H group ($d_{C\cdots O}$ 3.407(3) Å) whilst the crystal packing environment of the dimer in polymorph II includes the dimer acid oxygen and a neighbouring ring C—H ($d_{C\cdots O}$ 3.508(1) Å) and an anti-parallel π-contact between the acid carbonyl and a nitro group ($d_{\pi\cdots\pi}$ 2.927(1) and 3.026(1) Å). [97]

Pressure may also have effect on the ordering/disorder of protons in carboxylic acid hydrogen bonded $R_2^2(8)$ homo dimers. When pressure up to 2.21 GPa was applied to benzoic acid at room temperature; the proton ordering was observed to change from 50:50 at 0 GPa to 90:10 at 0.2 GPa; the increase in pressure resulted in closer contacts to the local environment and hence enhanced asymmetry in the potential. Further increases in pressure led to an increase in proton disorder attributed to a compressed dimer hydrogen bond distance lowering the potential barrier for hydrogen transfer between sites. [104]

Studies into solid state proton disorder may provide insight into the role of weak interactions on molecular conformation and hydrogen bond PES behaviour. Chapter 5 examines in detail the effect of changes to the local packing environment on temperature dependent proton disorder in additional molecular complexes containing 3,5-DNBA carboxylic acid hydrogen bonded $R_2^2(8)$ homo dimers, applying the technique of synchrotron X-ray diffraction.

1.3.2 Proton migration

Proton migration is a proton transfer process which involves the gradual shift in position of a hydrogen atom across a hydrogen bond. It is observed in very short hydrogen bonds, called short strong hydrogen bonds (SSHBs) with donor-acceptor distances of 2.4 to 2.55 Å, depending on the identity of D and A. The shape of the PES for these hydrogen bonds approaches that of a symmetric single well potential where the barrier to proton transfer is low such that proton migration may occur. [16, 105] The proton transfer pathways of migration across hydrogen bonds include from an off-centred position to a symmetrically located position, or *vice versa*, or by a switch from one side of the hydrogen bond to the other. As such, proton migration across a hydrogen bond is characterised by changes in the D—H and H···A distances. Proton migration may also be followed in Fourier difference maps (§2.4.1) suggested by either a shift in the position or by elongation of the hydrogen atom density along the hydrogen bond that often accompanies the migration process; a switch in the direction of the elongation along the hydrogen bond may also indicate migration. The shift in proton location within such migration processes in SSHBs tends to have a maximum value of around 0.1 Å.

Proton migration across SSHBs is a tuneable effect occurring as a result of the application of external variables including pressure, [106] electric fields [107] or temperature. The temperature dependence of proton migration, in particular, is of interest in this research project. Temperature dependent proton migration has been observed in a number of O—H···O and O^+—H···O^- SSHBs formed in urea organic acid molecular complexes including the 1:1 adduct of urea phosphoric acid (migration of 0.04 Å where $d_{O\cdots O}$ is approximately 2.4 Å), [108] the 2:1 complex of *N*,*N*-dimethylurea oxalic acid (migration of 0.045(9) Å where $d_{O\cdots O}$ is approximately 2.43 Å), and the 2:1 complex of *N*,*N*'-dimethylurea oxalic acid (migration of 0.031(9) Å where $d_{O\cdots O}$ is approximately 2.44 Å). [109] Temperature dependent proton migration has also been observed in a number of N^+—H···O^- SSHBs including in N-heterocycle organic acid molecular complexes in pyridine-3,5-dicarboxylic acid (migration of 0.09 Å where $d_{N\cdots O}$ is approximately 2.52 Å), [110] in 4,4'-bipyridine benzene-1,2,4,5-tetracarboxylic acid (migration of 0.1 Å where $d_{N\cdots O}$ is approximately 2.52 Å) [111] and in 4-methylpyridine pentachlorophenol (migration of 0.08 Å where $d_{N\cdots O}$ is approximately 2.50 Å). [112]

Other variables may lead to the tuning of proton migration behaviour. These include SSHB donor-acceptor distances; temperature dependent proton migration has not been observed for SSHBs with distances above 2.45 Å, for O—H···O or O^+—H···O^- SSHBs, or above 2.55 Å, for N^+—H···O^- SSHBs. The proton migration occurs in these molecular complexes where the SSHB donor-acceptor distance remains invariant as a function of temperature. In terms of designing potential proton migration systems, some previous efforts have gone into targeting the design of SSHBs

using ΔpK_a values of components; this is based on the premise that it may be possible to relate hydrogen bond strength and ΔpK_a values, [113] thus the latter may also be applicable in tuning proton migration behaviour; stronger hydrogen bonds may be expected to form between two components where their difference in pK_a approaches zero. [114] An increase in basicity of the hydrogen bond acceptor may lead to shorter SSHB donor-acceptor distances such as in molecular complexes of oxalic acids with substituted ureas; oxalic acid forms shorter O—H···O hydrogen bonds in this synthon with more basic *N*-methylurea ($d_{O\cdots O}$ 2.449(2) and 2.419(2) Å) [115] and *N,N*-dimethylurea ($d_{O\cdots O}$ 2.4398(15) and 2.4423(15) Å) [109] than with less basic urea ($d_{O\cdots O}$ 2.472(5) Å). [116]

The consideration of ΔpK_a values may also allow extent of proton migration to be tuned. Jones *et al.* (2012) [109] compared the extents of migration of a proton across O—H···O SSHBs in urea phosphoric acid (1:1), [108] *N,N*-dimethylurea oxalic acid (2:1) and *N,N*'-dimethylurea oxalic acid (2:1) [109] to values of ΔpK_a and observed a trend of increasing degree of migration as ΔpK_a became less negative. A similar effect was observed by Schmidtmann and Wilson (2008) [117] in molecular complexes of pentachlorophenol-lutidine; the value of ΔpK_a between components correlated with the extent of hydrogen transfer across an O···H···N hydrogen bond in the dimeric pentachlorophenol-lutidine complexes. No correlation was, however, observed in the equivalent trimeric complexes. As in the systems exhibiting proton disorder (§1.3.1), the nature of the local environment surrounding the O···H···N hydrogen bond in the pentachlorophenol-lutidine systems may be affecting its proton transfer behaviour; in the dimeric complexes the O···H···N hydrogen bond is isolated from a polar environment and follows a trend of ΔpK_a whilst strong polar interactions are present in the trimeric complexes and no such trend is observed. [117] The nature of the local environment is affected by molecular stoichiometry in these cases; changing where stoichiometry of components changes. Correlations between the extent of proton transfer and ΔpK_a values for related systems may therefore be affected by stoichiometry of components; a trend may only be applicable where the stoichiometry of acidic and basic components is the same across the related systems however, this does not appear to be the case of the substituted urea organic acid systems.

Proton migration may be favoured across SSHBs in certain hydrogen bond synthons. Proton migration occurs across O—H···O and N^+—H···O^- SSHBs which are frequently involved in the same type of hydrogen bonded synthon between the same molecular building blocks; O—H···O SSHBs form as part of a carboxylic acid:amide $R_2^2(8)$ hydrogen bond synthon between substituted ureas and organic acids whilst N^+—H···O^- SSHBs occur between organic acids and N-heterocycles, usually involving proton transfer, and either in a planar acid:pyridine $R_2^2(7)$ synthon

or a single N^+—H···O^- hydrogen bond between non co-planar pyridine and carboxylic acid groups (Figure 1.18).

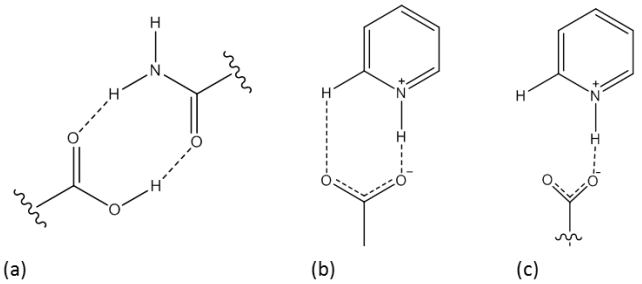

Figure 1.18 Synthons favouring SSHB formation: (a) carboxylic acid:amide $\boldsymbol{R_2^2(8)}$ hydrogen bond synthon, (b) planar acid:pyridine $\boldsymbol{R_2^2(7)}$ synthon and (c) a single N^+—H···O^- hydrogen bond between non-planar pyridine and carboxylic acid groups.

Migration of a proton across SSHBs may lead to certain physical properties including colour, such as in the 1:1 adduct between squaric acid and 4,4-bipyridine,[106] and ferroelectricity, such as in the molecular complex of phenazine chloranilic acid. [118] The low barrier to hydrogen transfer in SSHBs is thought to play an important role in enzyme catalysis, in transition state stabilisation [119] [120] and to be responsible for proton conduction in water. [10] The study of proton migration across SSHBs may therefore reveal details about the hydrogen bonding behaviour relevant to these properties; single crystal X-ray and neutron diffraction methods are commonly employed in its study. [121, 122] Chapter 6 applies crystal engineering strategies in the design of SSHBs with potential proton migration properties whilst Chapter 7 investigates temperature dependent proton migration using a combination of synchrotron and X-ray diffraction.

1.3.3 Static proton transfer

Subtle effects about proton transfer behaviour can be revealed when observing static proton transfer across a group of related molecular complexes. Static proton transfer is defined here as the situation where a proton is transferred from one molecular component to the other in the formation of a molecular ionic salt; this transfer state remains unchanged across a range of external variables over which the structure is studied.

The molecular complexes of DMAN (1,8-bis(dimethylamino)naphthalene) with organic acids are a good target for studying subtle "static" proton transfer effects. DMAN is a strongly basic derivative of naphthalene (pK_a 12, H_2O) [123] with a high proton affinity caused by the *syn peri*-planar arrangement of the amine substituents; protonation relieves the steric strain induced by the position of the nitrogen lone pairs close to each other in the *peri*-planar arrangement. [124] On protonation, a very stable intramolecular $[N—H···N]^+$ hydrogen bond (IHB) forms in DMAN [125]

between the amine substituents (the average protonated $d_{N\cdots N}$ is 2.59 Å) and the arrangement of the DMAN methyl groups changes from a staggered to an eclipsed arrangement (Figure 1.19).

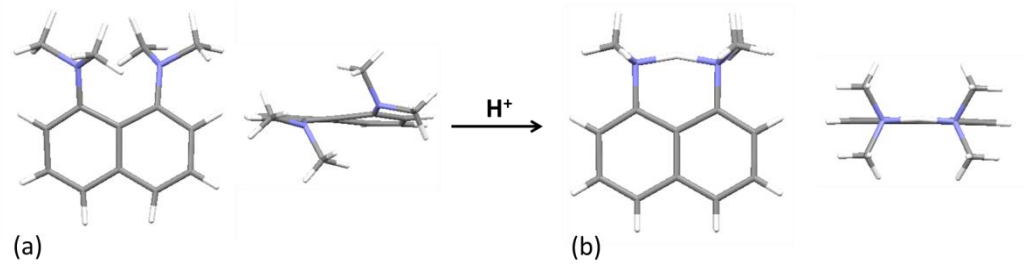

Figure 1.19 The change in arrangement of the DMAN methyl groups from (a) a staggered arrangement in the neutral state [126] to (b) an eclipsed arrangement in the protonated state. [127, 128]

The proton is shielded in its inter-nitrogen position within the IHB by the amine methyl groups, leading to a very slow rate of deprotonation, slower than the rate of diffusion ($\sim 10^{10}$ dm^3 mol^{-1} s^{-1}). [129] The high thermodynamic basicity coupled with the low kinetic basicity leads to the term 'proton sponge' for DMAN and other *peri* amino naphthalenes.

DMAN forms very stable ionic complexes with organic acids [124] including with 1,2,4,5-benzene-tetracarboxylic acid (pyromellitic acid), 4,5-dichlorophthalicacid, dicyanoimidazole, and *o*-benzoic sulfimide dehydrate (saccharin). [130] In the crystal structures of these complexes, packing occurs that is reminiscent of the close packing observed in inorganic compounds; either in pairs of stacked cations or anions, in an anti-parallel manner forming molecular planes, or by one single $DMANH^+$ interacting with six anions, or *vice versa*, in the local environment. [130] Within the crystal packing of $DMANH^+$ cations and deprotonated acid anions, a robust fragment $[Me_2N—H\cdots NMe_2]^+\cdots X^-$, where X^- is the nearest electronegative atom, is formed (Figure 1.20).

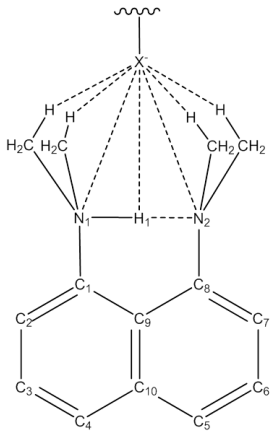

Figure 1.20 The $[Me_2N—H\cdots NMe_2]^+\cdots X^-$ fragment formed between the protonated DMAN and the nearest electronegative atom, X^-.

The $[Me_2N—H\cdots NMe_2]^+\cdots X^-$ fragment has multi-centre intermolecular bonding character containing the strong $[N—H\cdots N]^+$ intermolecular hydrogen bond (IHB) (major component), and weak hydrogen bonds between the methyl groups and X^- (the minor component); protonation of DMAN results in a +1 charge which is delocalised over the whole cation, increasing the charges at the methyl groups and hence their susceptibility to forming intermolecular interactions. [131] Variations in the anion may generate variation in the minor component of the fragment and also lead to structural changes in both the cation and anion; [131] protonation of DMAN leads to structural changes from the neutral base including the shortening of the C1—C2, C3—C4, C5—C6 and C7—C8 bond lengths, lengthening of the C—N distances, an increase in the *ipso* angles, $C_2C_1C_9$ and $C_9C_8C_7$, and NCC. [130]

In the $[Me_2N—H\cdots NMe_2]^+\cdots X^-$ fragment, the PES of the major component $[N—H\cdots N]^+$ IHB has the shape of an asymmetric double well [124] with a low barrier potential (typically 4.5 kcal mol^{-1}) for proton motion. [129] The motion of the proton in the low barrier potential appears to differ depending on the nature of the counter ion and aggregate state of the sample. [132] In an isolated $DMANH^+$ cation, the IHB proton would be centrally located, equally shared between the two nitrogen atoms, or disordered over two positions. [128] Any asymmetry in the proton position can therefore be attributed to weak intermolecular interactions in the crystal packing. [133, 134] The weak interactions of the minor component are thought to influence the position of the proton in the IHB; the proton is increasingly asymmetrically located where the arrangement of the weak interactions is increasingly asymmetric. [131] The behaviour of the proton in the IHB may also be related to the proximity of X^- in the minor component. X^- may act as a second acceptor to the IHB proton generating a bifurcated hydrogen bond. In this bifurcated hydrogen bond, X^- is almost always located slightly closer to the protonated nitrogen (N1) of the IHB; the $N_1H\ X^-$ hydrogen bond angle is also usually largest. [131] The range in which X^- may be having an effect on the IHB proton has been investigated in neutron diffraction studies on a number of molecular complexes of DMAN with halo-benzoic acids. X^- appeared to have an effect on the IHB proton behaviour when $H\cdots X^-$ distances were in the range of 2.61 to 2.81 Å; indicated by an equivalent movement of the thermal ellipsoids of the two atoms along the IHB. [135]

Where the $[Me_2N—H\cdots NMe_2]^+\cdots X^-$ fragment is formed in DMAN organic acid molecular complexes, the crystal packing and proton transfer behaviour across the $[N—H\cdots N]^+$ hydrogen bond appear related, and to be tuneable, by switching the anion, X^-. As discussed in §1.3.1 and §1.3.2, this is a further example of weak interactions in the crystal packing, secondary to the strong and moderate hydrogen bonds, 'tuning' proton transfer characteristics of hydrogen bonds. Chapter 8 investigates proton transfer effects in a number of molecular complexes of DMAN with halo and hydroxy benzoic acids, previously identified as containing the $[Me_2N—H\cdots NMe_2]^+\cdots X^-$

fragment. [136] This is carried out using synchrotron X-ray diffraction with an emphasis on the effect of the minor interactions on proton transfer behaviour and of changing the anion on elements of the crystal structure and packing.

The haloanilic acids are molecular building blocks that have also been reported to have interesting static proton transfer behaviour. [118] This behaviour is related to their ability to couple hydrogen bond formation with electron transfer and their being susceptible to different degrees of deprotonation (Figure 1.21). [137]

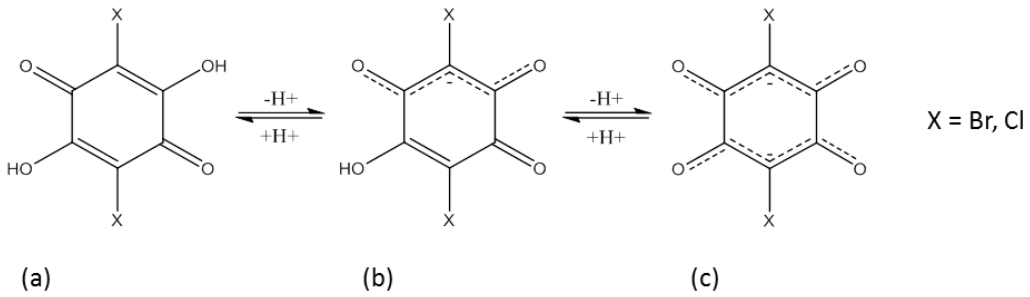

Figure 1.21 The differing degree of deprotonation of chloranilic acid (CAc): (a) doubly protonated (H_2CAc), (b) singly deprotonated (monoanion $HCAc^-$) and (c) doubly deprotonated (dianion CAc^{2-}). [137]

The haloanilic acids bromanilic and chloranilic acid are strongly acidic favouring SSHB formation through CAHBs. With *N*-heterocycles (N), the anilic acids (Ac) commonly form CAHBs, comprising a number of hydrogen bonding motifs related to its protonated state including an N:Ac:N hydrogen bonded motif, where a doubly deprotonated anilic acid forms bifurcated hydrogen bonds to *N*-heterocycle molecules on either side of the acid and an N:Ac:Ac:N motif for a singly deprotonated anilic acid comprised of an anilic acid hydrogen bonded dimer bifurcated on the deprotonated side by *N*-heterocycles (Figure 1.22).

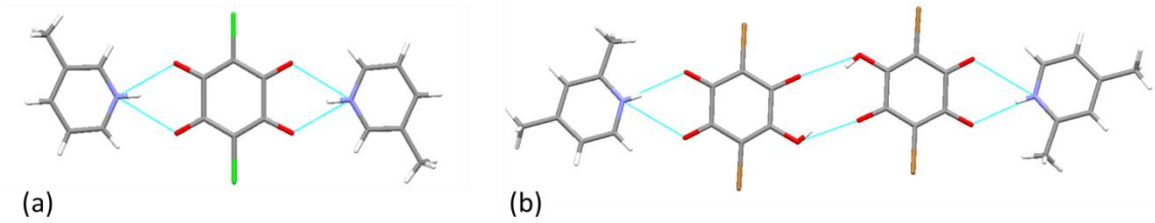

Figure 1.22 Anilic acid hydrogen bonding motifs for (a) a doubly deprotonated acid in an N:Ac:N motif and (b) a singly deprotonated acid in a N:Ac:Ac:N motif. [138, 139]

Chapter 2.

Theory

X-ray crystallography is an important tool in confirming the results of a crystal engineering design strategy or in the examination of hydrogen bonds, enabling the determination of the crystal structure of a prepared material. The theory behind this method is presented here.

2.1 The crystal

The crystal is a solid phase built up of a regular arrangement of atoms in three-dimensions. [140] Within this arrangement equivalent environments exist, related by translation and equally spaced, called lattice points; the regular array of equivalent points forms the crystal lattice.

2.1.1 The unit cell

Lattice points are joined in three dimensions forming a parallelopiped to define the smallest repeating three-dimensional unit of the crystal, called the unit cell. [141] The unit cell has three lengths defined by *a*, *b* and *c* and angles between these lengths defined by α, β and γ (Figure 2.1).

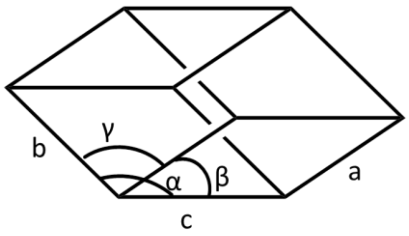

Figure 2.1 The crystal unit cell formed from four lattice points in the crystal with unit cell lengths *a*, *b*, *c* and angles α, β and γ.

The linking of lattice points to construct the unit cell may occur in four different ways (Figure 2.2) including linking at the four corners only (primitive), at the four corners with a lattice point at the centre of each face (face-centred), at the four corners with two extra lattice points positioned on opposite faces which intersect the C-axis (C-centred) and at the four corners with an extra lattice point at the body centre (body-centred). These are the four possible lattice types.

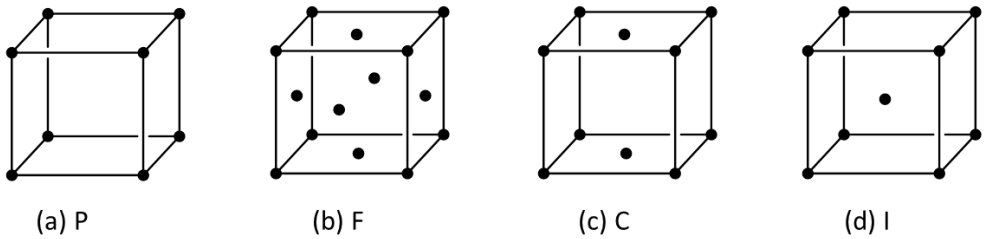

Figure 2.2 Four lattice types (a) primitive P, (b) face-centred F, (c) C-centred and (d) body centred I.

2.1.2 The seven crystal systems

In addition to the three-dimensional translational component, the crystal lattice is affected by symmetry, including by rotation or reflection symmetry. The presence of these symmetries imposes restrictions on the unit cell lengths and angles such that only seven crystal systems, distinguished from one another by shape, are possible (Table 2.1). [142] For each crystal system, only certain lattice types (PCIF) are allowed; in total this generates 14 so-called Bravais lattices.

Table 2.1 The seven crystal systems. [143]

Crystal System	Number of independent parameters	Axial Lengths (Å) & Angles (°)	Lattice types
triclinic	6	$a\neq b\neq c$, $\alpha\neq\beta\neq\gamma\neq 90$	P
monoclinic	4	$a\neq b\neq c$, $\alpha=\gamma\neq 90$, $\beta=90$	P, C
orthorhombic	3	$a\neq b\neq c$, $\alpha=\beta=\gamma=90$	P, I, C, F
Tetragonal	2	$a=b\neq c$, $\alpha=\beta=\gamma=90$	P, I
trigonal	2	$a= b\neq c$, $\alpha=\beta=90$, $\gamma=120$	P
hexagonal	2	$a=b\neq c$, $\alpha=\beta=90$, $\gamma=120$	P
Cubic	1	$a=b=c$, $\alpha=\beta=\gamma=90$	P, I, F

2.1.3 Crystal symmetry

The symmetry of a crystal is best described by the symmetry within the unit cell; the unit cell repeats *via* translational symmetry in three dimensions to form the crystal. The unit cell is generated from smaller asymmetric units (asu) related to one another by a combination of symmetry operations. An operation is a symmetry operation if, after being carried out, the properties of space remain unchanged. The symmetry operations (Figure 2.3) are performed on symmetry elements including points, axes or planes. There are four non-translational symmetry operations including rotation about an axis (n-fold= 2, 3, 4 and 6), reflection through a mirror plane, inversion through a point and a roto-inversion involving the rotation about an axis followed by an inversion through a point. The two translational symmetry operations include a screw axis, involving the rotation about an axis followed by a translation along the axial direction, and a glide

plane, involving the reflection of an object followed by its translation parallel to the reflection plane. [144]

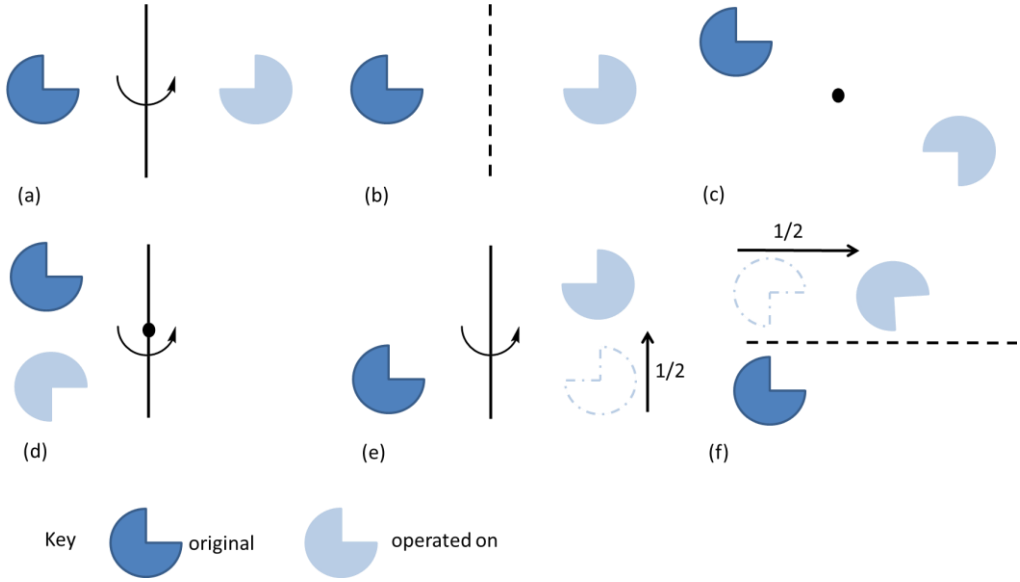

Figure 2.3 Symmetry operations of (a) a 2-fold rotation (180 °), (b) a reflection, (c) an inversion, (d) a rotoinversion, (e) a 2_1 screw axis and (f) a glide plane.

In crystals, multiple symmetry operations can co-exist; the combination of multiple non-translational operations generates a point group, so-called since the operators leave one point fixed. There are 32 possible crystal point groups. The next level of symmetry includes the translational components. By applying the 14 translational Bravais lattice symmetries and the translational symmetry operations to the 32 point groups, the 230 unique ways of arranging of points in space are generated – these are the space groups [143, 145] and describe the only ways in which identical objects can be arranged infinitely in the crystal.

2.1.4 Lattice planes

As well as forming unit cells, lattice points can be linked in two-dimensions to give a lattice plane. Lattice planes can be defined throughout the crystal, with different orientations and separations (Figure 2.4). The 'orientation' of a plane can be described by considering the intercepts *a*, *b*, *c* it makes on axes *x*, *y*, *z*. These points of interception are called the Weiss indices and have values that are unit lengths such as 1*a*, 1*b*, 1*c*. In the case where a plane runs parallel to an axis/axes with no intercept, the Weiss index has a value of infinity (∞). Because the Weiss indices may include fractions or values of ∞, this makes their use inconvenient and so are replaced by Miller indices *hkl* which are the reciprocal values of the Weiss indices with the fractions cleared. [146] Lattice planes separated by the same spacing, called *d*-spacing, are parallel and are described by the same Miller indices *hkl*; these are a family of crystal planes *hkl*. [147]

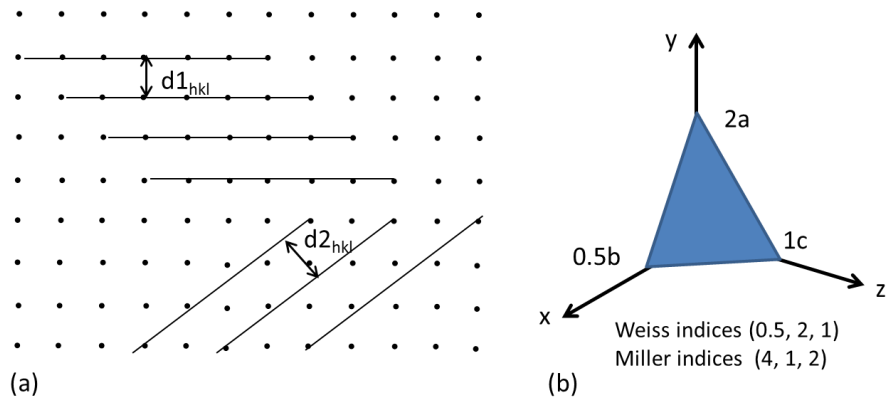

Figure 2.4 (a) Sets of parallel lattice planes with interlayer spacings $d1_{hkl}$ and $d2_{hkl}$ and (b) a crystallographic plane cutting *x*,*y*,z described by Weiss indices and the corresponding Miller indices.

2.1.5 The reciprocal lattice

The reciprocal lattice is an alternative way to describe the 'direct' crystal lattice; instead of a family of parallel crystallographic planes *hkl* separated by a certain *d*-spacing, the reciprocal lattice is built up of vectors (Figure 2.5). The vectors have a direction that is the normal of a family of crystal planes in 'direct' space and a length that is the inverse of the *hkl* *d*-spacing, d^*. A family of crystallographic planes may therefore be represented as a point called a reciprocal lattice point at the end of vector of length d^* and whose direction from the reciprocal space origin is given by the normal to the *hkl* lattice plane. [148]

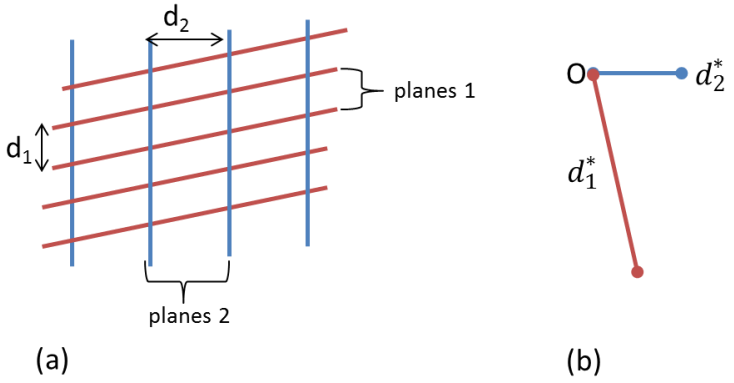

Figure 2.5 (a) Two families of parallel crystallographic planes *hkl* (red = planes 1 and blue = planes 2) separated by *d*-spacings d_1 and d_2 respectively and (b) the normal to these families of planes from a common origin with length $\boldsymbol{d_1^*}$ and $\boldsymbol{d_2^*}$.

Instead of being defined by *a*, *b* and *c*, the reciprocal lattice is defined by vectors a^*, b^* and c^* and is related to the direct lattice by:

Equation 2.1 $$\boldsymbol{a^* = \frac{b \times c}{V} \qquad b^* = \frac{c \times a}{V} \qquad c^* = \frac{a \times b}{V}}$$

Equation 2.2 $$\boldsymbol{V = a \cdot (b \times c) = b \cdot (c \times a) = c \cdot (a \times b)}$$

therefore:

Equation 2.3 $$\boldsymbol{a}^* \cdot \boldsymbol{a} = \boldsymbol{b}^* \cdot \boldsymbol{b} = \boldsymbol{c}^* \cdot \boldsymbol{c} = \mathbf{1}$$

and

Equation 2.4 $$\boldsymbol{a}^* \cdot \boldsymbol{b} = \boldsymbol{a}^* \cdot \boldsymbol{c} = \boldsymbol{b}^* \cdot \boldsymbol{a} = \boldsymbol{b}^* \cdot \boldsymbol{c} = \boldsymbol{c}^* \cdot \boldsymbol{a} = \boldsymbol{c}^* \cdot \boldsymbol{b} = \mathbf{0}$$

Equation 2.4 suggests that a^* is normal to the plane (b,c), b^* is normal to the plane (a,c) and c^* is normal to the plane (a,b). [144] A reciprocal lattice point thus defined at the end of vector d^*, lies along the a^*, b^* and c^* axes, which are the indices h, k and l. The length of the vector from the origin is (ha^*+kb^*+lc^*). The reciprocal lattice is important for understanding the geometry of diffraction from crystals. [144]

2.2 Diffraction of X-rays by crystals

2.2.1 Generation of X-rays

X-rays may be generated *via* a process of accelerating electrons through a potential difference (20 – 50 kV) and colliding them with a water cooled metal anode target. The electrons are generated initially from a heated filament supplied by an alternating current. The traditional laboratory method occurs in an evacuated X-ray tube and the anode is cooled where most of the electron collision energy leaves as heat. Collision of the high energy electrons on the anode target creates vacancies by ejecting electrons from the low-lying occupied atomic orbitals; subsequently, excited state electrons will drop into these vacant orbitals and the X-rays generated by this method are at characteristic energies (hence wavelengths) from the K_α and K_β transitions. The X-ray wavelengths generated are characteristic of the anode metal, and are generated alongside a continuous spectrum of white radiation. Usually monochromatic X-rays are employed and the K_α wavelength is selected preferentially. The most common anode metal targets in X-ray crystallographic studies are copper (Cu-K_α) and molybdenum (Mo-K_α) generating K_α wavelengths of 154.18 pm and 71.07 pm, respectively. [147, 149]

2.2.2 Scattering of X-rays by crystallographic planes

The periodic nature of crystals means that they may act as a three-dimensional diffraction grating for X-rays; [150] the diffraction occurs from the crystal lattice planes. For a set of parallel lattice planes with Miller indices hkl and interplanar spacing d_{hkl}, diffraction occurs provided several conditions are met. Incoming X-rays, incident to a set of lattice planes (hkl) at angle Θ (Figure

2.6), will only be observed as diffracted X-rays (reflections) if they interfere constructively on leaving the crystal. Constructive interference only occurs when the difference in path lengths of the diffracted beams (EF + FG) is an integral number of wavelengths ($n\lambda$). [147]

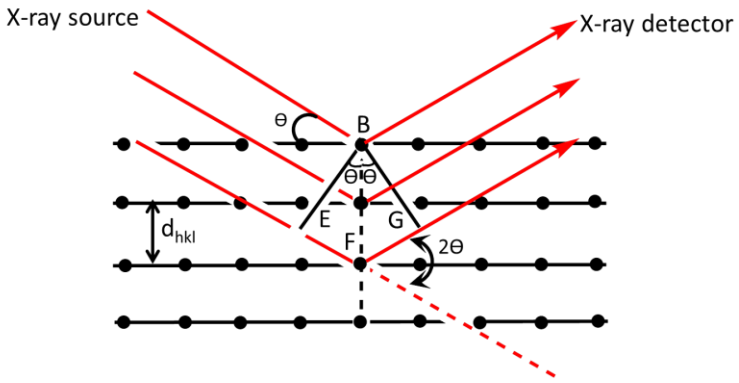

Figure 2.6 The Bragg condition for reflection of X-rays from a set of crystal planes with a spacing, $\boldsymbol{d_{hkl}}$.

Diffracted X-rays from a set of crystal planes, d_{hkl}, will also only be observed at particular Bragg angles of incidence (Θ_{hkl}) of the incoming beam. The Bragg equation describes fully the conditions for diffraction (Equation 2.5); combining the difference in path lengths and the relationship between d_{hkl} and Θ_{hkl}.

Equation 2.5 $$\boldsymbol{n\lambda = 2\, d_{hkl} sin\Theta_{hkl}}$$

2.2.3 The Ewald construction

The Ewald construction may be used to determine when the Bragg diffraction conditions are met for a set of *hkl* lattice planes (Figure 2.7(a)). In the basic construction, a sphere of radius $\frac{1}{\lambda}$, called the Ewald sphere (E), where λ is the wavelength of the incident X-rays, is drawn with the crystal at the centre. Incoming X-rays pass through the centre of the sphere. The origin of the reciprocal lattice is placed at the point where the direct X-ray beam leaves the sphere, point O, and the diffraction conditions for a set of *hkl* lattice planes are met by rotating the reciprocal lattice about O until a reciprocal lattice point cuts the sphere, at point P. Diffraction is observed from the set of planes at point P and the direction of diffraction, the normal to a set of *hkl* lattice planes d^*, is then given by drawing a line from the centre of the sphere to point P. There is a limit to the number of lattice points that may cut the Ewald sphere on rotating the reciprocal lattice and therefore reflections that may be observed. This is called the 'limiting sphere' (L) and is achieved by rotating the Ewald sphere around the point where the direct beam leaves it which generates a larger sphere of radius $\frac{2}{\lambda}$ (Figure 2.7(b)). [151]

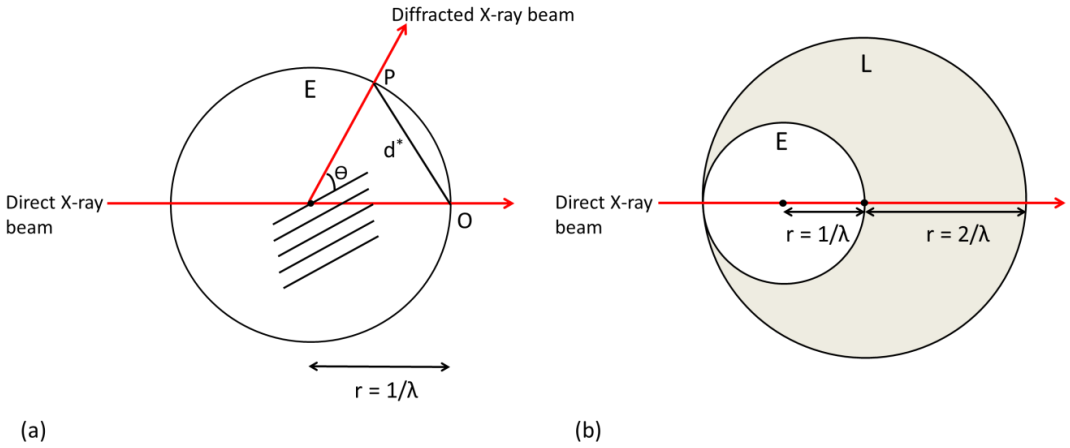

Figure 2.7 (a) The Ewald construction for meeting the Bragg condition and (b) the limiting sphere (L) of observable reflections.

2.2.4 Scattering of X-rays by atoms

The diffraction of X-rays by a crystal occurs due to the ability of the atomic electrons, within the crystal, to scatter X-rays. The scattering of X-rays by atoms can be described by an atomic scattering factor; this considers the sum of the contributions from all *Z* electrons; this contribution changes as a function of scattering angle (Equation 2.6). At a scattering angle of zero all scattered X-rays are in phase; the scattering amplitude is the contributions from all electrons and *f* is equal to *Z*. The X-rays become increasingly out of phase as the scattering angle increases such that the amplitude for each electron decreases and *f* falls off (Figure 2.8); the rate of fall off of *f* is affected by thermal motion of atoms, which modifies electron density and capacity to scatter, and is greatest for lighter atoms. For hydrogen, the scattering at an angle of zero is low, due to it having only one electron, and the fall of is rapid due to the high motion of these atoms. [144, 148]

Equation 2.6 $$\textit{atomic scattering factor } f = \frac{\textit{amplitude scattered by the atom}}{\textit{amplitude scattered by a single electron}}$$

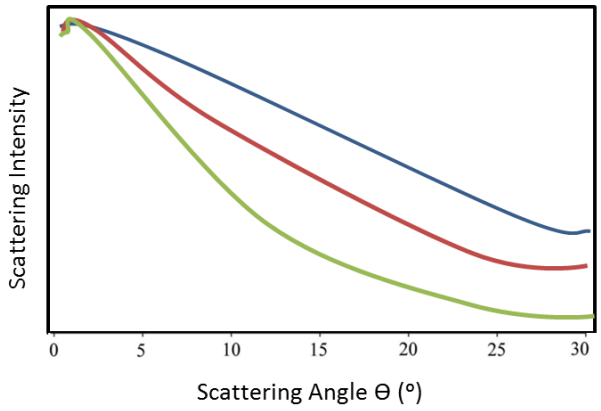

Figure 2.8 Scattering factor functions for elements iron (blue), carbon (red) and hydrogen (green). [152]

Thermal motion of atoms

Atoms in a crystal are not static entities; they undergo vibrations called thermal motion about their equilibrium positions (dynamic disorder). This thermal motion (expressed quantitatively in terms of atomic displacement parameters, ADP) is inversely proportional to atomic mass and leads to a reduction in the scattering factor as a function of $sin\Theta/\lambda$. [94] The motion may be isotropic, described by the single parameter $B\ (-8\pi^2U)$ or U and models a sphere for atomic motion where motion in all directions is equal, or anisotropic, described by six parameters U_{11}, U_{22}, U_{33}, U_{23}, U_{13}, U_{12} and models a three-dimensional ellipsoid for atomic motion where motion in all directions is not equal. [153] The thermal motion of atoms modifies atomic scattering (f) by causing the atomic electron density to be spread over an expanded volume such that intensity (f') is reduced.

Equation 2.7 $$\boldsymbol{f'(\Theta) = f(\Theta)e^{\left(\frac{-Bsin^2\theta}{\lambda^2}\right)}}$$

2.2.5 A single crystal X-ray diffraction experiment

In a single crystal X-ray diffraction experiment, a crystal is rotated around a fixed point in the incident X-ray beam. This allows the maximum number of possible reciprocal lattice points to cut the Ewald sphere and therefore reflections to be observed. Rotation of the crystal is achieved by mounting on a goniometer on a diffractometer commonly with three possible axes of crystal rotation including ϕ, χ and ω. The diffracted X-rays are observed using a detector which sweeps along a vertical 2Θ range adding a fourth rotation; [141] in modern diffractometers the detector angular sweep is achieved by using an area detector (Figure 2.9(a)). Diffraction, for crystal structure determination, is usually measured from a sample at very low temperature, typically at 100 or 150 K. At lower temperatures, the thermal motion of atoms is reduced, leading to a reduction in the fall off in atomic scattering with diffraction angle. [142] Often, it is beneficial to collect data on a sample at both low temperature and room temperature; phase transitions or some other structural change may be induced in a sample between the two temperatures. The detectors used in single crystal experiments include image plates, [154] charged coupled devices (CCD), [155] complementary metal oxide semi-conductors (CMOS) [156] and Pilatus hybrid pixel detectors. [157] In a typical diffraction pattern, the diffracted X-rays are observed as spots (Figure 2.9(b)).

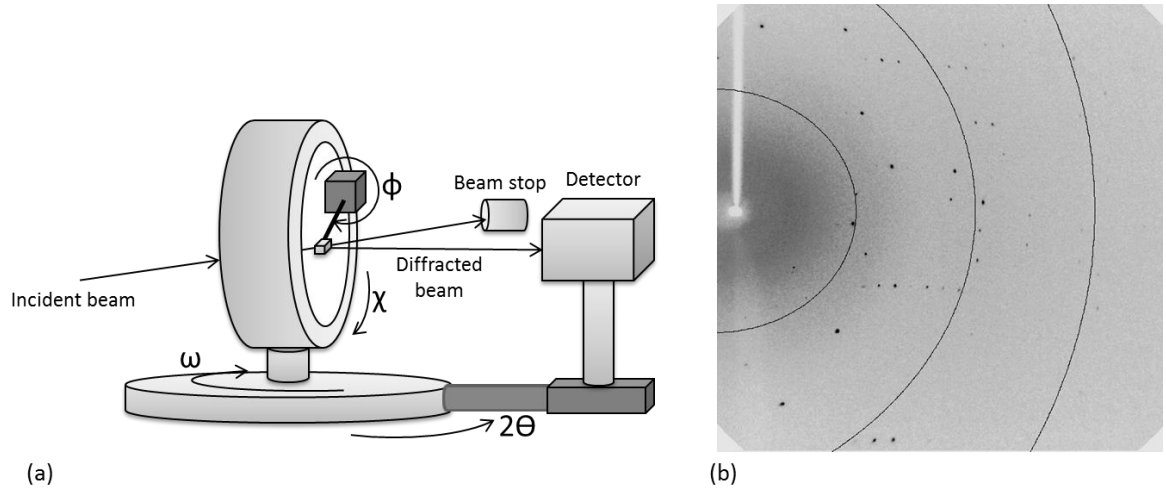

Figure 2.9 (a) A four circle goniometer [149] and a (b) single crystal X-ray diffraction pattern from a CCD detector.

2.3 Crystal structure determination using X-ray diffraction

The measurement of X-ray diffraction from a crystalline material can allow the structure of the material to be determined, recognising that the diffraction pattern is the Fourier transform of the crystal structure. This is related to the information held within the geometry and intensity of the diffracted X-rays in the recorded diffraction image.

2.3.1 Pattern geometry

The arrangement of spots in a diffraction pattern is related to both the size and shape of the unit cell and its crystal symmetry.

Unit cell determination

The distance of each diffraction spot from the centre of the diffraction pattern is proportional to *sinΘ*. Rearranging the Bragg equation (Equation 2.8) shows that each diffraction spot is equivalent to a reciprocal lattice point d_{hkl}^{*} ($1/d_{hkl}$) at position a^{*}, b^{*}, c^{*} or *h*, *k*, *l* on the reciprocal lattice.

Equation 2.8 $$\boldsymbol{sin\theta = \frac{\lambda}{2} \cdot \frac{1}{d_{hkl}}}$$

The position of d_{hkl}^{*} can only be known if the orientation matrix is first determined. The orientation matrix (A) is a 3 x 3 matrix which gives the components of the reciprocal lattice (a^{*}, b^{*}, c^{*}) in three directions of the goniometer axial system (Equation 2.9); the goniometer on which the crystal is mounted has three orthogonal axes, *x* points at the X-ray beam, *y* is at 90 ° to *x* in the horizontal plane and *z* is normal to the *xy* plane.

Equation 2.9

$$\boldsymbol{A} = \begin{pmatrix} \boldsymbol{a_x^*} & \boldsymbol{b_x^*} & \boldsymbol{c_x^*} \\ \boldsymbol{a_y^*} & \boldsymbol{b_y^*} & \boldsymbol{c_y^*} \\ \boldsymbol{a_z^*} & \boldsymbol{b_z^*} & \boldsymbol{c_z^*} \end{pmatrix}$$

The orientation matrix may be determined by using a set of reference reflections (diffraction spots), whose positions are then optimised to give a set of reciprocal lattice points which are calculated relative to the goniometer axial system. This gives the nine elements of A. The indices of all reflections are generated and the unit cell parameters are then extracted from the orientation matrix using its transpose (Equation 2.10). [142, 153]

Equation 2.10

$$(\boldsymbol{A'A})^{-1} = \begin{pmatrix} \boldsymbol{a.a} & \boldsymbol{a.b} & \boldsymbol{a.c} \\ \boldsymbol{b.a} & \boldsymbol{b.b} & \boldsymbol{b.c} \\ \boldsymbol{c.a} & \boldsymbol{c.b} & \boldsymbol{c.c} \end{pmatrix}$$

Symmetry determination

Information about crystal symmetry may be observed from the diffraction pattern including Laue class and the presence of translational symmetry elements. The crystal symmetry and space group may be assigned by comparing the intensities of reflections which are equivalent by symmetry. [141] Diffraction patterns are inherently centrosymmetric; two reflections (hkl) and –(hkl) (denoted $\bar{h}\,\bar{k}\,\bar{l}$) are related to one another *via* an inversion centre however since only the square of the amplitude of the intensity can be measured, the phase is lost, then they are considered equivalent, as described in Friedel's law. The centrosymmetric nature of the diffraction pattern limits the determinable symmetry to eleven Laue groups; centrosymmetric symmetries cannot be distinguished from non-centrosymmetric symmetries. [148]

Absences

Certain subsets of reflections in the diffraction pattern have zero intensity such that they are considered 'absent'; these absent reflections may also indicate information about crystal symmetry, being an effect of translational symmetry elements. [158] Absent reflections are caused by the destructive interference of X-rays for certain *hkl* reflections and affect a subset of reflections. The absence of certain reflections also occurs due to lattice centring which are called general absences; no absences occur in primitive lattice types whilst reflections are absent in I when the sum of $h + k + l$ is odd, in A when the sum of $k + l$ is odd, in B when the sum of $h + l$ is odd, in C when the sum of $h + k$ is odd and in F when *hkl* have mixed odd and even integers. Systematic absences occur due to the presence of translational symmetry elements of screw axes and glide planes, where planes of atoms are introduced part way along the cell and reflections from these planes interfere with those from other planes. For example, the presence of a 2_1 screw axis along *b* means that reflections will be absent from the *0k0* planes when *k* is odd. [142, 147, 159]

2.3.2 Reflection intensities

The intensities of the light scattered from objects allows them to be observed. Larger objects scatter visible light however as objects get smaller, magnification and smaller wavelengths of light are required. Atoms in a crystal scatter X-rays from their electrons (§2.2.4). The intensity of the scattered X-rays therefore holds information about the type and arrangement of atoms within the crystal. The intensities can be described by a term called the structure factor $F_{hkl.}$ (Equation 2.11) defined as the resultant of the waves scattered by all atoms in the unit cell in the *hkl* direction and is dependent on the scattering factor f_j and position (x_j, y_j, z_j) of each atom (Equation 2.12).

Equation 2.11 $$I_{hkl} \propto {F_{hkl}}^2$$

Equation 2.12 $$F_{hkl} = \sum_{j=1}^{j=n} f_j e^{2\pi(hx_j+ky_j+lz_j)}$$

An image of the atomic structure is then obtained in the form of the electron density ρ(*x*,*y*,*z*) by a recombination of the structure factors F_{hkl} using a Fourier transform (Equation 2.13) which gives $\rho(x,y,z)$ at position *x*, *y*, *z* in the unit cell, where *V* is the volume of the unit cell. [147]

Equation 2.13 $$\rho(x,y,z) = \frac{1}{V} \sum_h \sum_k \sum_l F_{hkl} e^{-2\pi i(hx+ky+lz)}$$

Equation 2.13 means that if the structure factors are known, the electron density distribution in the unit cell can be determined and the atoms located within it. In terms of the application of Equation 2.13 to determine electron density and hence atomic positions, one significant problem is the phase problem; the values of F_{hkl} obtained from the intensities are in fact its modulus, $|F_{hkl}|$. The amplitude of the F_{hkl} are thus known but their phases are unknown. Both are required for structure determination [141, 149] and so structure solution programmes aim to overcome this phase problem. Different methods may be employed by structure solution programs including direct methods, Patterson synthesis and charge flipping. The structure solution method employed in this research project is that of direct methods.

2.3.3 Direct methods of crystal structure determination

Direct methods are a trial and error method that aims to overcome the phase problem by using relationships between the intensities of different reflections to determine the missing phases. The F_{hkl} structure factors obtained from the diffraction experiment are first normalised (*E(h)*) to remove the effects of atomic shape. A restriction on the electron density is then imposed, $\rho(x,y,z)$ must be positive everywhere, which generates inequalities among *E(h)* and sets up the phase relationship between *E(h)* triplets *via* the Sayre Equation (Equation 2.14).

Equation 2.14 $$\boldsymbol{\phi(h) \approx \phi(h-k) + \phi(k)}$$

where h and k are reciprocal lattice vectors.

The reflections to be used for phase determination are then selected such that the strongest *E(h)* are chosen and that each *E(h)* is present in as large a number of phase relationships as possible. Initial phases are assigned which are then used in the tangent formula (Equation 2.15), derived by Karle and Hauptmann, to derive new phases using a large number of the triplet relationships; this process is iterated until the phases are converged to stable values.

Equation 2.15 $$\boldsymbol{tan\phi(h) \approx \frac{\sum_k |E(k)E(h-k)|\ \sin(\phi(k)+\phi(h-k))}{\sum_k |E(k)E(h-k)|\ \cos(\phi(k)+\phi(h-k))}}$$

Figures of merit are calculated for each phase set allowing their quality to be indicated and those with the highest values are used to calculate electron density maps. The peaks in the electron density map are then interpreted to form an initial structural model. [142, 153, 160]

2.4 Crystal structure refinement

The initial structural model obtained from direct methods will have substantial inaccuracies corresponding to incompleteness or errors in the model and in the data. To minimise these errors, structural parameters need to be optimised including atom types, positions and displacement parameters. This is done *via* the process of least squares structure refinement on F^2. In this process the structure factors from the model (F_c) are compared to those from the experiment (F_o); the aim of the least squares refinement is to minimise the difference between the two (Equation 2.16). In this minimisation, each reflection is assigned a weight (w) reflecting the confidence in the accuracy of the measured intensity; inversely proportional to the estimated variance of the amplitude of F (Equation 2.17). Only the amplitudes of F_o and F_c are compared as the phases of the structure factors are unknown from the experiment.

Equation 2.16 $$\boldsymbol{\sum w(|F_o|^2 - |F_c|^2)^2}$$

Equation 2.17 $$\boldsymbol{w = \frac{1}{\sigma^2(F_o{}^2)}}$$

During the least-squares procedure, the parameters to be optimised include atom types, positions and displacement parameters. In the initial structural model, only heavy atom types are assigned. Often these assignments may not be correct and should be corrected at this point; mis-assignment

of atoms may be indicated as residual peaks around the atom, if assigned too few electrons, or as troughs, if assigned too many. The displacement parameters of the heavy atoms are also optimised from an initial isotropic model to be anisotropic.

The progress of a refinement is monitored in residual *R*-factors, weighted (Equation 2.18) and non-weighted (Equation 2.19), and a goodness of fit parameter, *S* (Equation 2.20). During a refinement these values should reduce and a complete structure is indicated by an wR_2 of less than 0.2, an *R*-factor in the range of 0.02 to 0.05 and a goodness of fit of 1.

Equation 2.18 $$wR_2 = \left[\frac{\sum \mathrm{w}|F_o{}^2 - F_c{}^2|^2}{\sum w|F_o{}^2|^2}\right]^{1/2}$$

Equation 2.19 $$R = \frac{\sum ||F_o| - |F_c||}{\sum |F_o|}$$

Equation 2.20 $$S = \left[\frac{\sum w(F_o{}^2 - F_c{}^2)^2}{(N-P)}\right]^{1/2}$$

where *S* is the goodness of fit, *N* the number of data and *P* the number of refined parameters. [142, 153, 161]

2.4.1 Fourier difference maps

If a structure is approaching completion but still has a small section undefined, remaining atoms may be located by calculating a Fourier difference map $\Delta\rho(x,y,z)$, using a derivation of Equation 2.13, where the 'difference' structure factors ($|F_o|$ - $|F_c|$) are used alongside the calculated phases, α_{hkl}^c (Equation 2.21). The difference map $\Delta\rho(x,y,z)$ contains scattering density in F_o that has not been accounted for by F_c. [94]

Equation 2.21 $$\Delta\rho(x,y,z) = \sum_h \sum_k \sum_l (|F_o| - |F_c|) e^{-2\pi i(hx+ky+lz)+\alpha_{hkl}^c}$$

If all heavy atoms have been located and refined anisotropically, at this stage, the Fourier difference map will contain only peaks for the hydrogen atoms. The hydrogen atom positions may often be freely refined however, the low electron density of hydrogen atoms makes their refinement from X-ray data much less precise; often they may instead be fixed at riding positions relative to the heavy atom to which they are bonded. Hydrogen atoms are also refined with isotropic thermal parameters from X-ray data, involving just one *B* or *U* term. This is a consequence of the small contribution of a hydrogen atom to the scattering; refining hydrogen atoms with anisotropic displacement parameters would lead to an over interpretation of the data, reducing the observed data to parameter ratio which would compromise the accuracy of the overall

refinement. Hydrogen atom displacement parameters may be refined anisotropically from neutron data where hydrogen atoms have a larger relative contribution to the scattering. [94]

As well as the location of hydrogen atoms, Fourier difference maps may provide additional details about the structure. For high quality single crystal X-ray diffraction data, it may be possible to observe additional structural features including the bonding density between atoms or lone pairs.

Fourier difference maps may also be very useful in the study of hydrogen transfer processes such as proton disorder (§1.3.1) and migration (§1.3.2). Fourier difference maps can be generated for selected hydrogen bonding interactions with the hydrogen atom removed from the model such that the hydrogen atom density is observable in the map (Figure 2.10); the density may indicate information about the hydrogen atom behaviour in a certain type of hydrogen bond or as a function of an external variable. Fourier difference maps are frequently employed in temperature dependent proton disorder and migration studies.

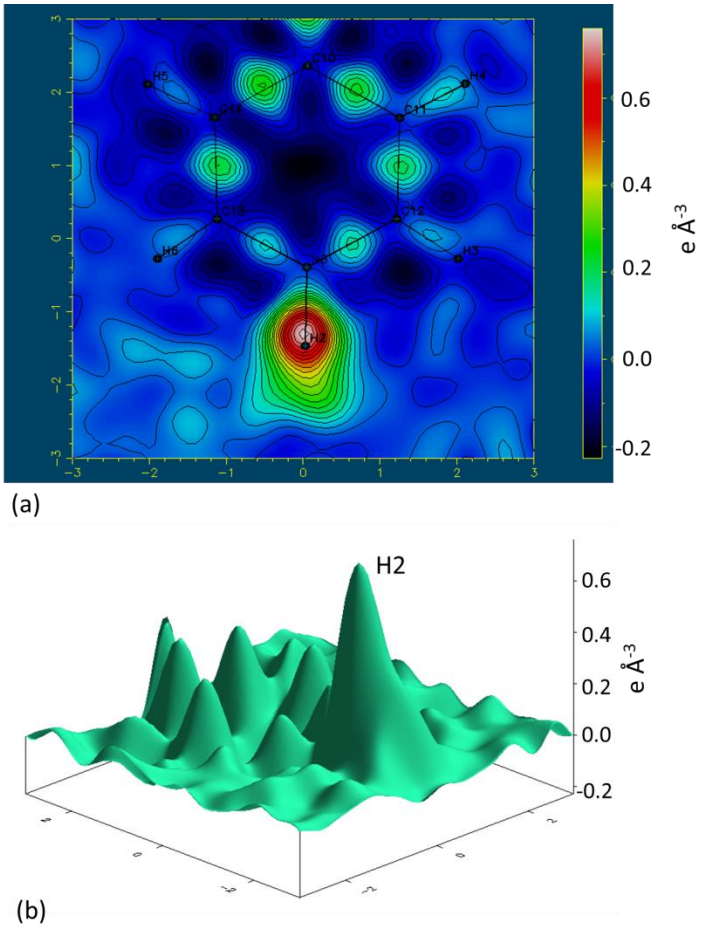

Figure 2.10 Fourier difference electron density maps through a molecular plane, showing the electron density (e $Å^{-3}$) associated with the H-atom by a peak maxima in (a) a two-dimension bitmap, (b) in a three-dimensional surface. In these maps, the e $Å^{-3}$ range is often between - 0.2 to 0.8 e $Å^{-3}$.

Interpretation of Fourier difference maps

The interpretation of Fourier difference maps for structure solution or the determination of proton behaviour may be affected by the presence of noise in the form of Fourier ripples or smearing of electron density. [94] The Fourier difference maps are generated from a Fourier series of the structure factors which in turn are derived from the diffraction intensities. The diffraction intensities are a measured quantity and so subject to error; the noise present in the Fourier difference maps, and therefore the quality of the final structure, will depend on the uncertainties in the measured intensities. [162] Noise in the Fourier difference maps may also occur related to the nature of the scattering material such as if molecules in the crystal are undergoing enhanced molecular vibrations, as a result of molecular disorder or due to collecting data at higher temperatures. [39]

Ideal diffraction data, for optimised Fourier difference maps, may be obtained when collected from a uniform crystal using an X-ray beam with a constant beam profile and image widths that are finely sliced relative to the crystal mosaicity. Background will be low whilst the intensities should have a high signal to noise ratio. Each reflection should be well defined and sampled multiple times, for an increased redundancy, and to a high resolution. The data set will also have good completeness.

2.4.2 Constraints and restraints

The optimisation of structural parameters during the refinement process may involve the use of constraints or restraints. Constraints involve either the use of equations to rigidly relate parameters or the assignment of fixed numerical values to parameters. Overall they reduce the number of independent refinable parameters. For example, when proton disorder is present across a hydrogen bond, in order to refine the ratio of the site occupancy factors for each proton site, their sum is constrained to unity. The fixing of hydrogen atoms using a riding model on a heavy atom involves a constraint applied to the D—H bond lengths and D'—D—H bond angles. Restraints are additional experimental observations and increase the overall number of parameters. They use a minimisation function involving a target value for a parameter which the actual restrained parameter will approach during refinement. For example, restraints may be applied to distances between atoms. [39]

2.4.3 Rigid body refinement

Atoms in a crystal undergo vibrations. If, when within a molecule, there are only small internal vibrations of atoms compared with the overall movement of the molecule, then a rigid body refinement may be applied. A rigid body refinement involves the constrained coordinate refinement of one or more groups of atoms that move, by rotations or translations around a fixed

axis, as a single body. The internal arrangement of atoms does not change. [153, 163] The use of a rigid body has the effect of reducing the number of overall refinement parameters.

Rigid body motion and TLS tensors

When a molecule is described by a rigid body, the vibrations of its atoms (atomic displacements) must be consistent with the overall molecular motion. This is the rigid body motion and it can be described by a harmonic approximation with translational, librational and screw components in a 3 x 3 matrix. The translational component, described by the tensor *T*, includes a backwards and forwards oscillation in three-dimensions whilst the libration component, described by the tensor *L*, includes rotary oscillation. The screw component, described by the tensor *S*, includes the complete motion of the molecule that does not lie on the centre of symmetry in the crystal structure. [153] This occurs when there is correlation between the translational and librational motion such that the librational axes do not intersect at a single point. [164]

In order to describe the rigid body motion of a molecule using the *TLS* tensors, the *x*, *y*, *z* coordinate system must first be converted to Cartesian orthogonal, *rx*, *ry*, *rz* coordinates using the matrix *[M]* (Equation 2.22 and Equation 2.23):

Equation 2.22
$$[\boldsymbol{M}] = \begin{pmatrix} \boldsymbol{A sin\gamma sin\omega} & \boldsymbol{0} & \boldsymbol{0} \\ \boldsymbol{A cos\gamma} & \boldsymbol{B} & \boldsymbol{C cos\alpha} \\ \boldsymbol{A sin\gamma cos\omega} & \boldsymbol{0} & \boldsymbol{C sin\alpha} \end{pmatrix}$$

Equation 2.23
$$\begin{bmatrix} \boldsymbol{rx} \\ \boldsymbol{ry} \\ \boldsymbol{rz} \end{bmatrix} = [\boldsymbol{M}] \cdot \begin{bmatrix} \boldsymbol{x} \\ \boldsymbol{y} \\ \boldsymbol{z} \end{bmatrix}$$

where A, B and C are the unit cell lengths, α and γ are the unit cell angles, and $sin\omega$ is described by Equation 2.24. [165]

Equation 2.24
$$\boldsymbol{sin\omega} = \frac{\boldsymbol{cos\beta - cos\alpha cos\gamma}}{\boldsymbol{sin\alpha sin\gamma}}$$

The *T*, *L* and *S* tensors are applied to the Cartesian coordinates to obtain the TLS description, in Cartesian format, of the heavy atom anisotropic thermal displacement parameters, U_{11}, U_{22}, U_{33}, U_{23}, U_{13} and U_{12} (Equation 2.25 to Equation 2.30).

Equation 2.25
$$\boldsymbol{U_{11}^{TLS} = L_{22} rz^2 + L_{33} ry^2 - 2L_{23} ryrz + 2S_{21} rz - 2S_{31} ry + T_{11}}$$

Equation 2.26
$$\boldsymbol{U_{22}^{TLS} = L_{11} rz^2 + L_{33} rx^2 - 2L_{13} rxrz - 2S_{12} rz - 2S_{32} rx + T_{22}}$$

Equation 2.27
$$\boldsymbol{U_{33}^{TLS} = L_{11} ry^2 + L_{22} rx^2 - 2L_{12} rxry - 2S_{23} rx - 2S_{13} ry + T_{33}}$$

Equation 2.28 $$U_{12}^{TLS} = -L_{33}rxry + L_{23}ryrxrz - L_{13}ryrz - L_{12}rz^2 - S_{11}rz + S_{22}rz + S_{31}rx - S_{32}ry + T_{12}$$

Equation 2.29 $$U_{13}^{TLS} = -L_{22}rxrz + L_{23}ryrx - L_{13}ry^2 + L_{12}ryrz + S_{11}ry - S_{33}ry + S_{23}rz - S_{21}rx + T_{13}$$

Equation 2.30 $$U_{23}^{TLS} = -L_{11}ryrz - L_{23}rx^2 + L_{13}rxry + L_{12}rxrz - S_{22}rx + S_{33}rx + S_{12}ry - S_{13}rz + T_{23}$$

When using the TLS description, corrections to the bond lengths are also usually applied as a result of inter-atomic distance 'shrinking' caused by the librational component. [166] Using the TLS description of molecular motion reduces the number of thermal parameters from six, for each atom, to 20 for the whole molecule. [153]

2.4.4 Parametric structure refinement

Parametric structure refinement (originally developed in the form of parametric Rietveld refinement) allows a large number of data sets, collected as a function of an external variable, to be refined against an evolving structural model. This differs from individual and sequential analysis in that the structural model is fitted simultaneously to all data sets. The simultaneous refinement leads to a higher precision in certain refined parameters, the standard uncertainty of a parameter is greatly reduced when derived from a large number of data sets. The method can also allow the modelling of evolving behaviour across the data, help to avoid false solutions and greatly reduces processing time compared to individual refinement against what can be hundreds of data sets. [167]

The application of a parametric structure refinement is based on the idea that, on collecting a large set of data as a function of an external variable, certain parameters (prm) will be either common across the data sets or may be related, such as the evolution of an atomic position with temperature. These parameters may be parametrised thus reducing the parameter to data ratio. An example input parametric refinement file is shown in Figure 2.11. The input file contains a section for the refinement choices, including turning models on or off or selecting data files, sections for each temperature, which contain the instructions required to perform refinement against each individual data set, and a section which contains information applicable to all data sets including the structural model. Parametric refinement may be performed using the Topas-Academic V5.0. [168]

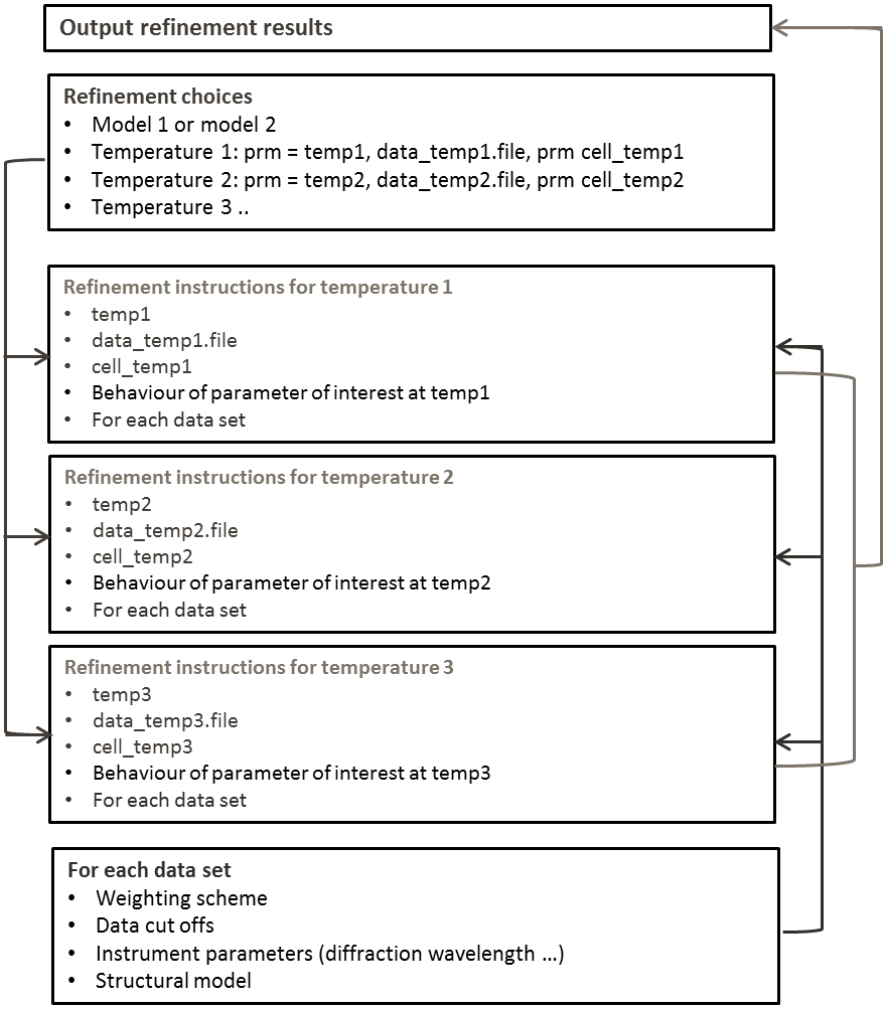

Figure 2.11 Schematic layout of parametric structure refinement file.

Parametric refinement has been employed in powder X-ray diffraction studies for a number of purposes including to carry out quantitative phase analysis and the determination of reaction mechanism in a photodimerisation reaction of 9-methylanthracene, [169] tested as one of many refinement strategies for determining the structural evolution of As_2O_5 [170] and to obtain a more reliable estimate of the optimised parameters in the study of dealumination of a zeolite catalyst. [171] Of particular relevance to this research project is the work by Ting *et al*. (2012) using parametric Rietveld refinement on neutron powder diffraction data to probe hydrogen atom positions in the hydrous compound $BaCl_2.2H_2O$; the changes in hydrogen atom positions as a function of temperature could be determined and monitored using the parametric method. [172] Parametric structure refinement is performed on single crystal X-ray diffraction data in the study of temperature dependent proton migration in Chapter 7.

2.5 Synchrotron crystallography

Laboratory X-ray sources are appropriate in the majority of cases for routine accurate determination of molecular structure from a single crystal. However, where samples and diffraction experiments are non-routine, it can be advantageous to use synchrotron radiation at a synchrotron source.

Synchrotron radiation is electromagnetic radiation covering the range from infrared to X-rays. It was first observed in 1947 and has been employed in research studies since the mid-1960s. Electromagnetic radiation is generated when a charged particle is accelerated [173] or forced along a circular path. [174] Electrons are charged particles and when they are accelerated to kinetic energies above the MeV range, and travelling close to the speed of light along a circular path, they emit 'synchrotron radiation'. [147] A typical synchrotron radiation research facility (Figure 2.12) has a linear accelerator (LINAC) which accelerates electrons from an electron gun into a booster ring where they are further accelerated to the speed of light. Once at speed, the electrons are injected into the storage ring, which is an evacuated ring shaped chamber, in bunches. [175]

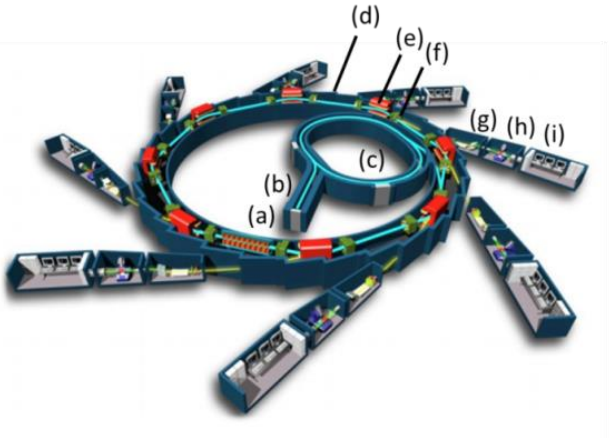

Figure 2.12 A typical synchrotron research facility: (a) electron gun, (b) the LINAC, (c) the booster ring, (d) the storage ring, (e) an insertion device, (f) a bending magnet, (g) the optics hutch, (h) the experimental hutch and (i) the control room. [176]

In the storage ring, sets of magnets are located at periodic points. Bending magnets maintain the electron direction of travel and speed along the circular path of the storage ring. [173] These magnets work on the principle that if a moving electron intersects a magnetic field which is perpendicular to the direction of travel, then it will experience a force perpendicular to both the direction of travel and the magnetic field. This force generates a centripetal acceleration causing the electron to move along a circular path and emit electromagnetic radiation. [177]

Additional sets of magnets are also located around the storage ring which produce the synchrotron radiation; these types of magnets determine the synchrotron 'generation'. In third generation synchrotrons, the generation of the synchrotrons used in this research project, magnets called insertion devices are used on straight sections. There are two types of insertion devices called wigglers and undulators (Figure 2.13). [178]

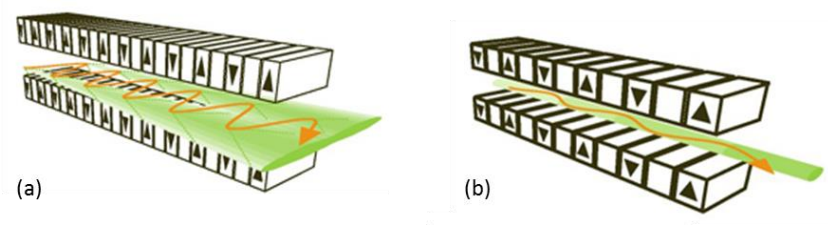

Figure 2.13 Insertion devices: (a) a wiggler and (b) an undulator. [179]

Wigglers contain dipole magnets which emit radiation with an energy (λ) characteristic to the circulating electron beam energy (E) and magnetic field (B) of the magnets. An electron beam passing through these magnets is 'wiggled' periodically away from and back to its curved path. A compensation effect occurs along the wiggle, using a very intense magnet, and results in a greater radial acceleration and the production of bright white light. [177, 179, 180] For multipole wigglers, the central emitted beam brightness is proportional to the number of wiggler periods. [181]

Undulators contain magnets with alternating low field magnetic poles. An electron beam passing through these magnets undergo a series of inward and outward electron accelerations where radiation is emitted on each 'undulation'. Downstream from the undulator, the emitted radiation may overlap interfering constructively or destructively and the result is a 'lumpy' spectrum, where each lump corresponds to a particular wavelength. Undulators therefore can produce very intense single wavelength radiation by magnet parameter tuning. [177]

The nature of the synchrotron radiation is a contracted narrow fan, in the forward direction of the electron bunches. Where there are several electron bunches circulating horizontally, passing a number of magnets, there is a continuum of such fans spread out over an arc creating a final fan that is wider horizontally than vertically; this property gives synchrotron radiation a greater intensity and collimation than ordinary laboratory sources. [177] Radiofrequency (RF) cavities are also present in sections along the storage ring to boost electron energy and momentum that has been lost due to bending and electron collisions.

The generated synchrotron radiation is utilised in beamlines, located at tangents to the storage ring and downstream of the insertion devices. In X-ray diffraction studies, a typical beamline set up

includes firstly an optics hutch, which takes the synchrotron radiation emitted by a wiggler or undulator and carries out 'tuning' by monochromation to select the desired wavelength of radiation and 'focusing' to a desired beam size and positioning for a particular diffraction experiment. Monochromation of the beam is carried out using a set of two monochromator crystals, one selects the wavelength by the application of Bragg's law whilst the other redirects the beam back to its original path. The beam is focused in the vertical and horizontal directions using mirrors. [181] The next section of a beamline is the experimental hutch where diffraction of the synchrotron X-rays from a sample is measured and the final section is the control room where the diffraction experiment is controlled and monitored. The single crystal beamlines of I19, Diamond Light Source. U.K. [1] and 11.3.1 at the Advanced Light Source, U.S.A. [2] are described in §4.2.6, respectively.

At a synchrotron X-ray source, the nature of the radiation called 'synchrotron radiation' differs from conventional laboratory source radiation by being highly intense, coherent, polarised, having a broad tuneable spectrum and a pulsed nature. [175] Each of these properties leads to particular applications. The high intensity of the X-rays means that data collections are extremely quick such that very fast reactions in solids can be followed [182] and the collection time for multi temperature or pressure experiments is significantly reduced. The pulsed-time structure of the synchrotron source means that time resolved studies, such as the decay of excited states may be studied. [183] Synchrotron X-rays also allow a higher coverage of reciprocal space with fewer detector settings and facilitates measurement of weak high order reflections, important in charge density studies. [184, 185] The tuneable spectrum of wavelengths means that resonance effects at or near the atomic absorption edge to carry out chemically specific diffraction can be exploited. [181] The intensity of the synchrotron radiation also means that small and weakly diffracting samples are no longer lost causes but can yield data of sufficient quality to allow structure solution and refinement.

2.6 Diffraction methods to follow proton transfer processes

Proton transfer across hydrogen bonds, including proton disorder or migration, has been followed in the solid state using both neutron and X-ray diffraction. Neutron diffraction remains the definitive technique for determining precise hydrogen atom positions and identifying the presence of proton transfer across hydrogen bonds. [98] However, advances in X-ray detector technology mean that hydrogen atoms may be routinely located and atomic positions and isotropic thermal parameters refined from X-ray diffraction data. [122] In particular, hydrogen atom behaviour can be determined when visualised in Fourier difference maps. [89] A number of combined neutron and

X-ray diffraction studies have revealed that the type of information obtained about the hydrogen atom behaviour is, however, not the same. This is related to the fact that the two techniques differ in what they observe; X-rays are scattered by atomic electrons whilst neutrons are scattered by atomic nuclei. When forming part of a D—H bond, the position of the one electron of the hydrogen atom is not localised on the hydrogen atom but located preferentially in the bonding region and closer to the heavy atom. Therefore, in an X-ray diffraction experiment, the hydrogen atom bonding density, and not the nuclear position as in neutrons, is being observed. Hydrogen atom positions given by neutrons are also shifted by 0.13 to 0.15 Å relative to those from X-rays. [94] This creates a problem when observing the proton transfer process of temperature dependent proton migration where larger apparent shifts in proton position are suggested from an X-ray study compared to a neutron study on the same material; in a study of the 1:1 adduct of urea phosphoric acid, a larger shift in the proton density maximum occurred with temperature in the X-ray data (0.1 Å) versus in the neutron data (0.04 Å). [121] Fourier difference maps will also reveal different information for the two techniques where those from X-ray data contain the bonding density whilst those from neutron data contain the nuclear density. X-rays therefore give information about electron sharing and thermal effects, whilst neutron data indicates thermal effects only. [109]

Due to hydrogen atoms being less precisely located by X-rays, standard uncertainties on bond lengths involving hydrogen atoms [153] and on hydrogen atom site occupancies are greater than for those in neutron refinement; for bond lengths the standard uncertainties are typically in the second decimal place for X-rays compared with the third for neutrons, while site occupancies have standard uncertainties of approximately 10% for X-rays [89] compared to approximately 1% for neutrons. [97] The difference in intensity of scattering between the two techniques also affects the information being observed about the hydrogen atom. In X-rays, hydrogen atoms have a low scattering intensity, where the one electron only is present. In contrast, in neutrons the scattering power, called the scattering length, is related to the properties of the nucleus which is strong for a hydrogen atom. This means that it is possible to refine hydrogen atoms anisotropically from neutron data whilst only isotropic refinement is possible from X-rays. Due to the neutrons interacting with nuclei rather than diffuse electrons in X-rays, there is also no fall off in scattering as a function of scattering angle, only that due to thermal motion of atoms. This means structural details about the hydrogen atom can be studied to a higher resolution in neutrons. [94]

Despite the different observations made by X-rays and neutrons, several combined diffraction studies of proton transfer across hydrogen bonds have shown that overall observed trends may be the same. Similar trends have been indicated in Fourier difference maps of hydrogen bonds including in the 1:1 adduct of urea phosphoric acid, where the hydrogen atom density was seen to

migrate across the bond with temperature in both X-ray and neutron Fourier difference maps; the effect was clearer in the X-ray maps (Figure 2.14), [121] and in cyclic hydrogen bonded dimers of 3,5-DNBA polymorph II where the emergence of proton disorder in the form of a second site in the dimer hydrogen bond was indicated in both X-ray and neutron Fourier difference maps at 300 K. [97]

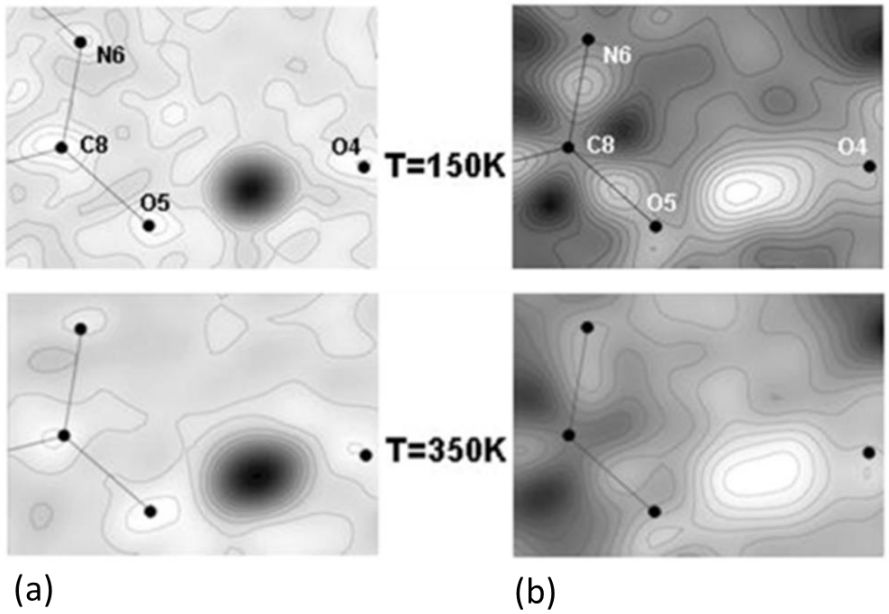

Figure 2.14 Fourier difference maps at 150 and 350 K for the (a) neutron and (b) X-ray structures of the O—H···O SSHB in the 1:1 adduct of urea phosphoric acid. The SSHB hydrogen atom is indicated by a peak maxima. [121]

Similar trends have also been observed in the occupancies of proton positions in X-ray and neutron proton disorder studies. One combined X-ray and neutron study on proton disorder in 4-DABA 3,5-DNBA demonstrated that it may be possible to refine hydrogen atom site occupancies provided high quality X-ray data are obtained. In this study, refined hydrogen occupancy values from X-ray data were in agreement with those from neutron data, at all temperatures. [97] In 3,5-DNBA polymorph II, the proton occupancies between the two techniques were also shown to follow the same trend of the second site increasing in occupancy with temperature; the final occupancy values at 300 K differed slightly (X-ray 72:28, neutron 81(2):19(2)) but were considered as being within the estimated 10 % error for the X-ray values. [97] The uncertainty in occupancy values from X-rays may be considered greater than this due to the small amount of electron density associated with each position and frequently Fourier difference maps are a more reliable route to extracting information on proton disorder. [121] In the case of dibenzoylmethane, there was no overall agreement in the observed trends found from neutron and X-ray structures. The nuclear density in variable temperature neutron Fourier difference maps showed an asymmetric hydrogen atom position which was invariant with temperature whilst electron density

in variable temperature X-ray Fourier difference maps suggested a migration from an asymmetric position at low temperature to a symmetric position at room temperature. [122]

Overall, the two diffraction techniques are in the most part complementary and where combined give a more complete picture of the proton transfer and hydrogen bonding; neutron diffraction probes the structural framework (positions of the atomic nuclei forming the molecule) whilst X-rays probe the bonding and therefore the chemistry. There is evidence to suggest, however, that X-ray diffraction offers potential in these studies of proton transfer. All previous diffraction studies of proton transfer processes have been carried out using neutron diffraction or a laboratory X-ray diffractometer. It would be advantageous if synchrotron X-ray diffraction could routinely be used in the study of proton transfer processes where X-rays are able to reveal interesting information about proton transfer processes. The high intensity of synchrotron X-rays means, for the multi temperature measurements which are usually carried out in the study of proton transfer, a greatly reduced data collection time compared to neutron and laboratory diffraction experiments. The number of samples that can be studied is also hugely increased at a synchrotron and, where the X-rays are stronger in intensity, the large crystal requirements of neutrons are not an issue. Synchrotron X-ray diffraction is applied in this research project in the study of temperature dependent proton disorder (Chapter 5) and proton migration (Chapter 7) processes and low temperature proton transfer behaviour (Chapter 8).

2.7 Powder X-ray diffraction

Powder X-ray diffraction (PXRD) is an alternative diffraction technique carried out on poly crystalline (powder) samples. It is usually a fixed λ method with a varying Θ and is based on the tendency of powder samples to be comprised of randomly oriented micro crystallites such that on exposure to X-rays, the Bragg condition is satisfied for a number of different *hkl* crystal planes simultaneously. The diffracted X-rays are observed as Debye Scherrer cones as a result of diffraction occurring from the same *hkl* crystal plane in a number of crystallites. [148] Detectors either record the whole of the diffraction cones, or take a vertical or horizontal slice. The cones or cone slices are then integrated to give the characteristic PXRD pattern containing peaks for reflections from particular *hkl* crystal planes at 2Θ positions related to the d_{hkl} with intensity I_{hkl} (Figure 2.15).

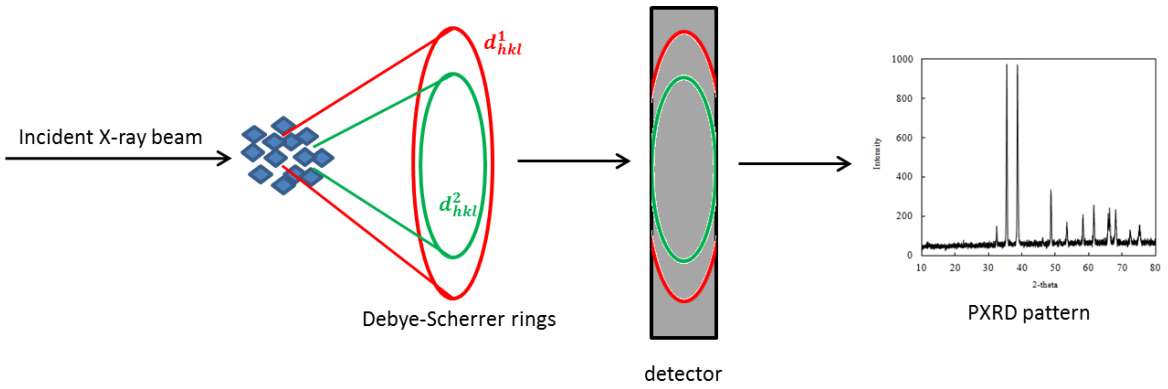

Figure 2.15 Diffraction of a powder crystalline product, its detection and data conversion to a PXRD pattern.

The diffraction observed by PXRD therefore differs to that observed by single crystal X-ray diffraction as the three-dimensional distribution of peaks is compressed down to one-dimensional lines. There is a significant loss of information in doing so, caused by an overlap of reflections from crystal planes of the same or similar *d*-spacing; this means that information on intensities and positions of the diffraction maxima is obscured. Crystal structure determination is thus less straight forward from PXRD data than from single crystal X-ray diffraction data. [186] The determination of unit cell parameters from a PXRD pattern is, however, relatively straight forward, provided good resolution of diffraction peaks. The unit cell determination process involves an initial peak selection, fitting and indexation process, using the positions of the maxima of typically the first twenty peaks to obtain the unit cell. A profile fitting technique, such as that of Pawley or LeBail is carried out which results in more accurate determinations of cell parameters by the refinement of variables that describe the different features of the diffraction pattern including the unit cell parameters, the background intensity and peak widths, shapes and intensities. [186] PXRD can be important when it is not possible to grow single crystals of a material, offering either the potential for the determination of unit cell parameters or, in favourable cases, structure solution.

PXRD has a number of applications related to the features of a PXRD pattern. Peak positions and their relative intensities serve as a 'fingerprint' for any crystalline material. This means that a PXRD pattern of a sample can identify the presence of a single component, a mixture and its phase composition, [14] structural changes as a function of an external variable such as temperature leading to new materials [187] or the preferred orientation of crystallites by a distortion of peak intensities. [188] Preferred orientation may occur in a powder sample when crystallite shape is increasingly anisotropic, such as plate or needle-like, resulting in distinctly non-random orientations due to natural preferences in packing of the anisotropic particles. The orientation of the crystallites is less random creating preferred orientation axes from which the intensity of reflections with reciprocal lattice vectors parallel to these axes are distorted. [188]

2.8 Thermal analysis of solids

The thermal analysis of a solid may allow its thermal properties to be determined. Once the structure of a material is obtained using X-ray crystallographic methods, it is then possible to link any observed properties to its structure. Thermal properties of crystalline materials frequently include thermally induced phase transitions. A phase transition involves the conversion of one phase of a substance to another phase and is often accompanied by a change in enthalpy; the rearrangement of atoms or molecules usually requires the intake (endothermic process) or results in the release (exothermic process) of energy. [189] In crystalline materials, thermal transformations include solid to liquid (melting), liquid to solid (recrystallisation) and solid to solid transformations; the last of these can correspond to structural rearrangement such as transition between polymorphs or loss of trapped guest molecules such as solvents. [14] By performing thermal analysis on materials, it may be possible to understand the structural transformations occurring. [190]

2.8.1 Differential scanning calorimetry

Differential scanning calorimetry (DSC) is a thermal analysis method which allows the thermal properties of a crystalline material to be studied and quantified.

A heat-flux DSC is commonly used to study crystalline samples. A typical heat-flux DSC set up involves a sample chamber, isolated from the external environment, and two disks that operate as temperature sensors and heaters (sample and reference). The crystalline sample is enclosed in a pan and placed on the sample heater whilst an empty sealed pan is placed on the reference heater (Figure 2.16). [191]

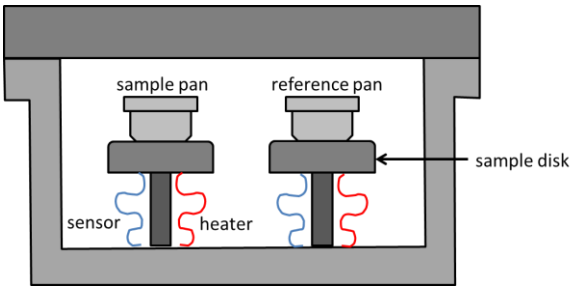

Figure 2.16 Sample chamber used in DSC, including sample and reference pans placed on sample disks connected to temperature sensors and heaters.

The sample disks with sensor/heater components work together in two control loops. One loop acts to increase the temperature of the sample and reference pans, during an experiment, at the same constant rate, which is recorded. The second ensures that, if a temperature difference occurs between the sample and the reference, as a result of a phase transition, the heat input is adjusted to remove this difference. The sensor records this difference between the heat flow to the sample and

reference (*dH/dt*) during an experiment as a function of temperature. [192] The heat flow is affected by the heat flux (*dQ/dt*), the heat capacity of the sample including the pan, C_s, the heat capacity of the reference including the pan, C_R, the temperature at constant pressure, T_P, and the thermal resistance of heat transfer to the chamber disks, R (Equation 2.31). A positive value of (*dH/dt*) corresponds to an absorbed thermal energy, caused by an endothermic transformation, whilst a negative value of (*dH/dt*) corresponds to a release of thermal energy, caused by an exothermic transformation. When (*dH/dt*) is null (no transformation), the heat capacity of the sample can be obtained using Equation 2.31. [193, 194]

Equation 2.31 $$\left(\frac{dH}{dt}\right) = -\left(\frac{dQ}{dt}\right) + (C_s - C_R)\left(\frac{dT_P}{dt}\right) - RC_S\left(\frac{d^2q}{dt^2}\right)$$

Examples of the type of endo and exothermic transitions observed in a typical ("exo up") DSC curve are shown in Figure 2.17. Endothermic transitions occur as dips whilst exothermic transitions occur as peaks. Types of endothermic transitions include solid to liquid transformations such as melting and loss of trapped guest molecules such as desolvation. In these transitions, the atoms/molecules take in energy in order to break away from the rigid structure. Types of exothermic transitions include liquid to solid transformations such as recrystallisation and often occur after a melt. [190] DSC curves can provide information about these transformations such as the onset temperature, the heat related to the transformation and transformation rate. [192]

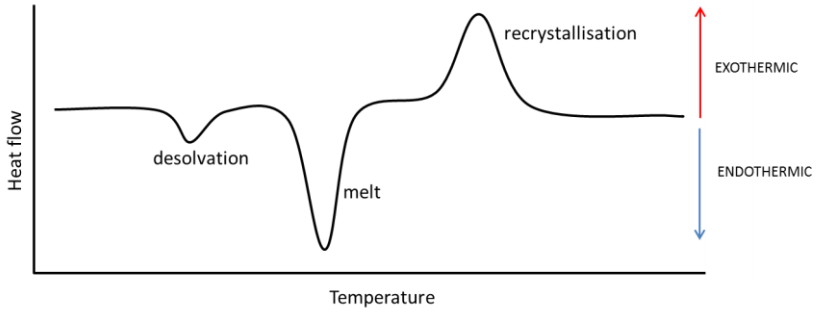

Figure 2.17 A DSC curve showing endo and exothermic transitions observed in crystalline materials.

DSC has a number of applications in addition to identifying thermal transitions including in the detection and determination of relative stability of polymorphic solid forms of a material, indicated by melting points (the higher melting polymorph is the more thermodynamically stable) [195] and identifying inclusion behaviour in materials; broad endotherms in the DSC curves indicate guest release. [196]

2.8.2 Thermogravimetric analysis

Thermogravimetric analysis (TGA) permits the mass of a crystalline sample to be continuously weighed as a function of temperature. [192] This is achieved in a setup which involves the sample being placed in a tared crucible on a precision balance which is positioned in a furnace (Figure 2.18). The precision balance records the mass of the sample during the experiment.

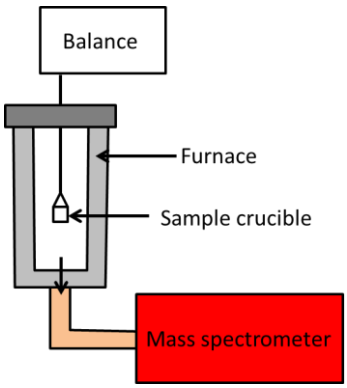

Figure 2.18 A TGA setup, coupled with a mass spectrometer.

In a TGA experiment, frequently the mass loss of a material is followed with temperature and the results are plotted in a mass loss curve (Figure 2.19) of sample weight% (Equation 2.32) versus temperature; mass loss is indicated by a 'step' in the curve.

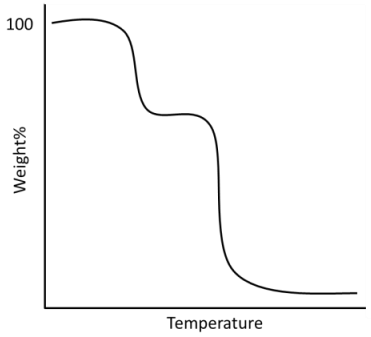

Figure 2.19 A typical TGA mass loss curve with temperature; each step corresponds to a mass loss from the sample.

Equation 2.32 $$\boldsymbol{Weight}\% = \frac{\boldsymbol{M_i - M_T}}{\boldsymbol{M_i}}$$

where M_i is the initial sample mass and M_T is the sample mass at temperature, T.

TGA may allow a number of characteristics of a material to be determined. Thermal stability of a material is indicated by the temperature of the first mass loss step (if any). [14] If a material is multi-component and the sample is pure, the size of each of the mass loss steps can indicate the ratio of

components [197] as well as the decomposition pathway of the material, including revealing its kinetics. [198] TGA may also indicate the ability of solids to retain guests and the temperature of their release. [199]

TGA coupled with mass-spectrometry

By coupling TGA with mass spectrometry, it is possible to confirm the identity of the component lost in a single mass loss step observed in TGA and indicated by endothermic events in DSC curves. In setting up the TGA-MS experiment, the mass spectrometer can be programmed to detect signals from certain molecular fragments as a function of TGA experiment time. [200] The technique is particularly useful in confirming guest loss from inclusion compounds. [201]

Chapter 3.

Aims and Objectives

In the research project upon which this thesis reports, the use of the technique of synchrotron X-ray diffraction is explored for the study of proton transfer processes in hydrogen bonded molecular complexes. These processes play an important role in a number of biological, chemical and physical phenomena. By the study of proton transfer processes in model systems, including those exhibiting both dynamic (proton disorder and migration) and static proton transfer behaviour, additional insight into the subtleties of these processes will be found. In particular, in this research project, we are interested to find where the hydrogen bonds form that exhibit proton transfer and what may 'tune' their transfer behaviour; thereby revealing the perturbation effects on the hydrogen bond potential energy surface.

Synchrotron X-ray diffraction is not commonly employed in the study of proton transfer processes; the method of choice is that of neutron diffraction, allowing a more reliable determination of hydrogen atom behaviour. However, there is a precedent for its application in these studies in previous work by Jones *et. al.* (2013) [97] which demonstrated that it is possible to observe equivalent trends in the proton transfer behaviour from X-ray data as that found from neutron data. There are many benefits to using the synchrotron method, and the associated high source brilliance, in these studies including offering the potential to collect very high quality data, for obtaining good quality Fourier difference maps in which the determination of hydrogen atom behaviour is most reliable for X-ray diffraction, and offering a rapid sample throughput, beneficial in proton transfer studies which are usually carried out as a function of temperature or over a range of molecular complexes and therefore require multiple measurements. In contrast to neutron diffraction, the probing of the electron density by X-ray diffraction, allows additional information about the evolving chemistry of the hydrogen bond to be found. It is hoped that this research project can contribute to making routine the use of synchrotron X-ray diffraction for the reliable determination of proton transfer behaviour such that the additional subtleties can be explored.

Two interlinked strands, therefore, comprise the work in this research project, namely (i) a crystal engineering component to target the design of materials (model systems) in which proton transfer behaviour may be studied and (ii) the application of synchrotron X-ray diffraction in the study of the proton transfer behaviour in those molecular complexes prepared. In a third strand (iii), the tuning of proton transfer behaviour will be explored.

For (i), the crystal engineering strand of the research project is driven by the need to have systems in which proton transfer behaviour can be studied by the synchrotron X-ray diffraction technique, in order to allow the development of this methodology. The molecular complexes in this research project are accessed *via* considered and developed crystal engineering strategies which target proton transfer effects. In these strategies, the hydrogen bond and weaker interactions are important; the potential of the hydrogen bond to exhibit a number of functions is also explored.

In carrying out (ii) there are a number of focus points. These include exploring the potential of the synchrotron technique in the study of a number of proton transfer processes including the dynamic processes of proton disorder, proton migration and the static process of proton transfer at different synchrotron sources including the Diamond Light Source, U.K. [1] and Advanced Light Source, U.S.A. [2] A number of data collection strategies are explored to optimise the use of the synchrotron technique in these studies. Different methods of crystal refinement, including implementing a parametric method in Topas-Academic V5.0, [168] are also investigated.

The strands of (i) and (ii) have consequences for (iii), affecting the potential to rationalise the proton transfer behaviour; in particular, this requires the reliable determination of the proton transfer behaviour using the synchrotron technique. Tuning effects are thus investigated for a number of proton transfer processes in the range of solid state organic molecular complexes including those of crystal packing, hydrogen bond donor-acceptor distances and variations in the molecular components.

Chapter 4.

Techniques and Instrumentation

Chapter 4 details the range of techniques and instrumentation used for the preparation and characterisation of the materials under study in this research project in order to realise the research goals outlined in Chapter 3. This is a general overview whilst the more specific details are included in an experimental section in each results chapter.

4.1 Materials preparation

Due to the focus of this research project on single crystal X-ray diffraction methods, the primary aim of the materials preparation was the growth of good quality single crystals of target materials. The target materials were multi-component crystalline molecular complexes.

The required characteristics of the single crystal, including size and quality, were further governed by the diffraction source employed; related to the intensity of the source. At high intensity synchrotron sources, diffraction data can be measured from smaller single crystal samples (less than 50 μ in all dimensions) compared to on an in-house laboratory source (crystal dimensions of 100 to 200 μ), where X-ray intensity is lower. The higher intensity of X-rays at a synchrotron source also means that this method is more sensitive than the home sources to crystal defects such as mosaic spread, defined as the degree of alignment and identical nature of the crystal unit cells, [141] or tiny crystallites on the surface of the crystal and so requires crystals of higher quality. Single crystallinity was also important for materials characterisation *via* the non-diffraction technique of hot stage microscopy (HSM). Analysing a single crystal in HSM ensures thermal transitions are clearly observed and can be attributed to a pure material. For some of the characterisation techniques performed during the work in this research project, the growth of micro crystalline powders was sufficient. These techniques include powder X-ray diffraction (PXRD), differential scanning calorimetry (DSC) and thermogravimetric analysis coupled with mass spectrometry (TGA-MS); for PXRD, the sample was required to be highly micro crystalline for a good resolution of diffraction peaks to observe changes in the diffraction peak positions for example as a result of a phase change.

4.1.1 Crystallisation

The growth of single crystals of single and multi-component molecular complexes is achieved *via* the process of crystallisation. A number of crystallisation methods are commonly employed including the slow evaporation of solvent (evaporative crystallisation), vapour diffusion, slow cooling and using batch or continuous methods. [195, 202]

The molecular complexes in this research project were prepared *via* evaporative crystallisation, a simple method that is commonly employed for single crystal growth and one that is largely successful, [203] [204] though it may be affected by crystallisation parameter variation. [205] The general experimental procedure of evaporative crystallisation involves the dissolution of target components in a 7 mm^3 glass vial with a 1 to 2 ml of volatile solvent. The target components are present in chosen stoichiometric ratios and usually with masses of each component in the range of 20 to 50 mg (1.25 to 2.5 x 10^{-4} mol). The stoichiometric ratios are often varied including a common choice of 1:1, 1:2 or 2:1 ratios, which may lead to variation in the ratio of the components in the formed molecular complex; the stoichiometric ratio of components in the crystallisation is, however, not always carried through to the molecular complex formed. Complete dissolution of components is important to allow recrystallisation of a new multi-component material from solution. [206] Dissolution is achieved either by agitation by hand, where components are more soluble, or using a sonicator with gentle heating, where solubility of components was lower. The crystallisation vial is sealed with a plastic cap in which holes are pierced (6 to 10 holes) to aid the slow evaporation of solvent. The sealed crystallisation vial should then ideally be left undisturbed during the crystallisation process. This may be at ambient temperature or in a controlled temperature environment. Over a period of time, the solvent evaporates from the vial increasing the concentration of the components in solution. Crystallisation then occurs when the concentration reaches supersaturation and the point of crystal nucleation (Figure 4.1). Single crystal samples may be taken from solution for analysis or the crystallisation vials may be left to dry completely at ambient conditions until studied.

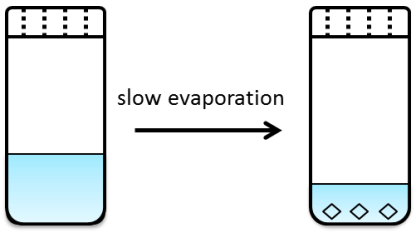

Figure 4.1 Crystallisation *via* the slow evaporation of solvent.

A number of parameters can be varied in the crystallisation procedure which may affect the sample reaching the supersaturation and crystal nucleation points; this has consequences for crystal

growth and crystallisation outcome. [205] Variations in the crystallisation procedure may therefore allow different crystal forms to be accessed or, where some crystallisation conditions are more successful than others, allow improved crystal growth. In the preparation of the molecular complexes during the experimental work conducted in this research project, the parameters of solvent and temperature were varied.

The choice of solvent in evaporative crystallisation can affect the crystallisation outcome related to component solubility, in a chosen solvent, as well as its volatility. Polar and non-polar, protic and aprotic solvents were trialled in the molecular complex preparation component of the research project including methanol, ethanol, acetonitrile, acetone, tetrahydrofuran (THF), ethyl acetate, water, diethyl ether, hexane and cyclohexane. In some cases, a combination of solvents was employed. Before each crystallisation experiment, the solubility of the target components in each solvent was trialled; the solubility of components in certain solvents is largely affected by their polarity where like usually dissolves in like. Solubility is important, since in order for recrystallisation of a component from solution, it must first be dissolved. Ideally, moderate and similar solubilities of the target components is preferred; in a two component solution, if one component is more soluble in the crystallisation solvent than the other, the less soluble component is likely to recrystallize alone first and without molecular complex formation. It is also important to consider the volatility of the solvent as this may affect evaporation rate which has consequences for crystal formation; solvents with a lower volatility evaporate more slowly whilst slower evaporation rates yield larger crystallites. In some cases, solvent may be co-crystallised alongside the target materials occupying holes in the crystal lattice; this may lead to the formation of hydrates or solvent inclusion complexes.

The choice of crystallisation temperature in evaporative crystallisation may also affect the crystallisation outcome related to the rate of solvent evaporation at each temperature; solvent evaporation occurs more quickly at higher temperatures whilst a quicker evaporation rate leads to the formation of smaller crystallites. A range of temperatures were trialled in the molecular complex preparation component of the research project including at 5, 20, 25, 30, 40 and 50 °C. The elevated temperatures (25 to 50 °C) were achieved using welled hot-plates (Figure 4.2) which were set to be held at a fixed temperature. The crystallisation vial was placed into a hot-plate well until all solvent was evaporated, at which point the sample is removed from the hot plate as further heating may lead to degradation of the sample. Crystallisation vials were also placed in the fridge, at 5 °C; this slowed the rate of evaporation and crystal formation.

Figure 4.2 Welled hot plates for crystallisation at elevated temperatures of 25, 30, 40 and 50 °C.

Once crystalline precipitates have formed, it may be favourable to test their stability to solvation; solvation may lead to solvent inclusion complexes. A method of vapour diffusion is employed and involves placing single crystal or powdered samples of a material into a vial into a sealed solvent environment (Figure 4.3). Over time, the solvent vapourises and diffuses into the dry sample, where the solvent concentration is low. This can lead to a solvated material.

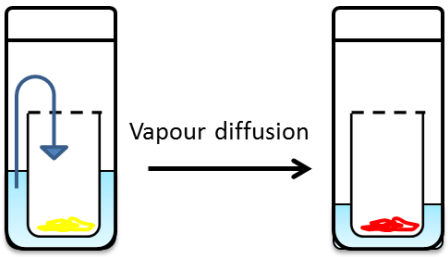

Figure 4.3 The process of vapour diffusion of solvent.

In this setup both the temperature and solvent choice can be varied, altering the rate of vapour diffusion; an increased temperature or volatility of the solvent increases the rate of vapour diffusion. Vapour diffusion was carried out in this research project to attempt the formation of solvent inclusion materials from non-solvated forms. The set up involved placing a powdered sample of a material in an open 7 mm^3 vial in a 100 ml sealed bottled with approximately 20 ml of solvent and leaving for up to 24 hours at a range of temperatures.

4.1.2 Crystal evaluation

The precipitates resulting from the crystallisation trials carried out in this research project were initially evaluated using optical microscopy. This method allows a range of information about the precipitates to be determined including crystalline nature and identity. This aids in determining the next appropriate experimental steps; indicating the most suited characterisation method for each precipitate or the need for additional crystallisation experiments.

The crystalline nature of the precipitate could be identified whether single crystals, micro crystalline powders or oils were formed. For those forming single crystals, their suitability for single crystal X-ray diffraction studies can be assessed in the quality of the crystal edges and faces or on crystal manipulation such as by cutting. The formation of non-single crystalline products in some cases, such as powders and oils, may indicate the need for the investigation of different crystallisation conditions. Where powders are formed, they may be characterised using powder X-ray diffraction (§4.3).

Information about the likely identity of the products may also be found using optical microscopy. A new product, whether single or multi-component, may be identified if there is a change in morphology or colour in the crystallisation product from the starting materials. The presence of a single morphology product formed from a two component crystallisation may indicate the formation of a multi-component system. The presence of multiple phases with differing morphologies and/or colours in the crystallisation vial may indicate the formation of multiple products. This could be an indication that a molecular complex has not formed and that the starting materials have crystallised separately. Additionally, a molecular complex may have formed alongside a starting material or molecular complexes of different crystal forms are present.

Of the crystalline precipitates formed from the crystallisation trials carried out in this research project, characterisation of single crystal samples was carried out using single crystal X-ray diffraction (§4.2) whilst powder crystalline samples were characterised using powder X-ray diffraction (§4.3).

4.2 Single crystal X-ray diffraction

Single crystal X-ray diffraction was performed on suitable single crystal samples resulting from the materials preparation component of this research project. Unit cell screening was first carried out on suitable single crystals resulting from the crystallisation trials *via* single crystal X-ray diffraction analysis to identify where new products had formed. The unit cell of the crystal under study was compared to those in the Cambridge Structural Database (CSD) [3] to confirm the formation of a new crystal structure, previously unreported and different to that of the starting materials or existing molecular complexes. Where a new crystal structure was indicated, single crystal X-ray diffraction analysis was carried out for crystal structure determination. The structures presented in subsequent chapters were determined using single crystal X-ray diffraction, conducted using both laboratory and synchrotron sources; the synchrotron sources were employed

for variable temperature or high throughput measurements. The experimental procedure was generally the same for both types of source.

4.2.1 Sample selection

The selection of single crystals for diffraction studies is carried out using polarised light microscopy. A good single crystal sample is one that appears visually of good quality with well-defined crystal edges and faces and free from tiny crystallites or cracks. Single crystallinity is important for the diffraction to occur as individual reflections [141] and is indicated for a crystal when extinguishing in plane polarised light on a 90 ° rotation. A good single crystal sample is also one that is of a certain size or one that can be cleanly cut to the appropriate size. Typically, crystal sizes with dimensions of 100 to 200 µ are recommended for laboratory sources whilst less than 50 µ can be measured at synchrotron sources; crystal size is dependent on X-ray source size as well as goniometer head sphere of confusion. The selected crystal is mounted on a glass fibre or loop attached to a magnetic mount using either fomblin or glue depending on the nature of the experiment. The magnetic mount is then placed on the diffractometer goniometer head. The temperature of the diffraction experiment is set and, once at the desired temperature, the crystal is centred in the X-ray beam position by adjustments to the vertical and horizontal axes of the goniometer head.

4.2.2 Screening, data collection and data processing

The process of collecting diffraction data from a single crystal, once mounted and centred at the desired temperature, involves a number of stages including crystal screening, data collection and data processing.

Initial screening is carried out *via* a 'pre-experiment' which involves the collection of a number of diffraction images from the crystal, when rotated through different positions. These screen images have a number of uses including indicating the diffraction quality of the sample, the identity of material forming the crystal (whether something new or previously reported) and the strategy required to collect a complete data set to allow crystal structure determination; all important factors for deciding whether or not to proceed to the data collection stage with a sample. The diffraction quality of the crystal is assessed in the intensity, peak shape and resolution of the reflections on the diffraction images. A crystal of good diffraction quality has reflections that have a good intensity and occur to a high resolution (typically $d_{min} < 0.84$ Å), that do not overload at low angle and which are not split. The reflections from the screen images are assigned *hkl* indices and used to determine the orientation matrix, unit cell parameters (a, b, c, α, β, γ) and Bravais lattice *via* an auto-indexing procedure. At this stage, the determined unit cell parameters should be

checked against those of existing materials to confirm a new material has been formed before commencing the data collection stage.

Once a new material is confirmed and a crystal of good diffraction quality is found, a full data collection for crystal structure determination can be carried out. A recommended data collection strategy is output at the end of the pre-experiment. The strategy suggests the required exposure time per diffraction image to obtain diffraction data to the required resolution, values of I/σ and completeness for accurate structure determination from the data collection. These parameters may change depending on experimental requirements but are typically d-spacing 0.8 Å resolution, an I/σ of 15, a redundancy of 5 and a completeness of 98 %. The extent of reciprocal space to be accessed during the data collection is also decided on, in terms either of the requirements of the unique data for the particular crystal system or in portions of the limiting sphere. The collection of a full hemisphere of data, if time allows, is recommended as this allows all unique data to be accessed even for the lowest symmetry triclinic system. The width of the diffraction image should also be considered depending on crystal mosaicity; image width should be less than the crystal mosaicity to enhance reflection sampling. The time for a full data collection may be affected by sample size and quality or X-ray source intensity and can be anything between 2 to 24 hours for laboratory diffractometers whilst for synchrotron sources the data collection can be completed in as little as 10 minutes. In some cases, the recommended full data collection time may be longer than the available experimental time; in these cases it is worth restarting the screening process. The result of the data collection process is a list of reflections that have assigned *hkl* Miller indices and a measured intensity. Each intensity has an associated standard uncertainty *σ(I)* which indicates the precision and reliability of the experiment; affected by both X-ray generation and diffraction experiment processes.

The data is processed *via* a 'data reduction' method that involves a number of stages. A redetermination of the unit cell is carried out *via* indexing of the Bragg reflections to determine their Miller indices *hkl* over a larger portion of the data and to obtain an improved set of unit cell parameters. This is followed by an integration step which integrates the intensity, in pixel counts, of each *hkl* reflection across the diffraction images. The intensities are corrected for background counts, these are estimated and removed, followed by additional Lorentz-polarization and absorption corrections. [207] A merging and averaging process of the repeated and symmetry equivalent data is then carried out to produce a set of unique and scaled data. The final intensities are converted to observed structure amplitudes $|F_o^2|$ (Equation 2.11) and the output is a list of reflections with *hkl* indices, intensity $|F_o^2|$ and with standard error $\sigma|F_o^2|$. [141]

Data collection and processing were performed in this research project using a number of software packages including Rigaku [208] CrystalClear™, [209] Rigaku Oxford Diffraction [210] CrysAlisPro, [211] DIALS [212] in Xia2, [213] Bruker AXS [214] Apex2 [215] with SADABS [216] and Bruker AXS [214] XPREP. [217]

4.2.3 Crystal structure solution and refinement

The theory of structure solution and refinement is described in §2.3 and §2.4, respectively. The process involves the location of atoms in the unit cell from the diffraction data for structure solution followed by optimisation of the solved structure *via* refinement.

In this research project, all crystal structures were solved by direct methods (§2.3.3) using the program SHELXS-2013 [218] followed by crystal structure refinement *via* a least-squares method using SHELXL-2013. [219] Where necessary, the programme PLATON [220] was used to check the space group assignment. All programs were used within the WinGX program suite. [221] In general, non-hydrogen atoms were refined freely with anisotropic thermal parameters. All hydrogen atoms were refined with isotropic thermal parameters and treated by a mixed of independent and constrained refinements. The specific refinement details for the treatment of the hydrogen atoms of interest are included in the experimental sections of each chapter. Crystal structures were viewed and analysed using the structure visualisation program Mercury. [222] The imaging of the hydrogen atom scattering density is carried out in two dimensional Fourier difference maps in the region of specific hydrogen bonds generated with the hydrogen atom of interest removed from the structural model. The Fourier difference maps are viewed in MAPVIEW within WinGX. [221] Additional programmes were used for crystal structure refinement *via* alternative methods. Jana2006 [223] was employed to allow the TLS refinement of anisotropic displacement parameters. In the refinement, a fully refined starting model from SHELXL-2013 [219] was input in which the hydrogen atom positions were recalculated and refined and each molecular component was modelled as a rigid body with TLS refined anisotropic displacement parameters.

Topas-Academic V5.0

Crystal structure refinement was also carried out in this research project using the program Topas-Academic V5.0. [168] Topas-Academic V5.0 [168] is a non-linear least squares system driven by a scripting language which may be employed in the fields of crystallography, solid state chemistry, optimisation and function minimisation. Its main features include a computer algebra system for function minimisation and linear/non-linear constraint applications, least squares refinement (including Rietveld methods) for single crystal and powder diffraction data (laboratory, neutron and synchrotron), a simulated annealing algorithm for structure solution from single crystal and powder X-ray diffraction data, an indexing algorithm and a command line TC.exe for batch data

processing. [168] In this research project, Topas-Academic V5.0 [168] was used for the purpose of single crystal structure refinement. The advantage of its use in this work, over standard single crystal refinement packages, is the potential to perform parametric refinements (§2.4.4) in which a single structure is refined simultaneously against a number of datasets.

The single crystal structure refinement method is based on the method originally developed for parametric Rietveld refinement, most commonly used in powder X-ray diffraction and one of the final stages of crystal structure determination *via* this method. Rietveld refinement employs a least-squares method *M* (Equation 4.1) to obtain the best fit between the experimental powder diffraction pattern (y_{obs}) and that calculated (y_{calc}) from a trial structure (this must be a good representation of the correct crystal structure to avoid leading to false minima); every point along the observed and calculated profiles are considered as an intensity measurement and compared. [224]

Equation 4.1 $$\boldsymbol{M = \sum_i w_i (y_{iobs} - y_{iobs})^2}$$

where y_{iobs} and y_{icalc} are the intensity of the ith data point in the experimental and calculated powder diffraction profiles, respectively, and w_i is a weighting factor for the ith data point.

The powder pattern is calculated for the trial structural model using the information of (1) the lattice parameters (to determine peak positions), (2) atomic positions and thermal parameters, (3) 2Θ-dependent functions that describe peak shape (affected by features of both the instrument and sample) and width and (4) a description of the background intensity. Selected parameters are adjusted by the least-squares refinement method to achieve the best fit between the observed and calculated powder patterns (Equation 4.1); achieved by turning parameters on or off within the input file. Additional parameters related to the sample, including sample height, may additionally be refined. The refinement is driven in Topas-Academic V5.0 [168] by an instruction file (inp file), edited in an external text editor programme JEdit V4.3, [225] which connects to the Topas-Academic V5.0 [168] GUI.

The agreement between the observed and calculated powder patterns is assessed by an R-factor R_{wp} (Equation 4.2); a good fit is indicated by R_{wp} values within the region of 5 to 20 %. [226] A visual comparison is also made on plotting the observed and calculated patterns alongside a difference curve ($y_{obs} - y_{calc}$) (Figure 4.4); the smaller the difference curve the better the fit.

Equation 4.2 $$\boldsymbol{R_{wp} = 100 \times \left(\frac{\sum_i w_j (y_i(obs) - y_i(calc))^2}{\sum_i w_j (y_i(obs))^2} \right)}$$

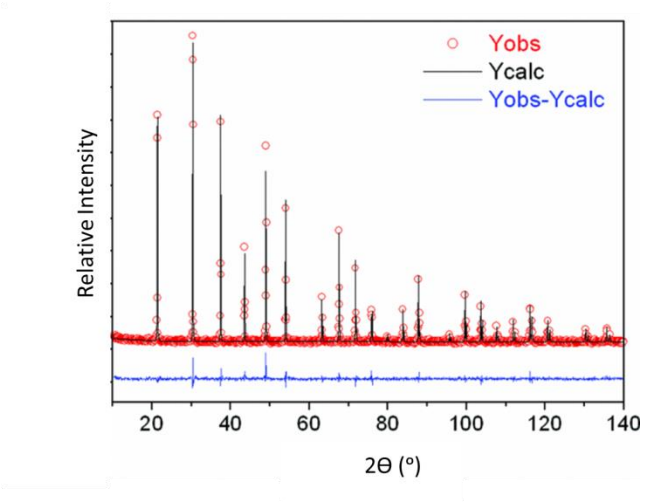

Figure 4.4 A plot of y_{obs}, y_{calc} and the $y_{obs} - y_{calc}$ difference curve versus 2Θ. [227]

In a single crystal structure refinement in Topas-Academic V5.0, [168] the least-squares method *M* (Equation 4.1) is also employed to obtain the best fit between a structure and the data. This method differs from the powder Rietveld refinement in that there is a greater certainty in the starting model, which can be obtained by a single crystal refinement of the same data in SHELX-2013. [219] The parameter y_{obs} is also different due to the data being a processed *hkl* reflection file which does not contain any peak shape or background information, and also does not suffer from the problems of peak overlap in powder data. The powder pattern y_{calc} is therefore calculated for the trial structural model using the information of (1) the lattice parameters (to determine peak positions) and (2) atomic positions and thermal parameters. During the least-squares minimisation, selected parameters within (2) are optimised, including the atomic positions and thermal parameters, to achieve the best fit between the observed and calculated powder patterns. A weighting scheme on y_{obs} may also be applied to optimise the best fit. The unit cell parameters are not refined, being determined within the single crystal data reduction that produced the *hkl* reflection file. As in the Rietveld refinement, the fit is indicated by R_{wp} factors and on plotting the observed and calculated patterns alongside a difference curve ($y_{obs} - y_{calc}$) (Figure 4.5). The refined structure can also be viewed within the Topas-Academic V5.0 [168] GUI.

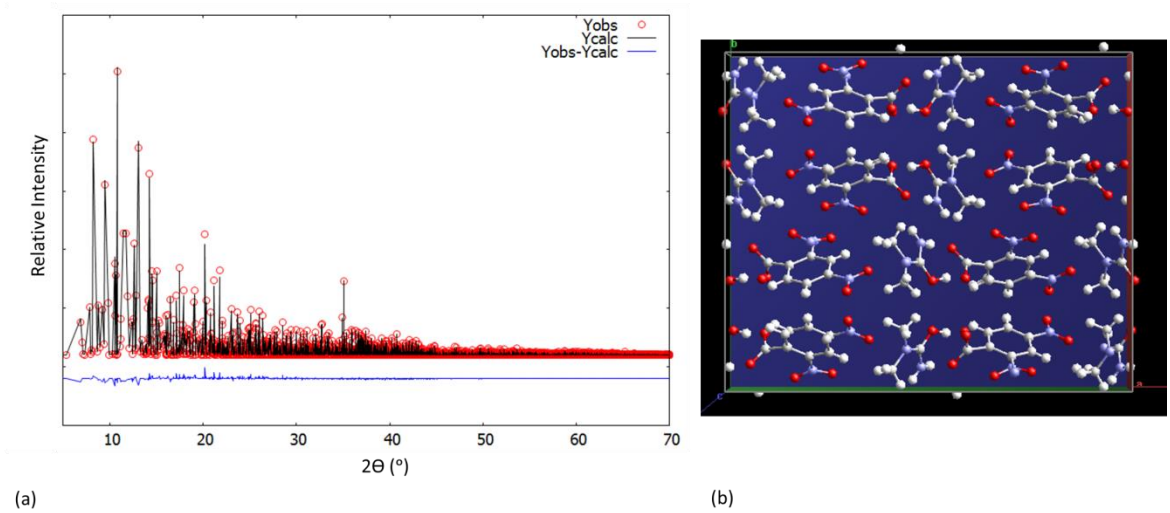

Figure 4.5 (a) A plot of y_{obs}, y_{calc} and the $y_{obs} - y_{calc}$ difference curve versus 2Θ for a single crystal *hkl* reflection file and (b) the 'view structure' option in the Topas-Academic V5.0 [168] GUI.

The use of Topas-Academic V5.0 [168] in this research project enabled single crystal refinement to be conducted over a number of variable temperature data sets using a parametric method (§2.4.4). This allowed the behaviour of certain parameters to be followed or driven over the temperature range whilst having advantages of an increased accuracy of parameters and a reduction in processing time.

4.2.4 Variable temperature measurements

The study of the proton transfer processes in the molecular complexes during the work in this research project required crystal structure determination at multiple temperatures, where proton migration and proton disorder are temperature dependent effects. This allowed the evolution of the hydrogen bond to be followed, including shifts in the refined hydrogen atom positions or changes in the occupancy of the proton sites in the hydrogen bond, as a function of temperature.

For the molecular complexes in which proton migration was studied, full data collections were first carried out in-house using laboratory X-ray diffraction at low (100 or 150 K) and high (300 or 350 K) temperature. This allowed potential proton migration materials to be identified. Multi-temperature measurements were also carried out at synchrotron X-ray diffraction facilities. These multiple temperature measurements were carried out in a range of temperature step sizes, from 10 to 100 K, and in a stepwise or continuous temperature ramping method, depending on the experimental requirements. In these variable temperature experiments, a different crystal mounting was required to that used in the low temperature crystal structure determinations; single crystal mounts with copper bases were used, to enhance the conduction of heat, and the crystal was glued to the loop attached to the mount using araldite to prevent it moving at the higher temperatures.

The sample position was also re-centred approximately every 40 K during the variable temperature measurement to account for expansion or shrinking in the mount on temperature variation.

Using a synchrotron source in the variable temperature measurements was advantageous allowing a more rapid data collection. The more rapid data collection introduced the possibility to probe the proton transfer behaviour at a greater number of points over the temperature profile; this could be done in a significantly shorter time than would be possible on an in-house source.

4.2.5 Laboratory single crystal X-ray diffraction

Four in-house laboratory X-ray diffractometers were used in the single crystal X-ray diffraction studies of the molecular complexes during the work in this research project. These include (1) a Rigaku [208] R-Axis/RAPID diffractometer which has a four-circle goniometer and is equipped with a Rigaku [208] image plate detector. The diffractometer has a standard sealed tube source (Mo-K_α radiation) and uses a graphite monochromator. (2) a Rigaku Oxford Diffraction [210] (formerly Agilent Technologies) Gemini A Ultra diffractometer which has a four-circle κ geometry goniometer and is equipped with an Agilent [228] Atlas CCD detector. The diffractometer has a dual source (Cu-K_α and Mo-K_α radiation) sealed tube with a graphite monochromator. (3) a Rigaku Oxford Diffraction [210] (formerly Agilent Technologies) Xcalibur diffractometer which has a four-circle κ geometry goniometer and is equipped with an Agilent [228] EoS2 CCD detector. The diffractometer has a standard sealed tube source (Mo-K_α radiation) and uses a graphite monochromator. (4) a Rigaku Oxford Diffraction [210] (formerly Agilent Technologies) SuperNova diffractometer which has a four-circle κ geometry goniometer and is equipped with an Agilent [228] EoS2 or Atlas CCD detector. The diffractometer has a dual source (Cu-K_α and Mo-K_α radiation) sealed tube with a graphite monochromator. Diffractometers 1 to 3 were used in-house at the University of Bath whilst diffractometer 4 was used both in-house at the University of Bath and at the Research Complex at Harwell (RCaH).

Despite the variations in the specific components across the diffractometers, their general set-up is the same (Figure 4.6). The four-circle goniometer can achieve rotation of the crystal through the three diffractometer axes ϕ, κ and ω (the fourth is 2θ of the detector) to access all the positions required to collect a complete set of diffraction data. Movement of the detector is also possible to vary the sample-to-detector distance; this may be required for a crystal with long unit cell axes to spread out reflections. A liquid nitrogen flow device (Oxford Cryosystems [229] Cryostream 700 or Oxford Instruments [230] CryojetXL) is additionally employed in the setup; this is aligned to point at the mounted crystal and allows the sample temperature to be controlled or manipulated during a diffraction experiment, such as in the variable temperature measurements. Single crystal diffraction data collections are commonly carried out at low temperature (100 or 150 K) or room

temperature (298 to 300 K). The experimental set-up is encased within an interlocked safety cabinet. Different detectors (§4.2.7) are employed between the Rigaku [208] R-Axis/RAPID (imaging plate) and Rigaku Oxford Diffraction [210] (previously Agilent Technologies) Xcalibur and SuperNova diffractometers (CCD). Each diffractometer is connected to a control computer.

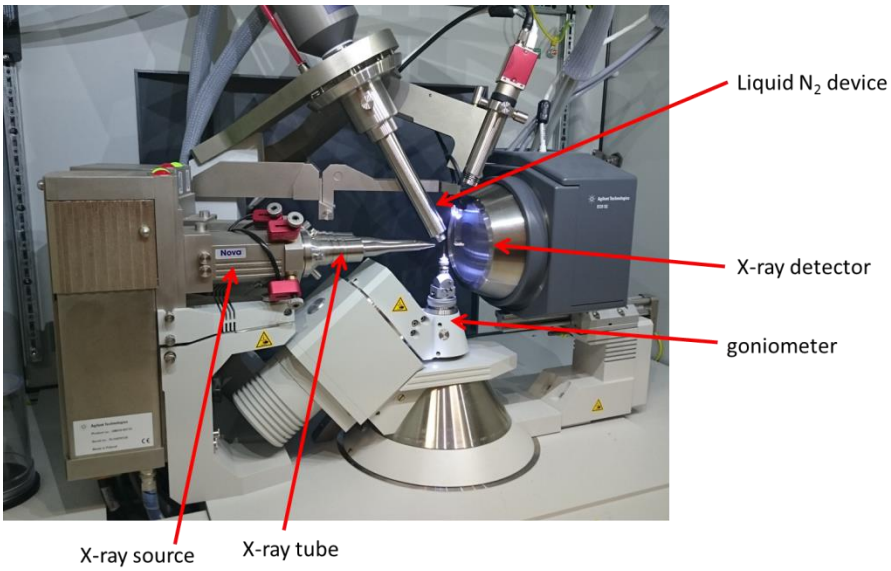

Figure 4.6 The experimental set-up for a laboratory single crystal X-ray diffractometer. Shown here is the Rigaku Oxford Diffraction [210] (previously Agilent Technologies) SuperNova.

Data collection and processing are carried out by software on the control computer and are specific to each type of machine. For the data collection and processing, the Rigaku [208] R-AXIS/RAPID diffractometer uses the Rigaku [208] CrystalClear™ [209] software package and the Rigaku Oxford Diffraction [210] Gemini, Xcalibur and SuperNova diffractometers use the Rigaku Oxford Diffraction [210] CrysAlisPro [211] software package.

4.2.6 Single crystal synchrotron X-ray diffraction

Single crystal synchrotron X-ray diffraction studies of the molecular complexes in this research project were carried out at two synchrotron facilities: Diamond Light Source, U.K [1] on Beamline I19, Harwell and the Advanced Light Source, U.S.A. [2] on Beamline 11.3.1, Lawrence Berkeley National Laboratory. The theory of synchrotron crystallography is described in §2.5. The high intensity of synchrotron X-rays gave two advantages in these studies; (1) the potential to collect good quality data for a more reliable determination of hydrogen atom behaviour and (2) a more rapid data collection for a high throughput of samples increasing the number of examples and number of temperatures across which possible proton transfer behaviour can be studied.

I19, the small-molecule single crystal diffraction beamline at the Diamond Light Source

I19 is a high flux, tuneable wavelength chemical crystallography beamline dedicated to single crystal structure determination including under a variety of conditions and sample environments. [231]

The I19 beamline is on a five metre straight section of the Diamond Light Source, U.K. [1] storage ring. It is supplied by synchrotron radiation being downstream of an in-vacuum undulator insertion device. The beamline schematic is shown in Figure 4.7.

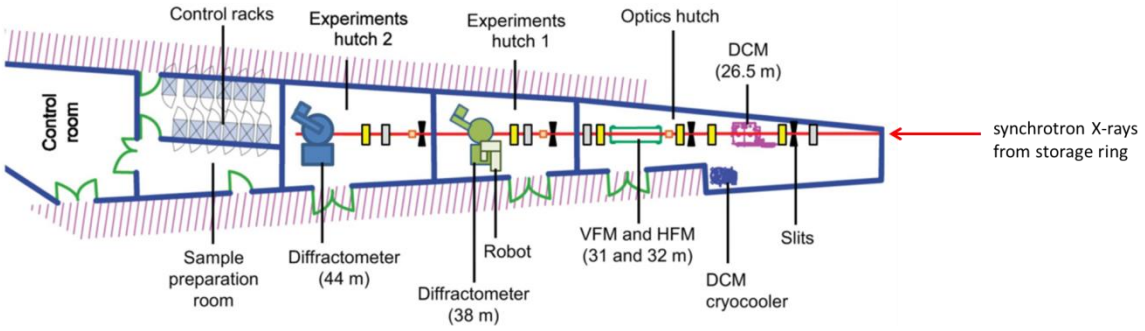

Figure 4.7 A schematic of the beamline I19, [231] Diamond Light Source, U.K. [1]

In the first section of the beamline, in the optics hutch, the wavelength of synchrotron radiation is selected in the 5 to 28 keV range by a cryo-cooled double crystal monochromator (DCM), equipped with Si-111 crystals; the double crystals of the DCM maintains the fixed-exit beam geometry. A pair of bimorph mirrors down-stream of the DCM focus the X-ray beam in the vertical and horizontal axes onto the sample position in the experimental hutches downstream of the optics hutch; the dimensions of the mirrors are matched to the divergence of the beam, and its 3 mrad incidence angle, allowing a maximised beam foot print over the mirrors. The focused beam has a Gaussian profile with a FWHM (full width half maximum) of 90 mm horizontally and 60 mm vertically at the first sample position in experimental hutch 1 (EH1) and 185 mm horizontally and 130 mm vertically at the second sample position in experimental hutch 2 (EH2). The beam size can be varied by defocusing the bimorph mirrors; this allows flexibility on sample size. A number of cameras are located along the beam path to monitor beam position whilst a number of attenuators along the beam path allow flux on the sample to be controlled. [231]

The two experimental hutches downstream of the optics hutch take beam controlled by an X-ray shutter. They house different experimental setups designed to support complementary areas of structural science . Single crystal synchrotron X-ray diffraction studies of the molecular complexes in this research project have been carried out in both experimental hutches. EH1 is designed for high-throughput chemical crystallography whilst EH2 can house significant sample environment

apparatus such as those using a laser and its position downstream of EH1 allows experiment preparation without disrupting the operation of EH1.

During this research project, EH1 (Figure 4.8) has been used in two different modes of operation, pre and post-upgrade. Pre-upgrade, data were collected using Si (111) monochromated radiation at $\lambda = 0.6889$ Å on a Crystal Logic [232] four-circle κ geometry diffractometer equipped with a Rigaku [208] Saturn 724+ CCD area detector. The sample temperature was controlled using an Oxford Cryosystems [229] Cryostream Plus. Data collection was performed using the Rigaku [208] CrystalClear™ [209] software package whilst data processing was performed using the Rigaku Oxford Diffraction [210] CrysAlisPro [211] software package. Post-upgrade, the data were collected using Si (111) monochromated radiation at $\lambda = 0.6889$ Å on a Fluid Film Devices Ltd [233] three-circle diffractometer in fixed χ geometry equipped with a DECTRIS [234] Pilatus 2M detector. The data collection process was controlled through the in-house Generic Data Acquisition (GDA) [235] software whilst the data processing was carried out using the in-house software DIALS [212] in Xia2. [213]

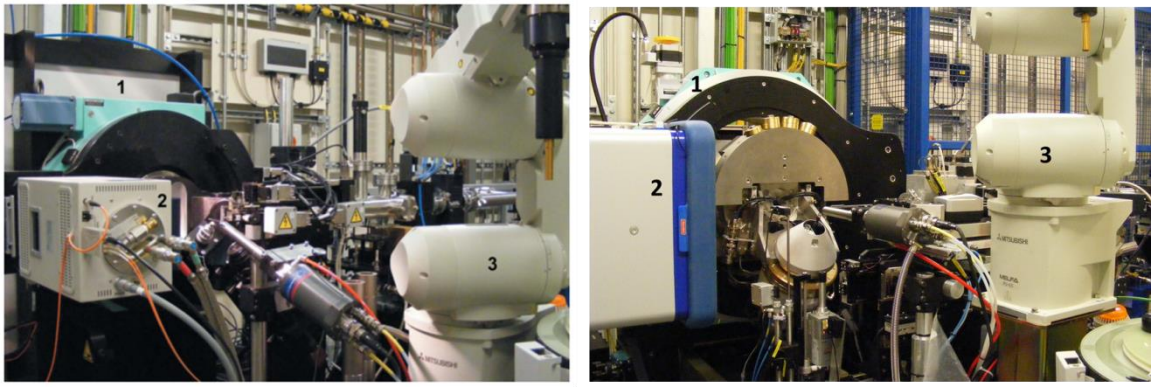

(a) (b)

Figure 4.8 The experimental set up of EH1 on I19 at the Diamond Light Source, U.K. [1] (a) pre-upgrade 1: Crystal logic[232] four-circle diffractometer, 2: Rigaku [208] Saturn 724+ CCD area detector and 3: robotic sample changer and (b) post-upgrade 2: Fluid Film Devices Ltd [233] three-circle diffractometer, 2: DECTRIS [234] Pilatus 2M detector and 3: robotic sample changer.

Data were collected in EH2 (Figure 4.9) using Si (111) monochromated radiation at $\lambda = 0.6889$ nm on a Newport [236] four-circle diffractometer in κ geometry equipped with a DECTRIS [234] Pilatus 300K hybrid pixel detector. The sample temperature was controlled using an Oxford Cryosystems [229] Cryostream Plus. The data collection process was controlled through the in-house Generic Data Acquisition (GDA) [235] software whilst the data processing was carried out using the in-house software DIALS [212] in Xia2. [213]

Figure 4.9 The experimental set up of EH2 on I19 at the Diamond Light Source, U.K. [1] 1: Newport [236] four-circle diffractometer, 2: DECTRIS [234] Pilatus 300K hybrid pixel detector.

Small molecule crystallography beamline 11.3.1, Advanced Light Source

Beamline 11.3.1 at the Advanced Light Source, U.S.A. [2] is dedicated to solving the structure of crystalline materials, too small for a home source, and under a range of experimental conditions. The beamline is on a six metre straight section of the Advanced Light Source, U.S.A. [2] coupled to a storage ring bending magnet allowing operation in the 6 to 17 keV (2 to 0.7 Å) energy range (Figure 4.10). Tuning across the energy range is achieved by a channel cut Si (111) monochromator cooled using a Joule-Thomson refrigerator whilst focusing is carried out by a toroidal mirror, located 14 metres from the X-ray source. [237]

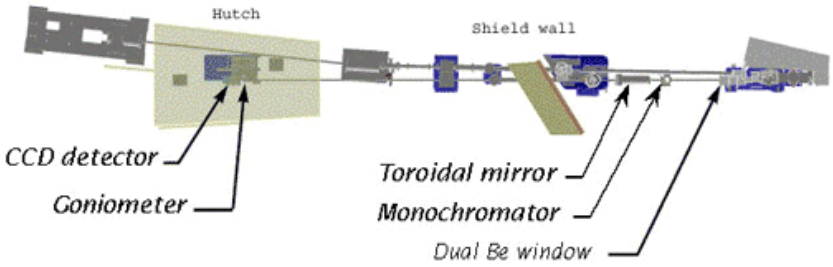

Figure 4.10 A schematic of the beamline 11.3.1, [237] Advanced Light Source, U.S.A. [2]

During this research project, beamline 11.3.1 has been used in two operational modes, pre and post detector upgrade. Pre-upgrade, data were collected using Si (111) monochromated radiation at λ = 0.7749 Å using a Bruker AXS [214] D8 three-circle diffractometer equipped with a Bruker AXS [214] Apex2 CCD detector (Figure 4.11). The sample temperature was controlled using an Oxford Cryosystems [229] Cryostream Plus. The data were collected using the Bruker AXS [214] Apex2 [215]

software and processed using the Bruker AXS [214] Apex2 [215] with SADABS-2012 [216] softwares. Post-upgrade, data were collected using Si (111) monochromated radiation at λ = 0.7749 Å using a Bruker AXS [214] D8 three-circle diffractometer equipped with a Bruker AXS [214] PHOTON 100 CMOS detector. The sample temperature was controlled using an Oxford Cryosystems [229] Cryostream Plus. The data were collected using the Bruker AXS [214] Apex2 [215] software and processed using the Bruker AXS [214] Apex2 [215] with SADABS-2014/5 [216] softwares.

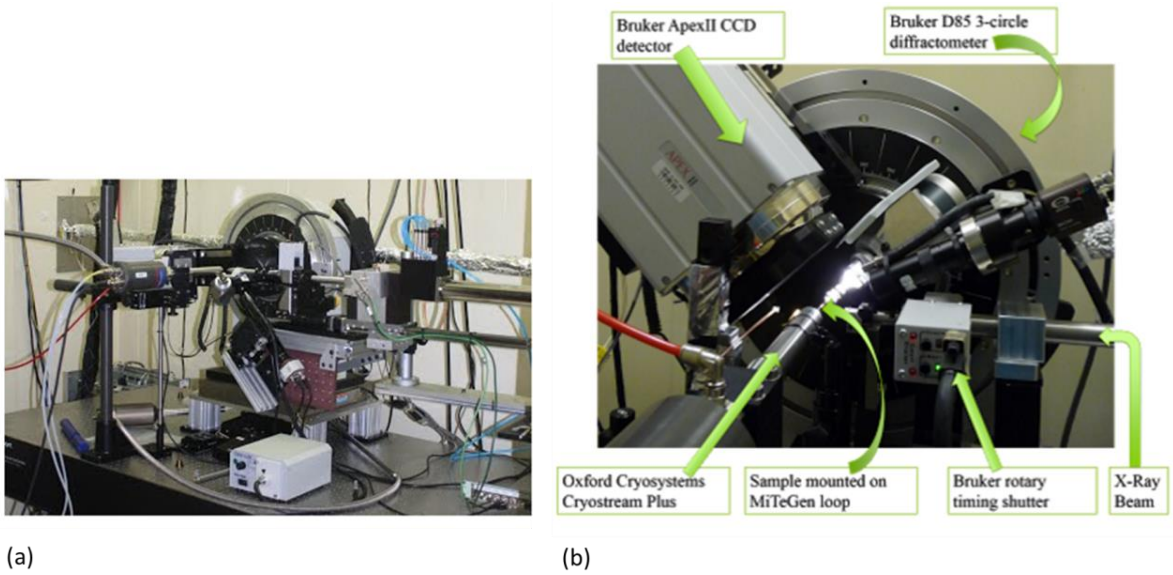

Figure 4.11 Beamline 11.3.1 at the Advanced Light Source, U.S.A. [2] (a) and (b) the experimental set-up pre detector upgrade. [237]

4.2.7 Single crystal X-ray detectors

A critical stage in an X-ray diffraction experiment is the detection of photons from the scattered X-ray. Where the photons are scattered from atomic electrons, they reveal information about molecular composition; the ability of an X-ray detector to count the number of photons with precision will affect the success of the crystal structure determination. [238] In this research project, a number of single crystal X-ray detectors were used in the data collection process. The X-ray detectors vary in the area and the mode of measurement of the diffracted intensities.

Image-plate detectors have a detection surface that, in the case of the instrument used in this project, is curved and made out of a photosensitive plastic sheet. On exposure to X-rays, a colour centre is created which is then read out, as a digital image, by a laser which scans across the photosensitive sheet. Image plates have high efficiency and high dynamic range and sample a large diffraction area. These detectors require long exposure and read out times (minutes) and so are less suited to synchrotron X-ray diffraction studies where, with the possible short exposures, the long read out time would slow an experiment down. [239] Image plate detectors are therefore also less

suited to variable temperature measurements; to collect at a number of temperatures would require a large amount of experimental time. The use of image plates for single crystal structure determination is, however, routine, particularly in the area of protein crystallography.

CCD (charge coupled device) detectors, such as the Agilent [228] CCD EoS2 or Atlas and Bruker AXS [214] APEX2 detector, have a significantly shorter exposure and read out time (seconds) in comparison to image plate detectors. [239] A CCD detector has the shape of a truncated cone with a phosphor at the wider end which produces visible light in response to X-rays. The pattern on the phosphor is then coupled, *via* fibre optics, to the CCD chip at the tapered end which encodes the resulting signal; [155] the read-out from the CCD chip occurs in a pixel-to-pixel manner *via* charge transfer. [156] The coupling and pixel-to-pixel charge transfer processes for CCD detectors can result in noise issues whilst blooming is also a problem; involving the overflow of potential wells into neighbours which results in a wrong intensity measurement. [238] These detectors are, however, widely used in diffraction studies and have been optimised to account for these problems. The faster read-out than image plate detectors makes these detectors well suited to use in synchrotron X-ray diffraction studies being able to cope with the shorter exposure times allowing complete data sets to be collected in a short amount of time.

Active pixel (AP) complementary metal oxide (CMOS) detectors such as the Bruker AXS [214] PHOTON 100 CMOS detector also use a phosphor layer to detect the X-rays, *via* the photoelectric effect, as AP CMOS chips cannot directly read X-rays. Optical coupling then transfers the resulting electronic signal to the CMOS chip occurring, in contrast to CCDs, per pixel in an independent manner *via* the AP sensor. [156] Due to the independent pixel read-out, image processing is more complicated to address the pixel to pixel non uniformities whilst the optical coupling means noise can also be an issue with these detectors. [239] CMOS detectors can, however, operate without the need for a mechanical shutter. This means faster image read outs are possible; this is advantageous in both synchrotron and variable temperature studies.

Pilatus hybrid pixel detectors such as the DECTRIS [234] Pilatus 300K and 2M are photon counting devices which perform direct detection of X-rays. They consist of a sensor layer (silicon pixels) which converts X-rays directly into electrical signal counted by a detector. [238] Features of these detectors include wide dynamic range, very short read out time (3 μs), shutterless operation, no read-out noise and a very high count rate leading to a good signal to noise ratio. The sensitivity and dynamic range of hybrid pixel detectors addresses the need to collect weak scattering alongside stronger signals, important in diffuse scattering studies. [240] Due to the very short read out times Pilatus detectors are well suited to both synchrotron and variable temperature measurements allowing complete data sets to be collected in a short amount of time. The good signal to noise

ratio offered by these detectors may also improve observation of the weakly scattering hydrogen atom in the proton transfer studies undertaken here. [121, 122]

4.3 Powder X-ray diffraction

Powder X-ray diffraction (PXRD) is an additional diffraction method used in the evaluation of the crystallisation products formed by slow evaporation of solvent; polycrystalline samples are those where crystallites are too small for single crystal X-ray diffraction studies. PXRD is a non-destructive method that requires little sample preparation and has a number of applications allowing both structural and phase information to be obtained. It is most widely used in phase identification (finger printing). A powder diffraction pattern is characteristic of a crystalline material and so, by comparing the powder diffraction pattern of a sample to simulated powder diffraction patterns of existing molecular complexes or starting materials, crystalline phases may be identified including new materials or different polymorphic forms and whether a mixed phase is present or if phase pure; in single crystal analysis it may also be of interest to determine whether a single crystal represents the bulk from which it was taken. Rietveld analysis can be carried out on mixtures of known components to determine their phase composition (quantitative phase analysis). Information about the microstructure of crystallites including morphology can also be obtained from a powder diffraction pattern.

Phase transitions, as a result of molecular rearrangements and caused by external variables such as temperature, pressure or time, may also be followed in crystalline materials using powder diffraction. This is of importance as the majority of molecular rearrangements occur *via* a single crystal to powder phase transition. In these cases, powder X-ray diffraction data are collected as an external variable is applied to the sample *in-situ*. Phase transitions are then indicated by shifts in the diffraction peaks of the powder patterns as a function of the external variable.

In favourable circumstances, it is possible to carry out indexing of a powder pattern to obtain unit cell parameters and space group information; the diffraction pattern should be of good quality with a good resolution of diffraction peaks. This is done using indexing programmes such as DICVOL [241] or Topas-Academic V5.0 [168] and can be performed for a pure or mixed powder phase where multiple phases may be indexed individually. Crystal structure determination using powder diffraction is also possible; the level of success is usually dependent on the quality of the data. It is an involved process which requires a start model and direct space global optimisation approaches [14] but offers a realistic alternative when single crystals of a material remain elusive; the

number of structures solved and refined successfully by this method has been rising in recent years.

In this research project, powder X-ray diffraction (PXRD) was performed for a number of purposes. Firstly, powder X-ray diffraction was carried out as an additional method to evaluate the precipitates from the crystallisation trials. The purpose was either to identity whether a single crystal sample represented the bulk crystallisation product or, where a powder precipitate only was formed, used as a fingerprinting tool to identify the solid phases present. Powder X-ray diffraction was also employed to follow thermal phase transitions of solvated materials. The heating of samples was not carried out *in-situ* due to the limitations of the in-house diffractometer setup; samples were instead preheated to a desired temperature on the hot stage and powder X-ray diffraction data measured on samples recovered to room temperature. In the solvent vapour diffusion trials, powder X-ray diffraction was carried out on a sample pre and post-vapour diffusion to identify phase transitions.

All powder diffraction experiments in this research project were carried out on a laboratory source. Powder samples were prepared for measurement by grinding 10 to 20 mg of single crystal or powder precipitates from the crystallisation vial using a pestle and mortar. Grinding was performed to achieve a homogenous microcrystalline powder mixture in order to prevent the preferred orientation of crystallites known to distort diffraction peak intensities. The ground samples were packed onto glass slides covering an area of approximately 10 mm^2; the samples were kept in place by a thin layer of fomblin oil on the glass slide. Once prepared, samples were mounted on the diffractometer in a centred positioned in the path of the direct X-ray beam. During data collection, the sample remained centred in the incident X-ray beam but was continuously rotated in the horizontal plane; this allowed the effects of preferred orientation to be minimised.

Samples were analysed at room temperature with a Bruker AXS [214] D8 Advance powder diffractometer equipped with a Bruker AXS [214] Vantec-1 detector, using graphite-monochromated copper radiation (Cu-K_α λ = 1.54184 Å) (Figure 4.12). The X-ray detector was scanned vertically, through a 5 to 50 ° 2Θ range and data collection times were approximately 30 minutes long (scan rate of ~2 °/minute). Qualitative analysis was carried out on the collected powder patterns by comparison to the simulated powder patterns of the molecular complexes characterised in this work or to existing molecular complexes and starting materials. The comparison was done visually by stacking the powder patterns in the plotting programme WGnuplot [242] and comparing peak positions and heights.

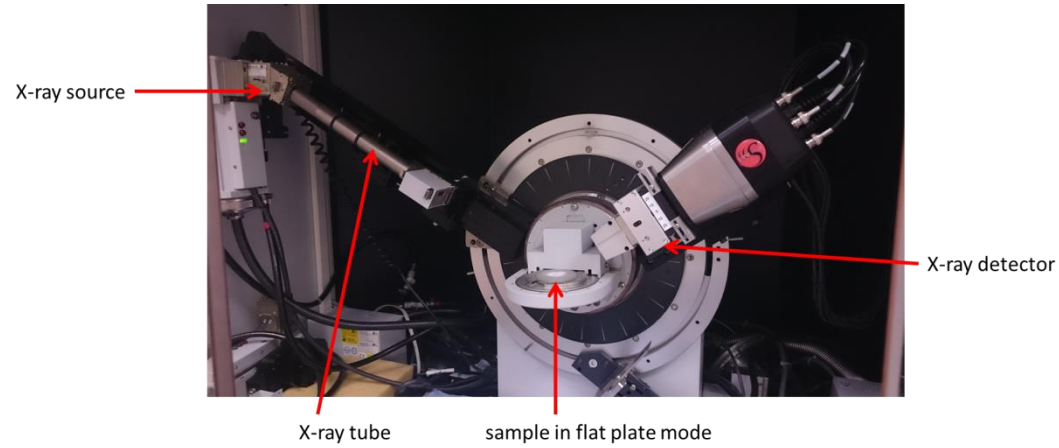

Figure 4.12 The experimental set-up for a laboratory powder X-ray diffractometer. Shown here is the Bruker AXS [214] D8 Advance powder diffractometer.

4.4 Thermal analysis

Thermal analysis was conducted for the identification of new materials based on sample melting points and to determine the thermal behaviour of the molecular complexes. The qualitative approach of hot-stage microscopy (HSM) and quantitative approaches of differential scanning calorimetry (DSC) and thermogravimetric analysis (TGA) coupled with mass spectrometry (MS) were employed. The three techniques were complementary; for example HS and TGA-MS revealed the nature of the endotherms in the DSC traces, whether attributable to melting or a phase transition as a result of desolvation.

4.4.1 HSM

Hot stage microscopy (HSM) combines microscopy and thermal analysis to allow the visual study of crystalline materials as a function of temperature and time. [243] The basic hot-stage configuration (Figure 4.13) includes an optical microscope equipped with a digital camera, a heating stage sample chamber coupled to a digital programmable temperature controller and a computer with software to record HSM images from the digital camera. HSM has a number of applications including assessing purity *via* observation of compound melt range, crystal nucleation and growth, inducing solid to solid transformations and also for co-crystal screening. HSM studies were particularly important in this research project in studying the thermal properties of solvent inclusion materials reported in Chapter 9.

Figure 4.13 The experimental set-up for conducting hot stage microscopy.

HSM analysis was conducted using a Mettler Toledo [244] FP82 hot stage equipped with a Leica Microsystems [245] DM1000 microscope. Single crystal and powder samples were placed on glass slides fixed in position in the heating-stage sample chamber. The powder samples were prepared by gently grinding single crystal or powder precipitates from the crystallisation vial using a pestle and mortar. Each sample was subjected to a programmed temperature regime using a Mettler Toledo [244] FP90 Central Processor. The single crystal samples were filmed using a Lumenera [246] Infinity 2 microscopy camera mounted on the microscope. A software package by Studio86Designs [247] was used for video capture (Studio Capture) and playback (Studio Player). Samples were typically heated using a ramp rate of 5 °C min^{-1} from a start temperature of 30 °C up to a desired temperature; either until the sample had melted, in the initial screen measurements, or to a specific temperature to investigate certain DSC transitions.

4.4.2 DSC

Differential scanning calorimetry (DSC) allows the thermal properties of a material to be studied on measuring the heat flow to a sample against that of a reference; differences between the two indicate thermal transitions in the sample. DSC was carried out in the work in this research project to probe the thermal stability of inclusion materials including desolvation properties, phase transitions and melt properties.

DSC studies were carried out using a TA Instruments [248] Thermal Advantage Q20 DSC equipped with TA Instruments [248] Thermal Advantage Cooling System 90 and operated with a dry nitrogen purge gas at a flow rate of 18 cm^3 min^{-1}. Samples of 3 to 6 mg, prepared by gently grinding single crystal or powder precipitates from the crystallisation vial using a pestle and mortar, were loaded into Tzero™ aluminium pans and sealed with a Tzero™ aluminium lid using a press. An empty sealed Tzero™ aluminium pan was used as the reference. HSM measurements of a sample from the same crystallisation vial were used as guide for the recommended heating regime; the target temperature was set to approximately 10 °C higher than the indicated melt point from HSM. A

heating regime of 5 °C min^{-1}, typically from 20 °C to 300 °C, was carried out on each sample, programmed using the TA Instruments [249] TA Advantage for Qseries[250] software. The temperature was allowed to equilibrate at the starting temperature (typically between 20 - 40 °C) and held isothermal for two minutes at the end temperature. In the DSC traces, the onset temperatures of endo and exotherms and the transition energies were determined using the TA Instruments [248] TA Universal Analysis software; [249] the onset temperature is the temperature at which a change in the DSC thermogram occurs and is defined as the intersection of the tangents of the peak with the extrapolated baseline.

4.4.3 TGA-MS

Thermogravimetric analysis (TGA) coupled with mass spectrometry (MS) allows the thermal decomposition pathway of a material to be followed by measuring sample weight loss as a function of temperature; when coupled with MS the identity of the lost components can be confirmed. TGA-MS was carried out to probe thermal stability of solvent inclusion materials including desolvation properties and decomposition pathway.

TGA was performed using a SETSYS Evolution TGA from Setaram Instrumentation, KEP Technologies. [251] Samples of 5 to 10 mg, prepared by gently grinding single crystal or powder precipitates from the crystallisation vial, using a pestle and mortar, were measured in a tared alumina crucible, 170 μl, under an argon gas purge, flow rate 20 ml min^{-1}. The weight of the sample was measured using a balance with 0.002 mg sensitivity. HSM and DSC measurements of a sample from the same crystallisation vial were used as a guide for the recommended heating regime; the target temperature was set to approximately 100 °C higher than the indicated melt point from HSM and DSC to ensure reaching the decomposition temperature. A heating regime of 5 °C min^{-1}, between 20 and 400 °C, was carried out on each sample, programmed using AKTS [252] Calisto [253] Thermal Analysis Software. The weight of the sample was measured over the regime by the AKTS [252] Calisto [253] Thermal Analysis Software. In the heating regime, the temperature was allowed to equilibrate at the start temperature (typically between 20 and 40 °C) for forty minutes and kept isothermal for two minutes at the end temperature.

For each batch of TGA-MS experiments, a blank measurement carrying out the same heating regime, 5 °C min^{-1} between 20 and 400 °C, was conducted on an empty crucible; this allowed the crucible contribution to each sample measurement to be removed. The crucible contribution includes buoyancy and gas convection effects, related to the argon gas temperature in the TGA furnace, which leads to an initial increase in weight at the start of the experiment. After blank subtraction, a mass loss profile (weight%) as a function of temperature was produced; the mass

loss in weight% was calculated by the Calisto Thermal Analysis Software. [251] The size of each mass loss step in the profile was then determined using the Calisto Thermal Analysis Software; [251] the mass difference (Δm) was calculated between selected points on the TGA curve, at the start and end of each mass loss step.

MS was coupled with the TGA using an OmniStar GSC 320 from Pfeiffer Vacuum, [254] under an argon atmosphere (2.3 bar outlet pressure) controlled using Pfeiffer Vacuum [254] Quadera [255] software. In the experimental set up, the MS was programmed to detect the first three to four significant MS peaks of each solvent. The signals of these peaks were recorded throughout the temperature regime and plotted alongside the TGA curve, as a function of temperature; this allowed the solvent mass loss step to be identified.

.

Chapter 5.

Synchrotron studies of proton disorder in 3,5-dinitrobenzoic acid dimers

Chapter 5 investigates the proton transfer process of proton disorder (§1.3.1) and its dependence on crystal packing environment using variable temperature synchrotron X-ray diffraction studies of a related series of molecular complexes.

5.1 Introduction and aims

Proton disorder is an effect which has been observed in a number of substituted benzoic acids containing centrosymmetric cyclic $R_2^2(8)$ hydrogen bonded carboxylic acid dimers. [89, 92, 95, 97, 98] In particular, crystal packing effects have been suggested to tune the proton disorder in these systems. [97] In order to understand further the role of weak interactions in the crystal packing on tuning the proton disorder, it is beneficial to identify and study further systems in which the effect is observed; variable temperature measurements will also reveal the temperature dependence of the proton disorder.

Molecular complexes of 3,5-dintrobenzoic acid (3,5-DNBA) containing the centrosymmetric $R_2^2(8)$ hydrogen bonded carboxylic acid dimers (Figure 5.1) are of interest in this study and are known to exhibit proton disorder with temperature including in the native forms of polymorphs I and II of 3,5-DNBA [97] and in the binary complex of 4-DABA (4-dimethylaminobenzoic acid) and 3,5-DNBA. [89 97]

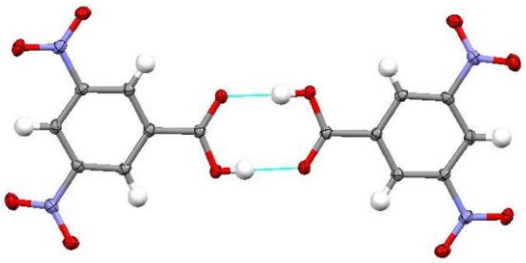

Figure 5.1 Centrosymmetric $\boldsymbol{R_2^2(8)}$ hydrogen bonded carboxylic acid dimers of 3,5-dinitrobenzoic acid (3,5-DNBA).

A search of the CSD was conducted to identify additional systems containing the centrosymmetric 3,5-DNBA hydrogen bonded dimer in which the proton disorder could be studied. The structures of KIZQIT, [256] VOCHOK, [257] YAFVOS [258] and PUQQIB [259] were revealed as potential candidates

as these had not previously been studied by variable temperature methods and have carboxylic acid C—O and C=O bond lengths suggestive of proton disorder (Table 5.1), deviating in length at room temperature from those of an ordered aromatic carboxylic acid. [93] The co-molecules were also readily available commercially, from Sigma-Aldrich (Figure 5.2).

Table 5.1 Candidates for variable temperature synchrotron X-ray diffraction studies. The average C—O and C=O carboxylic acid bond lengths for an ordered aromatic carboxylic acid group are 1.305 Å and 1.226 Å, respectively. [93]

CSD Refcode	T (K)	dC—O (Å)	dC=O (Å)	Co-molecule
YAFVOS [258]	283-303	1.271(3)	1.243(3)	3-aminobenzonitrile
KIZQIT [256]	283-303	1.265(2)	1.261(2)	*N*-methylcarbazole
VOCHOK [257]	283-303	1.27(1)	1.253(8)	indole-3-acetic acid
PUQQIB [259]	283-303	1.265(6)	1.253(6)	1,4-diiodobenzene

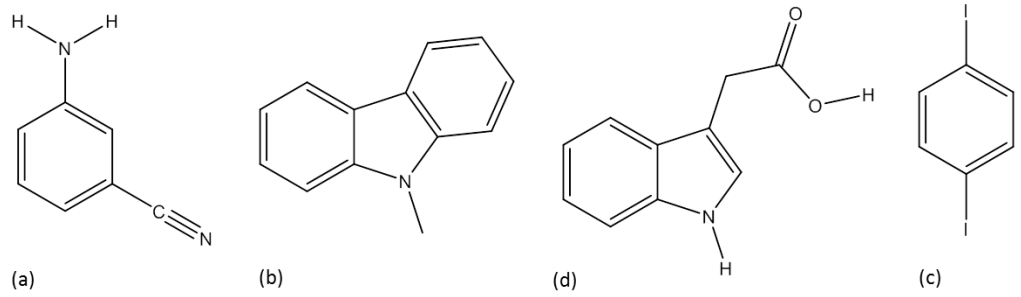

Figure 5.2 The co-molecules in structures (a) YAFVOS [258] (3-aminobenzonitrile), (b) KIZQIT [256] (N-methylcarbazole), (c) VOCHOK [257] (indole-3-acetic acid) and (d) PUQQIB [259] (1,4-diiodobenzne).

Previously, studies of proton disorder in $R_2^2(8)$ hydrogen bonded benzoic acid dimers have been carried out using the single crystal diffraction techniques of laboratory X-ray and neutron diffraction. Only a small number of systems have been studied to date, [89, 92, 97, 98] in the detailed way that is the focus of this work, limited by the availability of variable temperature and/or neutron diffraction measurements. There has, as yet, been no investigation into using X-rays from synchrotron sources to investigate such proton disorder effects, despite the high intensity and rapid throughput offered by this technique, both of which are potentially beneficial to multi-temperature studies of hydrogen transfer processes.

In the work presented in this chapter, variable temperature single crystal synchrotron X-ray diffraction is applied in the study of proton disorder in centrosymmetric 3,5-DNBA hydrogen bonded dimers using data collected on beamline I19, at the Diamond Light Source, U.K. (DLS), [1] and on beamline 11.3.1, at the Advanced Light Source, A.L.S. (ALS). [2] The study of these systems at multiple sources enables a greater reliability in the observations made about the proton disorder behaviour, where in agreement, by the synchrotron X-ray technique.

The synchrotron technique was investigated initially for 3,5-DNBA hydrogen bonded homo dimers in the C2/c polymorph (3,5-DNBA II) (§5.3), a system known to exhibit proton disorder at 300 K and which has been extensively studied previously by variable temperature laboratory X-ray and neutron diffraction. [97] The four additional systems of YAFVOS, KIZQIT, VOCHOK and PUQQIB were also studied using variable temperature single crystal synchrotron X-ray diffraction with the aim of assessing further the potential of the synchrotron technique in following proton disorder (§5.4) and in determining the effect of weaker interactions in the local environment of the centrosymmetric 3,5-DNBA hydrogen bonded dimer, particularly around the acid groups, on the presence and onset temperature of proton disorder (§5.5).

5.2 Experimental details

5.2.1 Preparation and crystallographic analysis

3,5-dinitrobenzoic acid polymorph II (3,5-DNBA II)

Colourless block crystals of 3,5-dinitrobenzoic acid form II were grown from slow evaporation of acetonitrile solvent at room temperature. Single crystal X-ray diffraction data were collected on 3,5-DNBA II samples on I19 at the Diamond Light Source, U.K. [1] in EH1, at 100, 200 and 300 K using Si (111) monochromated radiation at $\lambda = 0.6889$ Å on a Crystal Logic [232] four-circle κ geometry diffractometer equipped with a Rigaku [208] Saturn 724+ CCD detector, and in EH2, using a Newport [236] four-circle diffractometer equipped with a DECTRIS [234] Pilatus 300K detector at 120 and 300 K. The sample temperature was controlled using an Oxford Cryosystems [229] Cryostream Plus. Data were collected in EH1 using the Rigaku [208] CrystalClear™ [209] software whilst data processing was performed using Rigaku Oxford Diffraction [210] CrysAlisPro [211] version 1.171.36.28 (EH1 data). The data collection process was controlled through the in-house Generic Data Acquisition (GDA) [235] software whilst the data processing was carried out using the in-house software DIALS [212] in Xia2. [213] Single crystal X-ray diffraction data were also collected on 3,5-DNBA II samples on beamline 11.3.1 at the Advanced Light Source, U.S.A. [2] using Si (111) monochromated radiation at $\lambda = 0.7749$ Å on a Bruker AXS [214] D8 three-circle diffractometer equipped with a Bruker AXS [214] Apex2 CCD detector at 100, 200 and 300 K. The sample temperature was controlled using an Oxford Cryosystems [229] Cryostream Plus. Data were collected using Bruker AXS [214] Apex2 [215] and processed using Bruker AXS [214] Apex2 [215] with SADABS-2012. [216]

In all cases, the structures were solved using SHELXS-2013 [218] and refined using SHELXL-2013 [219] within the WinGX package. [221] A summary of the crystallographic data are given in Table 5.2 and Table 5.3.

3,5-dinitrobenzoic acid molecular complexes

3,5-dinitrobenzoic acid and 3-aminobenzonitrile 1:1 (3,5-DNBA 3-ABCN)

Colourless block shaped crystals of the 1:1 complex of 3,5-dinitrobenzoic acid and 3-aminobenzonitrile were grown from slow evaporation of a 1:1 stoichiometric ratio of the two components in a 50:50 solvent volume mix of water and methanol at room temperature.

3,5-dinitrobenzoic acid and *N*-methylcarbazole 1:1 (3,5-DNBA MCZ)

Orange needle shaped crystals of the 1:1 complex of 3,5-dinitrobenzoic acid and *N*-methylcarbazole were grown from slow evaporation of a 1:1 stoichiometric ratio of the two components in ethyl acetate at room temperature.

3,5-dinitrobenzoic acid and indole-3-acetic acid 1:1 (3,5-DNBA In-3-Ac)

Yellow needle shaped crystals of the 1:1 complex of 3,5-dinitrobenzoic acid and indole-3-acetic acid were grown from slow evaporation of a 2:1 stoichiometric ratio of the two components in acetone at room temperature.

3,5-dinitrobenzoic acid and 1,4-diiodobenzene 2:1 (3,5-DNBA 1,4-DIB)

Red plate shaped crystals of the 2:1 complex of 3,5-dinitrobenzoic acid and 1,4-diiodobenzene were grown from slow evaporation of a 2:1 stoichiometric ratio of the two components in acetonitrile at room temperature.

Single crystal diffraction data were collected for molecular complexes 3,5-DNBA 3-ABCN, 3,5-DNBA MCZ and 3,5-DNBA In-3-Ac at 100, 150, 200, 250 and 300 K and for 3,5-DNBA 1,4-DIB at 100, 200 and 300 K in EH1, on I19 at the Diamond Light Source, U.K. [1] using a Crystal Logic 4-circle κ geometry diffractometer equipped with a Rigaku [208] Saturn 724+ CCD detector. The sample temperature was controlled using an Oxford Cryosystems [229] Cryostream Plus. Data were collected using the Rigaku [208] CrystalClear™ [209] software whilst data processing was performed using Rigaku Oxford Diffraction [210] CrysAlisPro [211] version 1.171.36.28.

Single crystal diffraction data were collected for molecular complexes 3,5-DNBA 3-ABCN and 3,5-DNBA MCZ at 100, 200 and 300 K at the Advanced Light Source, U.S.A. [2] using a Bruker AXS [214] D8 Diffractometer equipped with a Bruker AXS [214] Apex2 CCD detector at 100, 200 and 300 K. The sample temperature was controlled using an Oxford Cryosystems [229] Cryostream Plus. Data were collected using Bruker AXS [214] Apex2 [215] and processed using Bruker AXS [214] Apex2 [215] with SADABS-2012. [216]

For all 3,5-DNBA molecular complexes, the structures were solved using SHELXS-2013 [218] and refined using SHELXL-2013 [219] within the WinGX package. [221] A summary of the crystallographic data are given in Table 5.4 to Table 5.6.

Refinement details

The refinement details include the treatment of the 3,5-DNBA carboxylic acid group hydrogen atom in each structure, during structure solution and refinement. Two refinement models were employed for the hydrogen atom in the 3,5-DNBA dimer hydrogen bonds. In both models, the hydrogen atoms were located based on Fourier difference maps. Model 1 involved the hydrogen atom position being restricted to one site but the isotropic thermal parameter and position being refined freely. In the sample 3,5-DNBA MCZ, for a stable refinement of the 3,5-DNBA hydroxyl hydrogen atom, a DFIX of 0.82 Å was applied to the O—H distance, a standard X-ray O—H bond length, and the hydrogen atom isotropic atomic displacement parameters was fixed at 1.5 times that of an equivalent hydrogen atom. In the sample 3,5-DNBA 1,4-DIB, for a stable refinement of the 3,5-DNBA hydroxyl hydrogen atom, a DFIX of 0.82 Å was applied to the O—H distance. Model 2 split the dimer hydrogen bond hydrogen atom over two positions, whose combined occupancy was constrained to unity and isotropic thermal parameters at each position constrained to be equal. The hydrogen atom positions were also fixed at 0.82 Å from the relevant donor oxygen.

Table 5.2 Crystallographic data for 3,5-dinitrobenzoic acid II (3,5-DNBA II) collected in EH1, on I19 at the Diamond Light Source, U.K. [1] (DLS) and on 11.3.1 at the Advanced Light Source, U.S.A. [2] (ALS).

Source	DLS		ALS		DLS		ALS		DLS		ALS	
Radiation (λ)	0.6889		0.7749		0.6889		0.7749		0.6889		0.7749	
Formula	$C_7H_4N_2O_6$		$C_7H_4N_2O_6$		$C_7H_4N_2O_6$		$C_7H_4N_2O_6$		$C_7H_4N_2O_6$		$C_7H_4N_2O_6$	
Mol. W ($gmol^{-1}$)	212.12		212.12		212.12		212.12		212.12		212.12	
T (K)	100		100		200		200		300		300	
Space group	C2/c		C2/c		C2/c		C2/c		C2/c		C2/c	
a (Å)	20.504(11)		20.3318(9)		20.782(15)		20.6328(12)		21.12(2)		21.0226(15)	
b (Å)	8.765(5)		8.7446(4)		8.756(6)		8.7372(5)		8.748(8)		8.7203(6)	
c (Å)	9.718(5)		9.6770(4)		9.759(7)		9.7130(5)		9.806(9)		9.7518(6)	
α (°)	90		90		90		90		90		90	
β (°)	110.181(6)		110.129(2)		110.675(8)		110.579(4)		111.202(12)		111.192(4)	
γ (°)	90		90		90		90		90		90	
Volume ($Å^3$)	1639.3(15)		1615.42(12)		1661(2)		1639.26(16)		1689(3)		1666.8(2)	
Z	8		8		8		8		8		8	
ρ_{calc} ($g\ cm^{-3}$)	1.719		1.744		1.696		1.719		1.668		1.691	
μ/mm^{-1}	0.097		0.143		0.153		0.141		0.138		0.139	
Θ range (°)	2.051-26.477		2.326-30.210		2.030-26.499		2.299-30.212		2.005-26.534		2.266-33.726	
Reflections collected	7902		7151		8080		7216		8102		9262	
Independent	1845		1845		1875		1872		1898		2544	
Observed I>2σ	1622		1678		1538		1622		1560		1795	
R_{int}	0.037		0.045		0.0477		0.0392		0.0468		0.0401	
Completeness (%)	99.7		99.0		99.7		99.1		99.3		99.0	
Refinement model	1	2	1	2	1	2	1	2	1	2	1	2
Parameters	152	156	153	156	152	156	153	156	152	156	153	156
GooF	1.065	1.062	1.063	1.075	1.054	1.048	1.093	1.073	1.043	1.043	1.076	1.077
R_1 (observed)	0.0342	0.0341	0.043	0.0429	0.04	0.0396	0.0395	0.039	0.0415	0.0411	0.0488	0.0485
R_1 (all)	0.0395	0.0394	0.045	0.0449	0.0493	0.0489	0.0442	0.0437	0.0502	0.0499	0.066	0.0656
wR_2 (all)	0.0890	0.0885	0.128	0.1281	0.1068	0.104	0.1188	0.1161	0.1165	0.1142	0.1528	0.1494
Δρ (max, min) ($e\ Å^{-3}$)	0.319, -0.267	0.319, -0.267	0.454 -0.289	0.454, -0.288	0.197, -0.267	0.197, -0.267	0.276, -0.291	0.275, -0.288	0.179, -0.187	0.179, -0.187	0.269, -0.231	0.266, -0.227

Table 5.3 Crystallographic data for 3,5-DNBA II from each optimisation strategy conducted on I19, at the Diamond Light Source, U.K. [1] in EH1, performed using a Rigaku [208] Saturn 724+ CCD detector: (1) a hemisphere, (2a) hemisphere (2b) plus an additional hemisphere, (3a) a hemisphere (3b) plus additional low angle data and (4a) a hemisphere (4b) plus additional high angle data and in EH2, performed using a DECTRIS [234] Pilatus 300K detector at (5) 120 K and (6) 300 K.

Detector	Rigaku Saturn 724+ CCD							Pilatus 300 K	
Strategy	1	2a	2b	3a	3b	4a	4b	5	6
Radiation (λ)	0.6889	0.6889	0.6889	0.6889	0.6889	0.6889	0.6889	0.6889	0.6889
Formula	$C_7H_4N_2O_6$	$C_7H_4N_2O_6$	$C_7H_4N_2O_6$	$C_7H_4N_2O_6$	$C_7H_4N_2O_6$	$C_7H_4N_2O_6$	$C_7H_4N_2O_6$	$C_7H_4N_2O_6$	$C_7H_4N_2O_6$
Mol. W ($gmol^{-1}$)	212.12	212.12	212.12	212.12	212.12	212.12	212.12	212.12	212.12
T (K)	100	100	100	100	100	100	100	120	300
Space group	C2/c	C2/c	C2/c	C2/c	C2/c	C2/c	C2/c	C2/c	C2/c
a (Å)	22.772(2)	22.8037(18)	22.7833(14)	22.7989(15)	22.7696(13)	22.7647(10)	22.7888(16)	20.384(7)	21.115(10)
b (Å)	8.7454(4)	8.7359(6)	8.7439(4)	8.7557(3)	8.7558(2)	8.74800(19)	8.7626(3)	8.7344(14)	8.723(2)
c (Å)	9.6720(9)	9.6839(8)	9.6772(6)	9.6874(6)	9.6839(5)	9.6800(4)	9.6895(6)	9.692(5)	9.777(9)
α (°)	90	90	90	90	90	90	90	90	90
β (°)	122.852(13)	122.879(11)	122.886(8)	122.871(9)	122.851(7)	122.890(6)	122.878(9)	110.177(12)	111.229(17)
γ (°)	90	90	90	90	90	90	90	90	90
Volume ($Å^3$)	1618.2(3)	1620.1(3)	1618.9(2)	1624.2(2)	1621.90(17)	1618.73(14)	1625.0(2)	1619.7(11)	1678.5(18)
Z	8	8	8	8	8	8	8	8	8
ρ_{calc} ($g\ cm^{-3}$)	1.741	1.739	1.741	1.741	1.737	1.735	1.734	1.740	1.679
μ/mm^{-1}	0.098	0.098	0.098	0.098	0.098	0.098	0.098	0.098	0.094
Θ range (°)	2.064-25.498	2.061-25.502	2.064-25.493	2.065-25.498	2.065-25.499	2.062-25.501	2.063-37.948	2.064-25.493	2.466-25.494
Reflections collected	7003	6835	11634	7019	9456	6930	15764	9673	10160
Independent	1649	1639	1644	1653	1495	1631	4287	1647	1688
Observed I>2σ	1445	1475	1521	1372	1641	1504	2762	1587	969
R_{int}	0.0301	0.0340	0.0423	0.0359	0.044	0.0260	0.0519	0.1058	0.0577
Completeness (%)	99.8	99.0	99.5	98.7	99.2	99.5	99.8	99.4	98.4
Parameters	152	152	152	152	152	152	152	152	152
GooF	1.033	1.062	1.051	1.040	1.083	1.055	0.994	1.063	0.820
R_1 (observed)	0.0313	0.0346	0.0308	0.0332	0.0314	0.0290	0.0509	0.0359	0.0348
R_1 (all)	0.0374	0.0385	0.0333	0.0431	0.0348	0.0318	0.0901	0.0366	0.0568
wR_2 (all)	0.0839	0.0954	0.0843	0.0861	0.0859	0.0815	0.1363	0.0983	0.0841
Δρ (max, min) ($e\ Å^{-3}$)	0.289, -0.226	0.372 -0.225	0.307, -0.277	0.280 -0.212	0.291, -0.243	0.308 -0.210	0.608, -0.434	0.246 -0.248	0.214 -0.176

Table 5.4 Crystallographic data for 3,5-dinitrobenzoic acid and 3-aminobenzonitrile (3,5-DNBA 3-ABCN) (1:1) collected in EH1, on I19 at the Diamond Light Source, U.K. [1] (DLS) and on 11.3.1 at the Advanced Light Source, U.S.A. [2] (ALS).

Compound	3,5-DNBA 3-ABCN															
Source	DLS		ALS		DLS		DLS		ALS		DLS		DLS		ALS	
Radiation (λ)	0.6889		0.7749		0.6889		0.6889		0.7749		0.6889		0.6889		0.7749	
Formula	$C_{14}H_{10}N_4O_6$		$C_{14}H_{10}N_4O_6$		$C_{14}H_{10}N_4O_6$		$C_{14}H_{10}N_4O_6$		$C_{14}H_{10}N_4O_6$		$C_{14}H_{10}N_4O_6$		$C_{14}H_{10}N_4O_6$		$C_{14}H_{10}N_4O_6$	
Mol. W ($gmol^{-1}$)	330.6		330.6		330.6		330.6		330.6		330.6		330.6		330.6	
T (K)	100		100		150		200		200		250		300		300	
Space group	P-1		P-1		P-1		P-1		P-1		P-1		P-1		P-1	
a (Å)	7.4006(2)		7.3873(15)		7.4101(2)		7.4299(6)		7.437(3)		7.4489(5)		7.4746(6)		7.478(8)	
b (Å)	14.0839(4)		14.062(3)		14.1309(3)		14.1868(10)		14.209(6)		14.2513(11)		14.3180(11)		14.332(15)	
c (Å)	14.7817(4)		14.737(3)		14.8079(3)		14.8301(7)		14.826(6)		14.8601(8)		14.8957(7)		14.862(15)	
α (°)	107.898(2)		107.936(3)		107.959(2)		107.992(5)		107.969(5)		107.997(6)		107.991(6)		107.831(15)	
β (°)	92.691(2)		92.667(3)		92.493(2)		92.312(5)		92.301(5)		92.097(5)		91.874(5)		91.805(15)	
γ (°)	91.587(2)		91.592(3)		91.916(2)		92.330(6)		92.390(6)		92.796(6)		93.353(6)		93.600(17)	
Volume ($Å^3$)	1463.08(7)		1453.6(5)		1471.82(6)		1483.22(18)		1486.7(10)		1496.31(18)		1511.45(19)		1511(3)	
Z	4		4		4		4		4		4		4		4	
ρ_{calc} ($g\ cm^{-3}$)	1.499		1.509		1.490		1.479		1.476		1.466		1.451		1.452	
μ (mm^{-1})	0.111		0.107		0.11		0.109		0.104		0.108		0.107		0.103	
Θ range (°)	1.474-26.572		2.629-30.209		1.470-26.573		1.465-26.571		2.609-30.211		1.678-26.573		1.672-26.571		2.592-28.672	
Reflections collected	24329		17212		24663		24804		17707		25017		25253		15966	
Independent	6621		6637		6665		6713		6795		6789		6837		5949	
Observed I>2σ	5457		4430		5338		4799		3607		4224		3736		2120	
R_{int}	0.0431		0.0551		0.034		0.0398		0.0765		0.0462		0.0438		0.1197	
Completeness (%)	99.4		99.8		99.3		99.4		99.8		99.4		99.3		99.8	
Refinement model	1	2	1	2	1	2	1	2	1	2	1	2	1	2	1	2
Parameters	513	521	513	521	513	521	513	521	513	521	513	521	513	521	513	521
GooF	1.031	1.03	0.969	0.962	1.05	1.047	1.029	1.031	0.949	0.947	1.038	1.036	1.032	1.032	0.905	0.906
R_1 (observed)	0.0392	0.0387	0.0464	0.0463	0.0396	0.039	0.0452	0.0446	0.0619	0.0615	0.0505	0.0498	0.053	0.0525	0.0644	0.0642
R_1 (all)	0.0489	0.0485	0.0793	0.0791	0.0509	0.0504	0.0658	0.0652	0.1239	0.1236	0.0816	0.0811	0.0954	0.095	0.1984	0.1983
wR_2 (all)	0.113	0.112	0.1248	0.1258	0.113	0.1103	0.1364	0.134	0.1795	0.179	0.1647	0.1619	0.1859	0.1852	0.1948	0.1957
Δρ (max, min) ($e\ Å^{-3}$)	0.353, -0.254	0.341, -0.248	0.273, -0.25	0.273, -0.258	0.321, -0.224	0.315, -0.219	0.247, -0.218	0.245, -0.212	0.211, -0.253	0.209, -0.249	0.197, -0.21	0.193, -0.205	0.185, -0.176	0.182, -0.171	0.167, -0.218	0.163, -0.218

Table 5.5 Crystallographic data for 3,5-dinitrobenzoic acid and *N*-methylcarbazole (3,5-DNBA MCZ) (1:1) collected in EH1, on I19 at the Diamond Light Source, U.K. [1] (DLS) and on 11.3.1 at the Advanced Light Source, U.S.A. [2] (ALS).

Source	DLS		ALS		DLS		DLS		ALS		DLS		DLS		ALS	
Radiation (λ)	0.6889		0.7749		0.6889		0.6889		0.7749		0.6889		0.6889		0.7749	
Formula	$C_{20}H_{15}N_3O_6$		$C_{20}H_{15}N_3O_6$		$C_{20}H_{15}N_3O_6$		$C_{20}H_{15}N_3O_6$		$C_{20}H_{15}N_3O_6$		$C_{20}H_{15}N_3O_6$		$C_{20}H_{15}N_3O_6$		$C_{20}H_{15}N_3O_6$	
Mol. W ($gmol^{-1}$)	393.35		393.35		393.35		393.35		393.35		393.35		393.35		393.35	
T (K)	100		100		150		200		200		250		300		300	
Space group	P-1		P-1		P-1		P-1		P-1		P-1		P-1		P-1	
a (Å)	6.7993(6)		6.793(3)		6.8303(7)		6.8750(6)		6.860(3)		6.9138(5)		6.9584(6)		6.914(14)	
b (Å)	8.3825(7)		8.382(3)		8.3977(8)		8.4241(8)		8.402(4)		8.4261(6)		8.4517(8)		8.395(17)	
c (Å)	15.656(2)		15.684(6)		15.706(2)		15.7587(19)		15.738(7)		15.7600(11)		15.791(2)		15.72(3)	
α (°)	81.198(9)		81.148(5)		81.428(10)		81.638(9)		81.572(6)		81.909(6)		82.217(10)		82.17(3)	
β (°)	89.075(9)		89.293(6)		89.039(10)		89.023(9)		89.200(6)		88.882(5)		88.345(10)		88.52(3)	
γ (°)	80.389(7)		80.783(6)		80.304(8)		79.982(7)		80.199(6)		79.570(6)		78.990(8)		79.12(3)	
Volume ($Å^3$)	869.38(16)		871.0(6)		878.09(17)		889.17(16)		884.2(6)		893.95(11)		903.18(17)		888(3)	
Z	2		2		2		2		2		2		2		2	
ρ_{calc} ($g\ cm^{-3}$)	1.503		1.500		1.488		1.469		1.477		1.461		1.466		1.472	
μ (mm^{-1})	0.068		0.098		0.103		0.102		0.096		0.102		0.101		0.134	
Θ range (°)	2.417-26.621		2.716-30.078		2.412-26.592		2.405-26.603		2.712-30.201		2.406-26.570		2.401-26.594		2.718-30.207	
Reflections collected	14343		10068		14636		14907		10167		14976		15209		10317	
Independent	3906		3921		3960		4008		4024		4026		4061		4038	
Observed I>2σ	3479		2803		3219		3129		2043		3049		2602		1393	
R_{int}	0.037		0.0358		0.0409		0.0375		0.068		0.0287		0.0343		0.0849	
Completeness (%)	98.9		99.7		99.4		99.3		99.8		99.2		99.2		99.8	
Refinement model	1	2	1	2	1	2	1	2	1	2	1	2	1	2	1	2
Parameters	310	315	310	315	310	315	310	315	310	315	310	315	310	315	306	315
GooF	1.041	1.039	1.031	1.031	1.08	1.069	1.046	1.052	0.976	0.966	1.041	1.047	1.049	1.055	0.895	0.894
R_1 (observed)	0.0543	0.0581	0.0543	0.0532	0.0564	0.0552	0.0555	0.0551	0.0682	0.0676	0.058	0.0576	0.0624	0.0617	0.0669	0.0669
R_1 (all)	0.0589	0.0534	0.0791	0.078	0.0664	0.0652	0.0683	0.0678	0.1335	0.1328	0.0731	0.0727	0.0887	0.0881	0.1927	0.1926
wR_2 (all)	0.1616	0.159	0.1621	0.1589	0.1775	0.1734	0.1768	0.1746	0.2099	0.2097	0.1846	0.183	0.2185	0.214	0.2178	0.2181
Δρ (max, min) ($e\ Å^{-3}$)	0.872, -0.311	0.877, -0.3	0.786, -0.309	0.779, -0.302	0.752, -0.283	0.748, -0.278	0.601, -0.269	0.601, -0.263	0.471, -0.284	0.4, -0.281	0.479, -0.226	0.482, -0.227	0.342, -0.228	0.349, -0.207	0.236, -0.188	0.241, -0.188

Table 5.6 Crystallographic data for 3,5-dinitrobenzoic acid and indole-3-acetic acid (3,5-DNBA In-3-Ac) (1:1) and 3,5-dinitrobenzoic and 1,4-diiodobenzene (3,5-DNBA 1,4-DIB) (2:1) collected in EH1, on I19 at the Diamond Light Source, U.K. [1] (DLS).

Compound	3,5-DNBA In-3-Ac										3,5-DNBA 1,4-DIB					
Source	DLS		DLS		DLS		DLS		DLS		DLS		DLS		DLS	
Radiation (λ)	0.6889		0.6889		0.6889		0.6889		0.6889		0.6889		0.6889		0.6889	
Formula	$C_{17}H_{13}N_3O_8$		$C_{17}H_{13}N_3O_8$		$C_{17}H_{13}N_3O_8$		$C_{17}H_{13}N_3O_8$		$C_{17}H_{13}N_3O_8$		$C_{10}H_6I_1N_2O_8$		$C_{10}H_6I_1N_2O_8$		$C_{10}H_6I_1N_2O_8$	
Mol. W ($gmol^{-1}$)	387.3		387.3		387.3		387.3		387.3		377.07		377.07		377.07	
T (K)	100		150		200		250		300		100		200		300	
Space group	$P2_1/c$		$P2_1/c$		$P2_1/c$		$P2_1/c$		$P2_1/c$		I2/a		I2/a		I2/a	
a (Å)	15.7986(5)		15.848(2)		15.861(3)		15.8620(5)		15.948(3)		9.5783(6)		9.5975(12)		9.6907(7)	
b (Å)	6.7209(2)		6.7509(6)		6.7731(6)		6.8003(3)		6.8487(7)		8.9641(7)		8.9485(17)		8.9681(8)	
c (Å)	16.0670(5)		16.1086(14)		16.1258(16)		16.1556(6)		16.2274(19)		27.610(2)		27.695(5)		27.963(4)	
α (°)	90		90		90		90		90		90		90		90	
β (°)	110.277(3)		110.469(11)		110.536(12)		110.504(4)		110.624(14)		94.957(10)		94.23(2)		93.467(13)	
γ (°)	90		90		90		90		90		90		90		90	
Volume ($Å^3$)	1600.28(9)		1614.6(3)		1622.3(4)		1632.24(11)		1658.8(4)		2361.8(3)		2372.1(7)		2425.7(4)	
Z	4		4		4		4		4		8		8		8	
ρ_{calc} ($g\ cm^{-3}$)	1.608		1.593		1.586		1.576		1.551		2.212		2.112		2.065	
μ (mm^{-1})	0.12		0.119		0.118		0.118		0.12		2.703		2.474		2.42	
Θ range (°)	2.494-26.572		2.486-26.572		2.483-26.565		2.479-26.569		2.467-26.564		2.316-26.599		2.319-26.610		2.312-26.591	
Reflections collected	15306		15485		15556		15562		15817		11429		11378		11557	
Independent	3678		3707		3719		3740		3792		2716		2733		2786	
Observed I>2σ	3136		3254		3152		3084		3013		2336		2182		1760	
R_{int}	0.0519		0.0387		0.0414		0.0805		0.0766		0.0416		0.0432		0.0711	
Completeness (%)	99.9		99.9		99.9		99.8		99.9		99.8		99.8		99.7	
Refinement model	1	2	1	2	1	2	1	2	1	2	1	2	1	2	1	2
Parameters	305	309	305	309	305	309	305	309	305	309	176	179	176	179	176	179
GooF	1.067	1.065	1.032	1.037	1.057	1.05	1.06	1.061	1.069	1.072	1.064	1.06	1.076	1.074	1.087	1.086
R_1 (observed)	0.0432	0.0427	0.037	0.0366	0.0398	0.0395	0.0497	0.0491	0.0538	0.0532	0.0441	0.0441	0.0481	0.0482	0.0592	0.0593
R_1 (all)	0.0499	0.0495	0.0421	0.0417	0.0471	0.0467	0.0585	0.0579	0.065	0.0645	0.0493	0.0494	0.0595	0.0596	0.0815	0.0816
wR_2 (all)	0.1258	0.1249	0.1054	0,.1037	0.1139	0.1125	0.1376	0.1364	0.155	0.1535	0.1235	0.1248	0.1445	0.1442	0.204	0.2049
Δρ (max, min) ($e\ Å^{-3}$)	0.381, -0.315	0.0427, 0.0495	0.303, -0.253	0.302, -0.25	0.263, -0.262	0.263, -0.262	0.254, -0.27	0.251, -0.274	0.264, -0.354	0.265, -0.348	4.228, -0.952	4.237, -0.962	3.305, -1.168	3.307, -1.172	1.96 -1.04	1.954, -1.041

5.3 A comparative diffraction study of proton disorder in 3,5-DNBA II

In order to benchmark the technique of variable temperature synchrotron X-ray diffraction in the study of proton disorder processes, it was first applied to the sample of 3,5-DNBA II in which the proton disorder had previously been studied extensively by Jones *et al.* (2013) by both variable temperature laboratory (Lab) X-ray and neutron diffraction. [97] A number of strategies were trialled in this work on 3,5-DNBA II initially to maximise data quality (§5.3.1). The best strategy was then applied in a variable temperature synchrotron X-ray diffraction study on 3,5-DNBA II and the results compared (§5.3.2) to those obtained by Jones *et al.* (2013) from Lab X-ray and neutron diffraction studies. [97]

5.3.1 Optimisation of synchrotron X-ray diffraction data for studying proton disorder

Fourier difference maps are one of the more reliable methods used to extract information about proton disorder behaviour in X-ray diffraction studies of substituted benzoic acids. [121] However, the reliability of this method is greatly affected by data quality; poor data quality leads to significant amounts of noise in the X-ray Fourier difference maps such that the signal from the hydrogen atom is obscured and therefore behaviour indeterminable. [39]

In order to optimise the use of synchrotron X-ray diffraction in the study of proton disorder *via* Fourier difference maps, a number of data collection strategies were trialled on the sample of 3,5-DNBA II, on I19, at the Diamond Light Source, U.K. [1] (DLS), in EH1 and EH2.

Strategy effects

The effects of changing certain data collection parameters, such as redundancy and resolution, on the quality of the Fourier difference maps by changing the data collection strategy such as the amount and/or type of diffraction data that was collected were investigated. Different image widths and exposure times were also trialled in initial screens before deciding on a 1.0 ° image with a 1 second exposure time. For each collection strategy trialled, a hemisphere of data was collected. For strategy 1, no further data was collected, for strategy 2, an additional hemisphere of data was collected (giving a sphere in total), for strategy 3, additional low angle data were collected and for strategy 4, additional high angle data were collected. These four strategies were implemented on four different single crystals of 3,5-DNBA II at 100 K using a Rigaku [208] Saturn 724+ CCD on I19, at the DLS, in EH1. For each strategy, the data collection parameters are in Table 5.7 whilst the generated Fourier difference maps are in Figure 5.3.

Table 5.7 Data collection parameters from each strategy employed on single crystals of 3,5-DNBA II in EH1 and EH2 at the Diamond Light Source, U.K. [1]

Strategy	Detector	Data collection information	T (K)	Processing	Resolution (Å)	Completeness (%)	Redundancy	R_{int} for selected resolution
1	Rigaku [208] Saturn 724+ CCD	Hemisphere 1.0 ° image width 1.0 sec. exposures	100	CrysalisPro [211]	0.8	99.9	4.13	0.030
2	Rigaku [208] Saturn 724+ CCD	a. Hemisphere 1.0 ° image width 1.0 sec. exposures	100	CrysalisPro [211]	0.8	99.2	4.04	0.034
		b. + additional hemisphere 1.0 ° image width 1.0 sec. exposures	100	CrysalisPro [211]	0.8	99.5	6.89	0.042
3	Rigaku [208] Saturn 724+ CCD	a. Hemisphere 1.0 ° image width 1.0 sec. exposures	100	CrysalisPro [211]	0.8	98.8	4.09	0.026
		b. + additional low angle 1.0 ° image width 1.0 sec. exposures	100	CrysalisPro [211] + SORTAV [260]	0.8	99.0	5.1	0.044
4	Rigaku [208] Saturn 724+ CCD	a. Hemisphere 1.0 ° image width 1.0 sec. exposures	100	CrysalisPro [211]	0.8	99.5	4.19	0.035
		b. + additional high angle 1.0 ° image width 1.0 sec. exposures	100	CrysalisPro [211] + SORTAV [260]	0.56	88.0	3.4	0.056
5	DECTRIS [234] Pilatus 300K	Sphere, 2.5 ml attenuation 0.4 ° image width 0.4 sec. exposures	120	Xia2 [213]	0.8	100	5.7	0.104
6	DECTRIS [234] Pilatus 300K	Sphere, 4 ml attenuation, 0.4 ° image width 0.4 sec. exposures	300	Xia2 [213]	0.8	100	5.8	0.058

Footnote 1 Data collection for each strategy was performed on a different crystal, where each crystal was of a similar size.

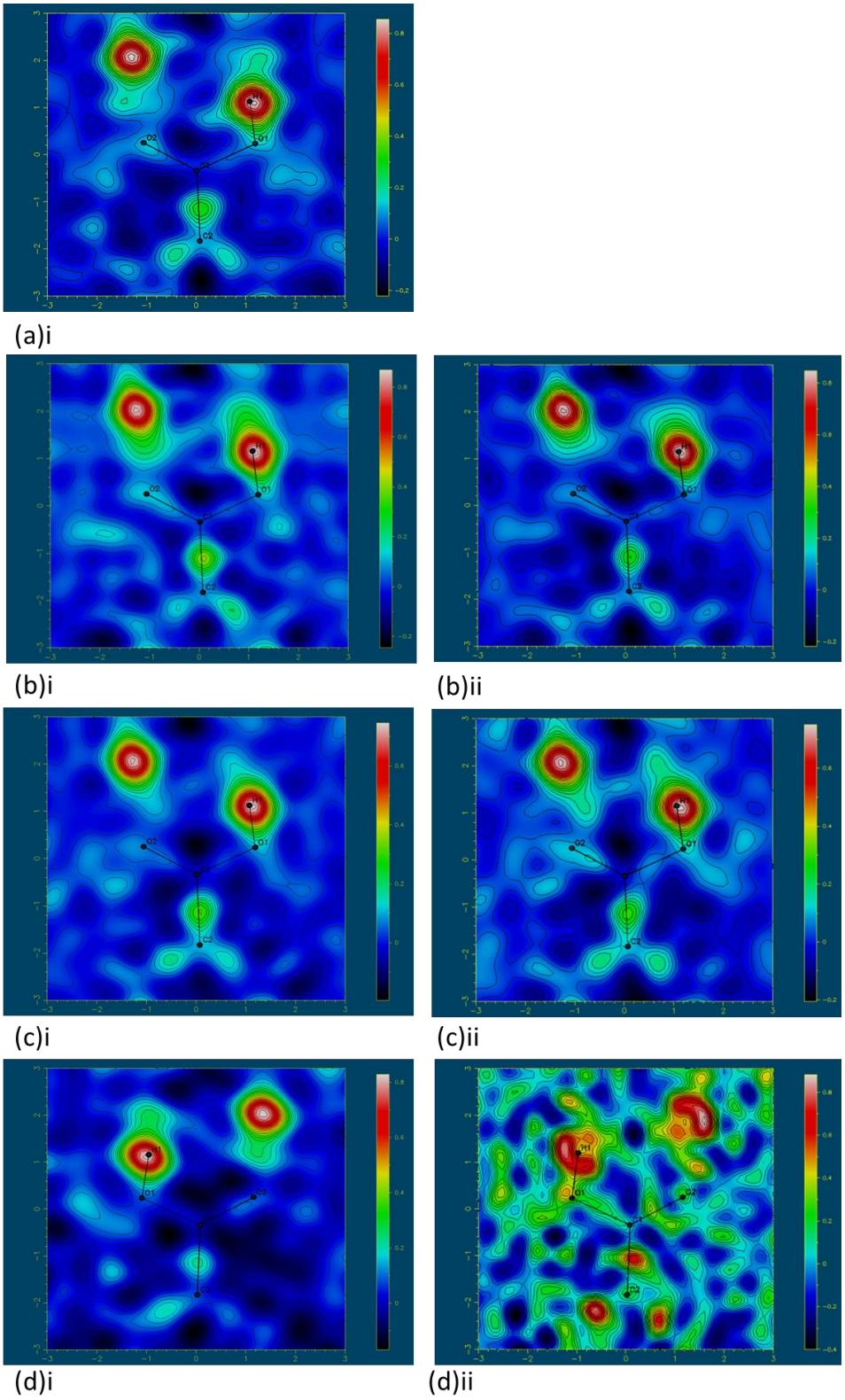

Figure 5.3 Fourier difference maps showing the electron density associated with the H-atom in the 3,5-DNBA dimer hydrogen bonds in 3,5-DNBA II from data collection using the CCD detector in EH1 on I19 at the Diamond Light Source, U.K. [1] at 100 K with (a) strategy 1 of a hemisphere, (b) strategy 2 of (i) a hemisphere sphere (ii) plus an additional hemisphere, (c) strategy 3 of (i) a hemisphere sphere (ii) plus additional low angle data and (d) strategy 4 of (i) a hemisphere (ii) plus additional high angle data.

Good quality clean Fourier difference maps, where the behaviour of the hydrogen atom density can clearly be seen, are generated from the hemisphere of data collected for each strategy; noise in the Fourier difference maps as a result of changes in crystal quality between strategies can therefore be ruled out and be attributed solely to the effects of the additional data. The good quality Fourier difference maps result in all cases where the completeness and redundancies are high and the values of R_{int}, the merging value of the data, are low.

The inclusion of the additional data, on top of a hemisphere, leads to varying changes in the Fourier difference maps and data collection parameters. The inclusion of the additional data for strategies 2 and 3 leads to the Fourier difference maps remaining of good quality with low levels of noise. The values of completeness and redundancy are also improved whilst a slight increase in the value of R_{int} occurred; a higher multiplicity of data usually increases R_{int}. [261] The collection of the additional hemisphere in strategy 2 results in a slight reduction in the noise in the Fourier difference map from that of the initial hemisphere. This reduction in noise indicates improved data quality; a result of collecting the unique data multiple times which offers the opportunity during the process of merging intensities to reject outliers and reduce the ratio of uncertainty in each intensity [261] and where the data to parameter ratio is improved; both factors are important for reliable structural solution and refinement. [153] The collection of additional low angle data on top of the initial hemisphere, as in strategy 3, may allow additional information about the hydrogen atom to be accessed. However, the noise in the Fourier map is actually unchanged. [39]

The inclusion of the additional high angle data (to 0.56 Å) in strategy 4 leads to a significant increase in noise in the Fourier difference maps from that of the initial hemisphere. The values of completeness and redundancy are lower whilst the value of R_{int} is higher; indicating a reduction overall in the quality of the data. The collection of additional high angle data can improve the resolution of the data which is important for unambiguous atom location where high angle reflections are primarily due to scattering by atomic cores; the accurate location of atoms in turn reduces noise in Fourier difference maps. Measuring more of the weaker reflections at the higher angle can also increase the data to parameter ratio. However, the weaker reflections have a low signal to noise ratio and so their inclusion may reduce the overall quality of the data, as observed here by the large amounts of noise in the Fourier difference maps. In addition, the lack of core electrons in bonded hydrogen atoms means that additional high angle data is unlikely to have a beneficial effect explicitly in their direct determination.

Detector effects

It was possible to obtain good quality Fourier difference maps, in which the behaviour of the hydrogen atom density was clearly visible, when using a Rigaku [208] Saturn 724+ CCD detector.

The potential of the DECTRIS [234] Pilatus 300K detector in the study of proton disorder in 3,5-DNBA II in Fourier difference maps was also investigated. The operation of a Pilatus detector differs from that of the CCD detector, operating as a photon counter rather than a photon integrator. This means that, in contrast to a CCD detector, the Pilatus detector has a significantly higher count rate and dynamic range, faster read out times and almost negligible background noise in the diffraction data. [155, 239, 240] These characteristics may benefit proton disorder studies by reducing noise in the Fourier difference maps, where the quality and resolution of the data may be significantly improved, and allowing the variable temperature data to be collected on shorter timescales.

Fourier difference maps were generated for a sphere of data (for 3,5-DNBA II) collected on the DECTRIS [234] Pilatus detector, in EH2 on I19 at the Diamond Light Source, U.K., [1] at 120 and 300 K. For each strategy, the data collection parameters are given in Table 5.7, with the generated Fourier difference maps in Figure 5.4. Different image widths and exposure times were also trialled for the DECTRIS [234] Pilatus detector in initial screens before deciding on a 0.4 ° image with a 0.4 second exposure time.

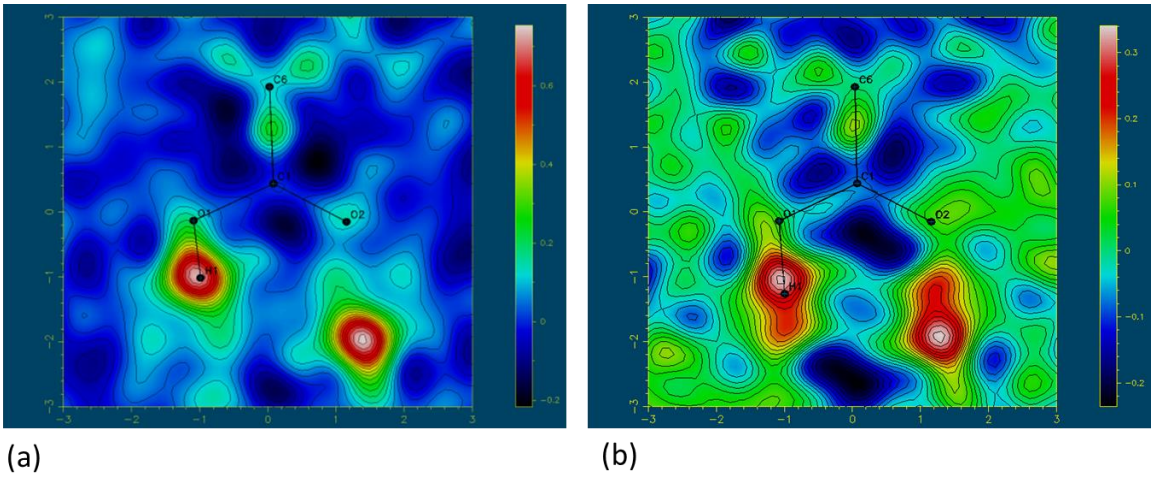

Figure 5.4 Fourier difference maps showing the electron density associated with the H-atom in the 3,5-DNBA dimer hydrogen bonds in 3,5-DNBA II from data collection using the DECTRIS [234] Pilatus detector, in EH2 on I19 at the Diamond Light Source, U.K. [1] at (a) 120 K and (b) 300 K.

The completeness and redundancy are high for both the 120 and 300 K data collections with values similar to those obtained for the collection of a sphere using the CCD detector. The Fourier difference maps are of reasonable quality at 120 K whilst larger amounts of noise are present at 300 K; likely a result of increased thermal motion or due to a difference in sample quality where the measurements were not carried out on the same crystal. The 120 K Fourier difference map has an increased amount of noise in comparison to those at 100 K from the CCD detector, for

strategies 1 to 3, however the hydrogen atom behaviour is still determinable. In the 300 K map there is also a suggestion of a second hydrogen atom peak, as observed in the literature laboratory X-ray study of this sample. [97] These initial results of using the DECTRIS [234] Pilatus detector in the study of proton disorder in Fourier difference maps therefore appear promising with proton disorder behaviour suggested at 300 K which agreed with that reported previously in the literature. [97] However, before the use of the Pilatus can be employed reliably in future studies further investigation into this method is required in order to obtain Fourier difference maps equivalent in quality to those obtained using the CCD detector.

Summary

For the data collection strategies which involved data collected using the Rigaku [208] Saturn 724+ CCD detector, the hemisphere data collection strategy appears to be best suited to the study of proton disorder, allowing good quality Fourier difference maps to be generated, comparable to those from a sphere of data but with the benefit of being collected in half the time; this is important in variable temperature studies that require measurements at multiple temperatures. Overall, the trials using the CCD detector gave better results than those using the DECTRIS [234] Pilatus 300K detector. However, it is important to note that the use of the DECTRIS [234] Pilatus 300K detector in these studies is still in the very early stages and these initial results are promising for its future use.

5.3.2 Variable temperature X-ray diffraction study of 3,5-DNBA II

The results from the first variable temperature synchrotron X-ray diffraction studies on 3,5-DNBA II at the Diamond Light Source, U.K. [1] (DLS) and the Advanced Light Source, U.S.A. [2] (ALS) are presented in this section and compared to those previously obtained by Jones *et al*. (2013) using laboratory (Lab) X-ray and neutron diffraction. [97] The focus is on the hydrogen bond dimer structural and atomic displacement parameters, occupancies of disordered sites and Fourier difference maps. The study of 3,5-DNBA II is performed at two sources to have greater confidence in the observations made about the proton disorder behaviour, where in support of one another, by the synchrotron X-ray technique.

Based on the findings in §5.3.1, a data collection strategy of collecting a hemisphere of data was employed at each synchrotron source and data collected using photon integrating CCD detectors of a Rigaku [208] Saturn 724+ CCD on I19, at the DLS, in EH1 and a Bruker AXS [214] Apex2 CCD detector on 11.3.1 at the ALS.

Hydrogen bond dimer structural parameters

A comparison of the 3,5-DNBA II hydrogen bonded dimer structural parameters over the 100 to 300 K temperature range revealed that the changes in the C—O and C=O bond lengths observed with temperature in the DLS and ALS synchrotron structures are in agreement and within error of those observed in the previously determined Lab X-ray and neutron structures [97] (Table 5.8 and Figure 5.5); the same trend of C—O decreasing and C=O increasing in length is observed as a function of temperature and therefore the same extent of proton disorder is indicated across the four structures. This is expected where parameters involving the heavy atoms of oxygen and carbon may be accurately refined from both X-ray and neutron data due to their strong scattering in both methods.

Table 5.8 Length of the C—O and C=O bonds in the carboxylic acid groups of the 3,5-DNBA II hydrogen bonded dimer at each temperature for each structure.

T (K)	100		200		300	
Structure	dC—O (Å)	dC=O (Å)	dC—O (Å)	dC=O (Å)	dC—O (Å)	dC=O (Å)
Synchrotron DLS	1.310(2)	1.227(2)	1.297(2)	1.231(2)	1.285(2)	1.241(2)
Synchrotron ALS	1.304(2)	1.226(1)	1.297(2)	1.228(1)	1.282(2)	1.233(2)
Lab X-ray [97]	1.308(1)	1.228(1)	1.299(1)	1.231(1)	1.281(2)	1.237(1)
Neutron [97]	1.309(2)	1.229(2)	1.299(2)	1.229(2)	1.283(2)	1.241(2)

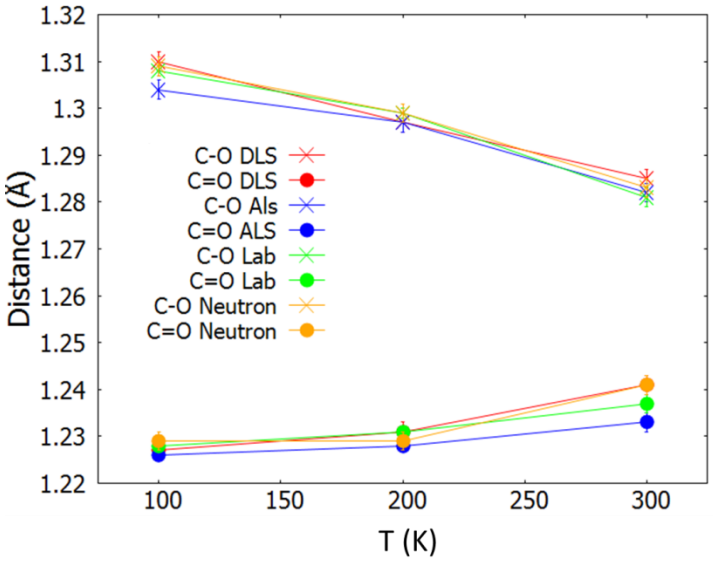

Figure 5.5 A comparison of the C—O and C=O bond lengths of the carboxylic acid groups forming the hydrogen bonded dimers as a function of temperature in the DLS, ALS, Lab X-ray and neutron structures. The standard uncertainties on the distances are plotted but are smaller than the symbols used to denote each data point.

The atomic distances in the dimer hydrogen bond were compared across the four structures (Table 5.9). The O···O distances of the dimer hydrogen bonds are similar in length between the DLS and ALS structures and to those in the Lab X-ray and neutron structures, at the different temperatures, and also invariant over the temperature range. The hydrogen bonded dimer lies along the *b*-axis and variations in the O···O hydrogen bond distances across the structures from the different sources appear to correspond to differences in the determined *b*-axis length; the longest O···O distance at 100 K occurs in the DLS structure which has the longest *b*-axis length at 8.765(5) Å whilst the shortest O···O distance at 100 K occurs in the ALS structure which has the shortest *b*-axis length at 8.7446(4) Å. When a hydrogen atom refinement model (model 1) with a single hydrogen atom site in the dimer is employed, with a freely refined position and thermal parameter, the refined O—H distances are in agreement for the three X-ray structures (DLS, ALS and Lab), over the temperature range, and indicate a slight movement of the refined hydrogen atom position towards the centre of hydrogen bond with increasing temperature; an indication of the onset of proton disorder. The refined O—H distances were longer in the neutron structure than all the measured X-ray lengths; the difference is as expected for bond lengths involving hydrogen atom positions determined by the two different techniques (§2.6). [94]

Table 5.9 Interatomic distances in the O—H···O hydrogen bond forming the 3,5-DNBA hydrogen bonded dimers at each temperature for each structure.

		Structure			
T (K)	Distance	DLS	ALS	Lab [97]	Neutron [97]
100	O···O (Å)	2.639(2)	2.627(1)	2.631(1)	2.629(2)
	O—H (Å)	0.92(2)	0.89(2)	0.91(2)	1.008(2)
	H···O (Å)	1.72(2)	1.74(2)	1.72(2)	1.621(2)
200	O···O (Å)	2.637(2)	2.628(2)	2.634(1)	2.633(2)
	O—H (Å)	0.91(2)	0.91(2)	0.86(2)	1.004(3)
	H···O (Å)	1.73(2)	1.72(2)	1.77(2)	1.630(3)
300	O···O (Å)	2.641(2)	2.631(2)	2.639(1)	2.622(3)
	O—H (Å)	1.03(3)	1.00(3)	1.00(2)	1.011(3)
	H···O (Å)	1.61(3)	1.63(3)	1.63(3)	-

Atomic displacement parameters

The atomic displacement parameters were compared across the different structures at the higher temperature of 300 K where thermal motion is increased (Figure 5.6). The anisotropic displacement parameters of the heavy atoms are in good agreement across all four methods, indicating similar atomic motion at this temperature. From X-rays, it is only possible to refine hydrogen atom displacement parameters isotropically. There is agreement in the size and

enlargement of the hydrogen atom isotropic displacement parameter, relative to those in the rest of the dimer, across the three X-ray structures (Lab, [97] DLS and ALS). In the neutron structure, the hydrogen atom displacement parameter is refined anisotropically and found to be larger than the displacement parameters of the hydrogen atoms in the rest of the dimer. The enlarged hydrogen atomic displacement parameter in all structures relative to the others indicates a similar apparent increased motion of the hydrogen atom at this temperature, indicative of proton disorder. However, the anisotropic modelling of the hydrogen atom in the neutron structure additionally allows the direction of the elongation and hence apparent motion along the dimer hydrogen bond to be determined. This is one disadvantage of the X-ray technique in these studies where only extent of motion and not direction is indicated by the isotropically refined hydrogen atom thermal parameter.

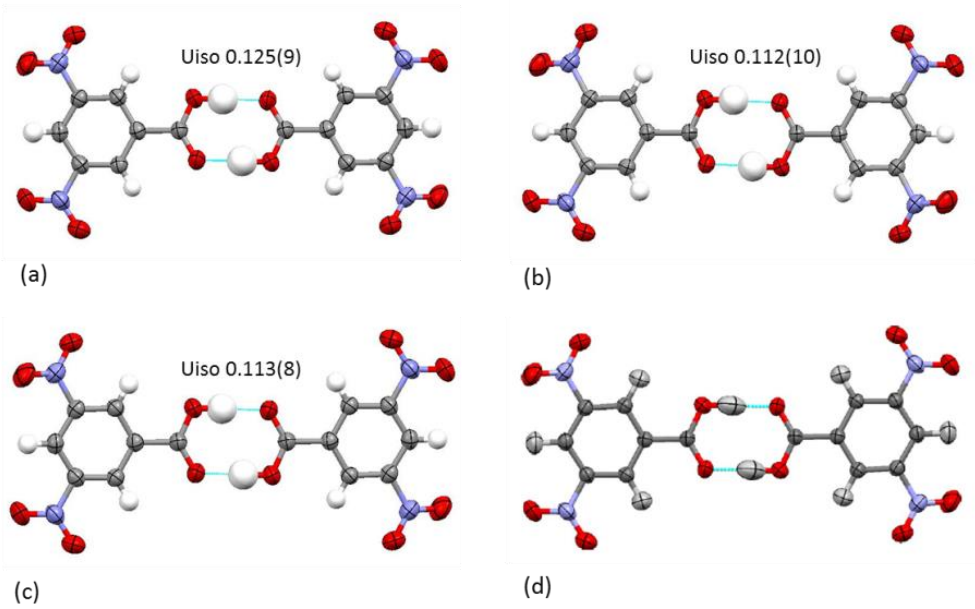

Figure 5.6 The atomic displacement parameters of the 3,5-DNBA hydrogen bonded dimer in 3,5-DNBA II in the (a) DLS, (b) ALS, (c) Lab X-ray [97] and (d) neutron structures [97] at 300 K.

Fourier difference maps

Fourier difference maps were generated for the dimer hydrogen bonds for the DLS and ALS structures (Figure 5.7) to visualise directly the behaviour of the hydrogen atom density relative to that seen in the Fourier maps of the Lab X-ray and neutron structures. [97] A single peak is present in the Fourier difference maps of the DLS and ALS structures at 100 K, in agreement with those of the Lab and neutron structures at the same temperature, and suggesting an ordered proton. The DLS and ALS Fourier maps both contain a potential second peak at 200 K, agreeing with that observed in the 200 K Fourier difference map of the Lab X-ray structure. The Fourier difference maps of the DLS and ALS structures contain two peaks at 300 K with differing intensities,

indicating proton disorder with unevenly occupied proton sites, which appear to have the same behaviour as those in the Fourier difference maps at 300 K of the Lab X-ray and neutron structures. There is better agreement in the shape of the hydrogen atom density in the DLS Fourier difference map at 300 K with the shape of the density in the Lab and neutron Fourier difference maps than in the ALS Fourier difference maps at the same temperature; the second peak is much more defined for this structure. The same trend of increasing proton disorder with temperature is therefore suggested by all Fourier difference maps.

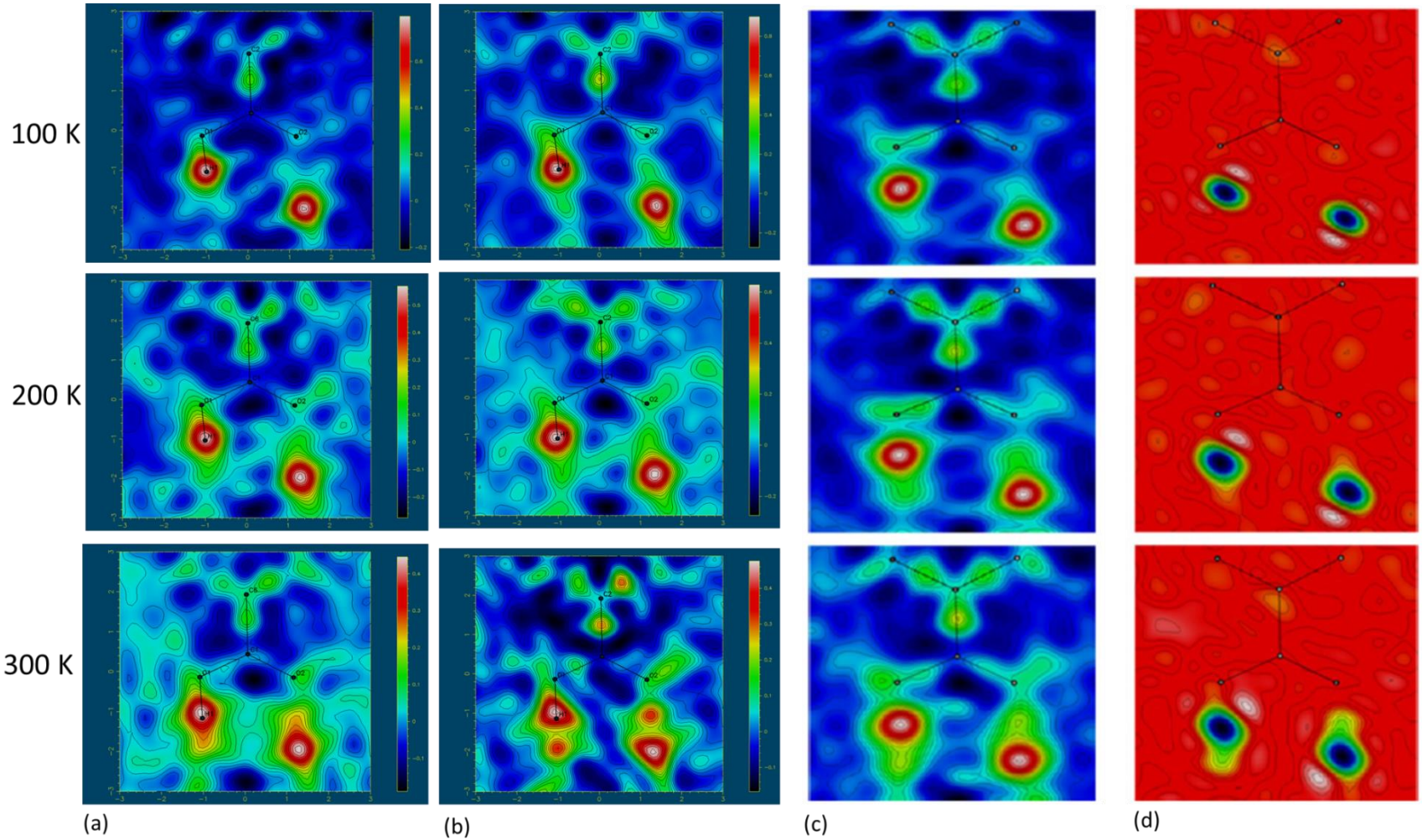

Figure 5.7 Variable temperature Fourier difference maps of the dimer hydrogen bonds in 3,5-DNBA II from the (a) DLS, (b) ALS, (c) Lab X-ray [97] and (d) neutron structures. [97]

Hydrogen atom site occupancies

A structural model (model 2) where the hydrogen atom is split over two positions in the dimer hydrogen bond was refined for both the DLS and ALS data to determine whether similar information about the site occupancies, to that available from the Lab X-ray and neutron structures, could be obtained (Table 5.10).

Table 5.10 Refined occupancies of the two proton configurations in the 3,5-DNBA hydrogen bonded dimer in 3,5-DNBA II in the DLS, ALS, Lab X-ray [97] and neutron structures. [97] The X-ray refined occupancy values have an estimated error of approximately 10 %. [89]

Method/T(K)	100	200	300
DLS	87:13	78:22	69:31
ALS	87:13	81:19	71:29
Lab [97]	100:0	78:22	72:28
Neutron [97]	100:0	100:0	81(1):19(2)

At 100 K, a small extent of proton disorder is indicated in the 3,5-DNBA dimer by the refined occupancy values of 87:13 for the two proton configurations in both the DLS and ALS structures. The occupancies at the same temperature are, in contrast, 100:0 for the Lab X-ray and neutron structures. It should be noted, however, that the estimated uncertainty on occupancy values of proton sites from X-rays is approximately 10 % [89] and the 13% occupation of the second site, suggested for the DLS and ALS structures, is equivalent to just 0.13 of an electron which could be equivalent to background noise. It may therefore be more sensible to assess these occupancies values alongside the C—O and C=O bond lengths and Fourier difference maps. In the DLS and ALS structures, at 100 K, the C—O and C=O bond lengths are in good agreement with the average C—O and C=O bond distances for an ordered aromatic carboxylic acid group [80] and the DLS and ALS dimer hydrogen bond Fourier difference maps show a lack of a second peak. It is therefore likely that the carboxylic acid group is fully ordered, with an occupancy ratio of 100:0, as refined in the Lab and neutron structures. Therefore, it appears that for synchrotron structures, when discussing site occupancies of the two proton sites, the C—O and C=O bond lengths and Fourier difference maps should also be considered.

There is good agreement in the overall trend of the disorder increasing with temperature suggested by the refined occupancies from the DLS and ALS structures with the Lab and neutron structures. The occupancies of the two sites are also in agreement at 200 and 300 K between the three X-ray structures and at 300 K, are close to being consistent with those refined in the neutron structures (81(1):19(2)); supported by consistent C—O and C=O bond lengths across the DLS, ALS, Lab and neutron structures and the presence of the second peak in the 300 K Fourier difference maps.

Summary

The DLS and ALS variable temperature synchrotron studies of proton disorder in 3,5-DNBA II revealed equivalent information about the proton disorder to that found by the previous Lab X-ray and neutron diffraction studies. [97] Synchrotron X-ray diffraction may therefore be suitable for the identification and quantification of proton disorder in 3,5-DNBA cyclic hydrogen bonded dimers. This is supported where the information revealed about the proton disorder is also in agreement between the two synchrotron sources. However, it is apparent that certain parameters should be given greater weighting during the analysis including using the C—O and C=O bond lengths and Fourier difference maps for the primary identification and quantification of the proton disorder with hydrogen atom refined parameters including position, displacement parameters and occupancies of proton sites only considered alongside this primary information.

This preliminary study therefore reveals how to optimise the information from the synchrotron X-ray technique to allow a more reliable determination of proton disorder behaviour.

5.4 Synchrotron studies of proton disorder in molecular complexes of 3,5-DNBA

In this section, the synchrotron technique is applied to additional molecular complexes containing centrosymmetric $R_2^2(8)$ hydrogen bonded 3,5-dinitrobenzoic acid dimers to assess further the potential of this technique in studies of proton disorder and to aid in determining the role of the local environment on tuning proton disorder characteristics, including its presence and onset temperature.

The proton disorder is studied in the four molecular complexes of 3,5-DNBA 3-aminobenzonitrile (3,5-DNBA 3-ABCN), 3,5-DNBA *N*-methylcarbazole (3,5-DNBA MCZ), 3,5-DNBA indole-3-acetic acid (3,5-DNBA In-3-Ac) and 3,5-DNBA 1,4-diiodobenzene (3,5-DNBA 1,4-DIB) so selected where, in their crystal structures at room temperature, the centrosymmetric $R_2^2(8)$ hydrogen bonded homo benzoic acid dimer is formed and proton disorder is suggested in the carboxylic acid C—O and C=O bond lengths. All samples have been studied in EH1 on I19, at the Diamond Light Source, U.K. [1] (DLS); for 3,5-DNBA 3-ABCN and 3,5-DNBA MCZ, they have also been studied on beamline 11.3.1, at the Advanced Light Source, U.S.A [2] (ALS).

5.4.1 3,5-DNBA 3-ABCN

In the crystal structure of 3,5-DNBA 3-ABCN at 100 K (DLS), the two components crystallise in a 1:1 ratio, with two formula units in the asymmetric unit, in space group $P\bar{1}$. Two symmetry independent 3,5-DNBA hydrogen bonded $R_2^2(8)$ dimers (dimer 1 and dimer 2) are present in the structure, where the 3,5-DNBA molecules are held together by strong to moderate strength O—H···O hydrogen bonds (dimer 1 $d_{O\cdots O}$ 2.588(1) Å and dimer 2 $d_{O\cdots O}$ 2.618(1) Å at 100 K) and are related by an inversion centre at the centre of the $R_2^2(8)$ hydrogen bonded ring (Figure 5.8(a)i and (b)i).

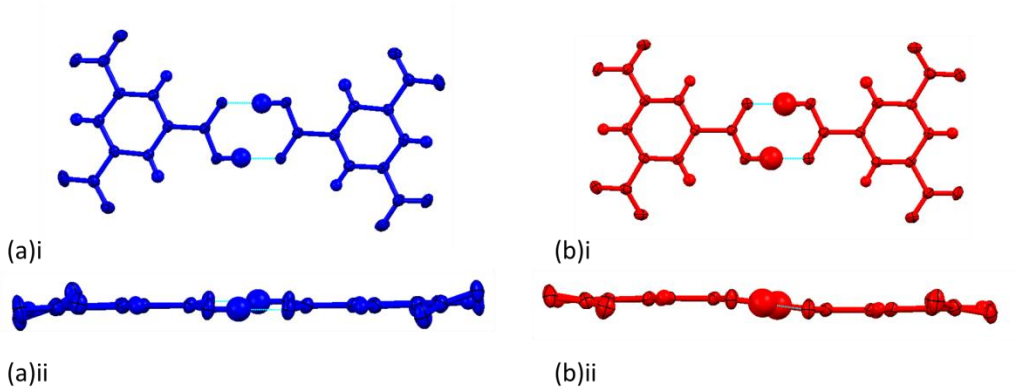

Figure 5.8 The 3,5-DNBA centrosymmetric hydrogen bonded $\boldsymbol{R_2^2(8)}$ dimers at 100 K in the molecular complex of 3,5-DNBA 3-ABCN: (a) dimer 1 and (b) dimer 2, i perpendicular to the dimer plane and ii in plane of the dimer.

Within the hydrogen bonded dimers, the aromatic rings of the two 3,5-DNBA molecules are in the same layer in dimer 1 (0.193 Å between aromatic ring planes) whilst they are slightly offset in dimer 2 (0.533 Å between aromatic ring planes) (Figure 5.8(a)ii and (b)ii). The hydrogen bonded carboxylic acid groups are essentially planar to the aromatic ring in both dimers; a twist of 5.6(2) ° occurs in dimer 1 and a twist of 0.8(2) ° occurs in dimer 2. In the $R_2^2(8)$ hydrogen bonded ring of each dimer, the carboxylic acid groups are tilted relative to one another (C—O···O angle of 111.30(8) ° in dimer 1 and 114.80(8) ° in dimer 2 and a C=O···O angle of 123.81(9) ° in dimer 1 and 120.25(8) ° in dimer 2). One of the nitro groups in dimer 1 lies slightly out of plane of the aromatic ring, with torsion angles of − 18.5(2) and 3.8(2) °, whilst both of the nitro groups lie out of plane of the aromatic ring in dimer 2, with torsion angles of 12.0(2) and − 9.9(2) °.

Molecular packing

In the crystal structure of 3,5-DNBA 3-ABCN, dimer 1 and dimer 2 are in different crystal packing environments. Several short contacts are formed to the hydrogen bonded carboxylic acid groups in both dimer 1 and dimer 2 (Figure 5.9).

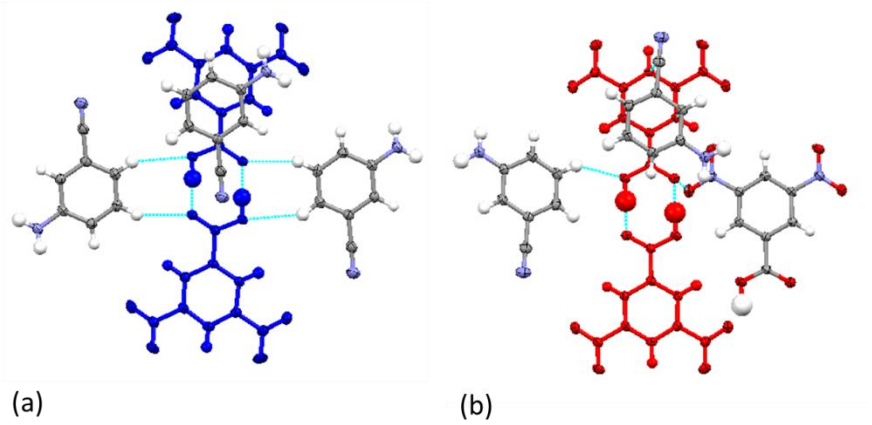

Figure 5.9 The local packing environments of the 3,5-DNBA hydrogen bonded dimer carboxylic acid groups in (a) dimer 1 and (b) dimer 2 in the molecular complex of 3,5-DNBA 3-ABCN. For clarity, the packing is shown for one side of the centrosymmetric dimer only.

In dimer 1, weak C—H···O hydrogen bonds form to both carboxylic acid oxygen atoms involving C—H groups donated from neighbouring 3-ABCN molecules. A shorter interaction forms to the carbonyl oxygen atom than the hydroxyl oxygen atom ($d_{C\cdots Ocarbonyl}$ 3.393(2) Å and <CHO 151(1) ° versus $d_{C\cdots Ohydrozyl}$ 3.546(1) Å and <CHO 147(1) °). A nitrile group of a neighbouring 3-ABCN molecule also stacks below the carboxylic acid group forming weak contacts to the acid π-density ($d_{\pi\cdots\pi}$ 3.294(2) and 3.378(2) Å). In the local environment of dimer 2, a weak C—H···O hydrogen bond forms to the hydroxyl oxygen atom involving a C—H group donated by a neighbouring 3-ABCN molecule ($d_{C\cdots O}$ 3.349(2) Å, <CHO 123(1) °). A 3-ABCN molecule also stacks below the carboxylic acid group forming weak contacts to the acid π-density ($d_{\pi\cdots\pi}$ 3.349(2) Å) whilst a weak O···O contact ($d_{O\cdots O}$ 2.948(1) Å), less than the sum of the van der Waals radii of the two atoms (3.04 Å) and therefore significant, forms between the acid carbonyl and a nitro group of a 3,5-DNBA molecule in a neighbouring dimer 2 unit.

Intermolecular interactions also occur between the 3,5-DNBA molecule, forming each centrosymmetric dimer, and to 3,5-DNBA and 3-ABCN molecules in the local environment (Figure 5.10). Interactions formed between 3,5-DNBA molecules are dimer specific such that no significant interactions form between dimer 1 and dimer 2.

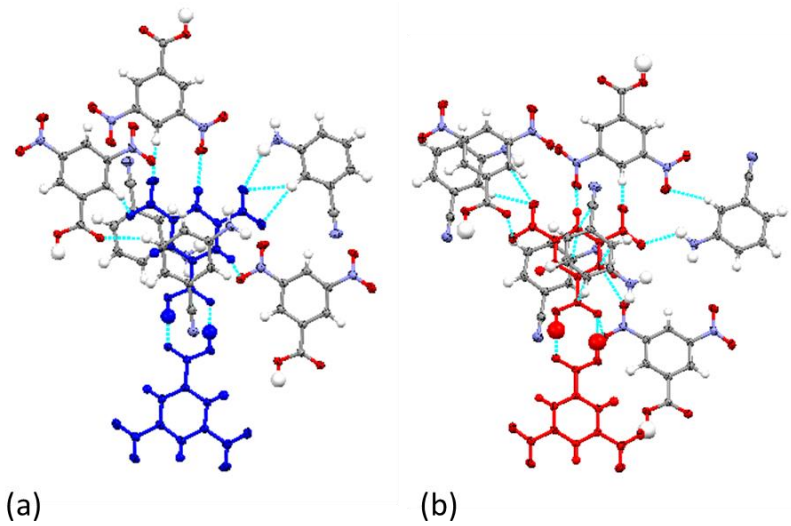

Figure 5.10 The local packing environments of each 3,5-DNBA molecule in (a) dimer 1 and (b) dimer 2 in the molecular complex of 3,5-DNBA 3-ABCN. For clarity, the packing is shown for one side of the centrosymmetric dimer only.

In the local environment of dimer 1, weak interactions form to both nitro groups of the 3,5-DNBA molecule forming the centrosymmetric dimer. The nitro group on the protonated side of the 3,5-DNBA molecule forms weak C—H···O hydrogen bonds, through both its oxygen atoms, to aromatic C—H groups from different 3,5-DNBA molecules in neighbouring dimer 1 units ($d_{C\cdots O}$ 3.212(2) and 3.269(2) Å). The nitro group on the non-protonated side of the 3,5-DNBA molecule interacts with a neighbouring 3-ABCN amino group *via* an N—H···O hydrogen bond ($d_{N\cdots O}$ 3.224(1) Å) and bifurcated C—H···O hydrogen bonds ($d_{C\cdots O}$ 3.395(2) and 3.606(2) Å). A weak C—H···O bond also form on the non-protonated side of the 3,5-DNBA molecule, involving an aromatic C—H at the 2-position, to a nitro group of a 3,5-DNBA molecule in a neighbouring dimer 1 unit ($d_{C\cdots O}$ 3.212(2) Å). In the middle of the 3,5-DNBA molecule, a ring C—H group at the 4-position forms a weak hydrogen bond to a nitro group of a 3,5-DNBA molecule in a neighbouring dimer 1 unit ($d_{C\cdots O}$ 3.269(2) Å). The amino end of a 3-ABCN molecule stacks below the 3,5-DNBA molecule forming weak π-contacts ($d_{\pi\cdots\pi}$ 3.332(2) Å).

In the local environment of dimer 2, weak interactions form to both nitro groups of the 3,5-DNBA molecule forming the centrosymmetric dimer. The nitro group on the protonated side of the 3,5-DNBA molecule forms a weak C—H···O hydrogen bond to aromatic C—H groups on a neighbouring 3-ABCN molecule ($d_{C\cdots O}$ 3.392(2) Å) and on a 3,5-DNBA molecule in a neighbouring dimer 2 unit ($d_{C\cdots O}$ 3.213(2) Å). The nitro group on the protonated side also forms a weak O···O contact to the acid group of a 3,5-DNBA molecule in a neighbouring dimer 2 unit ($d_{O\cdots O}$ 2.948(1) Å); less than the sum of the van der Waals radii of the two atoms (3.04 Å) and therefore significant. The nitro group on the non-protonated side of the 3,5-DNBA molecule

interacts with a neighbouring 3-ABCN amino group, *via* a moderate strength N—H···O hydrogen bond ($d_{N\cdots O}$ 2.948(2) Å), and with an aromatic C—H in a 3,5-DNBA molecule in a neighbouring dimer 2 *via* a weak C—H···O hydrogen bond ($d_{C\cdots O}$ 3.314(2) Å). A weak C—H···O bond also forms on the non-protonated side of the 3,5-DNBA molecule, involving an aromatic C—H at the 2-position to a nitro group of a 3,5-DNBA molecule in a neighbouring dimer 2 unit ($d_{C\cdots O}$ 3.213(2) Å). In the middle of the 3,5-DNBA molecule, one of the ring C—H groups forms a weak C—H···O hydrogen bond to a nitro group of a 3,5-DNBA molecule in a neighbouring dimer 2 ($d_{C\cdots O}$ 3.314(2) Å). 3-ABCN molecules also stack above and below the 3,5-DNBA molecule, at the benzonitrile ($d_{\pi\cdots\pi}$ 3.306(2) and 3.258(2) Å) and amino ends ($d_{\pi\cdots\pi}$ 3.322(2) Å).

The wider packing of each dimer in 3,5-DNBA 3-ABCN occurs in isolated layers of each component; the two symmetry independent dimers occupy different layers (Figure 5.11). The dimer acid groups are well integrated into the structure.

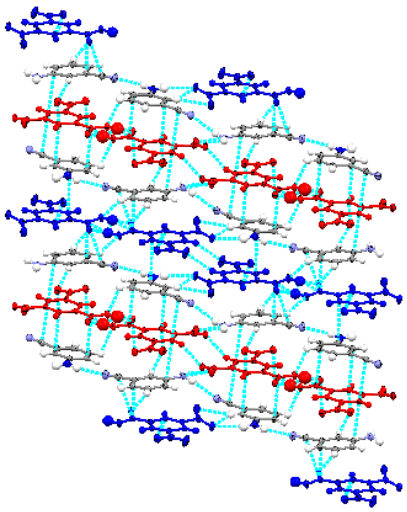

Figure 5.11 The wider packing in the molecular complex of 3,5-DNBA 3-ABCN. Dimer 1 is in blue and dimer 2 in red.

Variable temperature synchrotron X-ray diffraction measurements on 3,5-DNBA 3-ABCN

Variable temperature measurements were carried out on 3,5-DNBA 3-ABCN at the DLS at 100 to 300 K, in 50 K steps, and at the ALS at 100 to 300 K, in 100 K steps.

The C—O and C=O bond lengths of the carboxylic acid groups forming the hydrogen bonded dimers were followed as a function of temperature (Table 5.11 and Figure 5.12). Over the 100 to 300 K temperature range, a linear trend of the C—O bond lengths shortening and the C=O bond lengths lengthening with temperature occurs in both dimer 1 and dimer 2. This suggests the presence of temperature dependent disorder in this molecular complex. In general, the C—O and C=O bond lengths are closer in length over the temperature range for dimer 2 than they are for

dimer 1. At 100 K, the C—O and C=O bond lengths in dimer 2 also deviate from the average for an aromatic carboxylic acid (approximately 1.29 and 1.25 Å) whilst they do not for dimer 1 (approximately 1.31 and 1.23 Å). This suggests that the onset temperature and extent of proton disorder occurring is not the same for the two 3,5-DNBA dimers and that the effect is greater in dimer 2, though not such that a 50:50 split occupancy is suggested as the C—O and C=O bonds are not equalised at this temperature.

The C—O and C=O bond lengths from the DLS and ALS structures are consistent over the temperature range and indicate similar proton disorder behaviour; the apparent deviation at 300 K in the C—O and C=O distances in dimer 2 between the DLS and ALS structures is not large enough to be considered statistically significant.

Table 5.11 Carboxylic acid C—O and C=O bond lengths in dimer 1 and dimer 2, between 100 and 300 K, in the DLS and ALS structures of the molecular complex 3,5-DNBA 3-ABCN.

Dimer 1	DLS		ALS	
T (K)	dC—O (Å)	dC=O (Å)	dC—O (Å)	dC=O (Å)
100	1.309(1)	1.232(2)	1.305(1)	1.229(2)
150	1.300(1)	1.234(2)	-	-
200	1.290(2)	1.242(2)	1.294(3)	1.237(4)
250	1.281(2)	1.244(3)	-	-
300	1.277(2)	1.243(2)	1.272(4)	1.250(5)
Dimer 2	DLS		ALS	
T (K)	dC—O (Å)	dC=O (Å)	dC—O (Å)	dC=O (Å)
100	1.295(1)	1.248(2)	1.290(2)	1.247(2)
150	1.287(1)	1.250(2)	-	-
200	1.279(2)	1.253(2)	1.279(3)	1.255(3)
250	1.273(2)	1.256(3)	-	-
300	1.269(2)	1.254(3)	1.278(5)	1.240(5)

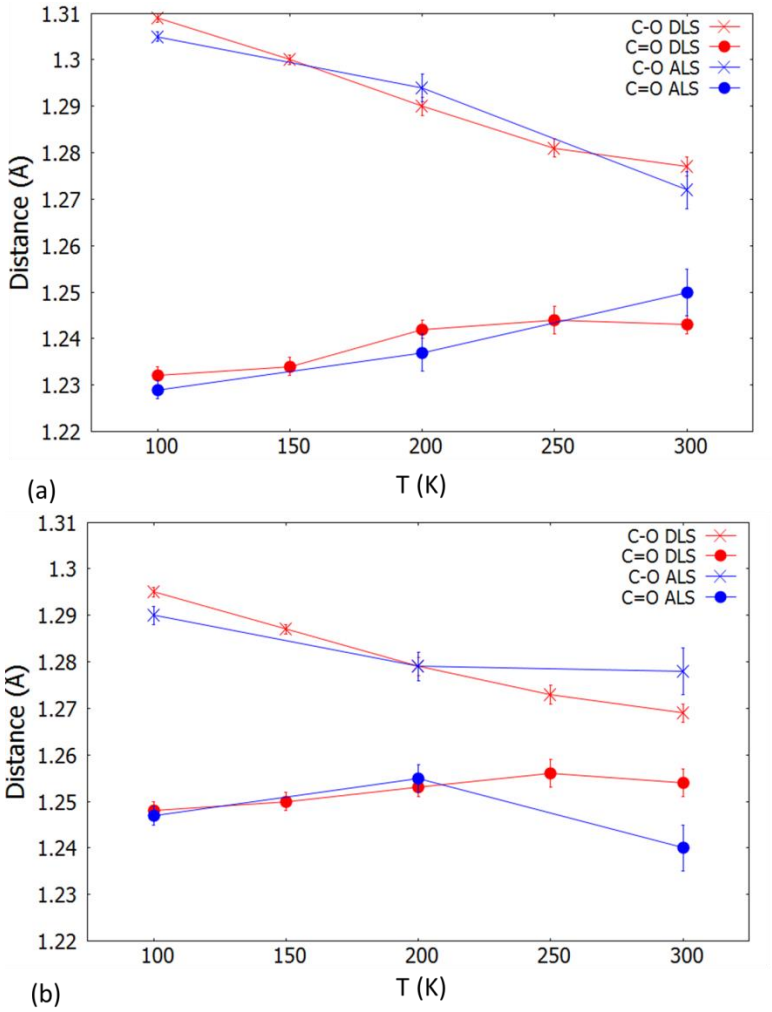

Figure 5.12 The C—O and C=O bond lengths of the carboxylic acid groups forming the hydrogen bonded dimers as a function of temperature in (a) dimer 1 and (b) dimer 2 in the DLS and ALS structures in 3,5-DNBA 3-ABCN.

The O—H···O hydrogen bond parameters in dimer 1 and 2 were also followed as a function of temperature (Table 5.12). The O···O hydrogen bond distance remains constant over the temperature range and between the DLS and ALS structures. The O—H distances lengthen and the H···O distances shorten linearly with temperature (Table 5.12 and Figure 5.13) as the refined hydrogen atom position moves towards the centre of the bond; behaviour that is characteristic of temperature dependent disorder and in agreement with the changes in the C—O and C=O bond lengths. The O—H and H···O distances suggest that the onset temperature of the proton disorder is different between the two dimers, where an elongated O—H distances occurs at temperatures as low as 100 K to 150 K in dimer 2 whilst in dimer 1 occurs more in the range of 150 to 200 K; this is in agreement with the deviations in the C—O and C=O bond lengths which are evident at 100 K in dimer 2 but are not indicated in dimer 1 until 200 K. The movement of the refined hydrogen atom position towards the centre of the bond is greater in dimer 2, coinciding with the C—O and C=O bond distances being closer in dimer 2 over the temperature range, and suggest a greater

extent of proton disorder occurring in this dimer. The O—H and H···O distances are also consistent between the DLS and ALS structures for each dimer, over the temperature range studied. The O—H and H···O distances, in conjunction with the C—O and C=O bond lengths, are therefore informative about the onset and temperature dependence of the proton disorder in this sample and the difference in the extents of disorder occurring between the two dimers.

The size of the thermal parameter (U_{iso}) of each dimer hydrogen atom increases linearly with temperature and can further suggest the presence of temperature dependent proton disorder in 3,5-DNBA 3-ABCN, in conjunction with the other indicators discussed here. The large value of U_{iso} in dimer 2 of 0.101(9) Å^2 at 100 K compared to 0.069(6) Å^2 in dimer 1, also suggests an earlier proton disorder onset temperature in dimer 2. The increase in size of the thermal parameters with temperature is similar between the two dimers and so indicates less about the extents of disorder occurring across the two dimers than is suggested by the C—O/C=O and O—H/H···O lengths as a function of temperature. Of course, in the absence of any corroborating information, the increase in size of the thermal parameter may also simply be an indicator of increased thermal motion at higher temperatures. In this case, the size of U_{iso} would only be useful for identifying the presence of proton disorder at low temperatures in this sample.

Table 5.12 Hydrogen bond parameters in dimer 1 and dimer 2, between 100 and 300 K in the DLS and ALS structures of 3,5-DNBA 3-ABCN.

Dimer 1	DLS				ALS			
T (K)	dO···O (Å)	dO—H (Å)	dH···O (Å)	U_{iso} (Å^2)	dO···O (Å)	dO—H (Å)	dH···O (Å)	U_{iso} (Å^2)
100	2.588(1)	0.98(2)	1.61(2)	0.069(6)	2.582(2)	1.07(3)	1.52(3)	0.072(9)
150	2.587(1)	1.05(3)	1.54(3)	0.099(7)	-	-	-	-
200	2.585(2)	1.12(3)	1.47(3)	0.119(9)	2.583(3)	1.14(6)	1.44(6)	0.17(2)
250	2.586(2)	1.16(3)	1.42(3)	0.142(11)	-	-	-	-
300	2.593(2)	1.14(4)	1.46(4)	0.157(12)	2.590(4)	1.19(7)	1.40(7)	0.20(3)
Dimer 2	DLS				ALS			
T (K)	dO···O (Å)	dO—H (Å)	dH···O (Å)	U_{iso} (Å^2)	dO···O (Å)	dO—H (Å)	dH···O (Å)	U_{iso} (Å^2)
100	2.618(1)	1.06(3)	1.56(3)	0.101(9)	2.608(2)	1.08(3)	1.53(3)	0.098(12)
150	2.613(1)	1.18(3)	1.43(3)	0.119(9)	-	-	-	-
200	2.613(2)	1.20(3)	1.41(2)	0.132(11)	2.616(3)	1.21(4)	1.42(4)	0.118(15)
250	2.612(2)	1.28(3)	1.34(3)	0.152(12)	-	-	-	-
300	2.615(2)	1.29(4)	1.33(4)	0.160(12)	2.605(5)	1.17(6)	1.44(6)	0.18(2)

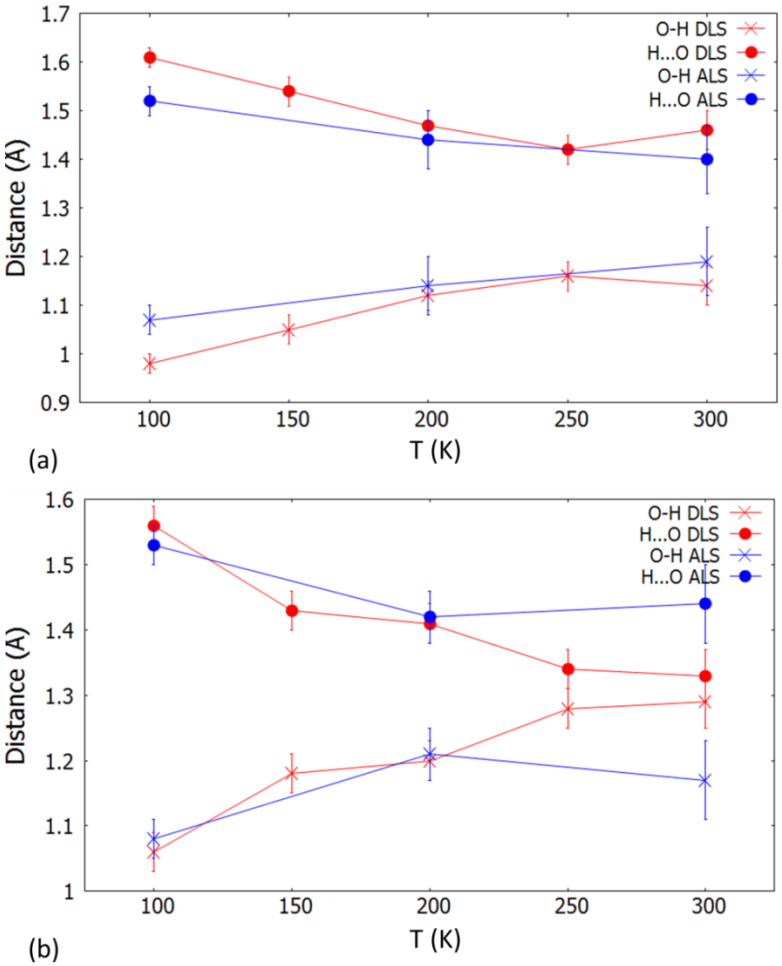

Figure 5.13 The O—H and H···O bond lengths in the O—H···O dimer hydrogen bonds with temperature in (a) dimer 1 and (b) dimer 2 in the DLS and ALS structures of 3,5-DNBA 3-ABCN.

Fourier difference maps were generated for the dimer 1 (Figure 5.14) and dimer 2 (Figure 5.15) hydrogen bonds over the temperature range. In agreement with the changes observed in the C—O/C=O and O—H/H···O bond lengths and hydrogen atom thermal parameters, a change in the hydrogen atom density in the Fourier difference maps for each dimer occurs with temperature and this change appears to be different between the two dimers. Unlike for the C—O/C=O and O—H/H···O bond lengths and hydrogen atom thermal parameters, the Fourier difference maps for each dimer are not consistent between the DLS and ALS structures. This lack of consistency may be caused by the presence of significant (and different) amounts of noise in the Fourier difference maps generated for the DLS and ALS structures and so the information about the behaviour of the hydrogen density in the dimer hydrogen bonds is less clear or reliable. There is less noise in Fourier difference maps generated for the DLS structures and so these are better used for identifying the presence and extent of proton disorder in this sample in conjunction with the other structural parameters.

For dimer 1, a single peak for the hydrogen atom density is present in the Fourier difference maps generated for the DLS structure at 100 and 150 K. The single peak suggests an ordered carboxylic acid; in agreement with the C—O and C=O bond lengths at this temperature ($d_{C—O}$ 1.309(1) Å and $d_{C=O}$ 1.232(2) Å). The first change in the shape of the hydrogen atom density occurs at 200 K; at this temperature, a second peak appears in the Fourier difference map generated for the DLS structure and suggests the onset of proton disorder at this temperature. This apparent change in the hydrogen atom density at 200 K coincides with the first significant deviation of the C—O and C=O bond lengths away from those of an ordered aromatic carboxylic acid; from 1.300(1) Å and 1.234(2) Å, respectively, at 150 K to 1.290(2) Å and 1.242(2) Å, respectively, at 200 K. The intensity of the signal for this peak increases between 200 and 300 K such that the second site is more apparent and indicates an increase in the extent of proton disorder between these two temperatures. The increase in intensity of the second peak between 200 and 300 K coincides with further shortening of the C—O and lengthening of the C=O bond distances to 1.277(2) and 1.243(2) Å, respectively.

For dimer 2, a weak signal in the Fourier difference maps of the dimer hydrogen bond at 100 K may indicate a second hydrogen atom position and the onset of proton disorder. This is not completely unlikely where the C—O and C=O bond lengths ($d_{C—O}$ 1.295(1) Å and $d_{C=O}$ 1.248(2) Å) are slightly shortened and lengthened, respectively, at this temperature for an ordered aromatic carboxylic acid group. The intensity of the signal for the second peak appears to increase with temperature at 200 K, suggesting an increase in the extent of proton disorder and coinciding with an increased shortening and lengthening, respectively, of the C—O and C=O bond lengths at this temperature ($d_{C—O}$ 1.279(2) Å and $d_{C=O}$ 1.253(2) Å). In the 250 and 300 K Fourier difference maps, the hydrogen atom density appears almost equally spit over the two sites, in two separate positions at 250 K and elongated over the two sites at 300 K. This could suggest an approaching towards a 50:50 disorder of the dimer proton above 250 K coinciding with the equalisation of the C—O and C=O bond lengths which are close in value to each other at 300 K ($d_{C—O}$ 1.269(2) Å and $d_{C=O}$ 1.254(3) Å).

In agreement with changes to the C—O and C=O bond lengths with temperature, the variable temperature Fourier difference maps for each dimer are able to identify temperature dependent proton disorder in 3,5-DNBA 3-ABCN and also reveal information about the extent of proton disorder occurring.

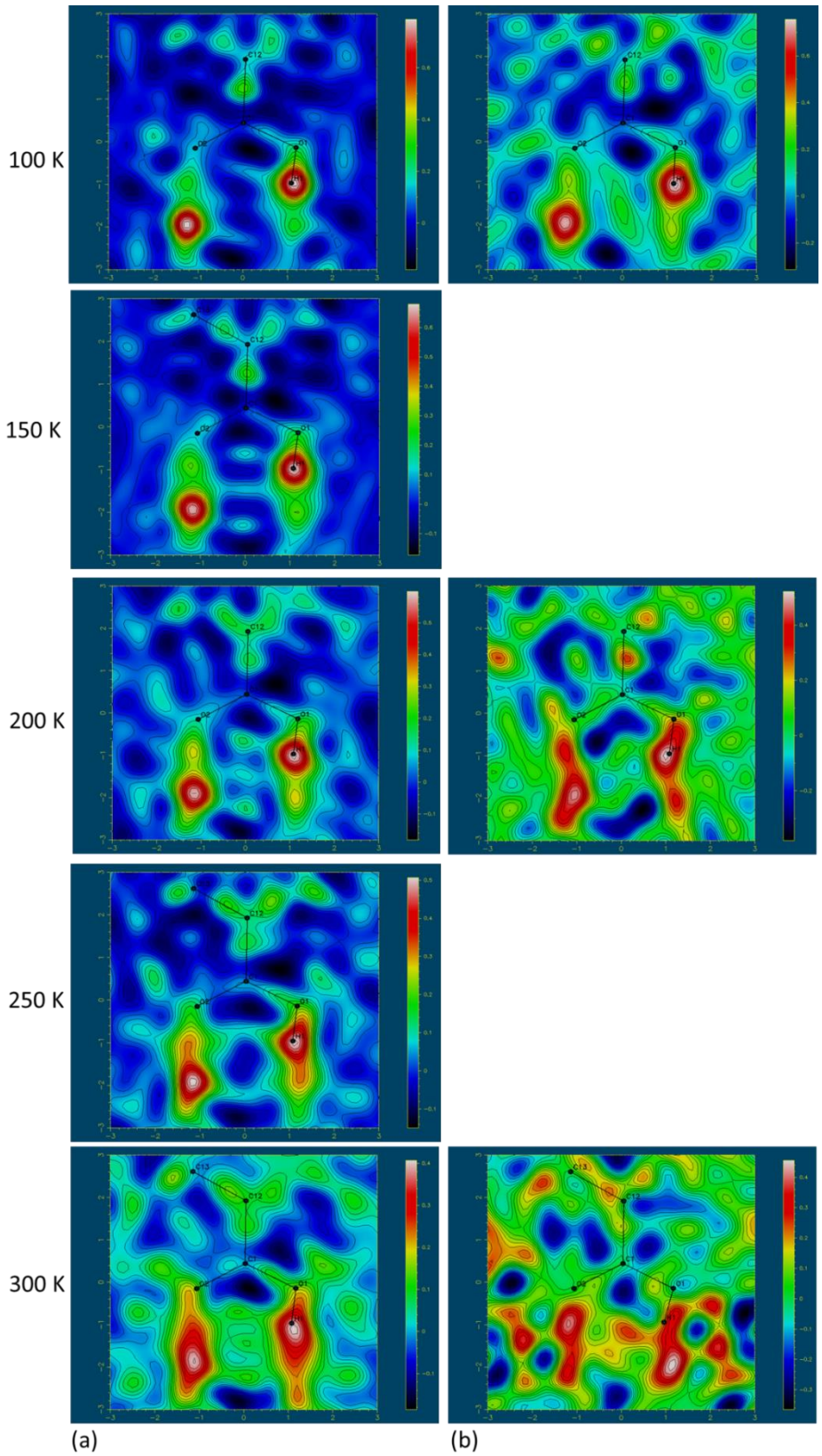

Figure 5.14 Variable temperature Fourier difference maps showing the electron density associated with the H-atom in the 3,5-DNBA dimer hydrogen bonds in 3,5-DNBA 3-ABCN dimer 1 generated for the (a) DLS and (b) ALS structures.

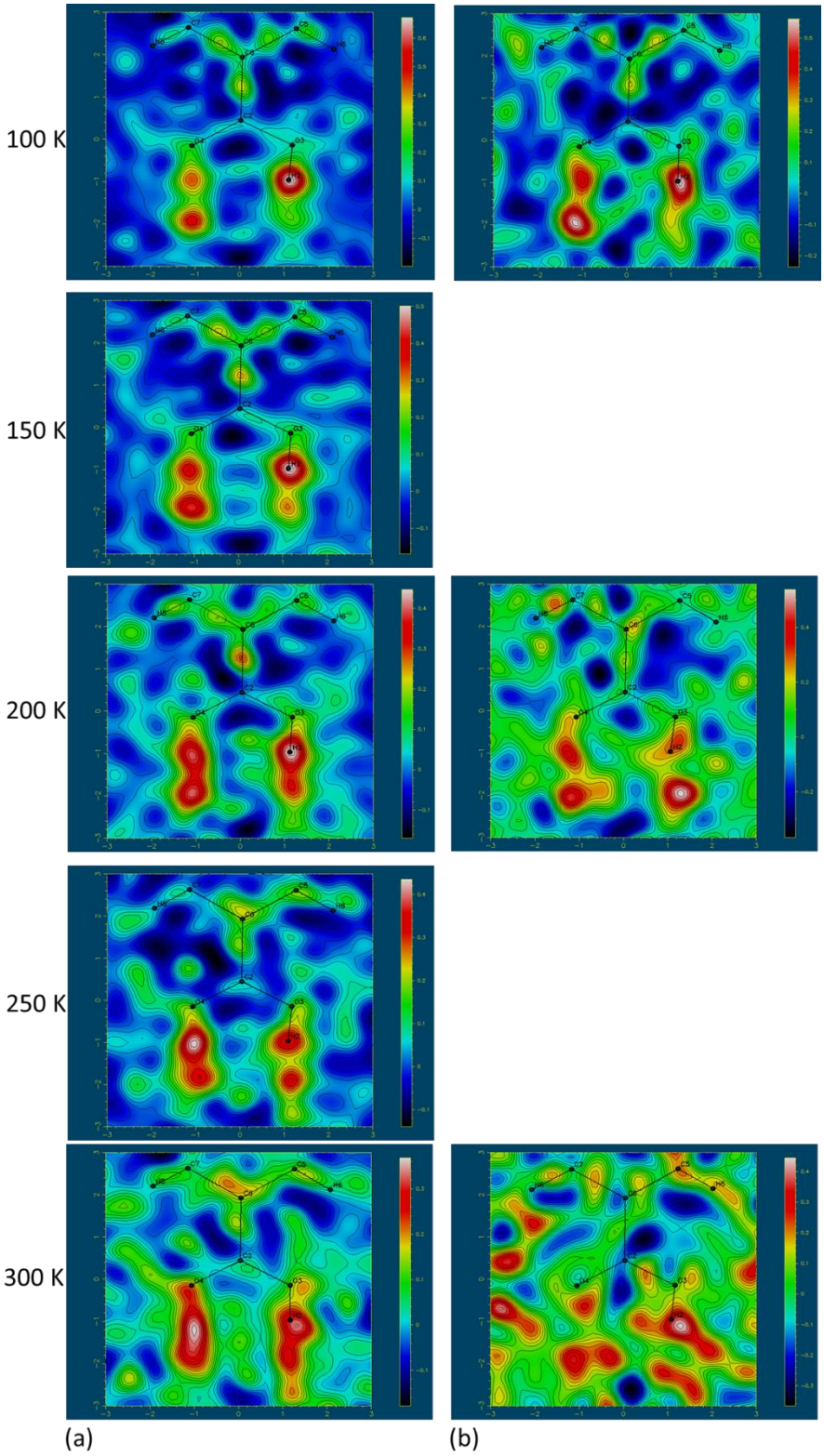

Figure 5.15 Variable temperature Fourier difference maps showing the electron density associated with the H-atom in the 3,5-DNBA dimer hydrogen bonds in 3,5-DNBA 3-ABCN dimer 2 generated for the (a) DLS and (b) ALS structures.

The potential to refine accurate occupancies for the proton sites as a function of temperature was investigated for 3,5-DNBA 3-ABCN. A structural model where the hydrogen atom is disordered

over two sites in the dimer hydrogen bond was refined for both the DLS and ALS structures (Table 5.13).

Table 5.13 Refined occupancies of the two proton configurations in dimer 1 and dimer 2 in the DLS and ALS structures of 3.5-DNBA 3-ABCN. The X-ray refined occupancy values have an estimated error of approximately 10 %. [89]

	Refined occupancy ratios			
	Dimer 1		Dimer 2	
T (K)	DLS	ALS	DLS	ALS
100	73:27	69:31	62:38	65:35
150	69:31	-	56:44	-
200	64:36	63:37	45:55	55:45
250	59:41	-	49:51	-
300	62:38	45:55	48:52	57:43

The refined proton site occupancies are consistent, considering the estimated 10% error, for dimer 1 and dimer 2 between the DLS and ALS structures. The occupancy values follow the trend of increasing disorder with temperature and a greater increase occurs in dimer 2, as suggested by both hydrogen bond dimer structural parameters and Fourier difference maps. However, the extent of disorder at each temperature does not appear to agree as well with the C—O and C=O bond lengths at each temperature. For example, a split occupancy of approximately 70:30 is estimated for dimer 1 at 100 K suggesting a significant amount of proton disorder to be occurring. This does not coincide with the C—O and C=O bonds lengths ($d_{C—O}$ 1.309(1) Å and $d_{C=O}$ 1.232(2) Å), which have values close to those of an ordered aromatic carboxylic acid, and the Fourier difference maps, which contain only one hydrogen atom peak, at this temperature. For dimer 2, at 300 K, an approximate 50:50 disorder is suggested by the refined occupancy values however the C—O and C=O bonds lengths are not equalised at this temperature in either the DLS ($d_{C—O}$ 1.269(2) Å and $d_{C=O}$ 1.254(3) Å) or ALS ($d_{C—O}$ 1.278(5) Å and $d_{C=O}$ 1.240(5) Å) structures, respectively. The proton site occupancies refined from the synchrotron X-ray data are thus shown here to be less reliable for determining the onset and extent of variable temperature disorder in this complex, 3,5-DNBA 3-ABCN, relative to the other structural parameters and Fourier difference maps.

5.4.2 3,5-DNBA MCZ

In the crystal structure of 3,5-DNBA MCZ at 100 K (DLS), the two components crystallise in a 1:1 ratio, in space group $P\bar{1}$. A 3,5-DNBA hydrogen bonded $R_2^2(8)$ dimer is present in the structure where the 3,5-DNBA molecules are held together by moderate strength O—H···O hydrogen bonds ($d_{O\cdots O}$ 2.626(2) Å at 100 K) and are related by an inversion centre at the centre of the $R_2^2(8)$ hydrogen bonded ring (Figure 5.16).

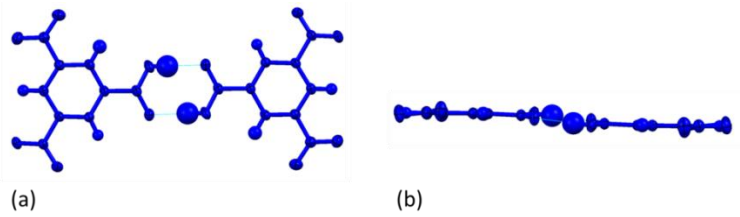

Figure 5.16 The 3,5-DNBA centrosymmetric hydrogen bonded $\boldsymbol{R_2^2(8)}$ dimer in the molecular complex of 3,5-DNBA MCZ at 100 K: (a) perpendicular to the dimer plane and (b) in plane of the dimer.

Within the hydrogen bonded dimer, the aromatic rings of the two 3,5-DNBA molecules are not in the same layer (offset by 0.447 Å between aromatic ring planes) and the hydrogen bonded carboxylic acid group is twisted slightly out of co-planarity of the 3,5-DNBA aromatic ring (5.9(2) °). On forming the $R_2^2(8)$ hydrogen bonded ring, the carboxylic acid groups are tilted relative to one another (C—O···O angle of 117.2(1) ° and a C=O···O angle of 117.6(1) °). One of the nitro groups is co-planar with aromatic ring (twisted by − 0.6(2) °) whilst the other is twisted slightly (7.1(2) °) out of co-planarity of the aromatic ring.

Molecular packing

In the crystal structure of 3,5-DNBA MCZ, there are short contacts in the local packing environment of the carboxylic acid groups forming the 3,5-DNBA dimer (Figure 5.17). These include those to MCZ molecules, in the neighbouring environment, which stack above ($d_{\pi\cdots\pi}$ 3.273(3) and 3.308(3) Å) the carboxylic acid groups. There are no significant interactions to the carboxylic acid oxygen atoms.

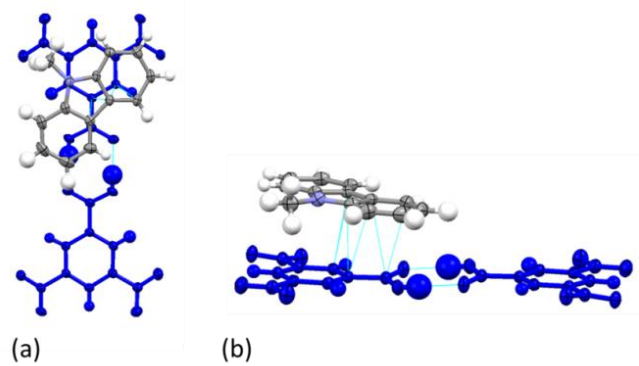

Figure 5.17 The local packing environments of the 3,5-DNBA hydrogen bonded dimer carboxylic acid groups in the molecualr complex of 3,5-DNBA MCZ. For clarity, the packing is shown for one side of the centrosymmetric dimer only.

Intermolecular interactions also occur between the 3,5-DNBA molecule, in each dimer, and the local environment (Figure 5.18). These interactions involve predominantly MCZ molecules with tail to tail interactions formed between 3,5-DNBA hydrogen bond dimers.

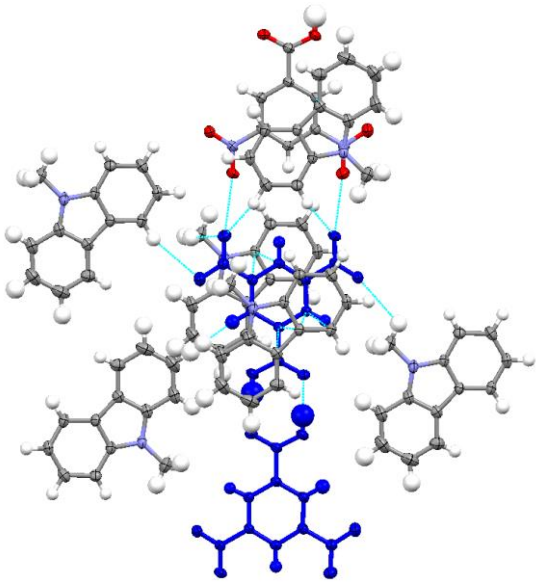

Figure 5.18 The local packing environments of the 3,5-DNBA molecule in the centrosymmetric hydrogen bonded dimer in the molecular complex of 3,5-DNBA MCZ. For clarity, the packing is shown for one side of the centrosymmetric dimer only.

Weak interactions form to both 3,5-DNBA nitro groups of the 3,5-DNBA molecule forming the centrosymmetric dimer. The nitro group on the protonated side of the 3,5-DNBA molecule forms weak C—H···O hydrogen bonds through interaction of both its nitro oxygen atoms to MCZ aromatic C—H ($d_{C\cdots O}$ 3.475(2) and 3.602(2) Å) and methyl C—H (3.257(2) Å) groups. The nitro group on the non-protonated side of the 3,5-DNBA molecule forms weak C—H···O hydrogen bonds through interaction of both the nitro oxygen atoms with C—H groups donated by an MCZ aromatic ring ($d_{C\cdots O}$ 3.454(2) Å) and a MCZ methyl group ($d_{C\cdots O}$ 3.217(2) Å). Both nitro groups form weak O···O contacts to a neighbouring 3,5-DNBA dimer unit ($d_{O\cdots O}$ 3.037(2) Å), just less than the sum of the van der Waals radii for the two atoms (3.04 Å) and therefore significant, occurring such that a nitro group on the protonated side on one 3,5-DNBA molecule links to the nitro group on the non-protonated side of the next 3,5-DNBA molecule. Equivalently orientated MCZ molecules stack above ($d_{\pi\cdots\pi}$ 3.340(2), 3.394(2) and 3.360(2) Å) and below (3.311(2), 3.317(2), 3.366(2) and 3.373(2) Å) the 3,5-DNBA molecule forming the dimer.

In the wider crystal structure, molecules of MCZ molecules pack around the 3,5-DNBA hydrogen bonded dimers such that the acid groups lie in a pocket, in an isolated environment (Figure 5.19).

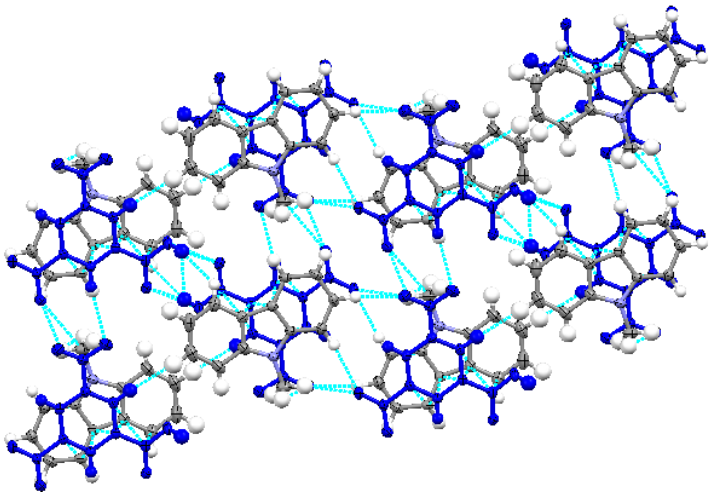

Figure 5.19 The wider packing in the molecular complex of 3,5-DNBA MCZ. The 3,5-DNBA hydrogen bonded dimer is shown in blue.

Variable temperature synchrotron X-ray diffraction measurements on 3,5-DNBA MCZ

Variable temperature measurements were carried out on 3,5-DNBA MCZ at the DLS at 100 to 300 K, in 50 K steps, and at the ALS at 100 to 300 K, in 100 K steps.

The C—O and C=O bond lengths of the carboxylic acid groups forming the hydrogen bonded dimers were followed as a function of temperature (Table 5.14 and Figure 5.20). Over the 100 to 300 K temperature range, only very small changes to the C—O and C=O bond lengths occur. At 100 K, the C—O and C=O bond lengths (at approximately 1.27 and 1.25 Å, respectively) deviate significantly from the average for an aromatic carboxylic acid in the DLS and ALS structures, suggesting a significant amount of proton disorder at this temperature. Between 100 and 200 K, the C—O and C=O bond lengths follow a linear trend of shortening and lengthening, respectively, indicating temperature dependent proton disorder, reaching equalisation at 200 K, in both the DLS and ALS structures. This suggests a 50:50 proton disorder at this temperature. Beyond 200 K, the C—O and C=O bond lengths appear to switch in the ordering; the C=O bond is now longer than the C—O. However, these values are consistent within error and so no further change to the proton disorder is suggested between 200 and 300 K. The C—O and C=O bond lengths between the DLS and ALS structures are consistent over the temperature range, in support of the same proton disorder behaviour; the apparent deviation at 300 K in the C—O and C=O distances between the DLS and ALS structures is not large enough to be considered significant.

Table 5.14 Carboxylic acid C—O and C=O bond lengths in the 3,5-DNBA dimer between 100 and 300 K, in the DLS and ALS structures of 3,5-DNBA MCZ.

	DLS		ALS	
T (K)	dC—O (Å)	dC=O (Å)	dC—O (Å)	dC=O (Å)
100	1.273(2)	1.258(2)	1.275(3)	1.262(3)
150	1.269(2)	1.264(2)	-	-
200	1.267(2)	1.266(2)	1.265(4)	1.265(4)
250	1.260(2)	1.266(2)	-	-
300	1.257(3)	1.264(3)	1.257(6)	1.250(5)

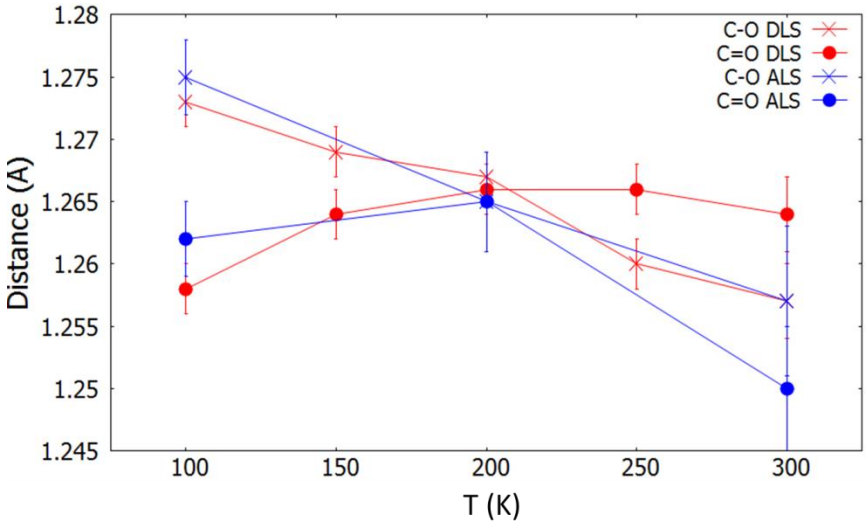

Figure 5.20 The C—O and C=O bond lengths of the carboxylic acid groups forming the hydrogen bonded dimers as a function of temperature in the DLS and ALS structures of 3,5-DNBA MCZ.

The O—H···O hydrogen bond parameters of the 3,5-DNBA hydrogen bonded dimer were also followed as a function of temperature (Table 5.15). A gradual increase in the O···O hydrogen bond distance occurs between 100 and 300 K for the DLS structures in accordance with thermal expansion of the cell. In the ALS structure, a shortening of the O···O hydrogen bond distance occurs between 200 and 300 K. This may be caused by the 3,5-DNBA dimer lying effectively along the *b* and *c*-axes which experience decreases in length between 200 K and 300 K; from 8.4261(6) to 8.395(17) Å for the *b*-axis and from 15.7600(1) to 15.72(3) Å for the *c*-axis. Little change is observed in the O—H and H···O distances as a function of temperature; a result of the distance restraint applied to the O—H distance in order to achieve a stable refinement of the hydrogen atom position. These parameters therefore cannot be used to identify or quantify the temperature dependent proton disorder in this sample. The size of the isotropic thermal parameter (U_{iso}) for the dimer proton is large at 100 K, at 0.11 Å^2, and may suggest the presence of proton disorder at this temperature in agreement with the deviating (from the ordered carboxylic group

distances) C—O and C=O bond lengths. The increase in the size of the isotropic thermal parameter as a function of temperature may also indicate an increase in the extent of proton disorder occurring. However, the thermal parameter continues to increase in size beyond 200 K with no further change in the proton disorder suggested by the C—O and C=O bond lengths, indicating on the basis of this corroborating factor that this is likely simply a result of the increase in thermal motion of atoms with temperature. In this case, the size of U_{iso} would therefore only be useful for identifying the presence of proton disorder at low temperature but reveals little about the temperature dependence or extent occurring. The hydrogen atom thermal parameters do not have errors as a result of a restraint being applied to the thermal parameter for a stable refinement. This makes this parameter even less reliable in determining proton disorder behaviour.

Table 5.15 Hydrogen bond parameters in the 3,5-DNBA dimer between 100 and 300 K in the DLS and ALS structures of 3,5-DNBA MCZ.

T (K)	DLS				ALS			
	dO···O (Å)	dO—H (Å)	dH···O (Å)	Uiso ($Å^2$)	dO···O (Å)	dO—H (Å)	dH···O (Å)	U_{iso} ($Å^2$)
100	2.626(2)	0.84(3)	1.79(3)	0.110	2.628(3)	0.85(3)	1.78(3)	0.098
150	2.633(2)	0.84 (3)	1.80(3)	0.143	-	-	-	-
200	2.639(2)	0.85(3)	1.79(3)	0.208	2.631(3)	0.84(4)	1.79(4)	0.152
250	2.637(2)	0.84(4)	1.80(3)	0.234	-	-	-	-
300	2.639(2)	0.85(5)	1.79(4)	0.283	2.621(5)	0.84(5)	1.79(5)	0.273

Variable temperature Fourier difference maps were generated for the 3,5-DNBA hydrogen bonded dimer (Figure 5.21). In agreement with changes being observed in the C—O/C=O bond lengths as a function of temperature, a change in the hydrogen atom density for the DLS structure also occurs. There is less agreement in the proton disorder behaviour indicated in the Fourier difference maps between the two sources. The Fourier difference maps of the ALS structures contain large amounts of noise and therefore determination of the hydrogen atom behaviour is more difficult.

At 100 K, a second peak is present in the DLS Fourier difference map suggesting the presence of proton disorder at this temperature. The second peak has a strong intensity, indicated by the white region at its centre which is just smaller than that of the first peak. The intensity of the second peak suggests a significant amount of proton disorder at this temperature and is in agreement with the C—O and C=O bond lengths at 100 K, which deviate significantly from the values of an ordered aromatic carboxylic acid. The intensity of the second hydrogen atom peak is increased at 150 and 200 K such that its maximum appears greater than that of the first peak. This suggests an increase in the extent of the proton disorder occurring between 150 and 200 K and may be an indicator of a

50:50 split in occupancies at 200 K, as suggested by the equalised C—O and C=O bond lengths. A similar effect is observed at 250 K, but with the intensity of the first site being slightly stronger, whilst at 300 K, the density for the hydrogen atom is significantly smeared such that it becomes difficult to resolve the two hydrogen atom positions; there is also additional noise in the Fourier difference maps. These fluctuations in the density between 200 and 300 K occur as the C—O and C=O bond lengths undergo minor fluctuations within error.

A second peak with strong intensity is also present in the Fourier difference map for the ALS structure at 100 K, indicating the presence of proton disorder. The intensity of this second peak appears to be greater than that of the peak for the refined hydrogen atom position and suggests more disorder to be occurring than indicated by the values of the C—O and C=O bond lengths at 100 K. Significant amounts of noise are present in the Fourier difference maps for the 200 and 300 K ALS structures such that determination of the hydrogen atom behaviour is unreliable.

The better quality variable temperature Fourier difference maps for the DLS structure are able to identify temperature dependent proton disorder in 3,5-DNBA MCZ and also reveal information about the extent of proton disorder occurring that is in reasonable agreement with changes to the C—O and C=O bond lengths as a function of temperature.

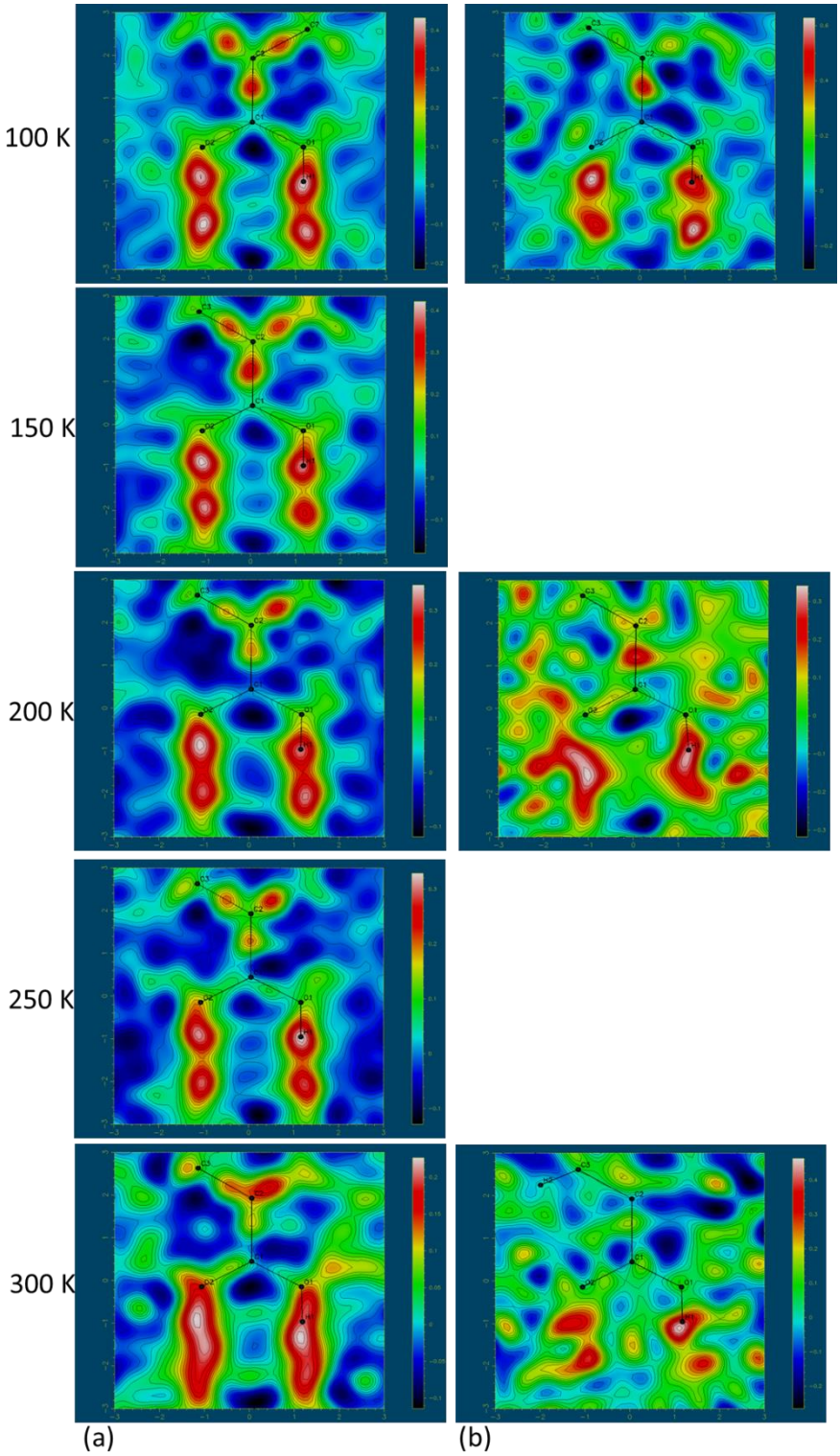

Figure 5.21 Variable temperature Fourier difference maps showing the electron density associated with the H-atom in the 3,5-DNBA dimer hydrogen bonds in 3,5-DNBA MCZ in the (a) DLS and (b) ALS structures.

The potential to refine accurate occupancies for the proton sites as a function of temperature was investigated for 3,5-DNBA MCZ. A structural model where the hydrogen atom is disordered over two sites in the dimer hydrogen bond was refined (Table 5.16).

At 100 K, the occupancies refined for the proton sites in the DLS and ALS structures both indicate the presence of proton disorder, in agreement with the deviation of the C—O and C=O bond lengths away from the values of an ordered aromatic carboxylic acid. However, there is not agreement in the extent of disorder suggested. For example, in each structure, at 100 K, the refined occupancies suggest a 50:50 disorder (considering the 10 % error on occupancies refined from X-rays) or a slight bias for the second site and a switch in carboxylic acid configuration; this is not in agreement with the disorder behaviour suggested by the C—O and C=O bond lengths at 100 K (approximately 1.27 and 1.25 Å, respectively). An increased occupancy of the second site is also suggested between 100 and 200 K in the DLS structure, agreeing with the Fourier difference maps where the second peak appears slightly more intense but in contrast to the C—O and C=O bonds which approach equalisation at 200 K, suggesting a 50:50 proton disorder. Occupancy values for the two proton sites at 300 K have been refined in the DLS structure, however a significant extent of smearing of the proton density is suggested in the Fourier difference maps; it therefore seems unlikely that during the refinement it is possible to attribute electron density to two separate positions with any confidence. There is also poor agreement in the refined occupancies between the DLS and ALS structures.

It appears that the refined occupancies are particularly unreliable for this molecular complex and so should be significantly down weighted when quantifying extents of proton disorder.

Table 5.16 Refined occupancies of the two proton configurations in the DLS and ALS structures of 3,5-DNBA MCZ. The X-ray refined occupancy values have an estimated error of approximately 10 %. [89]

T (K)	Refined occupancy ratios	
	DLS	ALS
100	44:56	42:58
150	43:57	-
200	39:61	54:46
250	57:43	-
300	40:60	33:77

5.4.3 3,5-DNBA In-3-Ac

In the crystal structure of 3,5-DNBA and In-3-Ac at 100 K (DLS), the two components crystallise in a 1:1 ratio, in space group $P2_1/c$. A 3,5-DNBA hydrogen bonded $R_2^2(8)$ dimer is present in the structure, where the 3,5-DNBA molecules are held together by strong to moderate strength O—H···O hydrogen bonds ($d_{O\cdots O}$ 2.633(2) Å at 100 K) and are related by an inversion centre at the centre of the $R_2^2(8)$ hydrogen bonded ring (Figure 5.22).

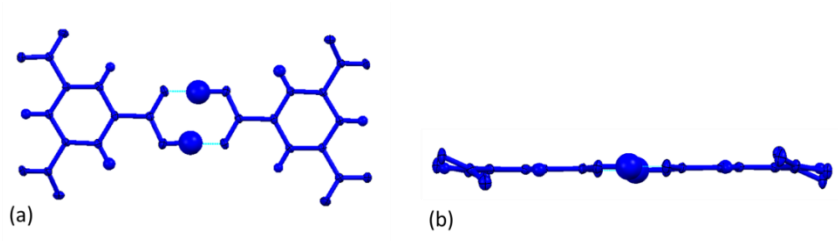

Figure 5.22 The 3,5-DNBA centrosymmetric hydrogen bonded $\boldsymbol{R_2^2(8)}$ dimer in the molecular complex of 3,5-DNBA In-3-Ac at 100 K: (a) perpendicular to the dimer plane and (b) in plane of the dimer.

Within the hydrogen bonded dimer, the aromatic rings of the two 3,5-DNBA molecules are in the same layer (0.136 Å between aromatic ring planes) and the hydrogen bonded carboxylic acid groups are essentially planar to the aromatic ring (twisted by − 3.9(2) °). In the $R_2^2(8)$ hydrogen bonded ring, the carboxylic acid groups are tilted relative to one another (C—O···O angle of 113(2) ° and a C=O···O angle of 118(1) °). The nitro groups are non co-planar with the aromatic ring, twisted by − 12.8(2) and 27.5(2) ° out of co-planarity.

Molecular packing

In the crystal structure of 3,5-DNBA In-3-Ac, there are short contacts in the local packing environment of the carboxylic acid groups forming the 3,5-DNBA dimer (Figure 5.23). These include those to In-3-Ac molecules, in the local environment, which stack above ($d_{\pi\cdots\pi}$ 3.393(2) and 3.338(2) Å) and below ($d_{\pi\cdots\pi}$ 3.387(2) Å) the carboxylic acid groups. There are no significant interactions formed to the carboxylic acid oxygen atoms.

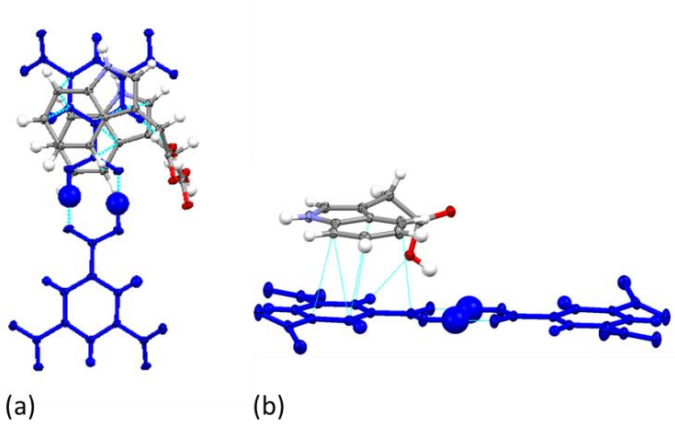

Figure 5.23 The local packing environments of the 3,5-DNBA hydrogen bonded dimer carboxylic acid groups in the molecular complex of 3,5-DNBA In-3-Ac. For clarity, the packing is shown for one side of the centrosymmetric dimer only and shown from different perspectives (a) and (b).

Intermolecular interactions also occur between the 3,5-DNBA molecules, in each dimer, and the local environment (Figure 5.24). These interactions involve In-3-Ac molecules only; there are no direct links between the 3,5-DNBA hydrogen bonded dimers.

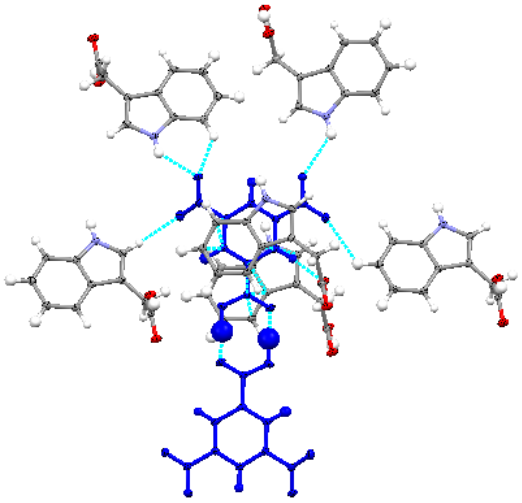

Figure 5.24 The local packing environments of the 3,5-DNBA molecule in the centrosymmetric hydrogen bonded dimer in the molecular complex of 3,5-DNBA In-3-Ac. For clarity, the packing is shown for one side of the centrosymmetric dimer only.

Weak interactions form to both 3,5-DNBA nitro groups of the 3,5-DNBA molecule forming the centrosymmetric dimer. The nitro group on the protonated side of the 3,5-DNBA molecule forms weak C—H···O hydrogen bonds through both its oxygen atoms to aromatic C—H groups from different In-3-Ac molecules in the local environment ($d_{C\cdots O}$ 3.206(2) and 3.172(3) Å). One nitro oxygen atom also interacts with an N—H group on a neighbouring In-3-Ac forming a moderate strength N—H···O hydrogen bond ($d_{N\cdots O}$ 2.991(1) Å). The nitro group on the non-protonated side of the molecule forms a weak C—H···O hydrogen bond through one of its oxygen atoms to a C—H group of a neighbouring In-3-Ac molecule ($d_{C\cdots O}$ 3.279(2) Å) whilst the other oxygen atom interacts with an N—H group on a neighbouring In-3-Ac forming a weak N—H···O hydrogen bond ($d_{N\cdots O}$ 3.023(2) Å). A weak C—H···O bond also form on the non-protonated side of the 3,5-DNBA molecule, involving one of its ring C—H and an In-3-Ac hydroxyl group ($d_{C\cdots O}$ 3.362(2) Å). In-3-Ac molecules in the local environment also stack above ($d_{\pi\cdots\pi}$ 3.328(2) and 3.383(2) Å) and below ($d_{\pi\cdots\pi}$ 3.329(2), 3.331(2), 3.353(2) and 3.355(2) Å) the 3,5-DNBA molecule forming the dimer.

In the wider crystal structure, similarly to 3,5-DNBA MCZ, molecules of In-3-Ac pack around the 3,5-DNBA hydrogen bonded dimer such that the acid groups lie in a pocket, in an isolated environment (Figure 5.25).

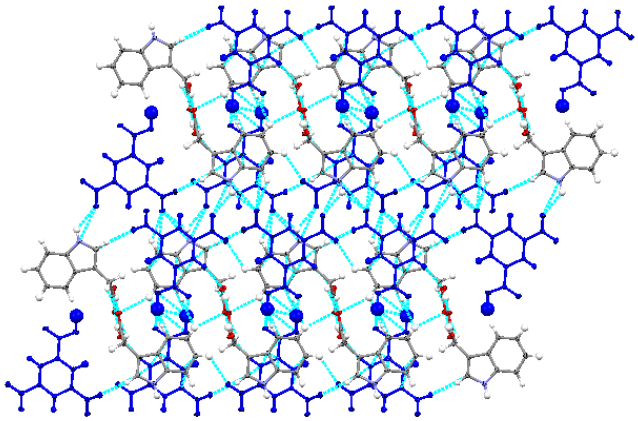

Figure 5.25 The wider packing in the molecular complex of 3,5-DNBA In-3-Ac. The 3,5-DNBA hydrogen bonded dimer is shown in blue.

Variable temperature synchrotron X-ray diffraction measurements on 3,5-DNBA In-3-Ac

Variable temperature measurements were carried out on 3,5-DNBA In-3-Ac at the DLS from 100 to 300 K, in 50 K steps.

The C—O and C=O bond lengths of the carboxylic acid groups forming the hydrogen bonded dimers were followed as a function of temperature (Table 5.17 and Figure 5.26). Over the 100 to 300 K temperature range, a linear trend of the C—O bond lengths shortening and the C=O bond lengths lengthening with temperature occurs. This suggests the presence of temperature dependent disorder in this molecular complex. At 100 K, the C—O and C=O bond lengths deviate from the average for an aromatic carboxylic acid, being 1.282(2) and 1.251(2) Å respectively. Proton disorder is therefore indicated at low temperature. At 300 K, the C—O and C=O bond lengths are very close in length, at 1.272(2) and 1.263(2) Å respectively, suggesting a high extent of disorder in the proton position at this temperature; though not such that a 50:50 split occupancy is suggested as the C—O and C=O bonds are not fully equalised.

Table 5.17 Carboxylic acid C—O and C=O bond lengths in the 3,5-DNBA dimer in 3,5-DNBA In-3-Ac between 100 and 300 K.

T (K)	dC—O (Å)	dC=O (Å)
100	1.282(2)	1.251(2)
150	1.277(2)	1.256(1)
200	1.274(2)	1.257(2)
250	1.270(2)	1.258(2)
300	1.272(3)	1.263(2)

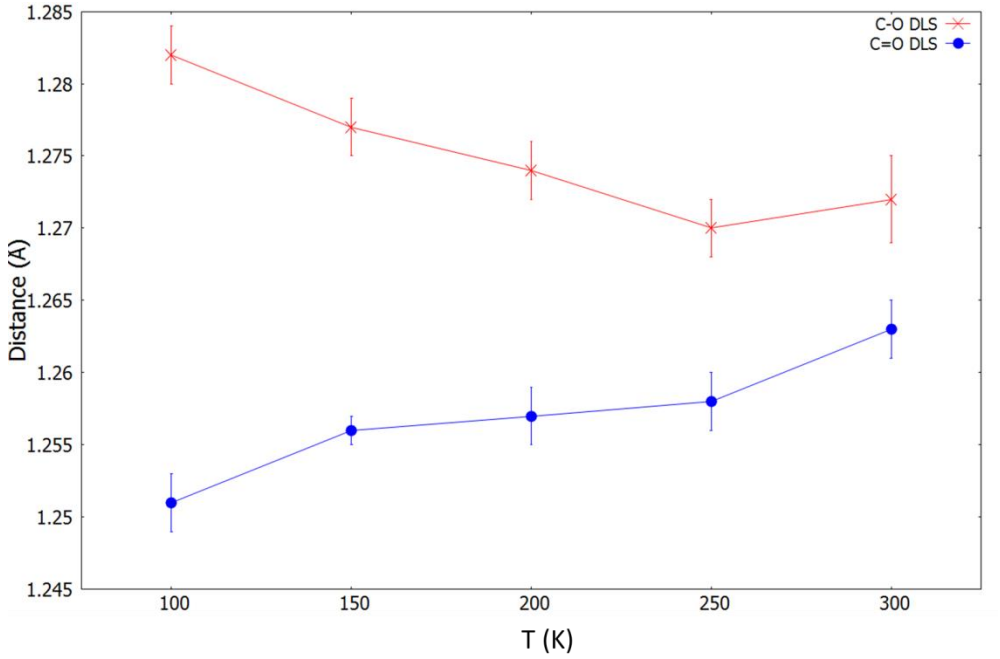

Figure 5.26 The C—O and C=O bond lengths of the carboxylic acid groups forming the hydrogen bonded dimer as a function of temperature in 3,5-DNBA In-3-Ac.

The O—H···O hydrogen bond parameters of the 3,5-DNBA dimer were also followed as a function of temperature (Table 5.18 and Figure 5.27). The O···O hydrogen bond distance remains constant between 100 and 250 K whilst a large increase occurs at 300 K. This jump may be caused by the 3,5-DNBA dimer lying parallel to the *a*-axis which experiences a sharp increase in length between 250 and 300 K from 15.8620(5) Å to 15.948(3) Å.

The hydrogen atom parameters in the O—H···O are less informative about the temperature dependent proton disorder in this molecular complex than the C—O and C=O bond lengths. The elongated O—H and shortened H···O bond distances indicate the presence of disorder at 100 K ($d_{O—H}$ 1.19(4) Å and $d_{H···O}$ 1.45(4) Å), however, over the temperature range, they indicate little about the change in disorder occurring, remaining essentially unchanged up to 200 K. At 250 K, the refined hydrogen atom position is moved towards the centre of the bond, this is an indicator of a possible increase in disorder at this temperature. The thermal parameter of the dimer proton is large at 100 K (0.112(13) $Å^2$) and may suggest the presence of disorder at this temperature however, there is little change in this value over the temperature range and so it does not give additional insight into how the disorder changes with temperature. In this molecular complex, the hydrogen atom parameters therefore may be tentatively used to identify the presence of proton disorder initially, but do not indicate how the disorder changes with temperature.

Table 5.18 Hydrogen bond parameters in the 3,5-DNBA dimer in 3,5-DNBA In-3-Ac between 100 and 300 K.

T (K)	dO···O (Å)	dO—H (Å)	dH···O (Å)	U_{iso} (Å^2)
100	2.633(2)	1.19(4)	1.45(5)	0.112(13)
150	2.636(1)	1.20(3)	1.44(3)	0.123(12)
200	2.636(2)	1.19(3)	1.45(3)	0.127(13)
250	2.636(2)	1.32(3)	1.32(3)	0.119(13)
300	2.647(2)	1.31(5)	1.34(5)	0.130(14)

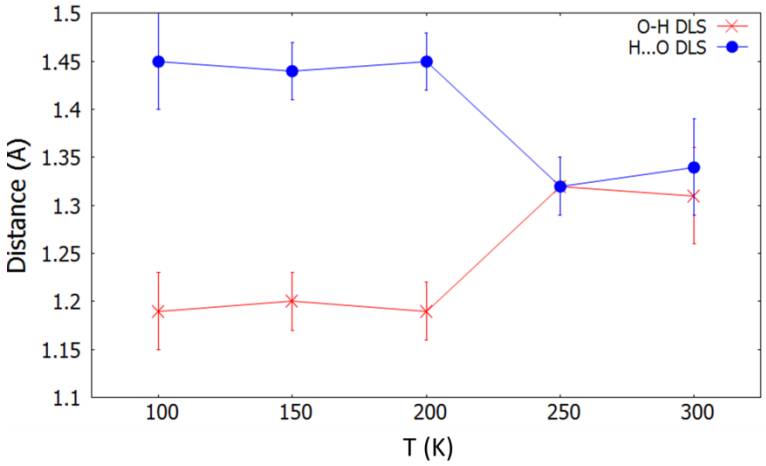

Figure 5.27 The O—H and H···O bond lengths of O—H···O dimer hydrogen bonds with temperature in 3,5-DNBA In-3-Ac.

Variable temperature Fourier difference maps were generated for the 3,5-DNBA hydrogen bonded dimer (Figure 5.28). In agreement with changes being observed in the C—O/C=O bond lengths with temperature, a change in the hydrogen atom density in the Fourier difference maps also occurs. However, this change is not as consistent as the trend seen in the C—O and C=O bond lengths as a function of temperature. At 100 K, a second peak with weak intensity is present in the Fourier difference map suggesting proton disorder at this temperature. This is in agreement with the C—O and C=O bond lengths, which deviate slightly at 100 K from the average distances for an aromatic carboxylic acid. A significant increase in the intensity of the second peak occurs at 150 K suggesting an increase in the extent of proton disorder; this is a greater increase than suggested by the C—O and C=O bond lengths which change in length by a relatively small amount between these temperatures. The signal of the second peak appears to decrease between 150 and 200 K whilst the C—O and C=O bond lengths continue along the linear trend of lengthening and shortening. The intensity of the second site then increases once more between 200 and 300 K. At 300 K, the intensities of the peaks for the two proton sites are almost equal, and suggest a large degree of proton disorder, approaching, but not quite equal to, a 50:50 occupancy,

coinciding with that suggested by the C—O and C=O bond lengths at this temperature ($d_{C—O}$ 1.272(3) Å and $d_{C=O}$ 1.263(2) Å).

The variable temperature Fourier difference maps are thus able to identify temperature dependent proton disorder in 3,5-DNBA In-3-Ac and also reveal some information about the extent of proton disorder occurring. However, the suggested proton disorder behaviour is only in agreement with that suggested by the C—O and C=O bond lengths at the temperature extremes of 100 and 300 K. This lack of agreement may be due to significant amounts of noise in the Fourier difference maps for these molecular complexes such that elements of the true proton disorder behaviour are hidden. For this molecular complex, the trend in the proton disorder is best assessed in the C—O and C=O bond lengths, but this interpretation is supported by the other factors observed; hydrogen atom parameters and Fourier difference maps.

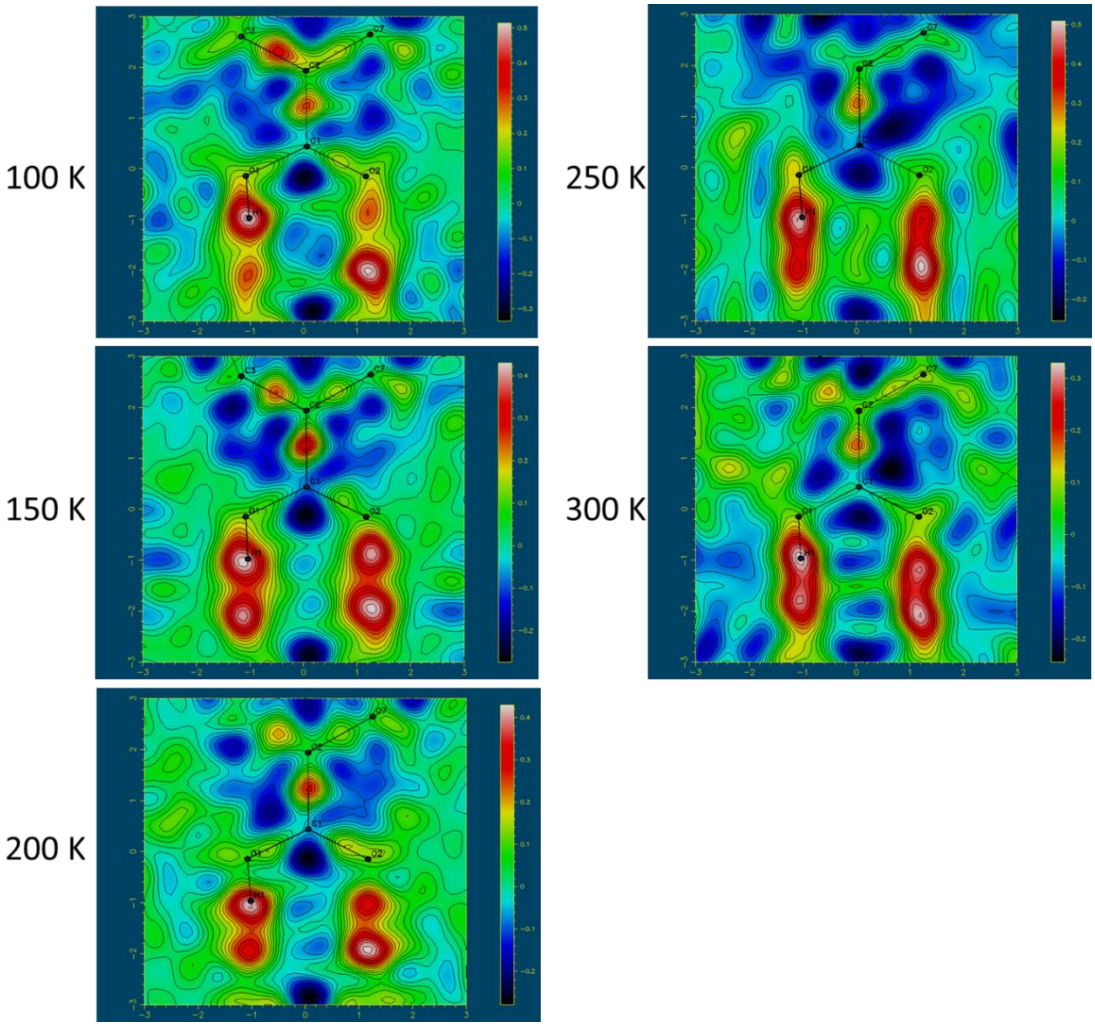

Figure 5.28 Variable temperature Fourier difference maps showing the electron density associated with the H-atom in the 3,5-DNBA dimer hydrogen bonds in 3,5-DNBA In-3-Ac.

The potential to refine accurate occupancies for the proton sites as a function of temperature was investigated for 3,5-DNBA In-3-Ac. A structural model where the hydrogen atom is disordered over two sites in the dimer hydrogen bond was refined (Table 5.19).

The refined occupancy values follow the trend of increasing disorder with temperature, as suggested by the C—O and C=O bond lengths and Fourier difference maps. However, the extent of disorder at each temperature is greater than that suggested by the equivalent C—O and C=O bond distances. For example, at 100 K, a split proton site occupancy of 56:44 has been refined. However, the C—O and C=O bond lengths at this temperature are far from being equivalent in length and the intensity of a second hydrogen site is only small in the Fourier difference maps. This suggests that, even considering the estimated 10 % error on refined occupancy values from X-rays, for this molecular complex, these values should be down weighted in importance when quantifying extents of proton disorder.

Table 5.19 Refined occupancies of the two proton configurations in the 3,5-DNBA dimer. The X-ray refined occupancy values have an estimated error of approximately 10 %. [89]

T (K)	Refined occupancy ratios
100	56:44
150	55:45
200	55:45
250	50:50
300	52:48

5.4.4 3,5-DNBA 1,4-DIB

In the crystal structure of 3,5-DNBA 1,4-DIB at 100 K (DLS), the two components crystallise in a 2:1 ratio, in space group *I2/a*. A 3,5-DNBA hydrogen bonded $R_2^2(8)$ dimer is present in the structure, where the 3,5-DNBA molecules are held together by strong to moderate strength O—H···O hydrogen bonds ($d_{O\cdots O}$ Å 2.668(4) at 100 K) and are related by an inversion centre at the centre of the $R_2^2(8)$ hydrogen bonded ring (Figure 5.29).

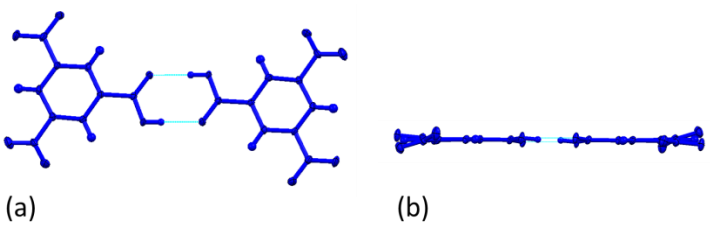

Figure 5.29 The 3,5-DNBA centrosymmetric hydrogen bonded $\boldsymbol{R_2^2(8)}$ dimer in the molecular complex of 3,5-DNBA 1,4-DIB at 100 K: (a) perpendicular to the dimer plane and (b) in plane of the dimer.

Within the hydrogen bonded dimer, the aromatic rings of the two 3,5-DNBA molecules are in the same layer (0.096 Å between aromatic ring planes) and the hydrogen bonded carboxylic acid group is twisted slightly out of co-planarity of the 3,5-DNBA aromatic ring on dimer formation (twisted by − 5.5(5) °). In the $R_2^2(8)$ hydrogen bonded ring, the carboxylic acid groups are tilted relative to one another (C—O···O angle of 108(3) ° and a C=O···O angle of 124(1) °). The nitro groups are non-planar, twisted by 18.9(5) and 5.6(5) ° out of co-planarity with the aromatic ring.

Molecular packing

In the crystal structure of 3,5-DNBA 1,4-DIB, there are short contacts in the local packing environment of the carboxylic acid groups forming the 3,5-DNBA dimer (Figure 5.30). Contacts form only to other 3,5-DNBA molecules in the local environment.

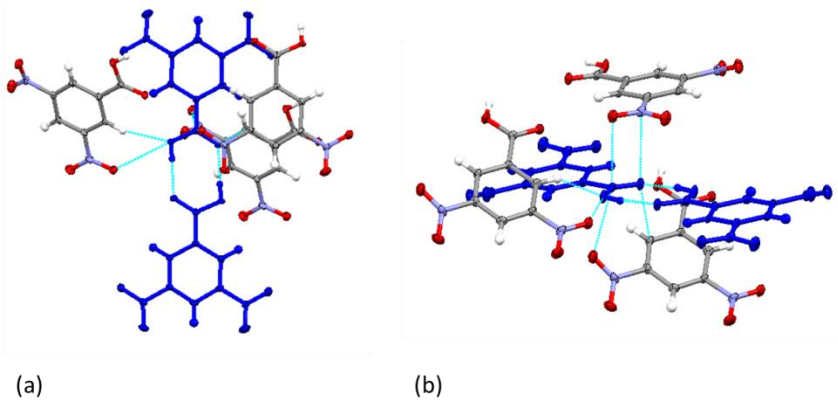

Figure 5.30 The local packing environments of the 3,5-DNBA molecule in the hydrogen bonded dimer in the molecular complex of 3,5-DNBA 1,4-DIB. For clarity, the packing is shown for one side of the centrosymmetric dimer only: (a) and (b) show the packing from different perspectives.

The carboxylic acid hydroxyl group interacts with the local environment *via* a weak C—H···O hydrogen bond ($d_{C\cdots O}$ 3.438(4) Å, <CHO 143.9 °) to an aromatic C—H group and a weak O···O ($d_{O\cdots O}$ 3.019(4) Å) to a nitro group in the same neighbouring 3,5-DNBA molecule; the interaction distance is just less than the sum of the van der Waals radii for the two atoms (3.04 Å) and therefore can be considered as significant. A number of π-interactions form to the carboxylic acid carbonyl group including an anti-parallel carbonyl-nitro π···π interaction ($d_{\pi\cdots\pi}$ 2.982(4) and 2.934(4) Å) to a nitro group in a neighbouring 3,5-DNBA molecule and a π-interaction to an aromatic carbon in a neighbouring 3,5-DNBA molecule ($d_{\pi\cdots\pi}$ 3.169(4) Å). A 3,5-DNBA molecule also stacks below the carboxylic acid group forming a π···π contact and interacting *via* its nitro group ($d_{\pi\cdots\pi}$ 3.149(5) Å).

Intermolecular interactions also occur between the 3,5-DNBA molecule, in each dimer, and the local environment (Figure 5.31) and involve both 3,5-DNBA and 1,4-DIB molecules.

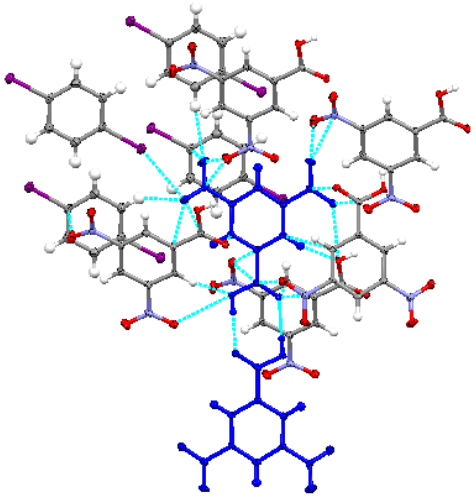

Figure 5.31 The local packing environments of the 3,5-DNBA molecule in the centrosymmetric hydrogen bonded dimer in the 2:1 complex of 3,5-DNBA 1,4-DIB. For clarity, the packing is shown for one side of the centrosymmetric dimer only.

Weak interactions form to both 3,5-DNBA nitro groups of the 3,5-DNBA molecule forming the centrosymmetric dimer. The nitro group on the protonated side of 3,5-DNBA molecule forms weak C—H···O hydrogen bonds to both nitro oxygen atoms through interaction with aromatic C—H groups donated from 1,4-DIB molecules ($d_{C\cdots O}$ 3.385(6) and 3.445(6) Å). One of the nitro oxygens forms a I···O halogen bond ($d_{I\cdots O}$ 3.432(3) Å) with a neighbouring 1,4-DIB molecule; the interaction distance is just less than the sum of the van der Waals radii for the two atoms (3.5 Å) and therefore can be considered significant. The other nitro oxygen forms an O···O contact to a neighbouring 3,5-DNBA nitro group ($d_{O\cdots O}$ 2.852(4) Å); considerably less than the sum of the van der Waals radii (3.04 Å) and therefore significant. Additional π-contacts form to aromatic π-density in neighbouring 3,5-DNBA ($d_{\pi\cdots\pi}$ 3.061(4) and 3.149(5) Å) and 1,4-DIB ($d_{\pi\cdots\pi}$ 3.138(5) Å) molecules involving both nitro oxygen atoms. Fewer interactions form to the nitro group on the non-protonated side of the 3,5-DNBA molecule forming the centrosymmetric dimer. Both nitro oxygen atoms interact with a nitro group of a neighbouring 3,5-DNBA forming O···O contacts ($d_{O\cdots O}$ 2.852(4) and 3.019(4) Å)); these are less than the sum of the van der Waals radii (3.04 Å) and therefore can be considered significant. One of the nitro oxygen atoms is also involved in anti-parallel nitro-carbonyl π-interactions to an acid group in a neighbouring 3,5-DNBA molecule ($d_{\pi\cdots\pi}$ 2.934(4) and 2.982(4) Å). An additional weak C—H···O hydrogen bond forms on the non-protonated side of the 3,5-DNBA molecule involving an aromatic C—H at the 2-position and a hydroxyl oxygen in a neighbouring 3,5-DNBA molecule ($d_{C\cdots O}$ 3.438(4) Å).

The wider packing of each dimer in 3,5-DNBA 1,4-DIB occurs in layers of each component; (Figure 5.32). This illustrates that the 3,5-DNBA hydrogen bonded dimer acid groups are involved in an extensive range of interactions within the local environment.

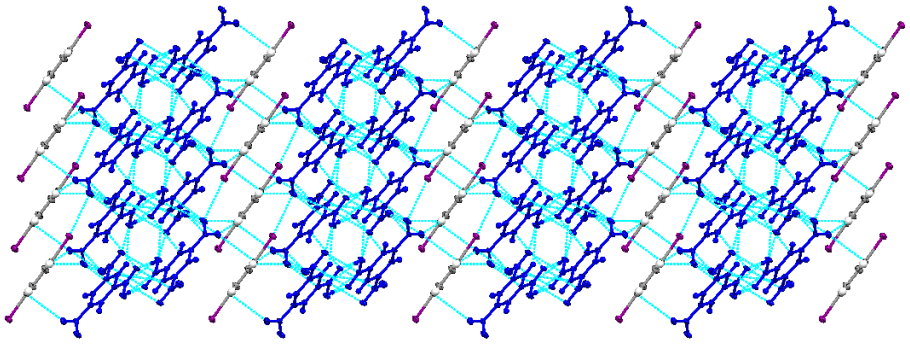

Figure 5.32 The wider packing in the molecular complex of 3,5-DNBA 1,4-DIB. The 3,5-DNBA hydrogen bonded dimer is shown in blue.

Variable temperature synchrotron X-ray diffraction measurements on 3,5-DNBA 1,4-DIB

Variable temperature measurements were carried out on 3,5-DNBA 1,4-DIB at the DLS from 100 to 300 K, in 100 K steps.

The C—O and C=O bond lengths of the carboxylic acid groups forming the hydrogen bonded dimers were followed as a function of temperature (Table 5.20 and Figure 5.33). Over the 100 to 300 K temperature range, a linear trend of the C—O bond lengths shortening and the C=O bond lengths lengthening with temperature occurs suggesting temperature dependent proton disorder. At 100 K, the C—O and C=O bond lengths ($d_{C—O}$ 1.306(5) Å and 1.227(5) Å) are equivalent to those for an ordered aromatic carboxylic acid suggesting there is no proton disorder at this temperature. The onset of proton disorder is indicated at 200 K, where the C—O and C=O bond lengths deviate from the values for an ordered aromatic carboxylic acid. At 300 K, there is a significant deviation of the C—O bond length ($d_{C—O}$ 1.265(6) Å) and some deviation of the C=O bond length ($d_{C—O}$ 1.239(6) Å). A significant extent of proton disorder occurring is therefore likely at 300 K however, not to the extent that 50:50 disorder is suggested.

Table 5.20 The carboxylic acid C—O and C=O bond lengths in the 3,5-DNBA dimer in 3,5-DNBA 1,4-DIB between 100 and 300 K.

T (K)	dC—O (Å)	dC=O (Å)
100	1.306(5)	1.227(5)
200	1.290(5)	1.222(5)
300	1.265(6)	1.239(6)

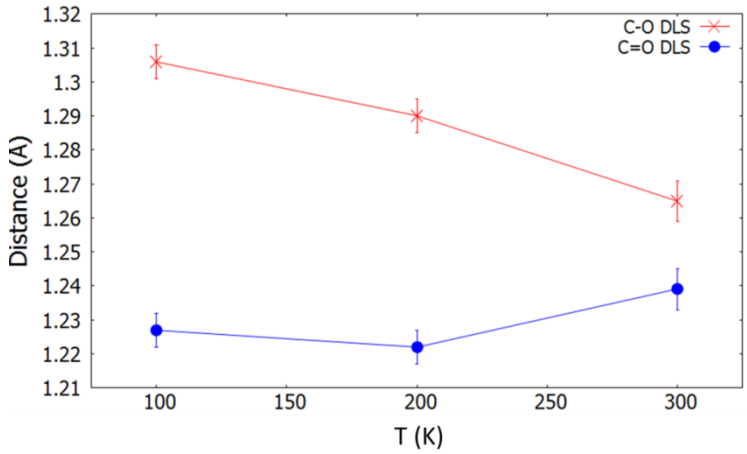

Figure 5.33 The C—O and C=O bond lengths of the carboxylic acid groups forming the hydrogen bonded dimer as a function of temperature in 3,5-DNBA 1,4-DIB.

The O—H···O hydrogen bond parameters of the 3,5-DNBA dimer were also followed as a function of temperature (Table 5.21). The O···O distance remains constant over the temperature range. Little change occurs in the O—H and H···O distances as a function of temperature; this is a result of the distance restraint applied to the O—H distance in order to achieve a stable refinement of the hydrogen atom position in the presence of the heavy iodine atom. These parameters therefore cannot be used to identify or quantify the temperature dependent proton disorder in this sample. The size of the isotropic thermal parameter (U_{iso}) for the dimer hydrogen bond hydrogen atom starts at a very small value at 100 K, again likely a result of the presence of the heavy iodine atom affecting the refinement, and then increases significantly at 200 K; this may indicate the onset of proton disorder at this temperature, as suggested by the deviating C—O and C=O bond lengths. There is no further change in the size of hydrogen atom thermal parameter at 300 K and so this parameter reveals little about how the disorder changes with temperature. In this molecular complex, the hydrogen atom parameters therefore may be tentatively used to identify the presence of proton disorder initially, but do not indicate how the disorder changes with temperature once present. The presence of the heavy iodine atom undoubtedly affects the capability of this parameter being exploited as an indicator of disorder in this case.

Table 5.21 Hydrogen bond parameters in the 3,5-DNBA dimer in 3,5-DNBA 1,4-DIB between 100 and 300 K.

T (K)	dO···O (Å)	dO—H (Å)	dH···O (Å)	U_{iso} (Å^2)
100	2.668(4)	0.80(4)	1.87(4)	0.011(12)
200	2.660(4)	0.80(7)	1.89(7)	0.09(3)
300	2.674(5)	0.82(6)	1.87(6)	0.10(3)

Variable temperature Fourier difference maps were generated for the 3,5-DNBA hydrogen bonded dimer (Figure 5.34). In agreement with changes observed in the C—O and C=O bond lengths with temperature, a change in the hydrogen atom density in the Fourier difference maps also occurs. At 100 K, a single hydrogen atom peak is present indicating an ordered carboxylic acid group, in agreement with the C—O and C=O bond lengths ($d_{C—O}$ 1.306(5) Å and 1.227(5) Å). At 200 K, a second, very weak hydrogen atom peak is present in the Fourier difference map suggesting a small extent of proton disorder at this temperature, similarly to the indications from the C—O and C=O bond lengths which deviate at this temperature. At 300 K, the intensity of the second hydrogen atom peak increases, suggesting an increase in extent of disorder, however this is only very slight in comparison to the more significant change in the C—O and C=O bond lengths. There are large amounts of noise in the Fourier difference maps for 3,5-DNBA 1,4-DIB as a result of the presence of the iodine atom. This makes it more difficult to distinguish the residual density of the hydrogen atom from the background noise and determine its behaviour.

The variable temperature Fourier difference maps are therefore able to identify temperature dependent proton disorder in 3,5-DNBA 1,4-DIB and also reveal some information about the extent of proton disorder occurring. However, with iodine present, there are large amounts of noise present in the maps, and the proton disorder is best assessed in the C—O and C=O bond lengths.

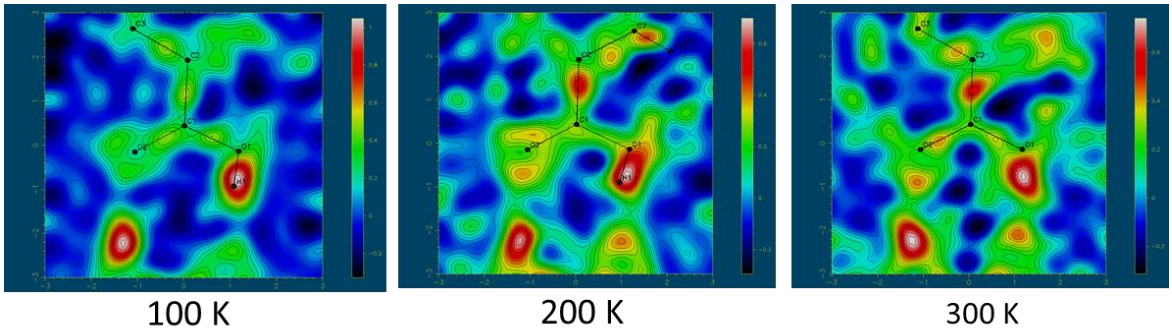

Figure 5.34 Variable temperature Fourier difference maps showing the electron density associated with the H-atom in the 3,5-DNBA dimer hydrogen bonds in 3,5-DNBA 1,4-DIB.

The potential to refine accurate occupancies for the proton sites as a function of temperature was investigated for 3,5-DNBA 1,4-DIB. A structural model where the hydrogen atom is disordered over two sites in the dimer hydrogen bond was refined (Table 5.22). Considering the noise present in the Fourier difference maps, it seems unlikely that it is possible to refine the proton occupancies accurately. At 100 K, occupancies of 89:11 are refined. Considering the ordered C—O and C=O bond lengths and the lack of a second peak in the Fourier difference maps, this is a reasonable approximation to the more likely situation of the occupancy split being 100:0, where no disorder is

present; the 89:11 refined occupancy split is likely to be the result of density in the form of Fourier ripples being mis-identified as a second site. The extent of proton disorder suggested by the refined occupancies increases from 89:11, at 100 K, to 78:22, at 200 K. This may be a reasonable estimate, as the C—O and C=O bond lengths and Fourier difference maps of the dimer hydrogen bonds also suggest some proton disorder at this temperature. At 300 K, the occupancies of the two proton sites are 54:46. This almost 50:50 occupancy is not reflected in the C—O and C=O bond lengths or the Fourier difference maps suggesting these values to be less reliable. Again, these refinements are likely to be affected by the presence of the iodine atom.

Table 5.22 Refined occupancies of the two proton configurations in the 3,5-DNBA dimer in 3,5-DNBA 1,4-DIB. The X-ray refined occupancy values have an estimated error of approximately 10 %. [89]

T (K)	Refined occupancy ratios
100	89:11
200	78:22
300	54:46

5.4.5 Determining the energy difference between proton configurations

An attempt was made to calculate the difference in energy, $\Delta H°$, between the two proton sites in the 3,5-DNBA molecular complexes, achieved by applying Arrhenius behaviour to the occupancy values using Equation 5.1 and Equation 5.4. [102]

Equation 5.1 $$\boldsymbol{K = \frac{P_A}{P_B} = \frac{P_A}{1 - P_A}}$$

where K is the configuration ratio, P_A is the occupancy of proton site one and P_B is the occupancy of the proton site two . The variation in K with temperature then allows thermodynamic parameters to be extracted as follows:

Equation 5.2 $$\boldsymbol{\Delta G° = -RTlnK}$$

Equation 5.3 $$\boldsymbol{\Delta G° = \Delta H° - T\Delta S°}$$

Equation 5.4 $$\boldsymbol{lnK = -\left(\frac{\Delta H°}{RT}\right) + \left(\frac{\Delta S°}{R}\right)}$$

The same analysis was attempted using the more reliable C—O and C=O bond lengths where the configuration ratio, K, was given by:

Equation 5.5 $$\boldsymbol{K = \frac{d(C-O) - 1.2}{d(C=O) - 1.2}}$$

where 1.2 Å is the approximate minimum C=O distance.

From these values, a plot of *lnK* vs (1/T) therefore gives ΔH^{o} and ΔS^{o} (Figure 5.35 and Table 5.23).

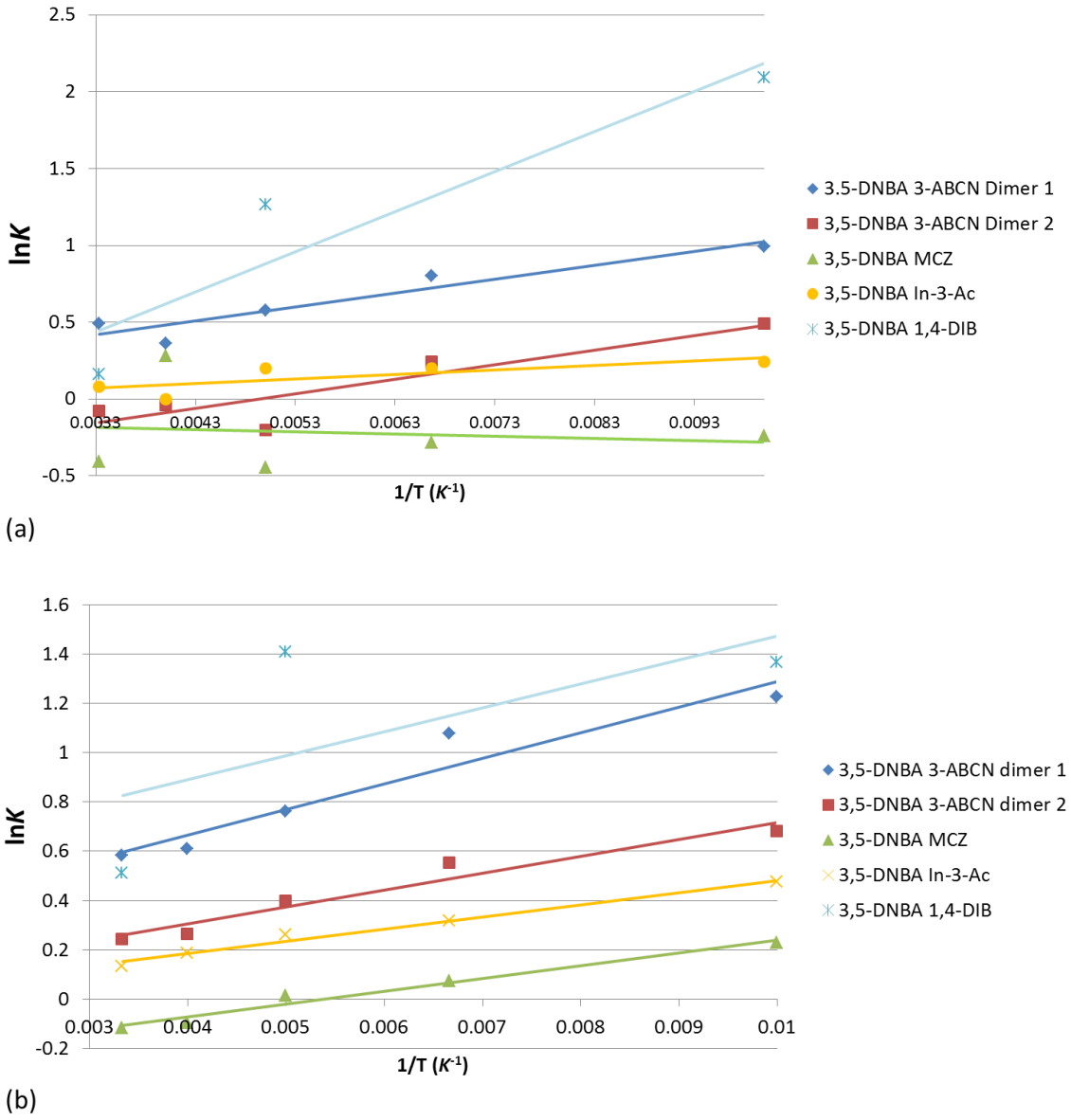

Figure 5.35 Plot of ln*K* versus *1/T* for each 3,5-DNBA molecular complex: (a) where *K* is calculated using the occupancy values of each proton site and (b) where *K* is calculated using the ratio of the C—O and C=O bond lengths.

Table 5.23 Δ*H*° and Δ*S*° between the two different proton configurations in each 3,5-DNBA molecular complex, calculated from applying Arrhenius behaviour the occupancy values and C—O/C=O bond lengths.

Molecular complex	Δ*H*° (kcal mol^{-1})		Δ*S*° (cal K^{-1} mol^{-1})	
	Occupancy	C—O and C=O	Occupancy	C—O and C=O
3,5-DNBA 3-ABCN (dimer 1)	-0.1786	-0.2058	0.2458	0.4990
3,5-DNBA 3-ABCN (dimer 2)	-0.1889	-0.1364	-0.9334	0.0618
3,5-DNBA MCZ	0.0285	-0.1035	0.2697	0.5568
3,5-DNBA In-3-Ac	-0.0581	-0.0977	-0.0497	-0.0196
3,5-DNBA 1,4-DIB	-0.5183	-0.1927	-0.8386	0.9999

When using the occupancy values of the proton configurations, the proton disorder follows classical Arrhenius jump behaviour between 100 and 300 K for the molecular complexes of 3,5-DNBA 3-ABCN and 3,5-DNBA In-3-Ac, shown by a linear increase in *K* with temperature. In the case of 3,5-DNBA MCZ and 3,5-DNBA 1,4-DIB, the fit to Arrhenius behaviour is less good, likely to be caused by incorrect occupancy values. When using the C—O and C=O bond lengths, the proton disorder strongly follows classical Arrhenius behaviour between 100 and 300 K for the molecular complexes of 3,5-DNBA 3-ABCN, 3,5-DNBA MCZ and 3,5-DNBA In-3-Ac; in the case of 3,5-DNBA 1,4-DIB, the fit to Arrhenius behaviour does not hold at 100 K, seen by a less steep increase in *K*. Where Arrhenius behaviour does not fit at low temperatures, this has previously been attributed to quantum tunnelling effects; occupation of the second site occurs without the same classical temperature dependence. [100, 102]

The energy difference between the two proton configurations (Δ*H*°) in hydrogen bonded dimers of benzoic acid is –0.12 kcal mol^{-1}. [102] Similar magnitudes of Δ*H*° are calculated here for the 3,5-DNBA molecular complexes. The negative values of Δ*H*° indicate an endothermic reaction; expected where an increase in population of the second site occurs with temperature, as described by Boltzmann statistics for a chemical system at equilibrium. [189] The values of Δ*H*° calculated using the occupancy values and C—O and C=O bond lengths indicate that 3,5-DNBA MCZ and 3,5-DNBA In-3-Ac have the lowest energy difference between the two proton configurations whilst larger energy differences between the two proton configurations are indicated for 3,5-DNBA 1,4-DIB, 3,5-DNBA 3-ABCN dimer 1 and dimer 2. This suggests a greater symmetry in the double wells of the dimer hydrogen bond potential energy surface in 3,5-DNBA MCZ and 3,5-DNBA In-3-Ac than in 3,5-DNBA 1,4-DIB, 3,5-DNBA 3-ABCN dimer 1 and dimer 2.

In cases where there is significantly less agreement in the refined occupancy values with the trends from the C—O and C=O bond lengths and Fourier difference maps as a function of temperature,

the energy differences between the two proton configurations is likely to be more accurate where calculated using the more reliable C—O and C=O bond lengths.

5.4.6 Following temperature dependent proton disorder using synchrotron X-ray diffraction

It was possible to follow proton disorder as a function of temperature in the molecular complexes studied, using the synchrotron X-ray diffraction technique. The determination is most reliable in the heavy atom C—O and C=O bond lengths, this is not unexpected as, provided good resolution of data, the carbon and oxygen atoms can be accurately located in the structure. In favourable circumstances, the Fourier difference maps revealing information about the onset and extent of proton disorder occurring at each temperature were found to be in agreement with the trends indicated in the C—O and C=O bond lengths. This is as indicated in the initial comparative diffraction study. In several cases, the determination of the proton disorder is hindered by large extents of noise in the Fourier difference maps; this is the case in 3,5-DNBA In-3-Ac and 3,5-DNBA 1,4-DIB; here, considering the changes in the C—O and C=O bond lengths is even more important for elucidating the proton disorder behaviour. This emphasises the importance of having good quality Fourier difference maps for the reliable determination of proton behaviour in these studies.

The refined carboxyl group hydrogen atom positions and isotropic thermal parameters, when considered in conjunction with the C—O/C=O bond lengths and Fourier difference maps, also indicate the presence of proton disorder in the molecular complexes but only when freely refined and in general do not reveal information about the extent occurring at each temperature; in the case of 3,5-DNBA MCZ and 3,5-DNBA 1,4-DIB, a stable refinement could only be achieved on applying a restraint to the O—H distance so the refined hydrogen atom parameters were less informative about the proton disorder. Beyond the comparative study on 3,5-DNBA II, the refined occupancy values are not particularly reliable in the majority of cases for the determination of proton disorder extent, disagreeing with the C—O/C=O bond lengths and density in the Fourier difference maps. This remains a disadvantage in using this technique, in that reliably refined proton sites occupancies only appear achievable when conditions are optimised, as for 3,5-DNBA II. The Arrhenius behaviour determined using the proton site occupancies therefore should be considered with caution whilst those determined using the C—O/C=O bond lengths may give a better indication of the difference in energy between the two proton configurations in future.

The measurements at the ALS, for 3,5-DNBA II, 3,5-DNBA 3-ABCN and 3,5-DNBA MCZ, in addition to those at the DLS and being consistent with the DLS results, provide further evidence in support of the proton disorder behaviour observed. This is in spite of these being generally lower

in data quality, indicated by greater noise in the Fourier difference maps, such that only the C—O/C=O bond lengths are reliable for the disorder behaviour determination.

Critically, the use of the synchrotron technique facilitates the study of the variable temperature proton disorder behaviour across a number of temperatures and in a number of systems. This allows greater details about the evolving nature of the proton disorder to be found and increases the set of materials over which the disorder behaviour can be rationalised.

5.5 The effect of local environment on proton disorder in 3,5-DNBA dimers

Varying degrees of proton disorder occurred in the 3,5-DNBA dimers across the molecular complexes, as a function of temperature which may be rationalised in the crystal packing.

Variable temperature proton disorder in the molecular complexes

Variable temperature proton disorder occurs in all four molecular complexes, observed most reliably in the C—O and C=O bond lengths and Fourier difference maps of the dimer hydrogen bonds. The temperature dependence of the proton disorder can be modelled by the classical Arrhenius jump model, where thermal activation on increasing the temperature leads effectively to hopping over the energy barrier to the second proton site. This means that population of the second site occurs with increased temperature, due to increased thermal energy; however, it should be noted that this may also be a consequence of the shape of the potential energy surface changing with temperature, a possibility not investigated in this work. One exception to this fit to Arrhenius behaviour is 3,5-DNBA 1,4-DIB, where this model does not hold at 100 K, and may suggest quantum tunnelling to be dominant in this molecular complex at this temperature.

3,5-DNBA MCZ and 3,5-DNBA In-3-Ac are the most disordered systems with the lowest disorder onset temperatures, at or below 100 K, and display the greatest extents of disorder occurring at each temperature; the proton disorder is greatest overall in 3,5-DNBA MCZ indicated by the C—O and C=O bond lengths being closer over the temperature range and the signal for the second hydrogen atom being stronger in the Fourier difference maps over the full temperature range studied. The smallest energy difference between the two proton configurations from the Arrhenius analysis is also suggested for these two molecular complexes. This suggests a more symmetric double well potential energy surface for the dimer hydrogen bond in these molecular complexes where there is little difference in energy between the two proton sites. Proton disorder is also present in 3,5-DNBA dimer 2 at 100 K, however the extents of disorder occurring at each

temperature is less than for 3,5-DNBA MCZ and 3,5-DNBA In-3-Ac. This indicates a more asymmetric double well potential energy surface for the dimer hydrogen bond and may also indicate a larger energy barrier between the two proton sites. 3,5-DNBA 3-ABCN dimer 1 and 3,5-DNBA 1,4-DIB are the least disordered systems having the higher disorder onset temperatures, at 200 K, and lower extents of disorder occurring at each temperature. Larger energy differences between the proton configurations are also indicated in these molecular complexes by Arrhenius analysis. This indicates a very asymmetric double well potential energy surface for the dimer hydrogen bonds in these molecular complexes with potentially a large barrier between the two proton sites.

Local packing effects on proton disorder

The proton disorder characteristics of each molecular complex may be rationalised in the crystal packing; where the proton behaviour reflects the nature of the hydrogen bond potential energy surface, this may indicate the role of the local environment in its tuning. This may allow certain proton disorder behaviour to be designed into future materials or where proton transfer processes lead to certain properties, may allow property tuning *via* crystal packing.

The proton disorder in molecular complexes 3,5-DNBA MCZ and 3,5-DNBA In-3-Ac occurs at a low onset temperature and to large extents at each temperature. A close to symmetric double well potential energy surface is therefore indicated for the dimer hydrogen bonds in 3,5-DNBA MCZ and 3,5-DNBA In-3-Ac. This proton disorder behaviour occurs in these molecular complexes where the local environment of the acid groups forming the dimer hydrogen bonds are in isolated pockets with no direct interactions to the carboxylic acid groups, with only π-contacts forming to the acid carbon atoms. The crystal packing environment where there are no interactions to the carboxylic acid oxygen atoms therefore appears to favour a more symmetric double well hydrogen bond potential where proton disorder is likely. A similar effect is observed in several reported molecular complexes containing the 3,5-DNBA hydrogen bonded dimer (CSD refcodes GAUTAM (3,5-DNBA and 4-dimethylamino benzoic acid), [262] KIZQOZ (3,5-DNBA and N-Isopropylcarbazole) [256] and KIZREQ (3,5-DNBA and N-Isobutylcarbazole)). [256] In these molecular complexes, there are no interactions between the carboxylic acid oxygens and the local environment, with only π-stacking above the acid carbon occurring. In this packing environment, the C—O and C=O bond length within the carboxylic acid are either equalised, or close to being so, at room temperature ($d_{C—O}$ and $d_{C=O}$ are 1.259(4) and 1.256(4) Å, respectively in GAUTAM, are 1.266(2) and 1.251(2) Å, respectively in KIZQOZ and are 1.269(3) and 1.253(4) Å, respectively, in KIZREQ) suggesting significant extents of proton disorder and therefore a close to symmetric double well potential energy surface for the dimer hydrogen bond.

In the molecular complexes where a lower extent of proton disorder occurs at each temperature, such as in 3,5-DNBA 3-ABCN dimer 2 or the onset temperature for proton disorder is higher, including in 3,5-DNBA 3-ABCN dimer 1 and 3,5-DNBA 1,4-DIB, less symmetric double well potential energy surfaces for the dimer hydrogen bonds are indicated. This proton disorder behaviour occurs where the 3,5-DNBA carboxylic acid groups are involved in a significant number of interactions to the local environment. Specifically, the local environments include weak C—H···O hydrogen bonds and O···O interactions of the carboxylic acid oxygen atoms with nitro groups. These interactions occur with varying strengths, and in different numbers and arrangements, to each end of the O—H···O dimer hydrogen bonds for each molecular complex. The presence and asymmetric arrangement of these interactions appears to be influencing an asymmetry in the dimer hydrogen bond, reflected in the lesser and different extents of proton disorder in these three complexes. A similar effect is observed in several reported molecular complexes containing 3,5-DNBA hydrogen bonded dimers (CSD refcodes ABUNOA, [73] AJIXOH, [263] YIVHUI01, [264] and ZUPJOJ). [265] In these molecular complexes, there is an asymmetric arrangement of interactions between the carboxylic acid oxygens and the local environment, including weak C—H···O hydrogen bonds and nitro-carbonyl group π-interactions. The C—O and C=O bond of the carboxylic acid indicate low extents of proton disorder in these complexes ($d_{C—O}$ and $d_{C=O}$ are 1.287(3) and 1.244(3) Å, respectively at 298 K in ABUNOA, are 1.306(2) and 1.225(2) Å, respectively in AJIXOH at 200 K, are 1.306(2) and 1.230(2) Å, respectively in YIVHUI01 at 100 K and are 1.279(6) and 1.229(5) Å in ZUPJOJ at 298 K) and therefore an asymmetric double well potential energy surface for the dimer hydrogen bond is indicated when in these packing environments.

These observations add further weight to the conclusion made by Jones *et al.* (2013) that weak interactions in the local environment of the dimer carboxylic acid groups play a role in determining the presence and nature of proton disorder in these systems; [97] having an effect of tuning the nature of the hydrogen bond potential energy surface.

Packing subtleties

It is apparent that the absence of intermolecular interactions in the local environment of the carboxylic acid groups of the dimer hydrogen bonds favours a symmetric hydrogen bond double well potential energy surface and therefore larger extents of proton disorder, whilst their presence favours an asymmetric hydrogen bond potential energy surface and proton ordering. There are, however, additional subtleties in the packing that should be explored.

In 3,5-DNBA MCZ and 3,5-DNBA In-3-Ac, the carboxylic acid groups of the dimer hydrogen bonds do not form any interactions with the local environment and as such the dimer hydrogen bond environment should be symmetric with a symmetry in the double wells of its potential energy surface; 50:50 proton disorder would be expected at 100 K. This is not the case in 3,5-DNBA MCZ and 3,5-DNBA In-3-Ac and the extents of disorder, suggested by the C—O and C=O bond lengths and Fourier difference maps at 100 K, is also different between these complexes; a greater extent is suggested in 3,5-DNBA MCZ. This may be due to a number of factors. The fact that 50:50 proton disorder is not achieved at 100 K in either complex may be caused by the local environment of the rest of the 3,5-DNBA molecule in each dimer (3,5-DNBA MCZ, see Figure 5.17 and 3,5-DNBA In-3-Ac, see Figure 5.24). In these two molecular complexes, the number of interactions, types of groups forming these, and interaction distances involved, differs between the protonated and non-protonated side of the 3,5-DNBA molecules forming the dimer. This may be sufficient to alter the electronics of 3,5-DNBA on each side of the molecule to different extents such that an imbalance in the symmetry of the carboxylic acid groups is created, preventing the formation of a symmetric double well potential energy surface for the dimer hydrogen bond and a 50:50 proton disorder resulting. The difference in the extents of disorder occurring at 100 K between 3,5-DNBA MCZ and 3.5-DNBA In-3-Ac may also be related to the nature of the co-molecule, which in 3,5-DNBA MCZ is a three fused ring structure with an acid group attached and in 3,5-DNBA In-3-Ac is a two fused ring structure with a methyl group attached. These co-molecules have different electronics and so may cause different perturbations to the 3,5-DNBA molecule on interaction. In general, the interactions formed between 3,5-DNBA and In-3-Ac molecules are shorter than those formed between 3,5-DNBA and MCZ molecules; this may lead to a greater perturbation effect in 3,5-DNBA In-3-Ac and cause the lower extent of proton disorder occurring in this complex.

A further subtlety in crystal packing effects on proton disorder may be investigated in the molecular complex of 3,5-DNBA 3-ABCN, where two 3,5-DNBA dimers are present which exhibit differing degrees of temperature dependent proton disorder; dimer 2 shows a greater extent of proton disorder than dimer 1. These dimers are free from electronic effects introduced by different components and so increaingly subtle packing effects can be studied. The centrosymmetric hydrogen bonded $R_2^2(8)$ ring formed between the 3,5-DNBA carboxylic acid groups is highly involved in interactions with the local environment in both dimer 1 and dimer 2. At a glance, the carboxylic acid groups of dimer 1 appear to be in a more symmetric environment than those of dimer 2 (Figure 5.9), where the same type of interaction, a weak C—H···O hydrogen bond, is formed on either side of the acid dimer. However, they are not of the same length. The nature of the C—H groups forming the weak C—H···O hydrogen bonds, to either end of the dimer hydrogen bond, also differ as a result of the functional groups on the 3-ABCN molecule; a strongly

electron withdrawing (EW) group (nitrile) and a strongly electron donating (ED) group (amino) are at the one and three position, respectively. ED groups may increase the acidity of an aromatic C—H at the *ortho* and *para* positions, whilst EW groups increase the acidity at the *meta* positions. For the 3-ABCN molecule interacting with acid dimer 1, the nitrile group directs to the C—H interacting with the carbonyl oxygen and the amino group directs to the C—H group interacting with the hydroxyl oxygen. Therefore, as the amino and nitrile group have differing directing abilities, the acidity of the two C—H groups involved in the weak C—H···O are very different and the interaction with the dimer oxygen atoms is different in each case leading to different perturbation effects at each end of the dimer hydrogen bond. The local environment of the dimer is therefore asymmetric. The C—O and C=O bond lengths and Fourier difference maps indicate a more symmetric environment in dimer 2, over the temperature range. This raises the question of what is causing the carboxylic acid environment to be more symmetric in dimer 2 than in dimer 1. This could be caused by a number of crystal packing effects. The greater symmetry in dimer 2 may be attributed to the interactions formed to each end of the dimer hydrogen bond being less significant; the local environment of dimer 2 includes a weak C—H···O hydrogen bond with low directionality (<CHO 123(1) °) and a weak O···O contact. In contrast, in the local environment of dimer 1, two weak C—H···O hydrogen bonds form with high directionality (<CHO 151(1) ° and 147(1) °); weak C—H···O hydrogen bonds formed to carboxylic acid dimers, if more directional, lead to a greater possibility of proton ordering. [26] Therefore, greater perturbation of the symmetry of the carboxylic acid or dimer hydrogen bonds may be being caused in dimer 1 than in dimer 2.

The arrangement of molecules around the dimer hydrogen bonds may also be the cause for the difference in extents of proton disorder occurring between dimer 1 and 2 in 3,5-DNBA 3-ABCN (Figure 5.36). Molecules of 3-ABCN are located above and below the plane of the acid dimer in dimer 1 and dimer 2. Around dimer 1, the 3-ABCN nitrile group points over the acid dimer with a slight bias towards the carboxylic acid hydroxyl oxygen (distances $N\cdots O_{hydroxyl}$ 3.377(2) Å *versus* $N\cdots O_{carbonyl}$ 3.467(2) Å). In contrast, around dimer 2, the nitrile groups are in a different position, located on either side of the acid dimer, again near the hydroxyl oxygen atom but this time at a much longer distance ($d_{N\cdots O}$ 3.782(2) Å). The closer proximity of the nitrile group to one side of the acid dimer in dimer 1, than in dimer 2, may be the cause for the greater asymmetry suggested in dimer 1; the nitrile group is very electron rich and may interact strongly with the nearby acid causing a greater perturbation effect on one side.

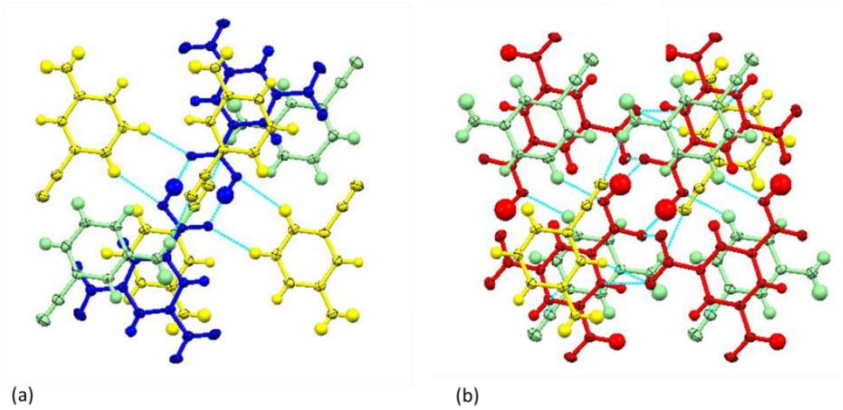

Figure 5.36 The arrangement of molecules around the 3,5-DNBA dimer in (a) dimer 1 (in blue) and (b) dimer 2 (in red) in 3,5-DNBA 3-ABCN: viewed perpendicular to the plane of the dimer hydrogen bond in each case. The two symmetry independent 3-ABCN molecules are shown in green and yellow.

Other effects suggested to influence proton disorder

Additional effects on proton disorder have been investigated in the literature for hydrogen bonded substituted benzoic acid dimers.

Planarity of the 3,5-DNBA molecule is not expected to affect the amount of disorder in 3,5-DNBA hydrogen bonded dimers. [97] This was indeed the case in the four 3,5-DNBA molecular complexes studied in this chapter. At 100 K, similar extents of proton disorder occur in 3,5-DNBA MCZ and 3,5-DNBA In-3-Ac, although very different twist angles of the nitro groups out of planarity with the aromatic ring occur. There is also no correlation between the changes in 3,5-DNBA substituent group planarity with the extent of proton disorder occurring as a function of temperature; proton disorder increases in each of the 3,5-DNBA molecular complexes as a function of temperature but the co-planarity of the two nitro groups with the benzene ring does not change in the same way across the complexes.

The extent of skew of carboxylic acid groups in a centrosymmetric hydrogen bonded $R_2^2(8)$ benzoic acid dimer may also reflect their interaction with the local environment. The 'skew' of carboxylic acid groups is defined by the C—O···O and C=O···O angles. Average values for an ordered carboxylic acid dimer are 112 and 125 °, respectively. [266] Extents of proton disorder may also be related to 'skew'; where the skew is small (C—O···O and C=O···O angles are equal) this favours proton disordering and a more symmetric hydrogen bond double well potential whilst where the skew is large (C=O···O angle is greater than the C—O···O angle), this favours proton ordering and a more asymmetric hydrogen bond double well potential. [266] In the molecular complexes in this chapter (Table 5.24), at 100 K, the most symmetric environment, indicated by the C—O···O and C=O···O angles, occurs in 3,5-DNBA MCZ whilst the least symmetric occurs in

3,5-DNBA 1,4-DIB and 3,5-DNBA 3-ABCN dimer 1; this agrees with the proton disorder behaviour observed. The skew of carboxylic acid groups is an additional measure of proton disorder which does not rely on accurately refined hydrogen atom positions and so may be useful to consider in X-ray studies where hydrogen atom positions are ambiguous.

Table 5.24 The C—O···O and C=O···O angles in each molecular complex at 100 K.

Molecular complex	<C—O···O (°)	<C=O···O (°)
3,5-DNBA 3-ABCN dimer 1	111.30(8)	123.81(9)
3,5-DNBA 3-ABCN dimer 2	114.80(8)	120.25(8)
3,5-DNBA MCZ	117.2(1)	117.6(1)
3,5-DNBA In-3-ac	113(2)	118(1)
3,5-DNBA 1,4-dib	108(3)	124(1)
Ordered hydrogen bonded carboxylic acid dimer [266]	110	120

5.6 Conclusions

In this chapter, the technique of synchrotron X-ray diffraction has been explored and developed in the study of proton disorder processes in hydrogen bonded benzoic acid dimers of 3,5-DNBA. This technique allows maximum throughput of samples, addressing the lack of variable temperature measurements on these systems to date. It was hoped that, by adding to the number of samples in which temperature dependent disorder has been studied, further understanding of the effect of the crystal packing on tuning proton disorder may be achieved. This work builds on that by Jones *et al.* (2013). [97]

The initial bench marking of the synchrotron technique for the previously well studied disorder system of 3,5-DNBA II allowed insight into data optimisation methods to access the higher quality Fourier difference maps for the reliable determination of proton behaviour. A hemisphere approach was recommended allowing the greatest speed of collection with little compromise in Fourier difference map quality compared to the other strategies. This aids in the design of future experiments allowing proton behaviour to be probed at an increased number of temperatures with a reduction in experimental time. The detector trials revealed both detector types to be applicable in synchrotron studies of proton behaviour where the CCD detector is currently the most suited, routinely allowing the collection of good quality data from which relatively noise free Fourier difference maps could be generated, however, the preliminary results from the Pilatus detector are promising and indicate the need for further investigation into the use of this detector in such studies.

Initial comparative diffraction studies of the high temperature proton disorder in 3,5-DNBA II revealed the synchrotron technique to be a promising method in the study of proton disorder processes; equivalent information about the disorder to that found previously from X-ray laboratory and neutron studies could be found. Certain caveats were noted including that, in the assessment of proton disorder behaviour from the synchrotron X-ray data, the more reliable C—O and C=O bond lengths and Fourier difference maps should be given greater weighting than the less accurately determined refined hydrogen atom parameters. These caveats are applicable to all studies of proton behaviour using X-rays; greater confidence can be had in proton behaviour indicated by the refined hydrogen atom positions when supported by the undisputable heavy atom parameters and by good quality Fourier difference maps.

Variable temperature single crystal synchrotron X-ray diffraction was applied to previously known molecular complexes of 3,5-DNBA. By considering the C—O and C=O bond lengths and Fourier difference maps alongside the refined hydrogen atom parameters, information about the degree and onset of proton disorder could be determined for each complex. As found in the optimisation studies, the C—O and C=O bond lengths and Fourier difference maps were the most informative about the proton disorder; information about the disorder was less reliable when observed in the hydrogen atom parameters. This emphasises the problems encountered in determining behaviour from hydrogen atom information refined from X-ray data. The greatest extent of disorder over the temperature range was indicated in 3,5-DNBA MCZ and 3,5-DNBA In-3-Ac whilst the least occurred in 3,5-DNBA 1,4-DIB.

The potential to follow the temperature dependent proton disorder in these molecular complexes allowed its rationalisation in the crystal packing, particularly in the variations in the 3,5-DNBA dimer local environment. It was found that a more symmetric double well hydrogen bond potential occurred, indicated by low onset temperatures and greater extents of proton disorder at each temperature, when the hydrogen bonded dimer carboxylic acid groups were isolated from direct interactions to the local environment, as in 3,5-DNBA MCZ and 3,5-DNBA In-3-Ac. The presence of weak interactions to the hydrogen bonded dimer carboxylic acid groups, in contrast, created a more asymmetric double well hydrogen bond potential, indicated by higher onset temperature lesser extents of proton disorder at each temperature, as in 3,5-DNBA 3-ABCN dimer 1 and 2 and 3,5-DNBA 1,4-DIB. Additional subtleties in the crystal packing were also suggested to tune proton disorder including variations in the type or number of interactions to each end of the hydrogen bonded dimer or variations in the nature or position of the interacting group or co-molecule. These observations add further weight to the hypothesis made by Jones *et al.* (2013) that weak interactions may affect the energetics of the dimer hydrogen bond and therefore play a role in tuning proton configuration in hydrogen bonded substituted benzoic acids. [97] This ability to tune

proton behaviour by changes to the crystal packing, achieved on co-former variation, adds further insight into the perturbing effect of different types of interactions on proton dynamics. The role of weak interactions in structure control is further explored in Chapter 8. To investigate further the effect of local environment on the proton disorder in 3,5-DNBA molecular complexes, additional examples containing the 3,5-DNBA dimer would be beneficial. Additional substituted benzoic acid co-formers were trialled in this work for the design of new molecular complexes containing 3,5-DNBA homo dimers, however these proved unsuccessful and further investigation is required.

In this study, the use of synchrotron X-ray diffraction to follow proton disorder processes was possible, when first benchmarked against the Lab X-ray and neutron technique. Issues remain in the accurate determination of refined hydrogen atom parameters, evident in the 3,5-DNBA molecular complexes, and therefore this study would benefit from complementary single crystal neutron diffraction studies for a more accurate determination of proton site occupancies. However, where the comparative diffraction study showed agreement across the synchrotron, Lab X-ray and neutron data, and where proton disorder trends were observed in synchrotron X-ray diffraction study of 3,5-DNBA molecular complexes, some confidence can be invested in the results presented in this chapter and the conclusions made about the effect of local environment on proton disorder behaviour. This is important where increasing knowledge about the susceptibility of hydrogen bonds to chemical environment may allow, in future, proton transfer behaviour to be designed into crystalline materials; this may be advantageous in the design of functional materials with properties that may be attributed to proton transfer.

.

Chapter 6.

Crystal engineering short strong hydrogen bonds (SSHBs) for potential proton migration studies

In this chapter, crystal engineering strategies are explored in the design of short strong hydrogen bonds (SSHBs) in the solid state for potential proton migration studies.

6.1 Introduction and aims

The short donor-acceptor distances of SSHBs (§1.1.2) leads to a hydrogen bond potential energy surface that has a low barrier to proton transfer such that the proton transfer process of proton migration may be observed (§1.3.2). [23] Proton migration across SSHBs may lead to certain physical properties within materials such as ferroelectricity [118] or colour change. [106] Its study in model systems may therefore aid in the understanding of these physical properties and their targeting in future materials; variable temperature diffraction methods are commonly employed. [108, 109, 121]

The predictable design of SSHBs in the solid state is difficult and even more so is the prediction of those that will have proton migration properties. It has been suggested that proton migration across SSHBs may occur only for very short donor-acceptor distances; proton migration has only been reported where the hydrogen bonding distance is less than 2.45 Å for O—H···O interactions [109] and in the region of 2.55 Å for N^+—H···O^- interactions. [110, 111, 267] There are, however, few examples of temperature dependent proton migration across these SSHBs reported in the literature.

In this chapter, several crystal engineering design strategies have been trialled to engineer SSHBs for potential proton migration studies. The design strategies include targeting the formation of the carboxylic acid:amide $R_2^2(8)$ hydrogen bonding synthon (§1.2.1, Figure 1.11) between substituted urea and organic acid molecular building blocks. This synthon has led previously to O—H···O SSHBs which exhibit proton migration properties in urea phosphoric acid, [108] *N*,*N*-dimethylurea oxalic acid and *N*,*N*'-dimethylurea oxalic acid. [109] A strategy of targeting charge transfer species such as the haloanilic acids alongside charge acceptor species such as *N*-heterocycles has also been trialled with the aim of forming charge assisted hydrogen bonds (CAHB) (§1.3.3); charges on the hydrogen bond donor or acceptor group as a result of charge transfer can lead to a strengthened hydrogen bond.[128] *N*-heterocycles with benzene carboxylic acids are also targeted where the

combination of these molecular components has led to a number of molecular complexes with N^+—H···O^- SSHBs including in pyridine-3,5-dicarboxylic acid, [110] 4,4-bipyridine 1,2,4,5-tetracarboxylic acid, [111] isoniazid with 4-aminosalicylic acid [267] or O—H···N SSHBs including in isonicotinamide oxalic acid; [268] in all the complexes containing N^+—H···O^-, temperature dependent proton migration occurs.

The effect of the acidity and basicity of molecular components on resulting hydrogen bond strength is also investigated by considering the nature of substituents and ΔpK_a values between components; the strongest and shortest of hydrogen bonds may be formed when ΔpK_a approaches zero. [269] The relationship between the hydrogen bonding and crystal packing in terms of the local environment of the hydrogen bonds and in terms of the wider packing including hydrogen bonding motifs is also explored; chemically equivalent hydrogen bonds in the same crystal structure have been shown to exhibit different proton transfer characteristics and is attributed to crystal packing. [117]

The molecular components investigated in this chapter in the design of SSHBs include basic components set 1, comprising substituted ureas and 3-deazauracil (Figure 6.1) and basic components set 2, containing *N*-heterocycles (Figure 6.2). Basic components sets 1 and 2 are combined with a range of organic acids (Figure 6.3). O—H···O and charge assisted N^+ —H···O^- SSHBs are targeted between molecular components; O—H···O SSHBs between set 1 basic components and the organic acids and charge assisted N^+—H···O^- SSHBs between set 2 basic components and the organic acids. Whereas previous studies have focused on substituted ureas with straight chain dicarboxylic acids in the design of O—H···O SSHBs [128] for potential temperature dependent proton migration, the focus of this study is on substituted ureas with benzene mono and di-carboxylic acids.

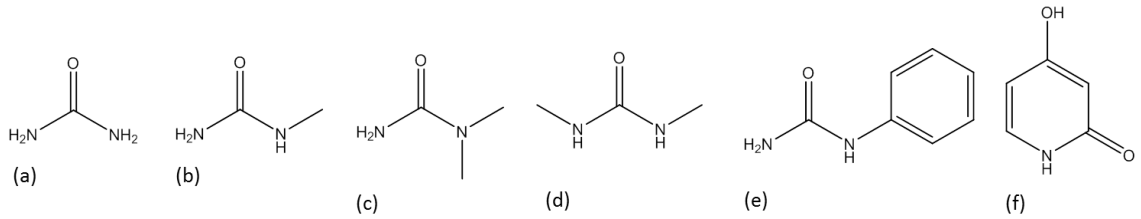

Figure 6.1 Set 1 basic molecular components of substituted ureas: (a) urea (U), (b) *N*-methylurea (MU), (c) *N,N*-dimethylurea (DMU), (d) *N,N'*-dimethylurea (D'MU), (e) *N*-phenylurea (PhU) and (f) 3-deazauracil (3-DAZA).

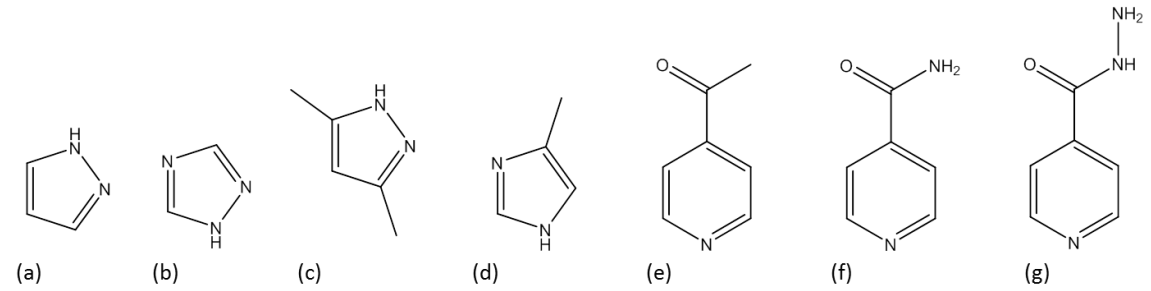

Figure 6.2 Set 2 basic molecular components of substituted *N*-heterocycles: (a) pyrazole (PY), (b) 1,2,4-*1H*-triazole (1,2,4-TZ), (c) 3,5-dimethylpyrazole (3,5-DMPY), (d) 4(5)-methylimidazole (4(5)-MIM), (e) 4-acetylpyridine (4-AP), (f) isonicotinamide (IN) and (g) isoniazid (IZN).

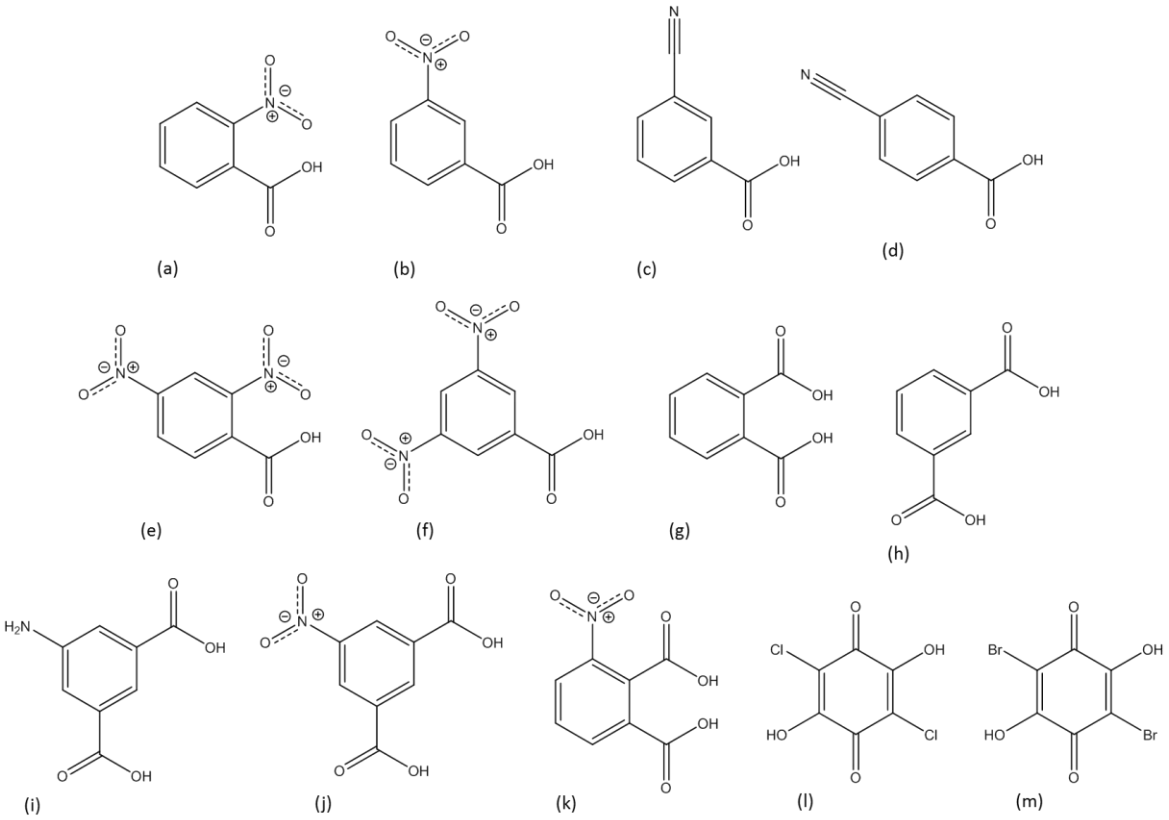

Figure 6.3 Substituted organic acid molecular components: (a) 2-nitrobenzoic acid (2-NBA), (b) 3-nitrobenzoic acid (3-NBA), (c) 3-cyanobenzoic acid (3-CBA), (d) 4-cyanobenzoic acid (4-CBA), (e) 2,4-dinitrobenzoic acid (2,4-DNBA), (f) 3,5-dinitrobenzoic acid (3,5-DNBA), (g) phthalic acid (P), (h) isophthalic acid (IP), (i) 5-aminoisophthalic acid (5-AIP), (j) 5-nitroisophthalic acid (5-NIP), (k) 3-nitrophthalic acid (3-NP), (l) chloranilic acid and (m) bromanilic acid.

The molecular components selected covered a range of pK_a values to examine the effect of ΔpK_a values between components on SSHB length (Table 6.1). The pK_a values were obtained, where possible, from literature sources. Where literature sources could not be found for a molecular component, the ACD-I Lab [270] was used to calculate or predict the values of pK_a. Values were also calculated for the molecular components with pK_a values obtained from literature sources, to check the calculation method; in most cases agreement was observed.

Table 6.1 The pKa values of each molecular component calculated using the ACD-I Lab (ACD pKa), [270] predicted using ACD-I Lab (pKa) [270] or obtained from the literature. The ACD pKa calculates 'accurate acid-base ionisation constants' for specific atoms/groups whilst those predicted are 'pKa and ion fractions' for molecular regions.

Molecular component	ACD pKa [270]	pKa [270]	Literature reference
urea	-	0.1	0.1 [93]
N-methylurea	-	0.1	0.9 [271]
N,*N*-dimethylurea	-	0.1	0.31 [135]
N,N'-dimethylurea	-	0.1	-
N-phenylurea	-	0.1	-0.30 [271]
3-deazauracil	1.40	-	1.37 [271]
pyrazole	2.83	-	2.49 [93]
3,5-dimethylpyrazole	4.06	-	4.38 [271]
4(5)-methylimidazole	7.68	-	7.52 [271]
isonicatinamide	3.39	-	3.61 [271]
Isoniazid	3.79	-	3.52 [271]
4-acetylpyridine	3.57	-	-
1,2,4-*1H*-triazole	2.70	-	-
2-nitrobenzoic acid	2.19	-	2.17 [93]
3-nitrobenzoic acid	3.48	-	3.46 [93]
3-cyanobenzoic acid	3.64	-	3.6 [93]
4-cyanobenzoic aicd	3.54	-	3.55 [93]
2,4-dinitrobenzoic acid	1.43	-	1.43 [93]
3,5-dinitrobenzoic acid	2.88	-	1.51 [93]
Phthalic acid	2.95	-	2.94 [93]
Isophthalic aicd	3.53	-	3.7 [93]
5-aminoisophthalic acid	3.69	-	-
5-nitroisophthalic acid	2.81	-	-
3-nitrophthalic acid	1.90	-	-
Chloranilic acid	1.38	-	1.38 [135]
Bromanilic acid	1.34	-	1.34 [135]

6.2 Experimental details

6.2.1 Preparation and crystallographic analysis

The molecular complexes prepared from the combination of set 1 and set 2 basic components with a range of organic acids are summarised in Table 6.2 and Table 6.3, respectively. The full details of their preparation are included in §A6.1 whilst the details of the crystallographic analysis are included in §A6.2 and in §7.2.

Table 6.2 The molecular complexes prepared from the combination of basic components set 1 and a range of organic acids.

Molecular complex	Code
N,*N*-dimethylurea and 2-nitrobenzoic acid 1:1	DMU2-NBA
N,*N*-dimethylurea and 3-nitrobenzoic acid 1:1	DMU3-NBA
N,*N*-dimethylurea and 3-cyanobenzoic acid 1:1	DMU3-CBA
N,*N*-dimethylurea and 4-cyanobenzoic acid 1:1	DMU4-CBA
N,*N*-dimethylurea and 2,4-dinitrobenzoic acid 1:1	DMU2,4-DNBA
N,*N*-dimethylurea and 3,5-dinitrobenzoic acid 1:1	DMU3,5-DNBA
urea and isophthalic acid 1:1	UIP
urea and 5-aminoisophthalic acid 1:1	U5-AIP
urea and 5-nitroisophthalic acid 4:1	U5-NIP
N-methylurea and phthalic acid 1:1	MUP
N-methylurea and isophthalic acid 1:1	MUIP
N-methylurea and 5-nitroisophthalic acid 2:1	MU5-NIP
N-methylurea and 5-aminoisophthalic acid 1:1	MU5-AIP
N,*N*-dimethylurea and phthalic acid 2:1	DMUP
N,*N*-dimethylurea and isophthalic acid 2:1	DMUIP
N,*N*-dimethylurea and 5-aminoisophthalic acid 2:1	DMU5-AIP
N,*N*-dimethylurea and 3-nitrophthalic acid 1:1	DMU3-NP
N,*N*-dimethylurea and 5-nitroisophthalic acid 2:1	DMU5-NIP
N-phenylurea and 2,4-dinitrobenzoic acid 1:1	PhU2,4-DNBA
N-phenylurea and 3-nitrophthalic acid 2:2	PhU3-NP
N-phenylurea and 5-nitroisophthalic acid 2:1	PhU5-NIP I
N-phenylurea and 5-nitroisophthalic acid 1:1	PhU5-NIP II
N,N'-dimethylurea and 5-aminoisophthalic acid 1:1	DM'U5-AIP
3-deazauracil and 3-nitrophthalic acid 2:1	3-DAZA3-NP
3-deazauracil and 2,4-dinitrobenzoic acid 1:1	3-DAZA2,4-DNBA
3-deazauracil and chloranilic acid 1:1	3-DAZAClA
3-deazauracil, bromanilic acid and water 2:1:2	3-DAZABrA hydrate

Table 6.3 The molecular complexes prepared from the combination of basic components set 2 and a range of organic acids.

Molecular complex	Code
isonicotinamide phthalic acid 2:2	INP
isonicotinamide 2,4-dinitrobenzoic acid 1:1	IN2,4-DNBA I
isonicotinamide 2,4-dinitrobenzoic acid 1:1	IN2,4-DNBA II
isonicotinamide 2,4-dinitrobenzoic acid methanol solvate 1:2:1	IN2,4-DNBA III
isoniazid 2,4-dinitrobenzoic acid 1:1	INZ2,4-DNBA
isoniazid phthalic acid 1:1	INZP
isoniazid 5-nitroisophthalic acid 1:1	INZ5-NIP
pyrazole bromanilic acid 1:1	PYBrA
pyrazole chloranilic acid hydrate 1:1 :1	PYClA hydrate
4(5)-methylimidazole bromanilic acid 1:1	4(5)-MIBrA
4(5)-methylimidazole chloranilic acid hydrate 2:1:1:2	4(5)-MIClA hydrate
4-acetylpyridine bromanilic acid 1:1	4-APBrA
4-acetylpyridine chloranilic acid 1:1	4-APClA
1,2,4-*1H*-triazole chloranilic acid hydrate 2:1:1	1,2,4-TZClA hydrate
3,5-dimethylpyrazole bromanilic acid hydrate 2:1:2	3,5-DMPYBrA hydrate
3,5-dimethylpyrazole chloranilic acid hydrate 2:1:2	3,5-DMPYClA hydrate
3,5-dimethylpyrazole chloranilic acid 1:1 (3,5-DMPYCLA has since been identified in the literature) [272]	3,5-DMPYClA

6.3 Engineering O—H···O SSHBs

Twenty-seven molecular complexes containing an O—H···O hydrogen bonding interaction were synthesised from the combination of the set 1 basic molecular components with the organic acids. The O—H···O hydrogen bond is commonly formed between the substituted ureas (U) and benzene carboxylic acids (Ac) molecular building blocks in a carboxylic acid:amide U:Ac $R_2^2(8)$ hydrogen bonding synthon containing a strong O—H···O hydrogen bond, alongside a moderate strength N—H···O hydrogen bond (Figure 6.4(a)). In the 3-deazauracil and organic acid molecular complexes, a single strong O—H···O hydrogen bond connects the two different molecular building blocks (Figure 6.4(b)).

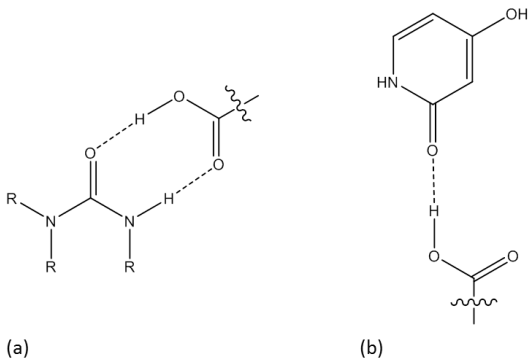

Figure 6.4 Hydrogen bond synthons formed in the basic set 1 organic acid molecular complexes of (a) a carboxylic acid:amide $\boldsymbol{R_2^2(8)}$ U:Ac hydrogen bonding synthon formed between substituted ureas (U) and benzene carboxylic acids (Ac) and (b) a single O—H···O hydrogen bond formed between the 3-deazauracil and organic acids.

6.3.1 Substituted urea and benzene carboxylic acid molecular complexes

In the substituted urea benzene carboxylic acid molecular complexes, the O—H···O hydrogen bonding interaction is formed in a carboxylic acid:amide U:Ac $R_2^2(8)$ hydrogen bonding synthon (Figure 6.4(a)). Related to the substitution of the molecular components and their crystallisation ratio, this synthon is utilised in forming a number of different hydrogen bonding motifs of varying stoichiometries; these include a U:Ac, U:Ac:U and Ac:U:Ac motif (Figure 1.11), as previously described by Alhalaweh *et al*. (2010). [44]

Substituted urea and benzoic acid molecular complexes

The combination of the substituted urea and benzoic acid molecular building blocks results in a 1:1 complex and the formation of the O—H···O hydrogen bonding interaction in a single carboxylic acid:amide $R_2^2(8)$ hydrogen bonding synthon generating a U:Ac hydrogen bonding motif (Figure 6.5). These molecular complexes include DMU2-NBA, DMU3-NBA, DMU3-CBA, DMU4-CBA, DMU3,5-DNBA, DMU2,4-DNBA and PhU2,4-DNBA. The di-substitution of the second amine group in the *N*,*N*-dimethylurea molecular complexes, the bulky group phenyl group in the *N*-phenylurea molecular complexes and the single carboxylic acid group on the benzoic acids prevents any further U:Ac synthons being formed. In DMU3-CBA, two independent U:A motifs are present and therefore can be better described as a 2:2 complex. In DMU2,4-DNBA, the formation of the U:A synthon occurs alongside the transfer of the 2,4-DNBA carboxylic acid hydrogen atom to the urea carbonyl and the SSHB is a O^+—H···O^- CAHB; DMU2,4-DNBA is therefore a salt. Proton transfer does not occur in any of the other U:Ac molecular complexes.

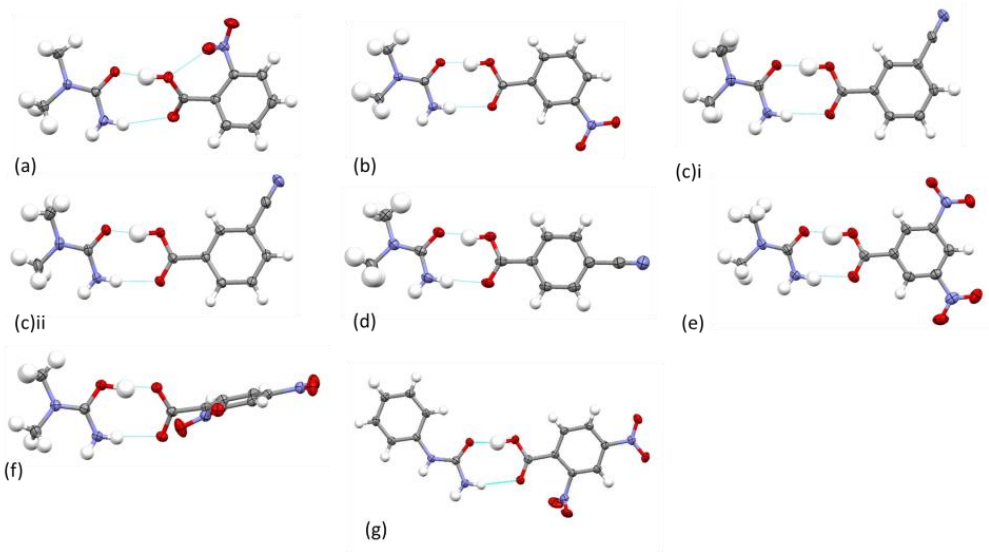

Figure 6.5 Carboxylic acid:amide $\boldsymbol{R_2^2(8)}$ U:Ac hydrogen bonding synthons in (a) DMU2-NBA, (b) DMU3-NBA, (c)i and ii DMU3-CBA, (d) DMU4-CBA, (e) DMU3,5-DNBA, (f) DMU2,4-DNBA and (g) PhU2,4-DNBA

The O—H···O hydrogen bonding interactions are short enough to be considered SSHBs, with O···O hydrogen bond distances in the range of 2.44 to 2.52 Å (Table 6.4). The shortest SSHB is formed in DMU2,4-DNBA, where it is charge assisted, with an O···O hydrogen bond distance of 2.446(1) Å and an elongated O—H distance of 1.08(2) Å; this is characteristic of an SSHB with a symmetric single well potential. DMU2,4-DNBA is the only molecular complex containing an O—H···O SSHB with an O···O hydrogen bond distance within the previously proposed limit of 2.45 Å where proton migration may occur. In DMU3-CBA, two O—H···O SSHB are present in the two different U:Ac synthons with significantly differing O···O hydrogen bond distances of 2.472(2) and 2.481(2) Å; this may be caused by crystal packing effects.

Table 6.4 Hydrogen bond parameters in each carboxylic acid:amide $\boldsymbol{R_2^2(8)}$ U:Ac hydrogen bonding synthon formed in the molecular complexes.

Complex	Interaction	D···A (Å)	D—H (Å)	H···A (Å)	<DHA (°)
DMU2-NBA	O2—H1···O5	2.465(1)	1.03(2)	1.45(2)	169(2)
	N1—H6···O1	3.197(2)	0.87(2)	2.40(2)	151(2)
DMU3-NBA	O1—H1···O3	2.506(2)	0.98(4)	1.53(4)	170(3)
	N2—H6···O2	2.995(2)	0.83(4)	2.67(4)	173(3)
DMU3-CBA	O2—H24···O6	2.472(2)	1.00(4)	1.48(4)	171(4)
	N5—H15···O1	2.911(2)	0.90(2)	2.03(2)	170(2)
	O3—H1···O5	2.481(2)	1.03(4)	1.46(3)	171(3)
	N1—H6···O4	2.933(2)	0.88(2)	2.06(2)	170(2)
DMU4-CBA	O2—H1···O3	2.516(2)	1.04(2)	1.48(2)	167(2)
	N4—H2···O1	2.932(2)	0.94(2)	2.00(2)	172(2)
DMU3,5-DNBA	O3—H1···O1	2.466(3)	1.03(7)	1.45(7)	166(6)
	N3—H3···O2	2.971(3)	0.98(5)	2.05(5)	155(4)
DMU2,4-DNBA	O3—H1···O2	2.446(1)	1.08(2)	1.39(2)	167(2)
	N3—H11···O1	2.906(1)	0.88(2)	2.03(2)	173(2)
PhU2,4-DNBA	O2—H1···O7	2.510(2)	1.00(3)	1.53(3)	168(3)
	N1—H6···O1	3.029(2)	0.88(2)	2.16(2)	167(2)

Substituted urea and benzene dicarboxylic acid molecular complexes

The combination of the substituted ureas with benzene dicarboxylic acids, where there is an additional carboxylic acid group compared to the benzoic acids, resulted in different crystallisation ratios of components and the formation of O—H···O hydrogen bonds in different hydrogen bonding motifs.

In nine of the substituted urea benzene dicarboxylic acid molecular complexes, components form a 2:1 complex, respectively, and the formation of the O—H···O hydrogen bonds occurs *via* two carboxylic acid:amide $R_2^2(8)$ hydrogen bonding synthons generating a U:Ac:U hydrogen bonding motif (Figure 6.6); for UIP, which is better described as a 2:2 complex, a second different hydrogen bonding motif is also present. There is no proton transfer across the O—H···O hydrogen bonds in any of the molecular complexes containing the U:Ac:U motif.

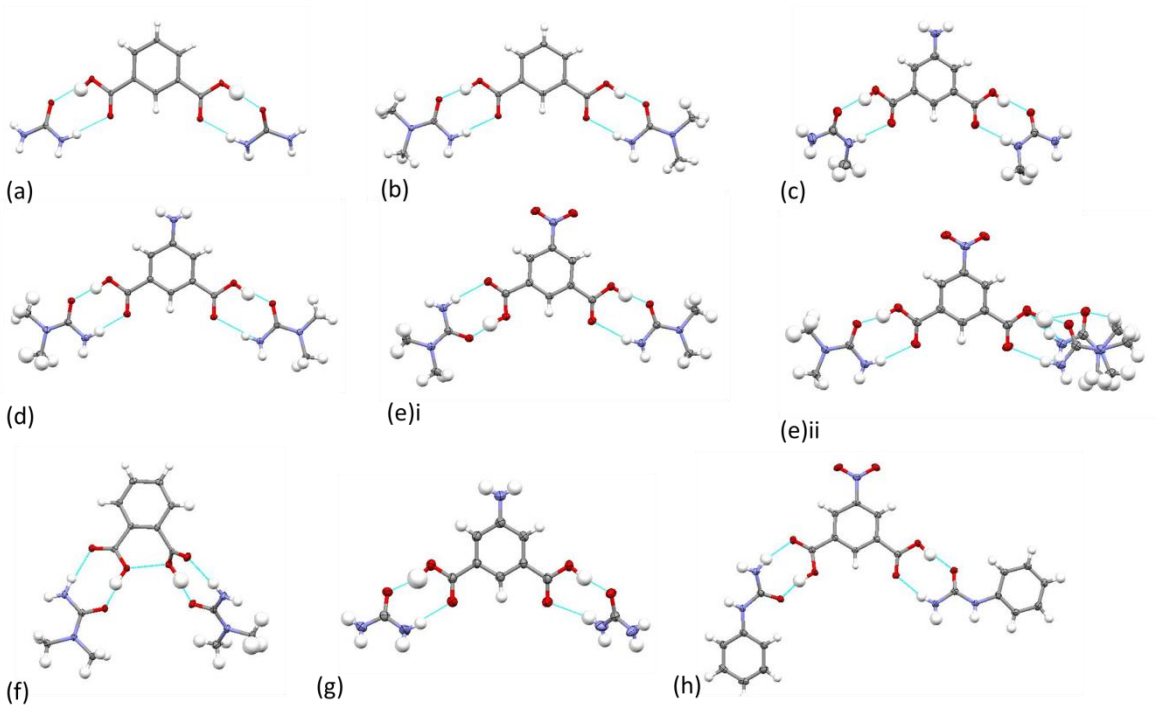

Figure 6.6 The U:Ac:U hydrogen bonding motif in molecular complexes (a) UIP, (b) DMUIP, (c) MU5-AIP, (d) DMU5-AIP, (e)i and ii DMUNIP, (f) DMUP and (g) U5-AIP and (h) PhU5-NIP II.

O—H···O hydrogen bonding interactions are formed in the U:Ac:U molecular complexes with a range of O···O hydrogen bond distances from 2.43 to 2.65 Å (Table 6.5). The O—H···O hydrogen bonding interactions short enough to be considered SSHBs are formed in DMUIP, DMU5-AIP, DMU5NIP, DMUP and PhU5-NIP II. Only in PhU5-NIP II for O11—H100···O10 is the O···O hydrogen bond distance within the previously proposed limit of 2.45 Å where proton migration may occur; an elongated O—H distance of 1.07(4) Å is also present and is characteristic of an SSHB with a symmetric single well potential. In DMUP, O2—H2···O5 is just above the limit at 2.452(2) Å whilst in O3—H1···O6, an elongated O—H distance of 1.09(3) Å is present in a longer SSHB ($d_{O\cdots O}$ 2.493(2) Å) and is again characteristic of an SSHB with a symmetric single well potential.

Table 6.5 Hydrogen bond parameters in each carboxylic acid:amide $\boldsymbol{R_2^2(8)}$ hydrogen bonding synthon formed in the U:Ac:U molecular complexes.

Complex	Interaction	D···A (Å)	D—H (Å)	H···A (Å)	<DHA (°)
UIP	O2—H1···O10	2.626(2)	0.87(5)	1.79(5)	160(4)
	N2—H9···O1	2.915(3)	0.89(3)	2.04(3)	166(3)
	O4—H2···O9	2.622(2)	0.95(5)	1.69(4)	167(4)
	N4—H13···O3	2.900(3)	0.96(4)	1.95(4)	170(3)
DMUIP	O2—H1···O3	2.508(1)	0.93(2)	1.59(2)	169(2)
	N1—H6···O1	2.91391)	0.91(2)	2.01(2)	170(1)
MU5-AIP	O4—H2···O10	2.618(2)	0.83(4)	1.80(4)	166(4)
	N4—H16···O3	2.908(3)	0.83(4)	2.09(4)	169(4)
	O1—H3···O9	2.659(2)	0.86(4)	1.82(4)	163(4)
	N6—H14···O2	2.886(3)	0.83(3)	2.06(3)	171(3)
DMU5-AIP	O2—H1···O3	2.504(1)	1.02(2)	1.51(2)	165(2)
	N2—H8···O1	2.978(1)	0.89(2)	2.12(2)	163(1)
	O6—H5···O4	2.534(1)	0.91(2)	1.63(2)	170(2)
	N4—H17···O5	2.884(1)	0.95(2)	1.95(2)	170(2)
DMU5-NIP	O1—H19···O3	2.459(2)	1.02(3)	1.45(3)	170(3)
	N1—H15···O2	2.967(2)	0.88(2)	2.10(2)	171(3)
	O5—H20···O17	2.482(2)	0.96(3)	1.53(3)	164(2)
	N8—H10···O4	3.125(2)	0.89(2)	2.26(2)	171(3)
	O14—H21···O9	2.450(2)	0.95(3)	1.51(3)	169(3)
	N4—H7···O13	3.021(2)	0.88(2)	2.16(2)	167(2)
	O11—H100···O10	2.434(2)	1.07(4)	1.38(4)	167(4)
	N8—H8A···O12	3.089(2)	0.860	2.242	168.1
DMUP	O3—H1···O6	2.493(2)	1.09(3)	1.44(3)	160(3)
	N3—H9···O4	2.978(2)	0.92(2)	2.06(2)	174(2)
	O2—H2···O5	2.452(2)	1.01(3)	1.45(3)	168(2)
	N4—H7···O1	2.974(2)	1.45(3)	2.03(2)	170(2)
U5-AIP	O1—H1···O3	2.651(4)	0.99(8)	1.71(8)	158(7)
	N2—H7···O2	2.857(5)	0.89(4)	2.01(4)	159(4)
	O5—H3···O3	2.605(4)	1.01(6)	1.60(6)	171(6)
	N1—H8···O3	3.177(6)	0.85(6)	2.57(6)	129(5)
PhU5-NIP II	O4—H1···O2	2.523(2)	1.02(3)	1.53(2)	165(3)
	N4—H12···O3	3.135(2)	0.94(3)	2.26(3)	156(2)
	O6—H21···O1	2.610(2)	0.96(3)	1.65(3)	170(3)
	N1—H8···O3	2.889(2)	0.93(2)	1.98(3)	168(2)

In eight of the substituted urea benzene dicarboxylic acid molecular complexes, O—H···O hydrogen bonds form in a carboxylic acid:amide $R_2^2(8)$ hydrogen bonding synthon involving one carboxylic acid group of the benzene dicarboxylic acid generating a U:Ac motif, whilst the second carboxylic acid group forms a single O—H···O hydrogen bond to a neighbouring substituted urea. In these molecular complexes, components are present in equivalent ratios; exceptions to this are MU5-NIP which is a 2:1 complex. In a number of cases, including MUIP, DMU3-NP, MUP and PhU3-NP, the single O—H···O hydrogen bond to a neighbouring substituted urea molecule connects U:Ac motifs (Figure 6.7). In MU5-NIP, the single O—H···O hydrogen bond forms to neighbouring *N*-methylurea which hydrogen bonds to an *N*-methylurea in a neighbouring U:Ac motif; motifs are connected by these *N*-methylurea:*N*-methylurea links (Figure 6.7(e)).

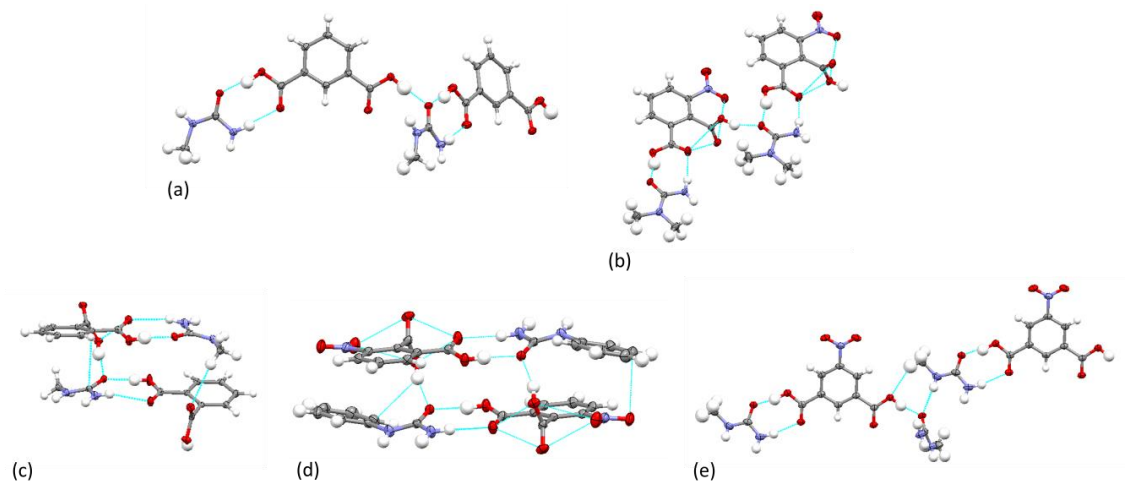

Figure 6.7 The connection of U:A motifs via a single O—H···O hydrogen bond link in (a) MUIP, (b) DMU3-NP, (c) MUP, (d) PhU3-NP and (e) MU5-NIP.

In the UIP and MU5-AIP structures, the single O—H···O hydrogen bond, formed between the second carboxylic acid group and a neighbouring substituted urea, forms a connection to the next U:Ac:U motif (Figure 6.8). The substituted urea in the U:Ac synthon also participates in a U:Ac:U hydrogen bonded motif. The result is a hydrogen bonded chain of U:Ac synthons, within which an Ac:U:Ac hydrogen bond motif is also present. In U5-NIP, the single O—H···O hydrogen bond, formed between the second carboxylic acid group and a neighbouring urea, connects to an extended hydrogen bonded chain of urea molecules which run through the structure (Figure 6.9).

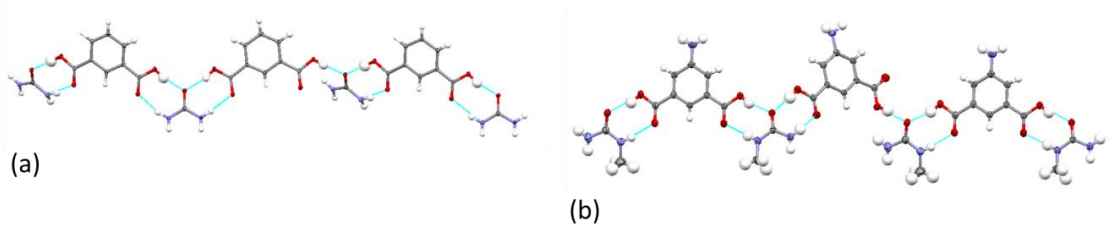

Figure 6.8 The U:Ac:U, Ac:U:Ac, U:Ac and single O—H···O hydrogen bond links in (a) UIP and (b) MU5-AIP.

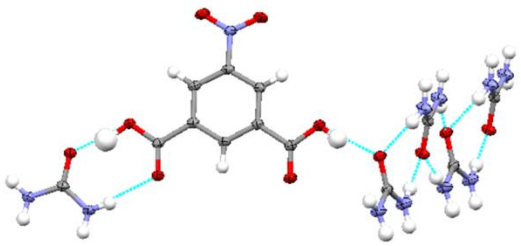

Figure 6.9 The hydrogen bond connections of U:Ac motifs and single O—H···O hydrogen bond links in U5-NIP.

There is no proton transfer across the O—H···O hydrogen bonds in any of the molecular complexes. The O—H···O hydrogen bonding interactions form with a range of O···O hydrogen bond distances from 2.47 to 2.66 Å (Table 6.6). SSHBs are formed in all molecular complexes, apart from PhU3-NP where the O···O hydrogen bond distances are greater than 2.6 Å. None of the SSHBs are below the previously proposed limit of 2.45 Å for proton migration to occur; the SSHB O4—H21···O10 is the closest in U5-NIP at 2.470(1) Å and also has an elongated O—H distance of 1.07(3) Å, characteristic of an SSHB with a symmetric single well potential.

Table 6.6 Hydrogen bond parameters of the U:Ac synthon and the single O—H···O hydrogen bond in the molecular complexes.

Complex	Interaction	D···A (Å)	D—H (Å)	H···A (Å)	<DHA (°)
UIP	O8—H3···O10	2.636(2)	0.89(3)	1.78(4)	164(3)
	N1—H11···O7	2.846(1)	0.88(3)	1.98(3)	170(3)
	O5—H4···O9	2.597(2)	0.85(4)	1.75(4)	175(4)
MUP	O7—H1···O5	2.558(1)	0.85(2)	1.72(2)	168(2)
	N1—H15···O6	3.134(2)	0.85(2)	2.38(2)	149(2)
	O9—H4···O8	2.595(2)	0.93(3)	1.67(3)	173(2)
	O2—H2···O8	2.578(1)	0.90(2)	1.69(2)	167(3)
	N4—H19···O1	3.156(2)	0.89(2)	2.31(2)	160(2)
	O3—H3···O5	2.591(1)	0.92(3)	1.68(3)	168(2)
MUIP	O4—H6···O5	2.594(2)	1.00(3)	1.61(3)	167(2)
	N1—H15···O6	2.905(2)	0.94(2)	1.97(2)	172(2)
	O2—H1···O5	2.674(2)	0.97(3)	1.71(3)	175(3)
MU5-AIP	O5—H1···O10	2.582(2)	0.84(4)	1.75(4)	174(4)
	N3—H18···O6	3.169(3)	0.87(4)	2.55(4)	129(3)
	O7—H4···O9	2.658(2)	0.83(4)	1.85(4)	167(4)
DMU3-NP	O2—H2···O7	2.563(2)	0.96(3)	1.62(3)	165(2)
	N2—H6···O1	2.971(2)	0.89(2)	2.10(2)	168(2)
	O4—H1···O7	2.589(1)	0.93(2)	1.71(2)	158(2)
U5-NIP	O4—H21···O10	2.470(1)	1.07(3)	1.42(4)	166(3)
	N8—H2···O3	2.878(2)	0.81(2)	2.07(2)	169(2)
	O1—H12···O7	2.614(1)	0.85(4)	1.78(4)	166(3)
MU5-NIP	O5—H5···O8	2.490(1)	0.99(2)	1.51(2)	168(2)
	N2—H7···O4	3.001(2)	0.94(2)	2.07(2)	170(2)
	O3—H1···O1	2.557(1)	0.93(2)	1.63(2)	170(2)
PhU3-NP	O2—H1···O3	2.643(2)	0.90(3)	1.74(3)	173(2)
	N2—H25···O1	2.895(2)	0.86(2)	2.05(2)	169(2)
	O11—H2···O3	2.605(1)	0.91(2)	1.77(2)	162(2)
	O6—H3···O10	2.607(2)	0.93(3)	1.69(3)	171(3)
	N4—H16···O7	2.995(2)	0.85(3)	2.16(3)	166(2)
	O4—H4···O10	2.618(1)	0.90(3)	1.73(2)	167(3)

The combination of *N,N'*-dimethylurea and 5-aminoisophthalic acid (DM'U5-AIP) leads to a very different structure to the other seventeen molecular complexes. The components crystallise in a 1:1 ratio in which the O—H···O hydrogen bond forms instead in a three membered hydrogen bonded ring, graphset notation $R_3^4(10)$, as a result of intramolecular hydrogen transfer between the 5-AIP amine group and one of its carboxylic acid groups, forming zwitterions (Figure 6.10); DM'U5-AIP

is therefore a salt. A charge-assisted moderate strength N^+—H···O^- hydrogen bond ($d_{N^+\cdots O^-}$ 2.826 Å) forms between the deprotonated carboxylic acid in one 5-aminoisophthalic acid molecule and the protonated amine group in another 5-aminoisophthalic acid molecule. A third 5-aminoisophthalic acid molecule completes the ring through a strong charge assisted O—H···O^- hydrogen bond to the deprotonated carboxylate group ($d_{O\cdots O}$ 2.591 Å), and a second O···H—N^+ hydrogen bond with the protonated amine group, *via* an N—H···O hydrogen bonding interaction ($d_{N\cdots O}$ 2.838 Å) (Table 6.7).

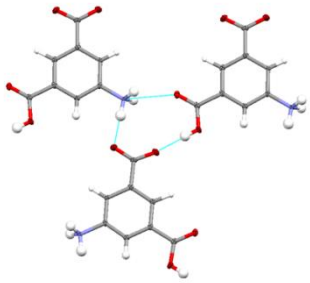

Figure 6.10 The three-membered hydrogen bonded ring formed by 5-aminoisophthalic acid molecules, $\boldsymbol{R_3^4}(10)$.

Table 6.7 Hydrogen bond parameters in the hydrogen bonded ring $\boldsymbol{R_3^4}(10)$ in DM'U5-AIP.

Complex	Interaction	D···A (Å)	D—H (Å)	H···A (Å)	<DHA (°)
DM'U5-AIP	O4—H4···$O2^-$	2.587	0.81	1.78	176
	$N1^+$—H15···$O1^-$	2.723	0.82	1.80	178
	N1—H14···O3	2.827	0.90	2.39	110

6.3.2 3-deazauracil organic acid molecular complexes

The molecular complexes formed between 3-deazauracil and organic acid molecular components have the common feature of a single O—H···O hydrogen bond link between the 3-deazauracil carbonyl group and the organic acid hydroxyl group but are otherwise very different (Figure 6.11). It is not possible to identify a common hydrogen bonding motif beyond this single O—H···O hydrogen bond link. The component ratios in each complex also differ; 3-DAZABrA hydrate is a 2:1:2 molecular complex, 3-DAZAClA and 3-DAZA2,4-DNBA are 1:1 complexes whilst 3-DAZA3-NP is a 1:2 molecular complex. A carboxylic acid:amide $R_2^2(8)$ hydrogen bond synthon forms alongside a single O—H···O hydrogen bond link in 3-DAZA2,4-DNBA. The formation of the O—H···O hydrogen bond link between components occurs with partial proton transfer of both BrA hydrogen atoms in 3-DAZABrA hydrate, complete proton transfer of one ClA hydrogen atom in ClA3-DAZA forming an O^+—H···O^- CAHB and with no proton transfer in 3-DAZA2,4-DNBA and 3-DAZA3-NP.

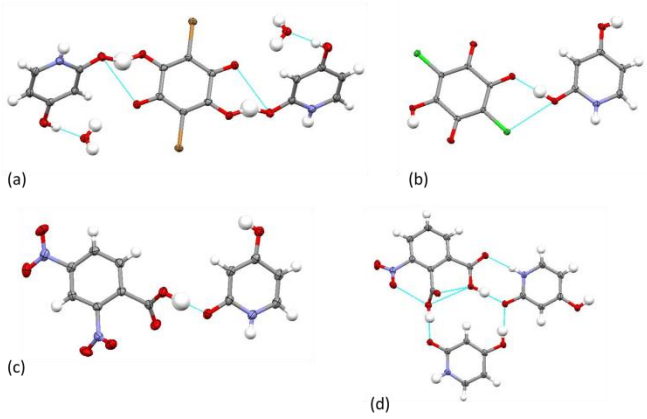

Figure 6.11 The molecular complexes of (a) 3-DAZABrA hydrate, (b) 3-DAZAClA, (c) 3-DAZA2,4-DNBA and (d) 3-DAZA3-NP.

The O—H···O hydrogen bonding links between the 3-deazuracil and organic acid component form with a range of O···O distances from 2.41 to 2.56 Å (Table 6.8). All the O—H···O hydrogen bonding links are short enough to be considered SSHBs. A very short O—H···O hydrogen bond is formed in 3-DAZABrA hydrate ($d_{O\cdots O}$ 2.411(2) Å) well below the previously proposed limit of 2.45 Å for proton migration to occur and where the hydrogen atom is symmetrically located, this is characteristic of an SSHB with a symmetric single well potential. In 3-DAZA2,4-DNBA, the SSHB O···O distance, at 2.449(1) Å, is just below the previously proposed limit for proton migration to occur.

Table 6.8 Hydrogen bond parameters in the 3-DAZA molecular complexes.

Complex	Interaction	D···A (Å)	D—H (Å)	H···A (Å)	<DHA (°)
3-DAZABrA hydrate	O2—H1···O3	2.411(2)	1.21(4)	1.28(4)	152(4)
3-DAZAClA	O6—H6···O2	2.560(1)	0.91(3)	1.65(3)	176(3)
3-DAZA2,4-DNBA	O1—H1···O7	2.449(1)	1.00(3)	1.45(3)	177(2)
3-DAZA3-NP	O2—H1···O9	2.504(1)	0.97(2)	1.54(2)	173(2)
	O4—H2···O7	2.542(1)	0.92(2)	1.63(2)	169(2)

6.4 Engineering charge assisted N^+—H···O^- SSHBs

Seventeen molecular complexes were synthesised containing an N^+—H···O^- charge assisted hydrogen bonding interaction between set 2 basic molecular components with the organic acid (benzene carboxylic acid or anilic acid) molecular building blocks.

In several of the six-membered substituted *N*-heterocycle and benzene carboxylic acid molecular complexes, the charge-assisted N^+—H···O^- hydrogen bond is assisted by a weak hydrogen bond

between the carboxylate group and a hydrogen bond donor adjacent to the protonated nitrogen; a pyridine:carboxylic acid $R_2^2(7)$ hydrogen bond synthon (Figure 6.12(a)) results. This synthon has been commonly reported in pyridine carboxylic acid molecular complexes. [273] In the *N*-heterocycles and anilic acid molecular complexes, the charge assisted N^+—H···O^- hydrogen bond is present in a number of motifs. Similar to other haloanilic acid molecular complexes, [31, 138] a bifurcated $R_2^1(5)$ $N^+H(O)O^-$ hydrogen bond prevails between the deprotonated anilic acid group and a protonated *N*-heterocycle nitrogen atom (Figure 6.12(b)). Single charge assisted N^+—H···O^- hydrogen bonds also form between the *N*-heterocycle and haloanilic acid molecular components either singly (Figure 6.12 (c)), or alongside a water molecule which forms a bifurcated hydrogen bond with the deprotonated group (Figure 6.12(d)).

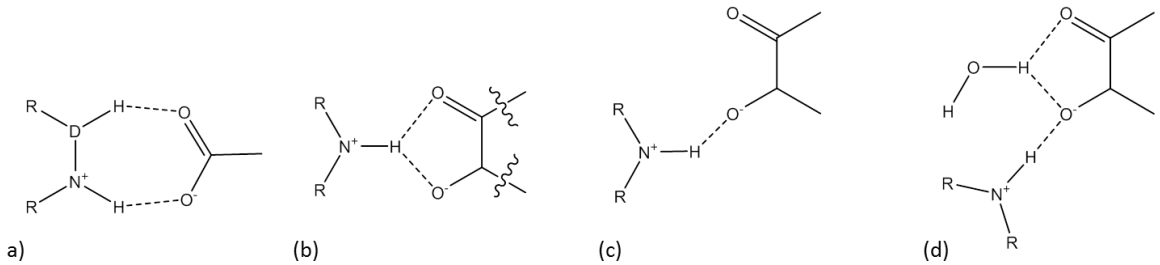

Figure 6.12 The hydrogen bonding motifs formed in the *N*-heterocycle organic acid molecular complexes: (a) a pyridine:carboxylic acid $\boldsymbol{R_2^2(7)}$ synthon in the substituted *N*-heterocycle and benzene carboxylic acid molecular complexes, (b) $\boldsymbol{R_2^1(5)}$ bifurcated N^+—H···O^- hydrogen bond and (c) a single N^+—H···O^- hydrogen bond forms to the deprotonated acid alone or (d) alongside a water molecule which forms a bifurcated hydrogen bond with the deprotonated acid group.

6.4.1 N-heterocycle and benzene carboxylic acid molecular complexes

The combination of the six-membered N-heterocycles and benzene carboxylic acid molecular building blocks formed 1:1 complexes in IN2,4-DNBA I, INZP and INZ2,4-DNBA and a 2:1 complex in INP. In IN2,4-DNBA II and INZ5NIP, two independent molecular motifs are present and therefore these complexes can be better described as 2:2 complexes. A methanol solvate of IN2,4-DNBA (IN2,4-DNBA III) was also formed as a 1:2:1 complex.

In the molecular complexes where components are present either in equivalent ratios or where the benzene carboxylic acid is the major component, a charge assisted N^+—H···O^- hydrogen bond forms in a pyridine:carboxylic acid $R_2^2(7)$ hydrogen bond synthon as a result of proton transfer between the benzene carboxylic acid and the *N*-heterocycle; in IN2,4-DNBA I, II and III and INZP the proton is transferred to the *N*-heterocycle nitrogen atom whilst in INZ2,4-DNBA, the proton is transferred to the diazo functional group (Figure 6.13). The assisting D—H···O interaction in the $R_2^2(7)$ hydrogen bond synthon is a weak C—H O hydrogen bond in IN2,4-DNBA I ($d_{C\cdots O}$

3.093(2) Å), IN2,4-DNBA II ($d_{C\cdots O}$ 3.007(2) Å) IN2,4-DNBA III ($d_{C\cdots O}$ 3.128(2) Å) and INZP ($d_{C\cdots O}$ 3.110(2) Å) whilst in INZ2,4-DNBA it is a moderate strength N—H···O hydrogen bond ($d_{N\cdots O}$ 2.777(1) Å). Proton transfer to the *N*-heterocycle occurs in both molecular units connected by the pyridine:carboxylic acid $R_2^2(7)$ hydrogen bond synthon in IN2,4-DNBA. In IN2,4-DNBA III, where a second IN molecule is not present, the second 2,4-DNBA molecule hydrogen bonds to the methanol solvent instead of undergoing proton transfer. In INZP, only one of the phthalic acid protons is transferred to the isoniazid co-component, the other forms a very short intramolecular O—H···O^- hydrogen bond with the carboxylate group ($d_{O\cdots O}$ 2.379(1) Å). These types of hydrogen bonds often occur between deprotonated and protonated carboxylic acid groups when in close proximity. [21]

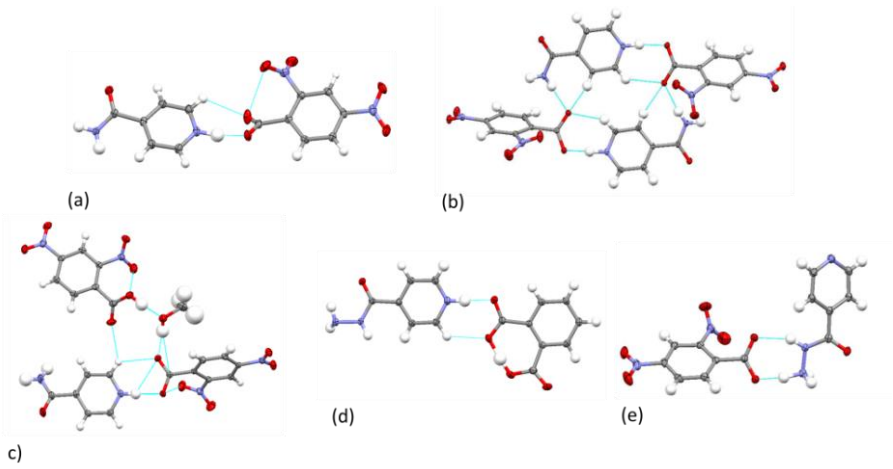

Figure 6.13 The pyridine:carboxylic acid $\boldsymbol{R_2^2(7)}$ hydrogen bond synthons comprised of a charge assisted N^+—H···O^- hydrogen bond and a weak D—H···O hydrogen bond between the *N*-heterocycle and the deprotonated carboxylic acid group in the molecular complexes: (a) IN2,4-DNBA I, (b) IN2,4-DNBA II (c) IN2,4-DNBA III, (d) INZP and (e) INZ2,4-DNBA.

Differences in the hydrogen bonding to IN2,4-DNBA I to III, INZP and INZ2,4-DNBA occur in INP and INZ5-NIP (Figure 6.14). In INP, the phthalic acid molecular component hydrogen bonds through both carboxylic acid groups to two isonicotinamide molecules *via* their nitrogen ring atoms. Proton transfer, to form a charge assisted N^+—H···O^- hydrogen bond, occurs across one INP hydrogen bond link only. This interaction does not form as part of a pyridine:carboxylic acid $R_2^2(7)$ hydrogen bond synthon, as in IN2,4-DNBA I to III and INZP, but is a single hydrogen bond where the carboxylate group and pyridine ring are twisted significantly out of co-planarity (72 °). The hydrogen bond link formed by the second phthalic acid carboxylic acid group is an O—H···N hydrogen bond and is formed in a hydrogen bond synthon that is a variation of the pyridine:carboxylic acid $R_2^2(7)$ hydrogen bond synthon; there is no proton transfer across the O—H···N hydrogen bond and this interaction is assisted by a weak C—H···O hydrogen bond ($d_{C\cdots O}$ 3.103(1) Å). In INZ5-NIP, charge assisted N^+—H···O^- hydrogen bonds form between each

symmetry independent molecular pair of isoniazid and 5-nitroisophthalic acid molecules. Transfer of a single hydrogen atom from one carboxylic acid group occurs for each 5-nitroisophthalic acid molecule to the diazo functional group of the isoniazid molecules. The non-deprotonated carboxylic acid group in each 5-nitroisophthalic acid molecule forms a side-on interaction with a carboxylate group of a neighbouring acid *via* an O—H···O^- hydrogen bond ($d_{O\cdots O}$ 2.586(3) and 2.609(3) Å).

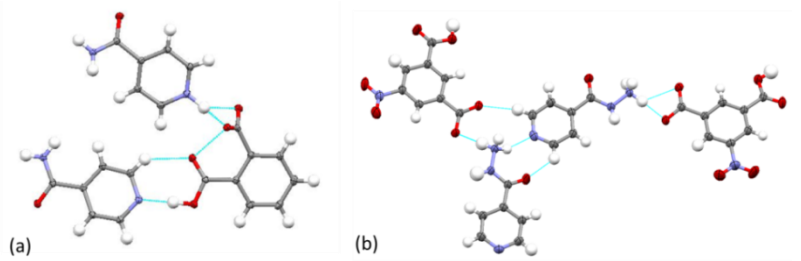

Figure 6.14 (a) The hydrogen bonding links between molecular components in (a) INP and (b) INZ5-NIP.

The distances of the charge assisted N^+—H···O^- hydrogen bonding interactions in the *N*-heterocycle benzene carboxylic acid molecular complexes range from 2.551(1) to 2.757(3) Å (Table 6.9). The charge assisted N^+—H···O^- hydrogen bonds that are short enough to be considered SSHBs are formed in IN2,4-DNBA I, II and III, INP and INZ2,4-DNBA. The shortest SSHB is formed in INP, with a N^+···O^- distance of 2.551(1) Å; this is on the limit of 2.55 Å where proton migration has previously been observed across charge assisted N^+—H···O^- SSHBs. In INP, the N^+—H distance is elongated at 1.07(2) Å; this is characteristic of an SSHB with a symmetric single well potential. In IN2,4-DNBA, the N^+···O^- distance of 2.555(1) Å is slightly longer but close to the previously observed proton migration limit and the N^+—H distance is elongated at 1.04(2) Å. Between IN2,4-DNBA II and IN2,4-DNBA III, the charge assisted N^+—H···O^- hydrogen bonding interactions have significantly different N^+···O^- distances; this may be caused by crystal packing effects.

Table 6.9 Hydrogen bond parameters of each N^+—H···O^- or O—H···N formed in the *N*-heterocycle organic acid molecular complexes.

Complex	Interaction	D···A (Å)	D—H (Å)	H···A (Å)	<DHA (°)
IN2,4-DNBA I	$N1^+$—H1···$O5^-$	2.596(2)	1.06(2)	1.54(2)	171(2)
IN2,4-DNBA II	$N1^+$—H2···$O5^-$	2.555(1)	1.04(2)	1.52(2)	177(2)
	$N2^+$—H1···$O9^-$	2.636(1)	0.98(2)	1.66(2)	169(2)
IN2,4-DNBA III	$N1^+$—H1···$O1^-$	2.599(2)	0.92(2)	1.68(2)	176(2)
INP	$N2^+$—H3···$O2^-$	2.551(1)	1.07(2)	1.48(2)	177(2)
	O1—H1···N1	2.696(1)	1.02(2)	1.68(2)	179(2)
INZP	$N3^+$—H2···$O1^-$	2.658(1)	0.98(2)	1.68(2)	178(2)
INZ2,4-DNBA	$N2^+$—H6···$O3^-$	2.583(1)	1.05(2)	1.54(2)	171(2)
INZ5-NIP	$N5^+$—H20···$O4^-$	2.736(2)	0.95(4)	1.80(4)	167(4)
	$N7^+$—H8···$O9^-$	2.757(3)	0.95(4)	1.82(4)	168(3)

6.4.2 *N*-heterocycle and anilic acid molecular complexes

The combination of the *N*-heterocycle (N) and anilic acid (Ac) molecular components formed ten molecular complexes in which proton transfer between the two molecular components resulted in a charge assisted N^+—H···O^- hydrogen bond.

In three of the molecular complexes, the charge assisted N^+—H···O^- hydrogen bond forms as part of a $N^+H(O)O^-$ bifurcated hydrogen bond synthon occurring on one side of the anilic acid where it is singly deprotonated (HAc^-) in the 1:1 complexes of 4-APClA and 4-APBrA and on both sides of the anilic acid where it is doubly deprotonated (Ac^{2-}) in the 2:1:1 complex of 1,2,4-TZClA hydrate. 4-APClA and 4-APBrA are isostructural, differing only in the halogen atom present. In their structures, two bifurcated hydrogen bond units connect *via* single O—H···O hydrogen bonds on the protonated side of the anilic acid molecule ($d_{O\cdots O}$ 4-APClA 2.671(3) Å, 4-APBrA 2.692(5) Å) (Figure 6.15(a) and (b)). The formation of the $N^+H(O)O^-$ bifurcated hydrogen bond synthon on both sides of the anilic acid in 1,2,4-TZClA hydrate results in a centrosymmetric N:Ac:N hydrogen bonding motif similar to that observed in other 2:1 molecular complexes of *N*-heterocycles with anilic acids including 2:1 picoline-bromanilic acid [139] and 2:1 picoline-anilic acid molecular complexes. [138] Water molecules also hydrogen bond to either side of the deprotonated acid *via* a weak O—H···O hydrogen bond ($d_{O\cdots O}$ 3.049(3) Å).

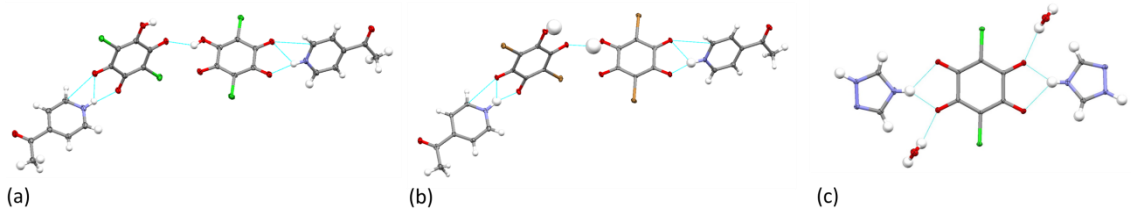

Figure 6.15 Charge assisted N^+—H···O^- hydrogen bonds present in a $N^+H(O)O^-$ bifurcated hydrogen bond synthon in (a) 4-APClA, (b) 4-APBrA and (c) 1,2,4-TZClA.

A bifurcated $N^+H(O)O^-$ hydrogen bond synthon also forms in the 1:1 molecular complexes of PYBrA and 4(5)-MIBrA occurring on one side of the anilic acid where it is singly deprotonated (Figure 6.16). A neighbouring 5-membered *N*-heterocycle also interacts with the deprotonated side of the anilic acid *via* an N—H···O^- hydrogen bond; with the presence of a second N—H group in pyrazole and 4(5)-methylimidazole, it is less clear in these complexes whether the charge assisted N^+—H···O^- hydrogen bond is that involved in forming the bifurcated $N^+H(O)O^-$ hydrogen bond synthon or the single N—H···O^- hydrogen bond. Two bifurcated hydrogen bond units dimerise over an inversion centre on the protonated side of the anilic acid *via* moderate strength O—H····O hydrogen bonds ($d_{O\cdots O}$ PYBrA 2.692(3) Å and 4(5)-MIBrA 2.655(3) Å) forming an N:Ac:Ac:N hydrogen bonded motif. This hydrogen bonded motif is commonly found in other 1:1 molecular complexes of the anilic acids and *N*-heterocycles including lutidine-bromanilic acid [139] and lutidine-chloranilic acid molecular complexes. [274]

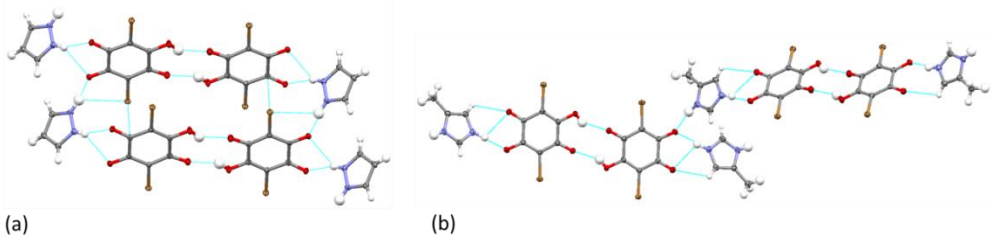

Figure 6.16 Charge assisted N^+—H···O^- hydrogen bonds present in N:Ac:Ac:N hydrogen bonded motifs in (a) PYBrA and (b) 4(5)-MIBrA.

A 1:1 molecular complex is also formed in 3,5-DMPYClA where the anilic acid is singly deprotonated (HAc^-) by the *N*-heterocycle. The charge assisted N^+—H···O^- hydrogen bond forms to the deprotonated side of the anilic acid. However, unlike in 4-APClA, 4-APBrA, 1,2,4-TRIAZClA, PYBrA and 4(5)-MIBrA, it occurs as a single interaction only and there is no bifurcated hydrogen bond formed to the deprotonated acid groups; this may be a result of the two molecules being twisted 84 ° out of co-planarity with one another. Two 3,5-DMPYClA units assemble *via* single O—H···O hydrogen bonds, as in 4-APClA and 4-APBrA, but this time formed

between the deprotonated and protonated sides of the anilic acid ($d_{O\cdots O}$ 2.681(1) Å) and resulting in a bent N:Ac:Ac:N hydrogen bonding motif (Figure 6.17).

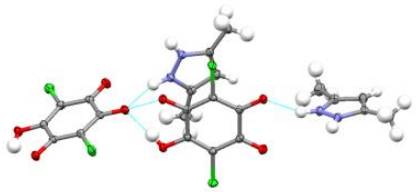

Figure 6.17 The charge assisted N^+—H···O^- hydrogen bonds present in hydrogen bonding motifs of 3,5-DMPYClA.

In four of the *N*-heterocycle anilic acid molecular complexes, water molecules replace the *N*-heterocycle in the bifurcated hydrogen bond synthon and interact with the deprotonated anilic acid groups. This occurs in 3,5-DMPYBrA hydrate, 3,5-DMPYClA hydrate, 4(5)-MIClA hydrate and PYClA hydrate. The charge assisted N^+—H···O^- hydrogen bond forms side-on to the deprotonated acid and as a single interaction (Figure 6.18). In 3,5-DMPYBrA hydrate, 3,5-DMPYClA hydrate and 4(5)-MIClA hydrate, the anilic acid is doubly deprotonated (Ac^{2-}) and the N-heterocycle and water molecules are in excess of the anilic acid. This generates a five membered hydrogen bonded motif which has inversion symmetry; the anilic acid occupies a special position of an inversion centre. 3,5-DMPYBrA hydrate and 3,5-DMPYClA hydrate are isostructural, differing only in the halogen atom present. The water:acid:water (W:Ac:W) hydrogen bonded unit is not unusual for hydrates of *N*-heterocycle haloanilic acid molecular complexes, also being observed in structures with CSD refcodes ABUHOU, [275] BARLOW, [31] GOMBEP [276] and NEQWEM [277] among others. A different hydrogen bonding motif forms in PYClA hydrate in the presence of water, where the *N*-heterocycle and anilic acid components are present in equivalent ratios (1:1) and where the anilic acid is singly deprotonated. Water forms an OH(O)O^- bifurcated hydrogen bond to one side of the anilic acid only. Two of these units assemble on the protonated side of the anilic acid *via* a single moderate strength O—H···O hydrogen bond ((Figure 6.18(d)). In the molecular complex of 4(5)-MIClA hydrate, a neutral chloranilic acid molecule (H_2Ac) is also present alongside the Ac^{2-}. This species does not interact *via* N—H···O hydrogen bonds with the *N*-heterocycle.

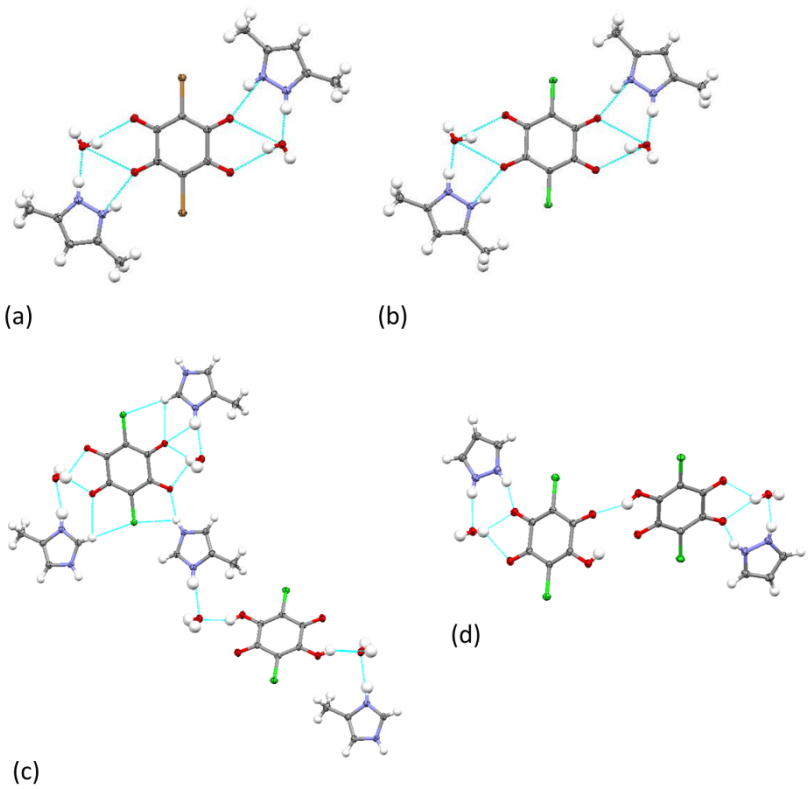

Figure 6.18 The charge assisted N^+—H···O^- hydrogen bonds in hydrogen bonded motifs in (a) 3,5-DMPYBrA hydrate, (b) 3,5-DMPYClA hydrate, (c) 4(5)-MIClA hydrate and (d) PYClA hydrate.

The charge assisted N^+—H···O^- and N—H···O^- hydrogen bonds formed in the seven *N*-heterocycle anilic acid molecular complexes have N···O distances in the range of 2.598(3) to 2.939(2) Å (Table 6.10). The N^+—H···O^- charge assisted hydrogen bonds in PYBrA, PYClA hydrate and 3,5-DMPYClA hydrate are at the limit of the N^+—H···O^- SSHBs whilst none are below the previously proposed limit for proton migration to occur. In general, shorter hydrogen bonding interactions were formed where not part of a bifurcated synthon.

Table 6.10 Hydrogen bond parameters in each N—H···O hydrogen bond formed in each molecular complex.

Complex	Interaction	HB type	D···A (Å)	D—H (Å)	H···A (Å)	<DHA (°)
PYBrA	N1—H4···O1	Single	2.598(3)	0.92(3)	1.71(3)	161(3)
	N2—H5···O2	Bifurcated	2.918(3)	0.85(2)	2.10(2)	163(3)
	N2—H5···O1	Bifurcated	2.914(3)	0.85(2)	2.39(3)	121(2)
4(5)-MIBrA	N1—H5···O1	Single	2.737(2)	0.88(4)	1.87(4)	167(4)
	N2—H4···O1	Bifurcated	2.744(3)	0.95(4)	1.80(4)	172(3)
	N2—H4···O2	Bifurcated	2.970(4)	0.95(4)	2.48(4)	112(3)
4-APClA	N1—H1···O4	Bifurcated	2.674(3)	0.85(4)	1.83(4)	171(4)
	N1—H1···O3	Bifurcated	2.793(3)	0.85(4)	2.38(4)	110(3)
4-APBrA	N1—H1···O3	Bifurcated	2.658(5)	1.02(7)	1.67(7)	164(5)
	N1—H1···O2	Bifurcated	2.793(5)	1.02(7)	2.32(5)	107(4)
PYClA hydrate	N1—H1···O4	Single	2.601(2)	0.88(2)	1.77(2)	157(2)
3,5-DMPYClA	N2—H4···O4	Single	2.700(1)	0.88(2)	1.86(2)	158(2)
3,5-DMPYBrA hydrate	N2—H4···O2	Single	2.621(1)	0.81(3)	1.89(3)	150(2)
3,5-DMPYClA hydrate	N1—H9···O1	Single	2.601(2)	0.85(3)	1.82(3)	151(2)
4(5)-MIClA hydrate	N1—H2···O4	Single	2.744(2)	0.88(3)	1.90(3)	161(3)
1,2,4-TZClA	N1—H1···O2	Single	2.611(2)	1.02(3)	1.62(3)	162(3)
	N2—H3···O1	Bifurcated	2.646(2)	0.87(3)	1.88(3)	146(3)
	N2—H3···O2	Bifurcated	2.904(2)	0.87(3)	2.23(3)	134(2)

6.5 SSHB formation in the molecular complexes

This study has investigated the combination of a range of molecular building blocks in the design of SSHBs for potential proton migration studies. In total, forty-four molecular complexes were synthesised, twenty-seven with O—H···O hydrogen bonds in the range of 2.41 to 2.66 Å and seventeen with charge assisted N^+—H···O^- in the range of 2.55 to 2.97 Å. Of the twenty-seven with O—H···O hydrogen bonds, nineteen can be considered SSHBs, with donor-acceptor distances less than 2.6 Å, whilst only five have donor-acceptor distances that are on or below the previously proposed limit of 2.45 Å for proton migration to occur. Of the seventeen molecular complexes with charge assisted N^+—H···O^- hydrogen bonds, eight can be considered SSHBs, with donor-acceptor distances less than 2.6 Å, whilst only two have donor-acceptor distances that are on or below the previously proposed limit of 2.55 Å.

The seven molecular complexes with O—H···O and N^+—H···O^- SSHBs below or near the respective proposed limits for proton migration are potential proton migration materials and include DMU2,4-DNBA ($d_{O\cdots O}$ 2.446(1) Å), DMUP ($d_{O\cdots O}$ 2.452(1) Å), 3-DAZA2,4-DNBA ($d_{O\cdots O}$ 2.449(1) Å), DMU5-NIP ($d_{O\cdots O}$ 2.434(2) Å), 3-DAZABrA hydrate ($d_{O\cdots O}$ 2.411(2) Å; a very short hydrogen bonding interaction), INP ($d_{N\cdots O}$ 2.551(1) Å) and IN2,4-DNBA II ($d_{N\cdots O}$ 2.555(1) Å). The potential for proton migration across SSHBs is further suggested in DMU2,4-DNBA, 3-DAZABrA hydrate, INP and IN2,4-DNBA where the D—H distance is elongated in the SSHB in the low temperature structures (100 or 150 K); this is characteristic of an SSHB with a symmetric single well potential and favours proton migration. These O···O SSHB distances in the molecular complexes of DMU2,4-DNBA, 3-DAZABrA hydrate are comparable to those previously reported for proton migration materials including urea phosphoric acid ($d_{O\cdots O}$ 2.411(2) Å), [108] *N,N*,-dimethylurea oxalic acid ($d_{O\cdots O}$ 2.4469(9) Å) [109] and *N,N'*-dimethylurea oxalic acid ($d_{O\cdots O}$ 2.4398(15) and 2.4423(15) Å). [109] The N···O SSHB distances of INP and IN2,4-DNBA are slightly longer than those previously reported for the proton migration materials isoniazid 4-aminosalicylic acid ($d_{N\cdots O}$ 2.548(2) Å), [267] pyridine-3,5-dicarboxylic acid ($d_{N\cdots O}$ 2.523(2) Å) [110] and 4,4'-bipyridine benzene-1,2,4,5-tetra carboxylic acid ($d_{N\cdots O}$ 2.5220(17) Å). [111]

A number of design strategies were trialled in this work to target the formation of SSHBs in the molecular complexes. The effect of these on SSHB formation is explored.

6.5.1 Molecular component selection and hydrogen bonding motif effects on SSHB formation

In this study, the success of the combination of different molecular components *via* different hydrogen bonded molecular motifs in accessing SSHBs is of interest.

The selection of substituted ureas and benzene carboxylic acid molecular components and of 3-deazauracil and organic acid molecular components proved to be a good strategy for obtaining O—H···O SSHBs, with SSHBs formed in nineteen out of the twenty seven molecular complexes prepared; in several cases the donor-acceptor distances are below the previously proposed proton migration limits. In general, there was a greater predictability in the motifs formed on combination of the organic acids with the substituted urea molecular components than with the 3-deazauracil molecular components; the substituted ureas repeatedly formed a carboxylic acid:amide $R_2^2(8)$ hydrogen bond synthon whilst there was more variation in the hydrogen bond motifs formed in the 3-deazauracil molecular complexes. The 3-deazauracil basic component was also particularly difficult to co-crystallise with the organic acids; only four such complexes formed compared to twenty-three from the combination of substituted ureas with benzene carboxylic acids. As found by Alhalaweh *et al.* (2010), [44] there was some relationship between ratio of molecular components

in the substituted urea benzene carboxylic acid complexes and the type of hydrogen bonding motif formed. The U:Ac hydrogen bond motif was formed in the 1:1 and 2:2 substituted urea benzene carboxylic acid molecular complexes whilst the U:Ac:U motif formed in the 2:1 substituted urea benzene carboxylic acid molecular complexes. Exceptions to this include the 2:1 complex of MU5-NIP, in which only a U:Ac motif formed, and the 2:2 complexes of UIP and MU5-AIP, in which a number of motifs formed including a Ac:U:Ac and a U:Ac:U hydrogen bonded motif. In all the 2:2 molecular complexes, a single U:Ac hydrogen bond motif was formed alongside a single O—H···O hydrogen bond involving the second carboxylic acid group. In general, in these complexes, the shorter O—H···O hydrogen bonds were formed in the U:Ac motif. This may be related to cooperative hydrogen bonding effects (resonance assisted HBs) occurring causing a strengthening of interactions in the U:Ac synthon. [8] This indicates that a strategy of targeting the carboxylic acid:amide $R_2^2(8)$ hydrogen bond synthon can allow shorter SSHBs to be accessed than for the single interactions. In the four 3-deazauracil organic acid molecular complexes synthesised, all showed a preference for the formation of a single O—H···O hydrogen bond whilst in one complex, 3-DAZA2,4-DNBA, a carboxylic acid:amide $R_2^2(8)$ hydrogen bond synthon was also formed. Unlike for the substituted urea benzene carboxylic acid molecular complexes, the single O—H···O hydrogen bonds were generally shorter than those in the carboxylic acid:amide $R_2^2(8)$ hydrogen bond synthon. This indicates that this carboxylic acid:amide $R_2^2(8)$ hydrogen bond synthon is not favoured for the formation of shorter SSHB in all cases.

In forming the N^+—H···O^- charge assisted hydrogen bonds, the *N*-heterocycles with the benzene carboxylic acids, rather than the anilic acids, proved to be more successful in synthesising molecular complexes containing SSHBs; five out of seven formed SSHBs with the benzene carboxylic acids whilst for the anilic acids no donor-acceptor distances were significantly lower than the 2.6 Å donor-acceptor distance limit. The lack of very short N^+—H···O^- charge assisted hydrogen bonds in the *N*-heterocycle anilic acid molecular complexes may be a result of bifurcated hydrogen bonds being commonly formed on proton transfer. Three-centre hydrogen bonds in a bifurcated motif are generally weaker than two-centre single hydrogen bonding interactions. [278] The geometry of the acid groups in the anilic acids favours the formation of bifurcated hydrogen bonds on deprotonation; the bifurcated motif is common in molecular complexes of *N*-heterocycles and haloanilic acids. [31, 138, 139, 274] Single N^+—H···O^- charge assisted hydrogen bonds were formed in some molecular complexes; in general these were shorter than those in the bifurcated motif. This indicates that, in future studies engineering SSHB, targeting bifurcated interactions is a less good strategy to implement for anilic acids. The combination of the *N*-heterocycles and anilic acids did, however, reveal information about the predictability of the design of different bifurcated motifs. In the 1:1 *N*-heterocycle anilic acid molecular complexes, the

anilic acid was singly deprotonated and formed a bifurcated hydrogen bond with a hydrogen bond donor (N^+—H or O—H_{water}) on the deprotonated side. Two of these bifurcated motifs then consistently interacted on the non-protonated side *via* single or dimer O—H···O hydrogen bonds; an exception to this was 3,5-DMPYClA where bulky methyl groups were adjacent to the N^+—H groups possibly preventing bifurcation. In the 2:1 *N*-heterocycle anilic acid molecular complexes, the anilic acid was doubly deprotonated and formed a bifurcated hydrogen bond with a hydrogen bond donor (N^+—H or O—H_{water}) on both sides of the acid. There was also some predictability in the hydrogen bonded motifs formed by the bromo and chloro analogues; several of the bromo and chloro molecular complexes were isostructural including 4-APBrA with 4-APClA, and 3,5-DMPYBrA hydrate with 3,5-DMPYClA hydrate.

In the molecular complexes of the *N*-heterocycles with benzene carboxylic acids, N^+—H···O^- charge assisted hydrogen bonds in a pyridine:carboxylic acid $R_2^2(7)$ hydrogen bond synthon were favoured. This synthon has been commonly reported in pyridine carboxylic acid molecular complexes. [273, 279] In INP, one of the N^+—H···O^- CAHBs formed singly and not as part of a pyridine:carboxylic acid $R_2^2(7)$ hydrogen bond synthon; this interaction was the shortest of those formed, at 2.551(1) Å. This may indicate that the formation of a N^+—H···O^- CAHB not in a pyridine:carboxylic acid $R_2^2(7)$ hydrogen bond synthon leads to shorter SSHBs. This was explored in several examples in the literature. In isonicotinamide 3,5-dinitrobenzoic acid, [280] the N^+—H···O^- CAHB was shorter ($d_{N^+\cdots O^-}$ 2.538(2) Å) when formed singly in the 1:1 molecular complex than when formed as part of a pyridine:carboxylic acid $R_2^2(7)$ hydrogen bond synthon in the 2:1 complex ($d_{N^+\cdots O^-}$ 2.564(2) Å). In the crystal structure of 4,4-bipyridine benzene-1,2,4,5-tetracarboxylic acid, a N^+—H···O^- CAHB in the pyridine:carboxylic acid $R_2^2(7)$ hydrogen bond synthon was longer ($d_{N^+\cdots O^-}$ 2.617(5) Å) than when formed singly ($d_{N^+\cdots O^-}$ 2.551(5) Å). [281] It may be that preventing the formation of the N^+—H···O^- CAHBs in the pyridine:carboxylic acid $R_2^2(7)$ hydrogen bond synthon is advantageous for accessing the shorter interactions. The shorter nature of the N^+—H···O^- CAHB when not formed in a pyridine:carboxylic acid $R_2^2(7)$ hydrogen bond synthon may be due to the closer molecular approach allowed in contrast to when the pyridine:carboxylic acid $R_2^2(7)$ hydrogen bond synthon is formed; in order for the weak D—H···O to form alongside the N^+—H···O^- CAHB in the synthon, molecular approach between the carboxylate and the protonated *N*-heterocycle may be more restricted.

6.5.2 Effects of acidity and basicity of molecular components on SSHB formation

The effect of the acidity and basicity of molecular components, indicated by pK_a values (§1.3), on SSHB formation is also of interest in this work; the pK_a values of two components interacting *via*

a hydrogen bond, and their differences (ΔpK_a) may affect the proton transfer properties across the hydrogen bond and the hydrogen bond strength.

The molecular complexes described in this chapter cover a ΔpK_a range of −4 to 6.5 (Table 6.11). The proton transfer behaviour observed is, in most cases, in agreement with the ΔpK_a values between the two components; all those with $\Delta pK_a < 0$ form a co-crystal, except for DMU2,4-DNBA and DM'U5-AIP which form salts, and all those with $\Delta pK_a > 3$ form salts. A large number of the N^+—H···O^- molecular complexes are in the 0 to 3 ΔpK_a range where the outcome is less predictable; the majority form salts except for 3-DAZABrA hydrate, which forms an intermediate between a salt and a co-crystal where the proton is symmetrically located in the SSHB. In INP and IN2,4-DNBA III, two molecular pairs of the basic and acid components are present; in one pair proton transfer occurs across the SSHB whilst it does not in the other and a mixed ionisation state molecular complex is formed. Similarly, in 4(5)-MIClA hydrate, a singly deprotonated and neutral acid are both present whilst the 4(5)-methylimidazole is always protonated. 4(5)-MIClA hydrate has a ΔpK_a value of 6.3 and so salt formation would be most likely; however, the stoichiometry is not 1:1 resulting in the coexistence of deprotonated and neutral ClA molecules.

The shortest of the SSHBs are formed in the molecular complexes where there is some degree of proton transfer occurring. For example, the O—H···O SSHBS in the molecular complexes DMU2,4-DNBA and 3-DAZABrA hydrate are two of the shortest formed; a CAHB is formed in DMU2,4-DNBA whilst in 3-DAZABrA hydrate the proton is partially transferred across the hydrogen bond, occupying a central position. For the *N*-heterocycle organic acid molecular complexes of INP and IN2,4-DNBA III, two molecular pairs of the IN and acid components are present, connecting *via* charge assisted and neutral hydrogen bonds between the same functional groups; the charge assisted N^+—H···O^- hydrogen bonds are significantly shorter than the neutral O—H···N hydrogen bonds where proton transfer had not occurred. In future design strategies for SSHB, the selection of components with $\Delta pK_a > 3$, where proton transfer is increasingly likely as occurring in the majority of cases in the complexes in this chapter, may be advantageous to form the shorter of the SSHBs.

Table 6.11 The ΔpK_a values for each molecular complex and the salt vs co-crystal outcome.

Complex	ΔpK_a	Outcome	Complex	ΔpK_a	Outcome
UIP	–3.6	co-crystal	3-DAZAClA	–0.01	salt
U5-AIP	–3.59	co-crystal	PhU5-NIP I	–3.11	co-crystal
U5-NIP	–2.71	co-crystal	PhU2,4-DNBA	–1.73	co-crystal
MU5-AIP	–1.19	co-crystal	PhU3-NP	–2.2	co-crystal
MUP	–3.14	co-crystal	IN2,4-DNBA I	2.18	salt
MUIP	–3.72	co-crystal	IN2,4-DNBA II	2.18	salt
MU5-AIP	–2.79	co-crystal	IN2,4-DNBA III	2.18	mixed
MU5-NIP	–1.91	co-crystal	INP	0.67	mixed
DMU2-NBA	–1.86	co-crystal	INZP	0.58	salt
DMU3-NBA	–3.15	co-crystal	INZ2,4-DNBA	2.09	salt
DMU3-CBA	–3.29	co-crystal	INZ5-NIP	0.98	salt
DMU3-CBA	–3.29	co-crystal	PYBrA	1.15	salt
DMU4-CBA	–3.24	co-crystal	4(5)-MIBrA	6.18	salt
DMU3,5-DNBA	–1.2	co-crystal	4-APClA	2.19	salt
DMU2,4-DNBA	–1.12	salt	4-APBrA	2.23	salt
DMU5-NIP	–2.5	co-crystal	PYClA	1.11	salt
DMU5-AIP	–3.38	co-crystal	DMPYClA	3	salt
DMU-3NP	–1.59	co-crystal	DMPYBrA hydrate	3.04	salt
DMUIP	–3.39	co-crystal	DMPYClA hydrate	3	salt
DMUP	–2.63	co-crystal	4(5)-MIClA hydrate	6.14	salt
D'MU5-AIP	–3.59	salt	1,2,4-TZClA	1.32	salt
3-DAZABrA hydrate	0.03	intermediate			

Potential correlation of the values of ΔpK_a for each molecular complex with the donor-acceptor distances of the hydrogen bond formed between the basic and acidic molecular components can also be examined (Figure 6.19). A correlation between ΔpK_a and SSHB length has previously been made, indicating that the strongest and shortest of hydrogen bonds between two components may be formed when ΔpK_a approaches zero. [117, 269] ΔpK_a values may therefore be a potential tool for tuning hydrogen bond strength. [109, 113]

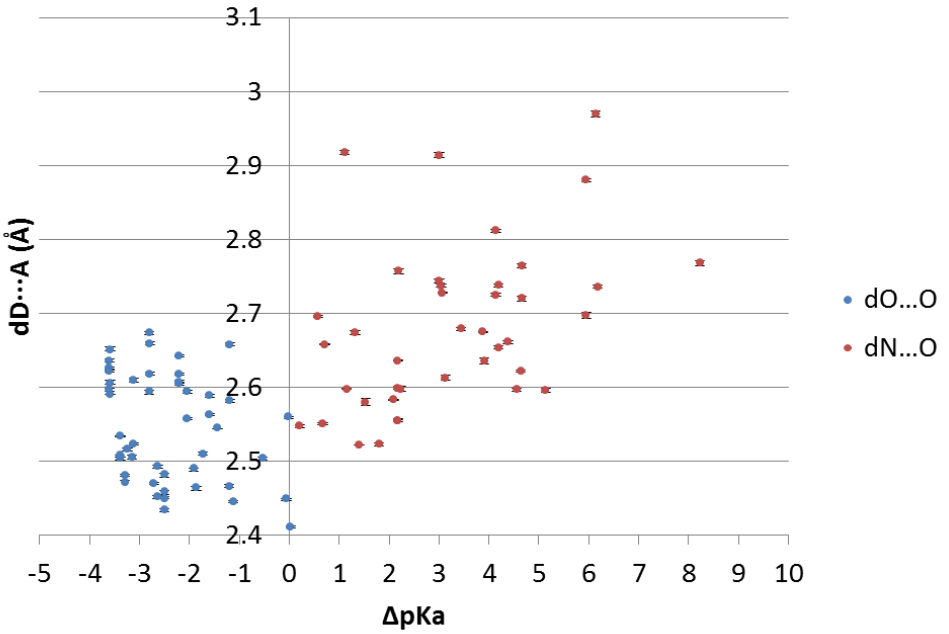

Figure 6.19 The donor-acceptor distances (dD···A) of the hydrogen bond formed between the basic and acidic molecular components versus ΔpK_a for the O—H···O and N^+—H···O^- molecular complexes. Literature values of similar N-heterocycle organic acid molecular components have been included in this plot to address the gap in the ΔpK_a range between 3.5 to 6, not covered by the molecular complexes in this chapter. These include CSD refcode HOLNIG01 (4(5)-methylimidazole succinic acid), [282] LOCJUJ (4(5)-methylimdazole terephthalic acid), [283] YUCQOD (4(5)-methylimdazole 2-((2-carboxyphenyl)disulfanyl)benzoic acid), [284] XIBWAH (Benzimidazole 2-nitrobenzoic acid), [285] NEQWEM01 (benzimidazole chloranilic acid monohydrate), [286] XEYQUO01 (benzimidazole picric acid), [287] AFORIY (9-Aminoacridine and 2,4-dinitrobenzoic acid), [288] VURVIO (3-methylpyridine chloranilic acid), [138] ACEWIP (bis(trimethylpyridine) chloranilic acid), [289] AYUSIX (bis(trimethylpyridine) 4-nitrobenzoic acid), [290] GODNOA (bis(trimethylpyridine benzoic acid), [291] GODNES (bis(trimethylpyridine 2-nitrobenzoic acid), [291] GODNIW (bis(trimethylpyridine 3,5-dinitrobenzoic acid), [291] GUHREG (bis(trimethylpyridine phthalic acid). [292] See §A6.3 for the values of ΔpK_a of molecular complexes taken from the literature. The standard uncertainties on the SSHB distances are plotted but are smaller than the symbols used to denote each data point.

In the molecular complexes in this chapter, a correlation between ΔpK_a values and SSHB length is not clear, with the data points being scattered. Some of the shorter O—H···O and N^+—H···O^- hydrogen bonds are formed between components with more similar proton affinities ($\Delta pK_a \approx 0$) however, as are some of the longer interactions. The hydrogen bonds with donor-acceptor distances less than the previously proposed proton migration limits (2.45 Å for O—H···O and 2.55 Å for N^+—H···O^-) were formed for O—H···O hydrogen bonds in the 0 to -2.5 range and for N^+—H···O^- hydrogen bonds in the 0 to +2.5 range. Longer hydrogen bond lengths were however also formed in these regions. It could be that by selecting molecular components with ΔpK_a values approaching zero it may be possible to access the shorter interactions however this it is not guaranteed. This lack of firm correlation between ΔpK_a and SSHB distances emphasises the

difficulties in transferring ΔpK_a values, determined under solution equilibrium conditions, to the solid state. [88]

Determining the effect of changes in basicity or acidity of molecular components on SSHB formation by substitution, instead of using the ΔpK_a values, may be a more reliable way to tune SSHB strength. For the O—H···O substituted urea benzene carboxylic acid molecular complexes, the shortest of the interactions were formed more consistently where the urea was increasingly substituted with methyl groups, in the *N*,*N*-dimethylurea molecular complexes. For example, the combination of substituted ureas with isophthalic acid leads to the shortest distance forming in combination with the most substituted urea (DMUIP $d_{O\cdots O}$ 2.508(1) Å, MUIP $d_{O\cdots O}$ 2.594(2) Å and UIP $d_{O\cdots O}$ 2.622(2) Å). This has also been seen previously in substituted urea oxalic acid molecular complexes where the O—H···O interaction distance shortened with increasing substitution of the urea. [109, 115, 293, 294] The shortening of the SSHB was attributed to the enhanced basicity of the urea when increasingly substituted with electron donating methyl groups. Ureas that are increasingly substituted with electron donating substituents therefore appear favourable for accessing the shortest of the O—H···O SSHBs in substituted urea benzene carboxylic acid molecular complexes.

For the molecular complexes of the benzene carboxylic acids with both set 1 and set 2 basic components, the SSHB length appears to be tuneable by substitution of the acid. In general, SSHBs with shorter donor-acceptor distances are found to be formed where the acids were substituted with electron withdrawing groups, in particular the shortest formed on nitro substitution, leading to enhanced acidity. For example, the O—H···O SSHBs O···O distances in UIP, MUIP and DMUIP are longer ($d_{O\cdots O}$ UIP 2.622(2) to 2.626(2) Å, MUIP $d_{O\cdots O}$ 2.594(2) Å and DMUIP $d_{O\cdots O}$ 2.508(1) Å), than in their respective nitro substituted molecular complexes of U5-NIP, MU5-NIP and DMU5-NIP ($d_{O\cdots O}$ U5-NIP 2.470(1) Å, MUIP $d_{O\cdots O}$ 2.490(1) Å and DMUIP $d_{O\cdots O}$ 2.434(2) to 2.482(2) Å). For the molecular complexes of the haloanilic acids with the set 2 basic components, the SSHB length also appear to be tuneable by acid substitution with increasingly electronegative substituent, again leading to enhanced acidity; in general shorter charge assisted N^+—H···O^- hydrogen bonds form in the bromo substituted molecular complexes than the chloro substituted such as when in complex with 4-acetylpyridine (4-APBrA $d_{N^+\cdots O^-}$ 2.658(5) to 2.793(5) Å and 4-APClA 2.674(3) to 2.793(3) Å) and with 3,5-dimethylpyrazole (3,5-DMPYBrA hydrate $d_{N^+\cdots O^-}$ 2.621(1) Å and 3,5-DMPYClA hydrate 2.700(1) Å). The shortest of the SSHBs formed between substituted urea or *N*-heterocycle basic components may therefore be accessible where organic acids are substituted with increasingly electron withdrawing species.

The *ortho* substitution of the benzene carboxylic acids also leads to shorter donor-acceptor distances. This might be expected where *ortho* substituted benzoic acids are more acidic and better

hydrogen bond donors than those that are *meta* or *para* substituted; attributed to the steric hinderance which forces the carboxylic acid group to twist out of co-planarity with the benzene ring. [295] This prevents conjugative electron donation of the acid group with the benzene ring and increases acidity; conjugation with the benzene ring destabilises the conjugate base thereby reducing acidity. For example, shorter O—H···O SSHBs are formed in DMUP ($d_{O\cdots O}$ 2.452(2) and 2.452(2) Å) than in DMUIP ($d_{O\cdots O}$ 2.508(2) Å) and in MUP ($d_{O\cdots O}$ 2.558(1) to 2.591(2) Å) than in MUIP ($d_{O\cdots O}$ 2.594(2) to 2.674(2) Å). Targeting *ortho* substituted organic acids therefore appears favourable for accessing the shortest of the O—H···O SSHBs in substituted urea benzene carboxylic acid molecular complexes.

6.5.3 Crystal packing effects on SSHB formation

In some of the molecular complexes, SSHBs are formed in identical hydrogen bonding motifs between the same molecular components with varying donor-acceptor distances. In these instances, the SSHBs are free from electronic effects and so the variations must be a result of changes to the crystal packing. The differences in SSHB distances are rationalised in the crystal packing in molecular complexes of IN2,4-DNBA I to III and in DMU3-CBA in which identical hydrogen bonding motifs are formed for each complex with the same ΔpK_a values but where there is variation in the SSHB distances.

IN2,4-DNBA I to III

Across the three IN2,4-DNBA I, II and III molecular complexes, the charge assisted N^+—H···O^- hydrogen bonds vary in length in the same pyridine:carboxylic acid $R_2^2(7)$ hydrogen bond synthons between the same pair of IN and 2,4-DNBA molecules (IN2,4-DNBA I $d_{N^+\cdots O^-}$ 2.596(2) Å, IN2,4-DNBA II SSHB1 $d_{N^+\cdots O^-}$ 2.555(1) Å and SSHB2 2.636(1) Å and IN2,4-DNBA III $d_{N^+\cdots O^-}$ 2.599(2) Å). The crystal packing of the local environment of the pyridine:carboxylic acid $R_2^2(7)$ hydrogen bond synthons varies (Figure 6.20).

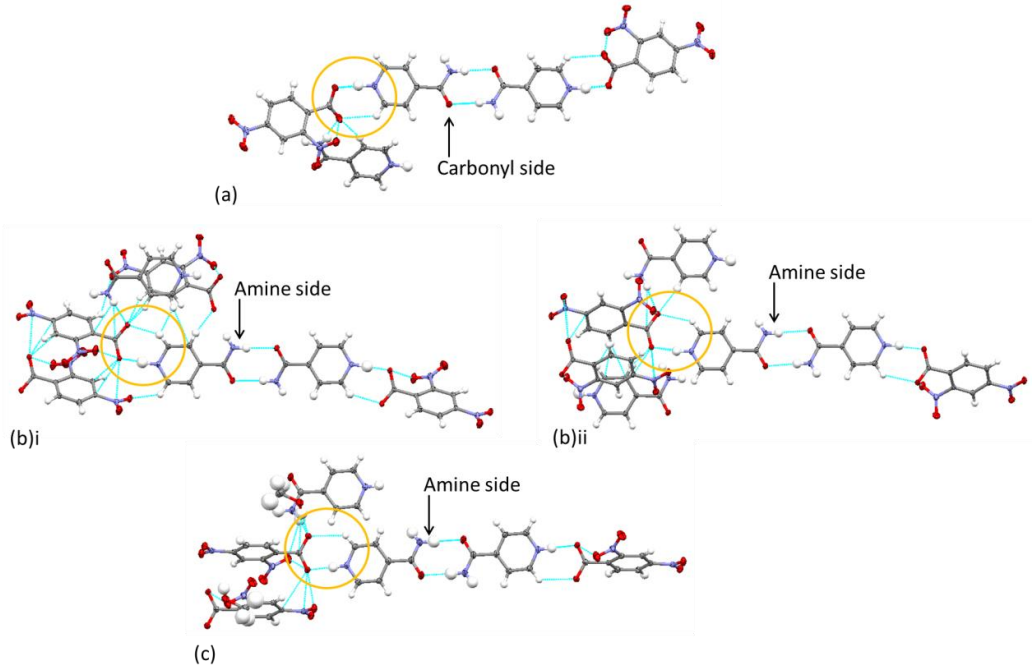

Figure 6.20 The crystal packing of the pyridine:carboxylic $\boldsymbol{R_2^2(7)}$ hydrogen bond synthons (circled) in the molecular complexes (a) IN2,4-DNBA I, (b) IN2,4-DNBA II and (c) IN2,4-DNBA III.

Variations in the crystal packing of each SSHB includes the side of the IN to which the pyridine:carboxylic acid $R_2^2(7)$ hydrogen bond synthon forms. This occurs on the amine side of the IN molecule in IN2,4-DNBA II and IN2,4-DNBA III whilst it occurs on the carbonyl side in IN2,4-DNBA I. The orientation of the 2,4-DNBA molecule forming the pyridine:carboxylic acid $R_2^2(7)$ hydrogen bond synthon form also varies, indicated by the location of the nitro group at the 2-position relative to the IN amide group (Figure 6.21). For one orientation of 2,4-DNBA, the nitro group at the 2-position is pointing in a similar direction to the IN amide carbonyl; the charge assisted N^+—H···O^- hydrogen bonds are shorter in this case including in IN2,4-DNBA I, IN2,4-DNBA II (SSHB1) and IN2,4-DNBA III. For the second orientation of 2,4-DNBA, the nitro group at the 2-position is pointing in a similar direction to the IN amide amine group; in this instance the charge assisted N^+—H···O^- hydrogen bond is longer, occurring in IN2,4-DNBA II (SSHB2).

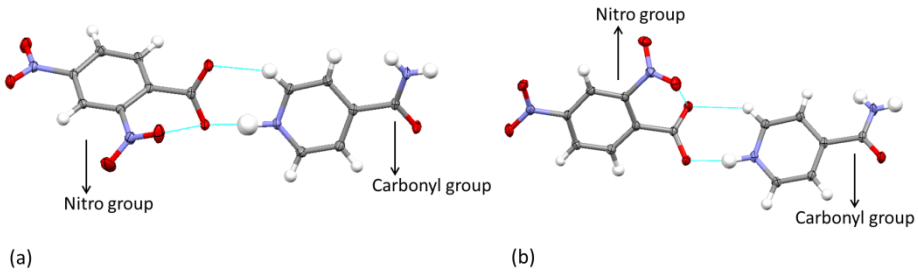

Figure 6.21 The orientation of the 2,4-DNBA 2-position nitro group relative to the IN carbonyl in the IN2,4-DNBA molecular complexes: (a) the nitro and carbonyl groups are oriented towards the same side and (b) the nitro and carbonyl groups are oriented to opposite sides.

The interactions of the nitro group at the 2-position on the 2,4-DNBA with the carboxylate group in the pyridine:carboxylic acid $R_2^2(7)$ hydrogen bond synthon also varies across the different forms where the SSHB distances vary. In IN2,4-DNBA I and IN2,4-DNBA II (SSHB2), the nitro interaction with the carboxylate group involves the oxygen forming the weak C—H···O interaction ($d_{O\cdots O}$ 2.849(2) and 2.972(2) Å, respectively) whilst in IN2,4-DNBA II (SSHB1) and in IN2,4-DNBA III they involve the oxygen forming the charge assisted N^+—H···O^- hydrogen bond ($d_{O\cdots O}$ 2.937(2) and 2.924(2) Å, respectively). Weak interactions in the local environment of the charge assisted N^+—H···O^- hydrogen bond also vary as the SSHB donor-acceptor distance varies. In IN2,4-DNBA I there are none formed directly to the SSHB, π-contacts form to the carboxylate end of the SSHB in IN2,4-DNBA II SSHB1 (including $d_{\pi\cdots\pi}$ 2.943(1) to 3.180(1) Å) and IN2,4-DNBA III ($d_{\pi\cdots\pi}$ 2.753(2) to 3.170(2) Å) whilst π-contacts ($d_{\pi\cdots\pi}$ 2.756(2) to 3.061(2) Å) and a weak C—H···O hydrogen bond ($d_{C\cdots O}$ 3.409(2) Å) form to the carboxylate end in IN2,4-DNBA II SSHB2. There does not appear to be any obvious correlation of these interactions with SSHB length.

In the crystal packing of each IN2,4-DNBA molecular complex there are also molecular structural variations. The angle between the planes of 2,4-DNBA carboxylate group and pyridine ring forming the pyridine:carboxylic acid $R_2^2(7)$ hydrogen bond synthon and the torsion angles of the nitro groups of 2,4-DNBA molecules vary; there does not appear to be any correlation in these variations with SSHB length (Table 6.12).

Table 6.12 Structural parameters in IN2,4-DNBA I, II and III.

Complex	Angle between planes of 2,4-DNBA carboxylate group and pyridine ring (°)	Torsion angle of nitro group at 2-position to 2,4-DNBA aromatic ring (°)	Torsion angle of nitro group at 4-position to 2,4-DNBA aromatic ring (°)
IN2,4-DNBA I	35.48	41.2(4)	13.2(2)
IN2,4-DNBA II (SSHB1 $d_{N+\cdots O-}$ 2.555(1) Å)	9.19	60.9(2)	13.3(2)
IN2,4-DNBA II SSHB2 ($d_{N+\cdots O-}$ 2.636(1) Å)	22.41	-49.5(2)	-5.8(2)
IN2,4-DNBA III	2.22	-68.5(2)	-8.6(2)

The pyridine:carboxylic acid $R_2^2(7)$ hydrogen bond synthon connects to the next *via* an amide:amide $R_2^2(8)$ hydrogen bond synthon. The N—H···O hydrogen bond distances in the

amide:amide $R_2^2(8)$ hydrogen bond synthon are shorter where the charge assisted N^+—H···O^- hydrogen bonds in the pyridine:carboxylic acid $R_2^2(7)$ hydrogen bond synthon are shorter and *vice versa* (Table 6.13). Here there appears to be some correlation evident between the crystal packing and the SSHB distances.

Table 6.13 Hydrogen bond lengths in the pyridine:carboxylic acid $\boldsymbol{R_2^2(7)}$ and amide:amide $\boldsymbol{R_2^2(8)}$ hydrogen bond synthons in the IN2,4-DNBA molecular complexes.

Complex	$dN^+\cdots O^-$ (Å) (pyridine:acid $R_2^2(7)$ synthon)	dN···O (Å) (amide:amide $R_2^2(8)$ synthon)
IN2,4-DNBA I	2.596(2)	2.845(2)
IN2,4-DNBA II ($d_{N+\cdots O-}$ 2.555(1) Å)	2.555(1)	2.864(1)
IN2,4-DNBA II ($d_{N+\cdots O-}$ 2.636(1) Å)	2.636(1)	2.949(1)
IN2,4-DNBA III	2.599(2)	2.862(2)

In summary, across the three molecular complexes of IN2,4-DNBA, variations in the donor-acceptor distances of the charge assisted N^+—H···O^- hydrogen bonds may be rationalised by variations in the crystal packing and in some cases it is possible to correlate the two effects.

DMU3-CBA

In the crystal structure of DMU3-CBA, two symmetry-independent units containing identical hydrogen bonded U:Ac motifs between the same two components are present. In each of the U:Ac motifs, the O—H···O SSHB donor-acceptor distance varies (U:Ac1 SSHB $d_{O\cdots O}$ 2.472(2) Å and U:Ac2 SSHB $d_{O\cdots O}$ 2.481(2) Å). The differences in lengths occur alongside interesting variations in crystal packing (Figure 6.22).

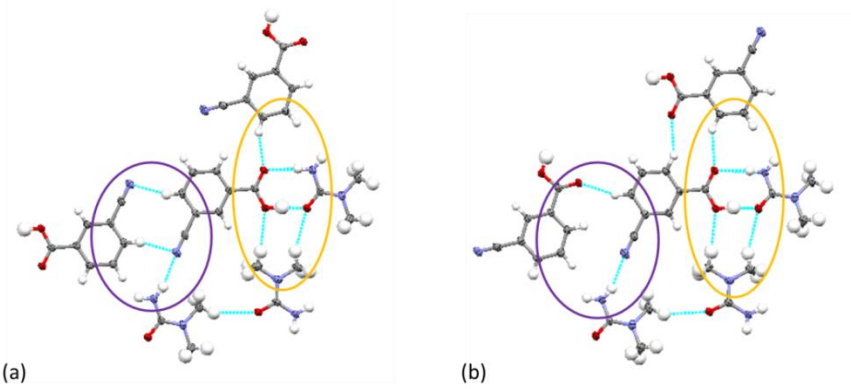

Figure 6.22 The crystal packing of the U:Ac motifs in DMU3-CBA (a) in U:Ac1 ($d_{O\cdots O}$ 2.472(2) Å) and (b) U:Ac2 ($d_{O\cdots O}$ 2.481(2) Å). The weak interactions formed to the U:Ac $\boldsymbol{R_2^2(8)}$ hydrogen bond synthon are circled in orange whilst those formed between the rest of the 3-CBA molecule and the local environment are circle in purple.

Variations in the crystal packing to the carboxylic acid:amide $R_2^2(8)$ hydrogen bond synthon occur between U:Ac1 and U:Ac2. Weak C—H···O hydrogen bonds form to either end of the O—H···O SSHB in both the U:Ac1 and U:A2 motifs with differing interaction strengths (U:Ac1 $d_{C\cdots Oacid}$ 3.493(3) Å and $d_{C\cdots Ourea}$ 3.552(3) Å and U:Ac2 $d_{C\cdots Oacid}$ 3.478(3) Å and $d_{C\cdots Ourea}$ 3.569(3) Å). The shorter O—H···O SSHB in U:Ac1 occurs where the weak C—H···O hydrogen bond to the acid end of the SSHB is shorter and the weak C—H···O hydrogen bond to the urea end is longer. In the crystal packing, a weak C—H···O hydrogen bond also forms to the 3-CBA carbonyl group of each U:Ac motif. The interactions are of different lengths (U:Ac1 $d_{C\cdots O}$ 3.275(2) Å and U:Ac2 $d_{C\cdots O}$ 3.464(3) Å) and the nature of the C—H forming the interaction also differs between the two motifs; in U:Ac1 the C—H is *ortho* to a cyano group and donated by a symmetry independent 3-CBA molecule whilst in U:Ac2, the C—H is *para* to a cyano group and is from a symmetry equivalent 3-CBA molecule. The C—H bond which is *ortho* to a cyano group in U:Ac1 is increasingly polarised, resulting in a shorter interaction distance than formed to U:Ac2 which experiences less polarisation in the *para* position.

The 3-CBA molecule also forms a different weak interaction with the surrounding environment *via* the C—H group at the 4-position to the carboxylic acid group. In U:Ac1, the C—H group forms a weak C—H···N hydrogen bond with a neighbouring nitrile group ($d_{C\cdots N}$ 3.558(3) Å) whilst in U:Ac2, the C—H groups forms a weak C—H···O bond to a neighbouring carboxylic acid group ($d_{C\cdots O}$ 3.275(2) Å). The interaction distances of the nitrile groups with a neighbouring amine in each U:Ac motif differs (U:Ac1 $d_{N\cdots N}$ 3.103(3) Å) and U:Ac2 $d_{N\cdots N}$ 3.146(3) Å). In general, where the weaker interactions involving the rest of the 3-CBA molecule in each U:Ac motif and the local environment are shorter, as in U:Ac1, the O—H···O SSHB is shorter. Between the two U:Ac motifs, there are variations in the crystal packing alongside variations in the length of the O—H···O SSHB and in some cases the two are effects may be correlated.

In summary, between the two U:Ac motifs in DMU3-CBA, variations in the donor-acceptor distances of the charge assisted O—H···O hydrogen bonds may be rationalised by variations in the crystal packing.

6.6 Conclusions

In this chapter, the design of organic molecular complexes containing O—H···O and N^+—H···O^- SSHBs for potential proton migration studies has been attempted.

Forty-four molecular complexes were synthesised from the combination of the benzene carboxylic acids with the set 1 basic components for the formation of O—H···O SSHBs and from the combination of organic acids with the set 2 basic components for the formation of charge assisted N^+—H···O^- SSHBs. From these forty-four molecular complexes, SSHBs were formed in twenty-seven whilst six of these had SSHBs with donor-acceptor distances below or near the proposed limits for proton migration; complexes DMU2,4-DNBA DMUP, 3-DAZA2,4-DNBA, DMU5-NIP and 3-DAZABrA hydrate, INP and IN2,4-DNBA II are thus recommended for variable temperature synchrotron X-ray diffraction proton migration studies. The strategies implemented in the design of SSHBs in this research project can therefore be considered relatively successful, where a large number have formed in the engineered molecular complexes. Only a small number of these are near the proposed limits for proton migration indicating that the design of SSHBs with potential proton migration behaviour remains a challenge and further development of crystal engineering strategies are required.

Despite the relative lack of success in accessing potential proton migration materials, the crystal engineering studies aid in identifying where they might be targeted in the future as well as revealing insight into molecular aggregation. In terms of component selection, the combination of substituted ureas and benzene carboxylic acids is recommended giving a greater predictability for O—H···O SSHB formation than the combination of 3-deazuracil with the organic acids, where the carboxylic acid:amide $R_2^2(8)$ synthon was found to be robust in governing molecular assembly and successful in the design of SSHBs. The combination of six-membered *N*-heterocycles with benzene carboxylic acids was the better approach for accessing charge assisted N^+—H···O^- SSHBs, frequently formed in a pyridine:carboxylic acid $R_2^2(7)$ hydrogen bond synthon, compared with the combination of *N*-heterocycles with the haloanilic acids. In the latter a bifurcated hydrogen bonding motif persisted within which the N^+—H···O^- SSHBs were generally weaker; this was a consequence of the arrangement of the acid groups and indicates molecular geometry is

an important consideration in these studies. Relatively few investigations of the six-membered *N*-heterocycles with benzene carboxylic acids were carried out and so more crystallisation trials are recommended; in particular the isonicotinamide co-former appears to be a good target for the formation of the shorter N^+—H···O^- SSHBs.

In terms of the acidity and basicity of molecular components, there did not appear to be a strong correlation between ΔpK_a and SSHB donor-acceptor distances; in some cases the shortest SSHBs were formed where ΔpK_a approached zero, as observed in the literature, however a range of SSHB distances were also formed for a single ΔpK_a value. This emphasises the problems of transferring pK_a values, determined under solution conditions, to the solid state and indicates their better use as a guide in these studies. The values of ΔpK_a may be useful in future strategies where there was mostly agreement with the predicted salt/co-crystal outcome and where the shortest of the hydrogen bonds were formed where an extent of proton transfer had occurred such as in DMU2,4-DNBA and 3-DAZABrA hydrate. Targeting charge transfer species is therefore a recommended strategy to implement in the design of SSHBs and can be achieved by targeting certain ΔpK_a values where salt formation is expected. In the complexes studied here, in preference to using ΔpK_a values, the consideration of the acidity or basicity of molecular components in terms of substituents proved to be more reliable way to access SSHBs. Certain substituents were favourable for SSHB formation; shorter O—H···O hydrogen bonds were formed where the ureas were increasingly substituted with electron donating groups, and more basic, whilst electron withdrawing substituents and substituents *ortho* to a carboxylic acid group, increasing acidity, in the benzene carboxylic acids led to shorter O—H···O and N^+—H···O^- hydrogen bonds being formed. The targeting of these types of co-formers is recommended in future SSHB design strategies.

Predictability in the resulting hydrogen bonding motifs formed was revealed between particular molecular components which, in some cases, were also relatable to molecular stoichiometry or protonation state. This was seen in the substituted urea organic acid molecular complexes, forming U:Ac, U:Ac:U and Ac:U:Ac motifs related to molecular stoichiometry, and in the *N*-heterocycle anilic acid molecular complexes, forming N:Ac:Ac:N and N:Ac:N or W:Ac:W motifs related to protonation state. This reoccurrence of motifs aids in the determining the likely aggregation of molecular components in future molecular complexes as well as the robust nature of certain hydrogen bonding synthons in the solid state.

By exploring the situation in which the SSHBs were present, crystal packing was also shown to tune the nature of SSHBs; this was observed from the study of DMU3-CBA and the different

forms of IN2,4-DNBA (I to III) where molecular orientation and weak intermolecular interactions appeared to influence SSHB donor-acceptor distances.

This study into the design of SSHBs for potential proton migration studies reveals insight into crystal engineering strategies to favour their formation as well as the different variables that may tune the SSHB strength in the solid state. These observations are important as they aid in accessing SSHBs more predictably in the future such that the studies of proton migration in the solid state may be added to, allowing the understanding of the manifestation of these properties in the solid state.

Chapter 7.

X-ray diffraction and synchrotron studies of proton migration across short strong hydrogen bonds (SSHBs)

Chapter 7 investigates the proton transfer process of proton migration across SSHBs, and its manifestation in the solid state, using a combination of variable temperature laboratory and synchrotron X-ray diffraction data and analysed by a combination of refinement techniques.

7.1 Introduction and aims

There are relatively few examples of temperature dependent proton migration (§1.3.2) across SSHBs reported in the literature and, where its study may reveal information about hydrogen bonding and proton transfer behaviour, it is beneficial to identify further systems. The manifestation of proton migration is, however, difficult to predict in materials. Certain combinations of molecular building blocks have repeatedly led to the formation of proton migration materials including the combination of substituted ureas and organic acids [108, 109] or the combination of six membered *N*-heterocycles with organic acids. [111] Proton migration has also only been observed across SSHBs with certain donor-acceptor distances; for O—H···O SSHBs where the O···O distance is less than 2.45 Å [108, 109] and for N^{+}—H···O^{-} SSHBs, where the N···O distance is less than 2.55 Å. [110-112, 267, 296] The extent of proton migration across an SSHB has also been rationalised on considering the ΔpK_a values of components forming the SSHB [109] or the crystal packing. [112, 297] Temperature dependent proton migration has been followed previously using single crystal X-ray laboratory and neutron diffraction methods; single crystal neutron diffraction remains the method of choice due to the possibility for accurate location of the hydrogen atom. There has, as yet, been no investigation into using X-rays from synchrotron sources in the study of proton migration.

In this chapter, temperature dependent proton migration is studied in the molecular complexes engineered in Chapter 6, where possible, by variable temperature X-ray diffraction methods with the aim of aiding the understanding of this process in the solid state. The technique of synchrotron X-ray diffraction is trialled in the study of proton migration in the most promising of these potential proton migration materials with the aim of investigating this technique in observing the finer points of the proton transfer process.

In the study of the temperature dependent proton migration using the synchrotron technique, two refinement methods are used. These include the traditional method of stepwise refinement in SHELXL, [219] for individual temperature steps (§7.3). A parametric structure refinement method (§2.4.4) in Topas-Academic V5 [168] is also trialled to probe evolving hydrogen atom positions as a function of temperature (§7.4). This method allows the evolving position of the migrating hydrogen atom to be refined as a function of temperature simultaneously over a range of data sets. This refinement method offers the potential for enhanced accuracy of parameters compared to individual structure refinement for each data set, while also saving time where large numbers of data sets are collected over a given temperature range. This approach has been implemented previously for variable temperature powder data and allowed quality structural information on the evolving hydrogen atom positions to be obtained. [172] As yet, no equivalent study has been carried out using variable temperature single crystal synchrotron X-ray diffraction data.

Two data collection approaches are also implemented related to the temperature ramping including (i) collecting data at each temperature with stepwise temperature ramping (STEP) and (ii) collecting data with a continuous ramping of temperature (CONT.). The continuous ramping method allows evolving hydrogen atom position information to be accessed along the temperature profile and is made possible by the use of the synchrotron X-ray source.

7.2 Experimental details

7.2.1 Preparation and crystallographic analysis

The molecular complexes featured in this chapter are summarised in Table 7.1. The full details of their preparation are included in §A6.1 and §A7.1.

Table 7.1 The molecular complexes studied using variable temperature synchrotron and X-ray diffraction methods.

Molecular complex	Code
N,*N*-dimethylurea and 2-nitrobenzoic acid 1:1	DMU2-NBA
N,*N*-dimethylurea and 3-nitrobenzoic acid 1:1	DMU3-NBA
N,*N*-dimethylurea and 3-cyanobenzoic acid 1:1	DMU3-CBA
N,*N*-dimethylurea and 4-cyanobenzoic acid 1:1	DMU4-CBA
N,*N*-dimethylurea and 2,4-dinitrobenzoic acid 1:1	DMU2,4-DNBA
N,*N*-dimethylurea and 3,5-dinitrobenzoic acid 1:1	DMU3,5-DNBA
Urea and isophthalic acid 1:1	UIP
N-methylurea and phthalic acid 1:1	MUP
N-methylurea and isophthalic acid 1:1	MUIP
N,*N*-dimethylurea and phthalic acid 2:1	DMUP
N,*N*-dimethylurea and isophthalic acid 2:1	DMUIP
N,*N*-dimethylurea and 5-aminoisophthalic acid 2:1	DMU5-AIP
N,*N*-dimethylurea and 3-nitrophthalic acid 1:1	DMU3-NP
N,*N*-dimethylurea and 5-nitroisophthalic acid 4:2	DMU5-NIP
N-phenylurea and 2,4-dinitrobenzoic acid 1:1	PhU2,4-DNBA
N-phenylurea and 3-nitrophthalic acid 2:2	PhU3-NP
3-deazauracil and 3-nitrophthalic acid 2:1	3-DAZA3-NP
3-deazauracil and 2,4-dinitrobenzoic acid 1:1	3-DAZA2,4-DNBA
3-deazauracil, bromanilic acid and water 2:1:2	3-DAZABrA hydrate
isonicotinamide phthalic acid 2:2	INP
isonicotinamide 2,4-dinitrobenzoic acid 1:1	IN2,4-DNBA I
isonicotinamide 2,4-dinitrobenzoic acid 1:1	IN2,4-DNBA II
isonicotinamide 2,4-dinitrobenzoic acid methanol solvate 1:2:1	IN2,4-DNBA III
isoniazid 2,4-dinitrobenzoic acid 1:1	INZ2,4-DNBA
isoniazid phthalic acid 1:1	INZP

Crystallographic analysis was carried out on the molecular complexes using variable synchrotron and X-ray diffraction methods.

Synchrotron X-ray diffraction measurements for single crystal refinement in SHELXL

Single crystal X-ray diffraction data were collected on molecular complexes DMU2,4-DNBA, DMU3,5-DNBA, INP and IN2,4-DNBA II on beamline 11.3.1 at the Advanced Light Source, U.S.A. [2] using Si (111) monochromated radiation at $\lambda = 0.8856$ Å on a Bruker AXS [214] D8 three-circle diffractometer equipped with a Bruker AXS [214] PHOTON 100 CMOS detector between 100 and 350 K, in 50 K steps. The sample temperature was controlled using an Oxford Cryosystems [229]

Cryostream Plus. The data were collected using Bruker AXS [214] APEX2 [215] and processed using Bruker AXS [214] APEX2 [215] and SADABS-2014/15 softwares. [216]

Single crystal diffraction data were collected on molecular complex DMUP on beamline 11.3.1 at the Advanced Light Source, U.S.A. [2] using Si (111) monochromated radiation at $\lambda = 0.7749$ Å on a Bruker AXS [214] D8 three-circle diffractometer equipped with a Bruker AXS [214] Apex2 CCD detector between 100 and 300 K, in 100 K steps. The sample temperature was controlled using an Oxford Cryosystems [229] Cryostream Plus. The data were collected and processed using Bruker AXS [214] APEX2 [215] software and processed using Bruker AXS [214] APEX2 [215] and SADABS-2014/2 softwares. [216]

All structures were solved using SHELXS-2013 [218] and refined using SHELXL-2013 [219] within the WinGX package. [221] Crystallographic data are given in Table 7.2 to Table 7.6.

Refinement details

The refinement details include the treatment of the SSHB hydrogen atom in each molecular complex, during structure solution and refinement. Two refinement models were employed. In both models, the hydrogen atoms were located based on Fourier difference maps. Model 1 involved the hydrogen atom position and isotropic thermal parameter being refined freely. Model 2 involved the hydrogen atom position being refined freely but the isotropic thermal parameter being constrained to 1.5 times that of the atom to which it is bonded.

Laboratory X-ray diffraction measurements for single crystal refinement in SHELXL

For molecular complexes UIP, MU, MUIP, DMU2-NBA, DMU3-NBA, DMU3-CBA, DMU4-CBA, DMU5-NIP, DMU5-AIP, DMU3-NP, DMUIP, PhU2,4-DNBA, PhU3-NP, 3-DAZA3-NP, 3-DAZA2,4-DNBA, INZ2,4-DNBA, INZP, IN2,4-DNBA I and IN2,4-DNBA III the single crystal diffraction data collection, processing, solution and general refinement details are included in §A6.2.

Refinement details

The refinement details include the treatment of the SSHB hydrogen atom in each molecular complex. A single refinement model was employed and involved the location of the SSHB hydrogen atom based on Fourier difference maps and the hydrogen atom position and isotropic thermal parameter being refined freely.

Synchrotron X-ray diffraction measurements for single crystal parametric refinement in Topas-Academic V5.0

Single crystal X-ray diffraction data were collected on single crystals of the molecular complex BZN4-OHBA *via* two temperature ramping methods (step and continuous). The step method (BZN4-OHBA STEP) involved the collection of single crystal variable temperature X-ray diffraction data in a step-wise temperature ramping approach collecting hemispheres in 20 K temperature steps, between 100 and 300 K. The continuous method (BZN4-OHBA CONT.) involved the continuous collection of hemispheres of data with a continuous ramping of temperature (120K hr^{-1}). A single average temperature was determined for each data set from experimental log files. In both the STEP and CONT. method, the single crystal diffraction data were collected in EH1 on I19 at the Diamond Light Source, U.K. [1] using Si (111) monochromated radiation at $\lambda = 0.6889$ Å on a Crystal Logic [232] four-circle κ geometry diffractometer equipped with a Rigaku [208] Saturn 724+ CCD detector. The sample temperature was controlled using an Oxford Cryosystems [229] Cryostream Plus. All data were collected using Rigaku [208] CrystalClear™ [209] software. Each temperature data set was processed using Rigaku Oxford Diffraction [210] CrysAlisPro [211] version 1.171.37.31 software. Structures were solved for the 100 and 290 K using SHELXS-2013 [218] and refined using SHELXL-2013 [219] within the WinGX package. [221]

Single crystal diffraction data were collected on single crystals of the molecular complex of DMU2,4-DNBA in EH1 on I19 at the Diamond Light Source, U.K. [1] using Si (111) monochromated radiation at $\lambda = 0.6889$ Å on a Fluid Film Devices Ltd. [233] three-circle diffractometer in fixed χ geometry equipped with a DECTRIS [234] Pilatus 2M detector collected *via* a step wise temperature ramping approach collecting in 10 K temperature steps, between 100 and 350 K. The sample temperature was controlled using an Oxford Cryosystems [229] Cryostream Plus. The data were collected through the in-house Generic Data Acquisition [235] (GDA) software and processed using the in-house software DIALS [212] in Xia2. [213] Structures were solved at 100 and 287 K using SHELXS-2013 [218] and refined using SHELXL-2013 [219] within the WinGX package. [221]

Crystallographic data are given in Table 7.7.

SHELXL refinement details

The refinement details include the treatment of the SSHB hydrogen atom in each molecular complex. A single refinement model was employed and involved the location of the SSHB hydrogen atom based on Fourier difference maps and the hydrogen atom position and isotropic thermal parameter being refined freely.

Topas-Academic V5.0 refinement details

The 100 K and approaching room temperature structures, obtained from the crystal structure solution and refinement in SHELXL-2013, [218] were refined in Topas-Academic V5.0 [168] against single and multiple diffraction data sets. The details of the refinement are included in §7.4.

Table 7.2 Crystallographic data for *N,N*-dimethylurea 2,4-dinitrobenzoic acid (DMU2,4-DNBA) (1:1) for variable temperature analysis on beamline 11.3.1 at the Advanced Light Source, U.S.A. [2]

Compound	DMU2,4-DNBA											
Diffractometer	Bruker AXS D8		Bruker AXS D8		Bruker AXS D8		Bruker AXS D8		Bruker AXS D8		Bruker AXS D8	
Wavelength (Å)	0.8856		0.8856		0.8856		0.8856		0.8856		0.8856	
Formula	$C_{10}H_{12}N_4O_7$		$C_{10}H_{12}N_4O_7$		$C_{10}H_{12}N_4O_7$		$C_{10}H_{12}N_4O_7$		$C_{10}H_{12}N_4O_7$		$C_{10}H_{12}N_4O_7$	
Mol. W ($gmol^{-1}$)	300.24		300.24		300.24		300.24		300.24		300.24	
T (K)	100		150		200		250		300		350	
Space group	Pbca		Pbca		Pbca		Pbca		Pbca		Pbca	
a (Å)	19.1778(10)		19.2246(11)		19.2605(9)		19.3010(8)		19.3399(8)		19.3762(14)	
b (Å)	5.8056(3)		5.8355(3)		5.8640(3)		5.8965(3)		5.9352(3)		5.9815(5)	
c (Å)	22.9749(11)		23.0024(12)		23.0318(11)		23.0621(10)		23.1175(10)		23.1959(16)	
α (°)	90		90		90		90		90		90	
β (°)	90		90		90		90		90		90	
γ (°)	90		90		90		90		90		90	
Volume ($Å^3$)	2558.0(2)		2580.5(2)		2601.3(2)		2624.7(2)		2653.6(2)		2688.4(4)	
Z	8		8		8		8		8		8	
ρ_{calc} ($g\ cm^{-3}$)	1.559		1.546		1.533		1.520		1.503		1.484	
μ (mm^{-1})	0.185		0.183		0.182		0.180		0.178		0.176	
Θ range (°)	2.209-39.231		2.206-39.256		2.204-39.283		2.201-39.278		2.195-39.280		2.188-39.267	
Reflections collected	40540		40003		41342		41174		42427		42048	
Independent	3906		3946		3981		4024		4070		4115	
Observed I>2σ	3208		3396		3250		3229		2864		2507	
R_{int}	0.0521		0.037		0.0556		0.033		0.0598		0.0396	
Completeness (%)	100.0		100.0		100.0		100.0		100.0		100.0	
Refinement model	1	2	1	2	1	2	1	2	1	2	1	2
Parameters	238	237	238	237	238	237	216	215	216	215	216	215
GooF	1.021	1.02	1.062	1.046	1.045	1.028	1.049	1.049	1.042	1.042	1.022	1.024
R_1 (observed)	0.039	0.039	0.0367	0.0367	0.0378	0.0378	0.0432	0.0432	0.0459	0.0459	0.0504	0.0504
R_1 (all)	0.0513	0.0513	0.0434	0.0435	0.0488	0.0488	0.0556	0.0556	0.0712	0.0712	0.0846	0.0847
wR_2 (all)	0.1051	0.105	0.1074	0.107	0.1105	0.1096	0.1256	0.1256	0.1362	0.1363	0.1539	0.1544
Δρ (max, min) ($e\ Å^{-3}$)	0.438, -0.293	0.439, -0.292	0.337, -0.245	0.339, -0.244	0.307, -0.235	0.306, -0.236	0.279, -0.234	0.279, -0.234	0.257, -0.211	0.257, -0.211	0.166, -0.205	0.166, -0.204

Table 7.3 Crystallographic data for *N*,*N*-dimethylurea 3,5-dinitrobenzoic acid (DMU3,5-DNBA) (1:1)) for variable temperature analysis on beamline 11.3.1 at the Advanced Light Source, U.S.A. [2]

Diffractometer	Bruker AXS D8				
Wavelength (Å)	0.8856	0.8856	0.8856	0.8856	0.8856
Formula	$C_{10}H_{12}N_4O_7$	$C_{10}H_{12}N_4O_7$	$C_{10}H_{12}N_4O_7$	$C_{10}H_{12}N_4O_7$	$C_{10}H_{12}N_4O_7$
Mol. W ($gmol^{-1}$)	300.24	300.24	300.24	300.24	300.24
T (K)	100	150	200	250	300
Space group	$P2_1$	$P2_1$	$P2_1$	$P2_1$	$P2_1$
a (Å)	7.4294(12)	7.4489(4)	7.4809(4)	7.5148(4)	7.5472(4)
b (Å)	11.3708(16)	11.3580(5)	11.3782(6)	11.4035(6)	11.4263(6)
c (Å)	7.8921(13)	7.8905(4)	7.8926(4)	7.8999(5)	7.9220(5)
α (°)	90	90	90	90	90
β (°)	103.692(5)	103.064(3)	102.336(3)	101.508(4)	100.761(4)
γ (°)	90	90	90	90	90
Volume ($Å^3$)	647.76(18)	650.29(6)	656.30(6)	663.37(7)	671.15(7)
Z	2	2	2	2	2
ρ_{calc} ($g\ cm^{-3}$)	1.539	1.533	1.519	1.503	1.486
μ (mm^{-1})	0.182	0.182	0.180	0.178	0.176
Θ range (°)	3.311-34.588	3.303-34.576	3.292-34.586	3.279-34.587	3.262-34.587
Reflections collected	9400	9481	9572	9700	9814
Independent	2830	2845	2877	2910	2940
Observed I>2σ	2578	2545	2354	2116	1846
R_{int}	0.0257	0.0235	0.0231	0.0237	0.0254
Completeness (%)	100.0	99.9	100.0	100.0	100.0
Parameters	216	216	216	216	216
Flack parameter	-0.3(2)	0.0(2)	-0.02(2)	-0.4(3)	0.1(3)
GooF	1.056	1.052	1.06	1.044	0.997
R_1 (observed)	0.0341	0.0361	0.0401	0.042	0.0415
R_1 (all)	0.0391	0.0422	0.0535	0.0639	0.0755
wR_2 (all)	0.0869	0.0902	0.1009	0.1001	0.105
Δρ (max, min) ($e\ Å^{-3}$)	0.201, -0.252	0.215, -0.200	0.189, -0.176	0.150, -0.197	0.146, -0.165

Table 7.4 Crystallographic data for 3-deazauracil bromanilic acid hydrate (3-DAZABrA hydrate) (2:1:2) for variable temperature analysis on beamline 11.3.1 at the Advanced Light Source, U.S.A. [2]

Compound	3-DAZABrA hydrate	3-DAZABrA hydrate	3-DAZABrA hydrate	3-DAZABrA hydrate	3-DAZABrA hydrate	3-DAZABrA hydrate
Diffractometer	Bruker AXS D8	Bruker AXS D8	Bruker AXS D8	Bruker AXS D8	Bruker AXS D8	Bruker AXS D8
Wavelength (Å)	0.8856	0.8856	0.8856	0.8856	0.8856	0.8856
Formula	$C_{16}H_{16}Br_2N_2O_{10}$	$C_{16}H_{16}Br_2N_2O_{10}$	$C_{16}H_{16}Br_2N_2O_{10}$	$C_{16}H_{16}Br_2N_2O_{10}$	$C_{16}H_{16}Br_2N_2O_{10}$	$C_{16}H_{16}Br_2N_2O_{10}$
Mol. W ($gmol^{-1}$)	556.13	556.13	556.13	556.13	556.13	556.13
T (K)	100	150	200	250	300	350
Space group	$P2_1/n$	$P2_1/n$	$P2_1/n$	$P2_1/n$	$P2_1/n$	$P2_1/n$
a (Å)	11.3767(6)	11.4019(6)	11.4301(5)	11.4598(5)	11.4906(5)	11.5354(5)
b (Å)	3.8643(2)	3.8811(2)	3.8992(2)	3.9153(2)	3.9287(2)	3.9393(2)
c (Å)	21.9158(12)	21.9123(11)	21.9205(10)	21.9385(11)	21.9710(10)	22.0340(10)
α (°)	90	90	90	90	90	90
β (°)	103.776(3)	103.745(2)	103.742(2)	103.807(2)	103.882(2)	104.049(2)
γ (°)	90	90	90	90	90	90
Volume ($Å^3$)	935.77(9)	941.89(8)	948.99(8)	955.91(8)	962.87(8)	971.31(8)
Z	2	2	2	2	2	2
ρ_{calc} ($g\ cm^{-3}$)	1.974	1.961	1.946	1.932	1.918	1.902
μ (mm^{-1})	7.702	7.652	7.595	7.540	7.485	7.420
Θ range (°)	2.322-39.235	2.318-39.238	2.313-39.238	2.307-39.225	2.301-39.238	2.290-39.231
Reflections collected	14863	14921	15099	15222	15417	15503
Independent	2861	2880	2903	2926	2941	2960
Observed I>2σ	2639	2620	2616	2562	2439	2960
R_{int}	0.0319	0.0323	0.0321	0.0341	0.0351	0.038
Completeness (%)	99.9	99.8	99.9	99.9	99.8	99.9
Parameters	168	168	168	168	168	168
GooF	1.09	1.085	1.073	1.111	1.04	1.03
R_1 (observed)	0.0241	0.0236	0.0247	0.0314	0.0293	0.0354
R_1 (all)	0.0276	0.0277	0.0289	0.0377	0.0397	0.0518
wR_2 (all)	0.0538	0.0538	0.0289	0.0676	0.0397	0.0518
Δρ (max, min) ($e\ Å^{-3}$)	0.466, -0.470	0.426, -0.408	0.411, -0.421	0.380, -0.493	0.294, -0.414	0.312, -0.495

Table 7.5 Crystallographic data for isonicotinamide phthalic acid (INP) (2:1) for variable temperature analysis on beamline 11.3.1 at the Advanced Light Source, U.S.A. [2]

Compound	INP											
Diffractometer	Bruker AXS D8		Bruker AXS D8		Bruker AXS D8		Bruker AXS D8		Bruker AXS D8		Bruker AXS D8	
Wavelength (Å)	0.8856		0.8856		0.8856		0.8856		0.8856		0.8856	
Formula	$C_{20}H_{18}N_4O_6$		$C_{20}H_{18}N_4O_6$		$C_{20}H_{18}N_4O_6$		$C_{20}H_{18}N_4O_6$		$C_{20}H_{18}N_4O_6$		$C_{20}H_{18}N_4O_6$	
Mol. W ($gmol^{-1}$)	410.38		410.38		410.38		410.38		410.38		410.38	
T (K)	100		150		200		250		300		350	
Space group	$P2_1/n$		$P2_1/n$		$P2_1/n$		$P2_1/n$		$P2_1/n$		$P2_1/n$	
a (Å)	7.0511(3)		7.0860(3)		7.1268(3)		7.1735(3)		7.2266(3)		7.2885(3)	
b (Å)	14.3222(6)		14.3239(6)		14.3224(5)		14.3192(5)		14.3175(5)		14.3164(6)	
c (Å)	18.2948(8)		18.3115(7)		18.3280(7)		18.3504(7)		18.3775(7)		18.4118(7)	
α (°)	90		90		90		90		90		90	
β (°)	92.967(2)		92.8563(18)		92.7424(18)		92.6147(18)		92.5064(18)		92.412(2)	
γ (°)	90		90		90		90		90		90	
Volume ($Å^3$)	1845.07(14)		1856.29(13)		1868.65(12)		1882.97(13)		1899.64(13)		1919.48(13)	
Z	4		4		4		4		4		4	
ρ_{calc} ($g\ cm^{-3}$)	1.477		1.468		1.459		1.448		1.435		1.420	
μ (mm^{-1})	0.147		0.146		0.145		0.144		0.143		0.141	
Θ range (°)	2.251-34.588		2.250-34.586		2.250-34.585		2.249-34.589		2.248-34.586		2.246-34.584	
Reflections collected	24727		24631		25374		24863		24882		25469	
Independent	4062		4092		4120		4156		4191		4236	
Observed I>2σ	3657		3662		3625		3598		3473		3291	
R_{int}	0.0344		0.032		0.0357		0.0312		0.0316		0.0342	
Completeness (%)	99.9		99.9		99.9		99.9		99.9		99.9	
Refinement model	1	2	1	2	1	2	1	2	1	2	1	2
Parameters	343	342	343	342	343	342	343	342	343	342	343	342
GooF	1.044	1.037	1.052	1.039	1.059	1.055	1.039	1.045	1.028	1.024	1.031	1.032
R_1 (observed)	0.0328	0.033	0.0336	0.0339	0.0345	0.0349	0.0363	0.0365	0.0376	0.0379	0.0405	0.0407
R_1 (all)	0.0367	0.0369	0.038	0.0383	0.0393	0.0397	0.0426	0.0429	0.0466	0.0469	0.0543	0.0545
wR_2 (all)	0.0906	0.0897	0.0928	0.0932	0.0973	0.0975	0.1014	0.102	0.1059	0.1064	0.1137	0.1143
Δρ (max, min) ($e\ Å^{-3}$)	0.341, -0.254	0.340, -0.255	0.302, -0.248	0.302, -0.248	0.267, -0.225	0.268, -0.224	0.224, -0.218	0.225, -0.218	0.178, -0.212	0.179, -0.212	0.140, -0.207	0.139, -0.205

Table 7.6 Crystallographic data for isonicotinamide 2,4-dinitrobenzoic acid (IN2,4-DNBA II) (1:1) and *N,N*-dimethylurea phthalic acid (DMUP) (2:1) for variable temperature analysis on beamline 11.3.1 at the Advanced Light Source, U.S.A. [2]

Compound	IN2,4DNBA II						DMUP		
Diffractometer	Bruker AXS D8	Bruker AXS D8	Bruker AXS D8	Bruker AXS D8	Bruker AXS D8	Bruker AXS D8	Bruker AXS D8	Bruker AXS D8	Bruker AXS D8
Wavelength (Å)	0.8856	0.8856	0.8856	0.8856	0.8856	0.8856	0.7749	0.7749	0.7749
Formula	$C_{26}H_{20}N_8O_{14}$	$C_{26}H_{20}N_8O_{14}$	$C_{26}H_{20}N_8O_{14}$	$C_{26}H_{20}N_8O_{14}$	$C_{26}H_{20}N_8O_{14}$	$C_{26}H_{20}N_8O_{14}$	$C_{14}H_{22}N_4O_6$	$C_{14}H_{22}N_4O_6$	$C_{14}H_{22}N_4O_6$
Mol. W ($gmol^{-1}$)	668.5	668.5	668.5	668.5	668.5	668.5	342.35	342.35	342.35
T (K)	100	150	200	250	300	350	100	200	300
Space group	P-1	P-1	P-1	P-1	P-1	P-1	$P2_1/c$	$P2_1/c$	$P2_1/c$
a (Å)	9.6471(4)	9.6655(3)	9.6941(4)	9.7324(4)	9.7821(4)	9.8459(5)	7.8576(5)	7.9905(5)	8.1487(4)
b (Å)	10.2736(4)	10.3072(4)	10.3377(4)	10.3593(4)	10.3740(4)	10.3748(6)	6.4443(4)	6.4455(4)	6.4317(3)
c (Å)	15.2260(6)	15.2772(6)	15.3331(6)	15.3563(6)	15.3741(6)	15.3937(8)	32.5997(18)	32.7612(18)	32.9567(15)
α (°)	79.376(2)	79.0693(18)	78.857(2)	93.235(2)	93.299(2)	93.219(3)	90	90	90
β (°)	72.012(2)	71.8380(17)	71.6211(19)	108.243(2)	107.985(2)	107.645(3)	94.616(3)	95.375(3)	96.369(3)
γ (°)	77.366(2)	77.2644(18)	77.256(2)	102.696(2)	102.548(2)	102.294(3)	90	90	90
Volume ($Å^3$)	1389.40(10)	1398.52(9)	1409.54(10)	1421.30(10)	1435.37(10)	1451.76(14)	1645.39(17)	1679.87(17)	1716.60(14)
Z	2	2	2	2	2	2	4	4	4
ρ_{calc} ($g\ cm^{-3}$)	1.598	1.587	1.575	1.562	1.547	1.529	1.382	1.354	1.325
μ (mm^{-1})	0.181	0.180	0.178	0.177	0.175	0.173	0.107	0.105	0.103
Θ range (°)	2.522-34.589	2.546-34.580	2.540-34.585	2.535-34.585	2.529-34.089	2.525-33.607	2.734-30.207	2.723-30.209	2.713-30.210
Reflections collected	20471	20741	20869	20941	20575	20415	21844	21540	23262
Independent	6134	6169	6224	6276	6096	5936	3775	3874	3948
Observed I>2σ	5347	5095	5003	4559	4099	3398	2843	2767	2435
R_{int}	0.0417	0.0314	0.0317	0.0265	0.0275	0.033	0.0691	0.0777	0.0542
Completeness (%)	99.8	99.8	99.9	99.8	99.8	99.8	99.9	100.0	100.0
Parameters	513	513	513	513	513	513	305	267	269
GooF	1.029	1.035	1.021	1.022	1.025	1.011	1.03	1.016	1.025
R_1 (observed)	0.0359	0.0373	0.0398	0.0431	0.0463	0.0518	0.0443	0.0448	0.0542
R_1 (all)	0.0418	0.0476	0.0515	0.064	0.0753	0.1032	0.0652	0.0783	0.0955
wR_2 (all)	0.1015	0.1026	0.1116	0.12	0.1337	0.1499	0.1103	0.1194	0.1573
Δρ (max, min) ($e\ Å^{-3}$)	0.309, -0.297	0.291, -0.260	0.228, -0.281	0.182, -0.233	0.151, -0.231	0.167, -0.192	0.291, -0.265	0.235, -0.275	0.224, -0.246

Table 7.7 Crystallographic data for benzimidazole 4-hydroxybenzoic acid (4:2) (BZN4-OHBA STEP or CONT.) and *N,N*-dimethylurea 2,4-dinitrobenzoic acid (DMU2,4-DNBA) (1:1) for variable temperature analysis in EH1 on I19 at the Diamond Light Source, U.K. [1]

Compound	BZN4-OHBA STEP						BZN4-OHBA CONT	DMU2,4-DNBA	
Wavelength (Å)	0.6889	0.6889	0.6889	0.6889	0.6889	0.6889	0.6889	0.6889	0.6889
Formula	$C_{42}H_{36}N_8O_6$	$C_{42}H_{36}N_8O_6$	$C_{42}H_{36}N_8O_6$	$C_{42}H_{36}N_8O_6$	$C_{42}H_{36}N_8O_6$	$C_{42}H_{36}N_8O_6$	$C_{42}H_{36}N_8O_6$	$C_{10}H_{12}N_4O_7$	$C_{10}H_{12}N_4O_7$
Mol. W ($gmol^{-1}$)	748.79	748.79	748.79	748.79	748.79	748.79	748.79	300.24	300.24
T (K)	100	140	180	220	260	300	287	100	300
Space group	$P2_1/c$	$P2_1/c$	$P2_1/c$	$P2_1/c$	$P2_1/c$	$P2_1/c$	$P2_1/c$	Pbca	Pbca
a (Å)	15.2677(4)	15.2719(4)	15.3073(5)	15.3150(4)	15.3151(5)	15.3711(6)	15.3478(7)	22.9629(13)	23.2603(14)
b (Å)	12.0747(3)	12.0935(3)	12.1381(4)	12.1620(3)	12.1823(4)	12.2465(4)	12.2091(7)	19.168(4)	19.326(4)
c (Å)	20.6846(7)	20.6893(6)	20.7376(9)	20.7493(7)	20.7579(8)	20.8417(9)	20.8063(11)	5.809(5)	5.996(7)
α (°)	90	90	90	90	90	90	90	90	90
β (°)	107.392(3)	107.521(3)	107.683(4)	107.865(3)	108.076(4)	108.294(5)	108.198(6)	90	90
γ (°)	90	90	90	90	90	90	90	90	90
Volume ($Å^3$)	3638.93(19)	3643.85(17)	3671.0(2)	3678.42(18)	3681.7(2)	3725.0(3)	3703.7(4)	2557(2)	2696(3)
Z	4	4	4	4	4	4	4	8	8
ρ_{calc} ($g\ cm^{-3}$)	1.367	1.365	1.355	1.352	1.351	1.335	1.343	1.560	1.480
μ (mm^{-1})	0.055	0.055	0.054	0.054	0.054	0.053	0.091	0.084	0.080
Θ range (°)	1.916-26.572	1.914-26.573	1.909-26.573	1.906-26.572	1.904-26.573	1.896-25.503	1.900-25.503	1.719-36.327	1.981-25.165
Reflections collected	59911	60217	60546	60598	61154	56843	33115	53279	32361
Independent	8337	8347	8418	8427	8435	7600	7533	6530	2651
Observed I>2σ	5457	5656	4942	5328	4593	4435	4067	5005	1866
R_{int}	0.0685	0.0595	0.0706	0.0586	0.0779	0.0598	0.0827	0.0317	0.0150
Completeness (%)	99.8	99.8	99.8	99.8	99.8	99.9	99.7	100.0	100.0
Parameters	653	653	653	653	653	653	653	227	208
GooF	1.020	1.030	1.012	1.019	1.016	1.025	1.019	1.048	1.046
R_1 (observed)	0.0603	0.0589	0.0624	0.0656	0.0686	0.0626	0.0647	0.0490	0.0569
R_1 (all)	0.1066	0.0964	0.1207	0.1070	0.1379	0.1131	0.1288	0.0603	0.0680
wR_2 (all)	0.1367	0.1503	0.1645	0.1892	0.1908	0.1881	0.1840	0.1581	0.2167
Δρ (max, min) ($e\ Å^{-3}$)	0.395, -0.264	0.358, -0.242	0.388, -0.256	0.444, -0.314	0.472, -0.254	0.388, -0.247	0.331, -0.196	0.564, -0.283	0.250, -0.193

7.3 Identifying temperature dependent proton migration across SSHBs using synchrotron and X-ray diffraction and refinement in SHELX

The temperature dependent proton migration properties of the molecular complexes identified in Chapter 6, where possible, were investigated using variable temperature single crystal X-ray diffraction. Variable temperature measurements were carried out first in the laboratory, generally involving two data collections performed at 100 or 150 K for the low temperature determination and 300 K for the higher. Where the results from these initial studies were promising, variable temperature measurements were also carried out at a synchrotron source over a 100 to 350 K temperature range. Temperature dependent proton migration across SSHBs was suggested in just two of the twenty-five molecular complexes investigated; those of DMU2,4-DNBA and INP.

7.3.1 Variable temperature synchrotron studies of proton migration

Variable temperature study of DMU2,4-DNBA (1:1)

An O^{+}—H···O^{-} SSHB with an O···O distance of 2.441(1) Å, at 100 K, is formed between the acid and urea components in the molecular complex of DMU2,4-DNBA. The 2,4-DNBA acidic proton resides on the DMU molecule at 100 K; the molecular complex DMU2,4-DNBA is therefore a salt at this temperature. This SSHB length is less than the previously proposed 2.45 Å limit, above which proton migration across O—H···O SSHBs is not expected to occur. Variable temperature measurements were carried out on this material at the Advanced Light Source, U.S.A. [2] between 100 and 350 K, in 50 K temperature steps.

The O^{+}—H···O^{-} SSHB hydrogen bond parameters were followed with temperature using refinement model 1, where the position and isotropic thermal parameter of the SSHB hydrogen atom were refined freely (Table 7.8 and Figure 7.1). At 100 K, the refined hydrogen atom position suggests that the proton resides on the urea with an elongated O—H distance of 1.09(2) Å and a H···O distance of 1.37(2) Å. As the temperature is increased, between 100 and 200 K, the refined hydrogen atom position shifts slightly closer to the urea oxygen atom, shown by a decrease in the O—H distance to 1.06(2) Å at 200 K but is within the error limits for the determination and not significant. Between 200 and 350 K, the proton shifts significantly towards the centre of the O^{+}—H···O^{-} hydrogen bond by approximately 0.12 Å. A second refinement model (model 2), employing a fixed thermal parameter for the SSHB hydrogen atom, was also refined at each temperature (§A7.2, Table A7.1 and Figure A7.1). Although there are larger errors on the O—H and H···O distances when employing this model, the same trend of proton migration was suggested, of the order of 0.1 Å. The consistent trends of the SSHB proton migrating towards the centre of the hydrogen bond as a function of temperature, indicated in the O—H and H···O bond

lengths in both refinement models, is promising for the presence of temperature dependent proton migration in this molecular complex.

There is a small variation in the SSHB donor-acceptor distance ($d_{O\cdots O}$) as a function of temperature. This occurs between 100 and 200 K where the O—H and H···O distances are within the error limits for the determination. However, where the most significant change in the O—H and H···O distances has occurred, between 200 and 350 K, the length of the SSHB is invariant. This is supportive of proton migration being the cause for the lengthening of the O—H distance as a function of temperature and not occurring as a consequence of an expanding hydrogen bond, caused by lattice expansion as a function of temperature.

Table 7.8 The O^{+}—H···O^{-} SSHB hydrogen bond parameters in DMU2,4-DNBA over the 100 to 350 K temperature range for refinement model 1.

T (K)	dO—H (Å)	dH···O (Å)	dO···O (Å)	<OHO (°)
100	1.09(2)	1.37(2)	2.441(1)	168(2)
150	1.07(2)	1.39(2)	2.446(1)	169(2)
200	1.06(2)	1.41(2)	2.448(1)	164(2)
250	1.11(2)	1.35(2)	2.448(1)	169(2)
300	1.16(3)	1.31(3)	2.448(2)	166(3)
350	1.18(3)	1.28(3)	2.448(2)	165(3)

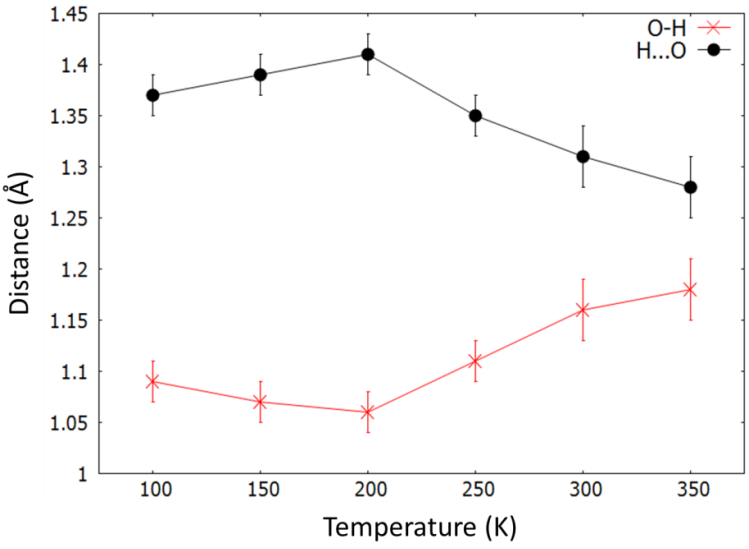

Figure 7.1 The O—H and H···O distances in DMU2,4-DNBA over the 100 to 350 K temperature range for refinement model 1.

Reasonable quality variable temperature Fourier difference maps of the O^{+}—H···O^{-} SSHB were generated from the data, in which it was possible to elucidate changes in the hydrogen atom

density as a function of temperature (Figure 7.2). A shift in position of the hydrogen atom density occurs towards the centre of the O^{+}—H···O^{-} SSHB, as a function of temperature. These observations support the proton migration indicated by the O—H and H···O distances as a function of temperature. It should be noted, however, that the refined hydrogen atom position does not coincide with the peak maxima at most temperatures; a shift in the refined position occurs relative to the peak maxima which is consistent across the maps. Between 100 and 250 K, the hydrogen atom density is elongated along the hydrogen bond, towards the deprotonated 2,4-DNBA. This behaviour is indicative of a hydrogen atom in an SSHB which is partially shared between two atoms and so may also confirm the presence of proton transferring effects.

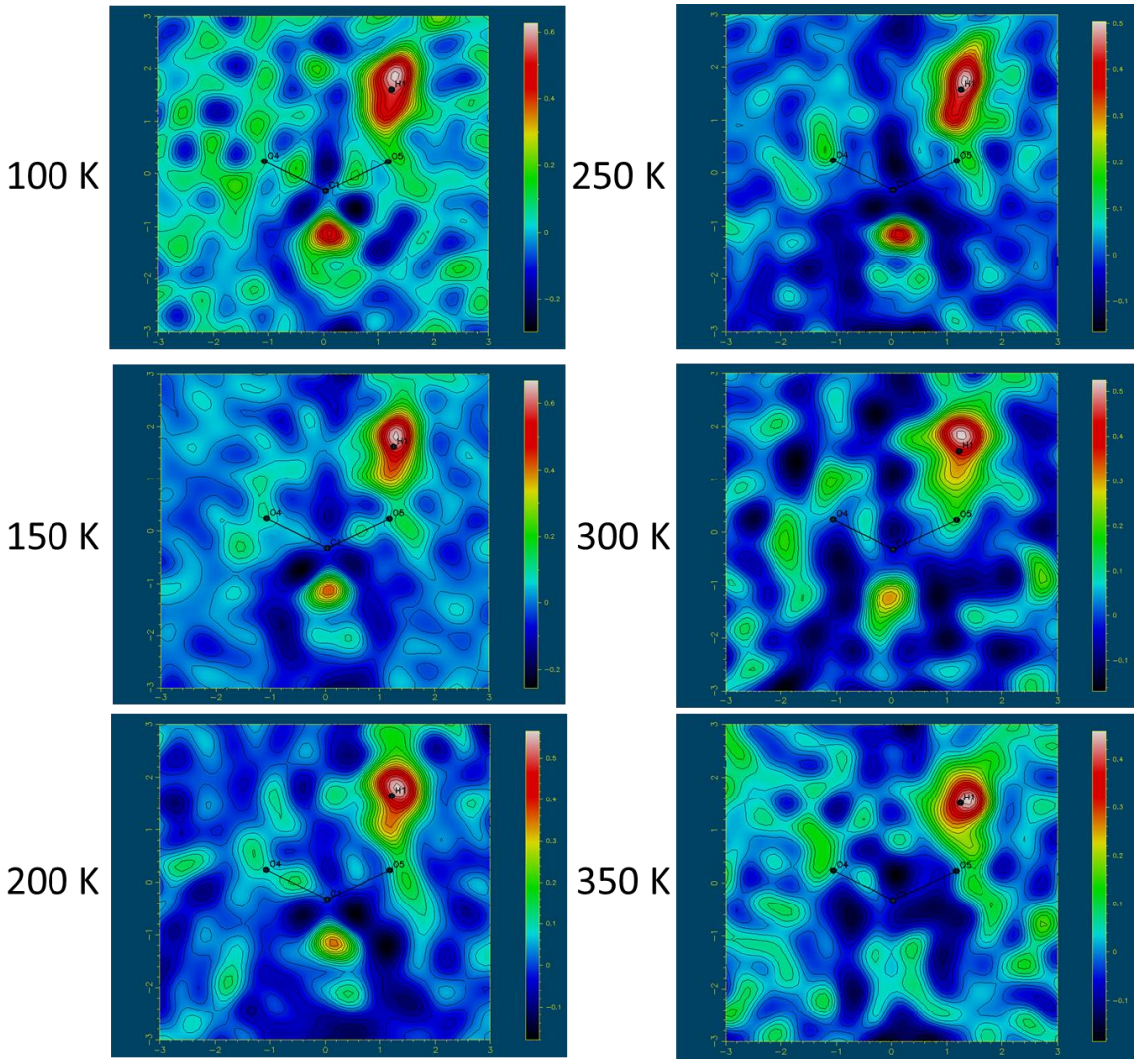

Figure 7.2 Fourier difference electron density maps showing the electron density associated with the H-atom in the O^{+}—H···O^{-} SSHB in DMU2,4-DNBA over the 100 to 350 K temperature range.

The bond distances of the groups forming the O^{+}—H···O^{-} SSHB were also followed as a function of temperature (Table 7.9). The DMU carbonyl C—O shortens, from 1.294(1) Å at 100 K to

1.282(2) Å at 350 K, reflecting a slight increase in bond order of this bond, approaching the C=O bond length for a neutral carbonyl in the native crystal structure of DMU [43] (1.245(2) Å at 273 K), and providing additional evidence in support of proton migration. The carbonyl group in DMU in the molecular complex therefore retains some protonated character at 350 K, in agreement with the elongated O—H distance at this temperature which indicates a bias to the DMU in the SSHB. Interesting behaviour is observed in the 2,4-DNBA carboxylate group, as the proton moves towards the centre of the O—H···O SSHB with increasing temperature. The deprotonated C—O bond decreases slightly in length as a function of temperature, from 1.274(1) Å at 100 K to 1.266(2) Å at 300 K. This suggests an increased deprotonation of this group and is not in support of migration of the proton, away from DMU towards 2,4-DNBA. This effect is, however, very small and could be caused by a redistribution of charge in the carboxylate group. The carboxylate carbonyl group, not involved in forming the SSHB, shortens from 1.237(1) Å at 100 K to 1.225(2) Å at 350 K, as would be expected for a carboxylic acid group which becomes increasingly protonated and is thus in support of proton migration.

Table 7.9 Bond distances of the groups forming the O^{+}—H···O^{-} SSHB in DMU2,4-DNBA over the temperature range.

T (K)	$dC{=}O_{DMU}$ (Å)	$dC{—}O^{-}_{2,4\text{-}DNBA}$(Å)	$dC{=}O_{2,4\text{-}DNBA}$ (Å)
100	1.294(1)	1.274(1)	1.237(1)
150	1.295(1)	1.273(1)	1.236(1)
200	1.293(1)	1.270(1)	1.233(1)
250	1.290(2)	1.267(2)	1.232(1)
300	1.287(2)	1.268(2)	1.230(2)
350	1.282(2)	1.266(2)	1.225(2)

In summary, a trend of temperature dependent proton migration is indicated in this molecular complex by all information, occurring most significantly between 200 and 350 K.

Variable temperature study of INP (2:1)

An N^{+}—H···O^{-} SSHB, with an N···O distance of 2.551(1) Å at 100K, forms between the isonicotinamide and phthalic acid components in the molecular complex of INP. The phthalic acid (P) acidic proton resides on the IN molecule at 100 K; the molecular complex INP is therefore a salt at this temperature. This SSHB donor-acceptor distance is just above the 2.55 Å limit where proton migration has previously been observed across N^{+}—H···O^{-} SSHBs. Variable temperature measurements were carried out on this material at the Advanced Light Source, U.S.A [2] between 100 and 350 K.

The N^+—H···O^- SSHB hydrogen bond parameters were followed with temperature using refinement model 1, where the position and isotropic thermal parameter of the SSHB hydrogen atom were refined freely (Table 7.10 and Figure 7.3). At 100 K, the proton resides on the isonicotinamide with an elongated N—H distance of 1.07(2) Å. As the temperature is increased, between 100 and 350 K, the refined proton position shifts gradually, but significantly, towards the centre of the N^+—H···O^- hydrogen bond, by approximately 0.1 Å. A second refinement model (model 2), employing a fixed thermal parameter for the SSHB hydrogen atom, was also refined at each temperature (§A7.2, Table A7.2 and Figure A7.2). Although there are larger errors on the N^+—H and H···O^- distances when employing this model, the same trend of proton migration is suggested, of the order of 0.1 Å. The consistent trends of the SSHB proton migrating towards the centre of the hydrogen bond as a function of temperature, indicated in the N^+—H and H···O^- bond lengths in both refinement models, is promising for the presence of temperature dependent proton migration in this molecular complex. The N^+···O^- SSHB distance remains invariant between 100 and 300 K with a very slight increase at 350 K. This is supportive of proton migration being the cause for the lengthening of the N^+—H distance as a function of temperature and not occurring as a consequence of an expanding hydrogen bond, caused by lattice expansion as a function of temperature.

An O—H···N hydrogen bond also forms in this structure between the other phthalic acid carboxylic acid group and a second isonicotinamide molecule. No proton migration is indicated across this hydrogen bond as a function of temperature.

Table 7.10 The N^+—H···O^- SSHB and O—H···N hydrogen bond parameters in INP between 100 and 350 K.

T (K)	Interaction	dD—H (Å)	dH···A (Å)	dD···A (Å)	<DHA (°)
100	N^+—H···O^-	1.07(2)	1.48(2)	2.551(1)	177(2)
	O—H···N	1.02(2)	1.68(2)	2.696(1)	179(2)
150	N^+—H···O^-	1.09(2)	1.46(2)	2.550(1)	177(2)
	O—H···N	1.02(2)	1.68(2)	2.700(1)	178(2)
200	N^+—H···O^-	1.09(2)	1.46(2)	2.550(1)	176(2)
	O—H···N	1.04(2)	1.66(2)	2.704(1)	180(2)
250	N^+—H···O^-	1.12(2)	1.43(2)	2.550(1)	175(2)
	O—H···N	1.04(2)	1.67(2)	2.707(1)	179(2)
300	N^+—H···O^-	1.15(2)	1.41(2)	2.552(1)	175(2)
	O—H···N	1.04(2)	1.67(2)	2.713(2)	178(2)
350	N^+—H···O^-	1.17(2)	1.39(2)	2.555(2)	174(2)
	O—H···N	1.01(2)	1.70(2)	2.718(2)	177(2)

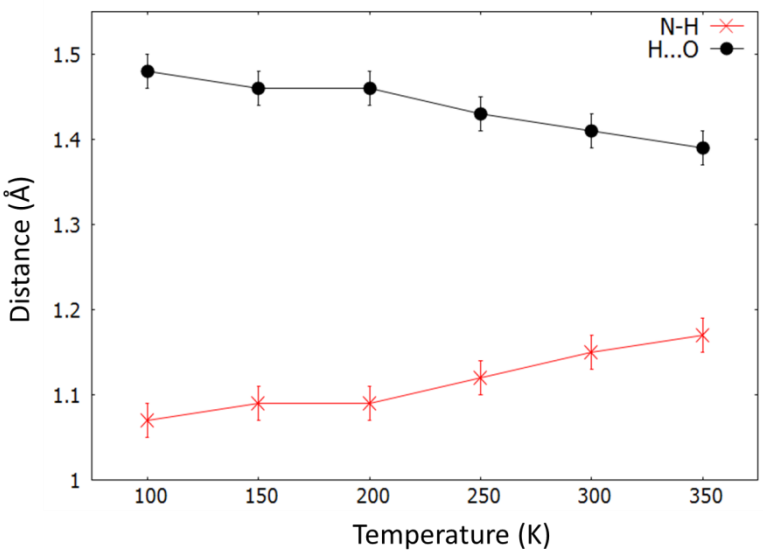

Figure 7.3 The N^{+}—H and H···O^{-} distances in INP over the 100 to 350 K temperature range for refinement model 1.

Good quality variable temperature Fourier difference maps of the N^{+}—H···O^{-} SSHB were generated from the data; in these it was possible to elucidate changes in the hydrogen atom density as a function of temperature (Figure 7.4). An increasing elongation of the hydrogen atom density occurs along the hydrogen bond towards the phthalic acid carboxylate group as the temperature increases. This elongation supports the occurrence of temperature dependent proton migration as indicated in the N^{+}—H and H···O^{-} distances as a function of temperature. The refined hydrogen atom positions are slightly offset from the hydrogen atom peak maxima, this effect occurring to the same extent at all temperatures.

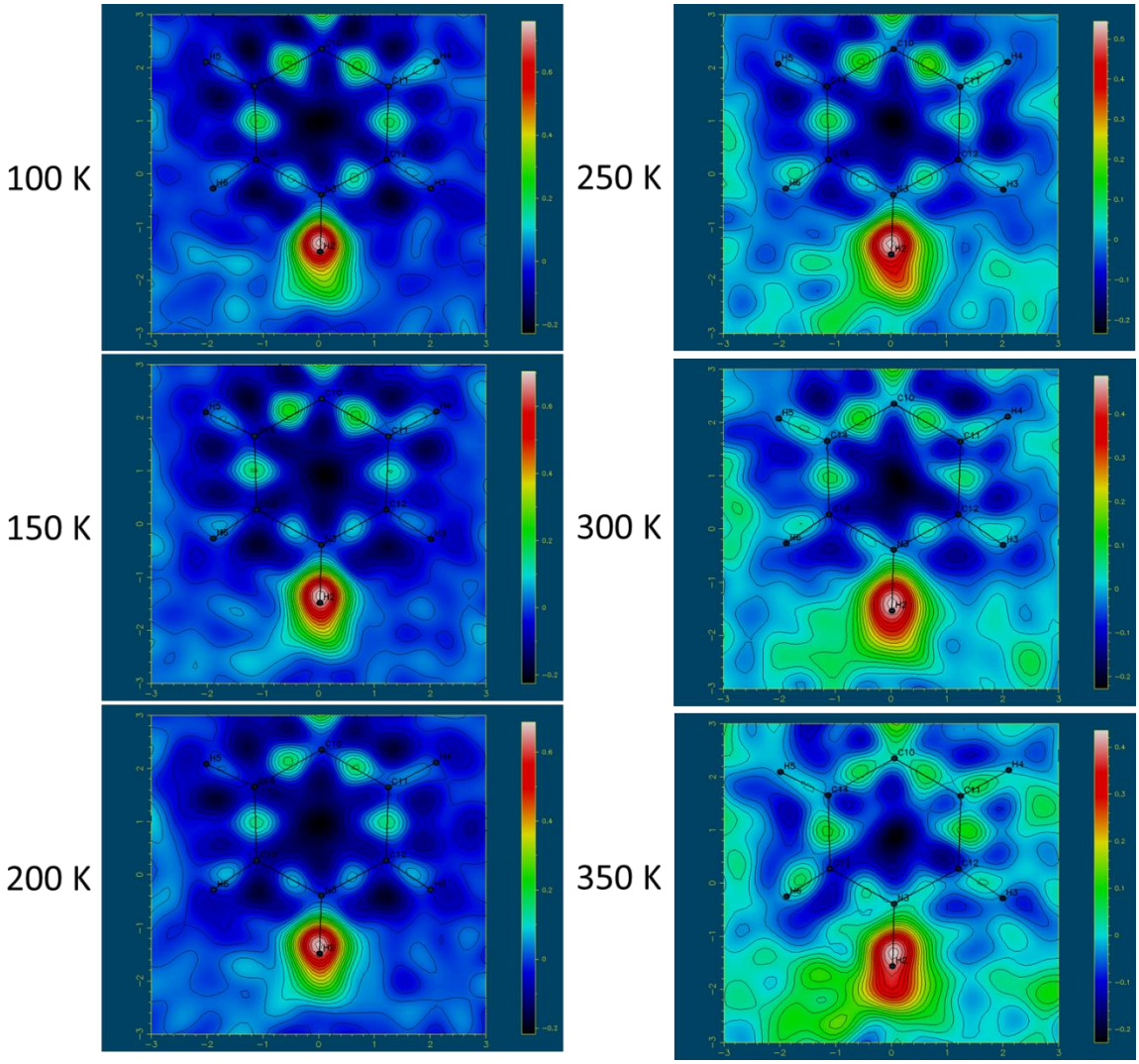

Figure 7.4 Fourier difference electron density maps showing the electron density associated with the H-atom in the N^+—H end of the N^+—H···O^- SSHB in INP over the 100 to 350 K temperature range.

The structural parameters of the groups forming the N^+—H···O^- SSHB were also followed as a function of temperature (Table 7.11). The C—N distances in IN shorten from 1.341(1) Å at 100 K to 1.329(2) Å at 350 K. The IN CNC angle also decreases from 121.10(9) ° at 100 K to 120.2(1) ° at 350 K. These structural changes in IN provide additional evidence in support of proton migration, away from the IN nitrogen atom; in the native crystal structure of the neutral IN, the C—N bond lengths are 1.337(2) Å and the CNC angle is 116.6(1) °. [298] In the phthalic acid carboxylate group forming the SSHB, there is little change in the phthalic acid deprotonated C—O bond length over the temperature range. A shortening of the C=O bond length occurs from 1.238(1) Å, at 100 K, to 1.228(2) Å at 350 K; this coincides with a transfer of H2 back towards to the carboxylic acid group and is in support of proton migration occurring.

Table 7.11 Structural parameters of the groups forming the N^+—H···O^- SSHB in INP over the temperature range.

T (K)	dC—N (Å)	dC—N (Å)	<CNC (°)	dC—O^- (Å)	dC=O (Å)
100	1.341(1)	1.341(1)	121.10(9)	1.287(1)	1.238(1)
150	1.340(1)	1.339(1)	121.0(1)	1.287(1)	1.237(1)
200	1.337(1)	1.336(1)	120.8(1)	1.286(1)	1.235(1)
250	1.336(2)	1.334(2)	120.7(1)	1.286(2)	1.232(2)
300	1.332(2)	1.332(2)	120.5(1)	1.285(2)	1.230(2)
350	1.329(2)	1.327(2)	120.2(1)	1.284(2)	1.228(2)

A trend of temperature dependent proton migration can be identified in INP, indicated by all information. Additional interesting thermal behaviour is observed for this molecular complex in the lattice parameters (§A7.2, Figure A7.3). A slight contraction of the *b*-axis and *β*-angle between 100 and 350 K occurs whilst the *a* and *c*-axes undergo significant increases in length. However, INP cannot be considered a negative thermal expansion material as the cell volume continues to increase with temperature.

Variable temperature study of 3-DAZABrA hydrate, a complex with a very short O—H···O hydrogen bond

The molecular complex of 3-DAZABrA hydrate contains an O—H···O SSHB between the anilic acid and 3-deazauracil components with a very short O···O distance of 2.411(2) Å at 100 K, well below the previously proposed 2.45 Å cut off; the proton in this SSHB also occupies a close to central position at 100 K, slightly closer in proximity to the BrA end of the SSHB ($d_{O—H}$ 1.16(4) Å and $d_{H···O}$ 1.30(4) Å); the molecular complex 3-DAZABrA hydrate is therefore in an intermediate proton transfer state at this temperature. Variable temperature measurements were carried out on 3-DAZABrA hydrate at the Advanced Light Source, U.S.A. [2] between 100 and 350 K.

The O—H···O SSHB hydrogen bond parameters were followed with temperature using refinement model 1, where the position and isotropic thermal parameter of the SSHB hydrogen atom were refined freely (Table 7.12 and Figure 7.5). Despite the very strong nature of the O—H···O hydrogen bond formed between the anilic acid and 3-deazauracil, no proton migration was suggested in the O—H or H···O bond lengths over the 100 to 350 K temperature range. Fourier difference maps of the O—H···O hydrogen bond do not show a consistent picture with temperature (Figure 7.6); an increased smearing of the proton density along the hydrogen bond occurs between 100 and 250 K but this does not persist above this temperature. This may be indicative of a change in the shape of a presumably single well potential for this SSHB, in which the proton occupies a fairly constant average position between the O atoms throughout the temperature range. The observation of the hydrogen atom density in the O—H···O hydrogen bond is more difficult in this

sample due to the present of the heavy bromine atom, which dominates the X-ray data, and due to the hydrogen atom not lying in the same plane as either of the molecules forming the SSHB; the hydrogen atom is twisted by 25(2) ° out of the plane of the BrA ring whilst it is twisted 3(2) ° out of the plane of the 3-DAZA ring. Also, the refined hydrogen atom position does not coincide with the peak maxima at most temperatures. Future neutron single crystal diffraction data might be of value for this complex if sufficiently large crystals can be obtained. The O···O distance in the SSHB increases by 0.02 Å with temperature; this increase is more substantial than observed in most of the other complexes studied in this chapter and is not suggestive of a situation that would support proton migration.

Table 7.12 The O—H···O SSHB hydrogen bond parameters in 3-DAZABrA hydrate over the 100 to 350 K temperature range.

T (K)	dO—H (Å)	dH···O (Å)	dO···O (Å)	<OHO (°)
100	1.16(4)	1.30(4)	2.412(2)	158(4)
150	1.17(3)	1.31(3)	2.416(2)	154(3)
200	1.17(4)	1.31(4)	2.421(2)	155(4)
250	1.16(4)	1.33(4)	2.424(2)	154(4)
300	1.09(4)	1.40(4)	2.428(2)	155(4)
350	1.20(4)	1.30(4)	2.432(4)	153(4)

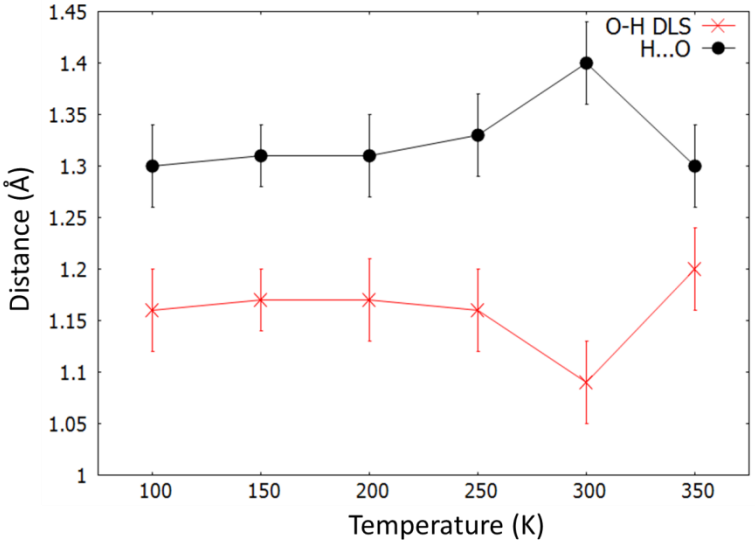

Figure 7.5 The O—H and H···O distances in 3-DAZABrA hydrate over the 100 to 350 K temperature range.

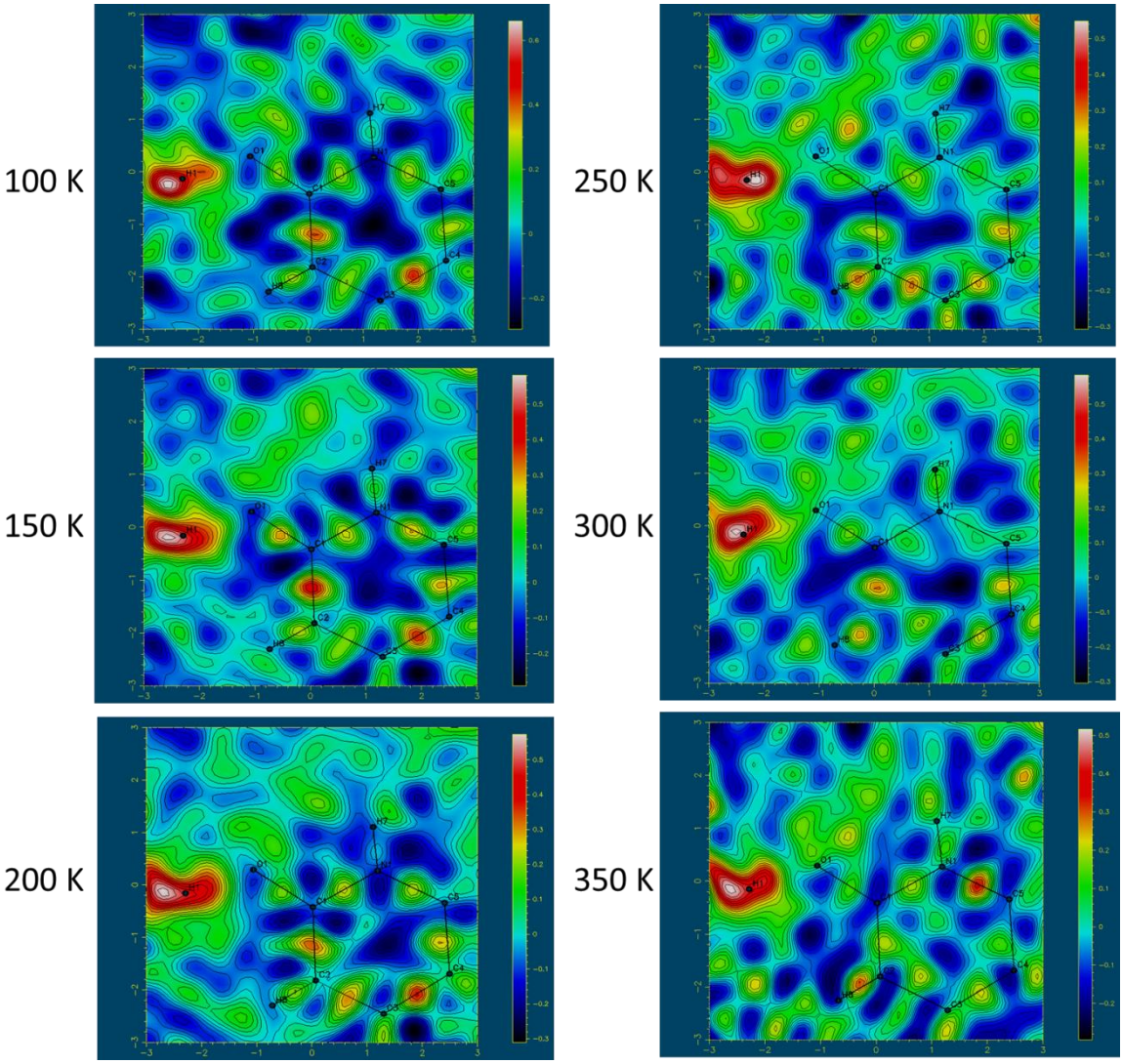

Figure 7.6 Fourier difference electron density maps showing the electron density associated with the H-atom in the O—H···O SSHB in 3-DAZABrA over the 100 to 350 K temperature range.

The bond distances of the 3-DAZA carbonyl group forming one end of the SSHB and the BrA carbonyl group not forming the SSHB shorten very slightly with temperature (Table 7.13) indicating some increase in protonation of the BrA hydroxyl group; this is not reflected in the O—H and H···O distances.

Table 7.13 Bond distances of the groups forming the O--H···O SSHB in 3-DAZABrA hydrate over the temperature range.

T (K)	$dC{=}O_{3\text{-}DAZA}$ (Å)	$dC{—}O_{BrA}$ (Å)	$dC{=}O_{BrA}$ (Å)
100	1.292(2)	1.292(2)	1.233(2)
150	1.291(2)	1.292(2)	1.235(2)
200	1.290(2)	1.291(2)	1.233(2)
250	1.287(2)	1.292(2)	1.231(2)
300	1.286(2)	1.294(2)	1.228(2)
350	1.286(2)	1.293(3)	1.227(2)

In summary, temperature dependent proton migration cannot be confirmed in the molecular complex of 3-DAZABrA hydrate.

Variable temperature study of DMU3,5-DNBA (1:1)

An O—H···O SSHB with an O···O distance of 2.472(3) Å at 100 K is formed between the acid and urea components in the molecular complex of DMU3,5-DNBA. The refined hydrogen atom positions show the SSHB proton occupies the centre of the hydrogen bond at 100K ($d_{O—H}$ 1.23(7) Å and $d_{H···O}$ 1.26(7) Å); the molecular complex DMU3,5-DNBA is therefore in an intermediate proton transfer state at this temperature. Variable temperature measurements were carried out on DMU3,5-DNBA at the Advanced Light Source, U.S.A. [2] between 100 and 300 K.

The O—H···O SSHB hydrogen bond parameters were followed with temperature using refinement model 1, where the position and isotropic thermal parameter of the SSHB hydrogen atom were refined freely (Table 7.14 and Figure 7.7). As a function of temperature, the proton position appears to shift away from the centre of the hydrogen bond towards the DMU molecule. However, the large errors on the bond lengths suggest that there is insufficient evidence for proton migration. The Fourier difference maps of the O—H···O hydrogen bond contain large amounts of noise, making determination of hydrogen atom density and hence thermal behaviour difficult (Figure 7.8). In these maps, the refined hydrogen atom position does not coincide with the peak maxima at most temperatures. The density of the hydrogen atom is biased towards the 3,5-DNBA oxygen atom at 100 K, with some smearing along the O—H···O hydrogen bond. A second peak is present at 200 K, indicating possible disorder of the proton over two positions, which remains up to 300 K. A structural model where the hydrogen atom is disordered was thus refined at each temperature and a 50:50 disorder was suggested at all temperatures, but again with a high degree of uncertainty. It is not possible to determine the hydrogen atom behaviour reliably as a function of temperature in this molecular complex. The O···O distance in the SSHB fluctuates with temperature; this behaviour is not suggestive of proton migration.

Table 7.14 The O—H···O SSHB hydrogen bond parameters in DMU3,5-DNBA over the 100 to 350 K temperature range.

T (K)	dO···O (Å)	dO—H (Å)	dH···O (Å)	<OHO (°)
100	2.472(3)	1.23(7)	1.26(7)	169(6)
150	2.466(3)	1.23(7)	1.24(7)	176(6)
200	2.470(4)	1.08(8)	1.40(8)	174(7)
250	2.472(2)	1.18(7)	1.30(8)	169(4)
300	2.469(4)	1.15(7)	1.34(8)	164(6)

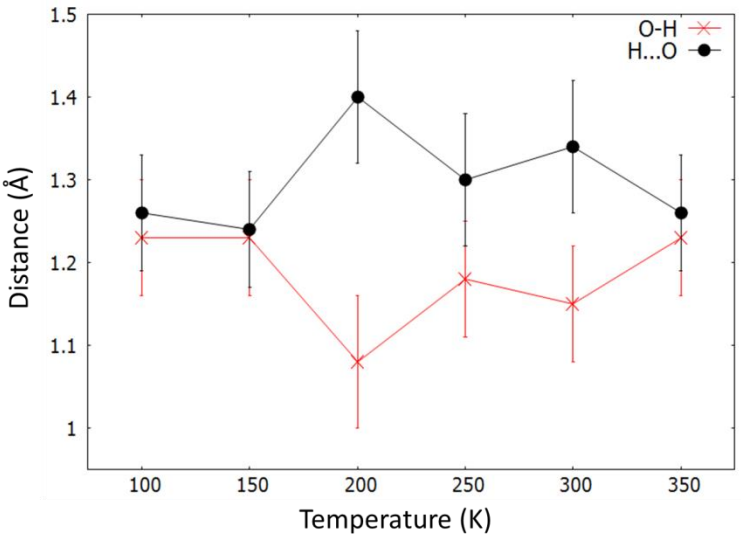

Figure 7.7 The O—H and H···O distances in DMU3,5-DNBA over the 100 to 350 K temperature range.

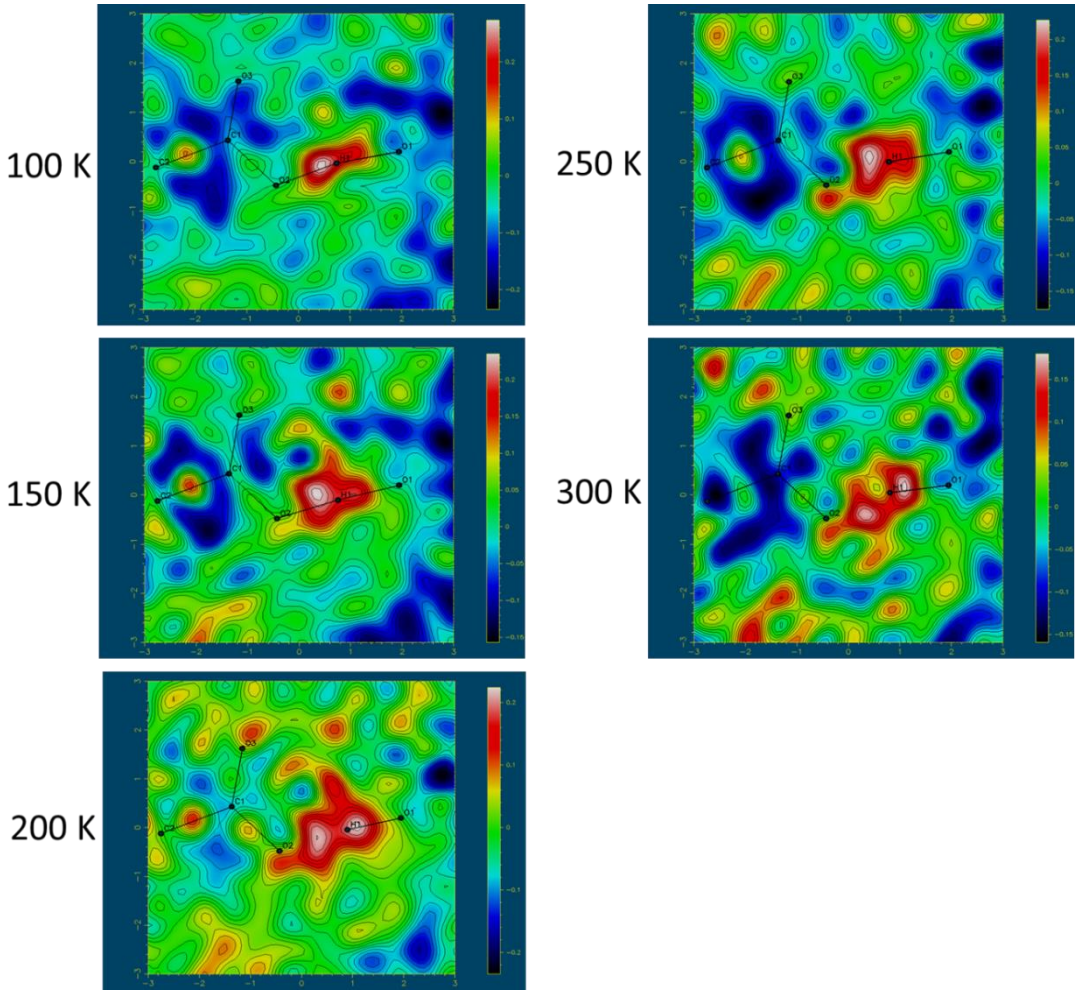

Figure 7.8 Fourier difference electron density maps showing the electron density associated with the H-atom in the O—H···O SSHB in DMU3,5-DNBA over the 100 to 350 K temperature range.

The structural parameters of the groups forming the SSHB (Table 7.15) add to the conclusion that no deduction of the presence or absence of migration can be made in this case, as they suggest a different trend to that of the O—H and H···O bond lengths over the temperature range; the C—O bonds instead suggest the proton resides on the 3,5-DNBA molecule and becomes increasingly bonded with temperature.

Table 7.15 Bond distances of the groups forming the O--H···O SSHB over the temperature range in DMU3,5-DNBA.

T (K)	dC=O_{DMU} (Å)	dC—$O_{3,5\text{-}DNBA}$ (Å)	dC=$O_{3,5\text{-}DNBA}$ (Å)
100	1.263(3)	1.306(4)	1.221(3)
150	1.259(3)	1.305(4)	1.214(3)
200	1.257(4)	1.301(5)	1.211(4)
250	1.248(4)	1.299(5)	1.210(4)
300	1.251(5)	1.303(5)	1.209(4)

In summary, the presence of temperature dependent proton migration cannot be confirmed in the molecular complex of DMU3,5-DNBA.

Variable temperature study of DMUP (2:1)

Two O—H···O SSHBs with O···O distances of 2.493(2) Å (O3—H1···O6) and 2.452(2) Å (O2—H2···O5) are formed at 100 K between the acid and urea components in the molecular complex of DMUP with both the SSHB protons residing on the phthalic acid molecule. Variable temperature measurements were carried out on DMUP at the Advanced Light Source, U.S.A [2] between 100 and 300 K.

The O—H···O SSHB hydrogen bond parameters were followed with temperature using refinement model 1, where the position and isotropic thermal parameter of the SSHB hydrogen atom were refined freely (Table 7.16 and Figure 7.9). An elongated O—H distance is found in both the O—H···O hydrogen bonds at 100 K; these lengthen as the temperature is increased to 300 K, although these changes are not significant enough to suggest proton migration. The Fourier difference maps contain large amounts of noise making determination of hydrogen atom behaviour difficult (Figure 7.10). The refined hydrogen atom positions also do not coincide with the peak maxima at most temperatures. The shape of the density of the hydrogen atom does not appear to change with temperature in either of the O3—H1···O6 and O2—H2···O5 hydrogen bonds; no temperature dependent proton migration is suggested across these interactions. The O···O distance in the O3—H1···O6 SSHB fluctuates whilst it increases in the O2—H2···O5 SSHB; neither behaviour is suggestive of proton migration.

Table 7.16 The SSHB hydrogen bond parameters in DMUP over the 100 to 300 K temperature range.

T (K)	O--H···O	dO···O (Å)	dO—H (Å)	dH···O (Å)	<OHO (°)
100	O3—H1···O6	2.493(2)	1.09(3)	1.44(3)	160(3)
	O2—H2···O5	2.452(2)	1.01(3)	1.45(3)	168(2)
200	O3—H1···O6	2.498(2)	1.09(3)	1.44(3)	163(2)
	O2—H2···O5	2.461(2)	1.05(3)	1.42(3)	169(3)
300	O3—H1···O6	2.493(2)	1.13(3)	1.38(3)	165(3)
	O2—H2···O5	2.474(3)	1.05(3)	1.43(3)	168(3)

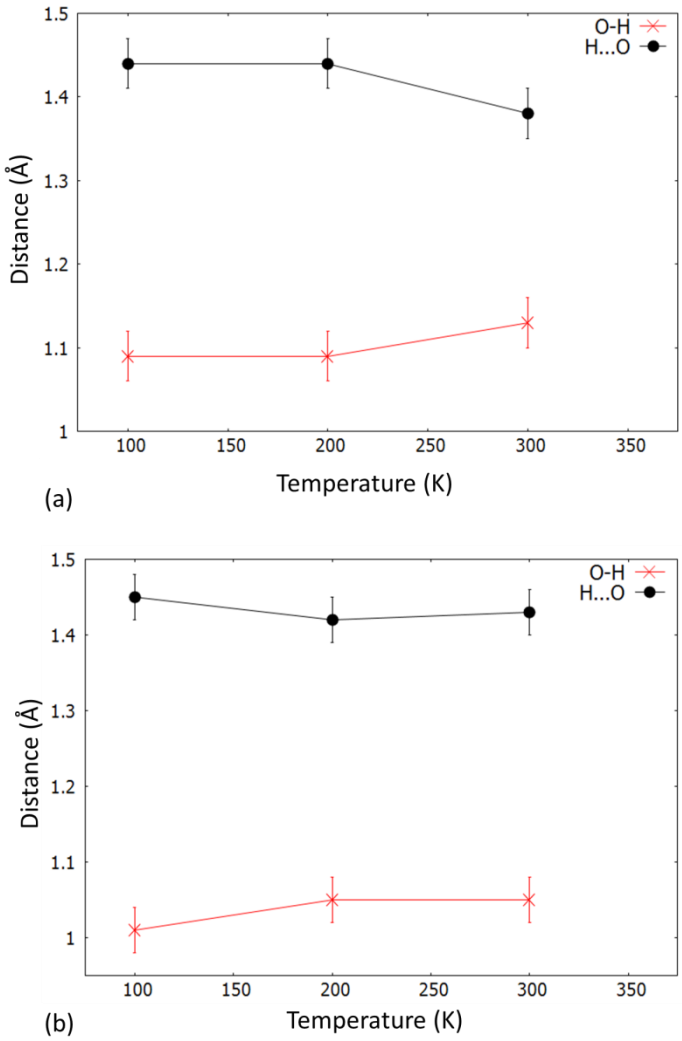

Figure 7.9 The O—H and H···O distances in DMUP over the 100 to 350 K temperature range in SSHB (a) O3—H1···O6 and (b) O2—H2···O5.

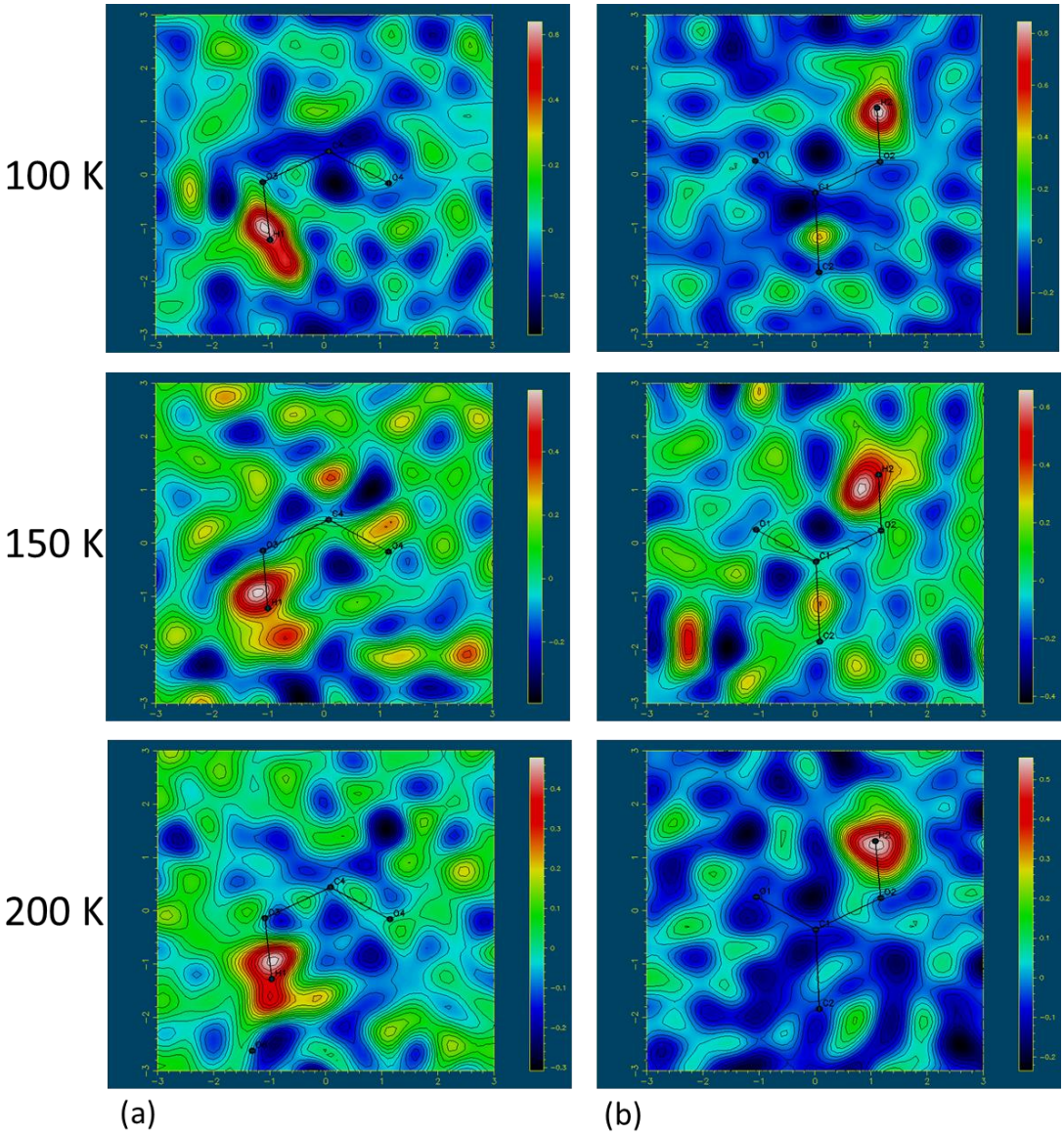

Figure 7.10 Fourier difference electron density maps showing the electron density associated with the H-atom in the (a) O3—H1···O6 and (b) O2—H2···O5 SSHB in DMUP over the 100 to 300 K temperature range.

The structural parameters of the groups forming the SSHB (Table 7.17) add to the conclusion that no deduction of the presence or absence of migration can be made in this case; the DMUP C=O distances shorten, indicating an increase in bond order, the opposite of what would be expected for transfer of the phthalic acid proton across the SSHB to DMU, whilst in the phthalic acid carboxylic acid groups there is no change in the C—O bond and the C=O bond fluctuates in length.

Table 7.17 Bond distances of the groups forming the O—H···O SSHB in DMUP over the temperature range.

T (K)	O—H···O	dC=O_{DMU} (Å)	dC—O_{PHA} (Å)	dC=O_{PHA} (Å)
100	O3—H1···O6	1.263(2)	1.309(2)	1.221(2)
	O2—H2···O5	1.264(2)	1.298(2)	1.230(2)
200	O3—H1···O6	1.259(2)	1.306(2)	1.220(2)
	O2—H2···O5	1.260(2)	1.301(2)	1.226(2)
300	O3—H1···O6	1.255(3)	1.308(3)	1.216(3)
	O2—H2···O5	1.251(3)	1.300(2)	1.255(3)

In summary, temperature dependent proton migration cannot be confirmed in the molecular complex of DMUP.

Variable temperature study of IN2,4-DNBA II (2:2)

Two N^+—H···O^- hydrogen bonds are formed between isonicotinamide and 2,4-dinitrobenzoic acid components in the molecular complex of IN2,4-DNBA II at 100 K; one is a charge assisted N^+—H···O^- SSHB with an N^+···O^- distance of 2.555(1) Å ($N1^+$—H2···$O5^-$) whilst the other is a charge assisted strong to moderate hydrogen bond with an N^+···O^- distance of 2.636(1) Å ($N2^+$—H1···$O9^-$). The molecular complex IN2,4-DNBA is a salt at 100 K as a result of the proton transfer between the IN and 2,4-DNBA species at this temperature. Variable temperature measurements were carried out on this material at the Advanced Light Source, U.S.A. [2] between 100 and 350 K.

The N^+—H···O^- SSHB hydrogen bond parameters were followed with temperature using refinement model 1, where the position and isotropic thermal parameter of the SSHB hydrogen atom were refined freely (Table 7.18 and Figure 7.11). At 100 K, the proton resides on the isonicotinamide in the $N1^+$—H2···$O5^-$ SSHB with an elongated N^+—H distance of 1.04(2) Å and an H···O^- distance of 1.52(2) Å. As the temperature is increased, between 100 and 350 K, the proton position shifts, in a fluctuating manner towards the centre of the $N1^+$—H2···$O5^-$ hydrogen bond. At 350 K, the N^+—H distance has lengthened to 1.12(2) and the H···O^- distance shortens to 1.46(2). Whilst this may indicate a migration of 0.08 Å, the trend is not consistent and not significant when the errors are taken into account. It was also not possible to confidently identify proton migration in the Fourier difference maps of the SSHB (Figure 7.12). The maps show an elongation of the hydrogen atom along the hydrogen bond but this does not increase consistently across the temperature range and by 350 K, the increased thermal motion of the entire system is reflected in the noise in the Fourier difference map. The refined hydrogen atom positions are slightly offset from the hydrogen atom peak maxima; occurring to the same extent at all

temperatures. The $N^{+}\cdots O^{-}$ distance in the SSHB increases by approximately 0.014 Å with temperature; this increase is substantial and is not suggestive of proton migration. No proton migration is indicated across the $N2^{+}$—H1···$O9^{-}$ hydrogen bond as a function of temperature as would be expected for the long $N^{+}\cdots O^{-}$ distance.

Table 7.18 The N^{+}—H···O^{-} SSHB hydrogen bond parameters over the 100 to 350 K temperature range in IN2,4-DNBA II.

T (K)	Interaction	dN···O (Å)	dN—H (Å)	dH···O (Å)	<NHO (°)
100	$N1^{+}$—H2···$O5^{-}$	2.555(1)	1.04(2)	1.52(2)	177(2)
	$N2^{+}$—H1···$O9^{-}$	2.636(1)	0.98(2)	1.66(2)	169(2)
150	$N1^{+}$—H2···$O5^{-}$	2.556(1)	1.08(2)	1.48(2)	176(2)
	$N2^{+}$—H1···$O9^{-}$	2.629(1)	1.01(2)	1.63(2)	170(2)
200	$N1^{+}$—H2···$O5^{-}$	2.560(1)	1.05(2)	1.51(2)	176(2)
	$N2^{+}$—H1···$O9^{-}$	2.627(1)	0.96(2)	1.67(2)	172(2)
250	$N1^{+}$—H2···$O5^{-}$	2.562(2)	1.09(3)	1.48(3)	176(2)
	$N2^{+}$—H1···$O9^{-}$	2.622(2)	1.00(2)	1.63(2)	172(2)
300	$N1^{+}$—H2···$O5^{-}$	2.566(2)	1.10(3)	1.47(3)	173(3)
	$N2^{+}$—H1···$O9^{-}$	2.619(3)	1.00(3)	1.63(3)	171(2)
350	$N1^{+}$—H2···$O5^{-}$	2.569(2)	1.12(3)	1.46(3)	173(3)
	$N2^{+}$—H1···$O9^{-}$	2.614(3)	1.05(3)	1.58(3)	171(3)

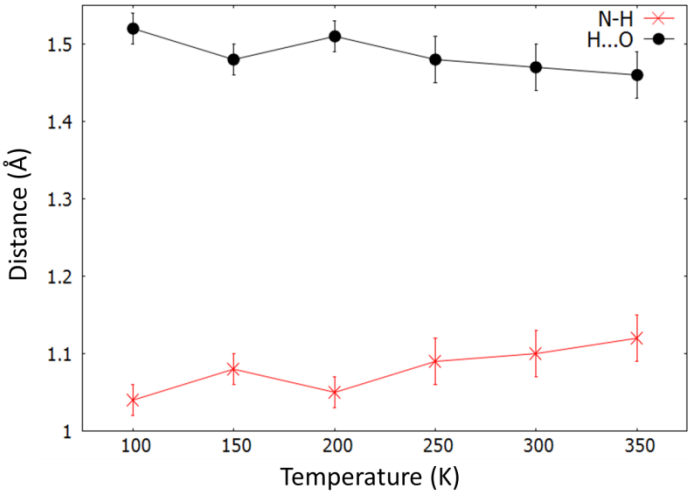

Figure 7.11 The N—H and H···O distances in IN2,4-DNBA II over the 100 to 350 K temperature range in SSHB $N1^{+}$—H2···$O5^{-}$.

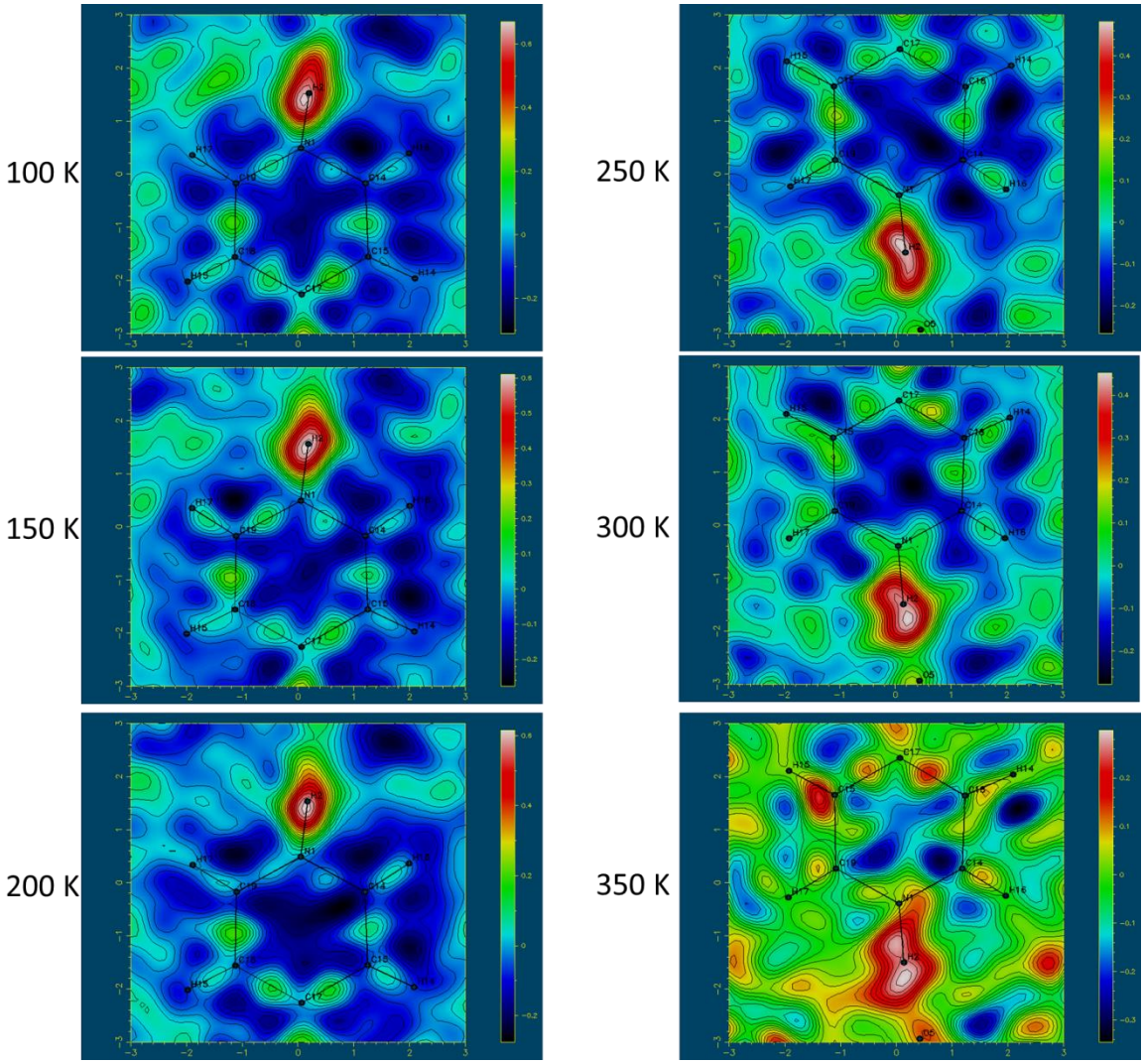

Figure 7.12 Fourier difference electron density maps showing the electron density associated with the H-atom in the $N1^{+}$—H2···$O5^{-}$ SSHB in IN2,4-DNBA II over the 100 to 350 K temperature range.

Structural changes in the groups forming the $N1^{+}$—H2···$O5^{-}$ SSHB were followed as function of temperature in IN2,4-DNBA II (Table 7.19). Over the temperature range, there is some shortening in both the C—O and C=O bond lengths of the 2,4-DNBA carboxylate group. Transfer of H2 from the protonated IN nitrogen atom back to the 2,4-DNBA acid group would be consistent with the shortening of C=O, but not the shortening of C—O. A shortening of the IN C—N bond lengths occurs, as the temperature increases, which could also suggest a transfer of H2 back to the carboxylic acid group. A clear picture of proton migration in this system is lacking, however.

Table 7.19 Bond distances of the groups forming the $N1^{+}$—H2···O5^{-} SSHB over the temperature range in IN2,4-DNBA II.

T (K)	dC—N (Å)	dC—N (Å)	<CNC (°)	dC—O^{-} (Å)	dC=O (Å)
100	1.338(2)	1.335(2)	120.7(1)	1.269(1)	1.240(1)
150	1.335(2)	1.332(2)	120.4(1)	1.266(2)	1.238(1)
200	1.328(2)	1.327(2)	120.31(1)	1.264(2)	1.237(1)
250	1.323(2)	1.325(3)	120.0(2)	1.262(2)	1.236(2)
300	1.320(1)	1.317(3)	119.7(2)	1.261(2)	1.233(3)
350	1.313(4)	1.308(4)	119.5(3)	1.263(3)	1.230(4

In summary, temperature dependent proton migration cannot be confirmed in the molecular complex of IN2,4-DNBA II.

7.3.2 Variable temperature studies of proton migration on a laboratory source

Variable temperature X-ray diffraction on a laboratory diffraction source was carried out on the molecular complexes, where possible, engineered in Chapter 6. Data collections were carried out at two temperatures to investigate for potential proton migration behaviour (Table 7.20 to Table 7.22). Due to the long $N^{+}\cdots O^{-}$ hydrogen bond distances in the N-heterocycle and anilic acid molecular complexes, all greater than 2.6 Å, these samples were not the focus for temperature dependent proton migration studies. The two data collections were generally carried out at 100 or 150 K for the low temperature determination and 300 K for the higher.

Proton migration was not suggested in these molecular complexes, based on the D—H and H···A distances and Fourier difference maps of the SSHBs at the two temperatures. In nearly all cases the D···A distance is greater than the previously proposed limits for proton migration to be observed across an O—H···O or N^{+}—H···O^{-} SSHB. Exceptions to this are DMU5-NIP and 3-DAZA2,4-DNBA with O—H···O SSHBs donor-acceptor distances below the migration limit at 150 K ($d_{O\cdots O}$ 2.434(2) and 2.449(1) Å, respectively); however, no proton migration is indicated in either of these molecular complexes between 150 and 300 K. A very short intramolecular O—H···O^{-} hydrogen bond is formed in INZP ($d_{O\cdots O}$ 2.379(1) Å). There is no significant change in the hydrogen atom position or the electron density within the intramolecular hydrogen bond over the 100 to 350 K temperature range (Figure 7.13). This is unsurprising in this case where these hydrogen bonds have a steric contribution and are often unsymmetrical, [7] and so are unlikely to exhibit proton migration.

Table 7.20 Hydrogen bond parameters in the molecular complexes, at low temperature (100 to 150 K) and at room temperature (298 to 300 K).

Complex	T (K)	O—H···O	dO···O (Å)	dO—H (Å)	dH···O (Å)
UIP	100	O2—H1···O10	2.626(2)	0.87(5)	1.79(5)
		O4—H2···O9	2.622(2)	0.95(5)	1.69(5)
		O8—H3···O10	2.636(2)	0.89(3)	1.78(4)
		O5—H4···O9	2.597(2)	0.85(4)	1.75(4)
	300	O2—H1···O10	2.653(2)	0.94(3)	1.73(3)
		O4—H2···O9	2.645(2)	1.10(3)	1.65(3)
		O8—H3···O10	2.653(2)	0.89(2)	1.77(2)
		O5—H4···O9	2.619(2)	0.96(3)	1.67(3)
MUP	100	O7—H1···O5	2.588(1)	0.85(2)	1.72(2)
		O9—H4···O8	2.595(2)	0.93(3)	1.67(3)
		O2—H2···O8	2.578(1)	0.90(2)	1.69(2)
		O3—H3···O5	2.591(1)	0.92(3)	1.68(3)
	300	O7—H1···O5	2.570(2)	0.86(2)	1.73(2)
		O9—H4···O8	2.611(2)	0.95(3)	1.68(3)
		O2—H2···O8	2.591(2)	0.87(3)	1.73(2)
		O3—H3···O5	2.601(2)	0.95(2)	1.66(2)
MUIP	100	O2—H1···O5	2.674(2)	0.97(3)	1.71(3)
		O4—H6···O5	2.594(2)	1.00(3)	1.61(3)
	298	O2—H1···O5	2.696(2)	0.94(3)	1.76(3)
		O4—H6···O5	2.610(2)	1.03(3)	1.60(3)
DMU2-NBA	150	O2—H1···O5	2.465(1)	1.03(2)	1.45(2)
	300	O2—H1···O5	2.478(2)	0.98(3)	1.51(3)
DMU3-NBA	150	O1—H1···O3	2.500(2)	0.98(4)	1.53(4)
	300	O1—H1···O3	2.504(2)	0.94(3)	1.57(3)
DMU3-CBA	150	O3—H1···O5	2.481(2)	1.03(4)	1.46(3)
		O2—H24···O6	2.472(2)	1.00(4)	1.48(4)
	300	O3—H1···O5	2.484(4)	1.02(4)	1.46(4)
		O2—H24···O6	2.476(2)	1.09(4)	1.39(4)
DMU4-CBA	150	O2—H1···O3	2.516(2)	1.04(2)	1.49(2)
	300	O2—H1···O3	2.522(2)	1.14(3)	1.39(3)

Table 7.21 Hydrogen bond parameters in the molecular complexes, at low temperature (100 to 150 K) and at room temperature (300 K) continued.

Complex	T (K)	O—H···O	dO···O (Å)	dO—H (Å)	dH···O (Å)
DMU5-NIP	150	O1—H19···O3	2.459(2)	1.02(3)	1.45(3)
		O5—H20···O17	2.482(2)	0.96(3)	1.53(3)
		O14—H21···O9	2.450(2)	0.95(3)	1.51(3)
		O11—H100···O10	2.434(2)	1.07(3)	1.38(4)
	300	O1—H19···O3	2.464(2)	1.01(3)	1.47(3)
		O5—H20···O17	2.486(2)	0.91(4)	1.58(4)
		O14—H21···O9	2.458(2)	1.04(4)	1.43(4)
		O11—H100···O10	2.448(3)	1.04(3)	1.44(3)
DMU5-AIP	150	O2—H1···O3	2.503(1)	1.02(2)	1.51(2)
		O6—H5···O4	2.534(1)	0.91(2)	1.63(2)
	300	O2—H1···O3	2.515(2)	0.97(2)	1.56(3)
		O6—H5···O4	2.531(2)	0.97(3)	1.57(3)
DMU3-NP	150	O4—H1···O7	2.589(1)	0.93(2)	1.71(2)
		O2—H2···O7	2.563(2)	0.96(3)	1.62(3)
	300	O4—H1···O7	2.603(2)	0.90(3)	1.73(2)
		O2—H2···O7	2.565(2)	0.98(3)	1.61(3)
DMUIP	100	O2—H1···O3	2.508(1)	0.93(2)	1.59(2)
	300	O2—H1···O3	2.515(2)	0.93(4)	1.61(4)
PhU2,4-DNBA	150	O2—H1···O7	2.510(2)	1.00(3)	1.53(3)
	300	O2—H1···O7	2.515(3)	1.07(5)	1.45(5)
PhU3-NP	100	O2—H1···O3	2.643(2)	0.90(3)	1.74(3)
		O11—H2···O3	2.650(1)	0.91(2)	1.77(2)
		O6—H3···O10	2.607(2)	0.93(3)	1.69(3)
		O4—H4···O10	2.618(1)	0.90(3)	1.73(2)
	300	O2—H1···O3	2.675(2)	0.91(2)	1.78(2)
		O11—H2···O3	2.661(1)	0.91(2)	1.78(2)
		O6—H3···O10	2.628(2)	0.88(3)	1.75(3)
		O4—H4···O10	2.627(1)	0.89(2)	1.75(2)

Table 7.22 Hydrogen bond parameters in the molecular complexes, at low temperature (100 to 150 K) and at room temperature (298 to 300 K) continued.

Complex	T (K)	O—H···O	dO···O (Å)	dO—H (Å)	dH···O (Å)
3-DAZA3-NP	100	O2—H1···O9	2.504(1)	0.97(2)	1.54(2)
		O4—H2···O7	2.542(1)	0.92(2)	1.63(2)
	300	O2—H1···O9	2.503(2)	0.97(2)	1.53(2)
		O4—H2···O7	2.546(2)	0.95(2)	1.60(2)
3-DAZA2,4-DNBA	150	O1—H1···O7	2.449(1)	1.00(3)	1.45(3)
	300	O1—H1···O7	2.451(2)	0.93(4)	1.52(4)
INZ2,4-DNBA	150	N2—H6···O3	2.583(1)	1.05(2)	1.54(2)
	300	N2—H6···O3	2.579(2)	1.09(2)	1.49(2)
INZP	150	O2—H1···O3	2.379(1)	1.07(2)	1.31(2)
		N3—H2···O1	2.658(1)	0.98(2)	1.68(2)
	300	O2—H1···O3	2.370(2)	1.05(3)	1.32(3)
		N3—H2···O1	2.650(1)	1.00(2)	1.65(2)
	350	O2—H1···O3	2.368(2)	1.02(2)	1.35(2)
		N3—H2···O1	2.653(2)	1.01(2)	1.64(2)
IN2,4-DNBA I	150	N1—H1···O5	2.596(2)	1.06(2)	1.54(2)
	300	N1—H1···O5	2.599(2)	1.04(2)	1.57(2)
IN2,4-DNBA III	150	N1—H1···O1	2.599(2)	0.92(2)	1.68(2)

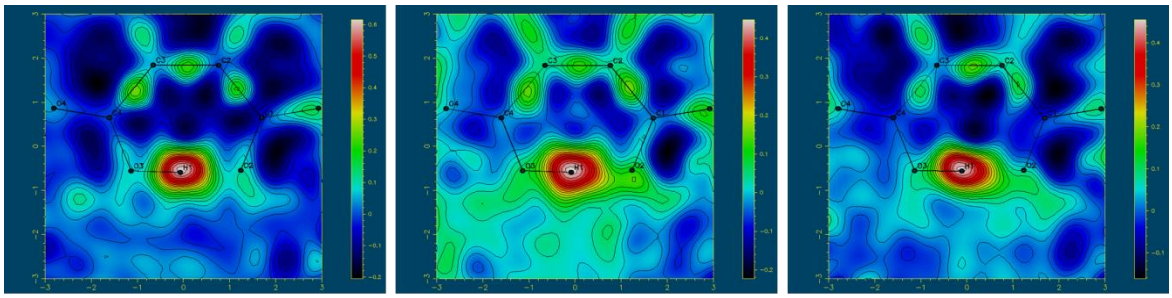

Figure 7.13 Variable temperature Fourier difference electron density maps showing the electron density associated with the H-atom in the O2—H1···O3 SSHB in INZP.

7.3.3 Following temperature dependent proton migration using synchrotron and X-ray diffraction

From the variable temperature synchrotron X-ray diffraction studies and refinement in SHELXL, [218] it was possible to identify temperature dependent proton migration in two molecular complexes DMU2,4-DNBA and INP.

Its identification, in these cases, is aided by consistent trends being observed across all information. In particular, the same migration trend is observed between the D—H and H···A lengths and the Fourier difference maps; this is important where Fourier difference maps give the most reliable picture of the hydrogen atom behaviour. [121] Trends in the reliably determined heavy atom positions, including donor-acceptor distances and bond lengths of the groups forming the SSHBs, also support the migration. There is not complete agreement in the refined hydrogen atom position and the peak maximum in the Fourier difference maps of these two systems. This is likely caused by the refined X-ray positions attempting to model the hydrogen atom density with a isotropic thermal parameter when, in an SSHB, it has a more anisotropic shape; this leads to an incorrect shifting of the atom away from its true position. [121] The difference is, however, small and consistent over the temperature range meaning the refined hydrogen atom positions can be relied on; this is further evidence of the importance of consistent trends being observed in these studies. The identification of temperature dependent proton migration in DMU2,4-DNBA and INP using the synchrotron technique is assisted by relatively noise free Fourier difference maps, for the reliable determination of hydrogen atom behaviour, and low values of error on the hydrogen atom bond parameters such that shifts in the proton positions are greater than the error limits for the determination and therefore significant; in DMU2,4-DNBA and INP the values of error on the D—H and H···A distances are relatively small at σ = 0.02 to 0.03, the errors increasing with determination temperature.

Temperature dependent proton migration is not identifiable in the other molecular complexes studied using synchrotron X-ray diffraction of 3-DAZABrA hydrate, DMU3,5-DNBA, DMUP and IN2,4-DNBA. In general, the Fourier difference maps are noisier than those of DMU2,4-DNBA and INP; this makes determination of hydrogen atom behaviour within them more difficult and in most cases, the combined evidence indicate a lack of proton migration. A conclusion that no proton migration is occurring in these molecular complexes would tend to be more reliable than proving that proton migration is present.

The use of the synchrotron technique, in these studies, therefore appears reliant on a number of factors. The importance of consistent trends across all information, particularly where supported by more reliable Fourier difference maps or heavy atom positions, is emphasised for confidence in the identification of temperature dependent proton migration using the synchrotron X-ray diffraction technique. This is not only of relevance here but also in all studies of proton transfer. Proton migration behaviour could also only be determined reliably where Fourier difference maps are relatively noise free; this emphasises the need for optimised Fourier difference maps in these studies. These studies implemented the same data collection strategy across the molecular complexes, collecting a fast scan to replace overloaded reflections followed by collecting

additional low angle data, where the hydrogen atom contribution to the scattering is more significant; with the speed of collection of the synchrotron and the intrinsically higher intensity, such a strategy can be deployed readily. The increased noise in the Fourier difference maps of 3-DAZABrA hydrate, DMU3,5-DNBA, DMUP and IN2,4-DNBA, compared to in those of DMU2,4-DNBA and INP, may therefore be a consequence of lower sample quality. Being able to determine the proton transfer behaviour using synchrotron X-ray diffraction may therefore also be dependent on the nature of the sample under study. Increased noise in some of the Fourier difference maps may also indicate the need for additional corrections such as for sample absorption or extinction. [142]

The potential of the synchrotron technique to collect diffraction data from which proton migration behaviour may be determined is indicated, provided conditions are optimised. The speed of data collection offered by the synchrotron technique is advantageous in the variable temperature studies allowing the proton transfer behaviour to be probed at a number of points along the 100 to 350 K temperature profile allowing a smoother observation of trends and in allowing these effects to be studied in an increased number of systems. The initial variable temperature studies carried out on a laboratory source were useful in the initial identification of molecular complexes to study at a synchrotron and in the identification of materials in which temperature dependent proton migration was unlikely to be occurring based on the D—H and H···A and SSHB donor-acceptor distances.

7.3.4 Proton migration effects

The study of temperature dependent proton migration in the molecular complexes allows an understanding of this process in the solid state.

The synchrotron X-ray diffraction studies indicated temperature dependent proton migration of 0.12 Å in DMU2,4-DNBA, between 200 and 350 K, and 0.1 Å in INP, between 100 and 350 K. The extents of temperature dependent proton migration across SSHB observed in molecular complexes in the literature are generally reported from neutron studies (Table 7.23). This makes a comparison of the extent of migration observed in DMU2,4-DNBA and INP to those previously reported more difficult; the neutron and X-ray diffraction techniques observe different characteristics of the hydrogen atom and as such hydrogen atom positions given by X-rays are shifted relative to those from neutrons. [94] However, it has been noted that, in a combined X-ray and neutron diffraction study of proton migration in urea phosphoric acid, a shift in the proton position as a result of migration was observed in neutron measurements to be 0.04 Å, while in X-ray measurements this was indicated to be 0.1 Å. [121] Considering this simple comparison, a shift of 0.12 Å, as observed for DMU2,4-DNBA from X-ray data, could be equivalent to a shift of 0.045 Å from neutron data. For DMU2,4-DNBA, a similar extent of proton migration to that in *N*,*N*-

dimethylurea oxalic acid is then found; [109] here the O—H···O hydrogen bond lengths are also similar suggesting that the conversion of apparent migration magnitudes between X-ray and neutron determinations may be a reasonable approximation. The extent of proton migration observed in DMU2,4-DNBA and INP is therefore in the range of that seen in previous proton migration studies (approximately 0.03 to 0.1 Å). The nature of the proton migration occurring for DMU2,4-DNBA is most similar to that in urea phosphoric acid [108] where the proton migrates across a charge assisted O^{+}—H···O^{-} SSHB, from the substituted urea end to the middle of the SSHB; the SSHB is however notably shorter in urea phosphoric acid. For INP, there are similarities in the nature of the proton migration occurring with 4,4-bipyridine 1,2,3,4-tetracarboxylic acid [110] and with pyridine-3,5-dicarboxylic acid [111] where the proton migrates across a charge assisted N^{+}—H···O^{-} SSHB away from the nitro end; however unlike in INP, in these molecular complexes the extent of migration is significantly greater such that at 300 K, the proton is closer to the oxygen atom.

Table 7.23 A comparison of the proton migration parameters for DMU2,4-DNBA and INP with those in the literature.

Complex	Interaction	dD···A (Å)	ΔpK_a	Migration T range (K)	Migration (Å)	Technique
Urea phosphoric acid [108]	O^+—H···O^- (at 100 K)	2.411(2)	-1.87	100 – 300	0.04	Neutron
N,N-dimethylurea oxalic acid [109]	O—H···O (at 100 K)	2.4469(9)	-1.56	150 to 300	0.045(9)	Neutron
N,N'-dimethylurea oxalic acid [109]	O—H···O (at 100 K)	2.4398(15) 2.4423(15)	-1.94	4 – 280	0.031(9)	Neutron
DMU2,4-DNBA	O^+—H···O^- (at 100 K)	2.446(1)	-1.12	200 – 350	0.12	X-ray
INP	N^+—H···O^-	2.551(1)	0.44	100 – 350	0.1	X-ray
Isoniazid 4-aminosalicylic acid [267]	O···H···N (H centrally located at 100 K)	2.548(2)	0.21	100 – 280	0.14	X-ray
Pyridine-3,5-dicarboxylic acid [110]	N^+—H···O^-	2.523(2)	1.8	15 – 296	0.09	Neutron
4,4'-bipyridine benzene-1,2,4,5-tetracarboxylic acid [111]	N^+—H···O^-	2.5220(17)	1.4	20 – 296	0.1	Neutron
Pentachlorophenol 4-methylpyridine [112]	O···H···N (H centrally located at 100 K)	2.506(2)	1.26	20 – 200 20 – 295	0.08 0.11	Neutron X-ray

Several explanations for the temperature dependent proton migration occurring across SSHBs have been suggested. A small number of studies attribute the migration to a static hydrogen bond potential with a shape such that the first excited state lies close to the acceptor atom and it becomes increasingly populated with temperature; the effect is observed as migration. [110, 111] In most cases, the effect of proton migration has been attributed to thermal fluctuations in the molecular environment induced by lattice vibrations; the result is a very subtle change in shape of the hydrogen bond potential energy well and a shift in the minimum, closer to the hydrogen bond acceptor atom. This explanation has been advanced for urea phosphoric acid, [299, 300] 3,5-pyridine dicarboxylic acid [110] and 4,4-bipyridine 1,2,4,5-tetracarboxylic acid. [111] In some cases no clear explanation has been advanced for the mechanism of proton migration, including in the case of

4-methyl pyridine pentachlorophenol, which is proposed to be caused by either a change in thermal population of a static unsymmetrical hydrogen bond potential well or by subtle changes in the potential well itself. [112] In molecular complexes of *N,N* and *N,N'*-dimethylurea oxalic acid, only a slight elongation in the hydrogen atom density was observed in Fourier difference maps calculated from neutron diffraction data, indicating that the apparent migration could be attributed to causes other than simply the effect of increased thermal motion. [109]

The temperature dependent proton migration behaviour occurring in the molecular complex of DMU2,4-DNBA is most similar to that in urea phosphoric acid, migrating from an off-centred to an increasingly centred position, with increasing temperature, in a charge assisted SSHB. As a function of temperature, there is also only a slight elongation in the hydrogen atom density in the X-ray Fourier difference maps indicating that the apparent migration can be attributed to causes other than just being an effect of increased thermal motion. Therefore, it could be that a similar proton migration mechanism, as occurring in urea phosphoric acid, [299, 300] occurs here in DMU2,4-DNBA; attributable to thermal fluctuations in the molecular environment induced by lattice vibrations. For INP, the nature of temperature dependent proton migration behaviour is most similar to that in 3,5-pyridine dicarboxylic acid [110] and 4,4-bipyridine 1,2,4,5-tetracarboxylic acid [111] where the proton migrates across a charge assisted N^{+}—H···O^{-} SSHB away from the nitrogen end. However, a significant smearing of the hydrogen atom density in the X-ray Fourier difference maps is observed with temperature and so it is less clear in this sample whether migration between 100 and 350 K is simply an effect of increased thermal motion or if the same mechanisms as those in 3,5-pyridine dicarboxylic acid and 4,4-bipyridine 1,2,4,5-tetracarboxylic acid are occurring, attributed to thermal fluctuations in the molecular environment induced by lattice vibrations.

<u>Manifestation of temperature dependent proton migration across SSHBs</u>

The observation of temperature dependent proton migration may allow insight into its manifestation in the solid state, and therefore design into future materials.

Temperature dependent proton migration has been reported for certain SSHB donor-acceptor distances only. For an O—H···O SSHB, a limit of 2.45 Å has been proposed, above which no proton migration is expected. In the molecular complexes containing O—H···O SSHBs, proton migration was only identifiable in DMU2,4-DNBA, where the O···O distance is 2.441(1) Å at 100 K. Proton migration is not indicated in any of the molecular complexes with O···O distances above 2.45 Å including molecular complexes with SSHB donor-acceptor distances just above the limit such as DMUP ($d_{O\cdots O}$ 2.493(2) and 2.452(2) Å at 100 K) and DMU3,5-DNBA ($d_{O\cdots O}$ 2.472(3) Å at 100 K). The previously proposed 2.45 Å limit for migration is therefore consistent with the

molecular complexes in this study. The shorter donor-acceptor distance favours the increasingly symmetric hydrogen bond potential energy surface and low barrier to proton transfer such that migration is possible. Being below the proposed 2.45 Å limit, however, does not appear to be a guarantee for the occurrence of proton migration. In 3-DAZABrA hydrate, an O—H···O SSHB is formed well below the limit ($d_{O\cdots O}$ 2.411(1) Å at 100 K) but no temperature dependent migration is indicated. Although the donor-acceptor distance is very short in this molecular complex, the hydrogen bond has low directionality (<OHO 152(4) °) and this may lead to a less symmetric potential well making proton migration less favourable. For an N^+—H···O^- SSHB, temperature dependent proton migration has not been identified above 2.55 Å; reported in isoniazid 4-aminosalicylic acid ($d_{N\cdots O}$ 2.548(2) Å), [267] pyridine-3,5-dicarboxylic acid ($d_{N\cdots O}$ 2.523(2) Å) [110] and 4,4'-bipyridine benzene-1,2,4,5-tetracarboxylic acid ($d_{N\cdots O}$ 2.5220(17) Å). [111] INP has the longest N^+—H···O^- hydrogen bond across which proton migration is identifiable ($d_{N\cdots O}$ 2.551(1) Å) and is just above the 2.55 Å limit. From variable temperature studies of IN2,4-DNBA, it was not possible to identify the presence of temperature dependent proton migration; in this complex the SSHB has a slightly longer donor-acceptor distance ($d_{N\cdots O}$ 2.555(1) Å) than INP. Therefore, it may be that the limit for proton migration across N^+—H···O^- SSHBs is somewhere in the narrow range of 2.551 and 2.555 Å. The SSHB distance is therefore shown to 'tune' the occurrence of proton migration across SSHBs.

The value of ΔpK_a has previously been correlated to the extent of proton migration occurring across O—H···O SSHBs in substituted urea organic acid molecular complexes; [109] a greater extent of proton migration was observed where the ΔpK_a of the two components forming the SSHB became increasingly less negative (i.e. approached zero). The values of ΔpK_a for each of the proton migration materials are included in Table 7.23. DMU2,4-DNBA has a value of ΔpK_a −1.12 and exhibits a large shift in proton position of 0.12 Å in the X-ray study, corresponding to an estimated shift of 0.045 Å from a neutron determination. Extents of proton migration observed in previous O—H···O SSHBs are, in increasing order, 0.031(9) Å for *N,N'*-dimethylurea oxalic acid, 0.04 Å for urea phosphoric acid, 0.045(9) Å for *N,N*-dimethylurea oxalic acid with increasingly less negative ΔpK_a values of −1.94, −1.87 and −1.56, respectively. DMU2,4-DNBA fits in this trend alongside *N,N*-dimethylurea oxalic acid with an estimated shift of approximately 0.045 Å for neutrons and a ΔpK_a value of −1.12. These findings are therefore in support of the trend suggested by Jones *et al*. (2012) on the nature of proton migration across SSHBs in substituted urea organic acid molecular complexes related to ΔpK_a values. [109] One finding of interest is the lack of variable temperature proton migration suggested in 3-DAZABrA hydrate, despite the presence of a very short SSHB ($d_{O\cdots O}$ 2.411(1) Å) and the ΔpK_a value of 0.06; this ΔpK_a is the closest to zero amongst the relevant complexes studied to date. It may be that that some imbalance in the pK_a values is

required for any proton migration to be observed between components. Across the previously studied N^+—H···O^- proton migration materials, including INP from this chapter, an opposite and less consistent trend is observed; the extent of proton migration appears to increase as the ΔpK_a values are more positive and further away from zero. The extents of proton migration observed in N^+—H···O^- SSHBs are, in increasing order, 0.1 Å for INP in the X-ray study, corresponding to an estimated shift of 0.04 Å from a neutron determination, 0.14 Å for isoniazid 4-aminosalicyclic acid in the X-ray study, corresponding to an estimated shift of 0.056 Å from a neutron determination, 0.08 Å for pentachlorophenol 4-methylpyridine, 0.09 Å for pyridine-3,5-dicarboxylic acid and 0.1 Å for 4,4-bipyridyl-benzene-1,2,4,5-tetracarboxylic acid. The corresponding ΔpK_a values are 0.44, 0.21, 1.26, 1.8 and 1.4, respectively. The problems of transferring pK_a values to the solid state, only valid under the solution equilibrium conditions at which they were determined, [88] are therefore indicated. It may be that ΔpK_a values may be used to access temperature dependent proton migration materials in crystal engineering strategies, seeming more likely for those containing O—H···O SSHBs proton migration, however further examples are required before this can be proven.

7.4 Parametric structural refinement in Topas-Academic V5.0

Parametric structural refinement in Topas-Academic V5.0 [168] has also been applied in the study of temperature dependent proton migration in this research project. The approach is trialled and developed on variable temperature single crystal synchrotron X-ray diffraction data collected on molecular complexes DMU2,4-DNBA, identified as a proton migration material in §7.3, and for the molecular complex of benzimidazole 4-hydroxybenzoic acid (BZN4-OHBA) which has been identified as having ambiguity in the proton transfer behaviour. [301]

Two approaches were applied for the single crystal synchrotron variable temperature X-ray diffraction data collections. These were (i) collecting data at each temperature with stepwise temperature ramping (STEP) and (ii) collecting data with a continuous ramping of temperature (CONT.). The continuous ramping method allows evolving information to be accessed along the temperature profile. For the sample DMU2,4-DNBA, single crystal variable temperature diffraction data were collected in a step wise approach collecting in 10 K temperature steps, between 100 and 350 K. For BZN4-OHBA, single crystal variable temperature diffraction data were collected in a step-wise temperature ramping approach collecting in 20 K temperature steps, between 100 and 300 K and also collected continuously, with a continuous ramping of temperature (120K hr^{-1}); the data could then be split into various temperature increments, with a single average temperature determined for each effective diffraction pattern from experimental log files.

7.4.1 Setting up the refinement of single crystal data in Topas-Academic V5.0

The setup of a parametric refinement in Topas-Academic V5.0 [168] was carried out in two stages. An input file for structural refinement at a single temperature was first set up in which the structural models for DMU2,4-DNBA and BZN4-OHBA were optimised and refinement choices finalised. This single temperature input file (single/rigid.inp) was then used as the 'seed' to generate the multi-temperature parametric input file (multi.inp) for structural refinement over the specified temperature range and variable temperature data.

Both the single and multi-temperature files were set up with the same format, having sections for:

- general refinement information including the output R-factors (R_{wp}) (§4.2.3);
- 'define…' to select refinement choices;
- 'use_t0000' for the selection of temperature/dataset against which to refine;
- 'xdd_scr' containing information for each data set (seed information) including unit cell parameters, selected structural information and refinement choices;
- 'for xdds' containing data treatment information for all data sets (weighting schemes and data cut-offs);
- 'for strs' within the 'for_xdds' section containing the structural model to be refined against the data.

Single.inp

Initial single temperature single crystal structural refinements were performed on the 100 K data set for each molecular complex in a single.inp file in Topas-Academic V5.0. [168] A number of refinement parameters were varied within the file to optimise the structural model. The structural model was assessed based on the value of the refined R-factor (R_{wp}).

The input starting model was that of the 100 K structure, in CIF format, for each molecular complex obtained from crystal structure solution and refinement against the 100 K data set using SHELX programs [218, 219] in the WingGX package. [221] The same starting model was used for BZN4-OHBA STEP and BZN4-OHBA CONT.; that of BZN4-OHBA STEP at 100 K. Each structure was refined against the data with a 2Θ cut off of 60 ° for DMU2,4-DNBA and 50 ° for BZN4-OHBA STEP and CONT., chosen where there were few reflections with significant intensity beyond these limits, and a standard Topas-Academic V5.0 [168] weighting scheme, weighting reflections with a value of 1 if Yobs<1, or equal to 1/Yobs, if Yobs > 1. An extinction coefficient was also applied as this was seen to improve the refinement.

In the structural model, the atomic coordinates were allowed to vary within minimum and maximum limits (±0.05) and the atomic thermal displacement parameters were also refined. The hydrogen atom isotropic thermal parameters were refined with B_{eq} values, constrained to be equal and allowed to vary within minimum and maximum limits (±5). The heavy atom thermal parameters were refined both isotropically and anisotropically, with individual U_{eq} values; anisotropic refinement in Topas-Academic V5.0 [168] was made possible by the quality of the single crystal data. A thermal correction was applied to the structure factors involving an isotropic scaling of the thermal parameters at each temperature using, either an isotropic temperature factor proportional to B_{eq} (Equation 7.1), Bfix, or proportional to U_{iso} (Equation 7.2), Ufix.

Equation 7.1 $$\boldsymbol{isotropic\ scaling\ Bfix = e^{[B_{eq}\ sin^2(\theta)/\lambda^2]}}$$

Equation 7.2 $$\boldsymbol{isotropic\ scaling\ Ufix = 8\pi^2 e^{[B_{eq}\ sin^2(\theta)/\lambda^2]}}$$

where 1 B_{eq} is equivalent to $8\pi^2 U_{iso}$

The success of each model was assessed in the output R-factors. Low R-factors were achieved for each model (Table 7.24) indicating a good refinement and in each case, well behaved structures were refined. Anisotropic refinement of the heavy atom thermal parameters gave lower R-factors than isotropic refinement suggesting it to be the better model. There were no differences in the R-factors on changing the type of thermal correction applied to the data; as Ufix values are more commonly used in small molecule crystallography, it will be the thermal correction applied in all models that follow.

Table 7.24 The R-factors for the different refinement models of the heavy atom thermal parameters for each molecular complex at 100 K.

		R-factor	
Molecular complex	Model for heavy atoms thermal parameters	Bfix	Ufix
DMU2,4-DNBA	Anisotropic	7.03	7.03
	Isotropic	13.13	13.13
BZN4-OHBA STEP	Anisotropic	10.52	10.52
	Isotropic	16.04	16.04
BZN4-OHBA CONT.	Anisotropic	10.59	10.59
	Isotropic	15.55	15.35

The data treatment information and structural model are included in single.inp in the ‘for_xdds’ section.

Rigid.inp

The structural model in the single.inp was developed to include refinement of molecules as rigid bodies (rigid.inp) with rotational and translational components defined about a central atom. This allowed a reduction in the number of overall refinement parameters. The rotations and translations of each molecule were included in the ‘xdd_scr’ section. Rigid bodies were refined for the isotropic and anisotropic thermal parameter models; there was no change in the R-factors on applying this model (Table 7.25) at 100 K. The stability of this rigid body model was also tested as the data collection temperature approached room temperature. In the case of the anisotropic refinement of thermal parameters, the R-factor experienced a small increase in each molecular complex and the structure remained stable. In contrast, the isotropic refinement of thermal parameters in the rigid body at 300 K led to an unstable refinement of the structural model in which the hydrogen atoms were no longer in sensible refined positions. For the stable refinement of hydrogen atoms at all temperatures, a model with anisotropic thermal parameters is therefore recommended.

A TLS approximation for rigid body motion was also trialled (§2.4.3) in order to introduce a low parameter method to describe heavy atom thermal parameter evolution as a function of temperature. This model was implemented in the ‘xdd_scr’ section. To implement the TLS model, the TLS tensors were set to starting values of zero and the atomic fractional coordinates, taken from the ‘for_strs’ in the ‘for_xdds’ section, were converted to Cartesian coordinates using Equation 2.22 and Equation 2.23 (§2.4.3). The Cartesian coordinates were then used, alongside the TLS tensors, as refined from the data to generate the TLS modelled anisotropic thermal parameters (U_{11}, U_{22}, U_{33}, U_{12}, U_{13}, U_{23}); the TLS modelled U_{ij} were output in Cartesian format for the non-orthorhombic complexes (BZN4-OHBA). Larger R-factors were refined for the TLS model (Table 7.25), particularly at the higher temperature, compared to normal refinement of the anisotropic thermal parameters. However, where the increase is small, the TLS model may be suitable for the refinement of the heavy atom thermal parameters.

Table 7.25 The R-factors for the different refinement models of the heavy atom thermal parameters at low and high temperature for each molecular complex. An 'x' denotes an unsuccessful refinement.

Molecular complex	Model for heavy atom thermal parameters	100 K	290 K	300 K
DMU2,4-DNBA	Isotropic	13.13	-	x
	Normal anisotropic	7.03	-	8.57
	TLS	10.76	-	17.82
BZN4O-HBA STEP	Isotropic	16.03	-	x
	Normal anisotropic	10.51	-	11.98
	TLS	12.80	-	16.99
BZN4-OHBA CONT.	Isotropic	15.35	x	-
	Normal anisotropic	10.59	10.42	-
	TLS	15.23	10.41	16.09

The high temperature heavy atom thermal parameters were compared visually between the anisotropic and TLS models for each molecular complex (§A7.3, Figure A7.4 to Figure A7.5). Figure 7.14 is representative of the comparison, shown for DMU2,4-DNBA. There was some agreement in the visual appearance of the thermal parameters between the normal and TLS modelled anisotropic thermal parameters in each molecular complex. Alongside the similarities in R-factors, this indicates the TLS model may be suitable for the refinement of the heavy atom thermal parameters in place of a normal anisotropic model. To further assess the correctness of the TLS model set up in Topas-Academic V5.0, [168] refinement of each high temperature structure was also carried out in Jana2006, [223] refined with both normal and TLS heavy atom anisotropic thermal parameters. There was some agreement in the visual appearance of the thermal parameters between the Topas-Academic V5.0 [168] and Jana2006 [223] TLS refinements (§A7.3, Figure A7.4 to Figure A7.5).

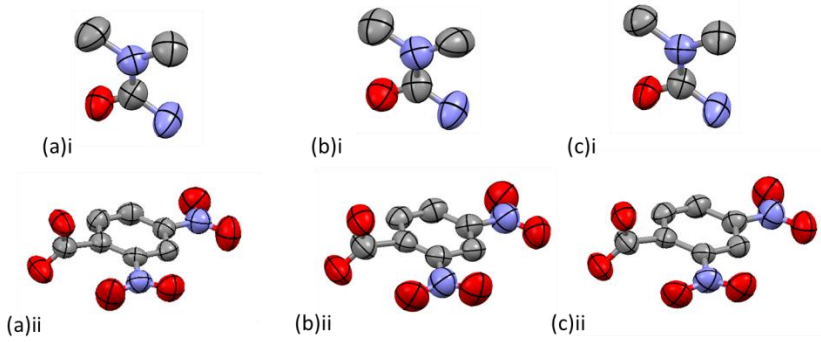

Figure 7.14 A comparison of the heavy atom thermal parameters modelled using (a) normal, (b) TLS refinement in Topas Academic V5.0 [168] and (c) TLS refinement in Jana2006 [223] in DMU2,4-DNBA at 300 K.

The TLS tensor values between the Topas-Academic V5 [168] and Jana2006 [223] refinements were also compared (§A7.3, Figure A7.6 to Figure A7.10). The S term was small to almost negligable for all molecular components and thus there was good agreement between the Topas-Academic V5.0 [168] and Jana2006 [223] output values. The L terms were also small for all molecular components and again there was good agreement between the Topas-Academic V5.0 [168] and Jana2006 [223] output values. The T tensors were the largest, with those output from Topas-Academic V5.0 [168] generally disagreeing with those output from Jana2006; [223] larger values were output from Topas-Academic V5.0. [168] The discrepancies in the TLS tensors between the different refinement programs indicate that the approximation in Topas-Academic V5.0 [168] may not be correct. This may be caused by differences in the refinement parameters between the software programs; in addition, in this case only a basic TLS refinement was carried out in Jana2006, [223] which may not be optimised. However, where the R-factors and visual appearance of the refined anisotropic thermal parameters indicated the Topas-Academic V5.0 [168] TLS approximation to be reasonable, it was trialled alongside a normal anisotropic refinement to model the heavy atom thermal parameters over the multi-temperature datasets.

Definition of the hydrogen atom behaviour

The hydrogen atom of interest in each molecular complex was defined in the 'xdd_scr' section of the rigid.inp file, separate from the rest of the molecular structure in the 'for_xdds' section. This allowed models to be applied to the hydrogen atom position as a function of temperature. Two models were employed, defined using 'ifdef' statements which could be selected or deselected in the general refinement choices section. Model 1 'H_{free}' allowed free refinement of the hydrogen position over the temperature range, within minimum and maximum limits (±0.05). Model 2 'H_{para}' applied parametric behaviour to the hydrogen atom position over the temperature range where an aim of this work was to 'drive' a linear migration trend (H_{para}) of the hydrogen atom position that could be benchmarked against the data during the parametric refinement. A modified version of the Taylors series expansion (Equation 7.3) [167] was used.

Equation 7.3 $$\boldsymbol{H_{xyz} = H_{x0y0z0} \times (1 + ax * 1e^{-6} \times T_{shift} + bx \times 1e^{-6} \times T_{shift}^{2})}$$

where H_{xyz} contains the atomic coordinates of the hydrogen atom, H_{x0y0z0} contains the initial atomic coordinates of the hydrogen atom, *a* and *b* are the Taylor expansion coefficients refined over the whole data and T_{shift} is defined by Equation 7.4 and is used to reduce correlations and bring the temperatures onto a -1 to +1 scale. [167]

Equation 7.4 $$\boldsymbol{T_{shift} = \left(\frac{(2\times(T_e - T_{min}))}{(T_{max} - T_{min})} - 1\right)}$$

Multi.inp

The single temperature refinement rigid.inp containing the finalised structural model and refinement choices were used to generate the multi-temperature parametric file (multi.inp). The rigid.inp file was modified to include 'use_t0000' for all temperatures over the studied range. The 'xdd_scr' section was also expanded for its application to each refinement temperature, carried out using the program Substitute. [302]

Several multi.inp files were set up in which different refinement models were applied. These included refining the heavy atom thermal parameters using a normal anisotropic model or modelled using the TLS approximation (the TLS behaviour was defined in the 'xdd_scr' at each temperature). The rigid-body rotations and translations were also defined by two models (defined in the 'xdd_scr' section at each temperature); allowed either to refine freely at each temperature, except at 100 K where they were fixed, or fixed at each temperature (at those of the 100 K structure) and having the effect of reducing refinement parameters.

An approach of refining over all data sets simultaneously (a surface approach) and carrying out consecutive single refinements (an independent approach) at each temperature was also trialled.

7.4.2 Parametric structural refinement using multi.inp in Topas-Academic V5.0

The multi-temperature multi.inp files for each molecular complex and for the different models were run in Topas-Academic V5.0. [168]

R-factors

Both independent and surface refinements were trialled for each multi.inp. The surface refinements were stable for all molecular complexes leading to well behaved structures and anisotropic thermal parameters. In contrast, the independent approach was only stable for the TLS refinement of anisotropic thermal parameters for DMU2,4-DNBA (H_{free} only) and BZN4-OHBA STEP (H_{free} and H_{para}). The overall R-factors for the surface refinements are presented in Table 7.26 and Table 7.27 for the different H_{free} and H_{para} models.

Between the different surface refinements, the refinement of the rigid body rotations and translations at each temperature (except at 100 K) was indicated as a better approach than their fixing at the same start values over the temperature range, giving lower overall R-factors for each molecular complex and being the most structurally stable. When all rigid in the TLS approach, the anisotropic thermal parameters became non-positive definite indicating the fixing of the rigid body rotations and translations at the same start values over the temperature range to be unsuitable here. Higher overall R-factors were obtained for the refinement of the anisotropic thermal parameters

using the TLS approach compared to when a normal anisotropic refinement was employed. However, the increase is small suggesting the TLS approach to be an appropriate model; the TLS anisotropic thermal parameters were also seen to increase in size as a function of temperature indicating this model to be working. There was little difference in the overall R-factors refined for H_{free} and H_{para} hydrogen atom behaviour models. Of interest, in the surface refinement of BZN4-OHBA CONT., where the refinement of the rigid body rotations and translations (except at 100 K) was carried out, the implementation of the H_{free} model led to a single nitrogen atom having non-positive definite thermal parameters at 100 K whilst the implementation of H_{para} led to sensible thermal parameters for this atom at 100 K; this indicates the importance of every parameter contributing to the overall structural refinement.

Table 7.26 Overall R-factors from the surface parametric refinement of each molecular complex employing H_{free}.

Thermal Parameters	Normal anisotropic		TLS	
Rigid-body refinement	100 K rigid only	All rigid	100 K rigid only	All rigid
DMU2,4-DNBA	14.92	19.34	19.77	-
BZN4-OHBA STEP	14.54	17.23	15.76	-
BZN4-OHBA CONT	15.25	18.06	18.18	-

Table 7.27 Overall R-factors from the surface parametric refinement of each molecular complex employing H_{para}.

Thermal Parameters	Normal anisotropic		TLS	
Rigid-body refinement	100 K rigid only	All rigid	100 K rigid only	All rigid
DMU2,4-DNBA	14.87	19.34	19.19	-
BZN4-OHBA STEP	14.54	17.23	15.80	-
BZN4-OHBA CONT	15.24	17.95	16.57	-

The R-factors for each molecular complex for each temperature data set were also recorded. (§A7.3, Figure A7.11 to Figure A7.18). Figure 7.15 is representative of the variable temperature R-factor (R_{wp}) plots. The free refinement of the anisotropic thermal parameters with an isotropic scaling led to a well-shaped plot of the R-factors as a function of temperature; the low and high temperatures had R-factors at extremes. The implementation of the TLS model of the anisotropic thermal parameters led to an increase in the R-factors at each temperature but also had a general effect of flattening out the well-shaped changes. The surface refinements led to much flatter trends in the R-factors than the independent refinements as a function of temperature (Figure A7.12 and Figure A7.15).

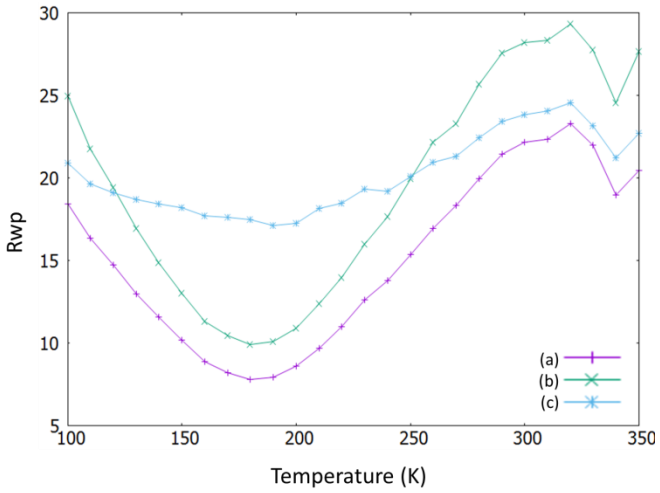

Figure 7.15 R_{wp} as a function of temperature for DMU2,4-DNBA for the surface refinement model H_{free} (a) normal anisotropic 100 K rigid only, (b) normal aniso all rigid and (c) TLS 100 K rigid only.

TLS tensors

The TLS tensors refined from the TLS model of anisotropic thermal parameters (§A7.3, Figure A7.19 to Figure A7.35) indicated that, as a function of temperature for DMU2,4-DNBA and BZN4-OHBA, the translational elements of the rigid body motion increased the most followed by the librational elements whilst there was little change in S tensors.

Proton migration effects

Across the molecular complexes, the best multi-temperature structural refinements in Topas-Academic V5.0 [168] were indicated as those which involved a surface approach where the rigid body rotations and translations (except at 100 K) were refined and where normal anisotropic thermal parameters were refined or modelled using the TLS method. The proton migration behaviour was assessed using these best approaches for each molecular complex in the D—H and H···A distances of the SSHB output from these approaches, for the H_{free} and H_{para} models.

DMU2,4-DNBA

The proton migration behaviour for each surface refinement is shown in Figure 7.16. For the H_{free} models (Figure 7.16(a)i and b(i)), there is good agreement in the proton migration behaviour suggested between the normal anisotropic and TLS refinement of the anisotropic displacement parameters; the hydrogen atom transfers from a central position in the hydrogen bond back towards the protonated DMU molecule as a function of temperature. For the H_{para} models (Figure 7.16(a)ii and (b)ii), there is good agreement in the proton migration behaviour suggested between 150 and 350 K by the normal anisotropic and TLS refinement models of the anisotropic displacement parameter; the hydrogen atom transfers from a central position in the hydrogen bond

back towards the protonated DMU molecule as a function of temperature. Below 150 K, the hydrogen atom start points differ; the TLS refinement of the anisotropic thermal parameters indicates a less central starting position for the hydrogen atom however this difference may be consistent within error.

The H_{para} and H_{free} models show similar proton transfer behaviour; the application of the H_{para} model appears to smooth the trend observed. The trend in the proton transfer behaviour suggested by these models is, however, not in agreement with that suggested in §7.3.1 from the single crystal refinements of variable temperature data in SHELXL-2013; [219] the proton migrates from the DMU towards the centre of the hydrogen bond between 200 and 350 K. It was, however, possible to obtain similar behaviour to that from SHELX on using a variation of the H_{para} model (H_{para_2}) where *a* and *b* were set to zero in Equation 7.3 and, at each temperature, the refinement was referred back to the starting H_{x0y0z0} in the 'for_xdds' section. This was applied in a surface refinement with the refinement of the rigid body rotations and translations (except at 100 K) (Figure 7.17).

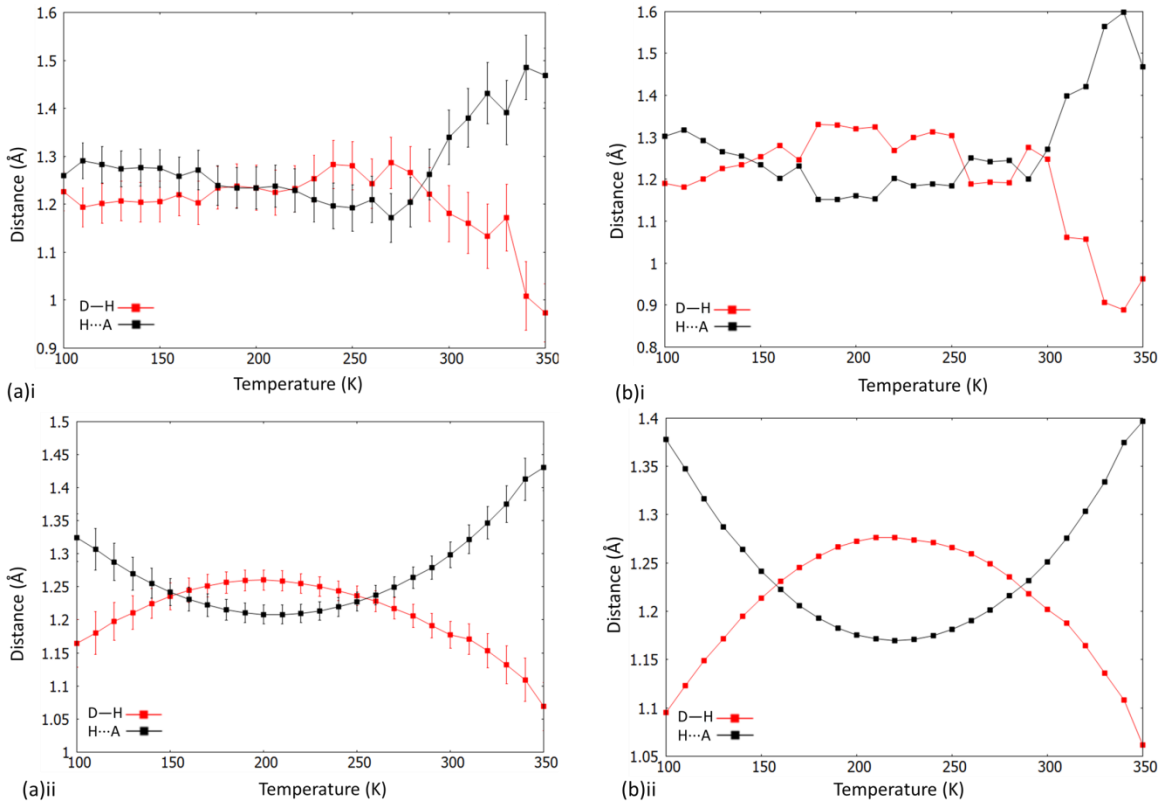

Figure 7.16 The change in the D—H and H···A distances in DMU2,4-DNBA over the 100 to 350 K temperature range for refinement model (a) normal anisotropic and (b) TLS modelled anisotropic thermal parameters for proton transfer model (i) H_{free} and (ii) H_{para}. Note: a stable refinement could not be achieved whilst calculating errors for the D—H and H···A distances using the TLS model.

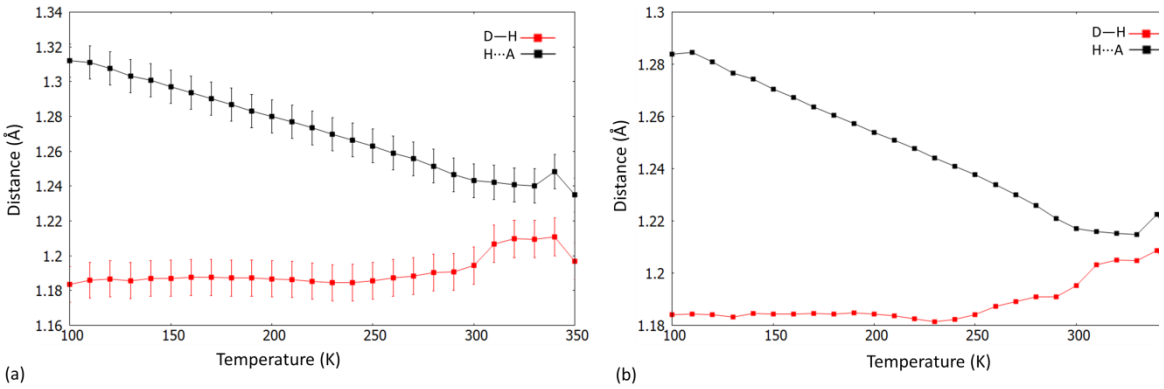

Figure 7.17 The change in the D—H and H···A distances in DMU2,4-DNBA over the 100 to 350 K temperature range for the H_{para_2} hydrogen transfer model for (a) normal anisotropic and (b) TLS modelled anisotropic thermal parameters. Note: a stable refinement could not be achieved whilst calculating errors for the D—H and H···A distances using the TLS model.

BZN4-OHBA STEP

The proton migration behaviour for each surface refinement is shown in Figure 7.18. For the H_{free} models (Figure 7.18 (a)i and (b)i), the proton migration behaviour suggested disagrees between the normal anisotropic and TLS refinement models of the anisotropic displacement parameters; the normal anisotropic displacement parameters model suggests migration of the proton towards the centre of the hydrogen bond as a function of temperature whilst the TLS refinement indicates little change in the hydrogen atom position. For the H_{para} models (Figure 7.18 (a)ii and (b)ii), there is some agreement in the proton migration behaviour suggested between normal anisotropic and TLS refinement models of the anisotropic displacement parameters; the hydrogen atom undergoes some transfer towards the centre of the hydrogen bond as a function of temperature. However, where this movement is only very slight, this could also be interpreted as no migration occurring. The surface refinement with H_{free} employed alongside the normal refinement of anisotropic thermal parameters results in the least similar behaviour to the other three models; the hydrogen atom moves from a less centred position at 100 K.

The single crystal refinement of variable temperature data in SHELXL-2013 [219] (Figure 7.19) does not indicate any significant proton migration in this molecular complex as a function of temperature. The surface models, excluding normal anisotropic thermal parameters, therefore appear to agree in this case with the SHELXL-2013 [219] refinements. A variation of the H_{para} model (H_{para_2}), where *a* and *b* were set to zero in Equation 7.3 and, at each temperature, the refinement was referred back to the starting H_{x0y0z0} in the 'for_xdds' section, was also applied in a surface refinement with the refinement of the rigid body rotations and translations (except at 100 K) for BZN4-OHBA (Figure 7.20). A similar trend of a slight shift in proton position, that could be

considered as indicating no migration, was observed for the normal anisotropic and TLS refined anisotropic displacement parameters.

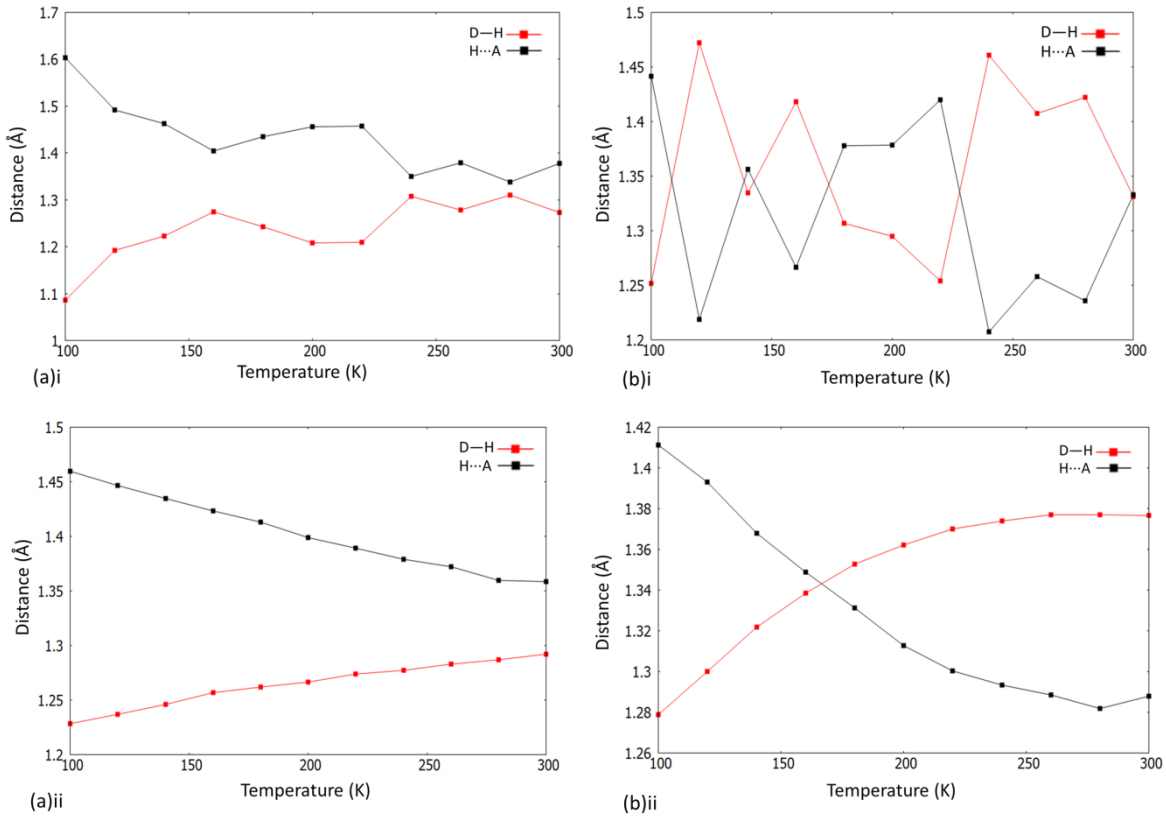

Figure 7.18 The change in the D—H and H···A distances in BZN4-OHBA STEP over the 100 to 300 K temperature range for refinement model (a) normal anisotropic and (b) TLS modelled anisotropic thermal parameters for proton transfer model (i) H_{free} and (ii) H_{para}. Note: it was not possible to calculate errors on the D—H and H···A distances for this molecular complex.

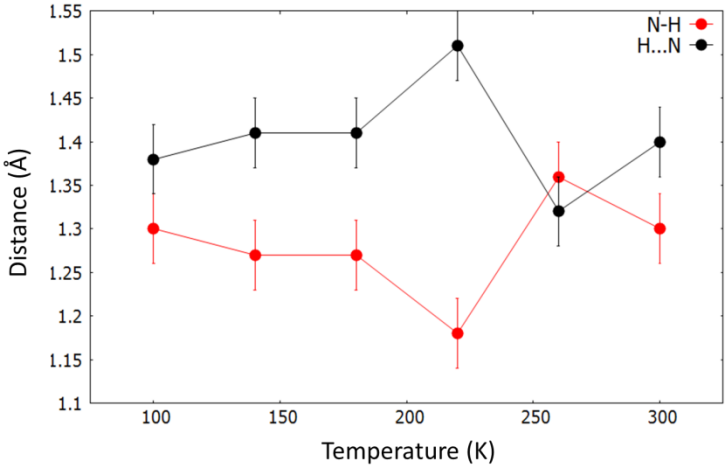

Figure 7.19 The change in the N—H and H···N distances in BZN4-OHBA over the 100 to 300 K temperature range from single crystal refinement in SHELX. [219]

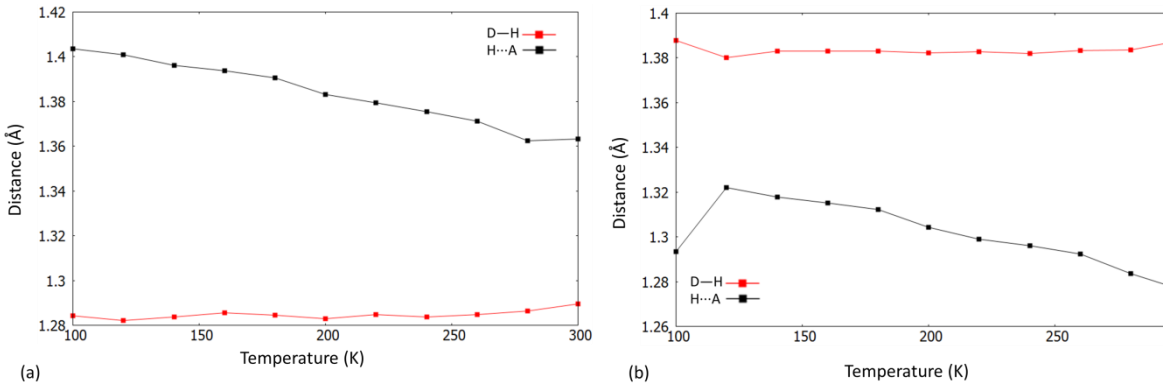

Figure 7.20 The change in the D—H and H···A distances in BZN4-OHBA STEP over the 100 to 300 K temperature range for the H_{para_2} hydrogen transfer model refined for (a) normal anisotropic and (b) TLS modelled anisotropic thermal parameters. Note: it was not possible to calculate errors on the D—H and H···A distances for this molecular complex.

BZN4-OHBA CONT.

The proton migration behaviour for each surface refinement is shown in Figure 7.21. For the H_{free} models (Figure 7.21(a)i and (b)i), the proton migration behaviour suggested in the normal anisotropic and TLS refinement of the anisotropic displacement parameter strongly agree; little change in the hydrogen atom position is indicated as a function of temperature. There is also strong agreement between the normal anisotropic and TLS refinement models of the anisotropic displacement parameter for the H_{para} model. The hydrogen atom position appears to shift slightly from an off-centre position on one side of the hydrogen bond to an off-centred position on the other side of the hydrogen bond; this shift may be within error and can be interpreted as indicating that no migration occurs over the temperature range.

For this continuous approach, the H_{para} models appear to give a smoother description of the hydrogen transfer behaviour occurring. The lack of proton migration being observed by the different refinements in models in Topas-Academic V5.0 [168] is in agreement with that suggested by the single crystal refinements in SHELXL-2013 [219] (Figure 7.19). This continuous temperature ramping data collection approach reveals more information about the changing nature of the hydrogen atom picture than obtained in the stepwise temperature ramping approach (BZN4-OHBA STEP) where points along the temperature profile are missed.

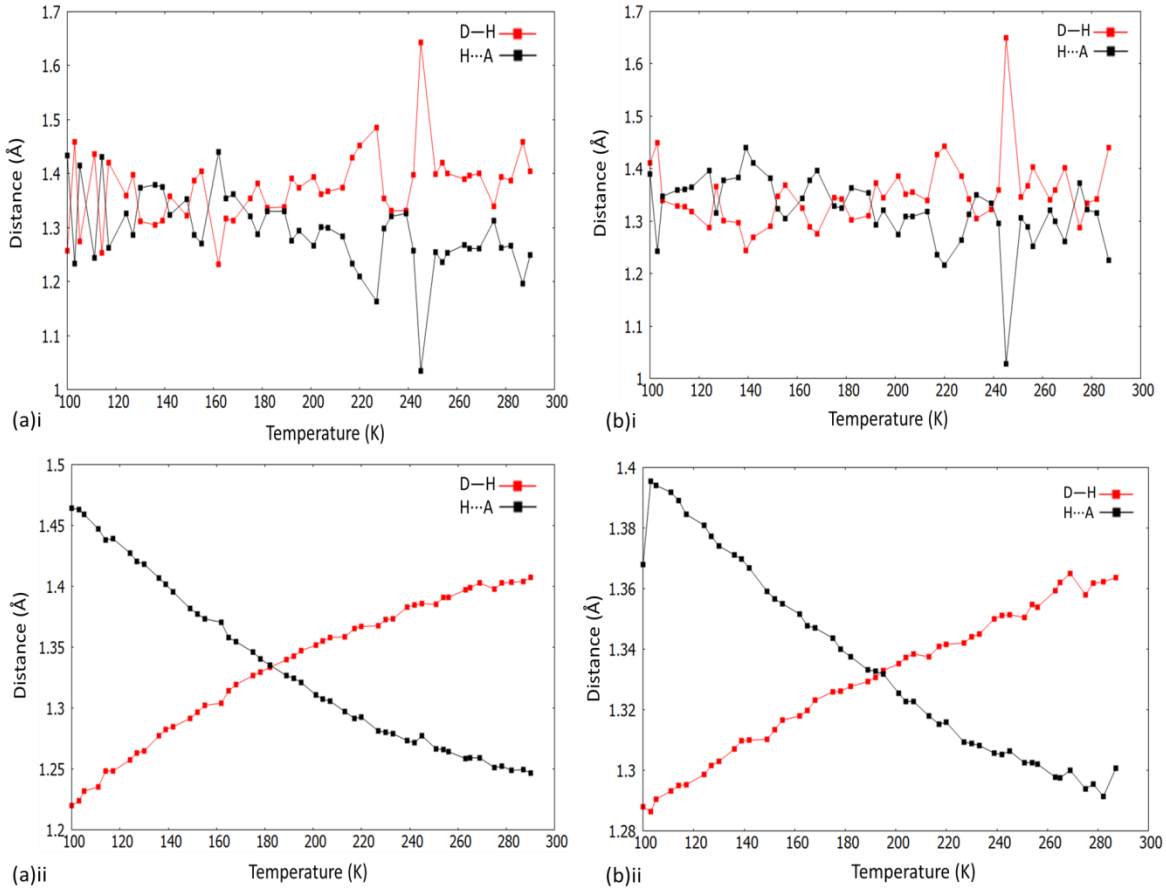

Figure 7.21 The change in the D—H and H···O distances in BZN4-OHBA CONT. over the 100 to 300 K temperature range for refinement model (a) normal anisotropic and (b) TLS modelled anisotropic thermal parameters for proton transfer model (i) H_{free} and (ii) H_{para}. Note: it was not possible to calculate errors on the D—H and H···A distances for this molecular complex.

7.4.3 Method assessment

The application of parametric structure refinement to multi temperature single crystal synchrotron X-ray diffraction data in Topas-Academic V5.0 [168] has been developed in this research project for variable temperature data collected on the molecular complexes of DMU2,4-DNBA and BZN4-OHBA.

In the initial stages of the development of the parametric structure refinement method, a number of models were trialled to determine how to achieve method optimisation. This method was found to be optimised, in terms of the refinement parameters, in surface refinements in which the molecular components are defined as rigid bodies whose rotations and translation may refine over the temperature range, except at 100 K, and where anisotropic thermal parameters are employed either refined freely with an isotropic scaling (normal anisotropic) or modelled using the TLS approach. In particular, the implementation of the TLS model allowed a flattening of the R-factors over the temperature range indicating that a reasonable fit of the refined structure to the data is occurring at

all temperatures compared to the normal anisotropic refinement approach in which the fit was significantly poorer at the temperature extremes. The parametric structure refinement method could also be optimised in terms of the raw data. Two methods were trialled for the variable temperature data collection for molecular complex BZN4-OHBA including a step wise temperature ramping approaching (STEP) and a continuous temperature ramping approach (CONT.). The CONT. approach allowed a more complete picture of the changes in the hydrogen atom position as a function of temperature to be accessed which was missed by the STEP approach collecting over larger stepwise 20 K temperature intervals.

The optimised method gave sensible structural outputs and allowed proton migration behaviour, defined by models, to be followed as a function of temperature in both DMU2,4-DNBA and BZN4-OHBA STEP and CONT. The proton migration behaviour suggested by the optimised models, however, was not always in agreement with that from single crystal refinements in SHELXL-2013. [219] This appeared to be heavily related to the model used to drive the hydrogen atom position as a function of temperature. For example, in DMU2,4-DNBA it was not possible to observe the same proton migration behaviour using the H_{free} and H_{para} models as found from single crystal refinements in SHELXL-2013. [219] In general, at a particular temperature, the hydrogen atom position was shifted in the surface refined structures relative to its position in a single temperature refinement; the D—H distances were longer in the surface refinements. For example, the N^{+}—H distance was elongated for the 100 K structure from 1.12 Å in a single temperature refinement (in a rigid.inp) to 1.22 Å in a H_{free} surface refinement (1.22 Å). It may be that, during the surface refinements, an averaging effect occurs on the positions of the hydrogen atom of interest across the temperature range. It was possible to observe similar proton migration behaviour to that found from the SHELXL-2013 [219] refinements for DMU2,4-DNBA when an altered version of the H_{para} model was used. In this model, at each temperature, the refinement was referred back to H_{x0y0z0} in the 'for_xdds' section, the 100 K coordinates for the hydrogen atom from the CIF. This is in contrast to the H_{free} and H_{para} models where the hydrogen atom of interest is included in each 'xdd_scr' section only and its position may be averaging over the data. In general, similar proton migration behaviour was observed between the H_{free} and H_{para} models and the H_{para} model gave a smoothing of the trend observed. The difference in the refined hydrogen atom behaviour observed between the hydrogen atom models (i.e SHELXL-2013 [219] versus Topas-Academic V5.0) [168] may indicate that, for these systems, it may be beyond the capabilities of the available data to constrain the hydrogen atom behaviour to be driven in a certain way (such as by the H_{para} models which may be pushing it too far).

The parametric structure refinement method developed in this research project is in the early stages of implementation and requires further investigation; the initial results indicate potential for

its application in these proton migration studies. The TLS description of anisotropic thermal parameters, in particular, requires more development where it appears to work for the systems of DMU2,4-DNBA and BZN4-OHBA but has not been confirmed as correct by other refinement programs. It would therefore be beneficial to explore the TLS implementation further. The choice of the model for the variable temperature hydrogen atom behaviour also gives significant variation in behaviour observed. It is therefore important in these studies to trial a number different models for hydrogen atom behaviour, it may be that one size does not fit all; further investigations into the different hydrogen atom behaviour models to implement are required. It would be interesting to develop this method further to study the evolution of the hydrogen atom thermal parameter as a function of temperature, with a D—H distance fixed, or to apply this type of investigation to studies of proton disorder, where site occupancies can be refined in Topas-Academic V5.0. [168]

7.5 Conclusions

In this chapter, single crystal synchrotron and X-ray diffraction has been applied in the study of proton migration across SSHBs. Two structural refinement methods have been applied to follow the proton migration behaviour.

The use of traditional refinement methods in SHELXL-2013 [219] allowed temperature dependent proton migration to be identified and followed from synchrotron X-ray diffraction data in the molecular complexes DMU2,4-DNBA and INP; the extent occurring was comparable to that reported in the literature. The synchrotron technique was found to be applicable in the study of proton migration behaviour provided consistent trends were observable across all information, including good correlation between the refined hydrogen atom positions and Fourier difference maps, and that Fourier difference maps were relatively noise free for the reliable determination of proton behaviour; aided by the availability of high quality data from this technique. Sample quality was also shown to have consequences for the success of the determination of the proton behaviour in the Fourier difference maps. These are reflections relevant in all studies of proton transfer and, if considered, may aid the success of this technique in future studies.

The use of the parametric structural refinement technique in Topas-Academic V5.0 [168] has been trialled in this research project for following proton migration in variable temperature synchrotron single crystal X-ray diffraction data. This refinement method offers the potential for increased accuracy on parameters and reduction in processing time. Its application to following proton migration behaviour was found to be possible with sensible results output; this is promising where this is the first implementation of a method of this type to single crystal data. The use of the

continuous temperature ramping method is also revealed to be worthwhile in these studies. The parametric refinement method was found to be improved by continuous temperature ramping during data collection allowing hydrogen atom behaviour to be followed continuously along the temperature profile; this is a novel method which is recommended in future studies of proton transfer. A significant caveat was, however, presented in the use of the parametric refinement method in that the proton migration behaviour observed appeared to be highly dependent on the model used for the evolving hydrogen atom behaviour. Further development of this method is therefore required but these early results indicate its potential in studies of proton transfer; its application to additional samples, such as where proton migration has been identified previously by single crystal X-ray or neutron diffraction measurements including in urea oxalic acid, [108] would be highly beneficial.

The study of these materials by single crystal synchrotron X-ray diffraction has allowed additional insight into the observed proton migration behaviour including its tuning by donor-acceptor distance or values of ΔpK_a. The proposed O—H···O SSHB donor-acceptor distance limit for observing temperature dependent proton migration was suggested to be rigid where no proton migration was observed above the 2.45 Å donor-acceptor distance. For the N^+—H···O^- SSHBs, additional insight into the donor-acceptor distance limit for proton migration to be observed was revealed to be longer than found previously, cases of proton migration have only been reported for N^+—H···O^- SSHBs with donor-acceptor distances below 2.55 Å, and potentially in the range of 2.551(1) and 2.555(1) Å; proton migration was indicated across the former SSHB but not the latter. The extent of proton migration occurring in these complexes followed the trend of increasing migration with less negative ΔpK_a for the O—H···O SSHBs in the substituted urea organic acid molecular complexes, supporting that observed by Jones *et al*. (2012). [109] In contrast, for the N^+—H···O^- SSHBs, there did not appear to be a clear trend between the value of ΔpK_a and the extent of proton migration occurring suggesting trends may only be applicable between similar molecular complexes. Details about the potential migration mechanism were also suggested from the variable temperature synchrotron X-ray diffraction studies contributing to the understanding of why such processes occur in the solid state.

The study of the tuning effects on the proton migration behaviour aids in the design of this property into additional systems, where the number of reported proton migration materials is still relatively few; in particular, strategies that target certain donor-acceptor distances or certain ΔpK_a values between components may be favourable. The synchrotron technique may contribute significantly to these studies allowing a greater number of systems to be studied reliably at an increased number of temperatures.

Chapter 8.

X-ray diffraction and synchrotron studies of proton transfer behaviour in molecular complexes of DMAN

In this chapter, synchrotron and X-ray diffraction is applied in the study of static proton transfer behaviour in the molecular complexes of the proton sponge molecule, DMAN (1,8-bis(dimethylamino)naphthalene), with organic acids. As in the systems studied in Chapter 5 and Chapter 6, weak intermolecular interactions are important.

8.1 Introduction and aims

In molecular complexes of DMAN with organic acids, proton transfer between components results in crystal packing in which a $[Me_2N—H\cdots NMe_2]^+\cdots X^-$ fragment, where X^- is the nearest electronegative atom, is formed (§1.3.3). The nature of the anion X^- appears to tune features of the crystal packing, [130] including the minor component of the fragment comprised of the weak $C—H\cdots X^-$ hydrogen bonds formed between the methyl groups and X^-; the transfer behaviour of the proton in the major component of the fragment, the intermolecular hydrogen bond (IHB) $[N—H\cdots N]^+$, in turn may be tuned by these weak interactions. [132]

To further understand the effect of the anion in tuning features of the crystal packing and to rationalise the IHB proton transfer behaviour, it is beneficial to identify and study further systems in which the $[Me_2N—H\cdots NMe_2]^+\cdots X^-$ fragment is formed. A number of molecular complexes of DMAN with halo and hydroxy benzoic acids have been identified as containing the $[Me_2N—H\cdots NMe_2]^+\cdots X^-$ fragment by laboratory X-ray diffraction. [128, 136] In these complexes, the DMAN and benzoic acid components crystallise in a 1:2 ratio. Proton transfer occurs between one acid and the DMAN whilst the second acid forms a negatively charged dimer ($ACID^-$) with the deprotonated acid *via* a strong $O—H\cdots O^-$ charge assisted hydrogen bond (CAHB). The acid dimer positions itself above the $[N—H\cdots N]^+$ IHB, forming the $[Me_2N—H\cdots NMe_2]^+\cdots X^-$ fragment (Figure 8.1); here X^- is the deprotonated carboxylate oxygen atom.

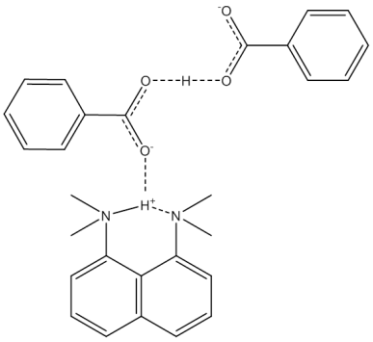

Figure 8.1 The interaction of the protonated DMAN ($DMANH^+$) and the charged acid dimer ($ACID^-$).

In these complexes, the positions of the hydrogen atoms in the $DMANH^+$ IHB and the $ACID^-$ dimer hydrogen bond could not be relied upon when determined from the laboratory X-ray diffraction data; the Fourier difference maps showed ambiguity in the location of these atoms. [128] It was therefore not possible to attempt rationalisation of the proton transfer behaviour using this technique. Neutron diffraction measurements were carried out by Jones *et al.* (2016) on several of the DMAN complexes, including DMAN with 2-fluoro, 2-iodo and 4-iodobenzoic acids; this method enables a precise determination of the hydrogen atom positions alongside the anisotropic refinement of hydrogen atom thermal parameters allowing the proton transfer behaviour to be accurately determined and thereby rationalised. [133] The proton behaviour in the IHB and the $ACID^-$ SSHB was found to be effected by combinations of weak interactions in the local environment. A correlation was also found between the thermal motion of the IHB proton and X^- when in close proximity; indicated by an equivalent movement of the thermal ellipsoids of two atoms when the $H\cdots X^-$ distances were in the range of 2.61 to 2.81 Å. [133, 135]

In this chapter, DMAN substituted benzoic acid molecular complexes containing the $[Me_2N—H\cdots NMe_2]^+\cdots X^-$ fragment are studied using a combination of synchrotron and X-ray diffraction. The molecular complexes under study include (i) the previously identified DMAN halo and hydroxy benzoic acids molecular complexes (co-former set 1) and (ii) new molecular complexes of DMAN with a range of substituted benzoic acids (co-former set 2). Across the molecular complexes, the effect of anion (X^-) variation, by substitution, on features of the crystal packing and molecular structure, including in the $[Me_2N—H\cdots NMe_2]^+\cdots X^-$ fragment, is investigated. Attempts to rationalise the low temperature IHB proton transfer behaviour using the X-ray technique are also made; conclusions are compared to those found in the neutron diffraction studies. [133]

In this work, a study of the previously identified molecular complexes of DMAN with halo and hydroxy benzoic acids (co-former set 1) [136] [128] has been conducted at a single low temperature (100 or 150 K) using the technique of synchrotron X-ray diffraction with the aim of improving on the

previously collected X-ray diffraction data; Fourier difference maps of higher quality are obtainable *via* this method such that more reliable hydrogen atom location and behaviour determination can be achieved. The synchrotron technique is first benchmarked for DMAN 2-iodobenzoic acid (§8.3), where the neutron diffraction data is available for comparison at the same temperature, [133] and subsequently applied to all those DMAN complexes with halo and hydroxy benzoic acids previously identified (Figure 8.2) (§8.4); it was not possible to prepare the previously found 2-chloro and 3-chloro benzoic acid analogues. [128, 136]

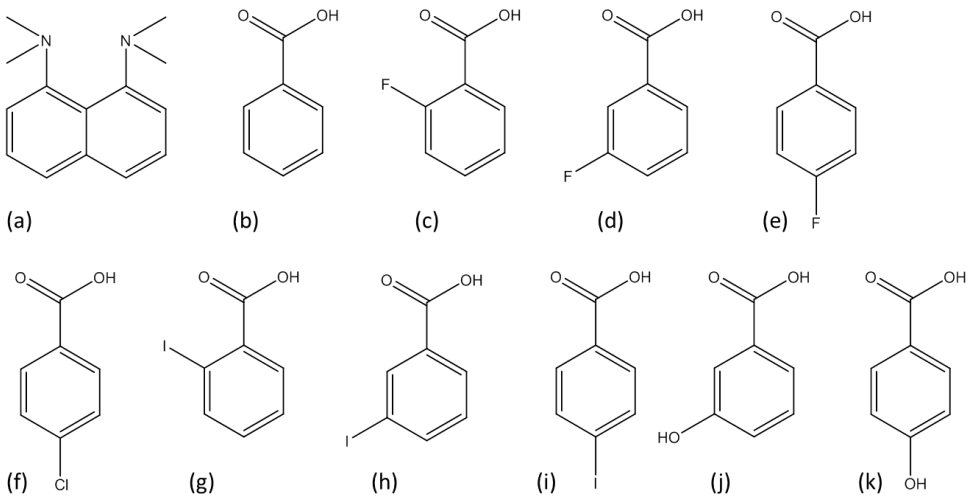

Figure 8.2 (a) DMAN with molecular co-components of co-former set 1: (b) benzoic acid (BA), (c) 2-fluorobenzoic acid (2-FBA), (d) 3-fluorobenzoic acid (3-FBA), (e) 4-fluorobenzoic acid (4-FBA), (f) 4-chlorobenzoic acid, (g) 2-iodobenzoic acid (2-IBA), (h) 3-iodobenzoic acid (3-IBA), (i) 4-iodobenzoic acid (4-IBA), (j) 3-hydroxybenzoic acid (3-OHBA) and (k) 4-hydroxybenzoic acid (4-OHBA).

The new molecular complexes of DMAN with a range of substituted benzoic acids (co-former set 2), prepared as part of crystal engineering study into the effect of anion substitution on the crystal packing, are also studied *via* a combination of the synchrotron technique and using laboratory X-ray diffraction with measurements conducted at 100 or 150 K. The benzoic acid co-formers contain a range of electron withdrawing and donating substituents (Figure 8.3). The formation of additional complexes in this study allows further understanding of the effect of anion substitution on the crystal packing and molecular structure and contributes to the number of instances across which the low temperature proton transfer behaviour can be studied.

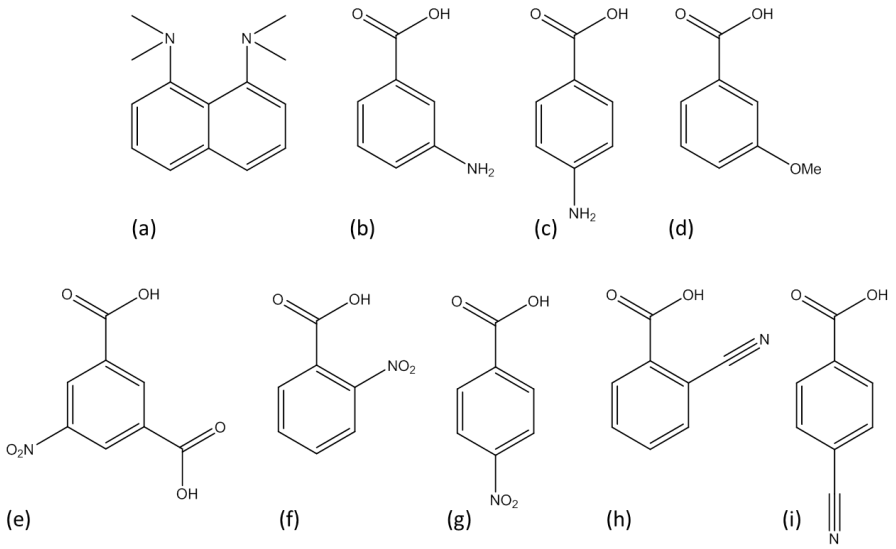

Figure 8.3 (a) DMAN with molecular co-components of co-former set 2: (b) 3-aminobenzoic acid (3-ABA), (c) 4-aminobenzoic acid (4-ABA), (d) 3-methoxybenzoic acid (3-OMBA), (e) 5-nitroisophthalic acid (5-NIP), (f) 2-nitrobenzoic acid (2-NBA), (g) 4-nitrobenzoic acid (4-NBA), (h) 2-cyanobenzoic acid (2-CBA), (i) 4-cyanobenzoic acid (4-CBA).

8.2 Experimental details

8.2.1 Preparation and crystallographic analysis

Co former Set 1

1,8-bis(dimethylamino)naphthalene benzoic acid 1:2 (DMANBA)

Colourless plate crystals of the 1:2 complex of 1,8-bis(dimethylamino)naphthalene and benzoic acid were grown by slow evaporation of a 1:2 stoichiometric ratio of the two components in diethyl ether solvent at room temperature.

1,8-bis(dimethylamino)naphthalene 2-fluorobenzoic acid 1:2 (DMAN2-FBA)

Colourless plate crystals of the 1:2 complex of 1,8-bis(dimethylamino)naphthalene and 2-fluorobenzoic acid were grown by slow evaporation of a 1:2 stoichiometric ratio of the two components in diethyl ether solvent at room temperature.

1,8-bis(dimethylamino)naphthalene 3-fluorobenzoic acid 1:2 (DMAN3-FBA)

Colourless plate crystals of the 1:2 complex of 1,8-bis(dimethylamino)naphthalene and 3-fluorobenzoic acid were grown by slow evaporation of a 1:2 stoichiometric ratio of the two components in diethyl ether solvent at room temperature.

1,8-bis(dimethylamino)naphthalene, 4-fluorobenzoic acid and water 1:2:1 (DMAN4-FBA hydrate)

Colourless plate crystals of the 1:2:1 complex of 1,8-bis(dimethylamino)naphthalene, 4-fluorobenzoic acid and water were grown by slow evaporation of a 1:2 stoichiometric ratio of the two components in diethyl ether solvent at room temperature.

1,8-bis(dimethylamino)naphthalene, 4-chlorobenzoic acid and water 1:2:1 (DMAN4-ClBA hydrate)

Brown needle crystals of the 1:2:1 complex of 1,8-bis(dimethylamino)naphthalene, 4-chlorobenzoic acid and water were grown by slow evaporation of a 1:2 stoichiometric ratio of the two components in methanol solvent at room temperature.

1,8-bis(dimethylamino)naphthalene 2-iodobenzoic acid 1:2 (DMAN2-IBA)

Colourless plate crystals of the 1:2 complex of 1,8-bis(dimethylamino)naphthalene and 2-iodobenzoic acid were grown by slow evaporation of a 1:2 stoichiometric ratio of the two components in acetone solvent at room temperature.

1,8-bis(dimethylamino)naphthalene 3-iodobenzoic acid 1:2 (DMAN3-IBA)

Colourless plate crystals of the 1:2 complex of 1,8-bis(dimethylamino)naphthalene and 3-iodobenzoic acid were grown by slow evaporation of a 1:2 stoichiometric ratio of the two components in dichloromethane solvent at room temperature.

1,8-bis(dimethylamino)naphthalene 4-iodobenzoic acid 1:2 (DMAN4-IBA)

Colourless plate crystals of the 1:2 complex of 1,8-bis(dimethylamino)naphthalene and 4-iodobenzoic acid were grown by slow evaporation of a 1:2 stoichiometric ratio of the two components in methanol solvent at room temperature.

1,8-bis(dimethylamino)naphthalene, 3-hydroxybenzoic acid and water 2:2:1 (DMAN3-OHBA hydrate)

Colourless plate crystals of the 2:2:1 complex of 1,8-bis(dimethylamino)naphthalene, 3-hydroxybenzoic acid and water were grown by slow evaporation of a 1:1 stoichiometric ratio of the two components in acetone solvent at room temperature.

1,8-bis(dimethylamino)naphthalene 4-hydroxybenzoic acid 1:2 (DMAN4-OHBA)

Colourless plate crystals of the 1:2 complex of 1,8-bis(dimethylamino)naphthalene and 4-hydroxybenzoic acid were grown by slow evaporation of a 1:1 stoichiometric ratio of the two components in diethyl ether solvent at room temperature.

1,8-bis(dimethylamino)naphthalene, 4-hydroxybenzoic acid and water 2:2:1 (DMAN4-OHBA hydrate)

Colourless plate crystals of the 2:2:1 complex of 1,8-bis(dimethylamino)naphthalene, 4-hydroxybenzoic acid and water were grown by slow evaporation of a 1:1 stoichiometric ratio of the two components in diethyl ether solvent at room temperature.

Single crystal X-ray diffraction data for all complexes were collected on beamline I19, in EH1 at the Diamond Light Source, U.K. [1] using using Si (111) monochromated radiation at λ = 0.6889 Å on a Crystal Logic [232] four-circle κ geometry diffractometer equipped with a Rigaku [208] Saturn 724+ CCD area detector. The sample temperature was controlled using an Oxford Cryosystems [229] Cryostream Plus. Data collection was performed using the Rigaku [208] CrystalClear™ [209] software whilst data processing was performed using the Rigaku Oxford Diffraction [210] CrysAlisPro [211] software version 1.171.37.28. All structures were solved using SHELXS-2013 [218] and refined using SHELXL-2013 [219] within the WinGX package. [221] Crystallographic data are given in Table 8.1 and Table 8.2.

Co-former Set 2

1,8-bis(dimethylamino)naphthalene and 5-nitroisophthalic acid 1:1 (DMAN5-NIP)

Colourless plate crystals of the 1:1 complex of 1,8-bis(dimethylamino)naphthalene and 5-nitroisophtlaic acid were grown by slow evaporation of a 1:2 stoichiometric ratio of the two components in methanol solvent at 30 °C.

1,8-bis(dimethylamino)naphthalene and 2-nitrobenzoic acid 1:1 (DMAN2-NBA)

Pale purple plate crystals of the 1:1 complex of 1,8-bis(dimethylamino)naphthalene and 2-nitrobenzoic acid were grown by slow evaporation of a 1:2 stoichiometric ratio of the two components in methanol solvent at 30 °C.

1,8-bis(dimethylamino)naphthalene and 3-methoxybenzoic acid 1:2 (DMAN3-OMBA)

Pale brown plate crystals of the 1:2 complex of 1,8-bis(dimethylamino)naphthalene and 3-methoxybenzoic acid were grown by slow evaporation of a 1:2 stoichiometric ratio of the two components in acetonitrile solvent at 4 °C.

1,8-bis(dimethylamino)naphthalene and 3-aminobenzoic acid 1:2 (DMAN3-ABA)

Pale brown plate crystals of the 1:2 complex of 1,8-bis(dimethylamino)naphthalene and 3-aminobenzoic acid were grown by slow evaporation of a 1:2 stoichiometric ratio of the two components in isopropanol solvent at 30 °C.

1,8-bis(dimethylamino)naphthalene, 4-aminobenzoic acid and water 3:6:4 (DMAN4-ABA hydrate)

Pale brown block crystals of the 3:6:4 complex of 1,8-bis(dimethylamino)naphthalene, 4-aminobenzoic acid and water were grown by slow evaporation of a 1:2 stoichiometric ratio of the two components in isopropanol solvent at room temperature.

1,8-bis(dimethylamino)naphthalene and 2-cyanobenzoic acid 1:3 (DMAN2-CBA)

Pale purple plate crystals of the 1:3 complex of 1,8-bis(dimethylamino)naphthalene and 2-cyanobenzoic acid were grown by slow evaporation of a 1:2 stoichiometric ratio of the two components in ethyl acetate solvent at 30 °C.

1,8-bis(dimethylamino)naphthalene and 4-cyanobenzoic acid 1:3 (DMAN4-CBA)

Pale purple plate crystals of the 1:3 complex of 1,8-bis(dimethylamino)naphthalene and 4-cyanobenzoic acid were grown by slow evaporation of a 1:2 stoichiometric ratio of the two components in isopropanol solvent at 50 °C.

1,8-bis(dimethylamino)naphthalene and 4-nitrobenzoic acid II 1:3 (DMAN4-NBA II)

Pale brown plate crystals of the 1:3 complex of 1,8-bis(dimethylamino)naphthalene and 4-nitrobenzoic acid were grown by slow evaporation of a 1:2 stoichiometric ratio of the two components in methanol solvent at 50 °C.

For samples DMAN5-NIP, DMAN2-NBA, DMAN3-OMBA, DMAN3-ABA, DMAN2-CBA and DMAN4-CBA, single crystal X-ray diffraction data were collected on beamline 11.3.1 at the Advanced Light Source, U.S.A. [2] using Si (111) monochromated radiation at $\lambda = 0.8856$ Å on a Bruker AXS [214] D8 three-circle diffractometer equipped with a Bruker AXS [214] PHOTON 100 CMOS detector. The sample temperature was controlled using an Oxford Cryosystems [229] Cryostream Plus. The data were collected using the Bruker AXS [214] Apex2 [215] software and processed using the softwares Bruker AXS [214] Apex2 [215] with SADABS-2014/5. [216]

For the sample DMAN4-ABA hydrate, single crystal X-ray diffraction data were collected using Mo-K_α radiation on a Rigaku Oxford Diffraction [210] Xcalibur four-circle diffractometer equipped with an Agilent [228] Atlas CCD detector at 150 K. The sample temperature was controlled using an Oxford Cryosystems [229] Cryostream Plus. For sample DMAN4-NBA II, single crystal X-ray diffraction data were collected using Cu-K_α radiation on a Rigaku Oxford Diffraction [210] SuperNova four-circle diffractometer equipped with an Agilent [228] Atlas CCD detector at 150 K. The sample temperature was controlled using an Oxford Cryosystems [229] Cryostream 700. The

data were collected and processed for DMAN4-ABA hydrate and DMAN4-NBA II using Rigaku Oxford Diffraction [210] CrysAlisPro [211] version 1.171.37.33.

All structures were solved using SHELXS-2013 [218] and refined using SHELXL-2013 [219] within the WinGX package. [221] Crystallographic data are given in Table 8.2 and Table 8.3.

Refinement details

The refinement details include the treatment of the $DMANH^+$ IHB hydrogen atom and the $ACID^-$ anion unit CAHB hydrogen atom during structure solution and refinement for co-former set 1 and 2 molecular complexes. The IHB and CAHB hydrogen atoms were located based on Fourier difference maps and the hydrogen atom position and isotropic thermal parameter were refined freely.

Table 8.1 Crystallographic data for DMAN benzoic acid (DMANBA) (1:2), DMAN 2-fluorobenzoic acid (DMAN2-FBA) (1:2), DMAN 3-fluorobenzoic acid (DMAN3-FBA) (1:2) and DMAN 4-fluorobenzoic acid hydrate (DMAN4-FBA hydrate) (1:2:1), DMAN 4-chlorobenzoic acid hydrate (DMAN4-ClBA hydrate) (1:2:1), DMAN 2-iodobenzoic acid (DMAN2-IBA) (1:2) collected on I19 at the Diamond Light Source, U.K. [1]

Compound	DMANBA	DMAN2-FBA	DMAN3-FBA	DMAN4-FBA hydrate	DMAN4-ClBA hydrate	DMAN2-IBA	DMAN2-IBA
Diffractometer	DTREK	DTREK	DTREK	DTREK	DTREK	DTREK	VIVALDI
Wavelength (Å)	0.6889	0.6889	0.6889	0.6889	0.6889	0.6889	0.80-5.20 (neutron) [135]
Formula	$C_{28}H_{30}N_2O_4$	$C_{28}H_{28}F_2N_2O_4$	$C_{28}H_{28}F_2N_2O_4$	$C_{28}H_{30}F_2N_2O_5$	$C_{28}H_{30}Cl_2N_2O_5$	$C_{28}H_{28}I_2N_2O_4$	$C_{28}H_{28}I_2N_2O_4$
Mol. W ($gmol^{-1}$)	458.54	494.52	494.52	512.54	545.44	710.32	710.32
T (K)	100	100	100	100	100	100	100
Space group	P-1	P-1	P-1	$P2_1/n$	$P2_1/n$	P-1	P-1
a (Å)	10.2878(7)	10.217(3)	10.242(3)	13.770(7)	13.8463(3)	10.4278(10)	10.440(5)
b (Å)	11.5980(8)	10.815(3)	11.852(4)	11.338(5)	11.1753(3)	11.0814(13)	11.080(5)
c (Å)	11.9944(8)	12.666(3)	12.172(3)	16.388(8)	17.3472(5)	12.7276(16)	12.700(5)
α (°)	76.950(6)	72.201(9)	76.335(13)	90	90	68.449(11)	68.470(10)
β (°)	67.760(6)	68.779(9)	68.135(14)	93.935(4)	92.681(2)	88.314(9)	88.310(10)
γ (°)	65.448(7)	88.848(14)	65.670(9)	90	90	79.641(9)	79.670(10)
Volume ($Å^3$)	1200.91(16)	1235.7(6)	1243.5(6)	2553(2)	2681.31(12)	1344.5(3)	1343.4(10)
Z	2	2	2	4	4	2	2
ρ_{calc} ($g\ cm^{-3}$)	1.268	1.329	1.321	1.334	1.351	1.755	1.755
μ (mm^{-1})	0.079	0.091	0.091	0.093	0.257	2.157	0.000
Θ range (°)	1.784-25.502	1.765-25.402	1.756-25.488	1.812-25.539	1.784-25.502	1.669-25.565	-
Reflections collected	18573	18673	19151	22614	24079	20577	13238
Independent	4869	4957	5028	5240	5454	5455	4013
Observed I>2σ	4062	4209	4098	4023	4312	4960	3057
R_{int}	0.0338	0.0439	0.0416	0.054	0.0617	0.0436	0.1121
Completeness (%)	99.5	99.5	99.6	100.0	99.8	99.5	99.6
Parameters	428	449	433	454	455	437	578
GooF	1.03	1.033	1.041	1.041	1.012	1.031	1.389
R_1 (observed)	0.0378	0.037	0.0426	0.0503	0.0412	0.0257	0.0439
R_1 (all)	0.0464	0.0446	0.0534	0.067	0.0567	0.0288	0.0705
wR_2 (all)	0.0997	0.0965	0.1129	0.139	0.1005	0.0645	0.0868
Δρ (max, min) ($e\ Å^{-3}$)	0.199, -0.185	0.225, -0.281	0.296, -0.223	0.460, -0.256	0.258, -0.350	0.936, -1.279	0.057, -0.055

Table 8.2 Crystallographic data for DMAN 3-iodobenzoic acid (DMAN3-IBA) (1:2) and DMAN 4-iodobenzoic acid (DMAN4-IBA), DMAN 3-hydroxybenzoic acid hydrate (DMAN3-OHBA hydrate) (2:2:1), DMAN 4-hydroxybenzoic acid (DMAN4-OHBA) (1:2), DMAN 4-hydroxybenzoic acid hydrate (DMAN4-OHBA hydrate) (2:2:1) collected on I19 at the Diamond Light Source, U.K. [1] and for DMAN 5-nitroisophthalic acid (DMAN5-NIP) (1:1) and DMAN 2-nitrobenzoic acid (DMAN2-NBA) (1:1) collected on 11.3.1 at the Advanced Light Source, U.S.A. [2]

Compound	DMAN3-IBA	DMAN4-IBA	DMAN 3-OHBA hydrate	DMAN 4-OHBA	DMAN 4-OHBA hydrate	DMAN5-NIP	DMAN2-NBA
Diffractometer	DTREK	DTREK	DTREK	DTREK	DTREK	Bruker AXS D8	Bruker AXS D8
Wavelength (Å)	0.6889	0.6889	0.6889	0.6889	0.6889	0.8856	0.8856
Formula	$C_{28}H_{28}I_2N_2O_4$	$C_{28}H_{28}I_2N_2O_4$	$C_{42}H_{50}N_4O_7$	$C_{28}H_{30}N_2O_6$	$C_{42}H_{50}N_4O_7$	$C_{22}H_{23}N_3O_6$	$C_{21}H_{23}\ N_3O_4$
Mol. W ($gmol^{-1}$)	710.32	710.32	361.43	490.54	722.86	425.43	381.42
T (K)	100	100	100	100	100	100	100
Space group	P-1	$P2_1/n$	Pbcn	$P2_1/c$	P-1	$P2_1/c$	$P2_1/n$
a (Å)	10.3833(3)	11.4093(3)	9.6592(2)	11.4729(5)	11.8405(3)	7.4488(3)	10.3320(4)
b (Å)	11.5170(3)	7.7352(2)	20.4656(3)	14.6030(3)	12.0843(4)	16.1665(7)	18.3951(7)
c (Å)	12.3062(4)	30.7454(7)	18.9364(3)	14.7655(5)	14.1221(3)	16.8622(8)	10.3744(4)
α (°)	110.490(3)	90	90	90	93.624(2)	90	90
β (°)	90.550(2)	96.809(2)	90	91.920(3)	96.041(2)	99.229(2)	103.652(2)
γ (°)	93.339(2)	90	90	90	111.330(3)	90	90
Volume ($Å^3$)	1375.48(7)	2694.24(12)	3743.37(11)	2472.40(15)	1860.52(9)	2004.28(15)	1916.03(13)
Z	2	4	4	4	2	4	4
ρ_{calc} ($g\ cm^{-3}$)	1.715	1.751	1.283	1.318	1.290	1.410	1.322
μ (mm^{-1})	2.108	2.153	0.081	0.086	0.082	0.136	0.119
Θ range (°)	1.713-25.502	1.785-25.501	2.085-25.499	1.721-25.502	1.764-25.504	2.188-42.136	2.759-41.120
Reflections collected	20985	23845	32210	21939	28563	37365	34754
Independent	5565	5508	3827	5028	7532	7291	6559
Observed I>2σ	5017	4593	3200	3691	6320	5697	4927
R_{int}	0.0335	0.055	0.0629	0.0661	0.0339	0.0328	0.0525
Completeness (%)	99.6	100.0	99.7	99.7	99.5	100.0	99.9
Parameters	437	437	340	445	678	372	345
GooF	1.032	1.007	1.037	1.04	1.030	1.024	1.026
R_1 (observed)	0.0215	0.027	0.0357	0.0436	0.0346	0.0455	0.0481
R_1 (all)	0.025	0.038	0.046	0.0697	0.0438	0.0636	0.0713
wR_2 (all)	0.0543	0.0597	0.0919	0.1092	0.0830	0.1232	0.1266
Δρ (max, min) ($e\ Å^{-3}$)	0.823, -0.679	0.622, -0.973	0.254, -0.161	0.228, -0.229	0.227, -0.186	0.463, -0.281	0.424, -0.284

Table 8.3 Crystallographic data for DMAN 3-methoxybenzoic acid (DMAN3-OMBA) (1:2), DMAN 3-aminobenzoic acid (DMAN3-ABA) (1:2), DMAN 4-aminobenzoic acid hydrate (DMAN4-ABA hydrate) (3:6:4), DMAN 2-cyanobenzoic acid (DMAN2-CBA) (1:3), DMAN 4-cyanobenzoic acid (DMAN4-CBA) (1:3) and DMAN 4-nitrobenzoic acid (DMAN4-NBA II) (1:3) collected on beamline 11.3.1 at the Advanced Light Source, U.S.A. [2]

Compound	DMAN3-OMBA	DMAN3-ABA	DMAN4-ABA hydrate	DMAN2-CBA	DMAN4-CBA	DMAN4-NBA II
Diffractometer	Bruker AXS D8	Bruker AXS D8	Xcalibur	Bruker AXS D8	Bruker AXS D8	SuperNova
Wavelength (Å)	0.8856	0.8856	Mo	0.8856	0.8856	Cu
Formula	$C_{30}H_{34}N_2O_6$	$C_{28}H_{32}N_4O_4$	$C_{84}H_{104}N_{12}O_{16}$	$C_{38}H_{33}N_5O_6$	$C_{38}H_{33}N_5O_6$	$C_{35}H_{33}N_5O_{12}$
Mol. W ($gmol^{-1}$)	518.59	488.57	1537.79	655.69	655.69	715.66
T (K)	100	100	150	100	100	150
Space group	$P2_1/c$	$P2_1/c$	P-1	$P2_1/c$	$P2_1/c$	P-1
a (Å)	9.8917(4)	9.8631(4)	13.3902(6)	11.2829(4)	21.5699(10)	14.6269(4)
b (Å)	23.8954(9)	21.3774(9)	17.4977(7)	12.5029(5)	9.1267(4)	18.1672(5)
c (Å)	12.0958(5)	12.5572(5)	19.3081(9)	23.4257(10)	18.2762(8)	20.9527(6)
α (°)	90	90	85.639(4)	90	90	93.416(2)
β (°)	112.040(2)	110.968(2)	70.634(4)	90.718(2)	112.449(2)	104.461(3)
γ (°)	90	90	69.986(4)	90	90	107.500(3)
Volume ($Å^3$)	2650.10(19)	2472.33(18)	4006.6(3)	3304.4(2)	3325.2(3)	5086.9(3)
Z	4	4	2	4	4	6
ρ_{calc} ($g\ cm^{-3}$)	1.300	1.313	1.275	1.318	1.310	1.402
μ (mm^{-1})	0.116	0.112	0.089	0.115	0.115	0.906
Θ range (°)	2.124-33.661	2.374-39.340	3.270-25.026	2.167-33.716	2.546-31.812	3.301-74.703
Reflections collected	37258	41246	36374	46488	42882	37803
Independent	5439	7542	14105	6806	5880	20174
Observed I>2σ	3754	5867	6958	4353	3924	16100
R_{int}	0.0561	0.042	0.059	0.0899	0.0734	0.0226
Completeness (%)	99.9	99.9	97.3	100.0	98.1	99.9
Parameters	479	453	1364	574	574	1801
GooF	1.025	1.032	1.002	1.006	1.014	1.021
R_1 (observed)	0.045	0.0445	0.0731	0.0474	0.0445	0.0396
R_1 (all)	0.0803	0.0609	0.1615	0.0942	0.0836	0.0524
wR_2 (all)	0.1022	0.1215	0.2091	0.112	0.1044	0.1083
Δρ (max, min) ($e\ Å^{-3}$)	0.189, -0.275	0.437, -0.285	0.641, -0.597	0.277, -0.246	0.181, -0.261	0.489, -0.423

8.3 A comparative diffraction study of proton transfer behaviour in DMAN 2-iodobenzoic acid

The reliable determination of proton transfer behaviour is important in this study to aid in its rationalisation across the DMAN substituted benzoic acid molecular complexes.

In order to benchmark the technique of synchrotron X-ray diffraction, in these studies of proton transfer behaviour, it was first applied to the molecular complex of DMAN2-IBA at 100 K, where the neutron diffraction data is available for comparison at the same temperature. [133, 135] The focus is on the $DMANH^+$ IHB and CAHB $ACID^-$ dimer structural and atomic displacement parameters, the observable IHB proton behaviour within the Fourier difference maps and the heavy atom parameters of the hydrogen bonding groups.

8.3.1 Hydrogen bond structural parameters

A comparison of distances involving hydrogen atoms in the $[N—H\cdots N]^+$ IHB and CAHB $ACID^-$ dimer SSHB for the synchrotron X-ray structure and neutron structure (Table 8.4) indicate that there is, in general, a difference in the order of 0.1 Å; this is as expected between X-ray and neutron determinations. [94] Despite the shift in the proton positions, similar proton location behaviour is suggested as, in both cases, the refined proton position appears asymmetric. The structural parameters of the groups forming the $[N—H\cdots N]^+$ IHB and CAHB $ACID^-$ dimer SSHB were generally in agreement between the synchrotron and neutron determinations (Table 8.5). In each case they supported the asymmetrical location of the protons in the $[N—H\cdots N]^+$ IHB and CAHB $ACID^-$ dimer SSHB; the bond distances of these groups differed in length at either end of the interaction. There is a slight variation in the C—N bond distances for the synchrotron X-ray structure but still indicate the same trend as neutron structure, that the C—N is longer for the protonated nitrogen atom.

The thermal parameters of the $[N—H\cdots N]^+$ IHB differ between the X-ray and neutron structures (Figure 8.4); refined isotropically for the X-ray case and anisotropically in the neutron case. The anisotropic refinement possible from neutron data means that the direction of movement of a hydrogen atom along a hydrogen bond can be indicated in the thermal ellipsoid. In the X-ray case, possible motion of a hydrogen atom along the bond may be indicated instead by an enlarged isotropic thermal parameter; however, the directionality remains unknown. Despite this difference, the same overall trend of a slight movement of the hydrogen atom along the hydrogen bond is indicated for DMAN2-IBA by each technique; a slightly enlarged isotropic thermal parameter is observed in the X-ray structure for the IHB proton alongside a slightly elongated anisotropic thermal parameter in the neutron structure.

Table 8.4 The $DMANH^+$ IHB and $ACID^-$ dimer SSHB structural parameters in the molecular complex DMAN2-IBA from the 100 K synchrotron and neutron determinations. [133, 135]

Source	Interaction	D···A (Å)	D—H (Å)	H···A (Å)	<DHA (°)
Synchrotron	$[N_1—H···N_2]^+$	2.566(3)	1.11(4)	1.49(4)	160(4)
Neutron [133, 135]	$[N_1—H···N_2]^+$	2.571(2)	1.199(4)	1.417(4)	158.6(3)
Synchrotron	$O—H···O^-$	2.463(2)	1.13(4)	1.34(4)	175(5)
Neutron [133, 135]	$O—H···O^-$	2.456(2)	1.211(3)	1.247(3)	176.5(4)

Table 8.5 The structural parameters of the groups forming the $DMANH^+$ IHB and $ACID^-$ dimer SSHB in the molecular complex DMAN2-IBA from the 100 K synchrotron and neutron determinations. [133, 135]

	Distance (Å)	
Bond	Synchrotron	Neutron [133, 135]
$C—N_1^+$	1.470(3)	1.462(2)
$C—N_2$	1.464(3)	1.452(3)
$C—O^-$	1.277(4)	1.279(3)
C=O	1.230(4)	1.233(3)
C—OH	1.294(3)	1.291(2)
C=O	1.227(3)	1.227(2)

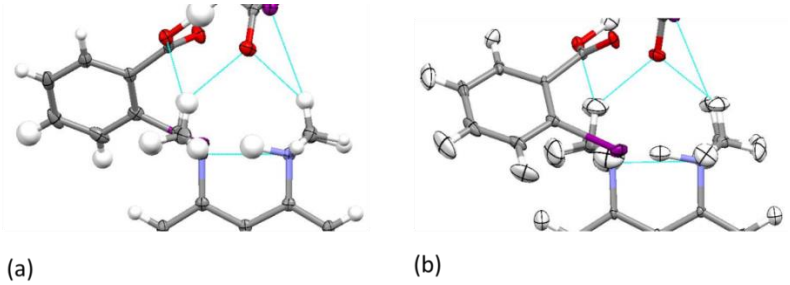

Figure 8.4 Thermal parameters of the IHB proton and X^- in the $[Me_2N—H···NMe_2]^+···X^-$ fragment in the (a) synchrotron and (b) neutron structure. [133, 135]

8.3.2 $DMANH^+$ IHB Fourier difference maps

In the Fourier difference maps of the $[N—H···N]^+$ IHB (Figure 8.5), the density of hydrogen atom in the synchrotron X-ray structure indicates an asymmetric hydrogen atom position as in the neutron structure and is in support of that indicated by the X-ray refined hydrogen atom position. There is, however, slightly different proton behaviour, imaged in the Fourier difference maps, suggested for the structure determined using each diffraction method; the shape of the density for the proton is different in the maps generated from the X-ray and neutron structures. The density for the hydrogen atom is significantly elongated along the IHB in the X-ray structure whilst in the neutron structure the density is better defined; this can be related to the bonding density being

observed in the X-ray Fourier difference map whilst nuclear density is observed in the neutron Fourier difference map. This difference is partly a result of the maps from neutron diffraction imaging nuclear density whilst those from X-ray diffraction, imaging electron density. There is also significant noise in the X-ray Fourier difference map as a consequence of the heavy iodine atom being present in the structure, obscuring the observation of the hydrogen atom; this may also be a contributing factor to the different proton behaviour being observed between the X-ray and neutron Fourier difference maps. The X-ray Fourier difference map, does however, give some indication about the direction of motion along the hydrogen bond where the hydrogen atom isotropic thermal parameter does not.

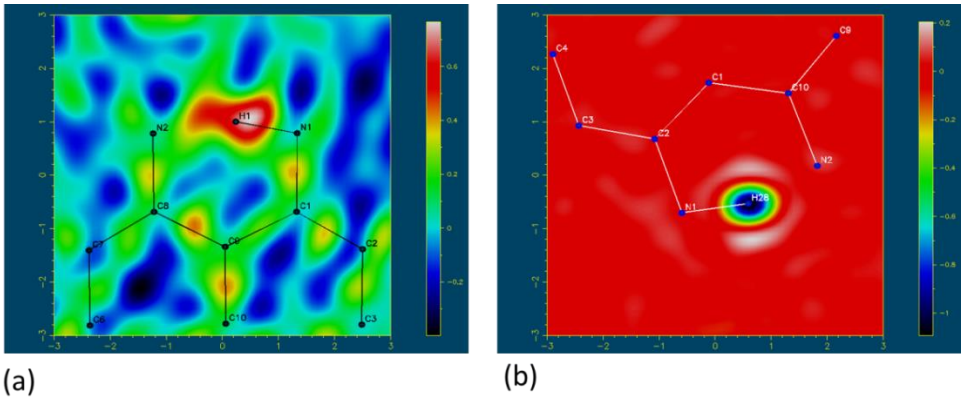

Figure 8.5 Fourier diference maps generated for the [N—H···N]$^{+}$ IHB in DMAN2-IBA: (a) generated for the X-ray structure showing the electron density associated with the H-atom in the IHB and (b) generated for the neutron structure [133, 135] showing nuclear density associated with the H-atom in the IHB.

8.3.3 Summary

Similar hydrogen atom positional information as that obtained by neutron diffraction [133, 135] is observed in the synchrotron X-ray hydrogen bond distances, with the well-established consideration that the equivalent neutron bond lengths will be longer by ~ 0.1 Å. This positional information is reliable when it is supported by the structural parameters of the groups forming the hydrogen bond and the Fourier difference maps, as is the case here. However, there is less agreement in the suggested hydrogen atom thermal behaviour between the two techniques; synchrotron X-ray diffraction may indicate increased thermal motion but lacking directional information. The direction of the hydrogen atom motion may instead be revealed in the synchrotron X-ray structures by considering the size of the isotropic thermal parameters alongside the shape of the density in the Fourier difference maps. This initial study therefore suggests that synchrotron X-ray diffraction may be suitable in studies of proton transfer behaviour on considering these points.

8.4 Synchrotron diffraction study of previously identified DMAN benzoic acid molecular complexes

In this section, synchrotron X-ray diffraction is applied to the previously identified molecular complexes of DMAN with halo and hydroxy benzoic acids. [128] The effect of anion (X^-) variation, by substitution, on features of the crystal packing and molecular structure is investigated and the low temperature $DMANH^+$ IHB proton transfer behaviour is studied.

8.4.1 Anion variation

In these molecular complexes, anions in the form of substituted $ACID^-$ dimers are present (Figure 8.6). The change in both the identity of the halo substituent (acidity order F< Cl < I) and its position (acidity order *ortho* > *meta*/*para*) alters the electronics of the $ACID^-$ dimer in conjugate base form.

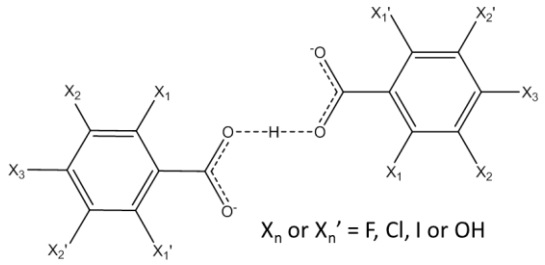

Figure 8.6 The $ACID^-$ anion substitution for BA, 2-FBA, 3-FBA, 4-FBA, 4-ClBA, 2-IBA, 3-IBA, 4-IBA, 3-OHBA and 4-OHBA.

8.4.2 Crystal packing

On substituting the anion, there are slight changes in the wider crystal packing, however the same inorganic type arrangement is adopted; the packing is built up from layers of pairs of $DMANH^+$ cations and pairs of the $ACID^-$ dimers (Figure 8.7). In the majority of the complexes the $DMANH^+$ cations are anti-parallel in each pair (Figure 8.8); an exception to this is in DMAN4-IBA, where they are parallel. In each pair, varying degrees of overlap of the $DMANH^+$ cations occur whilst its packing varies between the complexes. The $DMANH^+$ pairs pack in pockets in DMAN4-FBA, DMAN4-ClBA, DMAN3-IBA and DMAN2-FBA, in columns in DMANBA, DMAN3-OHBA hydrate, DMAN4-OHBA hydrate and in one dimensional chains in DMAN3-FBA, DMAN2-IBA, DMAN4-IBA and DMAN4-OHBA. Contacts linking the $DMANH^+$ cations include π···π stacking, methyl···methyl contacts and methyl···π contacts; dependent on the extent of eclipsed packing occurring.

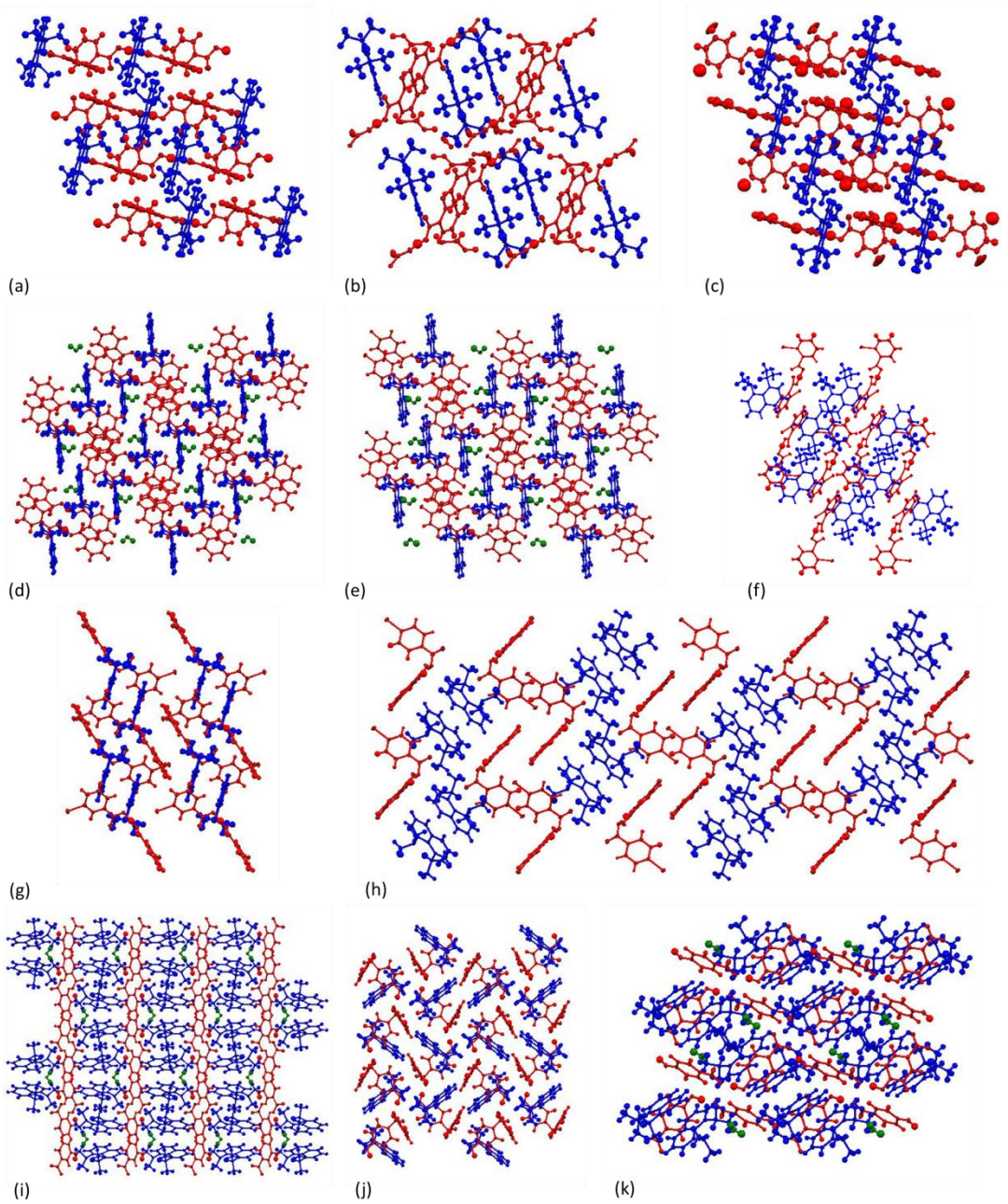

Figure 8.7 Molecular packing in the molecular complexes of (a) DMANBA, (b) DMAN2-FBA, (c) DMAN3-FBA, (d) DMAN4-FBA hydrate, (e) DMAN4-ClBA hydrate, (f) DMAN2-IBA, (g) DMAN3-IBA, (h) DMAN4-IBA, (i) DMAN3-OHBA hydrate, (j) DMAN4-OHBA, (k) DMAN4-OHBA hydrate. The $DMANH^+$ cation is shown in blue, the $ACID^-$ anion in red and water molecules in green.

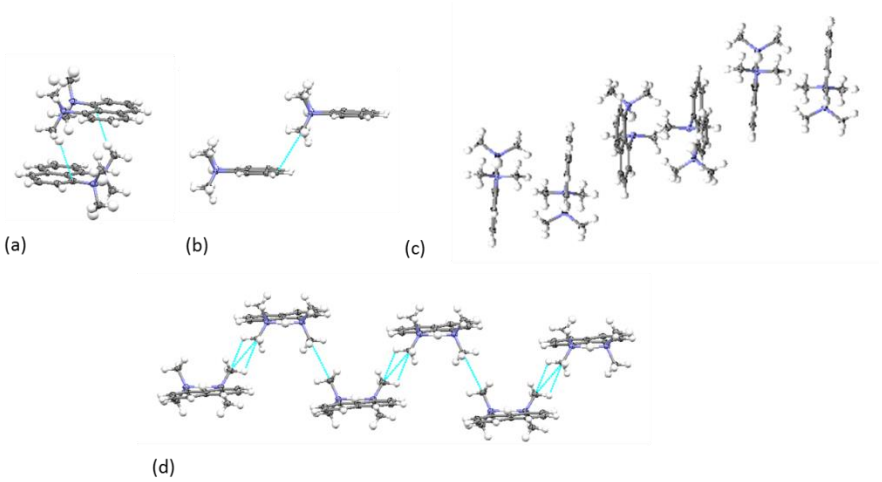

Figure 8.8 Molecular packing of the $DMANH^+$ cations in (a) anti-parallel pairs, (b) in parallel pairs, (c) in columns and (d) in chains.

At the more local level of the crystal packing, the $DMANH^+$ cation and $ACID^-$ dimer anions aggregate into the $[Me_2N—H\cdots NMe_2]^+\cdots X^-$ fragment (Figure 8.9); the fragment formation is robust and unaffected by changes to the anion. Anion variation, in a few cases, alters the motif formed by the acid molecules when in the aggregate. In DMAN3-OHBA hydrate and DMAN4-OHBA hydrate, the anion unit is not an $ACID^-$ dimer but a single deprotonated acid molecule; the deprotonated acid molecules link by interaction between the deprotonated carboxyl group and a hydroxyl group in the 3 or 4-position in the next acid. In DMAN4-OHBA hydrate, two symmetry independent protonated molecules of DMAN crystallise alongside two deprotonated acid molecules (DMAN A) and a molecule of water (DMAN B). The identity of X^- remains largely unchanged across the molecular complexes; in most cases X^- is the deprotonated carboxyl oxygen atom except for in DMAN4-OHBA hydrate B where a water molecule is inserted into the space above the $DMANH^+$ IHB. In DMAN3-OHBA hydrate and DMAN4-OHBA hydrate, the arrangement of X^- over the $DMANH^+$ IHB proton is different; two X^- atoms straddle the $[Me_2N—H\cdots NMe_2]^+$; both from the deprotonated acid.

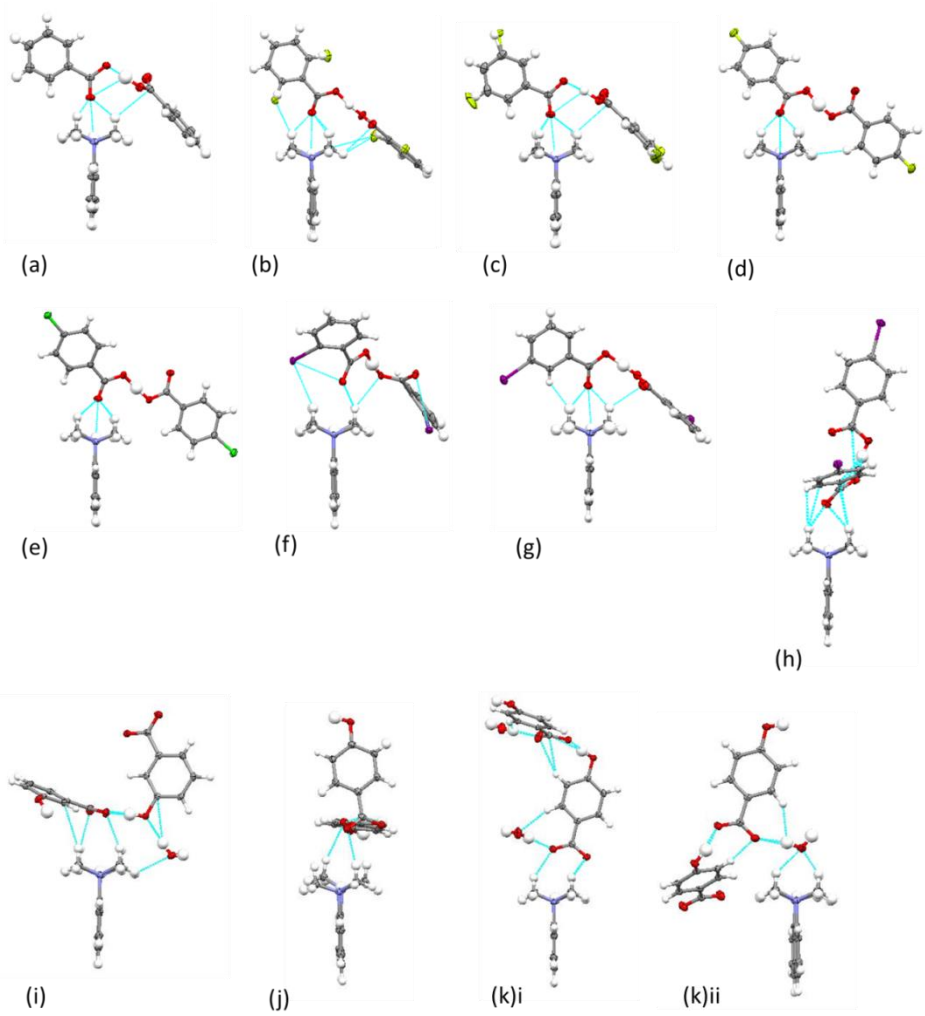

Figure 8.9 The aggregation of the $DMANH^+$ cation and $ACID^-$ dimer in (a) DMANBA, (b) DMAN2-FBA, (c) DMAN3-FBA. (d) DMAN4-FBA hydrate, (e) DMAN4-ClBA hydrate, (f) DMAN2-IBA, (g) DMAN3-IBA, (h) DMAN4-IBA, (i) DMAN3-OHBA hydrate, (j) DMAN4-OHBA, (k) DMAN4-OHBA hydrate i DMAN A and ii DMAN B.

The $[Me_2N—H\cdots NMe_2]^+\cdots X^-$ fragment minor components

Aggregation of the $DMANH^+$ cation and $ACID^-$ dimer anion is facilitated *via* the minor component of the $[Me_2N—H\cdots NMe_2]^+\cdots X^-$ fragment *via* weak $C—H\cdots X^-$ interactions (Table 8.6 and Table 8.7). In DMAN2-FBA, DMAN4-FBA hydrate, DMAN4-ClBA hydrate and DMAN2-IBA minor interactions also form to a halogen atom at the 2-position on the $ACID^-$ dimer. In all the molecular complexes, the $DMANH^+$ methyl groups are also involved in contacts to other neighbouring X^- in the local environment. The minor $C—H\cdots X^-$ interactions vary on varying the anion; the $C\cdots X^-$ interaction length increases with increasing electronegativity of the halogen substituent, in the order fluoro, chloro, iodo, whilst the longer $C—H\cdots X^-$ interactions occur where the anion is *ortho* substituted versus *meta* or *para* substituted. In general, the shortest or greatest number of the weak $C—H\cdots X^-$ interactions form to the most protonated $N_1(CH_3)_2$ group.

Table 8.6 The parameters of the minor component (C—H···X$^-$) of the $[Me_2N_1—H···N_2Me_2]^+···X^-$ fragment across the molecular complexes. $N(CH_3)_2$ group 1 is the most 'protonated' forming the IHB.

Complex	$N(CH_3)_2$ group	Interaction	dC···X$^-$ (Å)	dC—H (Å)	dH···X$^-$ (Å)	<CHX$^-$ (°)
DMAN	1	C14—H17···O4	3.246(2)	0.96(2)	2.60(2)	125(1)
BA	1	C13—H14···O4	3.046(2)	0.98(2)	2.35(2)	127(1)
	2	C11—H7···O4	3.130(2)	0.99(2)	2.43(2)	127(1)
	2	C12—H11···O4	3.303(1)	1.00(2)	2.63(1)	125(1)
	1	C14···O1	3.161(3)			
DMAN	1	C14—H18···O3	3.413(2)	1.02(2)	2.72(2)	125(1)
2-FBA	1	C13—H14···O3	3.305(2)	0.97(2)	2.61(2)	128(1)
	2	C11—H8···O3	3.228(2)	0.99(2)	2.49(2)	131(1)
	2	C12—H10···O3	3.221(2)	0.99(2)	2.48(2)	131(1)
	1	C14—H18···F2	3.537(2)	1.02(2)	2.60(1)	153(1)
	2	C11—H9···O4	3.565(2)	1.02(2)	2.66(2)	148(1)
DMAN	1	C11—H8···O4	3.107(3)	0.97(2)	2.40(2)	129(1)
3FBA	1	C12—H10···O4	3.244(2)	1.00(2)	2.57(2)	125(2)
	2	C13—H13···O4	3.316(2)	0.98(2)	2.67(2)	124(2)
	2	C14—H16···O4	3.124(2)	1.00(2)	2.44(2)	125(2)
	1	C11···O1	3.201(3)			
	2	C13···O2	3.194(3)			
DMAN	1	C26—H25···O1	3.166(3)	0.98(2)	2.47(2)	127(2)
4-FBA	1	C25—H24···O1	3.181(3)	0.99(2)	2.50(2)	126(2)
hydrate	2	C28—H20···O1	3.250(2)	1.00(3)	2.55(2)	127(2)
	2	C27—H17···O1	3.225(3)	1.00(2)	2.56(2)	124(1)
	2	C28—H21···F1	3.062(3)	1.01(3)	2.39(3)	123(2)
	1	C25—H23···O2	3.544(3)	0.93(2)	2.69(2)	152(1)
DMAN	1	C11—H12···O2	3.140(2)	0.95(2)	2.45(2)	129(2)
4-ClBA	1	C12—H9···O2	3.193(2)	0.97(2)	2.53(2)	125(1)
hydrate	2	C14—H14···O2	3.268(2)	0.99(2)	2.65(2)	121(1)
	2	C13—H13···O2	3.204(3)	0.96(2)	2.53(2)	127(2)
	1	C12—H9···Cl2	3.619(2)	0.97(2)	2.90(2)	132(1)
	2	C13—H19···Cl2	3.366(2)	1.01(2)	2.64(2)	129(2)
DMAN	1	C26—H17···O4	3.227(4)	0.97(4)	2.45(4)	137(3)
2-IBA	1	C25—H16···O4	3.554(4)	1.00(4)	2.83(3)	129(2)
	2	C28—H22···O4	3.624(4)	0.95(4)	2.94(4)	130(3)
	2	C27—H23···O4	3.293(4)	0.96(4)	2.54(3)	135(3)
	1	C25—H16···I1	4.075(3)	1.00(4)	3.15(4)	155(3)
	2	C27—H23···O2	3.255(4)	0.96(4)	2.48(3)	138(3)

Table 8.7 The parameters of the minor component (C—H···X^-) of the $[Me_2N_1—H···N_2Me_2]^+···X^-$ fragment (continued) across the molecular complexes. $N(CH_3)_2$ group 1 is the most 'protonated' forming the IHB.

Complex	$N(CH_3)_2$ group	Interaction	dC···X^- (Å)	dC—H (Å)	dH···X^- (Å)	<CHX^- (°)
DMAN	1	C27—H8···O1	3.277(4)	0.95(3)	2.61(4)	128(3)
3-IBA	1	C26—H12···O1	3.363(4)	0.99(3)	2.67(3)	127(2)
	2	C25—H6···O1	3.240(2)	0.99(3)	2.52(2)	130(2)
	2	C28—H2···O1	3.189(3)	0.95(2)	2.49(2)	130(2)
	1	C26—H12···O3	3.197(5)	0.99(3)	2.54(3)	124(2)
DMAN	1	C12—H10···O3	3.229(4)	0.99(4)	2.45(4)	135(3)
4-IBA	1	C11—H2···O3	3.394(3)	0.94(4)	2.65(4)	136(3)
	2	C13—H5···O3	3.534(4)	0.99(4)	2.85(3)	127(3)
	2	C14—H7···O3	3.403(4)	0.98(3)	2.63(3)	135(2)
	1	C12—H12···O4	3.549(4)	0.95(3)	2.64(3)	159(3)
	1	C11—H3···O3'	3.655(4)	0.98(3)	2.69(3)	169(3)
	1	C11—H4···O1	3.167(5)	1.00(3)	2.34(4)	140(3)
DMAN	1	C13—H8···O1	3.405(2)	1.00(2)	2.42(2)	167(1)
3-OHBA	1	C14—H11···O1	3.840(2)	0.98(2)	3.02(2)	142(1)
hydrate	2	C12—H3···O2	3.422(2)	0.99(2)	2.51(2)	153(1)
	2	C11—H5···O2	3.656(2)	0.98(2)	2.85(2)	140(1)
	1	C13—H10···O1'	3.555(2)	0.97(2)	2.68(2)	151(1)
	2	C14—H23···O1'	3.541(2)	0.99(2)	2.65(2)	150(1)
	2	C14—H22···O3	3.238(2)	0.99(2)	2.52(2)	129(1)
DMAN	1	C12—H11···O3	4.108(2)	0.99(2)	3.36(2)	134(1)
4-OHBA	1	C11—H8···O4	3.680(2)	0.99(2)	2.74(2)	158(2)
	2	C13—H12···O3	3.400(2)	0.94(2)	2.54(2)	153(2)
	2	C14—H15···O3	3.822(2)	0.99(2)	3.08(2)	133(1)
	2	C13—H16···O5	3.241(2)	0.98(2)	2.59(2)	124(1)
DMAN	1A	C70—H17···O7	3.142(2)	0.97(2)	2.37(2)	137(1)
4-OHBA	1A	C12—H19···O7	3.312(2)	0.98(2)	2.60(2)	130(1)
hydrate	2A	C50—H11···O7	3.593(2)	0.98(2)	2.89(2)	129(1)
	2A	C13—H14···O7	3.458(2)	0.99(2)	2.75(2)	129(1)
	1A	C12—H18···O3	3.553(2)	0.96(2)	2.61(2)	167(1)
	1B	C26—H36···O2	3.502(2)	0.99(2)	2.68(1)	141(1)
	1B	C25—H33···O1	3.131(2)	0.98(2)	2.43(2)	128(1)
	2B	C27—H31···O1	3.256(2)	0.97(2)	2.58(2)	126(1)
	2B	C28—H29···O2	3.602(2)	0.99(2)	2.80(2)	139(1)
	2B	C27—H30···O6	3.541(2)	0.99(2)	2.57(2)	167(1)

Within the $[Me_2N—H\cdots NMe_2]^+\cdots X^-$ fragment, X^- may also form an interaction with the $DMANH^+$ proton ($H\cdots X^-$); X^- acts as a second acceptor generating a bifurcated hydrogen bond. An interaction between H and X^- may be reflected in the bifurcated hydrogen bond parameters (Table 8.8).

Table 8.8 The bifurcated hydrogen bond parameters within the $[Me_2N_1—H\cdots N_2Me_2]^+\cdots X^-$ fragment across the molecular complexes.

Complex	$dN_1\cdots N_2$ (Å)	$dN_1—H$ (Å)	$dH\cdots X^-$ (Å)	$dN_1\cdots X^-$ (Å)	$dN_2\cdots X^-$ (Å)	$<N_1HX^-$ (°)	$<N_2HX^-$ (°)
DMAN BA	2.568(1)	1.24(2)	2.53(2)	3.037(1)	3.080(1)	102(1)	100(1)
DMAN 2-FBA	2.584(2)	1.31(3)	2.68(2)	3.240(2)	3.153(2)	103(1)	98(1)
DMAN 3-FBA	2.593(2)	1.06(2)	2.56(2)	3.051(2)	3.091(2)	107(1)	94(1)
DMAN 4-FBA hydrate	2.580(2)	1.19(2)	2.59(3)	3.055(2)	3.106(2)	102(1)	97(1)
DMAN 4-ClBA hydrate	2.590(2)	1.08(2)	2.56(2)	3.050(2)	3.104(2)	107(2)	95(1)
DMAN 2-IBA	2.566(3)	1.11(4)	2.92(4)	3.368(3)	3.408(3)	104(2)	96(2)
DMAN 3-IBA	2.581(3)	1.09(4)	2.69(3)	3.209(3)	3.148(3)	108(2)	92(1)
DMAN 4-IBA	2.606(3)	0.95(4)	2.82(4)	3.276(3)	3.389(3)	110(3)	93(2)
DMAN 3-OHBA hydrate	2.580(1)	1.15(2)	3.59(2)	4.202(1)	3.700(1)	115(1)	82.7(8)
DMAN 4-OHBA	2.566(2)	1.25(2)	3.46(2)	4.025(2)	3.713(2)	108(1)	90.0(9)
DMAN 4-OHBA hydrate	A 2.576(2) B 2.608(2)	1.19(2) 1.03(2)	3.16(2) 2.77(2)	3.581(1) 3.192(2)	3.618(2) 3.410(2)	101(1) 105(1)	97(1) 98.3(8)

Variation in the bifurcated hydrogen bond parameters occurs across the molecular complexes. The $H\cdots X^-$ distances vary in length depending on anion substituent; shorter $H\cdots X^-$ distances form for the least electronegative substituents and where the substituent is *meta* or *para* substituted. In

general, in the $[N—H\cdots N]^+$ IHB formed in $DMANH^+$ cations, the N—H and H···N distances are related; a short N—H leads to a long H···N. Therefore, in a bifurcated hydrogen bond, a short $H\cdots X^-$ separation may be expected to lead to a lengthened N—H and therefore an increased N···N distance. [303] However, there does not appear to be any particular correlation between the distances of N_1—H and $H\cdots X^-$ in the complexes here; a short $H\cdots X^-$ does not consistently lead to a lengthened N_1—H. There is, however, reasonable correlation between $N_1\cdots N_2$ and N_1—H where shorter N_1—H distances occur for longer $N_1\cdots N_2$ distances; DMAN2-FBA and DMAN2-IBA are outliers having $N_1\cdots N_2$ distances of 2.584(2) and 2.566(3) Å, respectively, alongside N_1—H distances of 1.31(3) and 1.11(4) Å, respectively. Other trends are apparent including that X^- is closest, in general, to the protonated N_1 and that the NHX^- angle is larger to the protonated nitrogen in the IHB (N_1), as observed in the literature. [131] There is also a strong correlation between $N_1\cdots X^-$ and $X^-\cdots H$.

Local environment of DMAN fused rings

The fused rings of the $DMANH^+$ cation also form interactions with X^- in the local environment involving the naphthalene C—H groups; the arrangement changing as the anion is varied.

Weak interactions to neighbouring X^- occur only on the more protonated side of the DMAN in complexes DMAN2-FBA, DMAN2-IBA, DMAN4-IBA and DMAN3-FBA (Figure 8.10). These are weak C—H···O hydrogen bonds involving the C2 position and forming a weak C—H···O hydrogen bond to an acid oxygen, in DMAN2-FBA ($d_{C\cdots O}$ 3.289(2) Å), DMAN2-IBA ($d_{C\cdots O}$ 3.293(2) Å) and DMAN4-IBA ($d_{C\cdots O}$ 3.188(4) Å) and at the C4 position involving an acid oxygen in DMAN3-FBA ($d_{C\cdots O}$ 3.351(2) Å). A weak C—H····F halogen bond also forms on the protonated side at the C3 position in DMAN2-FBA ($d_{C\cdots F}$ 3.42(4) Å).

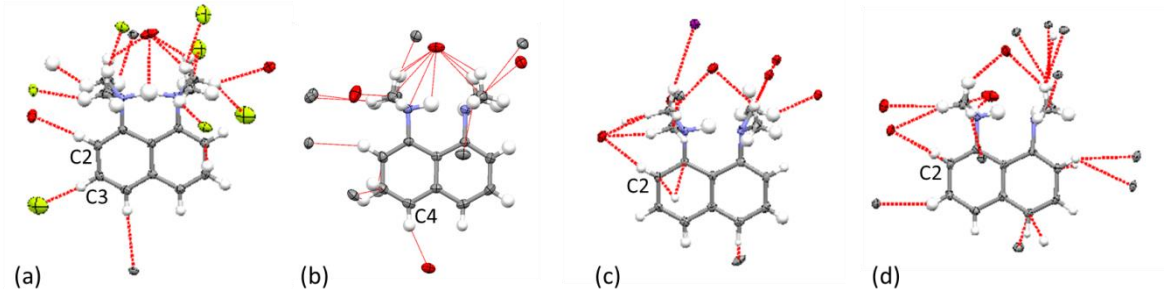

Figure 8.10 Weak interactions to the naphthalene C—H groups on the protonated side of the $DMANH^+$ cation in (a) DMAN2-FBA, (b) DMAN3-FBA, (c) DMAN2-IBA and (d) DMAN4-IBA.

In some cases, weak interactions to neighbouring X^- form to both sides of the fused rings of the $DMANH^+$ cation including in DMANBA, DMAN4-FBA hydrate, DMAN4-ClBA hydrate, DMAN3-OHBA hydrate and DMAN4-OHBA hydrate (Figure 8.11). On the protonated side, weak C—H···O hydrogen bonds occur at the C2 position involving an acid oxygen atom in

DMAN4-FBA ($d_{C\cdots O}$ 3.400(3) Å), DMAN4-ClBA hydrate ($d_{C\cdots O}$ 3.488(2) Å), DMAN3-OHBA hydrate ($d_{C\cdots O}$ 3.251(2) Å) and DMAN4-OHBA hydrate ($d_{C\cdots O}$ 3.229(2) Å). On the non-protonated side, weak C—H···O hydrogen bonds occur at the C6 position in DMAN3-OHBA hydrate ($d_{C\cdots O}$ 3.352(2) Å) to a water oxygen, in DMAN4-OHBA ($d_{C\cdots O}$ 3.216(2) Å) and DMAN4-OHBA hydrate B ($d_{C\cdots O}$ 3.626(2) Å) to a hydroxyl oxygen. In DMAN3-FBA, a weak C—H···O forms on the non-protonated side at the C5 position ($d_{C\cdots O}$ 3.430(3) Å) to a water oxygen and in DMAN4-ClBA hydrate a water bifurcates the C4 and C5 positions forming two C—H···O interactions ($d_{C\cdots O}$ 3.505(2) and 3.437(2) Å, respectively). In DMANBA, an acid oxygen bifurcates the C4 and C5 positions forming two C—H···O interactions ($d_{C\cdots O}$ 3.320(2) and 3.398(2) Å, respectively).

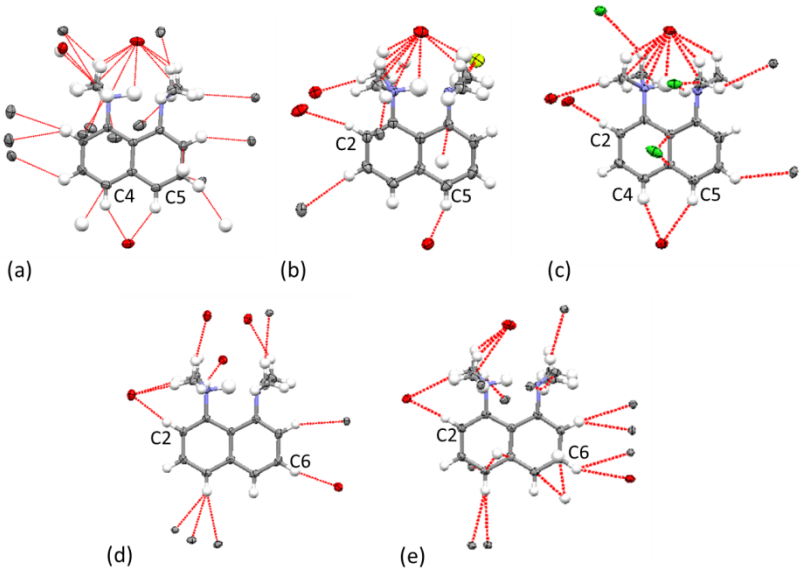

Figure 8.11 Weak interactions to the naphthalene C—H groups on both sides of the $DMANH^+$ cation in (a) DMANBA, (b) DMAN4-FBA hydrate, (c) DMAN4-ClBA hydrate, (d) DMAN3-OHBA hydrate and (e) DMAN 4-OHBA hydrate B.

In one case, DMAN4-OHBA hydrate (DMAN A), a weak interaction to a neighbouring X^- forms to the non-protonated side of the cation only; a weak C—H···O hydrogen bond forms to a hydroxyl oxygen atom ($d_{C\cdots O}$ 3.336(2) Å) at the C7 position (Figure 8.12).

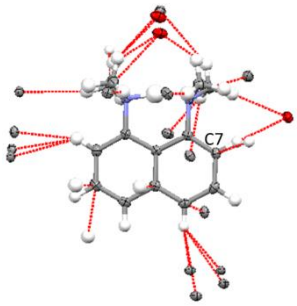

Figure 8.12 Weak interactions to the naphthalene C—H groups on the non-protonated side of the $DMANH^+$ cation (DMAN A) in DMAN 4-OHBA hydrate.

Overall, minor interactions between $DMANH^+$ and X^- in the local environment occurs more frequently to either the protonated side only or to both the protonated and the non-protonated side of the $DMANH^+$ cation.

8.4.3 Molecular structure

On anion variation, changes in the molecular structure of the DMAN and $ACID^-$ anion components occur.

[N—H···N]$^+$ IHB and O—H···O CAHB

In the $DMANH^+$ cation in each molecular complex, the proton position varies in the $[N—H···N]^+$ IHB. In the majority of cases, the proton is asymmetrically located (Table 8.9); the proton is symmetrically located only in DMAN2-FBA (N_1—H and H···N_2 are equivalent in length). The proton position in the IHB in DMANBA and DMAN4-OHBA is close to symmetric, being positioned just off-centre. The location of the proton in the O—H···O^- CAHB forming the $ACID^-$ dimer anion also varies (Table 8.10), and is found to be asymmetrically located and donated in all instances by the acid which does not sit above the $DMANH^+$ cation IHB. In DMAN2-FBA, DMAN4-FBA hydrate and DMAN4-ClBA hydrate, the proton sits just off centre in the O—H···O^- CAHB. There does not appear to be any correlation between the location of the proton in the $DMANH^+$ cation IHB and the location in the proton in the O—H···O^- hydrogen bond forming the $ACID^-$ dimer in the anion. There also does not appear to be any correlation between anion substituent and proton position in either hydrogen bond.

Table 8.9 The parameters of the IHB in the $[Me_2N_1—H···N_2Me_2]^+···X^-$ fragment across the molecular complexes.

Complex	$dN_1···N_2$ (Å)	$dN_1—H$ (Å)	$dH···N_2$ (Å)	$<N_1HN_2$ (°)
DMANBA	2.568(1)	1.24(2)	1.38(2)	158(2)
DMAN2-FBA	2.584(2)	1.31(3)	1.32(3)	159(2)
DMAN3-FBA	2.593(2)	1.06(2)	1.57(2)	158(2)
DMAN4-FBA hydrate	2.580(2)	1.19(2)	1.43(2)	161(2)
DMAN4-ClBA hydrate	2.590(2)	1.08(2)	1.56(2)	158(2)
DMAN2-IBA	2.566(3)	1.11(4)	1.49(4)	160(4)
DMAN3-IBA	2.581(3)	1.09(4)	1.54(4)	157(3)
DMAN4-IBA	2.606(3)	0.95(4)	1.71(4)	156(3)
DMAN3-OHBA hydrate	2.580(1)	1.15(2)	1.46(2)	163(2)
DMAN4-OHBA	2.566(2)	1.25(2)	1.35(2)	162(2)
DMAN4-OHBA hydrate	A 2.576(2) B 2.608(2)	1.19(2) 1.03(2)	1.42(2) 1.63(2)	160(2) 157(2)

Table 8.10 The parameters of the O—H···O^- CAHB in the $ACID^-$ dimers across the molecular complexes.

Complex	dO···O^- (Å)	dO—H (Å)	dH···O^- (Å)	<OHO (°)
DMANBA	2.470(1)	1.10(2)	1.38(3)	174(2)
DMAN2-FBA	2.453(2)	1.18(2)	1.28(2)	169(2)
DMAN3-FBA	2.489(2)	1.09(3)	1.41(3)	168(3)
DMAN4-FBA hydrate	2.454(2)	1.18(3)	1.27(3)	175(3)
DMAN4-ClBA hydrate	2.448(2)	1.19(3)	1.26(3)	176(2)
DMAN2-IBA	2.463(2)	1.13(4)	1.34(4)	175(5)
DMAN3-IBA	2.476(2)	1.13(3)	1.35(3)	175(4)
DMAN4-IBA	2.464(3)	1.00(4)	1.46(4)	176(4)
DMAN3-OHBA hydrate	2.524(1)	0.99(2)	1.55(2)	170(2)
DMAN4-OHBA	2.666(2)	0.97(2)	1.71(2)	170(2)
DMAN4-OHBA hydrate	2.530(1)	1.01(2)	1.54(2)	166(2)

Thermal parameters

The effect of the minor component, and its variation, on the thermal behaviour of the $[N—H···N]^+$ IHB proton may be monitored in Fourier difference maps. In neutron studies, many attempts have been made to relate the thermal parameters of a hydrogen atom in a hydrogen bond to the shape of the hydrogen bond potential well. [94] In X-rays, where the possibility of refining hydrogen atom parameters is more restricted, the shape of the electron density observed directly in a Fourier difference map may give some indication of the shape of the potential well and thermal behaviour. Differences in the shape of the hydrogen atom density for the IHB proton occur across the molecular complexes in the Fourier difference maps (Figure 8.13).

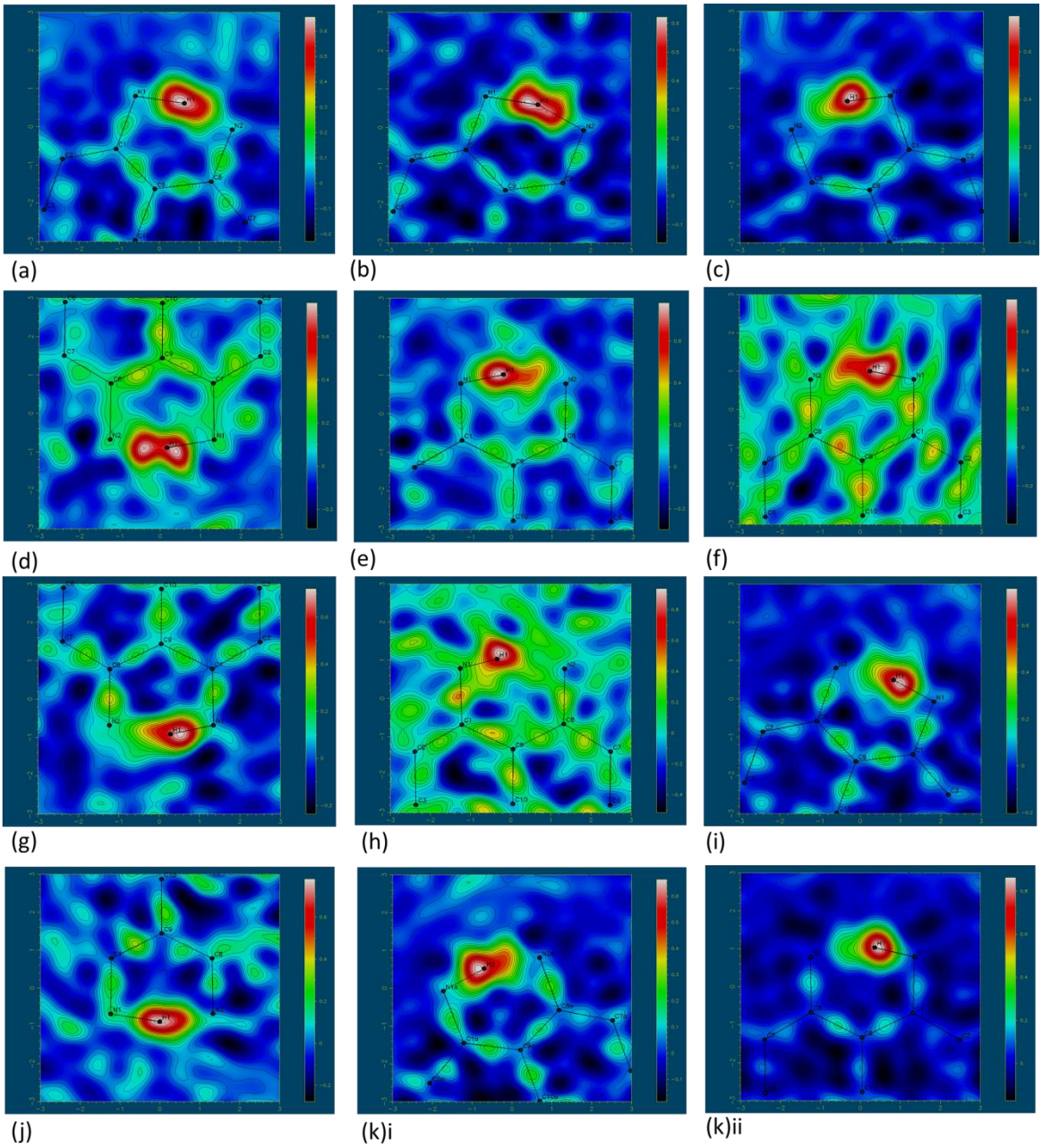

Figure 8.13 Fourier difference electron density maps showing the electron density associated with the H-atom in the [N—H···N]$^+$ IHB in (a) DMANBA, (b) DMAN2-FBA, (c) DMAN3-FBA, (d) DMAN4-FBA hydrate, (e) DMAN4-ClBA hydrate, (f) DMAN2-IBA, (g) DMAN3-IBA, (h) DMAN4-IBA, (i) DMAN3-OHBA hydrate, (j) DMAN4-OHBA, (k) DMAN4-OHBA hydrate i DMAN A and ii DMAN B.

The Fourier difference maps are of reasonable quality from the synchrotron X-ray structure determinations such that the determination of hydrogen atom behaviour is possible; in the maps of DMAN2-IBA and DMAN4-IBA large amounts of noise are present caused by the heavy iodine atom and make the determination more difficult. It should also be noted that the refined hydrogen atom position does not coincide with the peak maxima; a shift in the refined position occurs relative to the peak maxima which is consistent across the maps.

Ordered IHB protons are suggested for DMAN3-FBA, DMAN4-IBA and for DMAN4-OHBA hydrate DMAN B by a very spherical shape of electron density, suggesting an asymmetric double well potential for these hydrogen bonds and low proton thermal motion. This asymmetry supports the asymmetry observed in the refined hydrogen atom positions for these molecular complexes. Some elongation of the IHB proton density along the IHB occurs for DMAN3-IBA and DMAN3-OHBA hydrate whilst this elongation is more significant for DMAN4-ClBA, DMAN2-IBA and DMAN4-OHBA hydrate DMAN A; increased proton thermal motion is indicated for these molecular complexes in an IHB with a more symmetric double well potential. DMANBA, DMAN2-FBA and DMAN4-OHBA have symmetrically shaped elongated density at a more central position in the IHB, suggestive of a flatter single well potential and greater proton thermal motion; the flattest occurs for DMAN2-FBA. This symmetry is in support of the symmetry observed in the refined hydrogen atom positions for these molecular complexes. This increased thermal motion occurs in DMANBA, DMAN2-FBA and DMAN4-OHBA where the H···X^- distances are 2.53(2), 2.68(2) and 3.46(2) Å, respectively; no correlation between extent of proton thermal motion and the proximity of the IHB proton and X^- is therefore suggested. The density of the IHB proton in DMAN4-FBA hydrate appears as a split peak in the Fourier difference map, suggesting the possibility of proton disorder. This behaviour can be described by a double well potential with a low barrier to proton transfer. Refining the occupancies of the two proton sites results in a 56:44 disorder.

Significant differences in the shape of the hydrogen atom density for the $ACID^-$ dimer proton (Figure 8.14) are observed across the molecular complexes. The $ACID^-$ dimer proton density has a spherical shape for DMANBA, DMAN3-IBA, DMAN3-OHBA hydrate, DMAN4-OHBA, and DMAN4-OHBA hydrate DMAN A and is suggestive of an ordered proton with low thermal motion in an asymmetric O—H···O hydrogen bond double well potential. This asymmetry supports the asymmetry observed in the refined hydrogen atom positions for these molecular complexes. In DMAN2-FBA, DMAN2-IBA and DMAN4-IBA, the proton electron density is elongated along the hydrogen bond and could indicate a more symmetric double well potential and increased proton thermal motion. This symmetry is in support of the symmetry observed in the refined hydrogen atom positions for these molecular complexes in the case of DMAN2-FBA and DMAN2-IBA but not for DMAN4-IBA; the refined hydrogen atom position may therefore be less reliable for this complex. In DMAN2-FBA, DMAN4-FBA hydrate and DMAN4-ClBA hydrate, the proton electron density is symmetrically elongated, indicating a flatter single well potential for these O—H···O hydrogen bonds and increased thermal motion.

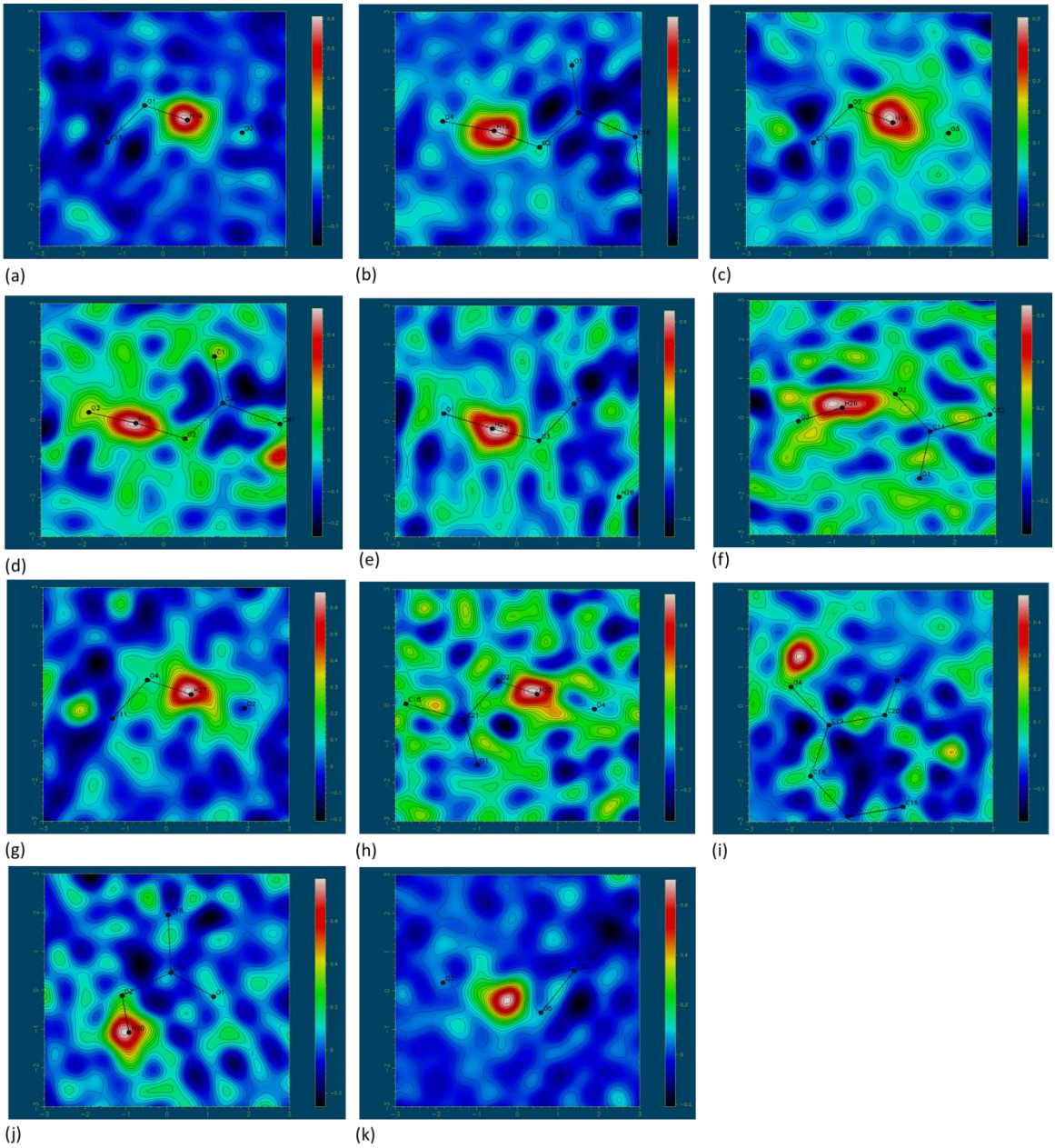

Figure 8.14 Fourier difference electron density maps showing the electron density associated with the H-atom in the $ACID^-$ dimer O—H···O hydrogen bond in (a) DMANBA, (b) DMAN2-FBA, (c) DMAN3-FBA, (d) DMAN4-FBA hydrate, (e) DMAN4-ClBA hydrate, (f) DMAN2-IBA, (g) DMAN3-IBA, (h) DMAN4-IBA, (i) DMAN3-OHBA hydrate, (j) DMAN4-OHBA, (k) DMAN4-OHBA hydrate DMAN A.

In general, hydrogen bonds with a shorter D···A distance should give a flatter potential energy well. [7] This is the case for the molecular complexes in this section. Increasingly flat single well potentials for the $[N—H···N]^+$ IHB are suggested for DMANBA, DMAN2-FBA and DMAN4-OHBA where the IHB N···N distances are some of the shortest whilst the most asymmetric double well potentials are suggested in DMAN3-FBA, DMAN4-IBA and DMAN4-OHBA hydrate DMAN B where the IHB N···N distances are some of the longest. Proton behaviour in hydrogen bonds in these complexes may therefore be more related to hydrogen bond

donor-acceptor distances than the proximity of the IHB proton and X^-. For the $ACID^-$ dimer O—H···O hydrogen bond, the flattest potential wells were again suggested where the O···O distances were the shortest (around 2.45 Å), in DMAN2-FBA, DMAN4-FBA hydrate and DMAN4-ClBA hydrate.

In the previous neutron diffraction studies of these molecular complexes, a correlated thermal motion of the IHB proton and X^- displacement parameters along the $[N—H···N]^+$ IHB indicated an interaction of the two atoms occurring when in close proximity ($d_{H···X^-}$ 2.61 to 2.81 Å). [133, 135] Here, only isotropic thermal parameters of the IHB proton can be determined from the synchrotron X-ray diffraction studies (Figure 8.15); in this case an enlarged hydrogen atom isotropic thermal parameter, relative to those in rest of the structure, can suggest movement along the $[N—H···N]^+$ IHB hydrogen bond. Enlarged IHB proton isotropic thermal parameters are observed for DMANBA, DMAN2-FBA, DMAN4-FBA hydrate and DMAN4-ClBA hydrate; in these cases the anisotropic thermal parameter of X^- also lies along the IHB suggesting interaction between the two atoms. The $H···X^-$ distances are correspondingly short (2.53(2), 2.68(2), 2.56(2) and 2.56(2) Å respectively). The correlation suggested in the thermal parameters of H and X^- in DMAN2-FBA is in agreement with that observed in the complex at 200 K in the neutron diffraction study. [133, 135] In DMAN4-OHBA hydrate A (Figure 8.15(k)), the thermal parameter of the water oxygen atom lies along the hydrogen bond but the IHB proton does not have an enlarged thermal parameter. Despite the short $H···X^-$ distance of 2.77(2) Å, interaction is therefore not suggested; this may be due to the $H···X^-$ having less of a charged attractive component. Smaller IHB proton thermal parameters occur where the thermal parameter of X^- does not lie along the bond including in DMAN4-IBA, DMAN3-OHBA hydrate, DMAN4-OHBA.

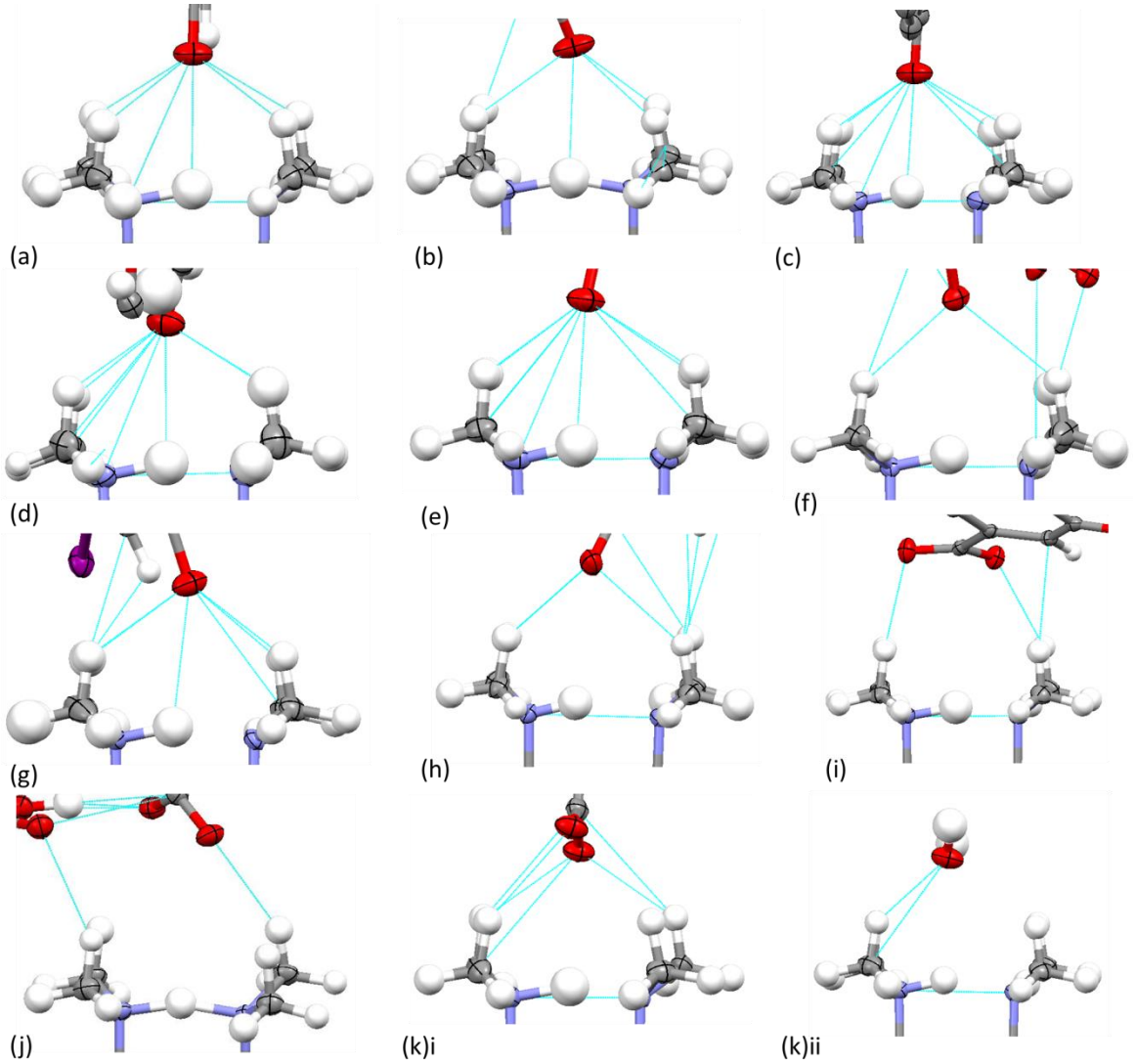

Figure 8.15 Thermal parameters of the IHB proton and X^- in the $[Me_2N—H\cdots NMe_2]^+\cdots X^-$ fragment in (a) DMANBA, (b) DMAN2-FBA, (c) DMAN3-FBA, (d) DMAN4-FBA hydrate, (e) DMAN4-ClBA hydrate, (f) DMAN2-IBA, (g) DMAN3-IBA, (h) DMAN4-IBA, (i) DMAN3-OHBA hydrate, (j) DMAN4-OHBA and (k) DMAN4-OHBA hydrate i DMAN A and ii DMAN B.

ACID⁻ anion and DMANH⁺ cation

The effect of altering the minor component by changing the anion is also reflected in structural changes within components of the $ACID^-$ dimer (Table 8.11) and the $DMANH^+$ cation (Table 8.12).

In the majority of the aggregates, the acid dimer is non-planar; the benzene rings of each acid are twisted by 70 to 90 ° degrees from planarity with one another (Figure 8.16). In DMAN4-FBA hydrate and DMAN4-ClBA hydrate the components of the acid dimers are close to being co-planar, with the benzene rings twisted by 12 to 14 ° from planarity with one another and the carboxylic acid groups flat relative to one another (COOC twist angles of 173.6(2) and −171.2(2) °

respectively). The moieties within the $ACID^-$ dimers are also all relatively planar; the largest twist out of planarity of the carboxylic acid group with the benzene ring occurs in DMAN2-FBA, DMAN2-IBA and DMAN4-IBA.

Table 8.11 Angles within the $ACID^-$ dimer in each DMAN molecular complex including the torsion angle of the carboxyl and carboxylate groups forming the SSHB (angle 1 COOC), the torsion angle between carboxylate group and benzene ring in the deprotonated acid (angle 2 $^-$OCCC where O^- is X^-), the torsion angle between carboxyl group and benzene ring in the protonated acid (angle 3 OCCC) and the co-planarity of the benzene rings of each acid (angle 4).

Complex	Angle 1 COOC (°)	Angle 2 OCCC (°)	Angle 3 HOCCC (°)	Angle 4 (°)
DMANBA	103.5(1)	–3.9(2)	–9.3(2)	86.31
DMAN2-FBA	120.4(1)	–34.0(2)	6.02(2)	83.83
DMAN3-FBA	90.5(2)	1.0(2)	–4.4(2)	89.90
DMAN4-FBA hydrate	173.6(2)	–7.3(2)	7.8(2)	12.23
DMAN4-ClBA hydrate	–171.2(2)	11.3(2)	-10.8(2)	13.92
DMAN2-IBA	–116.9(2)	–41.8(3)	52.3(3)	70.89
DMAN3-IBA	81.6(2)	4.2(3)	1.3(3)	89.64
DMAN4-IBA	–42.4(3)	–25.9(4)	–8.8(4)	74.15
DMAN3-OHBA hydrate	87.0(1)	–12.2(2)	-	76.28
DMAN4-OHBA	–24.98	8.5(2)	–28.1(2)	87.81
DMAN4-OHBA hydrate	–121.0(2)	3.3(2)	-	72.01

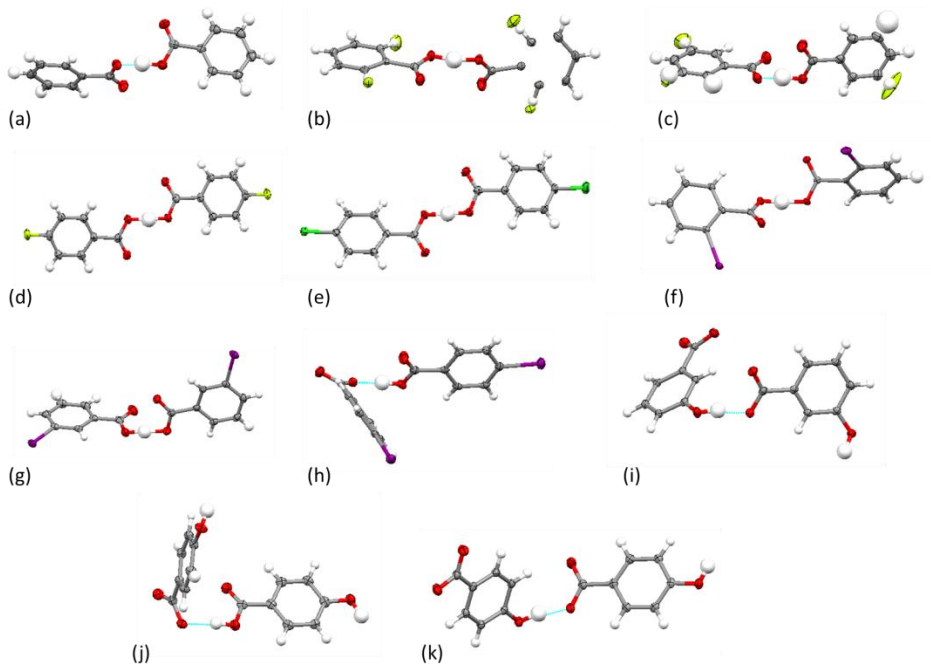

Figure 8.16 Torsions between carboxyl and carboxylate groups in the $ACID^-$ dimers in (a) DMANBA, (b) DMAN2-FBA, (c) DMAN3-FBA, (d) DMAN4-FBA hydrate, (e) DMAN4-ClBA hydrate, (f) DMAN2-IBA, (g) DMAN3-IBA, (h) DMAN4-IBA, (i) DMAN3-OHBA hydrate, (j) DMAN4-OHBA and (k) DMAN4-OHBA hydrate (DMAN A).

On protonation of DMAN, the *peri*-amino groups reorient from a staggered to an eclipsed arrangement (Table 8.12). [125] In DMAN2-FBA and DMAN4-OHBA, there is a significant deviation from the eclipsed arrangement (NCCN torsion angles of –3.4(1) and 7.2(1) ° respectively).

Table 8.12 The torsion angle between DMAN amino groups in each molecular complex.

Complex	$DMANH^+$ *peri*-amino group torsion (NCCN) (°)
DMANBA	–0.38(9)
DMAN2-FBA	–3.4(1)
DMAN3-FBA	–2.0(1)
DMAN4-FBA hydrate	–1.2(1)
DMAN4-ClBA hydrate	0.8(1)
DMAN2-IBA	–1.5(2)
DMAN3-IBA	0.9(2)
DMAN4-IBA	–0.3(2)
DMAN3-OHBA hydrate	0.89(9)
DMAN4-OHBA	7.2(1)
DMAN4-OHBA hydrate	A 2.17(9) B 0.78(9)

Different extents of changes in the structural parameters may be observed on different sides of the $DMANH^+$ cation, reflecting the symmetry of the IHB, whilst the changes in the $DMANH^+$ structural parameters across the different molecular complexes reflects the effect of changing the anion and the minor interactions (Table 8.13 and Table 8.14).

Across the DMAN molecular complexes, there is a difference in structural parameters due to the effect of the proton location and minor interactions with the anion. In the majority of the molecular complexes, except for DMAN2-FBA, the refined IHB proton position indicates an asymmetrically located proton. There is also a general asymmetry in the equivalent C—C bond distances on the protonated and non-protonated side of the molecule, in particular between C_1—C_2 and C_7—C_8, and between C_3—C_4 and C_5—C_6 (see Figure 1.20 for atom labelling scheme). In DMAN2-FBA, the refined hydrogen atom position suggests a proton that is symmetrically located in the IHB and, reflecting this, the equivalent C—C bond distances on the left and right hand side of the DMAN molecule are very similar in length. The C—N *peri*-amino distances are also slightly longer for the side on which the proton resides, C_1—N_1, in all the molecular complexes. In DMAN2-FBA, there is a slight asymmetry in the two C—N lengths suggesting a slight preference for one side of the IHB over the other. A larger *ipso* angle and smaller NCC angle is also observed on the protonated side of the $DMANH^+$ for all the molecular complexes in which the refined hydrogen atom positions indicate a proton that is asymmetrically located. The CNC angle between the methyl groups decreases slightly on protonation and an asymmetry in these values on either side of the IHB is also observed in all the molecular complexes. A lesser shortening of C_1—C_2 and C_7—C_8 occurs for DMAN2-FBA, DMAN3-FBA DMAN3-IBA whilst a greater shortening of C_3—C_4 and C_5—C_6 occurs for DMANBA, DMAN4-FBA hydrate and DMAN4-ClBA hydrate. DMANBA and DMAN3-FBA have significantly shorter C—N distances then the other molecular complexes.

Table 8.13 The C—C (Å) bond lengths in the neutral DMAN [124] and in the $DMANH^+$ cations of the molecular complexes (see Figure 1.20 for atom labelling scheme).

Complex	C_9—C_1	C_1—C_2	C_2—C_3	C_3—C_4	C_4—C_{10}	C_{10}—C_5	C_5—C_6	C_6—C_7	C_7—C_8	C_8—C_9	C_9—C_{10}
DMAN [124]	1.448(1)	1.394(1)	1.413(2)	1.370(2)	1.426(2)	1.419(2)	1.374(2)	1.412(2)	1.390(2)	1.450(1)	1.437(1)
DMANBA	1.426(2)	1.359(2)	1.404(2)	1.362(2)	1.408(2)	1.416(2)	1.355(2)	1.402(2)	1.363(2)	1.422(1)	1.427(2)
DMAN2-FBA	1.430(2)	1.374(2)	1.410(2)	1.367(2)	1.420(2)	1.420(2)	1.367(2)	1.411(2)	1.373(2)	1.435(2)	1.434(2)
DMAN3-FBA	1.425(2)	1.370(2)	1.406(2)	1.362(2)	1.421(2)	1.414(2)	1.365(2)	1.408(3)	1.367(2)	1.434(2)	1.431(2)
DMAN4-FBA hydrate	1.423(2)	1.364(3)	1.405(3)	1.361(3)	1.411(3)	1.415(3)	1.358(3)	1.397(3)	1.368(3)	1.431(2)	1.434(3)
DMAN4-ClBA hydrate	1.422(2)	1.364(2)	1.410(3)	1.360(3)	1.419(3)	1.415(3)	1.357(3)	1.407(3)	1.364(2)	1.432(2)	1.432(2)
DMAN2-IBA	1.429(3)	1.368(4)	1.409(4)	1.367(3)	1.417(4)	1.424(3)	1.366(4)	1.405(4)	1.363(3)	1.428(4)	1.437(4)
DMAN3-IBA	1.425(3)	1.376(4)	1.407(3)	1.368(3)	1.420(4)	1.420(3)	1.367(4)	1.400(3)	1.378(3)	1.435(4)	1.433(3)
DMAN4-IBA	1.430(3)	1.364(4)	1.400(5)	1.365(4)	1.413(4)	1.413(4)	1.368(4)	1.404(4)	1.374(4)	1.428(4)	1.428(4)
DMAN3-OHBA hydrate	1.432(2)	1.367(2)	1.408(2)	1.368(2)	1.415(2)	1.423(2)	1.362(2)	1.410(2)	1.372(2)	1.430(2)	1.429(2)
DMAN4-OHBA	1.427(2)	1.363(2)	1.410(2)	1.364(3)	1.421(2)	1.415(3)	1.369(3)	1.410(3)	1.366(2)	1.425(2)	1.434(2)
DMAN4-OHBA hydrate	A 1.433(2) B 1.428(2)	1.366(2) 1.369(2)	1.416(2) 1.409(2)	1.369(2) 1.365(2)	1.418(2) 1.422(2)	1.420(2) 1.417(2)	1.365(2) 1.369(2)	1.411(2) 1.412(2)	1.374(2) 1.369(2)	1.429(2) 1.436(2)	1.434(2) 1.432(2)

Table 8.14 The C—N *peri*-amino bond lengths and angles in the neutral DMAN [124] and in the $DMANH^+$ cations of the molecular complexes (see Figure 1.20 for atom labelling scheme).

Complex	C_1—N_1 (Å)	C_2—N_8 (Å)	$<C_2C_1C_9$ (°)	$<C_9C_8C_7$ (°)	$<N_1C_1C_9$ (°)	$< N_2C_8C_9$ (°)	$<CN_1C$ (°)	$<CN_2C$ (°)
DMAN [124]	1.402(1)	1.405(2)	119.09(9)	118.8(1)	120.57(9)	120.74(9)	111.92(9)	112.4(1)
DMANBA	1.464(1)	1.458(2)	121.3(1)	120.9(1)	118.1(1)	118.6(1)	111.0(1)	111.2(1)
DMAN2-FBA	1.471(2)	1.467(2)	121.4(1)	121.2(1)	118.2(1)	118.0(1)	110.6(1)	111.2(1)
DMAN3-FBA	1.469(2)	1.462(2)	121.5(1)	120.6(1)	119.0(1)	118.0(1)	111.4(1)	111.0(1)
DMAN4-FBA hydrate	1.473(2)	1.457(2)	121.8(2)	120.6(2)	118.1(1)	118.4(1)	111.0(1)	111.3(2)
DMAN4-ClBA hydrate	1.475(2)	1.463(2)	122.0(2)	121.0(2)	118.4(1)	118.2(1)	112.1(1)	112.0(1)
DMAN2-IBA	1.470(3)	1.464(3)	122.1(2)	120.8(3)	117.5(2)	117.9(2)	111.0(2)	111.7(3)
DMAN3-IBA	1.470(3)	1.462(3)	122.2(2)	120.9(2)	118.3(2)	117.8(2)	111.8(2)	110.6(2)
DMAN4-IBA	1.475(4)	1.448(4)	122.1(3)	120.6(3)	118.3(2)	118.5(2)	110.6(2)	111.7(2)
DMAN3-OHBA hydrate	1.471(2)	1.463(2)	122.4(1)	120.8(1)	117.7(1)	118.4(1)	111.7(1)	111.7(1)
DMAN4-OHBA	1.470(2)	1.465(2)	121.5(2)	121.1(2)	117.8(1)	118.2(1)	111.3(1)	110.9(1)
DMAN4-OHBA hydrate	A 1.468(2)	1.468(2)	121.8(1)	121.2(1)	118.0(1)	118.0(1)	111.4(1)	110.7(1)
	B 1.478(2)	1.458(2)	122.0(1)	120.8(1)	118.6(1)	118.2(1)	111.4(1)	111.2(1)

Variation in the bond lengths of the carboxylate groups (C—O^-, C=O_1) and the carboxyl (C—OH and C=O_2) groups occurs across the molecular complexes (Table 8.15). These variations may reflect the refined hydrogen atom position of the proton in the $ACID^-$ dimer hydrogen bond and be a result of being involved in the minor interactions in the $[Me_2N—H\cdots NMe_2]^+\cdots X^-$ fragment. Between the two acid molecules forming the dimer, the carboxyl bond lengths are most similar to those of the carboxylate where the refined hydrogen atom position indicates a proton that is most symmetrically located in the $ACID^-$ dimer O—H···O hydrogen bond and *vice versa*.

Table 8.15 The bond lengths of the carboxylate and carboxyl groups in the $ACID^-$ dimer across the molecular complexes.

Complex	Carboxylate group		Carboxyl group	
	dC—O^- (Å)	dC=O_1 (Å)	dC—OH (Å)	dC=O_2 (Å)
DMANBA	1.275(2)	1.232(2)	1.303(1)	1.219(2)
DMAN2-FBA	1.285(2)	1.230(2)	1.298(1)	1.225(2)
DMAN3-FBA	1.271(3)	1.240(2)	1.305(2)	1.217(2)
DMAN4-FBA hydrate	1.300(2)	1.220(2)	1.292(2)	1.232(2)
DMAN4-ClBA hydrate	1.299(2)	1.225(2)	1.296(2)	1.232(2)
DMAN2-IBA	1.294(3)	1.227(3)	1.277(4)	1.230(4)
DMAN3-IBA	1.277(3)	1.236(3)	1.303(3)	1.229(3)
DMAN4-IBA	1.294(4)	1.231(4)	1.304(4)	1.215(4)
DMAN3-OHBA hydrate	1.271(1)	1.245(2)	1.361(2)	-
DMAN4-OHBA	1.280(2)	1.256(2)	1.338(2)	1.218(2)
DMAN4-OHBA hydrate A	1.268(1)	1.256(1)	1.360(2)	-

8.5 Synchrotron and X-ray diffraction studies of new DMAN substituted benzoic acid molecular complexes

In this section, synchrotron X-ray diffraction is applied to new DMAN substituted benzoic acid molecular complexes. The effect of anion (X^-) variation, by substitution, on features of the crystal packing and molecular structure is investigated and the low temperature $DMANH^+$ IHB proton transfer behaviour is studied.

Eight previously unknown molecular complexes of DMAN with a selection of substituted benzoic acids containing both electron withdrawing and electron donating groups have been prepared containing the $[Me_2N—H\cdots NMe_2]^+\cdots X^-$ fragment.

8.5.1 Anion variation

The change in both the identity of the substituent and the ring position alters the electronics of the conjugate base X^-. In this new set of molecular complexes, components were found to crystallise in a number of ratios including 1:1, 1:2 and 1:3 of the DMAN organic acid components; in these, single $ACID^-$ units, $ACID^-$ dimers and trimers (Figure 8.17) are present.

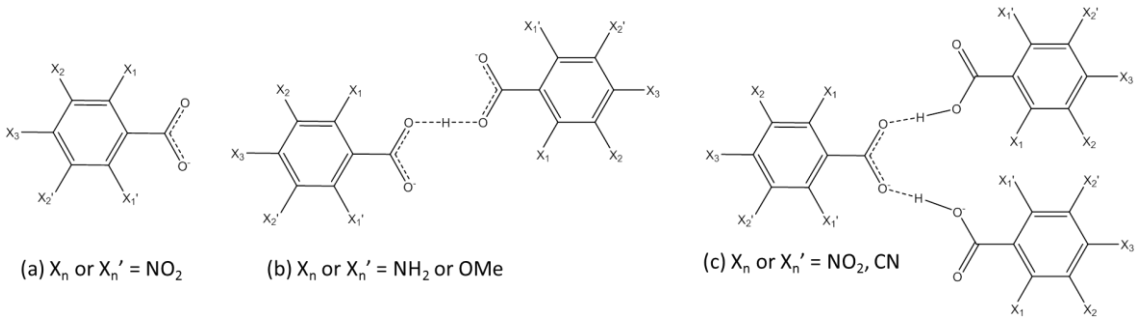

Figure 8.17 The $ACID^-$ anion substitution for a (a) single $ACID^-$ anion, (b) an $ACID^-$ dimer and (c) an $ACID^-$ trimer unit.

The effect of the anion and minor component on the crystal structure is again of interest in these materials particularly where changing the withdrawing or donating nature of the substituent altered the identity of X^- in the $[Me_2N—H\cdots NMe_2]^+\cdots X^-$ fragment. The molecular complexes were studied using synchrotron X-ray diffraction with the exception of DMAN 4-ABA and DMAN4-NBA II which were studied using X-ray diffraction from a laboratory source.

8.5.2 Crystal packing

On substituting the anion, there are changes to the wider crystal packing in the 1:1, 1:2 and 1:3 molecular complexes (Figure 8.18). In five of the molecular complexes, the inorganic type arrangement where the packing is built up from layers of pairs of $DMANH^+$ cations and pairs of the $ACID^-$ anion units is adopted.

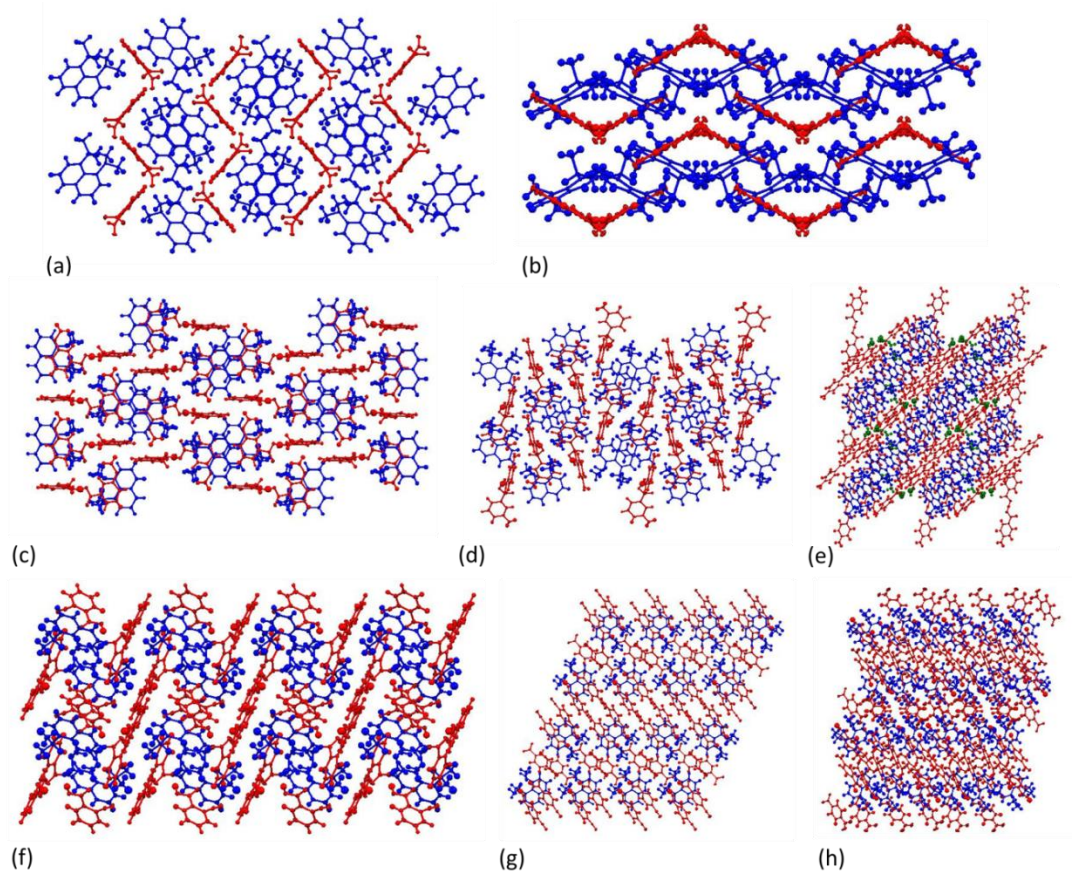

Figure 8.18 Molecular packing in the molecular complexes of (a) DMAN5-NIP, (b) DMAN2-NBA, (c) DMAN3-OMBA, (d) DMAN3-ABA, (e) DMAN4-ABA hydrate (f) DMAN2-CBA, (g) DMAN4-CBA, (h) DMAN4-NBA II. The $DMANH^+$ cation is shown in blue, the $ACID^-$ anion in red and water molecules in green.

In DMAN2-NBA, DMAN5-NIP, DMAN3-OMBA, DMAN3-ABA and DMAN4-ABA hydrate, the $DMANH^+$ cations stack in anti-parallel pairs. These are isolated pairs with the exception of DMAN5-NIP and DMAN4-ABA hydrate, which forms columns of interacting $DMANH^+$ cations (Figure 8.19(a) and (b)). In DMAN2-CBA, DMAN4-CBA and DMAN4-NBA II, the $DMANH^+$ cations adopt the other type of inorganic crystal packing; each cation is surrounded by six $ACID^-$ molecules; in DMAN2-CBA and DMAN4-CBA this packing forms chains of DMAN through the structure (Figure 8.19(c) and (d)).

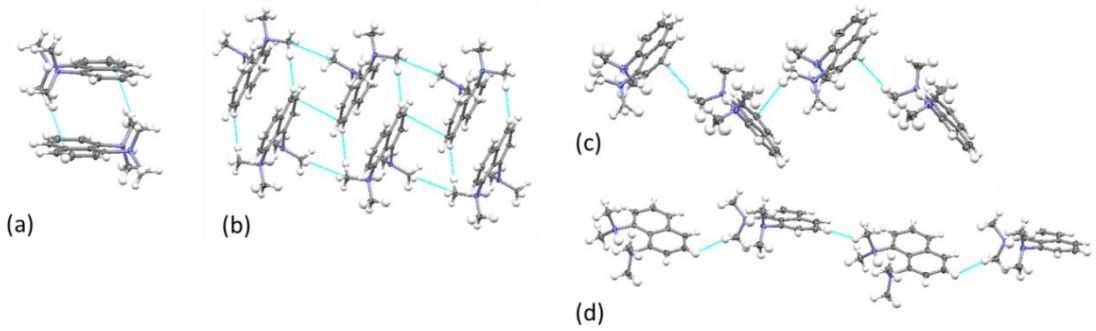

Figure 8.19 Molecular packing of the $DMANH^+$ cations in (a) isolated anti-parallel pairs, (b) anti-parallel in columns, (c) and (d) in single chains.

At the more local level of the crystal packing, the $DMANH^+$ cation and $ACID^-$ anion units aggregate into the $[Me_2N—H\cdots NMe_2]^+\cdots X^-$ fragment (Figure 8.20 and Figure 8.21); the substitution of the anion alters how this aggregation occurs. Where there are electron donating substituents on the benzoic acid ring, the aggregation of the $DMANH^+$ cation and $ACID^-$ units occurs in a 1:2 ratio and where X^- is the deprotonated oxygen atom, as seen in the complexes in §8.4. In contrast, where there are electron withdrawing substituents on the benzoic acid ring, the aggregation of the $DMANH^+$ cation and $ACID^-$ units occurs in a 1:1 or 1:3 ratio, and the electron withdrawing substituents are inserted into the space above the $DMANH^+$ IHB in preference to the deprotonated oxygen atom of the carboxylic acid group; one exception to this DMAN2-NBA where X^- is the deprotonated oxygen atom. The acid groups forming the dimer and trimer hydrogen bonded units do not catenate further. DMAN5-NIP forms a 1:1 aggregate *via* the $[Me_2N—H\cdots NMe_2]^+\cdots X^-$ fragment, however due the presence of the additional carboxylic acid group, continuous hydrogen bonded chains form between the $ACID^-$ molecules.

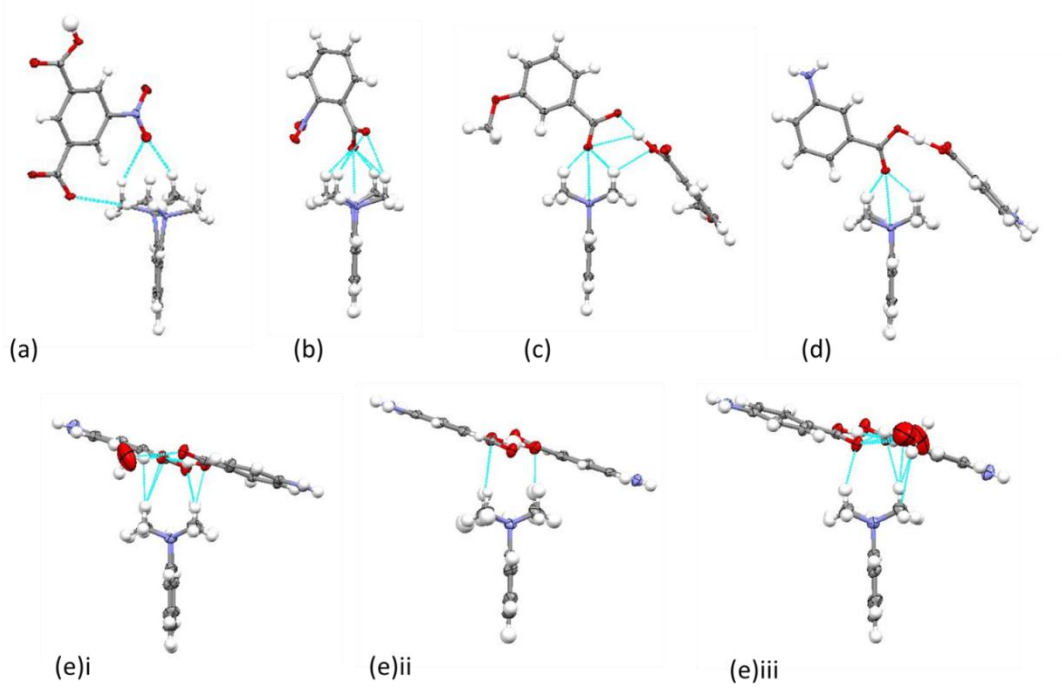

Figure 8.20 The aggregation of the $DMANH^+$ cation and $ACID^-$ anion unit in (a) DMAN5-NIP, (b) DMAN2-NBA, (c) DMAN3-OMBA, (d) DMAN3-ABA and (e) DMAN4-ABA hydrate i DMAN A, ii DMAN B and iii DMAN C.

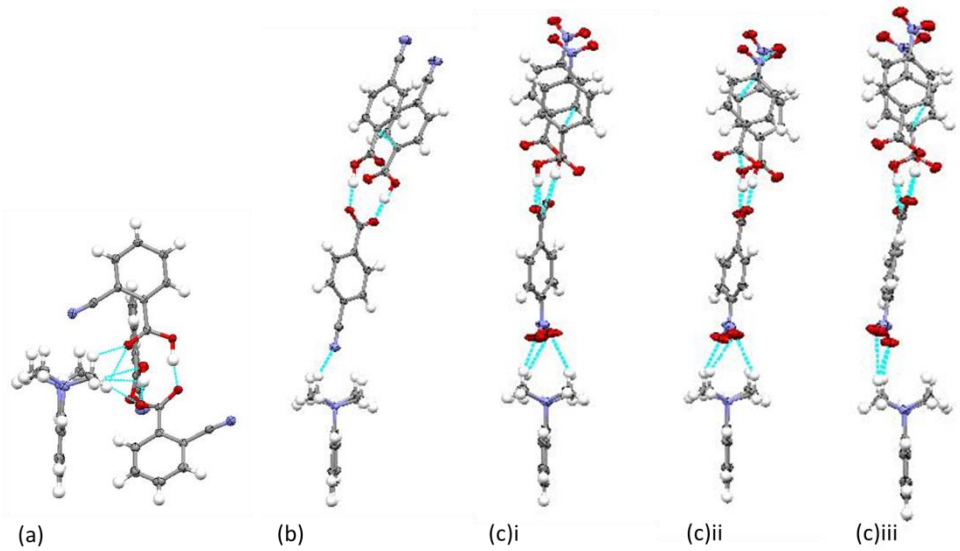

Figure 8.21 The aggregation of the $DMANH^+$ cation and $ACID^-$ anion unit in (a) DMAN2-CBA, (b) DMU4-CBA and (c) DMAN4-NBA II i DMAN A, ii DMAN B and iii DMAN C.

The $[Me_2N—H\cdots NMe_2]^+\cdots X^-$ fragment minor components

Aggregation of the $DMANH^+$ cation and $ACID^-$ anion units occurs *via* the minor component of the $[Me_2N—H\cdots NMe_2]^+\cdots X^-$ fragment *via* weak C—H$\cdots$ X^- hydrogen bonds (Table 8.16 to Table 8.18). X^- is the deprotonated carboxyl oxygen atom in DMAN2-NBA, DMAN3-OMBA, DMAN3-ABA and DMAN4-ABA whilst it is the non-carboxylic acid group substituent in DMAN5-NIP, DMAN2-CBA, DMAN4-CBA and DMAN4-NBA II. Additional minor interactions also form between the $[Me_2N—H\cdots NMe_2]^+$ component and neighbouring X^- atoms. In general, shorter minor interactions occur where X^- is the carboxylic acid group in contrast to where X^- is an electron withdrawing substituent. The shortest and greatest number of the weak C—H$\cdots X^-$ interactions form to the most protonated $N(CH_3)_2$ group; DMAN2-NBA is the only exception to this where the deprotonated oxygen is closest to the non-protonated dimethylamine, however the position of the carboxylic acid group overall is over the protonated dimethylamine; a second minor interaction forms between the methyl C—H and a second acid oxygen.

Table 8.16 The parameters of the minor component (C—H···X^-) of the $[Me_2N_1—H···N_2Me_2]^+···X^-$ fragment across the molecular complexes. $N(CH_3)_2$ group 1 is the most 'protonated' forming the IHB.

Complex	$N(CH_3)_2$ group	Interaction	dC···X^- (Å)	dC—H (Å)	dH···X^- (Å)	<CHX^- (°)
DMAN	1	C11—H14···O4	3.373(2)	0.98(1)	2.54(2)	143(1)
5-NIP	1	C12—H18···O4	3.393(3)	0.97(2)	2.56(2)	145(1)
	2	C14—H12···O4	4.439(1)	0.97(2)	3.86(1)	121(1)
	2	C13—H9···O4	3.970(1)	0.97(2)	3.28(2)	130(1)
	1	C11—H15···O2	3.285(1)	0.96(2)	2.37(2)	159(1)
	2	C13—H8···O1	3.559(2)	0.96(2)	2.65(1)	158(1)
DMAN	1	C14—H12···O2	3.363(1)	0.99(2)	2.70(1)	125(1)
2-NBA	1	C13—H10···O2	3.405(2)	0.96(2)	2.54(2)	150(1)
	2	C11—H14···O2	3.238(2)	0.98(2)	2.52(2)	130(1)
	2	C12—H17···O2	3.195(2)	0.99(2)	2.47(2)	130(1)
	1	C14—H12···O1	3.391(1)	0.99(2)	2.47(2)	156(1)
	1	C14—H11···O1'	3.234(2)	0.96(2)	2.33(2)	156(1)
	1	C13—H9···O1'	3.538(2)	0.98(2)	2.70(2)	143(1)
	1	C13—H8···O3	3.591(2)	0.97(2)	2.72(2)	151(1)
	2	C11—H16···O3	3.561(2)	0.96(2)	2.65(2)	160(1)
	2	C12 ···O4	3.180(2)			
DMAN	1	C13—H10···O1	3.154(2)	1.00(2)	2.45(2)	127(1)
3-OMBA	1	C14—H11···O1	3.083(3)	1.00(2)	2.39(2)	126(1)
	2	C12—H15···O1	3.196(2)	1.00(2)	2.51(2)	125(1)
	2	C11—H17···O1	3.301(3)	1.00(2)	2.64(2)	124(1)
	2	C11—H17···O4	3.241(2)	1.00(2)	2.62(2)	121(1)
DMAN	1	C11—H11···O1	3.203(2)	0.98(2)	2.52(2)	126(1)
3-ABA	1	C12—H8···O1	3.105(2)	0.98(2)	2.42(2)	127(1)
	2	C13—H17···O1	3.149(2)	0.97(2)	2.48(2)	126(1)
	2	C14—H15···O1	3.379(1)	0.97(2)	2.76(1)	122(1)
	1	C11—H12···O3	3.120(2)	0.98(2)	2.54(2)	118(1)
	2	C13—H19···O2	3.666(2)	0.98(2)	2.70(2)	168(1)

Table 8.17 The parameters of the minor component (C—H···X^-) of the $[Me_2N_1—H···N_2Me_2]^+···X^-$ fragment (continued) across the molecular complexes. $N(CH_3)_2$ group 1 is the most 'protonated' forming the IHB.

Complex	$N(CH_3)_2$ group	Interaction	dC···X^- (Å)	dC—H (Å)	dH···X^- (Å)	<CHX^- (°)
DMAN	1A	C14A—H10A···O6	3.477(7)	0.92(4)	2.68(4)	146(3)
4-ABA	1A	C13A—H13A···O5	3.516(6)	1.03(5)	2.51(5)	164(4)
hydrate	1A	C13A—H12A···N7	3.672(6)	0.98(5)	2.72(5)	163(4)
	2A	C11A—H16A···O6	4.040(6)	0.91(4)	3.38(5)	131(4)
	2A	C12A—H17A···O6	3.456(3)	1.01(4)	2.61(3)	141(3)
	1B	C13B—H19B···O1	3.555(5)	0.91(5)	2.65(5)	175(4)
	1B	C14B—H15B···O1'	3.226(6)	0.95(6)	2.42(5)	143(4)
	2B	C12B—H10B···O2	3.582(5)	1.03(4)	2.80(4)	133(3)
	2B	C11B—H12B···O2	3.628(7)	0.92(4)	2.86(3)	141(3)
	2B	C12B—H10B···N4	3.607(7)	1.03(4)	2.66(4)	153(3)
	2B	C12B—H8B···O12	3.344(6)	0.94(4)	2.53(5)	145(3)
	1C	C11C—H10C···O4	3.772(5)	0.98(4)	3.01(4)	135(4)
	1C	C12C—H12C···O4	3.358(5)	1.01(4)	2.43(4)	153(3)
	2C	C13C—H14C···O3	3.706(7)	0.93(6)	2.79(6)	172(5)
	2C	C14C—H17C···O5	3.313(6)	0.96(4)	2.42(3)	156(3)
	1C	C11C—H10C···O16	3.52(1)	0.98(4)	2.57(5)	161(4)
	1C	C11C—H8C···O8	3.543(7)	1.00(6)	2.71(6)	141(6)
DMAN	1	C12—H15···N3	3.697(3)	1.04(2)	2.83(2)	140(2)
2-CBA	1	C11—H11···N3	3.753(3)	1.04(2)	2.89(2)	141(2)
	2	C13—H8···N3	3.956(3)	1.00(2)	3.19(2)	135(2)
	2	C14—H18···N3	3.612(3)	1.00(2)	2.76(2)	143(2)
	1	C12—H15···O4	3.058(3)	1.04(2)	2.58(2)	107(2)
	1	C12—H14···O4	3.058(3)	1.00(2)	2.69(2)	102(2)
	2	C13—H7···O6	3.198(3)	1.03(2)	2.51(2)	124(2)
	2	C13—H9···O4	3.391(3)	0.98(2)	2.58(2)	140(2)
	2	C14—H16···O5	3.250(3)	1.00(2)	2.59(2)	124(2)
	2	C14—H16···O2	3.471(3)	1.00(2)	2.48(2)	171(2)
DMAN	1	C11—H12···N5	3.383(3)	1.02(2)	2.56(2)	138(2)
4-CBA	1	C14—H10···N5	3.534(3)	1.00(2)	2.76(2)	134(2)
	2	C12—H18···N5	3.551(4)	0.99(2)	2.81(3)	132(2)
	2	C13—H16···N5	3.615(3)	1.02(2)	2.86(2)	132(2)
	1	C11—H11···O1	3.452(3)	0.97(2)	2.49(2)	171(2)
	1	C14—H9···O2	3.249(2)	1.01(2)	2.49(2)	131(2)
	1	C14—H8···O5	3.464(3)	0.98(2)	2.57(2)	151(2)
	2	C12—H14···O4	3.508(3)	1.00(3)	2.54(3)	163(2)

Table 8.18 The parameters of the minor component (C—H···X$^-$) of the $[Me_2N_1—H···N_2Me_2]^+···X^-$ fragment (continued) across the molecular complexes. $N(CH_3)_2$ group 1 is the most 'protonated' forming the IHB.

Complex	$N(CH_3)_2$ group	Interaction	dC···X$^-$ (Å)	dC—H (Å)	dH···X$^-$ (Å)	<CHX$^-$ (°)
DMAN	1A	C13A—H11A···O2F	3.411(3)	0.95(2)	2.52(2)	157(2)
4-NBA II	1A	C14A—H10A···O2F	3.409(3)	1.01(2)	2.48(2)	154(2)
	2A	C11A—H17A···O1F	3.77(3)	0.99(3)	3.01(2)	135(2)
	2A	C12A—H14A···O1F	3.346(3)	0.99(2)	2.49(3)	144(2)
	1A	C13A···O4F	3.081(2)			
	1A	C13A—H13A···O1G	3.293(2)	0.97(2)	2.41(2)	151(2)
	1A	C14A—H8A···O2I	3.388(2)	1.01(2)	2.52(2)	144(2)
	1A	C14A—H9A···O4I	3.431(2)	0.96(2)	2.54(2)	154(2)
	1A	C14A—H9A···O2E	3.493(2)	0.96(2)	2.70(3)	141(2)
	2A	C12A—H16A···O1G	3.437(3)	1.02(3)	2.50(3)	153(2)
	1B	C13B—H11B···O4E	3.351(3)	0.98(2)	2.45(2)	152(2)
	1B	C11B—H8B···O4E	3.333(2)	0.99(2)	2.45(2)	149(2)
	2B	C15B—H19B···O3E	3.466(3)	0.97(2)	2.66(2)	140(2)
	2B	C14B—H15B···O3E	3.662(3)	1.00(3)	2.86(3)	137(2)
	1B	C13···O1K	3.108(2)			
	1B	C13B—H13B···O3J	3.280(2)	1.02(2)	2.60(2)	123(2)
	1B	C13B—H12B···O4L	3.380(3)	0.98(2)	2.45(2)	159(2)
	1B	C11B—H9B···O2H	3.233(2)	0.95(2)	2.32(2)	163(2)
	2B	C15B—H18B···O2H	3.541(2)	1.03(2)	2.55(2)	161(2)
	2B	C15B—H18B···O2G	3.317(2)	1.03(2)	2.70(2)	119(2)
	2B	C13···O3F	3.133(2)			
	1C	C11C—H11C···O4K	3.825(2)	0.99(2)	3.10(2)	131(1)
	1C	C12C—H9C···O3K	3.467(3)	0.98(2)	2.51(2)	166(2)
	2C	C14C—H15C···O4K	3.472(3)	1.00(3)	2.65(3)	139(2)
	2C	C13C—H18C···O4K	4.025(2)	1.00(3)	3.32(2)	129(2)
	1C	C11C—H12C···O3H	3.405(2)	0.99(2)	2.63(2)	135(2)
	1C	C11C—H13C···O4J	3.253(2)	2.34(2)	0.97(2)	157(2)
	1C	C12C—H10C···O3I	3.180(2)	0.99(2)	2.52(2)	124(2)
	1C	C12C—H9C···O4K	3.523(3)	0.98(2)	2.69(2)	143(2)
	2C	C13C—H19C···O4J	3.477(2)	1.00(2)	2.52(2)	159(2)

Within the $[Me_2N—H···NMe_2]^+···X^-$ fragment, X$^-$ may also form an interaction with the $DMANH^+$ proton (H···X$^-$); X$^-$ acts as a second acceptor generating a bifurcated hydrogen bond. An interaction between H and X$^-$ may be reflected in the bifurcated hydrogen bond parameters (Table 8.19).

Table 8.19 The bifurcated hydrogen bond parameters within the $[Me_2N_1—H\cdots N_2Me_2]^+\cdots X^-$ fragment across the molecular complexes.

Complex	$dN_1\cdots N_2$ (Å)	$dN_1—H$ (Å)	$dH\cdots X^-$ (Å)	$dN_1\cdots X^-$ (Å)	$dN_2\cdots X^-$ (Å)	$<N_1HX^-$ (°)	$<N_2HX^-$ (°)
DMAN 5-NIP	2.572(1)	1.20(2)	3.27(2)	3.528(1)	4.045(1)	92(1)	112(1)
DMAN 2-NBA	2.620(1)	1.02(2)	2.61(2)	3.181(1)	3.133(1)	115(1)	91.5(7)
DMAN 3-OMBA	2.588(2)	1.13(2)	2.55(2)	3.012(2)	3.107(2)	103(1)	97(1)
DMAN 3-ABA	2.587(1)	1.12(2)	2.55(2)	3.036(1)	3.121(1)	105(1)	97(1)
DMAN 4-ABA hydrate	A 2.568(5) B 2.564(5) C 2.568(5)	1.28(3) 1.27(5) 1.09(5)	3.29(4) 3.25(5) 3.45(4)	3.749(5) 3.808(5) 3.705(4)	3.752(4) 3.660(4) 4.123(5)	101(2) 106(3) 95(3)	100(2) 96(2) 105(2)
DMAN 2-CBA	2.555(2)	1.23(2)	3.30(2)	3.763(2)	3.796(2)	103(1)	100(1)
DMAN 4-CBA	2.589(3)	1.07(3)	2.97(2)	3.427(2)	3.519(3)	106(2)	96(1)
DMAN 4-NBA II	A 2.601(2) B 2.601(2) C 2.597(2)	1.01(2) 0.99(3) 1.05(2)	3.26(2) 3.27(3) 3.22(2)	3.772(2) 3.795(3) 3.675(2)	3.598(3) 3.609(3) 3.740(2)	113(1) 115(2) 107(1)	88.0(9) 87.9(9) 96(1)

Variation in the bifurcated hydrogen bond parameters occurs across the molecular complexes. Where the acid group occupies the space above the IHB proton, as in DMAN2-NBA, DMAN3-OMBA and DMAN3-ABA, the $H\cdots X^-$ interaction distance is shorter; the exception to this is in DMAN4-ABA hydrate where the $ACID^-$ dimer lies flat over the IHB. As in the DMAN complexes in §8.4, there does not appear to be any particular correlation between the N_1—H and $H\cdots X^-$ distances. There is a weak negative correlation between the $H\cdots X^-$ distance and the N···N IHB distance; longer $H\cdots X^-$ distances occur where the N···N donor-acceptor distance is shorter. There is reasonable correlation between $N_1\cdots N_2$ and N_1—H distances; shorter N_1—H distances occur for longer $N_1\cdots N_2$ donor-acceptor distances. Other trends are apparent including that X^- is closest, in general, to the protonated N_1 and that the NHX^- angle is larger to the protonated nitrogen in the IHB (N_1), as observed in the literature. [131] There is also a strong correlation between $N_1\cdots X^-$ and $X^-\cdots H$.

Local environment of DMAN fused rings

The fused rings of the $DMANH^+$ cation also form interactions with X^- in the local environment involving the naphthalene C—H groups; the arrangement changing as the anion is varied.

Weak interactions to neighbouring X^- occur only on the more protonated side of the DMAN in complexes DMAN2-CBA, DMAN4-CBA and DMAN4-ABA hydrate DMAN A and DMAN C (Figure 8.22). These are weak C—H···O hydrogen bonds formed between an acid oxygen and a DMAN aromatic C—H group at the C2 position in DMAN2-CBA ($d_{C\cdots O}$ 3.594(3) Å) and DMAN4-ABA hydrate DMAN C ($d_{C\cdots O}$ 3.352(2) Å). In DMAN4-ABA hydrate DMAN A, a weak C—H···O hydrogen bonds forms between a water oxygen and a DMAN aromatic C—H group at the C3 position ($d_{C\cdots O}$ 3.650(6) Å). In DMAN4-CBA, weak C—H···N hydrogen bonds form between a nitrile group and DMAN aromatic C—H groups at the C3 and C4 positions ($d_{C\cdots N}$ 3.450(2) and 3.457(3) Å).

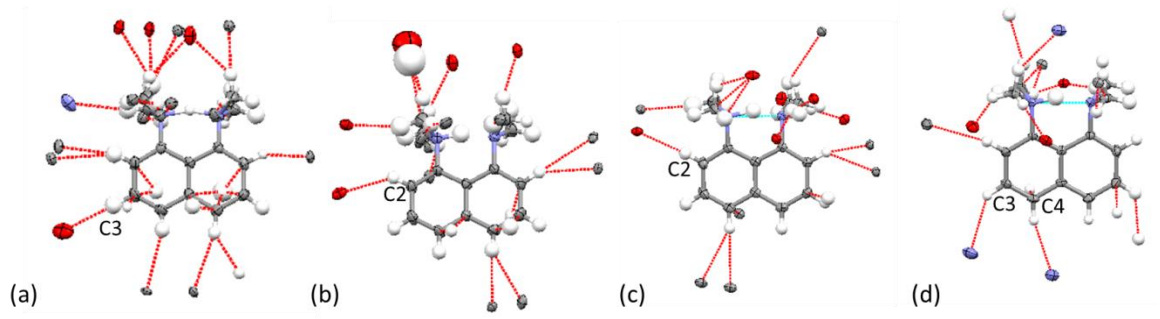

Figure 8.22 Weak interactions to the naphthalene C—H groups on the protonated side of the $DMANH^+$ cation in (a) DMAN4-ABA hydrate DMAN A (b) DMAN4-ABA hydrate DMAN C and (c) DMAN2-CBA and (d) DMAN4-CBA.

Weak interactions to neighbouring X^- occur to both sides of the $DMANH^+$ cation in DMAN5NIP, DMAN2-NBA, DMAN3-ABA, DMAN4-NBA II DMAN A, B and C (Figure 8.23). Weak C—H···O hydrogen bonds form at the C2 position to acid oxygen atoms in DMAN2-NBA ($d_{C\cdots O}$ 3.383(2) Å) and nitro oxygen atoms in DMAN4-NBA II DMAN A ($d_{C\cdots O}$ 3.466(2) Å), DMAN4-NBA II DMAN B ($d_{C\cdots O}$ 3.442(2) Å) and DMAN4-NBA II DMAN C ($d_{C\cdots O}$ 3.472(2) Å) whilst in DMAN5-NIP, weak C—H···O hydrogen bonds form at the C3 position to nitro oxygen atoms ($d_{C\cdots O}$ 3.637(1) Å). Additional weak C—H···O hydrogen bonds also form to nitro oxygen atoms on the protonated side in DMAN4-NBA II DMAN A, at the C4 position ($d_{C\cdots O}$ 3.503(3) and 3.375(2) Å), and in DMAN4-NBA II B, at the C3 and C4 positions ($d_{C\cdots O}$ 3.402(2) and 3.397 (2) Å). On the protonated side in DMAN3-ABA, C—H···N hydrogen bonds form to a neighbouring amine group ($d_{C\cdots N}$ 3.413(2) Å). On the non-protonated side of the $DMANH^+$ cation, weak C—H···O hydrogen bonds form to nitro oxygen atoms in DMAN2-NBA ($d_{C\cdots O}$ 3.455(2) Å), at the C6 position, and at the C5 position in DMAN4-NBA II DMAN B ($d_{C\cdots O}$ 3.455(2) Å) and

DMAN4-NBA II DMAN C ($d_{C\cdots O}$ 3.610(2) Å). On the non-protonated side of the $DMANH^+$ cation, weak C—H···O hydrogen bonds form to acid oxygen atoms in DMAN5-NIP ($d_{C\cdots O}$ 3.173(1) Å), at the C5 position, in DMAN3-ABA ($d_{C\cdots O}$ 3.407(2) and 3.362(2) Å), at the C5 and C7 position, and in DMAN4-NBA II A ($d_{C\cdots O}$ 3.377(2) Å) at the C6 position.

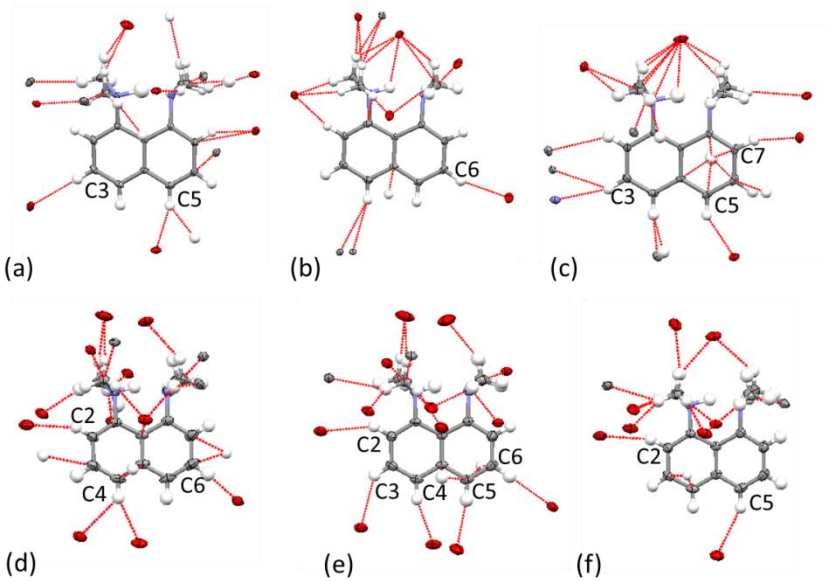

Figure 8.23 Weak interactions to the naphthalene C—H groups on both sides of the $DMANH^+$ cation in (a) DMAN5-NIP, (b) DMAN2-NBA, (c) DMAN3-ABA, (d) DMAN 4-NBA II DMAN A, (e) DMAN 4-NBA II DMAN B and (f) DMAN 4-NBA II DMAN C.

The weak interactions to neighbouring X^- occur on the non-protonated side only in in DMAN4-ABA hydrate DMAN B at the C7 position to a neighbouring acid oxygen (C—H···O ($d_{C\cdots O}$ 3.276(1) Å) and in DMAN3-OMBA, the methoxy oxygen atom bifurcates C—H groups at the C5 and C6 position forming weak C—H···O hydrogen bonds ($d_{C\cdots O}$ 3.258(2) and 3.248(2) Å) (Figure 8.24).

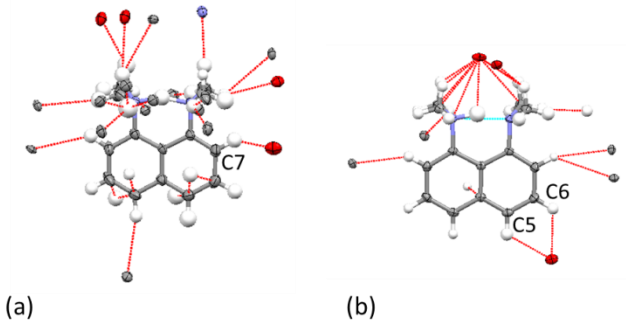

Figure 8.24 Weak interactions to the naphthalene C—H groups on the non-protonated side of the $DMANH^+$ cation in (a) DMAN4-ABA DMAN B and (b) DMAN3-OMBA.

In general, for the minor C—H··· X^- interactions involving the fused rings, the situation where interactions occur to either the protonated side only or to both the protonated and the non-protonated side of the $DMANH^+$ cation is more common than occurring only to the non-protonated side only.

8.5.3 Molecular structure

[N—H···N]$^+$ IHB and O—H···O CAHB

On anion variation, changes in the molecular structure of the DMAN and $ACID^-$ anion components occur. In the majority of the DMAN molecular complexes discussed in this section, the refined hydrogen atom positions indicate an IHB proton that is asymmetrically located in the IHB (Table 8.20), with the symmetric situation only in DMAN4-ABA hydrate, indicated by equivalent distances for N_1—H and H···N_2 in DMAN A and B. The refined hydrogen atom position is just off-centre in the IHB in DMAN5-NIP and DMAN2-CBA.

Table 8.20 The parameters of the IHB in the $[Me_2N—H···NMe_2]^+···X^-$ fragment across the molecular complexes.

Complex	$dN_1···N_2$ (Å)	$dN_1—H$ (Å)	$dH···N_2$ (Å)	$<N_1HN_2$ (°)
DMAN5-NIP	2.572(1)	1.20(2)	1.43(2)	155(2)
DMAN2-NBA	2.620(1)	1.02(2)	1.67(2)	153(2)
DMAN3-OMBA	2.588(2)	1.13(2)	1.50(2)	160(2)
DMAN3-ABA	2.587(1)	1.12(2)	1.51(2)	158(2)
DMAN4-ABA hydrate	A 2.568(5)	1.28(3)	1.32(3)	159(3)
	B 2.564(5)	1.27(5)	1.35(5)	156(4)
	C 2.568(5)	1.09(5)	1.52(5)	159(4)
DMAN2-CBA	2.555(2)	1.23(2)	1.38(3)	157(2)
DMAN4-CBA	2.589(3)	1.07(3)	1.58(3)	157(2)
DMAN4-NBA II	A 2.601(2)	1.01(2)	1.64(2)	157(2)
	B 2.601(2)	0.99(3)	1.66(2)	157(2)
	C 2.597(2)	1.05(2)	1.60(2)	157(2)

The location of the proton in the O—H···O^- CAHB forming the $ACID^-$ anion unit was also recorded (Table 8.21). The refined hydrogen atom positions indicate a proton that is asymmetrically located in the O—H···O^- CAHBs in all the molecular complexes with the exception of that interacting with DMAN B in DMAN4-ABA hydrate; the refined hydrogen atom position indicates a symmetrically located proton. In DMAN5-NIP, DMAN3-ABA and DMAN2-CBA, the O—H···O^- proton resides on the acid that sits above the $DMANH^+$ cation IHB whilst the opposite is true for DMAN3-OMBA, DMAN4-ABA hydrate, DMAN4-CBA and

DMAN4-NBA II; the proton resides on the acid which does not sit above the $DMANH^+$ cation IHB.

There does not appear to be any link between the location of the proton in the $DMANH^+$ cation IHB with the location of the proton in the O—H···O^- hydrogen bond forming the $ACID^-$ anion unit.

Table 8.21 The parameters of the O—H···O^- CAHB in the $ACID^-$ anion units across the molecular complexes.

Complex	Interaction	dO···O^- (Å)	dO—H (Å)	dH···O (Å)	<OHO (°)
DMAN5-NIP	O5—H22···O2	2.486(1)	0.99(2)	1.52(2)	166(2)
DMAN2-NBA	-	-	-	-	-
DMAN3-OMBA	O4—H27···O2	2.480(2)	1.03(3)	1.47(3)	169(3)
DMAN3-ABA	O2—H32···O3	2.450(1)	1.18(2)	1.272)	174(3)
DMAN4-ABA	A O3—H58···O5	2.513(4)	0.96(5)	1.57(5)	166(5)
hydrate	B O1—H83···O1’	2.448(4)	1.224	1.224	180.0
	C O3—H58···O5	2.513(4)	0.96(5)	1.57(5)	166(5)
	O10—H91···O12	2.480(3)	1.13(4)	1.37(4)	165(4)
	O8—H98···O8’	2.477(3)	1.239(2)	1.239(2)	180.0(2)
DMAN2-CBA	O3—H27···O1	2.540(2)	1.05(2)	1.51(2)	168(2)
	O5—H28···O2	2.560(2)	0.98(2)	1.58(2)	175(2)
DMAN4-CBA	O1—H29···O3	2.539(2)	1.05(3)	1.50(3)	167(3)
	O6—H28···O4	2.556(2)	1.02(2)	1.54(2)	176(3)
DMAN4-NBA II	A O2G—H5G···O3F	2.546(2)	0.97(3)	1.58(3)	176(3)
	A O1H—H1H···O4F	2.543(2)	1.00(3)	1.55(3)	173(3)
	B O4I—H1I···O2E	2.527(2)	0.93(3)	1.60(3)	171(3)
	B O2D—H1D···O1E	2.531(2)	1.02(3)	1.51(3)	174(3)
	C O3J—H1J···O1K	2.539(2)	0.96(3)	1.59(3)	167(3)
	C O3L—H1L···O2K	2.511(2)	0.98(4)	1.54(4)	177(4)

Thermal parameters

The effect of the minor component, and its variation, on the thermal behaviour of the $[N—H···N]^+$ IHB and O—H···O^- CAHB proton is investigated for this set of molecular complexes in Fourier difference maps.

Differences in the shape of the hydrogen atom density for the $[N—H···N]^+$ IHB proton occur across the molecular complexes in the Fourier difference maps (Figure 8.25).

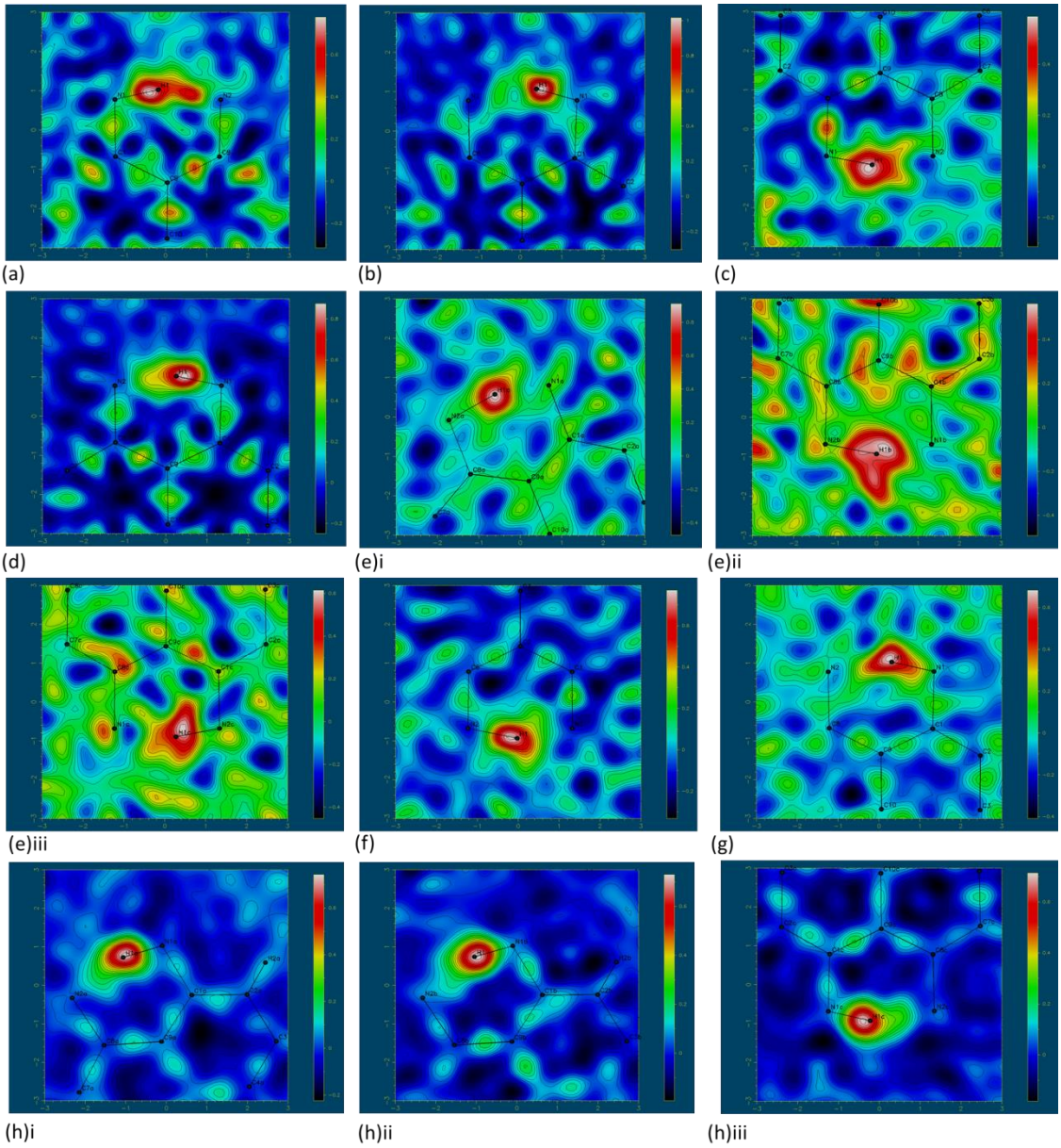

Figure 8.25 Fourier difference electron density maps showing the electron density associated with the H-atom in the $[N—H\cdots N]^+$ IHB in (a) DMAN5-NIP, (b) DMAN2-NBA, (c) DMAN3-OMBA, (d) DMAN3-ABA, (e) DMAN4-ABA hydrate (i) DMAN A, (ii) DMAN B and (iii) DMAN C, (f) DMAN2-CBA, (g) DMAN4-CBA and (h) DMAN4-NBA II i DMAN A, ii DMAN B and iii DMAN C.

The Fourier difference maps are of reasonable quality from the synchrotron and X-ray structure determinations such that the determination of hydrogen atom behaviour is possible in most cases; in the maps of DMAN4-ABA hydrate and DMAN4-CBA large amounts of noise are present making determination more difficult. It should be noted that the refined hydrogen atom position does not coincide with the peak maxima; a shift in the refined position occurs relative to the peak maxima which is consistent across the maps.

Ordered IHB protons are suggested for DMAN2-NBA, DMAN4-NBA II DMAN A and B by a spherical shape of proton electron density; the IHBs in these cases are therefore likely to have an asymmetric double well potential and low proton thermal motion. This low thermal motion occurs where the H···X^- distances are 2.61(2), 3.29(4), 3.26(2) and 3.27(3) Å, respectively. The asymmetry is in support of the asymmetry observed in the refined hydrogen atom positions for these molecular complexes. Some elongation of the IHB proton density along the interaction occurs for DMAN3-OMBA, DMAN3-ABA, DMAN4-CBA and DMAN4-NBA II DMAN C, whilst increased thermal motion of the proton is suggested in the Fourier difference map of DMAN4-ABA DMAN C. In these complexes, the IHB is more likely to have a more symmetric double well potential. This elongation of the IHB proton density in these molecular complexes is in support of the lengthened N_1—H distances indicated by the IHB proton refined hydrogen atom position. An ordered proton is indicated by the IHB proton density for DMAN4-ABA hydrate DMAN A. However, this density is symmetrically located and is in support of the symmetry observed in the refined hydrogen atom positions for this molecular complex. Large thermal motions are suggested for the IHB protons in DMAN5-NIP and DMAN4-ABA hydrate DMAN B by the smeared peak in the Fourier difference maps; in both cases this is suggestive of a more symmetric flat single well potential. This symmetry is in support of the symmetry observed in the refined hydrogen atom positions for these molecular complexes. The determination of proton behaviour from the Fourier difference map is less reliable for DMAN4-ABA hydrate DMAN B where there are significant amounts of noise present. The increased thermal motion occurs in DMAN5-NIP and DMAN 4-ABA hydrate DMAN B where the H···X^- distances are 3.27(2) and 3.25(5) Å, respectively; no correlation between extent of proton thermal motion and the proximity of the IHB proton and X^- is therefore suggested.

Differences in the shape of the hydrogen atom density for the $ACID^-$ unit protons are observed across the molecular complexes in the Fourier difference maps (Figure 8.26). The proton electron density has a spherical shape and appears to be well localised in almost all of the molecular complexes; an asymmetric double well potential is therefore suggested. In DMAN3-ABA, the density for the hydrogen atom appears split and is suggestive of proton disorder. Refinement of a model with the hydrogen atom split over two sites revealed a 54:46 occupancy of the two configurations. In this complex the O—H···O^- hydrogen bond is likely to have a symmetric double well potential with a relatively low barrier to proton transfer. This is in support of the symmetry observed in the refined hydrogen atom positions for DMAN3-ABA. The Fourier difference maps are extremely noisy for DMAN 4-ABA hydrate making the determination of the hydrogen atom behaviour unreliable from these maps.

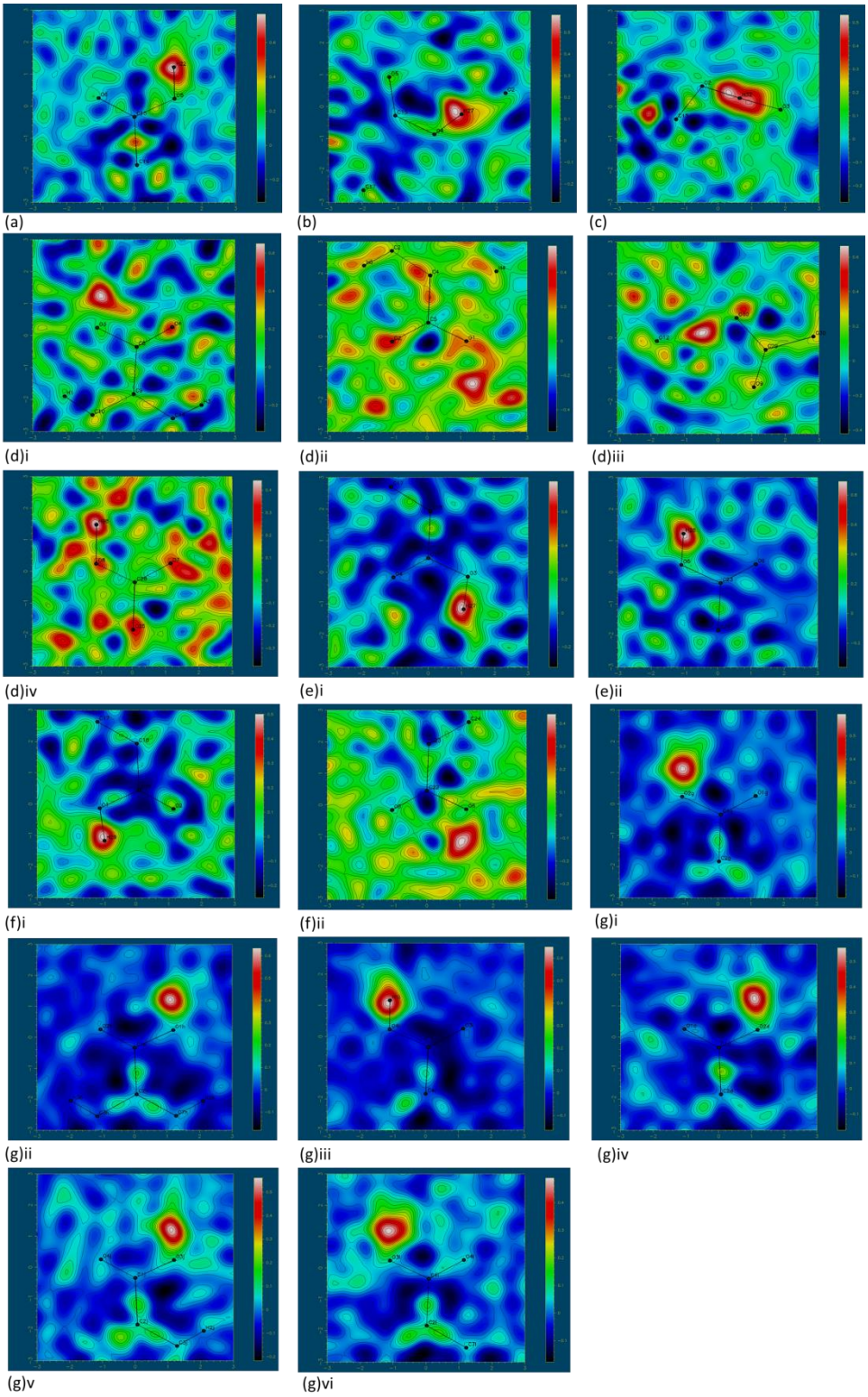

Figure 8.26 Fourier difference electron density maps showing the electron density associated with the H-atom in the $ACID^{-}$ anion unit O—H···O hydrogen bonds in (a) DMAN5-NIP, (b) DMAN3-OMBA, (c) DMAN3-ABA, (d) DMAN4-ABA hydrate i A, ii B, iii O10—H91···O12 and iv O8—H98···O8', (e) DMAN2-CBA i O3—H27···O1 and ii O5—H28···O4, (f) DMAN4-CBA i O1—H29···O3 and ii O6—H28···O4, (g) DMAN4-NBA II i A O2G—H5G···O3F, ii A O1H—H1H···O4F, iii B O4I—H1I···O2E, iv B O2D—H1D···O1E, v C O3J—H1J···O1K, vi C O3L—H1L···O2K.

There does not appear to be any correlation between the H···X^- distance and the thermal behaviour of the IHB proton in the Fourier difference maps. There is instead a stronger correlation with the IHB D···A distance. Hydrogen bonds with a shorter D···A distance should give a flatter potential energy well, which is reflected in the density corresponding to the hydrogen atom in the hydrogen bond. The shortest of the IHB donor-acceptor distances occur for DMAN4-ABA hydrate DMAN B ($d_{N\cdots N}$ 2.564(5) Å), DMAN5-NIP ($d_{N\cdots N}$ 2.572(1) Å), DMAN4-ABA hydrate DMAN C ($d_{N\cdots N}$ 2.568(5) Å) and DMAN4-ABA hydrate DMAN A ($d_{N\cdots N}$ 2.568(5) Å). In all but DMAN4-ABA hydrate DMAN A, a flatter potential well is suggested by the density in the Fourier difference maps for the IHB proton. The proton is symmetrically located as might be expected for a short hydrogen bond. The thermal motion of the proton decreases as the IHB donor-acceptor distance lengthens; the longest IHB donor-acceptor distances occur for DMAN2-NBA ($d_{N\cdots N}$ 2.620(1) Å) and DMAN4-NBA II DMAN A and DMAN B ($d_{N\cdots N}$ 2.601(2) and 2.601(2) Å respectively) and the shape of the proton density in the Fourier difference maps appears more ordered indicating a more asymmetric hydrogen bond potential. For the O—H···O^- interactions, one of the shortest donor-acceptor distances occurs in DMAN3-ABA ($d_{O\cdots O}$ 2.450(1) Å) and, in the Fourier difference map of this interaction, the proton density is split over two sites indicating a more symmetric double potential well. A similarly short donor-acceptor distance is formed in DMAN4-ABA hydrate O1—H83···O1' ($d_{O\cdots O}$ 2.448(4) Å), where the proton is again symmetrically located in the hydrogen bond. The longer O—H···O^- interactions have ordered protons and less symmetric shapes of the hydrogen bond potential well are suggested by the shape of the proton the density in the Fourier difference maps.

The possibility of correlation between the shape of the anisotropic thermal parameters of X^- and the isotropic thermal parameter of the IHB proton is investigated for this set of DMAN molecular complexes (Figure 8.27). Enlarged IHB proton isotropic thermal parameters are observed for DMAN5-NIP, DMAN3-OMBA, DMAN3-ABA and DMAN2-CBA where the anisotropic thermal parameter of X^- lies along the IHB. This may suggest interaction between the two atoms. The H···X^- distances are, however, distinctly varied (3.27(2), 2.55(2), 2.55(2) and 3.30(2) Å respectively). Unlike in the literature, [133] the correlation of the indicated thermal motions of the IHB proton and X^- does not occur here as an effect of their proximity.

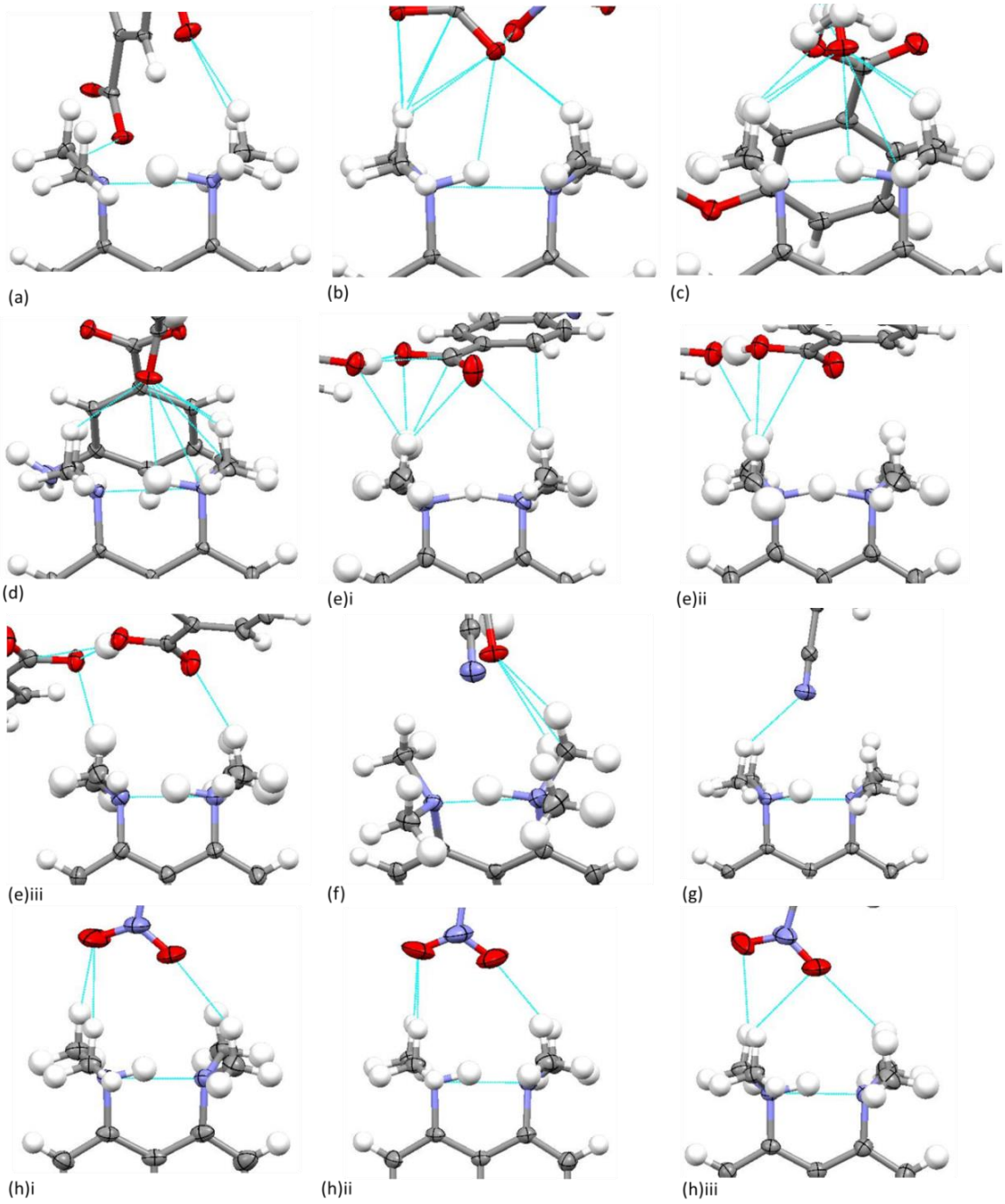

Figure 8.27 Thermal parameters of the IHB proton and X^- in the $[Me_2N—H\cdots NMe_2]^+\cdots X^-$ fragment in (a) DMAN5-NIP, (b) DMAN2-NBA, (c) DMAN3-OMBA, (d) DMAN3-ABA, (e) DMAN4-ABA hydrate i DMAN A, ii DMAN B, iii DMAN C, (f) DMAN2-CBA, (g) DMAN4-CBA and (h) DMAN4-NBA II i DMAN A, ii DMAN B, iii DMAN C.

ACID⁻ anion and DMANH⁺ cation

The effect of altering the minor component by changing the anion is also reflected in structural changes within components of the $ACID^-$ anion unit (Table 8.22) and the $DMANH^+$ cation (Table 8.23).

In the majority of the complexes, the acids within each unit are non-planar; an exception is in DMAN4-ABA hydrate where the molecules in each $ACID^-$ dimer are close to planarity, being twisted by 175 to 180 ° relative to one another (Figure 8.28). DMAN4-ABA hydrate also has the most planar benzene rings of the $ACID^-$ anion units (0 to 10 ° between the rings) whilst the benzene rings are significantly non co-planar in the rest of the molecular complexes (twisted by 32 to 90 °). The moieties within the $ACID^-$ units are also largely relatively planar ($^-$OCCC and HOCCC); the largest twist out of co-planarity of the carboxylic acid group with respect to the benzene ring occurs in DMAN2-NBA and DMAN2-CBA as a consequence of substituents *ortho* to the carboxylic acid group.

Table 8.22 Angles within the $ACID^-$ hydrogen bonded motif in each DMAN molecular complex including the torsion angle of the carboxyl and carboxylate groups forming the SSHBs (angle 1 COOC), the torsion angle between carboxylate group and benzene ring in the deprotonated acid (angle 2 $^-$OCCC where O is on X^-), the torsion angle between carboxyl group and benzene ring in the protonated acid (angle 3 OCCC) and the co-planarity of the benzene rings of each acid (angle 4).

Complex	Angle 1 COOC (°)	Angle 2 (OCCC) (°)	Angle 3 (HOCCC) (°)	Angle 4 (°)
DMAN 5-NIP	–87.5(1)	4.8(1)	15.9(2)	61.57
DMAN 2-NBA	-	34.6(2)	-	-
DMAN 3-OMBA	–92.7(2)	–7.9(2)	11.1(2)	88.51
DMAN 3-ABA	73.3(1)	6.4(2)	1.3(2)	86.33
DMAN 4-ABA hydrate	A 175.1(3) B -180.0(3) C 175.1(3)	-6.0(5) 2.8(6) -0.9(6)	0.7(5) –3.5(5) –4.4(5)	10.39 0.00 10.59
DMAN 2-CBA	1. 30.9(2) 2. 137.7(2)	-24.7(3)	–3.9(3) –16.8(3)	32.80 80.26
DMAN 4-CBA	1. –102.5(2) 2. –101.4(2)	9.6(3)	4.7(3) 4.4(3)	82.44 89.78
DMAN4NBA II	A G –76.4(2) H –103.8(2) B D 83.7(2) I 112.3(2) C J 103.7(2) L 93.8(2)	11.1(2) –16.4(2) 5.4(2)	12.5(2) 0.1(2) 8.3(2) –10.2(2) –1.9(2) 6.7(2)	76.77 70.5 79.08 83.43 79.16 70.76

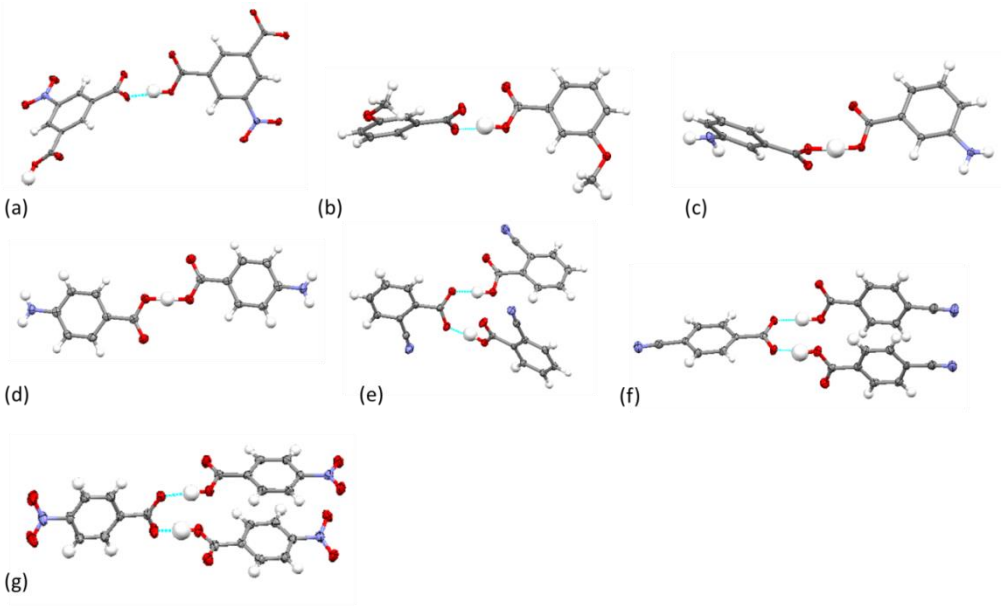

Figure 8.28 Torsions between carboxyl and carboxylate groups in the $ACID^-$ anion units in (a) DMAN5-NIP, (b) DMAN3-OMBA, (c) DMAN3-ABA, (d) DMAN4-ABA hydrate, (e) DMAN2-CBA, (f) DMAN4-CBA and (g) DMAN4-NBA II.

On protonation of DMAN, the arrangement of the *peri*-amino groups changes from a staggered to an eclipsed arrangement. [125] In DMAN-5NIP, DMAN2-NBA, DMAN2-CBA and DMAN4-CBA, there is a significant deviation away from the eclipsed arrangement (NCCN torsion angles of –14.59(7), -6.46(9), –7.8(1) and 5.8(1) ° respectively).

Table 8.23 The torsion angle between DMAN amino groups in each molecular complex.

Complex	$DMANH^+$ *peri*-amino group torsion (NCCN) (°)
DMAN5-NIP	–14.59(7)
DMAN2-NBA	–6.46(8)
DMAN3-OMBA	0.4(1)
DMAN3-ABA	2.70(8)
DMAN4-ABA hydrate	A –0.9(3) B –1.3(3) C 0.2(3)
DMAN2-CBA	–7.8(1)
DMAN4-CBA	5.8(1)
DMAN4-NBA II	A 0.8(1) B –3.8(1) C 3.2(1)

Across the DMAN molecular complexes, differences are observed in a number of structural parameters including the C—C (Table 8.24) and C—N bond lengths and the CCC, NCC and CNC angles (Table 8.25). These differences indicate the effect of changes to the minor component as a result of changing the anion. Protonation of DMAN leads to a shortening of the C1—C2, C3—C4, C5—C6 and C7—C8 bond lengths; a greater extent of shortening occurs for DMAN3-OMBA, DMAN4-ABA hydrate (DMAN C) and DMAN4-CBA whilst the least shortening of these bonds occurs in DMAN5-NIP. There is also a difference in the symmetry of the structural parameters on the two sides of each $DMANH^+$ cation in the presence of the different anions; notably in the equivalent C—C bond distances (see Figure 1.20 for labelling scheme), in particular between C_1—C_2 and C_7—C_8, and between C_3—C_4 and C_5—C_6. The C_1—N_1 bond lengths are also longer than C_8—N_2. This asymmetry reflects the asymmetry in the refined IHB proton position, evident in the majority of the molecular complexes. The most asymmetrically located proton indicated by the refined hydrogen atom position occurs in DMAN2-NBA and DMAN4-NBA II, which also show the greatest asymmetry in the C_1—N_1 and C_8—N_2 bond lengths. Larger *ipso* and smaller NCC angles and a decrease in the CNC angle between the dimethylamino methyl groups also occurs on the protonated side of the $DMANH^+$ cation. In DMAN4-ABA hydrate DMAN A and B, the proton is the most symmetrically located. Reflecting this, the C—N bond lengths and CCC, NCC and CNC angles are the most similar between the two sides of the molecule.

Table 8.24 The C—C bond lengths (Å) in the neutral DMAN [124] and in the $DMANH^+$ cations of the molecular complexes (see Figure 1.20 for atom labelling scheme).

Complex	C_9—C_1	C_1—C_2	C_2—C_3	C_3—C_4	C_4—C_{10}	C_{10}—C_5	C_5—C_6	C_6—C_7	C_7—C_8	C_8—C_9	C_9—C_{10}
DMAN [124]	1.448(1)	1.394(1)	1.413(2)	1.370(2)	1.426(2)	1.419(2)	1.374(2)	1.412(2)	1.390(2)	1.450(1)	1.437(1)
DMAN5-NIP	1.423(1)	1.374(2)	1.410(2)	1.368(2)	1.419(2)	1.416(1)	1.368(2)	1.411(2)	1.370(1)	1.430(1)	1.426(1)
DMAN2-NBA	1.424(2)	1.369(2)	1.410(2)	1.366(2)	1.414(2)	1.415(2)	1.363(2)	1.409(2)	1.374(2)	1.430(2)	1.434(2)
DMAN3-OMBA	1.425(2)	1.358(3)	1.403(2)	1.358(3)	1.414(3)	1.412(2)	1.356(3)	1.408(3)	1.366(2)	1.422(2)	1.432(2)
DMAN3-ABA	1.430(2)	1.367(2)	1.407(2)	1.363(2)	1.417(2)	1.418(2)	1.365(2)	1.410(2)	1.376(2)	1.427(2)	1.428(2)
DMAN4-ABA	A 1.422(4)	1.367(7)	1.404(6)	1.360(6)	1.415(7)	1.412(5)	1.363(7)	1.404(6)	1.350(5)	1.440(6)	1.431(5)
hydrate	B 1.418(4)	1.364(7)	1.397(6)	1.353(6)	1.428(7)	1.413(5)	1.367(7)	1.409(6)	1.355(5)	1.431(6)	1.420(5)
	C 1.442(6)	1.354(5)	1.409(6)	1.365(7)	1.405(5)	1.421(7)	1.356(6)	1.393(6)	1.369(7)	1.413(4)	1.429(5)
DMAN2-CBA	1.425(3)	1.364(3)	1.402(3)	1.356(3)	1.419(3)	1.413(3)	1.363(3)	1.411(3)	1.357(3)	1.426(3)	1.429(3)
DMAN4-CBA	1.420(3)	1.357(3)	1.403(3)	1.357(4)	1.412(3)	1.415(4)	1.359(3)	1.401(3)	1.363(4)	1.429(3)	1.424(2)
DMAN4-NBA II	A 1.421(2)	1.366(2)	1.407(3)	1.356(3)	1.416(3)	1.416(3)	1.352(3)	1.412(3)	1.369(3)	1.422(2)	1.431(2)
	B 1.427(2)	1.365(2)	1.407(3)	1.362(3)	1.415(2)	1.416(2)	1.361(3)	1.413(3)	1.370(2)	1.423(2)	1.432(2)
	C 1.425(2)	1.367(2)	1.408(3)	1.365(3)	1.416(2)	1.417(2)	1.359(3)	1.411(3)	1.372(3)	1.425(2)	1.432(2)

Table 8.25 The C—N *peri*-amino bond lengths and angles in the neutral DMAN [124] and in the $DMANH^+$ cations of the molecular complexes (see Figure 1.20 for atom labelling scheme).

Complex	C_1—N_1 (Å)	C_2—N_8 (Å)	$<C_2C_1C_9$ (°)	$<C_9C_8C_7$ (°)	$<N_1C_1C_9$ (°)	$< N_2C_8C_9$ (°)	$<CN_1C$ (°)	$<CN_2C$ (°)
DMAN [124]	1.402(1)	1.405(2)	119.09(9)	118.8(1)	120.57(9)	120.74(9)	111.92(9)	112.4(1)
DMAN5-NIP	1.468(1)	1.462(1)	121.8(1)	121.22(9)	117.47(9)	117.61(8)	111.62(9)	110.79(8)
DMAN2-NBA	1.473(1)	1.455(1)	122.2(1)	120.6(1)	118.89(9)	118.40(9)	111.39(9)	110.9(1)
DMAN3-OMBA	1.473(2)	1.460(2)	121.7(2)	121.0(2)	118.4(1)	118.4(1)	111.0(1)	111.2(1)
DMAN3-ABA	1.469(1)	1.455(2)	122.1(1)	121.0(1)	118.35(9)	118.17(9)	111.4(1)	111.05(9)
DMAN4-ABA hydrate	A 1.467(5)	1.468(5)	121.4(4)	121.2(4)	117.9(3)	117.2(3)	112.4(4)	111.2(4)
	B 1.471(5)	1.462(5)	121.8(4)	121.6(4)	118.3(3)	117.7(3)	112.5(4)	112.6(4)
	C 1.468(5)	1.460(5)	122.2(4)	121.1(4)	117.7(3)	118.0(3)	112.1(4)	111.1(4)
DMAN2-CBA	1.464(3)	1.462(2)	121.5(2)	121.3(2)	117.7(2)	117.4(2)	111.4(2)	112.3(2)
DMAN4-CBA	1.472(2)	1.453(2)	122.2(2)	120.6(2)	118.4(2)	118.2(2)	111.7(2)	111.3(2)
DMAN4-NBA II	A 1.475(2)	1.460(2)	122.1(2)	120.5(2)	118.7(1)	118.7(1)	112.3(1)	111.8(2)
	B 1.469(2)	1.457(2)	122.3(1)	120.5(1)	118.4(1)	118.9(1)	112.3(1)	112.1(1)
	C 1.471(2)	1.457(2)	122.2(1)	120.2(2)	118.4(1)	118.8(1)	112.0(1)	111.8(1)

Variation in the bond lengths of the carboxylate (C—O^-, $C=O_1$) and carboxyl (C—OH and $C=O_2$) groups occurs across the molecular complexes; this may reflect the position of the acid proton in the hydrogen bonded units (Table 8.26). Where the proton is most symmetrically located in the O—H···O^- hydrogen bond, the bond lengths of the carboxyl bond group are most similar to those of the carboxylate group, and *vice versa*.

Table 8.26 The bond lengths of the carboxylic acid groups in the $ACID^-$ anion unit.

	Carboxylate group		Carboxyl group	
Complex	dC—O^- (Å)	dC=O_1 (Å)	dC—OH (Å)	dC=O_2 (Å)
DMAN5-NIP	1.275(1)	1.236(1)	1.312(1)	1.213(1)
DMAN2-NBA	1.254(1)	1.248(2)	-	-
DMAN3-OMBA	1.279(2)	1.235(2)	1.304(2)	1.222(2)
DMAN3-ABA	1.294(2)	1.230(1)	1.289(1)	1.236(1)
DMAN4-ABA hydrate	A 1.290(4)	1.242(4)	1.315(5)	1.228(5)
	B 1.289(4)	1.238(4)	1.289(4)	1.238(4)
	C 1.315(5)	1.228(5)	1.290(4)	1.242(4)
DMAN2-CBA	1.257(2)	1.253(2)	1.323(2)	1.210(2)
			1.314(3)	1.211(3)
DMAN4-CBA	1.263(3)	1.254(3)	1.321(3)	1.215(2)
			1.323(2)	1.211(3)
DMAN4-NBA II	A 1.252(2)	1.252(2)	1.309(2)	1.215(2)
			1.317(2)	1.210(2)
	B 1.252(2)	1.249(2)	1.311(2)	1.210(3)
			1.315(2)	1.212(2)
	C 1.249(3)	1.249(2)	1.312(2)	1.219(2)
			1.316(2)	1.209(2)

8.6 Consequences of anion variation on the crystal packing

Variation of the anion has consequences for both the wider and local crystal packing in the DMAN molecular complexes studied in this chapter.

In most cases, the wider crystal packing of the $DMANH^+$ cation and $ACID^-$ anions is unaffected by anion substitution; the inorganic packing type occurs where units of each species are built up in layers. Changing the anion in DMAN2-CBA, DMAN4-CBA and DMAN4-NBA II leads to a different packing; in these complexes each $DMANH^+$ cation is surrounded by six $ACID^-$ anions. This difference is likely related to the crystallisation ratio of the components in DMAN2-CBA,

DMAN4-CBA and DMAN4-NBA II; all crystallised in a 1:3 ratio, where the $ACID^-$ anion is present in excess of the $DMANH^+$ cation. In order to accommodate the additional $ACID^-$ anion molecules there is a change in packing from pairs of counter ions to a cation surrounded by anions. This 1:3 crystallisation ratio occurs for the non-halogen electron withdrawing substituents, excluding 5-nitroisophthlalic acid and 2-nitrobenzoic acid. It may be that the wider crystal packing can be influenced by DMAN co-former selection.

The crystallisation ratio also reflects the aggregation of the $DMANH^+$ cation and $ACID^-$ anions into the $[Me_2N—H\cdots NMe_2]^+\cdots X^-$ fragment which in turn appears to be related to substituent on the benzoic acid ring of the anion. In the molecular complexes containing benzoic acids substituted by either halogen atoms or electron donating groups, the $[Me_2N—H\cdots NMe_2]^+\cdots X^-$ fragment forms where X^- is an $ACID^-$ dimer and where either the deprotonated acid or a water molecule, if present, occupies the space above the $[N—H\cdots N]^+$ IHB. In contrast, in the molecular complexes containing benzoic acids substituted by electron withdrawing groups, the crystallisation ratio changes to either 1:1 or 1:3 and in all but one case (DMAN2-NBA) the electron withdrawing substituent occupies the space above the IHB. This suggests that, by substitution of the anion, the way the $[Me_2N—H\cdots NMe_2]^+\cdots X^-$ fragment forms may be controlled. The exception to this, DMAN2-NBA, has the carboxylate group positioned above the IHB where there is no additional 2-NBA molecule to stabilise its negative charge; the DMAN and 2-NBA components crystallise in a 1:1 ratio. If a 1:2 molecular complex of DMAN2-NBA could be accessed, a switch in the identity of X^- may occur. In DMAN5-NIP, the components also crystallise in a 1:1 ratio however, the nitro substituent group is preferentially positioned above the IHB. In contrast to 2-NBA, 5-NIP has a second carboxylic acid group to stabilise the carboxylate group. The literature contains few examples of DMAN with substituted benzoic acids with electron withdrawing or donating groups. The complex of DMAN with 4,5-dichlorophthalic acid contains the same $[Me_2N—H\cdots NMe_2]^+\cdots X^-$ fragment. [130] In the presence of the halogen substituent, the carboxylate group is positioned over the IHB. This agrees with the arrangement observed in the halo benzoic acid complexes in this chapter.

Anion variation also appears to have local packing effects across the molecular complexes in this chapter. Within the $[Me_2N—H\cdots NMe_2]^+\cdots X^-$ assembly, the length of the minor $C—H\cdots X^-$ interactions appears to be tuneable, on changing the anion. In general, where the X^- located above the $[N—H\cdots N]^+$ IHB is from the $ACID^-$ unit, the minor interactions are shorter than those where X^- is an electron withdrawing substituent. This may be a result of the $C—H\cdots X^-$ interactions being formed between more strongly oppositely charged species where X^- is a carboxylate group compared to where X^- is an electron withdrawing substituent. A choice between an electron

withdrawing substituent or an electron donating or halogen substituent may therefore allow the length of these interactions to be tuned.

A change in the length of the minor C—H···X^- interactions also occurs, for those molecular complexes where X^- is the $ACID^-$ carboxylate group, depending on identity and position of the benzoic acid ring substituent; these effects are evident in the DMAN halo benzoic acid molecular complexes. The length of the minor C—H···X^- interactions increase with increasing electronegativity of the halogen in the order fluoro, chloro, iodo. This effect is due to the more electronegative ring substituents forming stronger acids, by the inductive effect, but in turn weaker conjugate bases for interaction of the deprotonated acid with the dimethylamino C—H groups; this means these interactions are longer. The position of the halogen substituent also leads to changes in the minor interactions. Carboxylic acid groups with *ortho* substituents have an increased acidity, compared to *meta* and *para* substituents, and consequently form weaker conjugate bases. This is reflected in the length of the C—H···X^- interactions formed in the two series of DMAN2-FBA, DMAN3-FBA and DMAN4-FBA hydrate and DMAN2-IBA, DMAN3-IBA and DMAN4-IBA. The *ortho* substituted acids (DMAN2-FBA and DMAN2-IBA) form weaker interactions to the $DMANH^+$ methylamino groups than the *meta* (3-position) and *para* (4-position) substituted equivalents. Substitution of an acid at a particular position or by a particular group therefore may allow tuning of the minor component.

The anion also appears to tune the symmetry and the number of the weak minor C—H···X^- interactions formed within the $[Me_2N—H···NMe_2]^+···X^-$ fragment across the molecular complexes. The symmetry in the arrangement of the C—H···X^- interactions appears to be affected by the identity of X^-. For example, in the molecular complexes where X^- is the carboxylate or a cyano group, X^- is positioned more centrally over $[Me_2N—H···NMe_2]^+$. In contrast, where X^- is a nitro group, it is positioned offset and closer to one of the DMAN dimethylamino groups. In the 1:3 molecular complexes, including DMAN2-CBA, DMAN4-CBA hydrate and DMAN4-NBA II, the type of packing adopted where the $ACID^-$ anions pack around the $DMANH^+$ cation leads to an increased number of minor C—H···X^- interactions forming to the local environment; this is usually biased to one dimethylamino group over the other. The substitution of the benzoic acids with hydrogen bond acceptor groups also leads to an increase in the numbers of minor C—H···X^- interactions occurring. Certain substituents on the anion therefore appear to favour particular arrangements and numbers of formation of the minor interactions within the $[Me_2N—H···NMe_2]^+···X^-$ fragment.

Varying the anion is therefore suggested to have significant packing effects in the DMAN molecular complexes. Certain substituents are shown to favour particular crystal packing and tune

the aggregation within the $[Me_2N—H\cdots NMe_2]^+\cdots X^-$ fragment. By selecting certain substituents the minor interactions are shown to be tuneable in length, number and also arrangement. This gives interesting insight into molecular packing in the solid state and the potential for targeting certain crystal packing in these DMAN benzoic acid molecular complexes.

8.7 Rationalising the proton transfer behaviour

8.7.1 Symmetry of the $DMANH^+$ cation

The symmetry of the $DMANH^+$ cation is found to vary over the molecular complexes. Of particular interest in this study is the effect of the minor interactions on the $[N—H\cdots N]^+$ IHB. In the nineteen molecular complexes studied in this chapter, the symmetry of the proton in the IHB changes from being asymmetrically located, such as in DMAN4-IBA and DMAN4-NBA II, to being centrally located in DMAN2-FBA and DMAN4-ABA hydrate DMAN A. In an isolated $DMANH^+$ cation, the proton is expected to be symmetrically located; [134] varying positions of the IHB proton when the $DMANH^+$ cation is in combination with different anions indicates that crystal packing forces play a role in tuning its position.

The symmetry of the $DMANH^+$ IHB appears to be strongly related to the weak $C—H\cdots X^-$ interactions forming the minor component of $[Me_2N—H\cdots NMe_2]^+\cdots X^-$ fragment. This has been suggested previously by Wozniak *et al* (2003); the weak minor interactions can influence the location of the proton in the $[N—H\cdots N]^+$ IHB [131] as changes in the distribution of these minor interactions alter the symmetry of the nitrogen atoms forming the interaction, altering the symmetry of the hydrogen bond potential well. In most cases, the IHB proton is located on the nitrogen atom whose methyl groups are involved in either the shortest or the greatest number of the weak $C—H\cdots X^-$ interactions; the weak $C—H\cdots X^-$ interactions of the minor component have a tuning effect on proton position. An exception to this is in DMAN2-FBA, where the refined hydrogen atom position and IHB Fourier difference map indicate a symmetrically located IHB proton and an equal number of minor interactions occur to the dimethylamino groups on each side of the IHB, however they are significantly shorter to one side than the other. Similarly in DMAN4-ABA hydrate DMAN A, the refined hydrogen atom position and IHB Fourier difference map indicate a symmetrically located IHB proton but there are a greater number of minor interactions, which are also shorter, to the dimethylamino groups on one side of the IHB. In these cases, other factors may be contributing including the N···N hydrogen bond distance. As noted above, as the donor-acceptor distance decreases in a hydrogen bond, the shape of the potential energy surface becomes increasingly flat changing from an asymmetric double well to a single well. [7] The position of proton in the hydrogen bond also becomes increasingly symmetric. In DMAN2-FBA

and DMAN4-ABA hydrate DMAN A the IHB inter nitrogen distances are 2.584(2) and 2.568(5) Å, respectively. These are short N···N distances; the neutral DMAN base has an N···N separation of 2.80 Å and the average protonated $DMANH^+$ N···N separation is 2.59 Å. [129] A flat potential well is therefore possible, the Fourier difference maps of the IHB for each complex indicate this, and may outweigh the influence of the weaker interactions to the dimethylamino groups.

Within the $[Me_2N—H···NMe_2]^+···X^-$ fragment, an interaction between X^- and the IHB proton also forms. As found in previous DMAN studies, X^- is closer to the DMAN methyl groups than the IHB proton, this means that the weak C—H··· X^- interactions are more significant than the $H···X^-$ interaction; [131] this is the case in the molecular complexes in this chapter where no correlation between IHB proton symmetry and $H···X^-$ is indicated but is between IHB proton symmetry and the weak C— $H···X^-$ minor interactions.

As with the minor interactions involving the dimethylamino groups, the weak $C—H···X^-$ interactions to the fused $DMANH^+$ cation rings appear to be strongly related to the symmetry of the IHB, in most cases forming either to the side of the cation on which the IHB proton is located or to both sides of the $DMANH^+$ cation. In particular, in DMAN4-OHBA hydrate DMAN A and DMAN4-ABA hydrate DMAN B, the $DMANH^+$ proton is positioned just off centre of the IHB despite the minor $C—H···X^-$ interactions involving the dimethylamino groups being biased towards the more protonated side of the cation. However, the interactions involving the $DMANH^+$ cation fused rings involve the non-protonated side only and are reasonably short ($d_{C···O}$ 3.336(1) and 3.276(1) Å). It may be that the weak interactions to the fused ring on the non-protonated side offset the minor interactions involving the dimethylamino groups on the protonated side and cause the elongation observed in the N—H distance towards the centre of the bond. This illustrates the subtle interplay of weak interactions in these molecular complexes. The effect of the minor interactions on the symmetry of the $DMANH^+$ cation is also reflected in the bond lengths and angles of the cation which are inequivalent on different sides of the molecule when the IHB proton is asymmetrically located and vice versa.

8.7.2 Behaviour of the IHB proton

Several studies have investigated the effect of the interaction of the IHB proton with X^- on its thermal behaviour within the $[Me_2N—H···NMe_2]^+···X^-$ fragment. X^- may act as a second acceptor to the IHB proton forming a bifurcated NHXN hydrogen bond. No link as yet has been found between the N—H and $H···X^-$ in the bifurcated hydrogen bond, [303] this is also the case in the molecular complexes in this chapter; a symmetrically located proton occurs in DMAN2-FBA where the $H···X^-$ distance is short (2.68(2) Å) and in DMAN4ABA hydrate DMAN A where this distance is long (3.29(4) Å).

There may yet be a connection between the thermal behaviour of the IHB proton and the nearest electronegative atom X^{-}, in agreement with that found by Jones *et al*. (2016). [133] In the molecular complexes in this chapter, enlarged isotropic thermal parameters for the IHB proton are observed where the anisotropic thermal parameter of X^{-} lies along the IHB. This occurs in DMANBA, DMAN2-FBA, DMAN4-FBA hydrate, DMAN4-ClBA hydrate, DMAN5-NIP, DMAN3-OMBA, DMAN3-ABA, DMAN2-CBA and may suggest interaction. However, unlike in the study by Jones *et al*. (2016), [133] where this similar behaviour in the thermal parameters for the IHB proton and X^{-} occurs where the two atoms are in close proximity (the H···X^{-} distance is in the range of 2.61 to 2.81 Å), this is not the case across the molecular complexes studied in this chapter; the similar behaviour of the thermal parameters occurs where the H···X^{-} distances are in a wide range: 2.53(2), 2.68(2), 2.56(2), 2.56(2). 3.27(2), 2.55(2), 2.55(2) and 3.30(2) Å, respectively. It is therefore difficult to make any definite conclusions about the effect of the length of the H···X^{-} interaction on the behaviour of the IHB proton from this study; a greater link is instead observed in the thermal parameters. It seems that the minor C—H···X^{-} and IHB N···N separations are more important in determining proton behaviour in these molecular complexes; the minor interactions may mitigate against a symmetrically located proton where it might otherwise be expected.

8.7.3 Behaviour of the $ACID^{-}$ proton

The proton in the O—H···O^{-} CAHB has differing behaviour across the molecular complexes which may also be related to the weak minor interactions. Symmetric and asymmetric protons with order or disorder are observed in these bonds. There does not appear to be any link between the behaviour of the IHB proton and the $ACID^{-}$ proton however a link is suggested between the H···X^{-} component of the minor interactions and the symmetry of the O—H···O^{-} CAHB; a more symmetric O—H···O^{-} CAHB forms where the H···X^{-} interaction is shorter. For example, in DMAN4-NBA II DMAN A, the O—H and H···O^{-} distances are 0.97(3) and 1.58(3) Å alongside a H···X^{-} distance of *ca*. 3.26(2) Å whilst in DMAN4-ClBA hydrate the O—H and H···O distances are 1.19(3) and 1.26(3) Å, respectively, alongside an H···X^{-} of 2.56(2) Å. The proton location in the O—H···O^{-} CAHBs formed in the $ACID^{-}$ anion units are all asymmetric in the 1:3 DMAN molecular complexes whilst there is greater variation in the 1:1 and 1:2 complexes. These O—H···O^{-} CAHBs are also generally longer in the 1:3 complexes likely due to the carboxylate sharing its negative charge over two oxygen atoms such that the charge assisted component is less. The H···X^{-} interaction distance therefore appears to have a greater effect on the O—H···O^{-} CAHB than the $[N—H···N]^{+}$ IHB.

8.8 Application of synchrotron X-ray diffraction in the study of proton transfer behaviour

As in Chapter 5 to Chapter 7, synchrotron X-ray diffraction is applied in the study of hydrogen atoms; here, its potential in the study of static low temperature proton transfer behaviour in the presence of weak interactions is explored.

In general, the data collected using the synchrotron technique is of high quality, shown by low errors on the D—H and H···A hydrogen bond distances (σ = 0.02 Å in some cases) and with a low level of noise in the Fourier difference maps. There is also consistency between the refined hydrogen atom positions and the position of the density for the hydrogen atoms in the Fourier difference maps; the relative shift between the two occurred consistently in the maps across the molecular complexes. For some samples, where there is increased noise in the Fourier difference maps and higher errors on hydrogen atom bond distances, this may be attributed to lower sample quality, the DMAN molecular complexes tended to produce more plate like crystals, or in some cases be due to the presence of heavy (e.g. iodine) atoms in the structure which generate additional Fourier ripples. There was an improvement, in most cases, in the quality of the Fourier difference maps generated from the synchrotron X-ray data in comparison to those generated from the laboratory X-ray data [128] (Figure 8.29(a)); where not improved, they were largely unchanged (Figure 8.29(b)). There was, however, little change in the uncertainties on the hydrogen atom positions between the two techniques; in DMAN2-FBA the IHB N—H and H···N distances were 1.31(3) and 1.32(3) Å, respectively, in the synchrotron structure and 1.30(3) and 1.32(3) Å, respectively, in the laboratory X-ray structure.

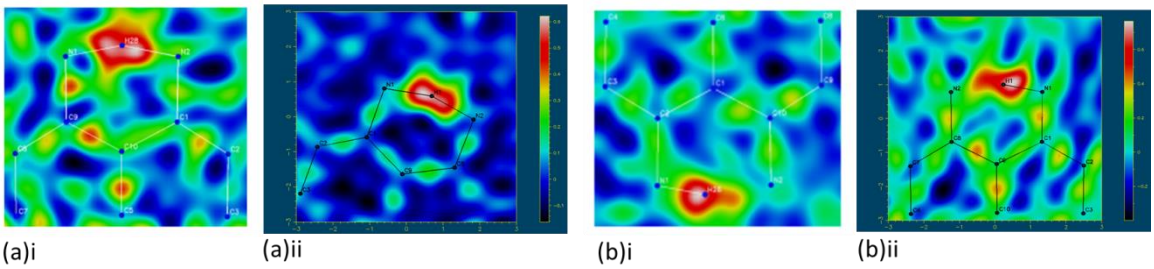

Figure 8.29 Fourier difference electron density maps showing the electron density associated with the H-atom in the $[N—H···N]^+$ IHB in (a) DMAN2-FBA and (b) DMAN2-IBA generated from the (i) the laboratory X-ray structure [128] and the (ii) synchrotron X-ray structure.

Synchrotron X-ray diffraction is deployed very effectively in the study of the packing and aggregation of the $DMANH^+$ cations and $ACID^-$ anions into the $[Me_2N—H···NMe_2]^+···X^-$ fragment, with rapid, accurate structure solution possible for each complex. The accurate structure solution allowed the asymmetry of the $[N—H···N]^+$ IHB and the $O—H···O^-$ CAHB to be

confirmed in the heavy atom parameters; including the C—N and C—C distances of the $DMANH^+$ cation and in the bond distances of the carboxyl and carboxylate groups of the $ACID^-$ anions. The subtle changes in the crystal packing, across the molecular complexes as a result of anion variation, and its effect on proton behaviour could also be followed with confidence; including in the minor C—H···X^- interactions where the heavy atom distances were the focus. A strong link is also suggested between the H···X^- and the N_1···X^- distances in the bifurcated [N—H···N]$^+$···X^- hydrogen bond such that the more reliable heavy atom distances may be used to infer the H···X^- interaction distance in future.

In this study, using X-rays, only the isotropic refinement of the hydrogen atom thermal parameters is possible; the potential of the interaction between H and X^- can be less clearly observed than in neutrons where hydrogen atom parameters may be refined anisotropically. It was therefore more difficult to determine when H and X^- were interacting on observation of the thermal parameters of the two atoms; this is exemplified in the comparative diffraction study in §8.3. However, there was some correlation between the size of the isotropic thermal parameter and the behaviour of the thermal parameter of X^-; an enlarged isotropic thermal parameter is observed when the thermal parameter of X^- lies along the [N—H···N]$^+$ IHB. This may be a useful indication of interaction between H and X^- in future X-ray studies.

Fourier difference maps give a good indication of the nature of the IHB potential, and here it was hoped that the synchrotron data may have given advantages. The expected shift of the position of the hydrogen atom for the X-ray structure relative to the neutron structure is observed reliably in both the Fourier difference maps and hydrogen atom bond lengths, and these maps have given consistent indication of elongation of hydrogen atom density that indicated freedom of movement along some of the SSHBs, for example. An increased amount of noise is present in some of the X-ray maps, however, which means that some of these findings must be treated with a degree of caution.

One of the main advantages of the use of the synchrotron technique is that it has allowed the study of a large number of these molecular complexes increasing the set over which the anion effects and low temperature proton transfer behaviour, and the associated hydrogen atom parameters and electron density, are studied. This allows a significant contribution to the understanding of crystal packing effects on molecular structure and proton behaviour.

8.9 Conclusions

In this chapter, the effect of anion variation on both the wider and finer details of the crystal structure have been investigated in existing and new molecular complexes of DMAN using a combination of synchrotron and X-ray diffraction. Attempts to rationalise the low temperature IHB proton transfer behaviour have also been made.

Across the molecular complexes, variation of the anion led to changes in the wider crystal packing. The formation of the $[Me_2N—H\cdots NMe_2]^+\cdots X^-$ fragment was, however, shown to be robust on anion substitution forming in all molecular complexes as a result of proton transfer between DMAN and the organic acids; aiding in the predictability of the outcome on the combination of these molecular components. The variation of the anion instead affected components within the $[Me_2N—H\cdots NMe_2]^+\cdots X^-$ fragment. It was shown that the identity of X^- could potentially be predicted or tuned based on the electronic characteristics of the substituted benzoic acid; electron donating or halogen substituents led to one $[Me_2N—H\cdots NMe_2]^+\cdots X^-$ arrangement whilst electron withdrawing substituents tended to lead to another. These electronic characteristics also appeared to influence crystallisation ratio of components forming the $[Me_2N—H\cdots NMe_2]^+\cdots X^-$ fragment; only 1:2 molecular complexes were formed for the electron donating and halobenzoic acid substituents. In the minor component of the $[Me_2N—H\cdots NMe_2]^+\cdots X^-$ fragment, the $C—H\cdots X^-$ interactions involving the dimethylamine C—H and nearest electronegative atom X^- were also suggested to be tuneable, in terms of length and arrangement, *via* changes to the identity of X^- as a consequence of varying the anion; this selection includes variation of electronics by nature and the ring position of the benzoic acid substituent. This knowledge is useful in the design of future DMAN molecular complexes where control of the composition of the $[Me_2N—H\cdots NMe_2]^+\cdots X^-$ fragment is desired; in terms of identity of X^- and the length of the minor interactions forming it. This is also a good example of ways to achieve more subtle structural variations in a crystal.

In agreement with that seen elsewhere, [130, 131] the crystal packing appeared to influence proton behaviour with a subtle balance of effects occurring. The minor interactions were suggested to cause localisation of the $[N—H\cdots N]^+$ IHB proton whilst the thermal behaviour of the proton within the IHB appeared to be related more to the N···N separation of the IHB than the proximity of the anion; this is in contrast to the previous neutron diffraction study by Jones *et al.* (2016) on several of these materials where an effect on the IHB proton thermal behaviour was indicated in the $H\cdots X^-$ distance range of 2.61 to 2.81 Å. [133] This lack of agreement may highlight limitations of the synchrotron technique in accurately determining the $H\cdots X^-$ distances. However, there did appear to be a similar link between the thermal behaviour of the IHB proton and that of the X^- anion,

suggesting interaction; enlarged isotropic thermal parameters are observed when the thermal parameter of X^- lies along the IHB.

This study aids in trying to rationalise the proton behaviour occurring in protonated DMAN systems. The influence of weak interactions on crystal structure has been shown, by which interactions to one part of the molecule cause structural perturbations at another. By taking these effects into account, it may be possible to achieve control over structure and proton transfer properties in future. The use of the synchrotron technique in these studies allowed data of good quality to be obtained, reflected in clean Fourier difference maps, from which hydrogen atom behaviour and position could be reliably determined across the molecular complexes. Again, the Fourier difference maps were shown to be important for the determination of the hydrogen atom thermal behaviour whilst heavy atom parameters allowed greater confidence in the refined hydrogen atom positions. This allowed the rationalisation of the proton behaviour in the crystal packing using the synchrotron X-ray technique. To draw more definitive conclusions, complementary neutron diffraction studies would be beneficial in these studies. The high throughput nature of the synchrotron technique also allowed the number of existing DMAN organic acid systems to be increased facilitating the study of the nineteen complexes in this chapter, adding further insight to the role of weak interactions in structure control, particularly in proton dynamics, and how these interactions may be controlled or changed by subtle changes to the anion.

This is the fourth study presented in this thesis applying the synchrotron technique in different aspects of the study of hydrogen atoms, and their behaviour.

Chapter 9.

Crystal engineering urea organic acid hydrogen bonded networks with solvent inclusion properties

In Chapter 6, the carboxylic acid:amide R_2^2 hydrogen bond synthon was shown to be robust for SSHB formation between substituted urea and benzene carboxylic acid molecular components. In this chapter, it is explored alongside additional synthons in the design of substituted urea organic acid hydrogen bonded networks with solvent inclusion properties. The work in this chapter has arisen from the investigations in Chapter 6.

9.1 Introduction and aims

Inclusion materials (§1.2.3) have guest hosting properties as a result of molecular packing. They are often targeted in crystal engineering because of their potential applications in pharmaceutics, [82] chemical sensing, [83] in the separation of alkanes [84] and in the capture of volatile organic compounds (VOCs). [85]

The predictable design of materials with inclusion behaviour in the solid state is difficult, requiring the formation of crystalline solids in which molecules do not efficiently fill space. [304] A number of factors may influence their formation including host component molecular size [75] and guest size and shape. [76] A number of inclusion materials have been reported based on hydrogen bonded networks [305-307] where particular hydrogen bonding synthons assemble to build up the host structure. [308-310] In these materials, the number, type and geometry of the hydrogen bond donor and acceptor groups of the host molecular building blocks influences the nature of the hydrogen bonded networks formed.

The two building blocks utilised in the synthesis of solvent inclusion compounds in this chapter are based on the urea and polycarboxylic acid core, each of which offer flexibility in hydrogen bonding functionality through various substitutions. Urea and substituted ureas have the potential to interact with a number of different co-formers *via* their different functional groups; interaction through the amide functionality facilitates urea-urea interactions, to form hexagonal channels around linear guests in urea inclusion compounds, [72, 311] and with carboxylic acids enables urea-carboxylic acid interactions, *via* the carboxylic acid:amide $R_2^2(8)$ hydrogen bonding synthon; three hydrogen bonding motifs

(U:Ac, U:Ac:U or Ac:U:Ac) (§1.2.1), [44] leading to hydrogen bonded chains in molecular complexes of substituted ureas and di-carboxylic acids, have previously been reported. [38, 113] It is also of relevance here to note that amine groups can form extended hydrogen bond networks with nitro group functionalities; for example in co-crystals of 3,5-dinitrobenzoic acid and 4-aminobenzoic acid, the nitro groups link to an amine group in the next molecule *via* bifurcated $R_2^1(4)$ and $R_2^2(8)$ hydrogen bond synthons. [36, 45] Polycarboxylic acids may form extended hydrogen bonded networks *via* carboxylic acid $R_2^2(8)$ hydrogen bonded dimer synthons such as in trimesic acid which has a honeycomb structure around coronene guest molecules; [73] network extension in two or three dimensions and directions may occur related to arrangement of the carboxylic acid groups. [312]

In this chapter, molecular building blocks of substituted ureas are combined with 5-nitroisophthalic acid in the design of hydrogen bonded networks with solvent-guest inclusion properties. Molecular recognition of substituted urea and 5-nitroisophthalic acid molecular building blocks, into extended networks, is possible *via* carboxylic acid $R_2^2(8)$ homo dimers, carboxylic acid:amide $R_2^2(8)$ and $R_2^1(6)$ hydrogen bond synthons, amide:amide $R_2^2(8)$ homo dimers, nitro:amide $R_1^2(4)$, $R_2^1(6)$ and $R_2^2(8)$ hydrogen bonded synthons (Figure 9.1).

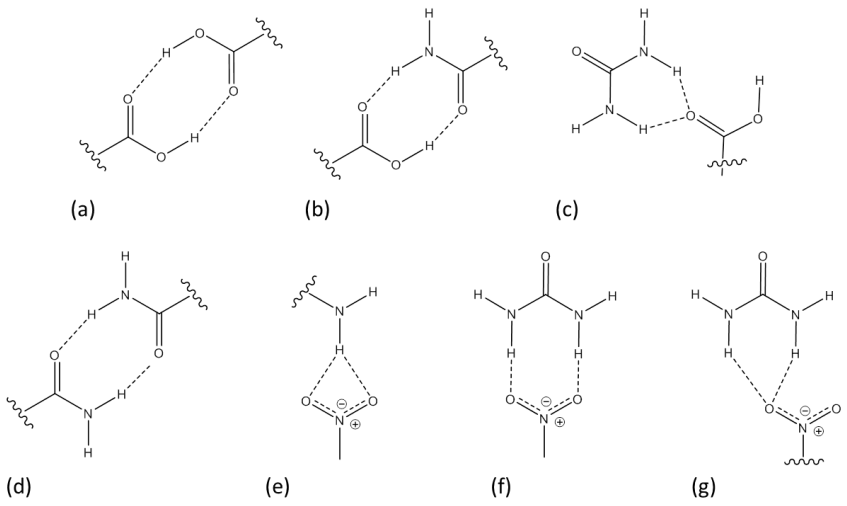

Figure 9.1 The possible hydrogen bond synthons on molecular recognition of substituted ureas and 5-nitroisophthalic acid: (a) carboxylic acid $\boldsymbol{R_2^2(8)}$ homo dimers, (b) carboxylic acid:amide $\boldsymbol{R_2^2(8)}$ and (c) $\boldsymbol{R_2^1(6)}$ hydrogen bond synthons, (d) amide:amide $\boldsymbol{R_2^2(8)}$ homo dimers, (e) nitro:amide $\boldsymbol{R_1^2(4)}$ and (f) $\boldsymbol{R_2^2(8)}$ and (g) $\boldsymbol{R_2^1(6)}$ hydrogen bonded synthons.

A systematic study of four substituted ureas with 5-nitroisophthalic acid in the presence of eight laboratory solvent molecules is carried out (Figure 9.2). A range of substituted urea molecular building blocks are investigated to determine the effect of different substituents, including altering the number of donor-acceptor sites available for hydrogen bond synthon formation, on inclusion

network generation. Where hydrogen bonded networks with solvent guest inclusion properties have been synthesised, their thermal stability is studied; these are included in a recent publication. [313]

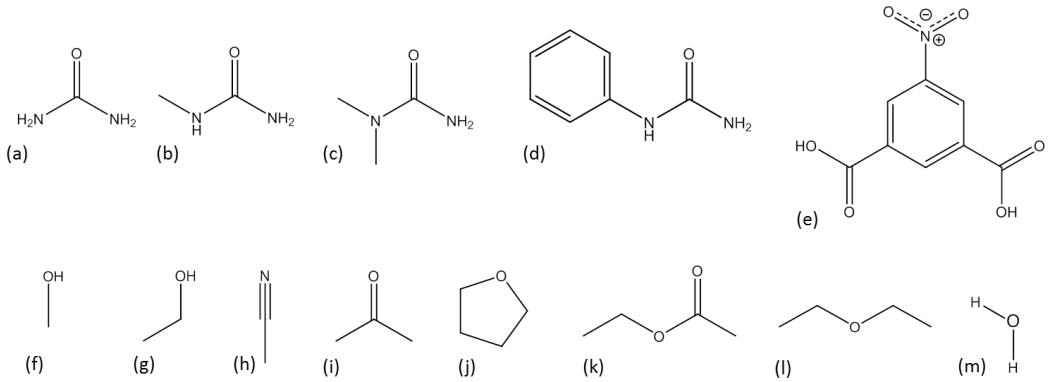

Figure 9.2 Top: Molecular building (a) urea, (b) *N*-methylurea, (c) *N*,*N*-dimethylurea, (d) *N*-phenylurea, (e) 5-nitroisophthalic acid, (f) methanol, (g) ethanol, (h) acetonitrile, (i) acetone, (j) tetrahydrofuran (THF), (k) ethyl acetate, (l) diethyl ether and (m) water.

9.2 Experimental details

9.2.1 Preparation and crystallographic analysis

***N*-phenylurea 5-nitroisophthalic acid molecular complexes**

7:4:2 *N*-phenylurea, 5-nitroisophthalic acid and methanol (IM1)

Triangular shaped yellow crystals of the 7:4:2 complex of *N*-phenylurea, 5-nitroisophthalic acid and methanol were grown by slow evaporation of a 2:1 stoichiometric ratio of the two components in methanol solvent at 40 °C.

3:2:1:1 *N*-phenylurea, 5-nitroisophthalic acid, ethanol and water (IM2)

Yellow needle shaped crystals of the 3:2:1:1 complex of *N*-phenylurea, 5-nitroisophthalic acid, ethanol and water were grown by slow evaporation of a 2:1 stoichiometric ratio of the two components in ethanol solvent at room temperature.

3:2:1 *N*-phenylurea, 5-nitroisophthalic acid and acetonitrile (IM3)

Yellow block shaped crystals of the 3:2:1 complex of *N*-phenylurea, 5-nitroisophthalic acid and acetonitrile were grown by slow evaporation of a 2:1 stoichiometric ratio of the two components in acetonitrile solvent at 40 °C.

3:2:1:1 *N*-phenylurea, 5-nitroisophthalic acid, acetone and water (IM4)

Yellow plate shaped crystals of the 3:2:1:1 complex of *N*-phenylurea, 5-nitroisophthalic acid, acetone and water were grown by slow evaporation of a 2:1 stoichiometric ratio of the two components in acetone solvent at 4 °C.

3:2:1:1 *N*-phenylurea, 5-nitroisophthalic acid, THF and water (IM5)

Yellow block shaped crystals of the 3:2:1:1 complex of *N*-phenylurea, 5-nitroisophthalic acid, THF and water were grown by slow evaporation of a 2:1 stoichiometric ratio of the two components in THF solvent at 30 °C.

3:2:1 *N*-phenylurea, 5-nitroisophthalic acid and ethyl acetate (IM6)

Yellow plate shaped crystals of the 3:2:1 complex of *N*-phenylurea, 5-nitroisophthalic acid and ethyl acetate were grown by slow evaporation of a 2:1 stoichiometric ratio of the two components in ethyl acetate solvent at room temperature.

2:2:1:2 *N*-phenylurea, 5-nitroisophthalic acid, THF and methanol (IM7)

Pale yellow plate crystals of the 2:2:1:2 complex of *N*-phenylurea, 5-nitroisophthalic acid, THF and methanol were grown by slow evaporation of a 2:1 stoichiometric ratio of the two components in a 1:1 solvent mixture of methanol and THF at room temperature.

1:1:1 *N*-phenylurea, 5-nitroisophthalic acid and water (CIM1)

Yellow fine needle shaped crystals of the 1:1:1 complex of *N*-phenylurea, 5-nitroisophthalic acid and water were grown by slow evaporation of a 1:2 stoichiometric ratio of the two components in ethyl acetate solvent at room temperature.

1:1:1 *N*-phenylurea, 5-nitroisophthalic acid and acetone (CIM2)

Colourless rectangular crystals of the 1:1:1 complex of *N*-phenylurea, 5-nitroisophthalic acid and acetone were grown by slow evaporation of a 2:1 stoichiometric ratio of the two components in acetone solvent at 4 °C.

2:1 *N*-phenylurea and 5-nitroisophthalic acid (NS1)

Pale yellow block crystals of the 2:1 complex of *N*-phenylurea and 5-nitroisophthalic acid were grown by slow evaporation of a 2:1 stoichiometric ratio of the two components in water at room temperature.

1:1 *N*-phenylurea and 5-nitroisophthalic acid (NS2)

Yellow plate crystals of the 1:1 complex of *N*-phenylurea and 5-nitroisophthalic acid were grown by slow evaporation of a 2:1 stoichiometric ratio of the two components in diethyl ether solvent at 30 °C.

Single crystal X-ray diffraction data were collected on **IM1**, **IM4** and **NS1** using Mo-K_α radiation on a Rigaku Oxford Diffraction [210] Xcalibur diffractometer equipped with an Agilent [228] EosS2 detector and collected on **IM3**, **IM5**, **IM6**, **IM7**, **CIM1**, **CIM2** and **NS2** using Cu-K_α radiation on a Rigaku Oxford Diffraction [210] SuperNova diffractometer equipped with an EosS2 detector (**IM5**, **IM6**, **CIM1** and **CIM2**) or an Atlas (**IM3** and **IM7**) detector. The sample temperature was controlled on the Xcalibur diffractometer using an Oxford Cryosystems [229] Cryostream Plus and on the SuperNova using an Oxford Cryosystems [229] Cryostream 700. The data were processed using the Rigaku Oxford Diffraction [210] CrysAlisPro [211] software version 1.171.37.33 (version 1.171.37.35 in the case of **CIM1**). Single crystal X-ray diffraction data were collected on **IM2** at the Advanced Light Source, USA [2] using radiation λ = 0.9538 Å on a Bruker AXS [214] D8 three-circle diffractometer diffractometer equipped with a Bruker AXS [214] PHOTON 100 CMOS detector. The sample temperature was controlled using an Oxford Cryosystems [229] Cryostream Plus. The data were collected using Bruker AXS [214] APEX2 software and and processed using Bruker AXS [214] APEX2 [215] and SADABS-2014/15 softwares. [216] All structures were solved using SHELXS-2013 [218] and refinement was carried out in SHELX-2013 [219] within the WinGX package. [221] Crystallographic data are given in Table 9.1 and Table 9.2.

Substituted urea 5-nitroisophthalic acid molecular complexes

The syntheses of molecular complexes U5-NIP, MU5-NIP and DMU5-NIP are described in §A6.1. The data collection, data processing, structure solution and refinement details and the summary of the crystallographic data for U5-NIP, MU5-NIP and DMU5-NIP are given in §A6.2.

Refinement details

The refinement details include treatment of the solvent molecule guests. All solvent molecule non-hydrogen atoms were refined anisotropically except in the case of **IM2** and **IM7** where the solvent guests were disordered and so refined isotropically.

Table 9.1 Crystallographic data for the inclusion materials **IM1** to **IM7**.

Material	**IM1**	**IM2**	**IM3**	**IM4**	**IM5**	**IM6**	**IM7**
Diffractometer	Xcalibur	Bruker AXS	SuperNova	Xcalibur	SuperNova	SuperNova	SuperNova
Radiation (K_α) / wavelength (Å)	Mo	0.9538	Cu	Mo	Cu	Cu	Cu
Formula	$C_{83}H_{84}N_{18}O_{33}$	$C_{39}H_{42}N_8O_{17}$	$C_{39}H_{37}N_9O_{15}$	$C_{40}H_{42}N_8O_{17}$	$C_{41}H_{44}N_8O_{17}$	$C_{41}H_{42}N_8O_{17}$	$C_{18}H_{21}N_3O_{8.5}$
Mol. W ($gmol^{-1}$)	1861.8	894.80	871.78	906.81	920.84	918.82	415.38
T (K)	150	100	150	150	150	150	150
Space group	P-1	P-1	P-1	P-1	P-1	P-1	P-1
a (Å)	12.2579(6)	6.9335(3)	10.0887(5)	12.3639(7)	12.3606(5)	9.8732(4)	9.9483(8)
b (Å)	14.7289(9)	12.4902(7)	12.3161(5)	13.0486(10)	13.4644(6)	10.9970(3)	9.9564(8)
c (Å)	23.5050(14)	25.4854(13)	17.3345(10)	13.8208(10)	14.3535(6)	20.4449(6)	10.6641(7)
α (°)	94.490(5)	89.062(5)	70.478(5)	71.686(7)	81.404(4)	80.035(2)	66.488(7)
β (°)	91.215(4)	83.694(4)	87.122(4)	89.156(5)	83.684(4)	89.288(3)	75.790(7)
γ (°)	90.291(4)	74.923(3)	87.659(4)	87.439(5)	64.194(4)	77.290(3)	71.335(7)
Volume ($Å^3$)	4229.6(4)	2118.02(19)	2026.83(18)	2114.7(3)	2123.73(17)	2131.99(12)	909.16(13)
Z	2	2	2	2	2	2	2
ρ_{calc} ($g\ cm^{-3}$)	1.462	1.403	1.428	1.424	1.440	1.431	1.517
μ (mm^{-1})	0.115	0.190	0.952	0.113	0.967	0.963	1.042
Θ range (°)	3.282-25.681	2.266-34.590	3.809-74.405	3.292-25.026	4.769-71.918	4.393-71.995	4.564-75.016
Reflections collected	37793	20333	14449	15520	15570	16547	6117
Independent	16015	7477	7975	7468	8144	8157	3565
Observed I>2σ	9340	3492	6311	2729	6568	6377	3029
R_{int}	0.0423	0.0901	0.022	0.097	0.029	0.039	0.0141
Completeness (%)	99.8	97.5	99.8	97.6	99.8	99.9	99.7
Parameters	1518	561	716	606	760	763	274
GooF	1.015	1.005	1.041	0.959	1.034	1.008	1.081
R_1 (observed)	0.0553	0.1019	0.0396	0.0834	0.0509	0.0539	0.0642
R_1 (all)	0.1125	0.1972	0.0526	0.2373	0.0633	0.0687	0.0721
wR_2 (all)	0.1460	0.3331	0.1125	0.2000	0.1470	0.1547	0.2040
Δρ (max, min) ($e\ Å^{-3}$)	0.309, -0.329	1.124, -0.676	0.239, -0.274	0.534, -0.434	0.423, -0.308	0.246, -0.292	0.399, -0.975

Table 9.2 Crystallographic data for the inclusion materials **CIM1**, **CIM2**, **NS1** and **NS2**.

Material	**CIM1**	**CIM2**	**NS1**	**NS2**
Diffractometer	SuperNova	SuperNova	Xcalibur	SuperNova
Radiation (K_α) / wavelength (Å)	Cu	Cu	Mo	Cu
Formula	$C_{30}H_{30}N_6O_{16}$	$C_{18}H_{19}N_3O_8$	$C_{22}H_{21}N_5O_8$	$C_{15}H_{13}N_3O_7$
Mol. W ($gmol^{-1}$)	730.6	405.36	483.44	347.28
T (K)	150	150	150	150
Space group	P-1	$P2_1/c$	P-1	$P2_1/c$
a (Å)	6.8562(5)	7.7787(1)	8.9131(7)	15.1254(3)
b (Å)	11.9649(9)	18.8747(2)	9.7105(8)	12.7462(2)
c (Å)	20.6362(10)	13.0343(1)	13.3778(11)	16.2905(4)
α (°)	78.951(5)	90	71.440(7)	90
β (°)	88.870(5)	91.528 (1)	78.479(7)	107.286(3)
γ (°)	76.106(6)	90	83.019(7)	90
Volume ($Å^3$)	1612.26(19)	1913.02(4)	1073.43(16)	2998.81(12)
Z	2	4	2	8
ρ_{calc} ($g\ cm^{-3}$)	1.505	1.407	1.496	1.538
μ (mm^{-1})	1.069	0.958	0.116	1.068
Θ range (°)	3.878-72.174	4.123-71.919	3.321-29.343	4.485-74.591
Reflections collected	11673	12893	8876	20298
Independent	6168	3711	4920	6023
Observed I>2σ	5069	3376	3277	4827
R_{int}	0.0291	0.0272	0.026	0.031
Completeness (%)	99.7	100.0	99.7	99.8
Parameters	483	338	400	555
GooF	1.087	1.029	1.023	1.123
R_1 (observed)	0.0848	0.0345	0.052	0.0526
R_1 (all)	0.0975	0.0376	0.093	0.0659
wR_2 (all)	0.2446	0.0969	0.1101	0.1426
Δρ (max, min) ($e\ Å^{-3}$)	0.608, -0.366	0.222, -0.240	0.240, -0.300	0.279, -0.230

9.3 Molecular complexes of substituted ureas with 5-nitroisophthalic acid

In the design of hydrogen bonded networks with solvent guest inclusion properties from substituted ureas and 5-nitroisophthalic acid molecular components in the presence of a range of laboratory solvents, fourteen molecular complexes have been prepared. Nine of the fourteen can be considered solvent inclusion materials whilst five are non-solvated. Only the combination of *N*-phenylurea with 5-nitroisophthalic acid led to hydrogen bonded networks with solvent inclusion properties.

9.3.1 Inclusion materials of *N*-phenylurea 5-nitroisophthalic acid

Nine hydrogen bonded networks with solvent inclusion properties have been prepared from the combination of molecular building blocks *N*-phenylurea and 5-nitroisophthalic acid (Table 9.3). **IM1**-**IM7** are inclusion materials (IM), while **CIM1** and **CIM2** are classed here as condensed inclusion materials (CIM).

Table 9.3 *N*-phenylurea 5-nitroisophthalic acid solvent inclusion materials and included solvents.

Inclusion Material (IM)	Solvent(s) included
IM1	methanol
IM2	ethanol, water
IM3	acetonitrile
IM4	acetone, water
IM5	THF, water
IM6	ethyl acetate
IM7	disordered THF/methanol
CIM1	water
CIM2	acetone

Host Framework

In inclusion materials **IM1** – **IM7**, *N*-phenylurea and 5-nitroisophthalic acid molecules assemble into hydrogen bonded ring host networks around solvent guest molecules (Figure 9.3 (a) to (g)). The hydrogen bonded ring networks are comprised of eight molecular building blocks in **IM1** to **IM6** and in each case molecular assembly is *via* four carboxylic acid:amide $R_2^2(8)$ hydrogen bond synthons, in both U:Ac and U:Ac:U hydrogen bonded motifs, and *via* two carboxylic acid:amide $R_2^1(6)$ and two nitro:amide $R_2^2(8)$ hydrogen bond synthons. In contrast, six molecular building blocks form the hydrogen bonded ring in **IM7** and molecular assembly occurs *via* two carboxylic acid:amide $R_2^2(8)$ hydrogen bond synthons, in a U:Ac motif, and *via* two nitro:amide $R_2^1(6)$

hydrogen bond synthons and two carboxylic acid dimer $R_2^2(8)$ hydrogen bond synthons. Condensed hydrogen bonded networks form in **CIM1** and **CIM2** (Figure 9.3 (h) and (i)), each containing different portions of the ring networks present in **IM1** – **IM6**; carboxylic acid:amide $R_2^2(8)$ hydrogen bond synthons, in a U:Ac motif, form in both complexes alongside a nitro:amide $R_2^2(8)$ hydrogen bond synthon in **CIM1** and a carboxylic acid:amide $R_2^1(6)$ synthon in **CIM2**. Ring formation does not occur in **CIM1** and **CIM2**, where there is a 1:1 stoichiometry of the host components such that no U:Ac:U motifs form and where solvent molecules hydrogen bond to the second 5-nitroisophthalic acid carboxylic acid group.

In these hydrogen bonded networks, the phenyl and urea moieties of the *N*-phenylurea molecular building blocks experience varying degrees of molecular distortion. These are most significant for *N*-phenylurea occurring in the angles between the urea and phenyl moiety planes; variation occurs across the IMs and within the same crystal structure. In general, the co-planarity of the phenyl and urea moieties is increased in the IMs compared to the native crystal structure; angles between the plane of the two moieties range from ca. 0 to 35 ° in **IM1** – **IM7** versus ca. – 48 ° in the native crystal structure, CSD Refcode PHUREA01. [314] The *N*-phenylurea molecular building blocks have the most co-planar phenyl and urea moieties in **IM4** (angles between moiety planes are 3 to 6 °) whilst in **CIM1** and **IM5**, the moieties of the *N*-phenylurea molecular building blocks are the least co-planar (angle between moiety planes are 33 and 35 °, respectively). Variations in the co-planarity of the phenyl and urea moieties also occur within the same molecular complex; the co-planarity is most similar in **IM4** (angles between moiety planes are 3 to 6 °) and **IM6** (6 to 14 °). For the IMs with hydrogen bonded ring networks, there does not appear to be any link between position in the ring, or hydrogen bond synthon involvement, and the angles between the moiety planes within *N*-phenylurea. The variation in the torsion angles of the 5-nitroisophthalic acid carboxylic acid groups with the benzene ring across the IMs is only small in comparison (OCCC torsions in the range of 0 to 12 °) covering a slightly wider range than in the native crystal structure, CSD Refcode COFDUW10 (OCCC torsions in the range of 2 to 6 °). [315] The largest twist of a 5-nitroisophthalic acid carboxylic acid group out of planarity of the benzene occurs in **IM4** (OCCC torsion −11.6(9) °) whilst the smallest occurs in **IM1** (OCCC torsions in the range of 0 to 3.5(4) °) and **IM2** (OCCC torsions in the range of 0 to 2(1) °).

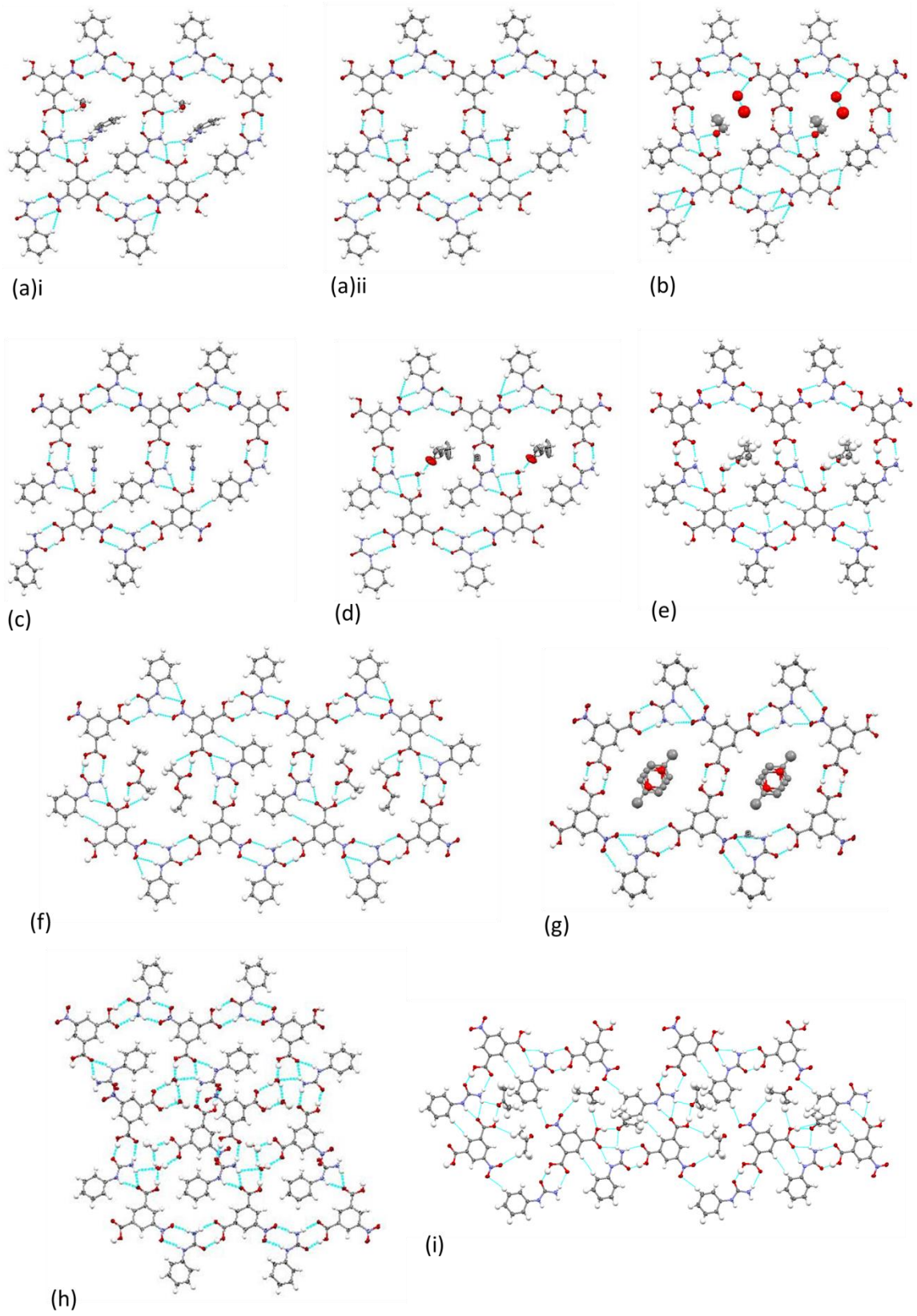

Figure 9.3 Hydrogen bonded ring networks in (a)i and ii **IM1**, (b) **IM2**, (c**) IM3**, (d) **IM4**, (e) **IM5**, (f) **IM6**, (g) **IM7**, (h) **CIM1** and (i) **CIM2**.

At first glance, the host ring networks in **IM1** – **IM5** appear isostructural, having the same graphset notation $R_8^8(42)$. However, the arrangement of the hydrogen bond synthons in space and the orientation of the molecular building blocks differ (Figure 9.4).

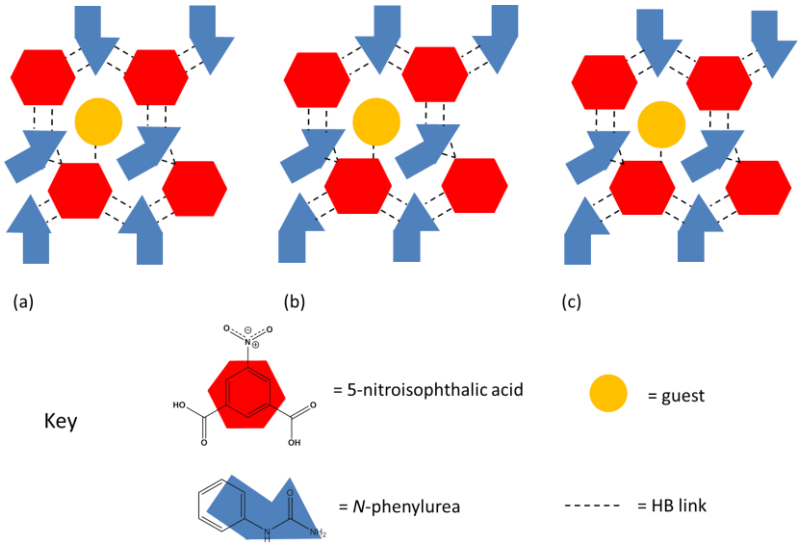

Figure 9.4 The different orientations of the *N*-phenylurea molecular building blocks in structurally similar (a) **IM1**, **IM2** and **IM4**, (b) **IM3**, (c) **IM5**.

The hydrogen bonded network in **IM6** contains the same number of each hydrogen bond synthon as in **IM1** to **IM5** but has an expanded ring structure with a different graphset notation of $R_8^8(40)$. In **IM7**, a different combination of synthons to **IM1** – **IM6**, is present and the overall hydrogen bonding network is altered, with graphset notation $R_6^6(36)$. Similar hydrogen bond lengths in the hydrogen bonded synthons of the ring network are observed for the IMs (Table 9.4 to Table 9.7).

Table 9.4 The hydrogen bond donor-acceptor (D···A) distances of each hydrogen bonded ring in **IM1** and **IM2**.

IM	Carboxylic acid:amide synthon $R_2^2(8)$		Carboxylic acid:amide synthon $R_2^1(6)$		Nitro:amide synthon $R_2^2(8)$	
	D—H···A	d(D···A) (Å)	D—H···A	d(D···A) (Å)	D—H···A	d(D···A) (Å)
IM1	N14—H26···O8	3.044(3)	N13—H28···O20	2.899(3)	N3—H41···O29	3.064(3)
	O7—H102···O14	2.500(2)	N14—H27···O20	3.085(3)	N4—H56···O30	3.157(3)
	N3—H42···O32	2.877(3)	N2—H53···O28	2.927(3)	N6—H16···O10	3.273(3)
	O31—H79···O26	2.632(2)	N1—H52···O28	3.042(3)	N7—H17···O9	2.980(3)
	N1—H51···O5	2.984(3)			N9—H72···O1	3.006(3)
	O6—H80···O(25)	2.520(3)			N8—H74···O2	3.265(3)
	N9—H73···O4	2.882(3)			N11—H14···O16	2.986(3)
	O3—H81···O21	2.555(2)			N10—H12···O15	3.179(3)
	N11—H77···O18	2.850(3)				
	O17—H83···O13	2.595(2)				
	N7—H101···O11	2.902(3)				
	O12—H82···O23	2.559(2)				
IM2	O1—H3···O14	2.534(6)	N4—H12···O7	3.150(7)	N5—H19···O3	3.384(7)
	N6—H20···O2	2.961(7)	N3—H13···O7	2.923(7)	N6—H21···O4	3.043(7)
	O6—H1···O13	2.514(6)			N7—H29···O11	3.371(7)
	N4—H11···O5	3.061(7)			N8—H28···O12	3.020(7)
	O10—H6···O15	2.580(6)				
	N8—H27···O9	2.904(6)				

Table 9.5 The hydrogen bond donor-acceptor (D···A) distances of each hydrogen bonded ring in **IM3** to **IM5**.

IM	Carboxylic acid:amide synthon $R_2^2(8)$		Carboxylic acid:amide synthon $R_2^1(6)$		Nitro:amide synthon $R_2^2(8)$	
	D—H···A	d(D···A) (Å)	D—H···A	d(D···A) (Å)	D—H···A	d(D···A) (Å)
IM3	O6—H21···O1	2.5566(15)	N1—H6···O2	3.0254(16)	N6—H13···O14	2.9580(18)
	N3—H14···O10	2.8559(17)	N7—H5···O2	2.9087(17)	N5—H27···O12	3.2791(17)
	O3—H20···O4	2.5256(15)			N2—H16···O13	3.2152(17)
	N7—H4···O9	2.9706(17)			N3—H15···O15	2.9873(18)
	O8—H23···O5	2.5538(15)				
	N6—H12···O11	2.8939(19)				
IM4	O7—H42···O5	2.572(5)	N7—H52···O13	2.914(6)	N3—H3B···O9	3.038(6)
	N4—H4A···O10	2.862(6)	N10—H10B···O13	3.113(6)	N2—H51···O6	3.280(6)
	O1—H1···O4	2.506(6)			N4—H4B···O8	3.021(6)
	N10—H10A···O12	2.966(7)			N6—H50···O15	3.236(7)
	O3—H60···O11	2.576(5)				
	N3—H3A···O14	2.894(5)				
	O7—H42···O5	2.572(5)				
IM5	O4—H43···O13	2.5333(19)	N7—H38···O11	3.153(2)	N4—H6···O1	3.363(2)
	N7—H39···O3	3.022(2)	N8—H37···O11	2.942(2)	N3—H7···O2	2.964(2)
	O6—H41···O15	2.5115(19)			N5—H15···O8	3.034(2)
	N3—H8···O5	2.918(2)			N6—H16···O9	3.270(2)
	O7—H4···O14	2.6112(19)				
	N5—H14···O10	2.900(2)				

Table 9.6 The hydrogen bond donor-acceptor (D···A) distances of each network in **CIM1** and **CIM2**.

IM	Carboxylic acid:amide synthon $R_2^2(8)$		Carboxylic acid:amide synthon $R_2^1(6)$		Nitro:amide synthon $R_2^2(8)$	
	D—H···A	d(D···A) (Å)	D—H···A	d(D···A) (Å)	D—H···A	d(D···A) (Å)
IM6	O4—H33···O8	2.5288(19)	N7—H29···O15	2.928(2)	N6—H21···O1	3.342(2)
	N8—H13···O3	2.927(2)	N8—H14···O15	2.927(2)	N5—H19···O2	3.001(2)
	O5—H42···O7	2.525(2)			N4—H1···O6	2.929(2)
	N4—H1···O6	2.929(2)			N3—H3···O12	3.257(2)
	O9—H20···O11	2.574(2)				
	N5—H18···O10	2.871(2)				
CIM1	O13—H13···O1	2.516(4)	N4—H4A···O3	2.955(4)	N2—H2A···O6	3.137(4)
	N5—H5A···O12	2.954(4)	N5—H5B···O3	2.977(4)	N3—H3B···O7	2.962(4)
CIM2	O1—H3···O7	2.5057(11)	N3—H8···O3	3.0673(13)		
	N3—H9···O2	2.9600(13)	N2—H7···O3	2.9058(12)		

Table 9.7 The hydrogen bond donor-acceptor (D···A) distances of the hydrogen bonded ring in **IM7**.

IM	Carboxylic acid:amide synthon $R_2^2(8)$		Carboxylic acid dimer synthon $R_2^2(8)$		Nitro:amide synthon $R_2^1(8)$	
	D—H···A	d(D···A) (Å)	D—H···A	d(D···A) (Å)	D—H···A	d(D···A) (Å)
IM7	O2—H5···O7	2.534(2)	O6—H1···O5	2.623(2)	N3—H6···O4	3.045(3)
	N3—H7···O1	3.007(3)			N2—H8···O4	3.143(2)

The hydrogen bonded ring networks in **IM1** to **IM7** have an elongated ellipsoid shape (Figure 9.5 and Table 9.8). The longest dimension of the hydrogen bonded ring in each inclusion material is *ca.* 12 Å in **IM1** – **IM5** and 15 Å in **IM6** and **IM7**, where the ring networks are expanded. These dimensions are comparable to those for the inclusion materials of trimesic acid (14 Å), if there is no pore interpenetration, [316] 2,4,6-tris-(4-bromophenoxy)-1,3,5-triazine (BrPOT) (12 Å) [317] and in some zeolites. [318]

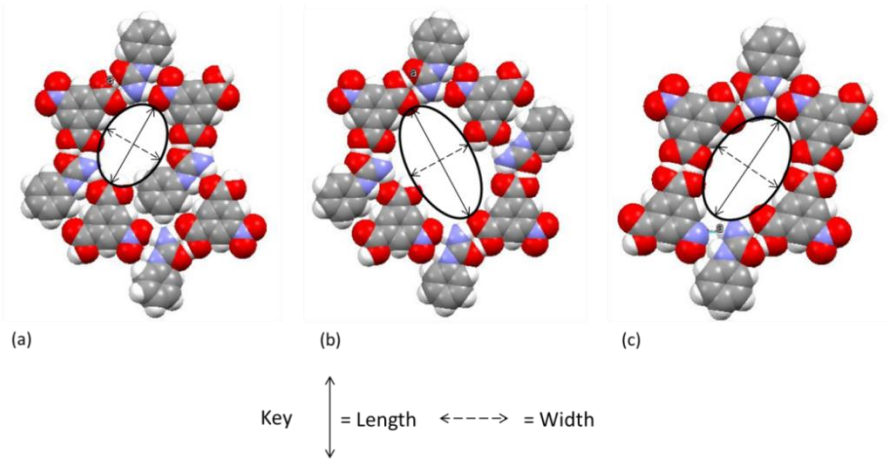

Figure 9.5 The size of the hydrogen bond ring in (a) **IM1** – **IM5**, (b) **IM6** and (c) **IM7** in terms of a ring cross section; ellipsoid axis lengths are given in Table 9.8.

Table 9.8 The hydrogen bonded ring cross sections in **IM1** to **IM7**, in terms of an ellipsoid with length (L) and width (W).

IM	Ellipsoid length, L (Å)	Ellipsoid width, W (Å)
IM1 i	12.100(3)	9.25(3)
IM1 ii	11.970(3)	9.43(3)
IM2	11.924(9)	9.8516
IM3	12.334(2)	8.84(3)
IM4	11.869(7)	9.700(7)
IM5	11.485(2)	10.11(4)
IM6	15.437(3)	8.99(5)
IM7	15.639(3)	9.5401

Guest inclusion

Guests (G) are included in the centre of the hydrogen bonded ring in each IM and in the close packed space in the CIMs. The host:guest ratios are presented in Table 9.9. In **IM1**, **IM3**, **IM6**, **CIM1** and **CIM2**, a single type of guest species is included in the host structure. In contrast, in **IM4**, **IM5** and **IM7**, two types of guest species are included; in **IM4** and **IM5** a volatile solvent and a water molecule are included whilst in **IM7** a disordered THF and methanol molecule are included. In **IM7**, the guest is disordered over an inversion centre making its determination more

difficult. Crystallisation was carried out from methanol and THF solvent whilst the electron density in the asymmetric unit resembled that of half a THF alongside an additional solvent molecule. To aid in the guest identification, Squeeze, [319] within the WinGX package, [221] was carried out on the host structure without the solvent modelled. The residual electron count per unit cell was 49. It is likely a THF molecule is present (an electron count of 40) alongside an additional guest which may be a molecule of water (electron count of 10) or methanol (electron count of 18). The identity of this guest is investigated further in §9.4.2.

Table 9.9 Host-guest ratios of the IMs, per asymmetric unit.

IM	No. of *N*-phenylurea molecules	No. of 5-nitroisophthalic acid molecules	No. of guest molecules
IM1	7	4	2
IM2	3	2	2
IM3	3	2	1
IM4	3	2	2
IM5	3	2	2
IM6	3	2	1
IM7	1	1	1.5
CIM1	1	1	1
CIM2	1	1	1

Guest inclusion occurs in **IM1** – **IM6**, **CIM1** and **CIM2** by tethering to a carboxylic acid hydroxyl group of the host, *via* an O—H···O or O—H···N hydrogen bond, that is not involved in formation of the hydrogen bonded host network; the hydroxyl group interacts with an oxygen or nitrogen atom on the solvent guest. Similar tethering of the guest to the host framework *via* hydrogen bonding interactions has been reported in other inclusion materials including in an orthogonal bis(resorcinol)-anthracene compound, [320] in an AL-MIL-53 metal organic framework [321] and in the 1,1'-binaphthyl-2,2'-dicarboxylic acid clathrate with DMF. [322] Guest-guest interactions have also been reported. [323] In contrast, in **IM7**, the hydrogen bonding capacity of the host building blocks is satisfied in network formation and there is no carboxylic acid hydroxyl group to which the guest can tether; this may account for the disordered nature of the solvent. Instead, the guest species are held in place by π-interactions to host rings in the layers above and below ($d_{\pi\cdots\pi}$ 3.220(5) – 3.316(8) Å).

In **IM1**, two types of guest inclusion occur (Figure 9.3 (a) i and ii). In one host ring, a methanol guest is tethered to the host by interaction to the carboxylic acid hydroxyl group. In the second host ring, a molecule of *N*-phenylurea hydrogen bonds instead to the carboxylic acid hydroxyl

group, through an O—H···O hydrogen bond, and the methanol guest interacts with the host through an O—H···O hydrogen bond to a carbonyl oxygen in an carboxylic acid:amide synthon. In **IM4** and **IM5**, water tethers to the host framework by interacting with the carboxylic acid hydroxyl group and the second solvent molecule is held in place by a guest-guest O—H···O hydrogen bond to the water. Additional interactions hold the water guest species in place in **CIM1**; one water hydrogen bonds to a second carboxylic acid group, this time to the carbonyl oxygen, whilst the other water molecule is held in place by an additional interaction to a nitro group and a urea carbonyl in neighbouring 5-nitroisophthalic acid and *N*-phenylurea molecules, respectively. Guest-guest interactions also occur between the two water molecules. The host-guest and guest-guest interaction distances in all the IMs and CIMs are presented in Table 9.10.

Table 9.10 Host-guest (Ho-G), guest-guest (G-G) interaction distances (D···A) in the IMs.

IM	Interaction type	D—H···A	d(D···A) (Å)
IM1	Ho-G (host-methanol1)	O27—H78···O100	2.603(3)
	Ho-G (host-methanol1)	O100—H106···O26	2.801(3)
	Ho-G (host-methanol2)	O101—H107···O8	2.783(3)
	Ho-G (host-methanol2)	N16—H48···O101	2.918(3)
	Ho-G (host-N-phenylurea)	O19—H100···.O22	2.561(3)
IM2	Ho-G (host-ethanol)	O8—H10···O16	2.611(9)
	G-G (ethanol-water1)	O16···O17	2.75(2)
	G-G (water1-water2)	O17···O18	2.17(2)
IM3	Ho-G (host-acetonitrile)	O7—H22···N9	2.762(2)
IM4	Ho-G (host-water)	O2—H2···O17	2.626(7)
	Ho-G (host-water)	O17—H53···O10	2.859(8)
	G-G (water-acetone)	O17—H54···O100	2.795(10)
IM5	Ho-G (host-water)	O12—H5···O17	2.594(2)
	Ho-G (host-water)	O17—H22···O14	2.867(2)
	G-G (water-THF)	O17—H23···O16	2.805(3)
IM6	Ho-G (host-ethyl acetate)	O14—H32···O16	2.630(2)
IM7	Ho-G (host-THF/methanol)	π···π	3.220(5) – 3.316(8)
CIM1	Ho-G (host-water1)	O2—H2B···O16	2.555(4)
	Ho-G (host-water1)	O16—H100···O10	2.783(4)
	Ho-G (host-water2)	O11—H105···O15	2.690(4)
	Ho-G (host-water2)	O15—H103···O8	2.840(4)
	Ho-G (host-water2)	O15—H102···O14	2.691(4)
	G-G (water1-water2)	O16—H101···O5	2.778(5)
CIM2	Ho-G (host-acetone)	O4—H1···O8	2.6433(12)
	Ho-G (host-acetone)	N3—H8···O8	3.0691(13)

In addition to the tethering of each guest species to the ring network, *via* interaction with a host hydroxyl group, secondary interactions occur as the host components pack around the guest forming the solvated pockets or channels. In **IM1**, in the hydrogen bonded ring where the methanol guest interacts with the host hydroxyl tether group, the methanol guest also forms several hydrogen bonding interactions to *N*-phenylurea molecules in the surrounding framework including an N—H···O ($d_{N\cdots O}$ 3.119(3) Å) and an O—H···O ($d_{O\cdots O}$ 2.802(3) Å) hydrogen bond and a weaker C—H···O ($d_{C\cdots O}$ 3.444(6) Å) hydrogen bond. In the other hydrogen bonded ring, where an *N*-phenylurea molecule interacts with the host hydroxyl tether group, the second methanol guest is held in the host structure *via* two N—H···O hydrogen bonds ($d_{N\cdots O}$ 2.919(3) and 3.171(3) Å) to the tethered *N*-phenylurea molecule in the middle of the ring and a weak C—H···O hydrogen bond to a 5-nitroisophthalic acid molecule ($d_{C\cdots O}$ 3.290(3) Å) host molecule. In **IM2**, the ethanol guest is further held within the hydrogen bonded ring *via* O—H···O and C—H···O hydrogen bonds to a 5-nitroisophthalic acid host molecule ($d_{O\cdots O}$ 2.555(2) Å and $d_{C\cdots O}$ 3.49(2), 3.58(2) Å). The water molecules do not form additional interactions to the host framework. In **IM3**, the acetonitrile guest is packed in the host framework *via* π-π interactions and weak C—H···O hydrogen bonds to a carboxylic acid group in the layer below ($d_{\pi\cdots\pi}$ 3.099(2) and $d_{C\cdots O}$ 3.199(2) Å). In **IM4**, the water guest species tethered to the host hydroxyl group also interacts with an *N*-phenylurea molecule of the host *via* an N—H···O hydrogen bond ($d_{N\cdots O}$ 3.202(6) Å) and with a 5-nitroisophthalic acid molecule in the layer above *via* an O—H···O hydrogen bond ($d_{O\cdots O}$ 2.853(8) Å). The pairs of acetone guests in each pocket interact *via* weak C—H···H—C ($d_{C\cdots C}$ 3.71(1) Å) interactions. There are no host-guest interactions involving the acetone solvent, only guest-guest interactions. In **IM5**, the water guest species tethered to the host hydroxyl group also interacts with an *N*-phenylurea molecule in the ring above *via* an O—H···O hydrogen bond ($d_{O\cdots O}$ 2.867(2) Å). The THF guest is located below the hydrogen bonded ring layer and interacts with the host framework through a weak C—H···O hydrogen bond ($d_{C\cdots O}$ 3.391(5) Å) to a 5-nitroisophthalic acid host oxygen atom. Pairs of THF molecules in each pocket also interact *via* weak C—H···H—C contacts ($d_{C\cdots C}$ 3.809(6) Å). Additional interactions holding the guest species in place in **IM6** include π-π interaction between an ethyl acetate oxygen and a 5-nitrosiophthalic acid molecule ($d_{\pi\cdots\pi}$ 3.214(3) Å) and in **IM7** include π-π interactions between the guest and 5-nitroisopthalic acid molecules ($d_{\pi\cdots\pi}$ 3.185(5) to 3.351(5) Å). There are no additional interactions holding the water guest in place in **CIM1**. In **CIM2**, the guest is additionally held in place by an N—H···O hydrogen bond to an *N*-phenylurea molecule and several C—H···O weak interactions to a 5-nitroisophthalic acid molecule ($d_{N\cdots O}$ 3.069(1) Å and $d_{C\cdots O}$ 3.432(2) – 3.567(2) Å).

The hydrogen bonded rings in **IM1** – **IM7** form one-dimentionsal chains that pack in layers through the crystal structure. In **IM1**, **IM3**, **IM4** and **IM5**, pairs of rings stack on top of one another in opposite orientations creating pockets of guests; this arrangement is characteristic of

inclusion clathrates (Figure 9.6). In **IM1** and **IM3**, the pair wise packing of hydrogen bonded rings means two molecules of guest are present per pocket. The guest molecule is also co-planar with the hydrogen bonded ring layer. In contrast, in **IM4** and **IM5**, four molecules of solvent are present per pocket as two types of guest are included per ring (volatile solvent and water molecule); only the water molecules are co-planar with the hydrogen bonded ring layer whilst the volatile solvents sit in the space between the layers. In **IM2**, **IM6** and **IM7**, hydrogen bonded rings stack continuously on top of one another, creating channels; this is characteristic of inclusion compounds (Figure 9.7). In **IM2**, the layers are not planar but have a wave like structure and, in the case of **IM6** and **IM7**, the hydrogen bonded rings are stacked offset from one another and the guest channel runs diagonally through the structure. In **CIM1** and **CIM2**, the hydrogen bonded networks extend in two-dimensions generating layers, within which the guests occupy pockets, in pairs (Figure 9.6).

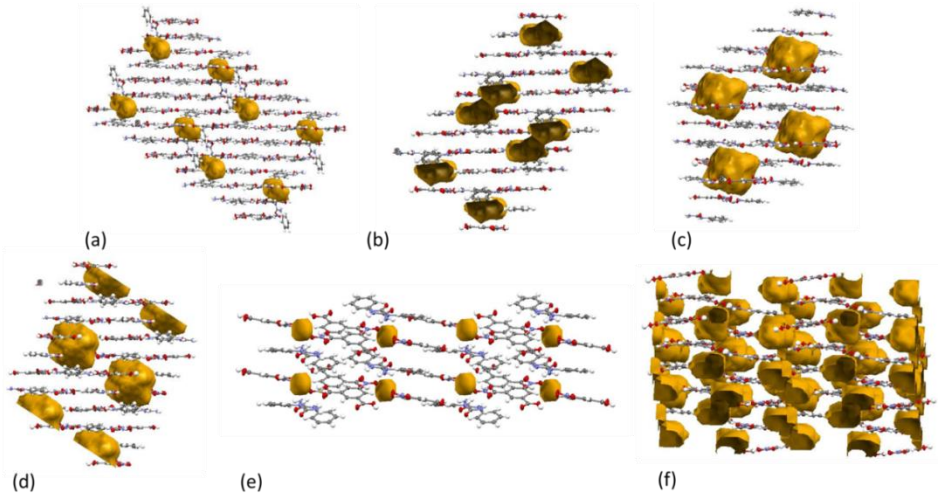

Figure 9.6 Pockets occupied by the guest molecules in the *N*-phenylurea and 5-nitroisophthalic acid host framework in (a) **IM1**, (b) **IM3**, (b) **IM4**, (c) **IM5**, (d) **IM5**, (e) **CIM1** and (f) **CIM2**.

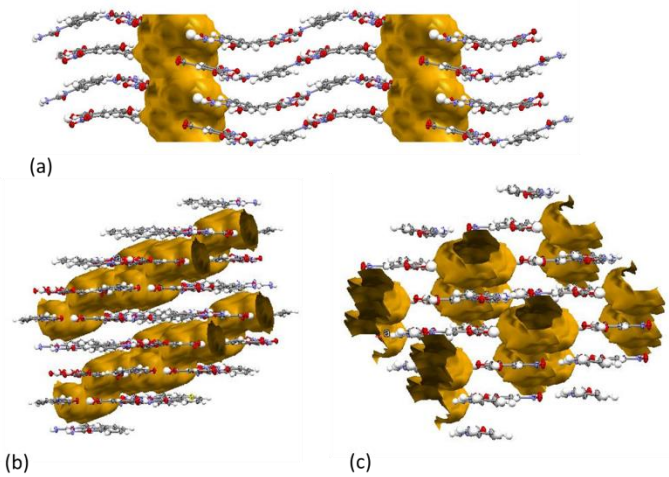

Figure 9.7 Channels occupied by the guest molecules in the *N*-phenylurea and 5-nitroisophthalic acid host framework in (a) **IM2**, (b) **IM6** and (c) **IM7**.

The void spaces of the pockets and channels occupied by the guest molecules in **IM1** to **IM7**, **CIM1** and **CIM2** were mapped in Mercury [222] on a structural model with the solvent molecule(s) removed; the void spaces are also shown in Figure 9.6 and Figure 9.7 in yellow. The void calculation in Mercury [222] used a contact surface with parameters of a 1.2 Å probe radius and 0.7 Å grid spacing (Table 9.11). Small void volumes were indicated in **CIM1** (< 14 $Å^3$ per unit cell), whilst the largest void volume was present in **CIM2** (~336 $Å^3$ per unit cell). **CIM2** was also shown to be the least dense 'empty framework' whilst **IM1** was the most dense.

Table 9.11 Calculated void volumes and densities in **IM1** – **IM7**, **CIM1** and **CIM2**.

IM	Unit cell volume occupied by void (%)	Void volume per unit cell ($Å^3$)	Calculated density with solvent removed ($gmol^{-1}Å^{-3}$)
IM1	3.2	136.34	1.4368
IM2	12.8	270.32	1.3026
IM3	5.9	119.51	1.3612
IM4	11.5	243.00	1.3046
IM5	13.1	279.23	1.2991
IM6	12.6	268.28	1.2941
IM7	19.7	178.80	1.2309
CIM1	0.9	13.73	1.4308
CIM2	17.6	336.24	1.2058

In **IM1**, **IM3** and **IM5**, parts of the host framework occupy the space between the stacked layers. In **IM1**, an *N*-phenylurea molecular building block is oriented almost perpendicular to the hydrogen bonded ring plane, by 82 °, and in **IM3** and **IM5**, a phenyl ring bends into the interlayer space, out of co-planarity of the layers by 29.84 ° and 25.82 °, respectively. The layers of hydrogen bonded ring networks, in each IM, pack *via* π-π stacking interactions between the phenyl rings of both the *N*-phenylurea and 5-nitroisophthalic acid and between phenyl rings and lone pair density on the nitrogen and oxygen atoms of the intermolecular building blocks. A range of interlayer spacings occur for the different inclusion materials (Table 9.12). The shortest interactions form in **CIM2**, where the hydrogen bonded ring motif is not present. The closest packing of layers where the hydrogen bonded ring motif is present occurs in **IM3** whereas the most spaced layers are in **IM5**; likely a consequence of the large THF molecules positioned in the interlayer spacing.

Table 9.12 The π-π stacking interactions between the layers of the hydrogen bonded ring networks in **IM1** – **IM7**, **CIM1**, **CIM2**.

IM	Interlayer spacing (Å)
IM1	3.153(3) to 3.351(3)
IM2	3.014(7) to 3.396(8)
IM3	2.916(2) to 3.386(2)
IM4	3.187(8) to 3.680(1)
IM5	3.027(2) to 3.697(2)
IM6	3.046(3) to 3.359(3)
IM7	3.184(2) to 3.516(5)
CIM1	3.093(5) to 3.332(5)
CIM2	2.987(1) to 3.318(1)

9.3.2 Non-solvated (NS) *N*-phenylurea 5-nitroisophthalic acid molecular complexes

Two non-solvated forms of *N*-phenylurea 5-nitrosiophthalic acid were also prepared, **NS1**, in a 2:1 ratio of components and in space group $P\bar{1}$, and **NS2**, in a 1:1 ratio of components and in space group $P2_1/c$ (Figure 9.8). **NS1** has a structurally similar hydrogen bonded ring network to that formed in **IM1** to **IM5**, comprised of four carboxylic acid:amide $R_2^2(8)$ hydrogen bond synthons, in both U:Ac and U:Ac:U hydrogen bonded motifs, and two carboxylic acid:amide $R_2^1(6)$ and two nitro:amide $R_2^2(8)$ hydrogen bond synthons.

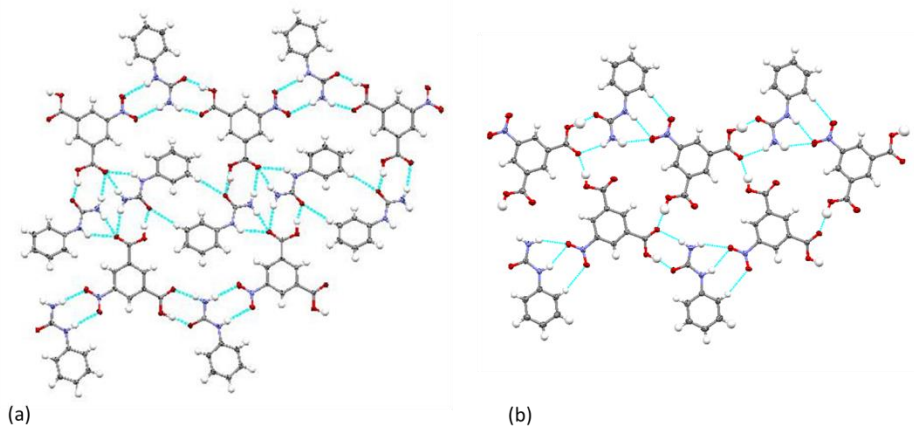

Figure 9.8 Hydrogen bonding networks in non-solvated *N*-phenylurea 5-nitroisophthalic acid (a) **NS1** and (b) **NS2**.

In contrast to **IM1** to **IM5**, in **NS1**, an *N*-phenylurea molecule sits in place of the guest in the centre of the hydrogen bonded ring network and an additional carboxylic acid:amide $R_2^2(8)$ hydrogen bond synthon is formed. **NS2** has a very different structure to all other complexes discussed here. A single carboxylic acid:amide $R_2^2(8)$ hydrogen bond synthon is formed, in a U:Ac motif, alongside a nitro:amide $R_2^1(6)$ hydrogen bond synthon and a single O—H···O interaction,

formed between symmetry independent 5-nitroisophthalic acid molecules and involving a carboxylic acid hydroxyl group of one and a carbonyl oxygen atom of the other. A weak C—H···O hydrogen bond between the nitro group and an *N*-phenylurea aromatic C—H group ($d_{C\cdots O}$ 3.402(3) Å) also forms. The hydrogen bonding interactions in **NS1** and **NS2** are listed in Table 9.13 and Table 9.14, respectively.

Table 9.13 Hydrogen bond donor-acceptor distances in the hydrogen bond networks of **NS1**.

Carboxylic acid:amide synthon $R_2^2(8)$		Carboxylic acid:amide synthon $R_2^1(6)$		Nitro:amide synthon $R_2^2(8)$	
D—H···A	d(D···A) (Å)	D—H···A	d(D···A) (Å)	D—H···A	d(D···A) (Å)
O6—H21···O1	2.610(2)	N4—H11···O3	3.045(2)	N2—H15···O7	3.151(2)
N3—H14···O5	2.889(3)	N5—H10···O3	3.113(2)	N3—H13···O8	3.084(3)
O4—H(1···O2	2.5232(18)				
N4—H12···O3	3.135(2)				

Table 9.14 Hydrogen bond donor-acceptor distances in the hydrogen bond networks of **NS2**.

Carboxylic acid:amide synthon $R_2^2(8)$		Nitro:amide synthon $R_2^1(6)$		O—H···O Single HB	
D—H···A	d(D···A) (Å)	D—H···A	d(D···A) (Å)	D—H···A	d(D···A) (Å)
O8—H24···O1	2.479(2)	N1—H16···O12	3.127(3)	O6—H23···O14	2.655(2)
N4—H21···O7	3.068(3)	N2—H14···O12	3.121(3)	O10—H1···O7	2.661(2)
O13—H100···O2	2.481(2)	N3—H17···O4	3.082(3)		
N2—H15···O14	3.010(3)	N4—H22···O4	3.157(3)		

The hydrogen bonded networks in **NS1** and **NS2** extend in one dimension forming a hydrogen bonded chain. Infinite numbers of these hydrogen bonded chains interconnect through weak C—H···O interactions into two dimensional sheets (**NS1** $d_{C\cdots O}$ 3.374(2) and 3.442(2) Å, **NS2** $d_{C\cdots O}$ 3.446(3) and 3.506(3) Å). Packing of the hydrogen bonded sheets in **NS1** and **NS2** occurs in layers (Figure 9.9) where each layer is oppositely oriented to the next. π-π stacking interactions form connections between the layers (**NS1** $d_{\pi\cdots\pi}$ 3.311(4) to 3.367(3) Å and **NS2** $d_{\pi\cdots\pi}$ 2.974(4) to 3.330(4) Å). The *N*-phenylurea molecule occupying the centre of the hydrogen bonded ring in **NS1** is twisted relative to the hydrogen bonded ring network, out of co-planarity by 21 °, packing diagonally across the ring layers.

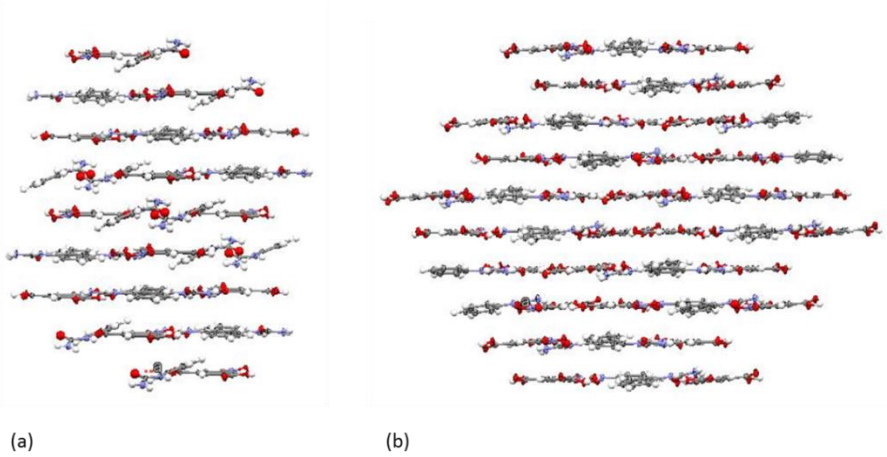

Figure 9.9 Layered structures of the *N*-phenylurea 5-nitroisophthalic acid non-solvated forms (a) **NS1** and (b) **NS2**.

9.3.3 Non-solvated substituted urea 5-nitroisophthalic acid molecular complexes

Three non-solvated molecular complexes of urea 5-nitroisophthalic acid (U5-NIP), *N*-methylurea 5-nitroisophthalic acid (MU5-NIP) and *N*,*N*-dimethylurea 5-nitroisophthalic acid (DMU5-NIP) have also been prepared. U5-NIP and DMU5-NIP are 4:1 and 2:1 complexes of the substituted urea and 5-nitroisophthalic acid molecular components, respectively, formed in space group $P\bar{1}$. MU5-NIP is a 2:1 complex formed in space group $P2_1/n$. In these molecular complexes, substituted urea and 5-nitroisophthalic acid molecules assemble into hydrogen bonding networks (Figure 9.10). Unlike the IMs of *N*-phenylurea and 5-nitroisophthalic acid, these do not have solvent inclusion behaviour.

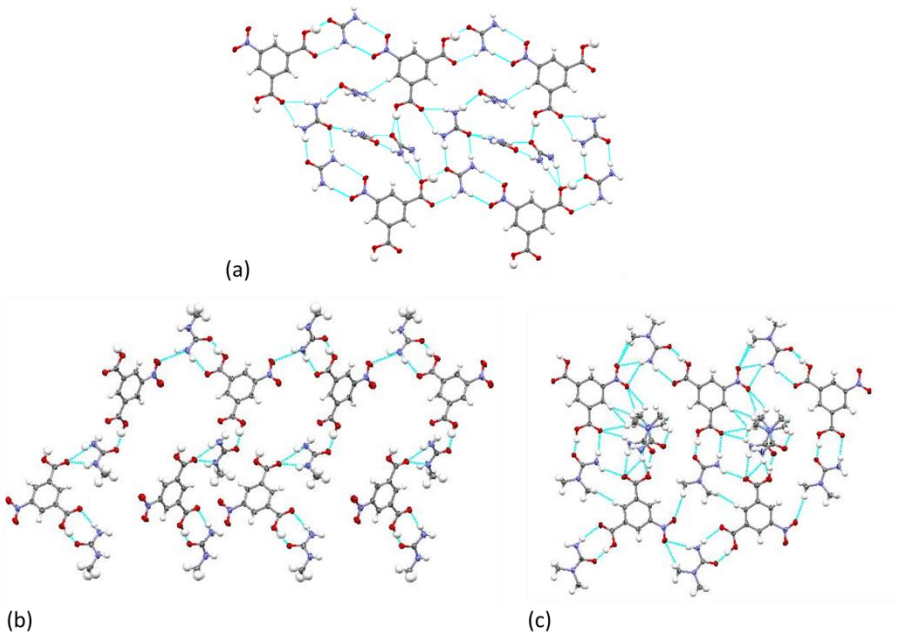

Figure 9.10 Hydrogen bonded networks formed in (a) U5-NIP, (b) MU5-NIP and (c) DMU5-NIP.

In U5-NIP and DMU5-NIP, the hydrogen bonded networks have a ring structure comprised of eight molecular building blocks, as in the *N*-phenylurea 5-nitroisophthalic acid IMs. The ring network in DMU5-NIP is close to being isostructural with those formed in the *N*-phenylurea 5-nitroisophthalic acid IMs. In MU5-NIP, the hydrogen bonded network does not have a ring structure but is more chain like.

In the networks of U5-NIP, MU5-NIP and DMU5-NIP, molecular assembly occurs *via* carboxylic acid:amide $R_2^2(8)$ hydrogen bond synthons, in a U:Ac motif as in the *N*-phenylurea 5-nitroisophthalic acid IMs. In U5-NIP, molecular assembly also occurs in the ring network *via* nitro:amide $R_2^2(8)$ and carboxylic acid:amide $R_2^1(6)$ hydrogen bond synthons, as in the IMs, and *via* an amide:amide $R_2^2(8)$ hydrogen bonded dimer. In MU5-NIP, the hydrogen bonded chain is additionally comprised of a carboxylic acid:amide $R_2^1(6)$ hydrogen bond synthon between MU and 5-NIP molecules, as in the IMs, alongside a single N—H···O link between a 5-NIP nitro group and MU amine N—H group ($d_{N\cdots O}$ 2.934(2) Å) and a single O—H···O hydrogen bond ($d_{O\cdots O}$ 2.614(1) Å) between a 5-NIP hydroxyl group and a MU carbonyl. In DMU5-NIP, in the ring network, each 5-NIP molecule is involved in two carboxylic acid:amide $R_2^2(8)$ hydrogen bond synthons forming a U:Ac:U hydrogen bond motif; this motif also forms in **IM1** – **IM6**, and **NS1**. The disubstitution of one nitrogen atom in the DMU molecule means that a nitro:amide $R_2^2(8)$ hydrogen bond synthon is blocked from forming between the 5-NIP nitro group and the DMU molecule in the hydrogen bond ring; instead they link *via* a nitro:amide $R_2^1(6)$ hydrogen bond synthon. This disubstitution also means that a carboxylic acid:amide $R_2^1(6)$ hydrogen bond synthon is blocked from forming between the 5-NIP carboxylic acid group and the DMU molecule; instead they link *via* a single N—H···O hydrogen bond ($d_{N\cdots O}$ 3.038(2) Å). The hydrogen bonding ring interactions are given in Table 9.15.

Table 9.15 Hydrogen bonding network interactions in U5-NIP, MU5-NIP and DMU5-NIP.

Complex	Synthon	D—H···A	d(D···A) (Å)
U5-NIP	Carboxylic acid:amide synthon $R_2^2(8)$	O4—H21···O10	2.4703(14)
		N8—H2···O3	2.8780(17)
	Carboxylic acid:amide synthon $R_2^1(6)$	N4—H14···O2	3.0501(17)
		N5—H15···O2	2.9956(17)
	Nitro:amide synthon $R_2^2(8)$	N8—H1···O8	2.9435(17)
		N9—H3...O9	3.2943(16)
	Amide:amide $R_2^2(8)$	N4—H13···O10	2.9592(16)
		N9—H4···O5	2.8368(16)
MU5-NIP	Carboxylic acid:amide synthon $R_2^2(8)$	O5—H5···O8	2.4901(12)
		N4—H14···O2	3.0628(15)
	Carboxylic acid:amide synthon $R_2^1(6)$	N5—H12···O2	2.9181(14)
		N4—H14···O2	3.0628(15)
	Single D—H···A	N2—H6···O6	3.0036(15)
DMU5-NIP	Carboxylic acid:amide synthon $R_2^2(8)$	O3—H1···O1	2.5568(12)
		O5—H20···O17	2.4824(16)
		N8—H10···O4	3.1250(19)
		O1—H19···O3	2.4586(16)
		N1—H15···O2	2.9674(19)
	Nitro:amide synthon $R_2^1(4)$	N8—H9···O6	3.2310(19)
		N8—H9···O7	3.303(2)
	Single D—H···A	N1—H14···O12	3.038(2)
		N4—H8 ···O15	3.223(2)

'Guest' substituted urea molecules occupy the centre of the hydrogen bonded ring networks in U5-NIP and DMU5-NIP. In U5-NIP, the 'guest' urea molecules form hydrogen bonded chains that run almost perpendicular to the plane of the ring network (non-planar by ca. 70 to 80 °). One chain is tethered to the 'host' *via* an O—H···O hydrogen bonding interaction with a 5-NIP hydroxyl group, not satisfied on hydrogen bond network formation ($d_{O\cdots O}$ 2.614(1) Å), as in the IMs, and a carboxylic acid:amide $R_2^1(6)$ hydrogen bond synthon with a urea of the host ($d_{N\cdots O}$ 2.971(2) and 2.945(2) Å) whilst the other chain is tethered by a single N—H···O hydrogen bond to a host urea molecule ($d_{N\cdots O}$ 2.934(2) Å). In DMU5-NIP, a disordered *N.N*-dimethylurea molecule occupies the centre of the hydrogen bonded ring (occupancy split of 84:16) tethered to the host on interaction with the 5-NIP hydroxyl group *via* a carboxylic acid:amide $R_2^2(8)$ hydrogen bond synthon ($d_{O\cdots O}$ 2.434(2) Å and $d_{N\cdots O}$ 3.089(2) Å).

The packing of the hydrogen bonding networks in U5-NIP, MU5-NIP and DMU5-NIP forms layered structures in U5-NIP and DMU5-NIP whilst in MU5-NIP, molecules are arranged with alternate orientations (Figure 9.11).

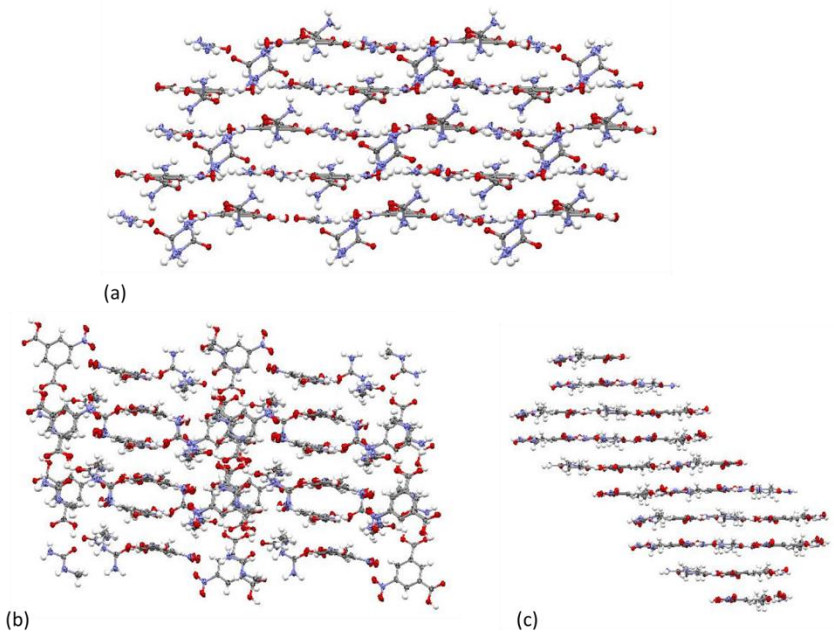

Figure 9.11 The crystal packing in (a) U5-NIP, (b) MU5-NIP and (c) DMU5-NIP.

In U5-NIP, the layers are formed of two dimensional planar sheets of the hydrogen bonded rings. The sheets stack on top of one another in the crystal structure such that each hydrogen bonded ring lies over the next; this creates the channels which are occupied by the one dimensional chains of urea molecules. The interlayer separations in U5-NIP are in the range of 2.948(2) to 3.295(2) Å. In DMU5-NIP, the hydrogen bonded rings extend in one dimensional chains. These chains connect in two dimensions to form planar sheets via weak C—H···O hydrogen bonds; formed between DMU methyl groups and both oxygen atoms in the O—H···O hydrogen bond of the carboxylic acid:amide $R_2^2(8)$ hydrogen bond synthon ($d_{C\cdots O}$ 3.309(2), 3.535(2), 3.332(2) and 3.561(3) Å) and between a methyl group and a 5-NIP nitro oxygen atom ($d_{C\cdots O}$ 3.171(2) Å). The planar sheets of DMU5-NIP stack on top of one another such that two oppositely oriented hydrogen bonding rings form a pocket of two disordered DMU molecules. The interlayer separations in DMU5-NIP are in the range of 3.206(2) to 3.486(2) Å. There is no layered structure in MU5-NIP. Instead, molecules pack in three-membered pseudo planar units, consisting of a U:Ac hydrogen bonded motif linked to a second MU molecule by a carboxylic acid:amide $R_2^1(6)$ hydrogen bond synthon. These motifs stack in offset columns by π-π interactions ($d_{\pi\cdots\pi}$ 2.958(1) to 3.333(2) Å) and each column is alternately oriented to the next (rotated by 79 °), connected by O—H···O hydrogen bonds formed between MU and 5-NIP molecules ($d_{O\cdots O}$ 2.918(2) Å) and between MU molecules ($d_{O\cdots O}$ 2.955(2) Å).

9.4 Experimental characterisation of the properties of *N*-phenylurea 5-nitroisophthalic acid inclusion materials

9.4.1 Crystallisation trials

Not all the solvents trialled generated the *N*-phenylurea 5-nitroisophthalic acid IMs; the host components were set up in a range of polar (methanol, ethanol, acetonitrile, acetone, THF, ethyl acetate, water) and non-polar solvents (diethyl ether, hexane and cyclohexane). Only the polar solvents were included in the host structures; diethyl ether produced **NS2** whilst the host components were insoluble in hexane and cyclohexane.

9.4.2 Thermal behaviour of N-phenylurea 5-nitroisophthalic acid inclusion materials

Thermogravimetric analysis (TGA) coupled with mass spectrometry (MS), Differential Scanning Calorimetry (DSC) and Hot Stage Microscopy (HSM) were carried out on **IM1** – **IM7**, **CIM1** and **CIM2** to determine the thermal stability of these materials. The thermal stability of **NS1** and **NS2** was also investigated.

TGA-MS

TGA coupled with MS was carried out on the IMs according to the procedure detailed in §4.4.3. The TGA curves with MS data for **IM1** – **IM7**, **CIM1** and **CIM2** are shown in Figure 9.12 to Figure 9.14. The TGA shows well defined three-step mass loss profiles in each of the IM and CIM curves. The first step corresponds to the loss of the guest, with the identity of each lost guest confirmed by MS analysis (Figure 9.12 to Figure 9.14). The second and third mass loss steps correspond to the *N*-phenylurea and 5-nitroisophthalic acid components, respectively, of the host framework. In the TGA-MS of **CIM2** (Figure 9.14(c)), a small amount of **IM4** may be indicated by a weak MS signal for a water peak (m/z = 18). There is reasonable agreement between the expected and observed weight loss values for each step (Table 9.16). Discrepancies between the expected and observed weight losses can be attributed to an impure sample in each case; calculated values were based on the asymmetric unit. The size of the first mass loss step in **IM7** indicates the likely identity of the disordered solvent as THF only. However, in the MS data, methanol solvent is detected alongside THF. Therefore in **IM7**, it is likely that both THF and methanol solvent are included in the host structure.

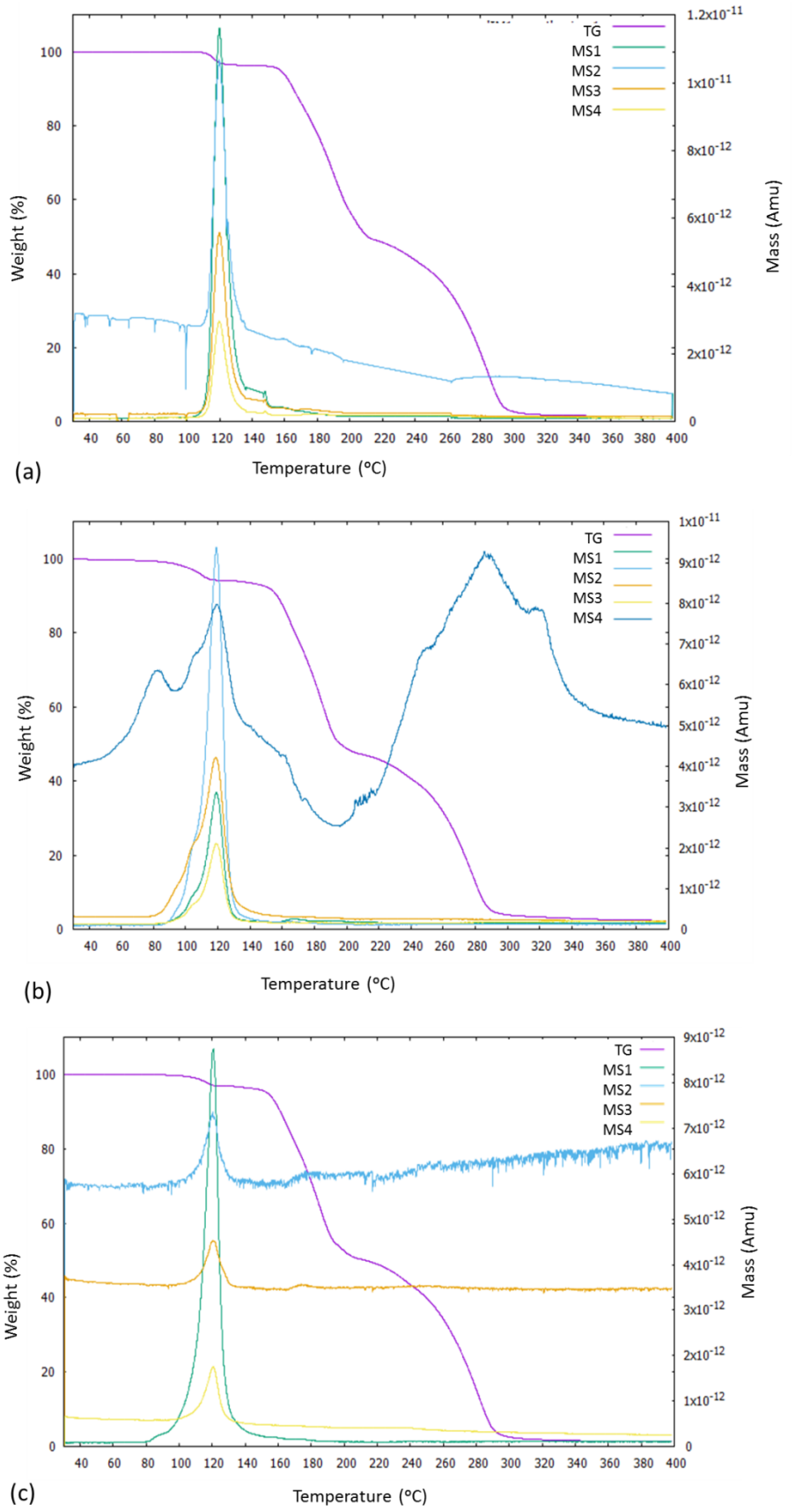

Figure 9.12 The TGA-MS for (a) **IM1**: methanol peaks MS1 = 31 m/z, MS2 = 32 m/z, MS3 = 29 m/z, MS4 = 15 m/z, (b) **IM2**: ethanol peaks MS1 = 31 m/z, MS2 = 45 m/z, MS3 = 27 m/z, MS4 = 29 m/z, water peak MS5 = 18 m/z and (c) **IM3**: acetonitrile peaks MS1 = 41 m/z, MS2 = 39 m/z, MS3 = 28 m/z, MS4 = 14 m/z.

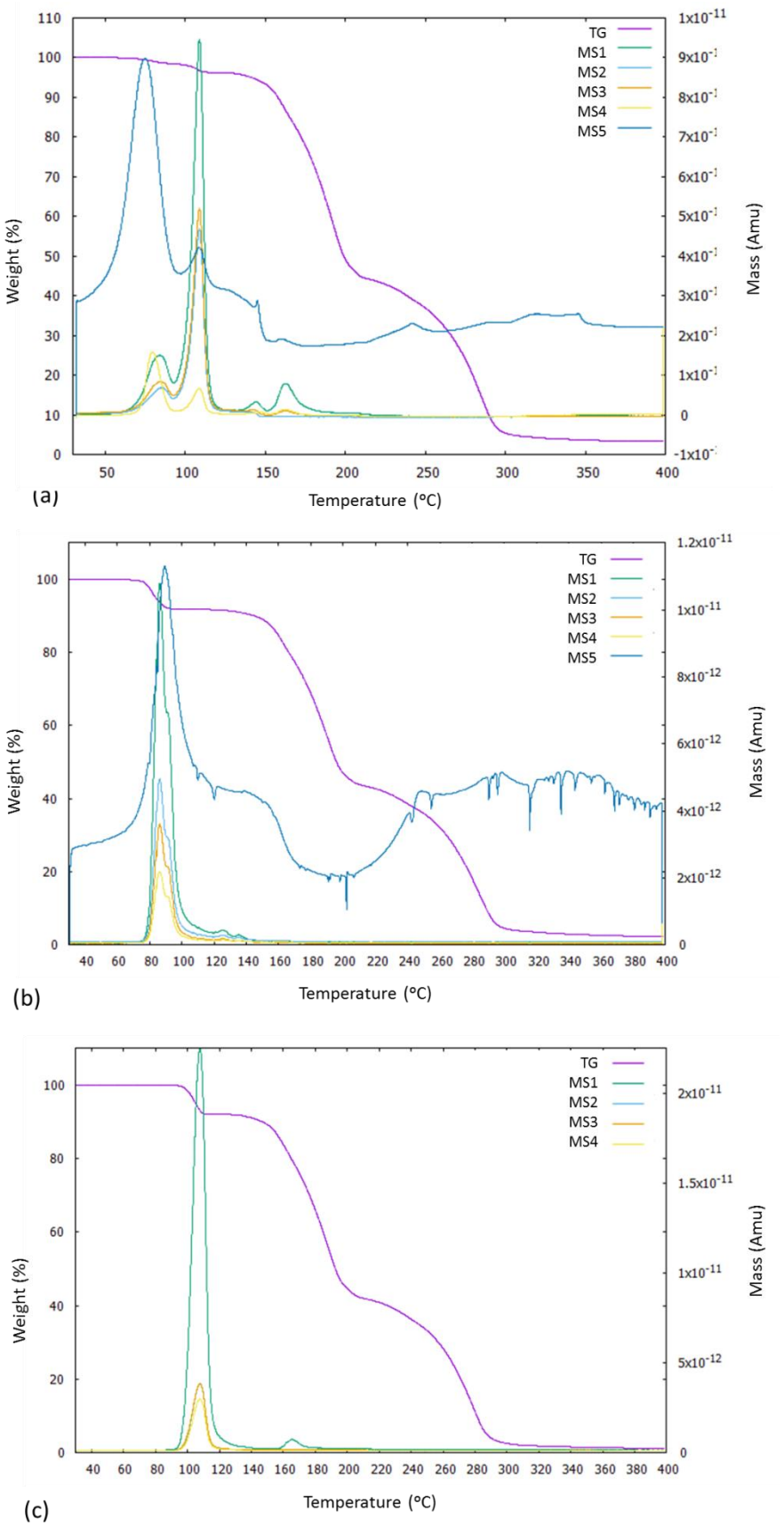

Figure 9.13 The TGA-MS for (a) **IM4**: acetone peaks MS1 = 43 m/z, MS2 = 58 m/z, MS3 = 15 m/z, MS4 = 42 m/z, water peaks MS5 = 18 m/z, (b) **IM5**: THF peaks MS1 = 42 m/z, MS2 = 41 m/z, MS3 = 71 m/z, MS4 = 43 m/z, water peak MS5 18 m/z and (c) **IM6**: ethyl acetate peaks MS1 = 43 m/z, MS2 = 61 m/z, MS3 = 45 m/z, MS4 = 70 m/z.

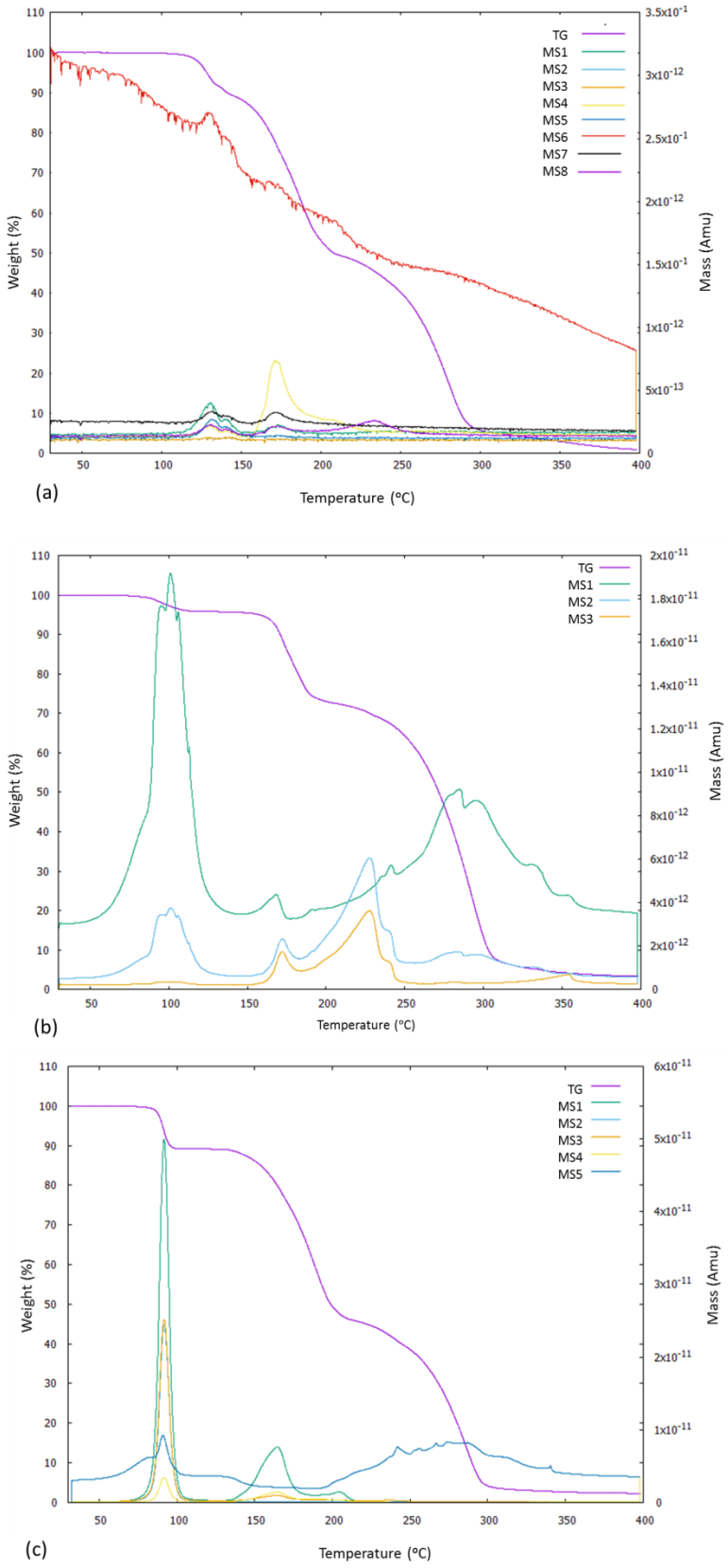

Figure 9.14 The TGA-MS for (a) **IM7**: THF peaks MS1 = 42, MS2 = 41, MS3 = 71, MS4 = 43, methanol peaks and MS5 = 31, MS6 = 32, MS7 = 29, MS8 = 15, (b) **CIM1**: water peaks MS1 = 18 m/z, MS2 = 17 m/z, MS3 = 16 m/z, (c) **CIM2**: acetone peaks MS1 = 43 m/z, MS2 = 58 m/z, MS3 = 15 m/z, MS4 = 42 m/z, water peaks MS5 = 18 m/z.

Table 9.16 Mass loss data for TGA of **IM1** – **IM7**, **CIM1** and **CIM2**.

IM	Step 1: solvent		Step 2: *N*-phenylurea		Step 3: 5-nitroisophthalic acid	
	Expected loss (%)	Observed loss (%)	Expected loss (%)	Observed loss (%)	Expected loss (%)	Observed loss (%)
IM1	3.4	3.4	45.3	47.6	51.1	46.2
IM2	7.2	5.2	45.6	46.2	47.1	43.2
IM3	4.7	3.2	46.9	46.0	48.4	48.0
IM4	8.4	1.7, 2.0	45.0	51.7	46.6	39.2
IM5	9.8	8.1	44.4	46.5	45.9	40.9
IM6	9.6	7.9	44.4	50.4	45.9	40.1
IM7	13.0	10.9	34.0	39.6	52.8	45.2
CIM1	4.9	4.2	37.3	22.8	57.8	68.9
CIM2	14.3	10.7	33.6	43.7	52.0	43.0

DSC

DSC analysis was carried out on the IMs, **NS1** and **NS2**, according to the procedure detailed in §4.4.2. The DSC traces for each IM and the non-solvated materials, **NS1** and **NS2**, are shown in Figure 9.15 and the thermal data is tabulated in Table 9.17. The broad endotherms, below 130 °C, in the DSC trace for each IM correspond to the loss of the solvent guest from the host; these occur within the temperature range of the first mass loss step in the TGA curves of each IM. Two endotherms are present in the case of **IM2**, **IM4** and **IM5**, where two types of guests occupy the host structure. The desolvation endotherm in the DSC trace of **IM7** is less broad and occurs at a higher temperature than in the other IMs. The differing onset temperatures of the desolvation endotherms indicate that there is a significant difference in energy required to remove each guest molecule from the host structure across the different IMs (Table 9.18).

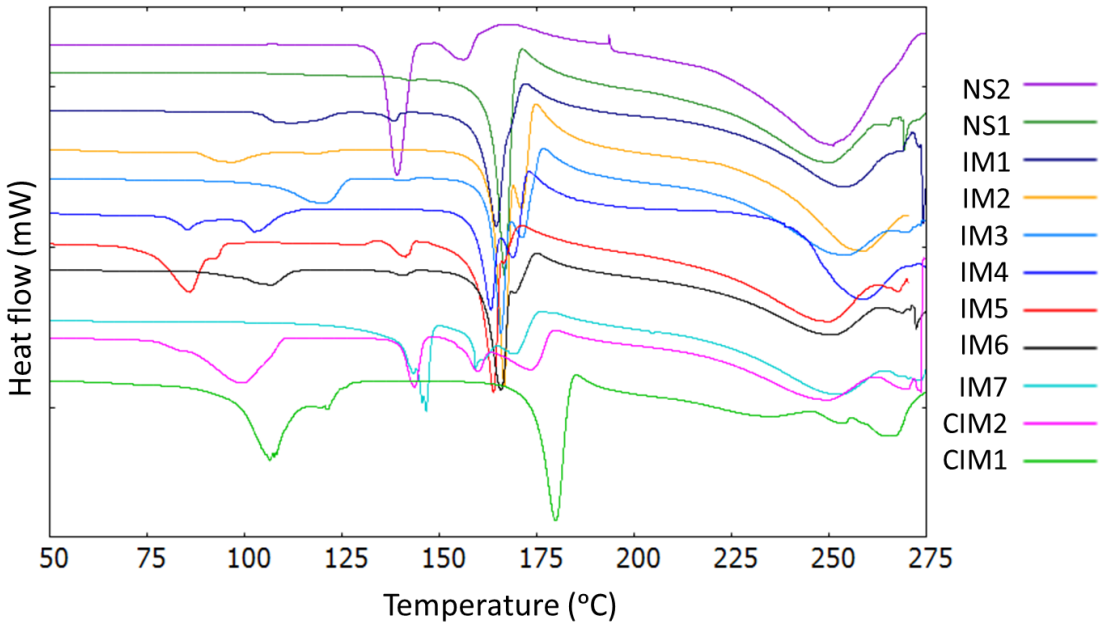

Figure 9.15 DSC traces of **IM1** – **IM7**, **CIM1**, **CIM2**, **NS1** and **NS2**, recorded at a 5 °C min^{-1} heating rate.

Table 9.17 Thermal data (T_{onset}) of **IM1** – **IM7**, **CIM1**, **CIM2**, **NS1** and **NS2** from the DSC analysis.

	T_{onset}					
IM	Endotherm 1 (°C)	Endotherm 2 (°C)	Melt 1 (°C)	Melt 2 (°C)	Melt 3 (°C)	Recrystallisation 1 (°C)
IM1	103.3	-	138.6	159.7	-	169.2
IM2	86.9	112.8	-	163.4	169.0	172.2
IM3	106.6	-	138.1	162.7	168.8	174.1
IM4	80.8	99.8	-	159.1	166.1	170.7
IM5	76.0	89.5	136.1	159.8	165.7	167.8
IM6	95.8	-	136.6	161.2	168.2	170.1
IM7	143.4	-	-	158.6	167.0	172.3
CIM1	96.6	-	-	-	174.2	185.7
CIM2	83.2	-	140.1	155.5	164.9	177.8
NS1	-	-	-	163.0	-	169.4
NS2	-	-	134.8	149.6	-	157.1

Table 9.18 The corresponding energies of the desolvation endotherm for **IM1** – **IM7**, **CIM1** and **CIM2**.

IM	T_{onset} (°C)	Energy (J g^{-1})	Solvent boiling point (°C)
IM1	103.3	33.8	64.5 (methanol) [93]
IM2	86.9, 112.8	26.0, 1.7	78 (ethanol), 100 (water) [93]
IM3	106.6	79.4	81 (acetonitrile) [93]
IM4	80.8, 99.8	17.3, 21.8	56 (acetone), 100 (water) [93]
IM5	76.0, 89.5	68.7	66 (THF) [93]
IM6	95.8	38.8	77 (ethyl acetate) [93]
IM7	143.4	81.8	66 (THF), 64.5 (methanol) [93]
CIM1	96.6	0.2	100 (water) [93]
CIM2	83.2	104.5	56 (acetone) [93]

A melt present in the DSC traces of **IM1** – **IM7** and **CIM2**, post desolvation at T_{onset} ca. 150 °C, matches the main melt of **NS1**, suggesting the identity of the desolvation product as **NS1**. The short melt in the DSC trace of **NS2**, at T_{onset} 149.6 °C, also matches the main melt of **NS1**, suggesting conversion to **NS1** at this temperature. A second smaller melt peak in the DSC traces for **IM1**, **IM3**, **IM5**, **IM6** and **CIM2** at T_{onset} 136 °C, matches the main melt peak of **NS2**. This may indicate some conversion to this non-solvated form, post desolvation, before conversion to **NS1** at the higher temperature. The recrystallisation peak in the DSC traces of **IM1** – **IM7**, **CIM2**, **NS1** and **NS2** at *ca.* T_{onset} 170 °C suggest conversion to the same unidentified product (**UN1**) at this temperature. Different thermal behaviour, post desolvation, is observed for **CIM1**. The main melt in the DSC trace occurs at a higher temperature of T_{onset} 174.2 °C followed by a recrystallisation at T_{onset} 185.7 °C; **CIM1** is not suggested to convert to **NS1** on desolvation but to a different unidentified product (**UN2**) which then converts to a further different unidentified product (**UN3**) post recrystallisation.

HSM

HSM was carried out on single crystals of **IM1** – **IM7**, **CIM1** and **CIM2**, according to the procedure detailed in §4.4.1. Single crystals were heated by ramping from room temperature to past the desolvation temperature as indicated in the DSC traces and the TGA curves for IM. A single crystal to powder phase transition was indicated through the desolvation temperature for each of the IMs; a powder product was formed in each case. HSM on single crystals of **NS1** and **NS2** was also carried out. Single crystals of **NS1** were heated from room temperature to up to 290 °C, beyond the decomposition temperature. On heating **NS1**, a melt in line with that in the DSC trace of **NS1** occurred at *ca.* T_{onset} 160 °C. This was followed by a recrystallisation to a powder product between 172 and 180 °C, in line with that in the DSC trace of **NS1**. Single crystals of **NS2**

were heated from room temperature to 290 °C, beyond the decomposition temperature. At ca. T_{onset} 134 °C, in line with that in the DSC trace of **NS2**, a melt occurred with a retention of single crystallinity. A small melt in line with that in the DSC trace of **NS2** occurred at *ca.* T_{onset} 150 °C. This was followed by a recrystallisation to powder product at T_{onset} 157 °C in line with that in the DSC trace of **NS2.**

Powder X-ray diffraction (PXRD) analysis

The thermal transitions indicated in the DSC traces for each material were investigated by PXRD according to the procedure detailed in §4.3. PXRD analysis on **IM1** – **IM7** and **CIM2** on samples at 25 °C and after preheating to 145 °C or 150 °C, past the desolvation point and just below the melt temperature, confirmed a structural change (Figure 9.16 to Figure 9.18) and indicated conversion to **NS1** post-desolvation (Figure 9.20). PXRD analysis on **NS2** at 25 °C and after preheating to 150 °C, past the main melt and just below the second smaller melt peak, also confirmed a structural change (Figure 9.18) and indicated conversion to **NS1** (Figure 9.20). PXRD analysis of **IM1** – **IM7**, **CIM2**, **NS1** and **NS2**, preheated to 184 °C beyond the recrystallisation point, confirmed conversion to the same unidentified (**UN1**) product (Figure 9.21). PXRD analysis of **CIM1** at 25 °C and on samples preheated to 145 °C, past the desolvation point just below the melt temperature, confirmed a structural change (Figure 9.19) and indicated that desolvation did not lead to **NS1** (Figure 9.20) but to an unidentified product (**UN2**). PXRD analysis of **UN2**, preheated further to 189 °C, confirmed a further structural change and indicated the formation of a different unidentified recrystallisation product **(UN3)** to that of **UN1** (Figure 9.21).

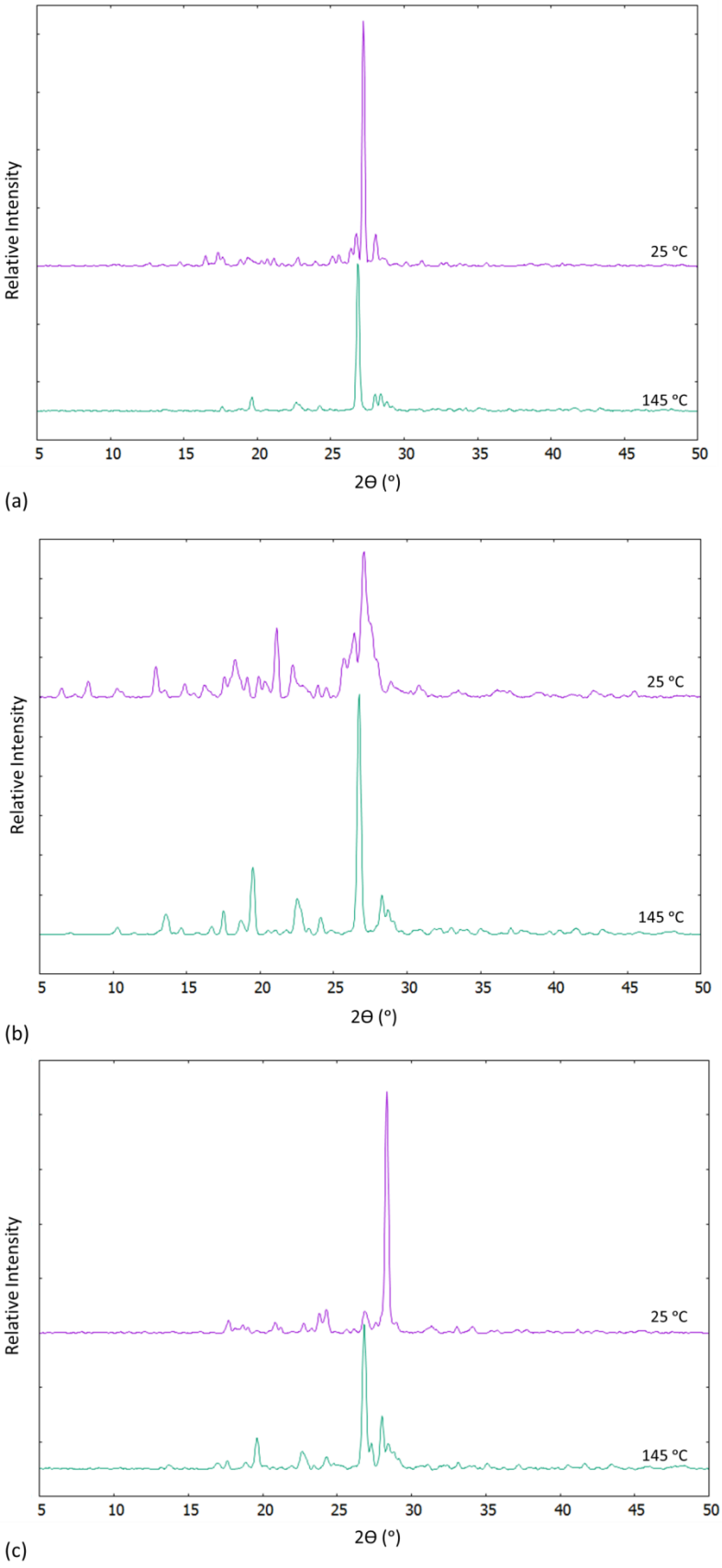

Figure 9.16 PXRD patterns for (a) **IM1**, (b) **IM2** and (c) **IM3** on samples at 25 °C and after preheating to 145 °C.

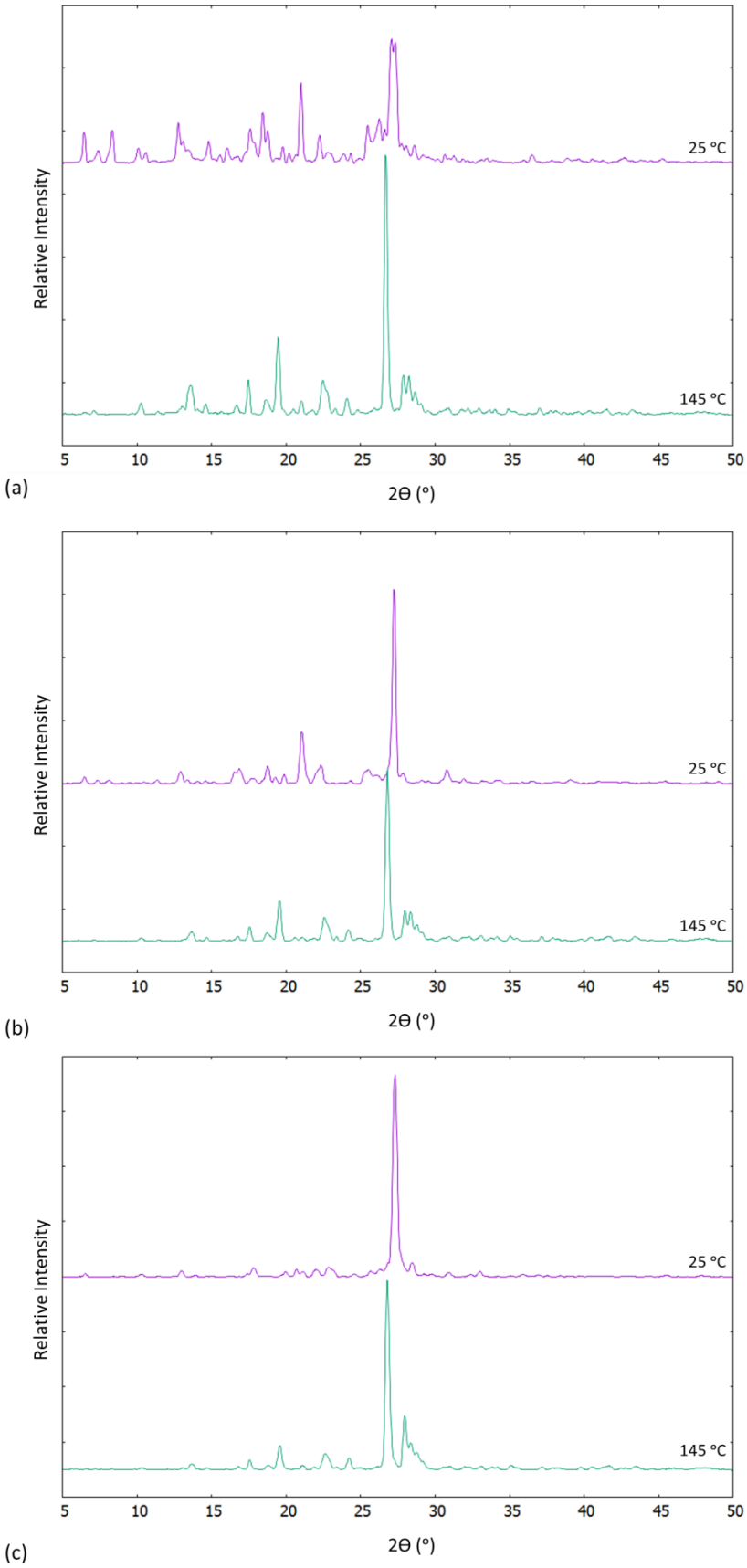

Figure 9.17 PXRD patterns for (a) **IM4**, (b) **IM5** and (c) **IM6** on samples at 25 °C and after preheating to 145 °C.

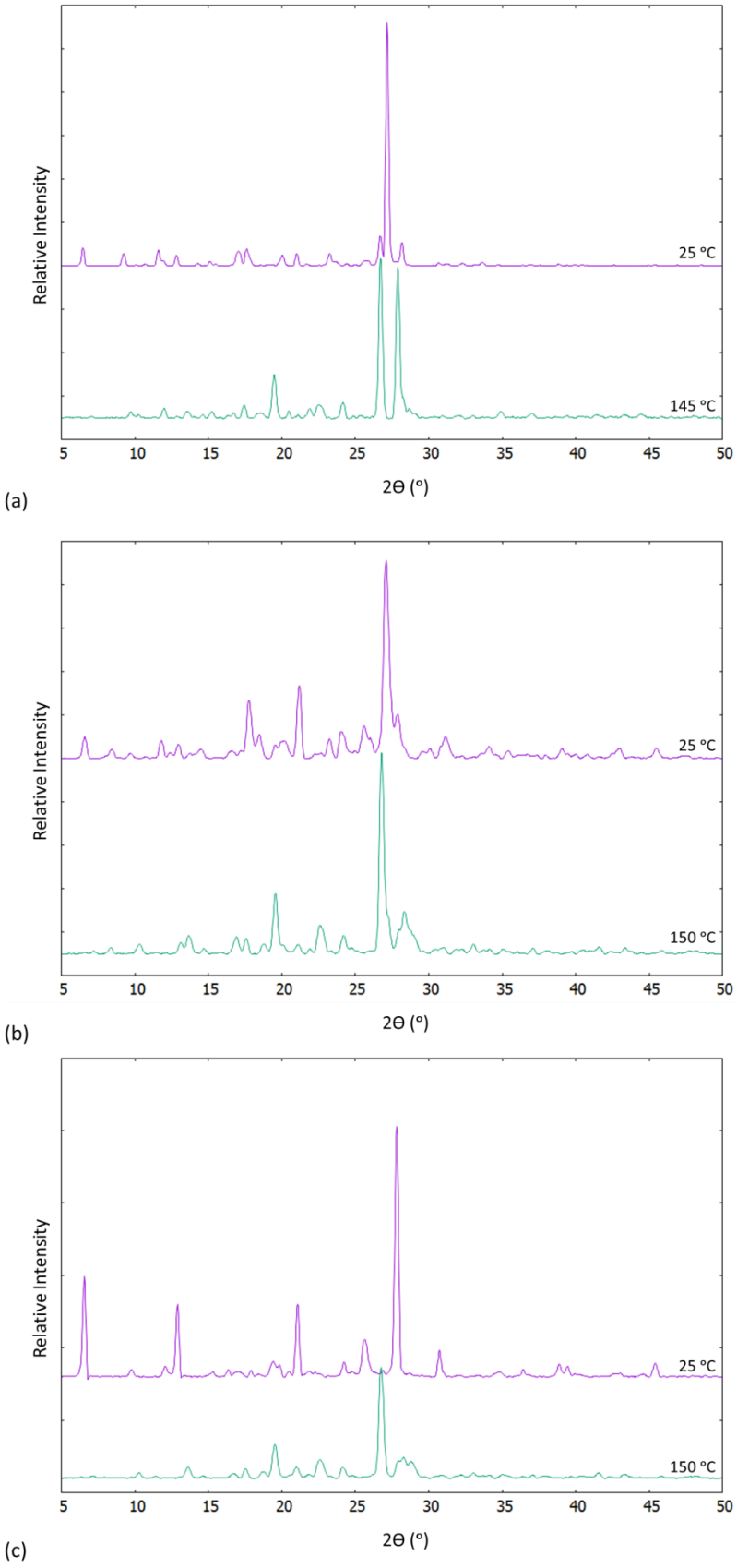

Figure 9.18 PXRD patterns for (a) **IM7**, (b) **CIM2** and (c) **NS2** on samples at 25 °C and after preheating to 145 or 150 °C.

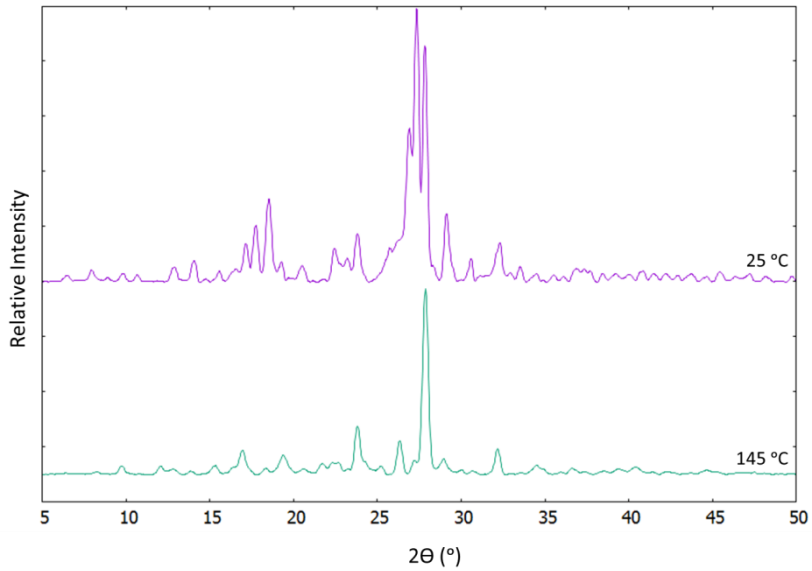

Figure 9.19 PXRD patterns for **CIM1** on samples at 25 °C and after preheating to 145 °C.

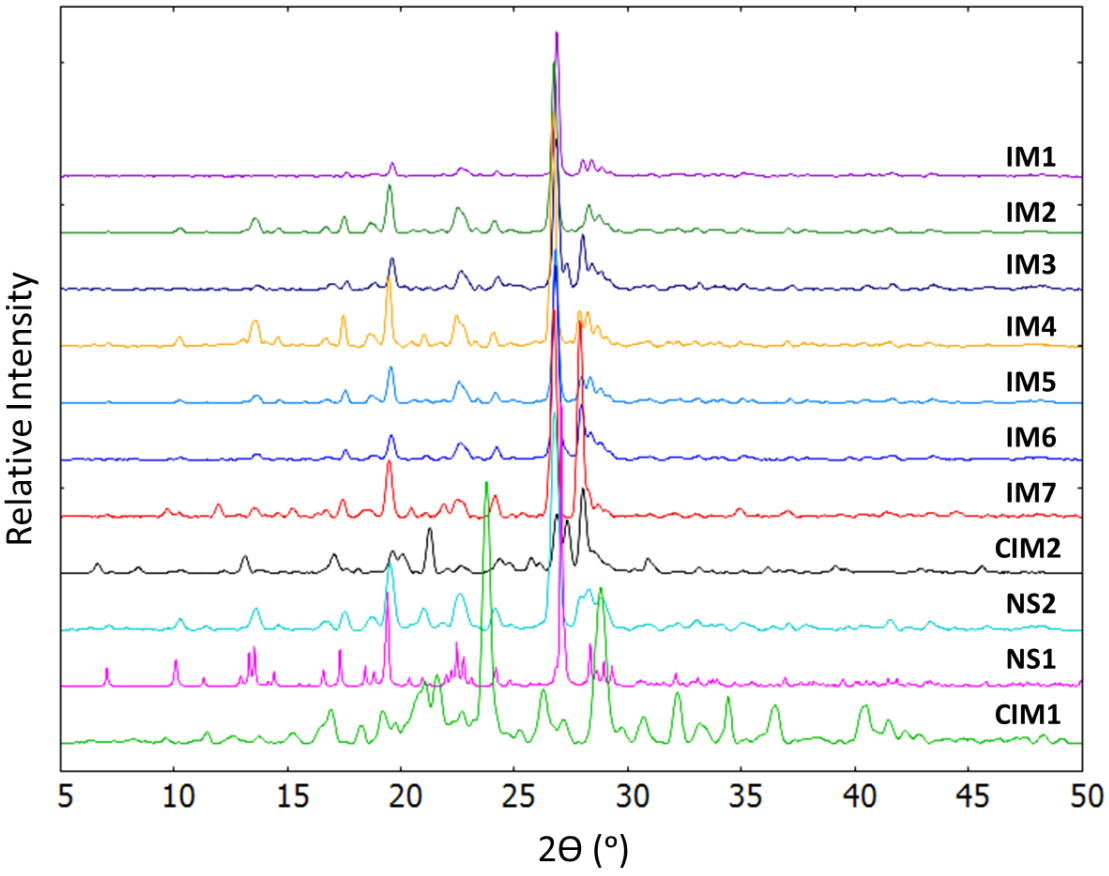

Figure 9.20 PXRD patterns of **IM1** – **IM7**, **CIM1**, **CIM2** and **NS2** preheated to 145 or 150 °C compared to the simulated powder pattern of **NS1** (150 K structure).

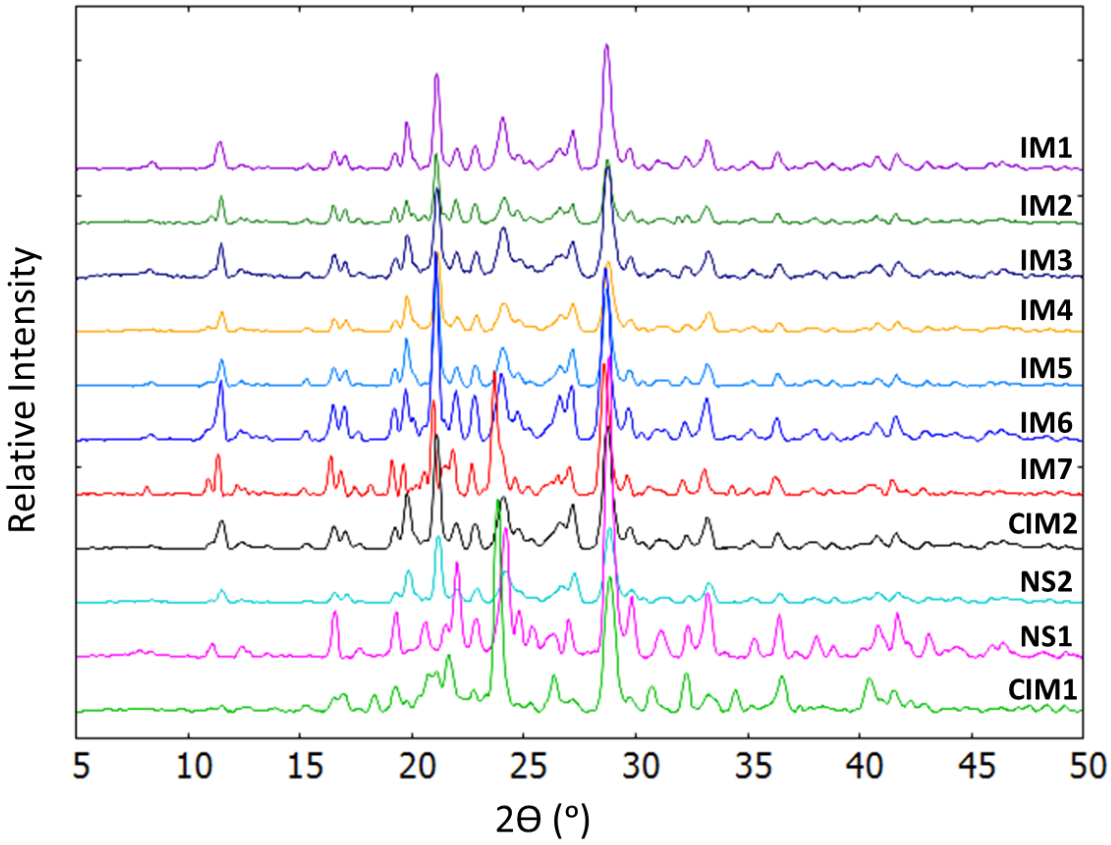

Figure 9.21 PXRD patterns of the resulting products after preheating **IM1** – **IM7**, **CIM1**, **CIM2**, **NS1** and **NS2** past the recrystallisation point, to 184 °C (189 °C for **CIM1**).

The conversion of **IM1** – **IM7**, **NS1** and **NS2** to the recrystallisation product **UN1**, on heating to 184 °C, was accompanied by a colour change from yellow to cream in the powdered sample. This is most striking in **NS2** (Figure 9.22).

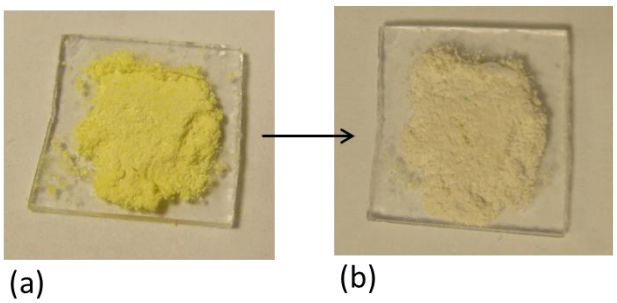

Figure 9.22 Powder samples of **NS2** (a) at 25 °C and (b) after preheating to 184 °C.

The presence of a more stable higher temperature form of **NS1** (**UN1**) is suggested by both DSC and PXRD analysis however the identity of this product is unknown. Unlike **IM1** – **IM7** and

CIM2, **CIM1** does not convert to **NS1**; instead different unidentified desolvation (**UN2**) and recrystallisation (**UN3**) products are formed. Preliminary indexing and Pawley fits were carried out on the powder patterns of **UN1**, **UN2** and **UN3** in Topas-Academic V5.0 [168] to obtain unit cell parameters for these materials. The indexing was inconclusive and further investigation is required to confirm their identity; synchrotron powder X-ray diffraction data collections would be beneficial to allow accurate indexing of diffraction peaks.

In the DSC trace of **IM1**, **IM3**, **IM4**, and **IM5**, an additional small endotherm is present at T_{onset} 136 – 138 °C matching that of the melt for **NS2** (Figure 9.15), at T_{onset} 134.8 °C. This may indicate that in these IMs, post-desolvation, an initial conversion to **NS2** occurs at a lower temperature before converting to **NS1** at 145 °C. PXRD analysis was carried out on **IM1**, **IM3**, **IM4**, and **IM5** after preheating to 126 – 127 °C, post desolvation and below the melt of **NS2** (Figure 9.23). The powder patterns are most similar to that of **NS1** at this temperature however an additional peak is present at *2Θ* ca. 28 °, which does not occur in the patterns for the IMs at room temperature but matches the strongest peak in the simulated powder pattern of **NS2**. It may be that there is some conversion of **IM1**, **IM3**, **IM4**, and **IM5** to **NS2** upon desolvation, alongside **NS1**. Although not conclusive, this is not an unreasonable suggestion as organic inclusion compounds have been reported to undergo multiple phase transitions upon thermal desolvation. [322, 324]

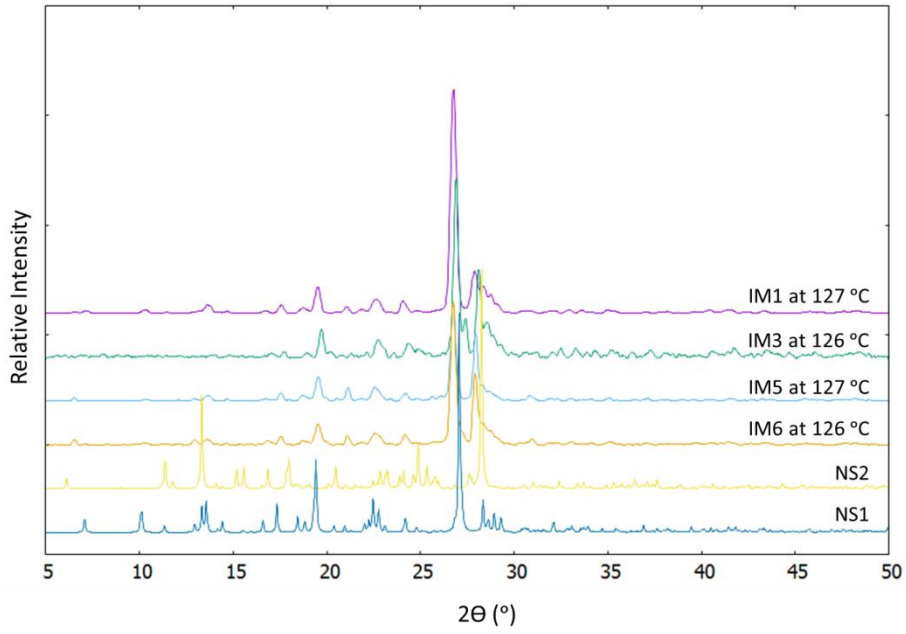

Figure 9.23 The PXRD patterns of **IM1**, **IM3**, **IM5** and **IM6** preheated to 126 or 127 °C and the simulated powder patterns for crystal structures of **NS1** (150 K) and **NS2** (150 K).

9.4.3 Ambient temperature desolvation

The IMs may be desolvated using heat; this method leads to desolvation *via* a single crystal to powder phase transition. By using more gentle methods, it was thought that desolvation may be possible *via* a single crystal to single crystal phase transition. Desolvation under vacuum was trialled for the IMs where the solvent occupied channels in the host structure, in **IM2**, **IM6** and **IM7**, and therefore more accessible.

IM6 and **IM7** were selected for vacuum studies, being the better quality crystals for diffraction studies. Single crystals of **IM6** and **IM7** were put under vacuum at 0.1 mbar pressure for 24 to 48 hours. Batches of crystals were screened before and after being under vacuum. After being under vacuum, the crystal sample quality had deteriorated significantly for both samples. It was only possible to collect a single crystal data set on **IM7** to determine whether the solvent had been removed from the channels. The disorder THF/methanol solvent remained within the channels and there was no change in the output electron count per unit cell from Squeeze. [319]

Powdered samples of **IM2** and **IM6** were also put into a desiccator to determine whether dessication would lead to **NS1**. PXRD patterns of the sample pre and post dessication, after a two week dessication period, did not indicate a structural change or desolvation.

9.4.4 Resolvation studies

Vapour diffusion studies were carried out on powdered samples of **NS1** and **NS2** to attempt their resolvation. Powder samples of **NS1** and **NS2** were placed in a small vial in a sealed bottle in the presence of solvent forming a vapour diffusion chamber (Figure 4.3). Solvents methanol, ethanol, acetonitrile, acetone, THF and ethyl acetate were used in this setup.

Vapour diffusion was trialled initially at a range of temperatures (–18, 25, 30, 40 and 50 °C) and it was found that the lowest temperature of –18 °C was the best condition for vapour diffusion of all the solvents; higher temperatures resulted in rapid sample wetting by the solvent vapour. A vapour diffusion time period of 24 hours was chosen; beyond this, samples were wet by the solvent vapour. In the case of THF solvent, vapour diffusion was stopped after three hours when signs of sample wetting were observed.

Powder diffraction data were collected on **NS1** and **NS2**, before and after vapour diffusion with each solvent (Figure 9.24). Changes in the powder patterns of **NS1** were only indicated after 24 hours of vapour diffusion in acetone solvent (at –18 °C) however it was not possible to confirm the nature of the structural change. Changes in the powder patterns of **NS2** were indicated after 24

hours of vapour diffusion in methanol, acetone, THF and ethyl acetate solvent (at –18 °C) however it was again not possible to confirm the nature of the structural change. Vapour diffusion of a powdered sample of **NS2** with acetone resulted in a colour change from yellow, pre-vapour diffusion, to white post vapour diffusion and inside the vapour diffusion chamber (Figure 9.25). Since **CIM2** is an acetone IM and forms colourless crystals, this may indicate the formation of this CIM by resolvation. On removing the powder from the chamber into ambient conditions, the colour of the powder returned to yellow. **CIM2** shows similar colour change behaviour, forming colourless blocks on crystallisation but turning to a yellow powder once exposed to air.

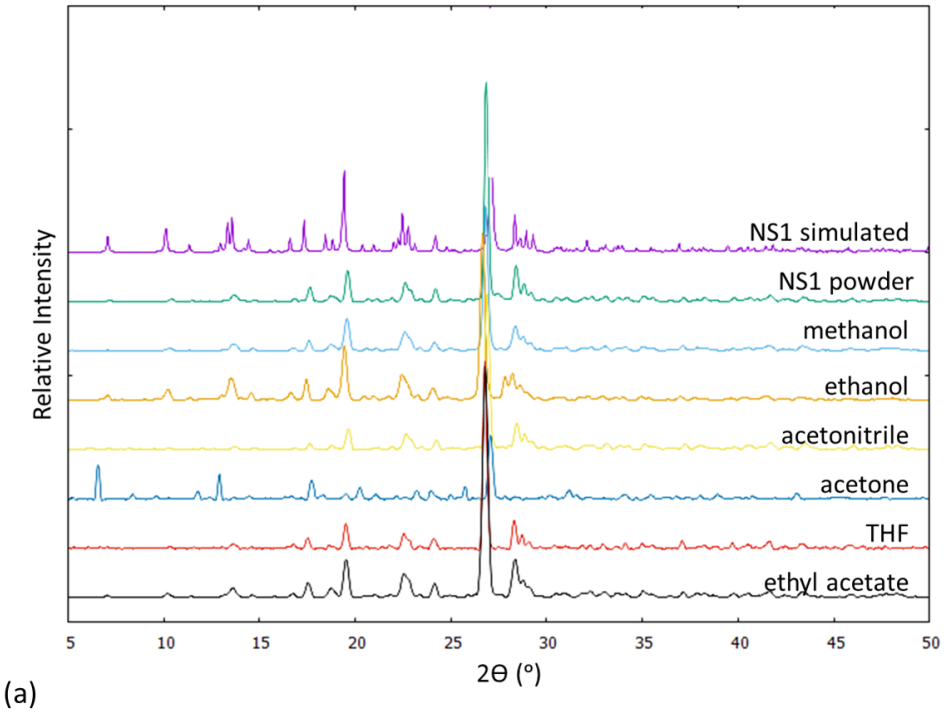

(a)

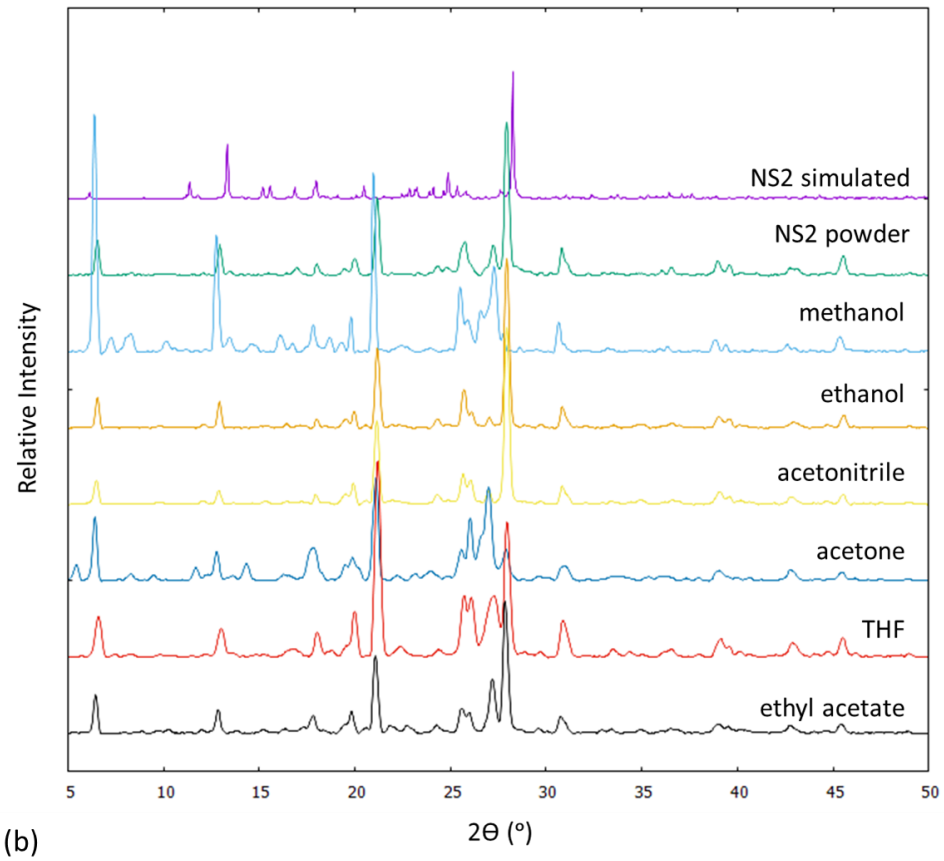

(b)

Figure 9.24 PXRD patterns of the simulated structure and pre vapour diffusion powders of (a) **NS1** and (b) **NS2** and post vapour diffusion with solvents methanol, ethanol, acetonitrile, acetone, THF and ethylacetate at -18 °C.

Figure 9.25 The colour change between (a) **NS2** pre vapour diffusion, (b) in sealed environment post vapour diffusion with acetone (potentially resolvated to **CIM2**) and (c) after exposure to air.

9.4.5 Competition experiments

Host frameworks may selectively include some guests over others. The selectivity of the hydrogen bonded ring network formed by *N*-phenylurea and 5-nitroisophthalic acid towards particular solvent guest inclusion was investigated for 1:1 solvent mixtures and the same 2:1 stoichiometric ratio of the *N*-phenylurea and 5-nitroisophthalic acid molecular components.

The competition experiment outcomes are shown in Table 9.19; the evidence for each outcome is included in §A9.1. The non-solvated **NS1** is the most formed material in the solvent competition studies, forming in six out of seven instances when water comprised part of the solvent mix and three instances for the combination of non-water solvents. In no instances is **NS2** formed. This suggests a preference for the host to be non-solvated, and in the **NS1** form, where possible. The host framework had the greatest preference for ethanol and acetonitrile; these solvents are selectively included over the competing solvent in the solvent mix in the most instances (four out of seven). Medium preference by the host is shown for methanol and ethyl acetate; each is included in three out of seven instances. The methanol acetonitrile 1:1 solvent mix resulted in both **IM1** and **IM3** forming indicating these solvents to be equally favourable for inclusion by the host. The host framework appeared to have the lowest preference for acetone or THF; these solvents are selectively included over the competing solvent in the solvent mix in the fewest (two out of seven) instances. The 1:1 methanol and THF solvent mixture led to a design route for a new inclusion material, involving the inclusion of both solvents, resulting in **IM7**; indicating these solvents to be equally favourable for inclusion by the host.

For the combination of acetonitrile and THF, acetone and water or acetone and diethyl ether, the powder pattern of the crystallisation product is most similar to the simulated powder pattern of **IM2**. It is unknown which solvent or whether one or both are included from these mixtures but this result indicates that the structure in **IM2**, where solvent guests occupy channels in the structure, may be favourable for mixed solvent systems; this is indeed the case for **IM7**.

Table 9.19 The solvent included on crystallisation of a 2:1 stoichiometric ratio of the *N*-phenylurea and 5-nitroisophthalic acid molecular components in a 1:1 solvent mixture. Evidence for each outcome is given in §A9.1.

Solvent	Methanol	Ethanol	Acetonitrile	Acetone	THF	Ethyl acetate	Water	DEE
Methanol		**NS1**			**IM7**		**NS1**	
Ethanol				**NS1**			**NS1**	
Acetonitrile						**IM2** structure	**NS1**	
Acetone							**IM2** structure	**IM2** structure
THF						**NS1**	**NS1**	
Ethyl acetate							**NS1**	
Water								**NS1**
DEE								

9.4.6 Variation of stoichiometry

The host components were set up in three different ratios of 1:1, 2:1 and 1:2 with the different solvents; it was thought that on changing the stoichiometry, different hydrogen bonding networks might result as the number of different groups available for each type of synthon formation is changed. In particular, the formation of the carboxylic acid:amide $\boldsymbol{R_2^2(8)}$ hydrogen bond synthon (U:Ac) is likely to be affected by the set up ratio of the *N*-phenylurea (U) and 5-nitroisophthalic acid (Ac) components; a 1:1 set up ratio would favour the formation of this synthon involving one 5-nitroisophthalic acid carboxylic acid group (in a U:Ac motif) whilst a 2:1 ratio would favour its formation involving both carboxylic acid groups (in a U:Ac:U motif). [44] In fact, changing the stoichiometry of components does not appear to change the host network; the same network is favoured for each solvent regardless of stoichiometry of components. Changes in the host network are instead achieved on changes to the guest (§9.6).

9.5 IM desolvation to NS1

The desolvation of **IM1** – **IM7** and **CIM2** does not lead to a porous structure with accessible void space, instead there is conversion to **NS1**, meaning the IMs have virtual porosity only (Figure 9.26). The loss of cavity structure on guest removal is typical for organic inclusion compounds [317] and there are only a few examples in the literature where an empty framework is stable on guest removal. [74, 325] This lack of stability of an empty host framework is unsurprising in the IMs studied here as guest removal leads to an unsatisfied hydrogen bonding group (5-nitroisophthalic acid hydroxyl group) which should be fulfilled according to Etter's rules. [36] The conversion to **NS1** results in the fulfilment of the hydrogen bonding capabilities of this group, accompanied by the replacement of the solvent in the hydrogen bonded ring host network with an *N*-phenylurea molecular building block. In the case of **IM7**, the fact an empty host network is not formed is more surprising; guest removal can occur from the channels without disrupting the hydrogen bonded ring. This suggests that the formation of **NS1** is highly favourable.

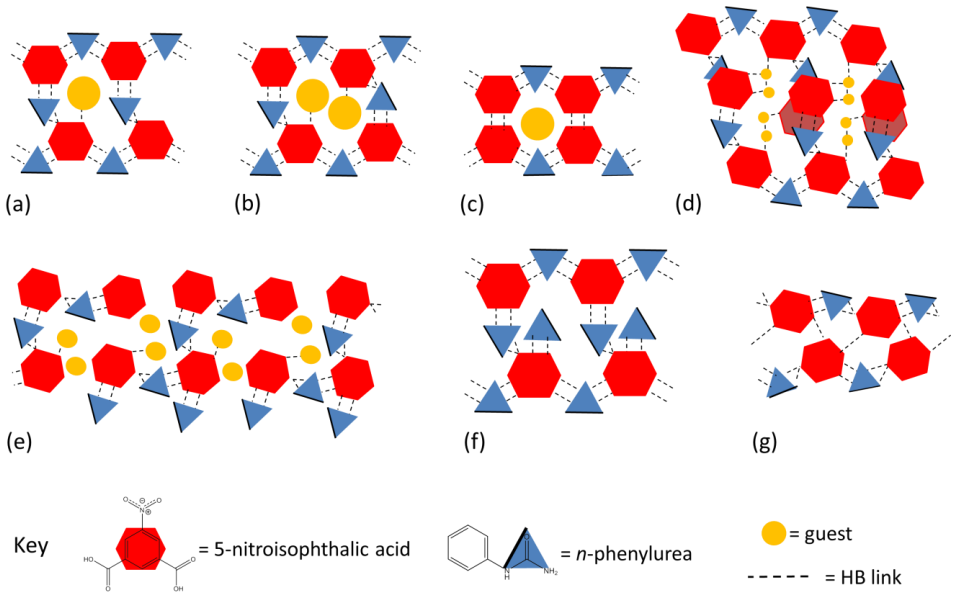

Figure 9.26 A comparison of the arrangement of molecular building blocks in (a) **IM1** – **IM5**, (b) **IM6**, (c) **IM7**, (d) **CIM1**, (e) **CIM2**, (f) **NS1**, (g) **NS2**.

9.5.1 Structural changes on desolvation

On desolvation of **IM1** – **IM7**, and **CIM2**, to **NS1** a layered structure is retained which, in the case of **IM2**, becomes increasingly flat. *N*-phenylurea remains the major component where the ratio of molecular building blocks changes from 3:2 in the IMs (7:4 in the case of **IM1**) to 2:1 in **NS1**, for the *N*-phenylurea and 5-nitroisophthalic acid molecular building blocks, respectively. In contrast, upon desolvation of **CIM2** to **NS1**, the ratio of molecular building blocks changes from 1:1, where the host components are present in equal amounts, to 2:1, where *N*-phenylurea is the major component. The structural changes on desolvation are most significant for **IM6**, where the expanded hydrogen bond network condenses, for **IM7**, which switches a carboxylic acid dimer $R_2^2(8)$ hydrogen bond synthon for a carboxylic acid:amide $R_2^2(8)$ hydrogen bond synthon, and for **CIM2**, which adopts a more planar structure and a significant molecular rearrangement occurs. The desolvation to **NS1** leads to a reduction in cell volume and retention of triclinic symmetry in the majority of cases; exceptions to this are **IM7**, where desolvation instead leads to a marginal increase in cell volume, and **CIM2**, where desolvation occurs alongside a change in symmetry from monoclinic to triclinic. The desolvation of **IM1** – **IM6**, and **CIM2**, to **NS1** also leads to an increase in crystal density (Table 9.20) and a change in the interlayer spacing (Table 9.21); the largest change is observed in **IM4** and **IM5**. This is not case for **IM7**, crystal density is instead reduced on converting to **NS1**.

Table 9.20 Crystal density for **IM1** – **IM7**, **CIM1** and **CIM2** and **NS1** and **NS2**.

Complex	Density (M gm^{-3})
IM1	1.462
IM2	1.403
IM3	1.428
IM4	1.424
IM5	1.44
IM6	1.431
IM7	1.517
CIM1	1.505
CIM2	1.407
NS1	1.496
NS2	1.538

Table 9.21 Interlayer spacing for **IM1** – **IM7**, **CIM1** and **CIM2** and **NS1** and **NS2**.

Complex	Interlayer spacing (Å)
IM1	3.137(3) – 3.405(3)
IM2	3.008 (9) – 3.389(9)
IM3	2.916(2) – 3.386(2)
IM4	3.187(8) – 3.680(1)
IM5	3.027(2) –3.697(2)
IM6	3.046(3) – 3.359(3)
IM7	3.182(3) – 3.397(4)
CIM1	3.093(5) – 3.332(5)
CIM2	2.987(1) – 3.318(1)
NS1	3.190(3) – 3.367(3)
NS2	2.9974(4) – 3.330(4)

9.5.2 Selective conversion to NS1

The selective conversion of **IM1** – **IM7** and **CIM2**, to **NS1**, on desolvation, rather than to **NS2** (which is only produced here by crystallisation from diethyl ether) may be related to several factors including thermal stability, stoichiometries and the nature of the hydrogen bond network.

NS1 has a greater thermal stability than **NS2**, shown by conversion of **NS2** on heating to **NS1**, and is therefore likely to be the thermodynamically more favourable desolvation product; the main melt for **NS2** occurs at T_{onset} 134.7 °C compared with 163.0 °C for **NS1**. The ratio of host molecular building blocks, where *N*-phenylurea is in the majority, is also retained in **NS1** whereas

in **NS2**, *N*-phenylurea and 5-nitroisophthalic acid components crystallise in an equivalent 1:1 ratio; it may be that the stoichiometries with excess *N*-phenylurea are more favourable. In **CIM2**, the ratio of host molecular building blocks is actually most similar to **NS2** where the *N*-phenylurea and 5-nitroisophthalic acid components are present in equivalent proportions. The selective conversion of **CIM2** to **NS1** may further suggest the favourability of stoichiometries with excess *N*-phenylurea. The hydrogen bonded ring host network is the most similar between **NS1** and **IM1** – **IM7**, and **CIM2**, where molecular building blocks assemble *via* more similar hydrogen bonded synthons in contrast to the situation in **NS2**, where only one of the hydrogen bond synthons present in the IMs leads to molecular building block assembly in this structure. **CIM1** does not convert to **NS1** on desolvation, forming **UN2**, and also forms a different recrystallisation product of **UN3**. The fact that **CIM1** does not convert to **NS1** may be related to **CIM1** and **NS1** having similar crystal densities (1.505 M gm^{-3} and 1.496 M gm^{-3}, respectively) such that conversion would not lead to any favourable gain in crystal density. It could also be that, due to the small size of the guests, the space created on desolvation is too small to allow molecular rearrangement to **NS1**; in the other IMs, where larger solvent molecules are present, rearrangement to **NS1** occurs.

The relative stability of **NS1** compared to the IMs and **NS2** was also indicated in the resolvation studies; only vapour diffusion with acetone resulted in a shift in the peak position of the powder pattern of **NS1**, pre and post vapour diffusion. In contrast, **NS2** appeared more susceptible to solvent vapours indicated by a shift in peak positions of the powder pattern of **NS2**, pre and post vapour diffusion with methanol, acetone, THF and ethyl acetate. The competition studies also indicated the relative stability of **NS1** compared to the IMs and **NS2**. **NS1** was formed preferentially in a number of instances over inclusion of a solvent whilst **NS2** was not preferentially formed in a single instance from solvent mixtures containing diethyl ether; the form of the second solvent resulted each time.

9.5.3 Thermal behaviour

A relationship between fine structure and thermal transformations of a compound is possible. [326] Guest removal energy may be related to crystal density, where a more dense inclusion material is more stable and more energy will be required to disrupt the system, [80] or to host-guest interaction strength. [327] This is not the case in the materials discussed in this chapter and the energy required to remove each guest correlates more strongly with guest boiling point (Table 9.18 and §A9.2).

9.6 Guest templation of host network formation

Guest molecules appear to exert control on the host structure formed in the IMs. Changes to the combination of guest species led to alterations in the hydrogen bonded host network formed. For example, in **IM4**, a hydrogen bonded ring network forms in the presence of acetone and water whilst in **CIM1** and **CIM2**, condensed networks form where water or acetone are present singly. In **IM5**, one hydrogen bonded ring network forms in the presence of THF alongside water whilst in **IM7**, the hydrogen bonded ring network is altered in the presence of THF alongside methanol.

Changes in the hydrogen bonded host network were also observed on changing the molecular size of the solvent. For example, an expanded hydrogen bonded ring network occurs for the long chain ethyl acetate solvent (in **IM6**) whereas a smaller hydrogen bonded ring network occurs in **IM1** and **IM3** where the solvent molecules are smaller (methanol and acetonitrile, respectively). The second non-solvated form **NS2** is only produced by crystallisation from diethyl ether and it can be proposed that the large volume of the solvent molecules in this case precludes the initial formation of a solvated IM and instead favours **NS2** formation. The location of the included solvent changed in the isostructural IMs, **IM1** to **IM5**, related to solvent size. In **IM1** to **IM3**, the solvent molecules (methanol, ethanol and acetonitrile) are included in the plane of the hydrogen bonded ring whilst in **IM4** and **IM5**, the larger solvent molecules of acetone and THF occupy the space between the layers.

The guest may also be exerting control over the host networks related to its polarity and hydrogen bonding ability; inclusion in the majority of cases (except **IM7**) was *via* a hydrogen bonding interaction to the host. Only IMs with polar guests included were prepared; although a number of polar and non-polar solvent guests were trialled. **NS2** was formed direct by crystallisation from diethyl ether and the fact that no ring network was formed around a diethyl ether guest may be related to it being non-polar with a hydrogen bond acceptor oxygen atom which is sterically hindered by the diethyl groups. The multiple hydrogen bond donor and acceptor groups of the water guest may prevent a ring type network forming in **CIM1**. Water was also only included as a guest when crystallised from ethyl acetate from a 1:1 stoichiometric ratio of the *N*-phenylurea and 5-nitroisophthalic acid host components; crystallisation from water from a 2:1 stoichiometric ratio of components presented a direct route to **NS1**. Attempts were made to alter the hydrogen bonding network by changing the set up ratio of components, however in all cases (except in the formation of **CIM1** occurring from a different solvent to that which was included) this had no effect on the network formed. This further suggests the greater templating role of guest molecules in these materials.

9.6.1 Host preference for guests

The preliminary competition experiments carried out in §9.4.5 indicated that guest uptake by the *N*-phenylurea 5-nitroisophthalic acid host network may occur preferentially although it is difficult to form any particular trends. There was a general preference for the guest that could be included in the layer of the hydrogen bonded ring network rather than occupying the space between layers; methanol, ethanol, acetonitrile or ethyl acetate were included preferentially over acetone or THF. This may suggest that a more efficient packing may be achieved in this arrangement. [307] In some cases, the guest giving the most dense packing was included preferentially such as for the 1:1 ethanol acetonitrile solvent mix (**IM2** 1.435 $gmol^{-1}Å^{-3}$ versus **IM3** 1.428 $gmol^{-1}Å^{-3}$) which gave **IM2**, and for the 1:1 acetone THF solvent mix (**IM4** 1.424 $gmol^{-1}Å^{-3}$ versus **IM5** 1.440 $gmol^{-1}Å^{-3}$) which gave **IM5**. However, this was not true of all combinations. No particular link was found between guest size or host-guest interaction strength and inclusion preference. In general, there was a significant preference for a structure that matched that of **IM2**, even from solvent mixtures that did not involve ethanol. In the **IM2** structure guests, occupy channels; this type of inclusion may be favourable for mixed solvent systems, as seen in **IM7**.

These studies are merely indicative at this stage and would benefit from further investigations including trialling further solvent mix ratios; this may allow a selectivity coefficient to be determined. [80] There are also some caveats in the analysis carried out. When a powder precipitate was formed on crystallisation from a solvent mixture, it was not possible to make a firm conclusion about the product identity due to the presence of multiple phases and when single crystals were obtained, not every single crystal in the vial was screened and so some products may have been missed and the bulk may be misrepresented.

9.7 Engineering hydrogen bond networks with inclusion properties

In the design of hydrogen bonded networks with inclusion behaviour, a number of substituted urea molecular building blocks alongside 5-nitroisophthalic acid were trialled.

The strategy of targeting the polycarboxylic acid 5-nitroisophthalic acid proved to be successful for forming extended hydrogen bonded networks with inclusion behaviour. The trigonal arrangement of the hydrogen bonding groups (carboxylic acid and nitro groups) allowed network extension in three directions and aided the generation of structural voids, filled by guest molecules, by hindering the close packing of molecules. The 5-nitroisophthalic acid carboxylic acid groups participated in a number of hydrogen bond synthons which led to network formation including carboxylic acid:amide $R_2^2(8)$ and $R_2^1(6)$ synthons to substituted urea amide groups. The

5-nitroisophthalic acid nitro group was also versatile in network formation participating in a number of hydrogen bond synthons including nitro:amide $R_2^2(8)$ and $R_2^1(6)$ synthons to substituted urea amide groups. The planarity of the 5-nitroisophthalic acid molecule was carried through to the hydrogen bonding synthons it formed; this may have encouraged the formation of the hydrogen bonded rings.

The variation of the substituted urea in combination with 5-nitroisophthalic acid appeared to affect the hydrogen bonded inclusion network formation. Hydrogen bonded networks with inclusion type behaviour were formed for U5-NIP, DMU5-NIP and for the *N*-phenylurea IMs. In these complexes, the hydrogen bonded networks had ring structures formed around 'guest' molecules; in U5-NIP and DMU5-NIP these guests were the substituted urea whilst in the *N*-phenylurea IMs, the guests were solvent molecules. No inclusion type behaviour occurs in the hydrogen bonded networks of MU5-NIP; hydrogen bonded chains of molecules formed instead.

Within the networks, differing effects related to the substituted nature of the urea were observed. Changes to the substitution of the urea led to changes in the extended nature of the hydrogen bonded ring networks formed between U5-NIP, DMU5-NIP and the IMs, affecting the number of hydrogen bond donor-acceptor groups available. In U5-NIP, where the urea was unsubstituted and had the maximum number of urea donor and acceptor groups available for hydrogen bonding, the hydrogen bonded ring networks extended in two dimensions, forming a hydrogen bonded planar sheet. In contrast, in DMU5-NIP and for the *N*-phenylurea IMs, one side of the urea molecule was blocked by substitution and the hydrogen bonded ring networks extending in a one-dimensional chain only.

The substituent size also appeared to have an effect on the type of hydrogen bonding network formed. In MU5-NIP, despite having the same number of hydrogen bonding sites available as *N*-phenylurea, the same ring network does not form. The single methyl substituent is significantly smaller than the phenyl ring (Figure 9.27). It may be that larger urea substituents are required to stabilise the type of ring network formed in the *N*-phenylurea IMs. This is supported by almost isostructural hydrogen bonding ring networks forming for DMU5-NIP; the dimethyl substituents are also bulky on one side of the urea. The bulky substituents may have an effect of protecting the ring unit from disruption at the extremities giving it a closed favourable structure. A similar effect is seen in host frameworks based on hydrogen bonded hydroxyl rings which are stabilised by bulky, rigid groups. [328, 329]

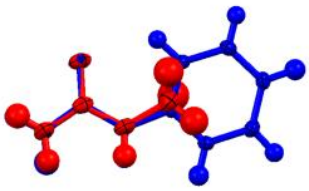

Figure 9.27 A structural overlay of molecules *N*-methylurea (red) and *N*-phenylurea (blue).

Changes in the urea substitution appeared to tune the hydrogen bonded network cavity size. This was observed between the hydrogen bonded ring networks formed in DMU5-NIP and in the *N*-phenylurea 5-nitroisophthalic acid IMs **IM1** to **IM5**. A structural overlay of the two hydrogen bonded networks indicates that the cavity formed by the hydrogen bonded ring network in DMU5-NIP is smaller than in **IM1** to **IM5** (Figure 9.28). This is related to urea substituent size where the *N*-phenyl substituent on the urea acts as a larger spacer and shifts the position of the 5-nitroisophthalic acid molecule, relative to its in position in DMU5-NIP, causing the ring to widen. The smaller cavity size in DMU5-NIP may be the cause for only DMU molecules being included in this material where its flexibility to solvent guest molecules is reduced. The fact that no solvent guests are included in the DMU5-NIP network may also be related to the strength of the host-guest interaction formed; a very short O—H···O hydrogen bond ($d_{O\cdots O}$ 2.434(2) Å) forms to the DMU 'guest' in DMU5-NIP which may be too strong to be disrupted by solvent guest molecules.

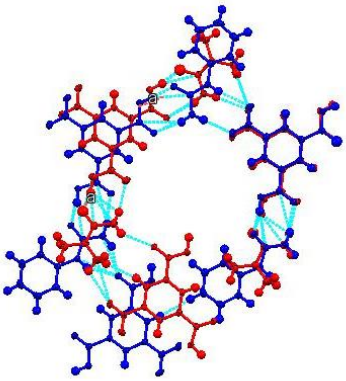

Figure 9.28 A structural overlay of the hydrogen bonded ring network in **IM1** to **IM5** (blue) and DMU5-NIP (red).

The variations in the urea substitution also appear to have a consequence for the guest inclusion in the hydrogen bonded networks. In U5-NIP where the urea was unsubstituted and therefore smaller, 'guest' molecules formed chains that penetrated the hydrogen bonded ring network; this allowed the hydrogen bonding of the urea molecules to be satisfied. In contrast, in DMU5-NIP or **NS1**, where the 'guest' was substituted on one side by bulky groups, it was included in the layer of the hydrogen bonded network.

Variation in the substitution of the ureas also led to variation in the hydrogen bonding synthons that were formed. Across the different substituted urea 5-nitroisophthalic acid complexes, the formation of the carboxylic acid:amide $R_2^2(8)$ synthon was prevalent and unaffected by substitution; this indicates the robust nature of this motif for the assembly of carboxylic acid and amide groups. In contrast, the type of nitro:amide synthon formed and whether the carboxylic acid:amide $R_2^1(6)$ synthon was present was affected by urea substitution. This is evident between the IMs and DMU5-NIP where the hydrogen bonding network is almost isostructural except for the type of nitro:amide hydrogen bond synthons present. In DMU5-NIP, the disubstitution of the DMU nitrogen atom blocks hydrogen bonding sites and led to a nitro:amide $R_2^1(6)$ synthon forming, in place of a $R_2^2(8)$ synthon in the IMs, and a single N—H···O hydrogen bond, in place of a carboxylic acid:amide $R_2^1(6)$ synthon in the IMs. The change in synthons had little effect on the overall ring network formation. The carboxylic acid:amide $R_2^1(6)$ synthon was present in all non or singly substituted urea molecular complexes. The nitro amide $R_2^2(8)$ synthon formed for U5-NIP and the *N*-phenylurea IMs, where the urea was increasingly less substituted; it was not formed in MU5-NIP despite the single substitution of the urea however this structure is most different to that of U5-NIP and the *N*-phenylurea IMs.

9.8 Conclusions

In this chapter, substituted ureas with 5-nitroisophthalic acid have been investigated for the design of hydrogen bonded networks with inclusion behaviour *via* a number of hydrogen bonding synthons. Fourteen molecular complexes were prepared, nine of which had solvent inclusion behaviour (IMs); these latter were formed for the combination of *N*-phenylurea with 5-nitroisophthalic acid.

In the synthesised inclusion materials, the hydrogen bond was shown to be an important tool both in host formation and guest inclusion; host networks were based on a number of hydrogen bond synthons whilst guest tethering occurred in most cases *via* hydrogen bonding to the host. This reaffirms the potential of the hydrogen bond in inclusion material design. Certain hydrogen bonding synthons prevailed in the networks between the 5-nitroisophthalic acid and substituted urea components including carboxylic acid:amide and nitro:amide hydrogen bond synthons; in particular the carboxylic acid:amide $R_2^2(8)$ synthon was robust for network formation. This aids in the predictability of the assembly of urea, carboxylic acid and nitro group containing molecular building blocks in the solid state.

The molecular components of 5-nitroisophthalic acid and substituted ureas were shown to be suitable targets in the design of hydrogen bonded networks with inclusion behaviour. The arrangement of hydrogen bonding groups in 5-nitroisophthalic acid favoured the formation of ring networks which led to the inclusion behaviour whilst substitution of the urea allowed tuning of the resulting hydrogen bonding networks, including network shape and size; an increased substitution of the urea with bulkier groups favour inclusion behaviour in the resulting networks and is recommended in further design strategies. The nitro functionality of the 5-nitroisophthalic acid molecule proved to be a valuable crystal engineering tool allowing network extension and variation being versatile in hydrogen bond synthon formation. This reveals the potential for network modification by modifications to the molecular components.

The synthesised IMs were not thermally stable but desolvated on heating, as is typical for organic inclusion compounds, which did not lead to an empty structure but to a material where a host molecular building block replaced the solvent guest in the cavities. These materials therefore do not offer the potential for porous frameworks on guest removal; this is likely a result of the host hydrogen bonding group pointing into the guest cavity which must be fulfilled on guest release. The study of thermal behaviour allows physical properties to be related to structure; this may aid in the prediction of the thermal behaviour of future inclusion materials where the structure is known.

In the design of these materials, the guest is shown to have an important role in determining host structure having a ‘templating’ effect; different host networks were formed for different combinations of single and multiple guests. The templating of host structures by guest molecules is useful in the design of inclusion materials, allowing the introduction of diversity into the networks and providing the potential for making subtle modifications to structure and therefore properties. The inclusion of different guests in different networks, or not, may also indicate the determining factors in guest selection; here molecular size and hydrogen bond donor-acceptor ability appeared to be important. Preliminary competition studies investigated the host selectivity of guests, however these potential properties require further investigation.

Chapter 10.

Conclusions and future work

The work in this research project has demonstrated the potential of synchrotron X-ray diffraction to reveal information about proton transfer behaviour, across hydrogen bonds, in the solid state. The synchrotron X-ray diffraction technique was found to be applicable in the studies of proton transfer behaviour when both the data collection and refinement procedures were optimised. It was therefore possible to correlate a number of effects to the proton transfer behaviour including the hydrogen bond local and wider crystal packing and hydrogen bond donor-acceptor distances. This aids in the understanding of these processes and in the future design of proton transfer materials. The study of these effects in the range of molecular complexes accessed from crystal engineering studies also provides insight into the predictability of molecular recognition and crystal packing where common hydrogen bond motifs repeatedly formed for combinations of certain co-formers. Where the crystal packing leads to a certain physical property, such as proton transfer or inclusion behaviour, this contributes to the predictable design of functional materials.

10.1 Synchrotron X-ray diffraction studies of proton transfer behaviour

The synchrotron X-ray diffraction technique was found to be applicable in the study of proton transfer processes allowing the collection of diffraction data from which proton transfer behaviour could be determined. In particular, the speed of data collection offered by this method was found to be invaluable allowing multiple measurements across which the proton transfer processes could be studied; whether multi-temperature measurements, such as for the investigations of the temperature dependent effects of proton disorder and migration, or across a number of molecular complexes. The success of the synchrotron technique in these studies was, however, found to rely upon certain factors which should be considered upon its implementation in future studies.

Having high quality data was shown to be important in these studies in order to allow the reliable determination of proton transfer behaviour in the Fourier difference maps; reduced data quality led to increased noise in the Fourier difference maps and to large errors on the hydrogen bond parameters such that hydrogen atom behaviour, or changes in it, became indeterminable. This was seen in a number of cases and was likely a cause of sample quality therefore emphasising the need for optimum conditions in order to rely on the use of the technique in studying proton transfer behaviour. The optimisation studies attempted to probe where these optimum conditions could be

achieved during the data collection stages. The trialling of a number of data collection strategies, between which the portions of data collected and X-ray detectors were varied, revealed that collecting a hemisphere of data using a CCD detector is an appropriate strategy to employ in these studies allowing good quality Fourier difference maps to be obtained without compromising experimental time. Promising results were found in the preliminary studies using the DECTRIS [234] Pilatus 300K detector; this detector offers enhanced speeds of collection and improved signal to noise ratios and therefore may be the way forward in future studies of this type. Varied temperature steps and ramping methods were trialled during the data collection process and it was found that smoother and more reliable trends in the hydrogen atom parameters could be found when probing the proton transfer behaviour at an increased number of points along the temperature profile. The collection of data, as the temperature is ramped continuously, also allows a more detailed account of the proton transfer behaviour over the range studied. The approach of continuous temperature ramping was pioneered in this work, having not previously been implemented in single crystal X-ray diffraction studies, and was made possible by the use of the synchrotron X-ray source.

The choice of refinement method was shown to have consequences for the determination of proton transfer behaviour using the synchrotron technique. The different refinement strategies trialled, targeted both the way information about the transferring hydrogen atom was refined from the synchrotron data and the way it was modelled during the refinement. Single temperature step data set refinement in SHELXL [219] was shown to be successful and a simple method to implement in following the proton transfer processes, whether static or as a function of temperature. The employment of the parametric refinement method in Topas-Academic V5.0 [168] was shown to be both possible and potentially advantageous in the studies of proton migration allowing shifts in proton position to be followed by its simultaneous refinement over a large number of data sets and saving significant data processing time. There were, however, limitations presented with the use of this method. Parametric refinement has the potential to offer an enhanced accuracy in the refined proton position, where refined over a large sample of data, however, the model chosen to drive the hydrogen atom position with temperature significantly affected the migration behaviour indicated by the refined hydrogen atom positions. The use of parametric refinement in studies of this type is, however, promising and while it is a more involved method, this work has gone some way to making its implementation in studies of proton transfer more routine and further investigation is recommended. Care was also required in the treatment of the transferring hydrogen atom in the SHELXL [219] refinements. In some cases, such as following proton migration, it was appropriate to apply different models to the proton thermal behaviour; freely refined and fixed thermal parameters indicated similar proton transfer behaviour allowing confidence in the observed proton migration. In other cases, such as following proton disorder, modelling the hydrogen atom

behaviour in a certain way, including models with the proton position split over two sites in the hydrogen bond, was less appropriate; in most cases the refined occupancies were not supported by the carboxyl bond lengths or the Fourier difference maps. This emphasises the problems presented in attempting to follow or to model the behaviour of potentially a fraction of an electron.

The determination of the proton transfer behaviour occurring in each system using the synchrotron technique was found to be most reliable when all available information extracted from the data were in support of the behaviour suggested and when following a consistent trend. It was also found that greater weight, in the determination, should be given to the Fourier difference maps, a direct imaging approach that is not dependent on models assumed for the proton structural parameters and hence offers high potential to allow proton behaviour to be determined reliably from X-ray diffraction, and to the heavy atom parameters, accurately refined by this technique. This allows greater confidence in the results obtained from synchrotron X-ray diffraction. This may appear a disadvantage in comparison to neutron diffraction methods, which allow unambiguous determination of proton transfer behaviour without the need of supporting information. However, these disadvantages are compensated for by the high throughput offered by the synchrotron radiation methods assessed here allowing the collection of a single data set in minute time scales compared to hours for a neutron diffraction measurement.

These findings therefore contribute to the development of the synchrotron X-ray diffraction method such that it can be used routinely and more confidently in future studies of proton transfer behaviour. Further development is required, including exploring the use of Pilatus detectors in these studies, as well as maximising the potential of the parametric refinement processes in Topas-Academic V5.0. [168]

10.2 Tuning proton transfer behaviour

Proton transfer in the form of temperature dependent proton disorder and migration and static proton transfer processes was studied using the synchrotron technique. Changes in hydrogen atom density or shifts in refined hydrogen atom positions, as a function of temperature or across a set of complexes, were observable in agreement with structural parameters and density in the Fourier difference maps. This allowed details about the proton transfer behaviour to be revealed including mechanistic information and temperature dependency. Proton disorder and migration were both shown to be temperature dependent and gradual effects; the effect more subtle in the case of proton migration. Proton disorder occurred *via* Arrhenius behaviour whilst the proton migration observed was most likely attributable to lattice fluctuations with temperature. In the case of the

static proton transfer, this transfer was well defined in each complex whilst subtle effects were shown to occur on the length scale, across the complexes. The proton transfer behaviour in turn revealed the details about the likely shape of the hydrogen bond potential energy surface. These studies therefore contribute towards the understanding of the different proton transfer processes.

The study of the different proton transfer processes allowed variations in the transfer behaviour to be rationalised in the variations across the molecular complexes. A number of effects were revealed to 'tune' the transfer behaviour occurring across the molecular complexes.

Crystal packing, including in the local environment of the hydrogen bond and the wider packing, was indicated to tune the proton transfer behaviour occurring. This effect was apparent in the proton disorder (Chapter 5) and static proton transfer (Chapter 8) studies. Proton transfer effects were reduced where interactions formed in the local environment of the hydrogen bond. This was evident in the 3,5-DNBA molecular complexes; decreased extents of proton disorder occur at each temperature where there is a direct interaction between the dimer hydrogen bonds and the local environment in contrast to complexes in which this interaction is not present. In the DMAN molecular complexes, the $[N—H\cdots N]^{+}$ IHB proton appears localised by the interactions between the nitrogen donor-acceptor atoms and X^{-}; asymmetrically located and undergoing reduced extents of transfer, on the side of the IHB that forms the shortest interactions to X^{-}. Similar thermal behaviour was also observed in the DMAN molecular complexes between the IHB proton and X^{-}, potentially indicating an influence of X^{-} on the proton behaviour. Proton transfer effects were also reduced where interactions were formed in the wider crystal packing. This was evident in the DMAN molecular complexes; the $[N—H\cdots N]^{+}$ IHB proton appears localised by the $[Me_2N—H\cdots N\ Me_2]^{+}\cdots\ X^{-}$ minor interactions, located on the side of the IHB where they are shortest. In some of the 3,5-DNBA molecular complexes (3,5-DNBA MCZ and 3,5-DNBA In-3-Ac), despite the dimer hydrogen bonds being in an isolated environment, a 50:50 disorder is not observed; this occurs where there the arrangement of interactions to rest of 3,5-DNBA molecule are not the same on the protonated and non-protonated side which may be sufficient to imbalance the symmetry of the carboxylic acid dimer groups. The observed tuning effect of the crystal packing on proton transfer behaviour in this research project is in support of that found by Jones *et al* (2013) [97] and contributes further insight to what the specific effects might be. The 'tuning' of the proton transfer behaviour by the crystal packing also indicates the sensitivity of the hydrogen bond potential energy surface; perturbed by the weaker interactions.

Proton transfer behaviour was also found to be related to the hydrogen bond donor-acceptor distances. As is well known, the strength of the hydrogen bond affects the proton transfer process occurring, related to the shape and barrier height of the hydrogen bond potential energy surface for

the different interactions. Proton disorder occurred for moderate strength hydrogen bonds whilst proton migration occurred for the shortest of the interactions (SSHBs). The proton transfer process of temperature dependent proton migration appeared particularly sensitive to donor-acceptor distance, only occurring in the molecular complexes across O—H···O SSHBs with donor--acceptor distance of less than 2.45 Å or N^+—H···O^- SSHBs with donor-acceptor distances in the region of 2.551 Å or less. These observations are in agreement with studies in the literature. [110, 111, 117, 267] For O—H···O SSHBs, the previously proposed 2.45 Å limit appeared strict, where proton migration was observed in DMU2,4-DNBA for an O···O distance of 2.441(1) Å but not for DMUP for an O···O distance of 2.449(2) Å. This emphasises the need for very short donor-acceptor distances for the proton migration process to occur; this is related to a reduction in the barrier to proton transfer and to the increasingly symmetric hydrogen potential energy surface as the donor-acceptor distance reduces. In the case of the N^+—H···O^- SSHBs, the donor-acceptor distance is the longest in INP of those previously reported to exhibit proton migration. No limit has been yet been suggested for these interactions however, it may within the range of 2.551(1) to 2.555(1) Å, where proton migration could not be confirmed in IN2,4-DNBA whose N^+···O^- distance was the latter. More studies are required to examine the N^+—H···O^- SSHB donor-acceptor range to identify a potential limit above which temperature dependent proton migration is not expected to occur. In the molecular complexes, the donor-acceptor distance also appeared to tune the transfer occurring at low temperature (100 or 150 K); in the SSHBs studies, elongated D—H distances occurred for the shortest donor-acceptor distances whilst in the DMAN molecular complexes, the static transfer behaviour appeared to be related to the donor-acceptor distance (more so than the H···X^- distances). This indicates the effect of donor-acceptor distances on the shape of the hydrogen bond potential energy surface. These studies aid in understanding proton transfer behaviour and contribute to the knowledge of where it may be expected in similar materials, in terms of donor-acceptor distances, or those donor-acceptor distances to target; this is important where relatively few examples exist in the literature.

The potential for ΔpK_a values to tune proton transfer behaviour was also indicated; the extent of temperature dependent proton migration across O—H···O SSHBs in substituted urea organic acid molecular complexes [109] has previously been correlated to ΔpK_a values. The single O—H···O proton migration material identified in this research project (DMU2,4-DNBA) agrees with the suggested trend of increasing extent of migration as the ΔpK_a values become increasingly less negative (i.e. approaches zero). However, no such trend was indicated for the N^+—H···O^- SSHBs on comparing the single N^+—H···O^- proton migration material identified in this research project (INP) with those previously reported. Two issues arise in this work on correlating ΔpK_a and proton migration including the difficulties in transferring pK_a values to the solid state, including that they

are determined from solution but applied in the solid state, and on comparing extents of migration obtained from different diffraction methods; proton shifts determined from X-ray diffraction are longer than those determined from neutron diffraction. [121] The tuning effects of ΔpK_a on proton transfer therefore should be considered more tentatively. If applicable, however, this factor would be beneficial in these studies allowing extents of proton migration to be targeted through co-former selection.

Proton transfer behaviour therefore appears tuneable by a subtle balance of a combination of effects. This reveals the potential to control proton transfer behaviour in future materials where crystal packing has an element of predictability or in targeting certain hydrogen bond donor-acceptor distances. By targeting certain transfer behaviour, it may be possible to target certain functions, attributable to proton transfer, in solid state materials.

10.3 Crystal engineering

The implementation of crystal engineering strategies allowed the preparation of a number of molecular complexes. A number of design strategies were employed including targeting the formation of (1) SSHBs, in the design of potential proton migration materials, (2) the $[Me_2N—H\cdots NMe_2]\cdots X^-$ fragment, for the study of proton transfer behaviour and anion effects, and (3) extended hydrogen bonded networks with inclusion behaviour. Across the crystal engineering strategies, elements of predictability were noted, contributing to knowledge of molecular assembly in the solid state.

There was some predictability in the tuning of the intermolecular interaction distances between components. This was found in both the studies involving the engineering of SSHBs and in the DMAN organic acid molecular complexes and occurred as a result of molecular substitution and molecular motif formation. Molecular substitution appeared to affect the interaction distances of the SSHBs and the minor interactions in the DMAN molecular complexes related to the basicity of the hydrogen bond acceptors. A strategy of selecting increasingly acidic hydrogen bond donors and increasingly basic hydrogen bond acceptors is recommended to access the shortest of the SSHBs whilst targeting increasingly acidic substituted benzoic acids or those with non-halogen electron withdrawing groups in the DMAN molecular complexes led to weaker minor interactions. Certain hydrogen bonding motifs also appeared to have consequences for interaction distances; SSHBs were favoured in hydrogen bonding motifs of the carboxylic acid:amide and single CAHB $N^+—H\cdots O^-$ hydrogen bonds whilst a $[Me_2N—H\cdots NMe_2]\cdots X^-$ fragment, where X^- was a deprotonated acid, led to shorter minor interactions than where it was an electron withdrawing

group. A correlation between interaction distances and ΔpK_a values was less conclusive, however, the ΔpK_a values were mostly correct in predicting the occurrence of proton transfer; this is interesting where the shorter hydrogen bonds generally formed where proton transfer had occurred. Interaction distances were found, whether those in the local or wider packing, to tune proton transfer behaviour. Understanding the ways in which these interactions distances may be tuned or targeted is of interest where they appear to influence proton transfer behaviour; their tuning *via* component selection and combination may allow certain proton transfer behaviour to be targeted in materials.

There was also predictability in molecular aggregation occurring across the molecular complexes. Aggregation appeared affected by hydrogen bonding groups; certain hydrogen bonding groups assembled repeatedly *via* the same hydrogen bonding motifs such as the combination of the carboxylic acid and amide functionalities and the anilic acids with *N*-heterocycles. The ring position or nature of the substituent also caused variation in the aggregation including in the DMAN:$ACID^-$ anion units formed, in terms of the identity of X^- or the ratio of components forming the $[Me_2N—H\cdots NMe_2]\cdots X^-$ fragment, or the urea organic acid motifs formed, whether extended or isolated, as the number of available hydrogen bonding sites or size of molecular substituent varied. The geometry of the hydrogen bond donor-acceptor groups also favoured certain molecular aggregation. For example, the arrangement of the acid groups in the anilic acids favoured bifurcation on deprotonation whilst the pseudo trigonal symmetry of hydrogen bonding groups in 5-nitroisophthalic acid favoured hydrogen bond network extension in three directions for inclusion network formation. In the case of the inclusion networks, guests were also shown to play a role in templating the networks revealing additional ways to influence molecular assembly in the solid state as well as introducing diversity into networks formed. The predictability in the molecular aggregation observed in the complexes in this research project indicates ways in which control of crystal packing may be achieved by certain co-former selection or combination. Where molecular aggregation can determine material properties, such as proton transfer or inclusion behaviour, increased knowledge of molecular assembly, as found in this work, aids in the deliberate design of functional materials.

As well as contributing knowledge to the design of materials in the solid state with desired structure related functions, the work in this research project is also an excellent example of the robust nature and versatility of the hydrogen bond in crystal engineering; able to exhibit a number of proton transfer processes or facilitate host-guest chemistry, contributing to both host network design and guest inclusion.

10.4 Future work

The work presented here has the potential to be developed in aspects of both the synchrotron X-ray diffraction studies of proton transfer behaviour and in the crystal engineering studies.

Related to the use of the synchrotron X-ray diffraction technique, developments in both the data collection and crystal structure refinement methods are still required where this is the first reported instance of its implementation in studies of this type. The optimisation of the hybrid pixel detectors such as the DECTRIS [234] Pilatus range would be advantageous in these studies for a more rapid data collection, particularly useful in the continuous temperature ramping studies allowing many more points along the temperature profile to be probed, and for reduced noise for potentially cleaner Fourier difference maps for proton transfer behaviour determination. The continuous temperature ramping method should also be further explored, trialled only in one case, allowing the evolving proton transfer behaviour to be followed. The single crystal parametric refinement method developed in Topas-Academic V5.0 [168] should be built on, currently allowing a stable refinement but where there is room for its optimisation. Trialling further models for proton transfer would also be of interest, including one that restricts the hydrogen atom position but allows the thermal parameters to refine, to determine what else can be refined parametrically or applying the method to further examples. In general, improvement in the refinement of proton site occupancies in the disorder studies is also required; this was achieved somewhat reliably in the benchmarking study of 3,5-DNBA but remained unreliable for the 3,5-DNBA molecular complexes. Using the carboxyl bond lengths may be one solution, but a better method for treating the split proton density is required.

In using the synchrotron X-ray technique to elucidate information about the proton transfer occurring such that it can be rationalised, this study would benefit from complementary neutron diffraction measurements; this is particularly true in the determination of the disordered proton split site occupancies. The aim here, however, was to assess the potential of X-ray methods in the absence of neutron studies. A number of systems were studied reasonably successfully using the synchrotron technique and correlations between proton transfer behaviour and other effects could be identified. The study of further systems would add further weight and insight to the conclusions made in this research project about the tuning effects on proton transfer behaviour, particularly those of the weaker interactions, and therefore how to achieve the design of proton transfer behaviour into additional materials. There was also no attempt made to quantify the tuning effects of the weaker interactions in this work. This could be performed using computational methods and would allow the energy of stabilisation/destabilisation associated with the crystal packing to be determined. [330] The tuning effects could also be investigated by conducting charge density studies

to determine atomic charges and electron density of components of the weak interactions; this may reveal their perturbation effects or strength. [131]

Developments to the crystal engineering strand would target further proton transfer materials considering what has been found in this research project. The design of the charge assisted N^+—H···O^- was not as well investigated as those of the O—H···O SSHBs and should be investigated further, particularly those for the 6-membered ring *N*-heterocycles, favouring the shorter of the interactions. If successful, this may allow the donor-acceptor distance limit for migration across charge assisted N^+—H···O^- hydrogen bonds to be determined. Where proton transfer led to the shortest of the O—H···O SSHBs, the ΔpK_a range where proton transfer is expected should be probed for their future design. Despite the contributions from this research project, the number of reported studies of proton disorder systems remains low. Further investigation into the circumstances under which the 3,5-DNBA centrosymmetic hydrogen bonded dimers form would be of interest. Where attempts to crystallise 3,5-DNBA dimers in the presence of a range of substituted benzoic acids were unsuccessful, a strategy of using different types of co-molecules should be implemented. The substituted benzoic acid co-molecules used were selected with the aim of determining whether certain benzoic acid substituents favoured homo (3,5-DNBA dimer alongside a co-molecule dimer) or hetero-dimer formation; in all cases, the co-molecules crystallised separately. The combination of 5-nitroisophthalic acid with ureas whose substituents are more bulky than that of *N*-phenylurea would be interest to determine if similar hydrogen bonding inclusion networks can be obtained for other substituents *via* the same hydrogen bonding synthons. This may lead to a range of inclusion materials based on the same synthons and network motif.

10.5 Concluding remarks

The work in this research project is by no means definitive in the studies of proton transfer behaviour using synchrotron X-ray diffraction but hopes to go some way in demonstrating its potential for routine use in these studies, offering the potential to reveal insight into the transfer process and aspects of molecular structure control.

Crystal engineering is shown to remain a significant tool in the design of solid state functional materials with the hydrogen bond being robust for materials formation. It is hoped that the design strategies trialled in this work can be used in the development of functional materials, whose function is dependent on the proton behaviour, as in the proton transfer systems, or molecular packing, as in the inclusion networks.

References

1. *Diamond Light Source*, http://www.diamond.ac.uk/Home.html, Accessed 06//06/2016.
2. *Advanced Light Source*, http://www-als.lbl.gov/, Accessed 06/06/2016.
3. F. Allen, *Acta Crystallogr. Sect. B*, 2002, **58**, 380-388.
4. W. M. Latimer and W. H. Rodebush, *J. Am. Chem. Soc.*, 1920, **42**, 1419.
5. R. Arunan, G. R. Desiraju, R. A. Klein, J. Sadlej, S. Scheiner, I. Alkorta, D. C. Clary, R. H. Crabtree, J. J. Dannenberg, P. Hobza, H. G. Kjaergaard, A. C. Legon, B. Mennucci and D. J. Nesbitt, *Pure Appl. Chem.*, 2011, **83**, 1637-1641.
6. G. C. Pimental and A. L. McClellan, *The Hydrogen Bond*, W. H. Freeman and Company, San Francisco, 1960.
7. G. A. Jeffrey, *An Introduction to Hydrogen Bonding*, Oxford University Press, New York, 1997.
8. T. Steiner, *Angew. Chem. Int. Ed.*, 2002, **41**, 48-76.
9. A. L. McClellan, *J. Chem. Educ.*, 1967, **44**, 547.
10. R. Vuilleumier and D. Borgis, *Nat Chem*, 2012, **4**, 432-433.
11. L. N. Ferguson, *J. Chem. Educ.*, 1956, **33**, 267.
12. P. A. Kollman and L. C. Allen, *Chem. Rev.*, 1972, **72**.
13. A. Novak, *Large Molecules*, Springer, Berlin, 1974.
14. D. Braga and F. Grepioni, *Making Crystals by Design: Methods, Techniques and Applications*, Wiley-VCH, Weinheim, 2007.
15. G. R. Desiraju and T. Steiner, *The Weak Hydrogen Bond in Structural Chemistry and Biology*, Oxford University Press, Oxford, 1999.
16. C. L. Perrin, *Acc. Chem. Res.*, 2010, **43**, 1550-1557.
17. C. A. Coulson, *Hydrogen Bonding*, Symposium Publications Division Pergamon Press, New York, 1957.
18. G. Gilli and P. Gilli, *J. Mol. Struct.*, 2000, **552**, 1-15.
19. D. Braga, L. Maini, F. Grepioni, A. De Cian, O. Felix, J. Fischer and M. W. Hosseini, *New J. Chem.*, 2000, **24**, 547-553.
20. G. Gilli, F. Bellucci, V. Ferretti and V. Bertolasi, *J. Am. Chem. Soc.*, 1989, **111**, 1023-1028.
21. K.-L. Zhong, *Acta Crystallogr. Sect. C*, 2013, **69**, 1537-1540.
22. C. C. Wilson and C. A. Morrison, *Chem. Phys. Lett.*, 2002, **362**, 85-89.
23. C. L. Perrin and J. B. Nielson, *Annu. Rev. Phys. Chem.*, 1997, **48**, 511-544.

24. S. Nagaoka, T. Terao, F. Imashiro, A. Saika, N. Hirota and S. Hayashi, *Chem. Phys. Lett.*, 1981, **80**, 580-584.
25. U. Koch and P. L. A. Popelier, *J. Phys. Chem.*, 1995, **99**, 9747-9754.
26. G. R. Desiraju, *Crystal Engineering: The Design of Organic Solids*, Elsevier, Amsterdam, 1989.
27. I. Olovsson and P. G. Jonsson, *The Hydrogen Bond*, Elsevier, Amsterdam, 1976.
28. R. Taylor and O. Kennard, *J. Am. Chem. Soc.*, 1982, **104**, 5063-5070.
29. J. Bernstein, M. D. Cohen and L. Leiserowitz, *The Chemistry of Quinoid Compounds*, Interscience, New York, 1974.
30. I. Rozas, I. Alkorta and J. Elguero, *J. Phys. Chem. A*, 1998, **102**, 9925-9932.
31. M. B. Zaman, M. Tomura and Y. Yamashita, *J. Org. Chem.*, 2001, **66**, 5987-5995.
32. I. Y. Torshin, I. T. Weber and R. W. Harrison, *Protein Eng.*, 2002, **15**, 359-363.
33. D. Braga, *Chem. Commun.*, 2003, 2751-2754.
34. C. B. Aakeröy, N. R. Champness and C. Janiak, *CrystEngComm*, 2010, **12**, 22-43.
35. M. C. Etter, Z. Urbanczyk-Lipkowska, M. Zia-Ebrahimi and T. W. Panunto, *J. Am. Chem. Soc.*, 1990, **112**, 8415-8426.
36. M. C. Etter, *Acc. Chem. Res.*, 1990, **23**, 120-126.
37. F. H. Herbstein, *Crystalline Molecular Complexes and Compounds: Structures and Principles*, Oxford University Press, Oxford, 2005.
38. R. Custelcean, *Chem. Commun.*, 2008, 295-307.
39. P. Muller, R. Herbst-Irmer, A. L. Spek, T. R. Schneider and M. R. Sawaya, *Crystal Structure Refinement: A Crystallographer's Guide to SHELXL*, Oxford University Press, Oxford, 2006.
40. W. Dannecker, J. Kopf and H. Rust, *Cryst. Struct. Commun.* , 1979, **8**, 429.
41. C. Nather, C. Doring, I. Jess, P. G. Jones and C. Taouss, *Acta Crystallogr. Sect. B*, 2013, **69**, 70-76.
42. C. Huiszoon and G. W. M. Tiemessen, *Acta Crystallogr. Sect. B*, 1976, **32**, 1604-1606.
43. G. Song, F.-Y. Bai, N. Xing, C. Chen, H. Shan and Y.-H. Xing, *Chem. Res. Chin. Univ.*, 2013, **29**, 408-413.
44. A. Alhalaweh, S. George, D. Boström and S. P. Velaga, *Cryst. Growth Des.*, 2010, **10**, 4847-4855.
45. M. C. Etter and G. M. Frankenbach, *Chem. Mater.*, 1989, **1**, 10-12.
46. F. F. Awwadi, D. Taher, S. F. Haddad and M. M. Turnbull, *Cryst. Growth Des.*, 2014, **14**, 1961-1971.
47. P. Metrangolo, F. Meyer, T. Pilati, G. Resnati and G. Terraneo, *Angew. Chem. Int. Ed.*, 2008, **47**, 6114-6127.
48. P. Politzer, J. S. Murray and T. Clark, *Phys. Chem. Chem. Phys.*, 2010, **12**, 7748-7757.

49. N. W. Alcock, in *Advances in Inorganic Chemistry and Radiochemistry*, eds. H. J. Emeléus and A. G. Sharpe, Academic Press, New York, 1972, vol. 15, pp. 1-58.
50. N. W. Alcock and R. M. Countryman, *J. Chem. Soc., Dalton Trans.*, 1977, 217-219.
51. T. Sakurai, M. Sundaralingam and G. A. Jeffrey, *Acta Crystallogr.*, 1963, **16**, 354-363.
52. G. R. Desiraju and R. Parthasarathy, *J. Am. Chem. Soc.*, 1989, **111**, 8725-8726.
53. B. B. Averkiev, A. A. Korlyukov, M. Y. Antipin, A. B. Sheremetev and T. V. Timofeeva, *Cryst. Growth Des.*, 2014, **14**, 5418-5427.
54. M. Albrecht, M. Muller, A. Valkonen and K. Rissanen, *CrystEngComm*, 2010, **12**, 3698-3702.
55. J. W. Steed and J. L. Atwood, *Supramolecular Chemistry*, John Wiley & Sons Ltd., Chichester, 2000.
56. C. R. Martinez and B. L. Iverson, *Chem. Sci.*, 2012, **3**, 2191-2201.
57. M. Watt, L. K. E. Hardebeck, C. C. Kirkpatrick and M. Lewis, *J. Am. Chem. Soc.*, 2011, **133**, 3854-3862.
58. F. H. Allen, C. A. Baalham, J. P. M. Lommerse and P. R. Raithby, *Acta Crystallogr. Sect. B*, 1998, **54**, 320-329.
59. R. Taylor, *CrystEngComm*, 2014, **16**, 6852-6865.
60. T. S. Thakur, M. T. Kirchner, D. Blaser, R. Boese and G. R. Desiraju, *CrystEngComm*, 2010, **12**, 2079-2085.
61. D. Braga and F. Grepioni, *Chem. Commun.*, 2005, 3635-3645.
62. D. Braga, F. Grepioni, L. Maini and M. Polito, *Struct. Bond*, 2009, **132**, 25-50.
63. S. L. Childs, G. P. Stahly and A. Park, *Mol. Pharm.*, 2007, **4**, 323-338.
64. L. Yu, *Acc. Chem. Res.*, 2010, **43**, 1257-1266.
65. R. Chadha, S. Gupta and G. Shukla, *Acta Pharm. Sin. B*, 2011, **1**, 129-135.
66. J. Li, L. Wang, Y. Q. Ye, X. Fu, Q. Ren, H. Zhang and Z. Deng, *Eur. J. Pharm. Sci.*, 2016, **85**, 47-52.
67. J. Bernstein, *Polymorphism in Molecular Crystals*, Oxford University Press, Oxford, 2002.
68. C. Sun and D. J. W. Grant, *Pharm. Res.*, 2004, **21**, 382-386.
69. P. Van Der Sluis and J. Kroon, *J. Cryst. Growth*, 1989, **97**, 645-656.
70. A. J. Cruz-Cabeza, G. M. Day and W. Jones, *Chemistry*, 2009, **15**, 13033-13040.
71. J. E. D. Davies, *Nat. Chem.*, 1981, **289**, 224.
72. K. D. M. Harris and J. M. Thomas, *J. Chem. Soc., Faraday Trans.*, 1990, **86**, 2985-2996.
73. O. Ermer and J. Neudörfl, *Helv. Chim. Acta*, 2001, **84**, 1268-1313.
74. P. Sozzani, A. Comotti, R. Simonutti, T. Meersmann, J. W. Logan and A. Pines, *Angew. Chem. Int. Ed.*, 2000, **39**, 2695-2699.
75. A. Jacobs, L. R. Nassimbeni and J. H. Taljaard, *CrystEngComm*, 2006, **7**, 731-734.

76. S. Thakral and A. K. Madan, *J. Pharm. Pharmacol.*, 2007, **59**, 1501-1507.
77. M. Fogagnolo, G. Fantin and O. Bortolini, *Int. J. Mol. Sci.*, 2007, **8**, 662-669.
78. L. J. Barbour, *Chem. Commun.*, 2006, 1163-1168.
79. M. A. Little, M. E. Briggs, J. T. Jones, M. Schmidtmann, T. Hasell, S. Y. Chong, K. E. Jelfs, L. Chen and A. I. Cooper, *Nat. Chem.*, 2014, **7**, 153-159.
80. H. Wahl, D. A. Haynes and T. le Roex, *CrystEngComm*, 2015, **17**, 1549-1555.
81. W. Xiao, C. Hu and M. D. Ward, *J. Am. Chem. Soc.*, 2014, **136**, 14200-14206.
82. O. Danylyuk, H. Butkiewicz, A. W. Coleman and K. Suwinska, *CrystEngComm*, 2015, **17**, 1745-1749.
83. K. Buhlmann, J. Reinbold, K. Cammann, K. Skobridis, A. Wierig and E. Weber, *Fresenius J. Anal. Chem.*, 1994, **348**, 549-552.
84. A. Goldup and G. W. Smith, *Sep. Sci. Technol.*, 1971, **6**, 791-817.
85. E. Barea, C. Montoro and J. A. Navarro, *Chem. Soc. Rev.*, 2014, **43**, 5419-5430.
86. A. R. Eberlin, M. D. Eddleston and C. S. Frampton, *Acta Crystallogr. Sect. C*, 2013, **69**, 1260-1266.
87. J. Reijenga, A. van Hoof, A. van Loon and B. Teunissen, *Anal. Chem. Insights*, 2013, **8**, 53-71.
88. S. Mohamed, D. A. Tocher, M. Vickers, P. G. Karamertzanis and S. L. Price, *Cryst. Growth Des.*, 2009, **9**, 2881-2889.
89. A. Parkin, C. C. Seaton, N. Blagden and C. C. Wilson, *Cryst. Growth Des.*, 2007, **7**, 531-534.
90. J. A. Kanters, G. Roelofsen and J. Kroon, *Nature*, 1975, **257**, 625.
91. P. Fischer, P. Zolliker, B. H. Meier, R. R. Ernst, A. W. Hewat, J. D. Jorgensen and F. J. Rotella, *J. Solid State Chem.*, 1986, **61**, 109-125.
92. C. C. Wilson, N. Shankland and A. J. Florence, *J. Chem. Soc., Faraday Trans.*, 1996, **92**, 5051-5057.
93. W. M. Haynes, *CRC Handbook of Chemistry and Physics*, CRC Press, Boca Raton, 96th edn., 2016.
94. C. C. Wilson, *Single Crystal Neutron Diffraction from Molecular Materials*, World Scientific, Singapore, 2000.
95. G. A. Sim, J. M. Robertson and T. H. Goodwin, *Acta Crystallogr.*, 1955, **8**, 157-164.
96. G. Klausberger, K. Furic and L. Colombo, *J. Raman. Spectrosc.*, 1977, **6**, 277.
97. A. O. F. Jones, N. Blagden, G. J. McIntyre, A. Parkin, C. C. Seaton, L. H. Thomas and C. C. Wilson, *Cryst. Growth Des.*, 2013, **13**, 497-509.
98. L. H. Thomas, N. Blagden, M. J. Gutmann, A. A. Kallay, A. Parkin, C. C. Seaton and C. C. Wilson, *Cryst. Growth Des.*, 2010, **10**, 2770-2774.
99. K. Furić, *Chem. Phys. Lett.*, 1984, **108**, 518-521.

100. E. F. Caldin, *Chem. Rev.*, 1969, **69**, 135-156.
101. A. J. Horsewill, *J. Phys. Org. Chem.*, 2010, **23**, 580-585.
102. C. C. Wilson, N. Shankland and A. J. Florence, *Chem. Phys. Lett.*, 1996, **253**, 103-107.
103. S. Hayashi and J. Umemura, *J. Chem. Phys.*, 1974, **60**, 2630-2633.
104. W. Cai and A. Katrusiak, *CrystEngComm*, 2012, **14**, 4420-4424.
105. C. L. Perrin, *Pure Appl. Chem.*, 2009, **81**, 571-583.
106. D. M. S. Martins, D. S. Middlemiss, C. R. Pulham, C. C. Wilson, M. T. Weller, P. F. Henry, N. Shankland, K. Shankland, W. G. Marshall, R. M. Ibberson, K. Knight, S. Moggach, M. Brunelli and C. A. Morrison, *J. Am. Chem. Soc.*, 2009, **131**, 3884-3893.
107. E. H. Lee, *Asian J. Pharm. Sci.*, 2014, **9**, 163-175.
108. C. C. Wilson, K. Shankland and N. Shankland, *Z. Kristallogr.*, 2001, **216**, 303-306.
109. A. O. F. Jones, M.-H. Lemee-Cailleau, D. M. S. Martins, G. J. McIntyre, I. D. H. Oswald, C. R. Pulham, C. K. Spanswick, L. H. Thomas and C. C. Wilson, *Phys. Chem. Chem. Phys.*, 2012, **14**, 13273-13283.
110. J. A. Cowan, J. A. K. Howard, G. J. McIntyre, S. M. F. Lo and I. D. Williams, *Acta Crystallogr. Sect. B*, 2005, **61**, 724-730.
111. J. A. Cowan, J. A. K. Howard, G. J. McIntyre, S. M.-F. Lo and I. D. Williams, *Acta Crystallogr. Sect. B*, 2003, **59**, 794-801.
112. T. Steiner, I. Majerz and C. C. Wilson, *Angew. Chem. Int. Ed.*, 2001, **40**, 2651-2654.
113. A. O. F. Jones, C. K. Leech, G. J. McIntyre, C. C. Wilson and L. H. Thomas, *CrystEngComm*, 2014, **16**, 8177-8184.
114. P. Gilli, L. Pretto, V. Bertolasi and G. Gilli, *Acc. Chem. Res.*, 2009, **42**, 33-44.
115. S. Harkema, J. H. M. Ter Brake and H. J. G. Meutstege, *Acta Crystallogr. Sect. B*, 1979, **35**, 2087-2093.
116. S. Harkema, J. W. Bats, A. M. Weyenberg and D. Feil, *Acta Crystallogr. Sect. B*, 1972, **28**, 1646-1648.
117. M. Schmidtmann and C. C. Wilson, *CrystEngComm*, 2008, **10**, 177-183.
118. K. Lee, B. Kolb, T. Thonhauser, D. Vanderbilt and D. C. Langreth, *Phys. Rev. B*, 2012, **86**, 104102.
119. J. A. Gerlt, M. M. Kreevoy, W. W. Cleland and P. A. Frey, *Chem. Biol.*, 1997, **4**, 259-267.
120. W. Cleland and M. Kreevoy, *Science*, 1994, **264**, 1887-1890.
121. A. Parkin, S. M. Harte, A. E. Goeta and C. C. Wilson, *New J. Chem.*, 2004, **28**, 718-721.
122. L. H. Thomas, A. J. Florence and C. C. Wilson, *New J. Chem.*, 2009, **33**, 2486-2490.
123. R. W. Alder, P. S. Bowman, W. R. S. Steele and D. R. Winterman, *J. Chem. Soc., Chem. Commun.*, 1968, 723.
124. P. R. Mallinson, K. Woźniak, C. C. Wilson, K. L. McCormack and D. S. Yufit, *J. Am. Chem. Soc.*, 1999, **121**, 4640-4646.

125. H. A. Staab and T. Saupe, *Angew. Chem. Int. Ed.*, 1988, **27**, 865-879.
126. H. Einspahr, J.-B. Robert, R. E. Marsh and J. D. Roberts, *Acta Crystallogr. Sect. B*, 1973, **29**, 1611-1617.
127. R. T. Stibrany and J. A. Potenza, *CSD Communication*, 2006.
128. L. H. Thomas, A. O. F. Jones, A. A. Kallay, G. J. McIntyre and C. C. Wilson, *Cryst. Growth Des.*, 2016, **16**, 2112-2122.
129. A. F. Pozharskii and V. A. Ozeryanskii, *Mendeleev Commun.*, 2012, **22**, 117-124.
130. P. R. Mallinson, G. T. Smith, C. C. Wilson, E. Grech and K. Wozniak, *J. Am. Chem. Soc.*, 2003, **125**, 4259-4270.
131. K. Wozniak, P. R. Mallinson, G. T. Smith, C. C. Wilson and E. Grech, *J. Phys. Org. Chem.*, 2003, **16**, 764-771.
132. L. Sobczyk, *J. Mol. Struct.*, 2010, **972**, 59-63.
133. A. O. F. Jones, A. A. Kallay, H. Lloyd, G. J. McIntyre, C. C. Wilson and L. H. Thomas, *Cryst. Growth Des.*, 2016, **16**, 2123–2129.
134. Y. Horbatenko and S. F. Vyboishchikov, *ChemPhysChem*, 2011, **12**, 1118-1129.
135. A. O. F. Jones, PhD Thesis, University of Bath, 2012.
136. A. A. Kallay, PhD Thesis, University of Glasgow, 2012.
137. K. Molcanov and B. Kojic-Prodic, *CrystEngComm*, 2010, **12**, 925-939.
138. M. S. Adam, A. Parkin, L. H. Thomas and C. C. Wilson, *CrystEngComm*, 2010, **12**, 917-924.
139. L. H. Thomas, M. S. Adam, A. O'Neill and C. C. Wilson, *Acta Crystallogr. Sect. C*, 2013, **69**, 1279-1288.
140. A. R. West, *Basic Solid State Chemistry*, John Wiley & Sons Ltd., Chichester, 2nd edn., 1991.
141. W. Clegg, *Crystal Structure Determination*, Oxford University Press, Oxford, 1998.
142. W. Massa, *Crystal Structure Determination*, Springer, Berlin, 2000.
143. G. H. Stout and L. H. Jensen, *X-ray Structure Determination*, John Wiley & Sons Ltd., New York, 1989.
144. G. Giacovazzo, H. Monaco, G. Artioli, D. Viterbo, G. Ferraris, G. Gilli, G. Zanotti and G. Catti, *Fundamentals of Crystallography*, Oxford University Press, Oxford, 2002.
145. M. F. C. Ladd, *Symmetry in Molecules and Crystals*, Ellis Horwood Limited, Chichester, 1989.
146. M. A. Jail, H. J. Sawant and A. P. Kulkarni, *Applied Science - I*, Technical Publications Pune, Pune, 2009.
147. L. E. Smart and E. A. Moore, *Solid State Chemistry: an Introduction*, CRC Press, Taylor and Francis Group, Boca Raton, 2005.

148. C. Hammond, *The Basics of Crystallography and Diffraction*, International Union of Crystallography, Oxford University Press, Oxford, 3rd edn., 2009.
149. H. Shmueli, *Theories and Techniques of Crystal Structure Determination*, International Union of Crystallography, Oxford University Press, Oxford, 2007.
150. P. P. Ewald, *Fifty Years of X-ray Diffraction*, International Union of Crystallography, Springer, Chester, 1st edn., 1962.
151. R. Copley, presented in part at the The 14th BCA/CCG Intensive Teaching School in X-ray Structure Analysis, Trevelyan College, Durham, U.K., April 2013.
152. R. I. Cooper, A. L. Thompson and D. J. Watkin, *J. Appl. Crystallogr.*, 2010, **43**, 1100-1107.
153. W. Clegg, A. J. Blake, R. O. Gould and P. Main, *Crystal Structure Analysis: Principles and Practice*, Oxford University Press, Oxford, 2001.
154. Z. Dauter and K. S. Wilson, *Acta Phys. Pol. A*, 1994, **8G**, 477-486.
155. S. M. Gruner, M. W. Tate and E. F. Eikenberry, *Rev. Sci. Instrum.*, 2002, **73**, 2815-2842.
156. A. Hoffman, M. Loose and V. Suntharalingam, *Exp. Astron.*, 2006, **19**, 111-134.
157. C. Broennimann, E. F. Eikenberry, B. Henrich, R. Horisberger, G. Huelsen, E. Pohl, B. Schmitt, C. Schulze-Briese, M. Suzuki, T. Tomizaki, H. Toyokawa and A. Wagner, *J. Synchrotron Rad.*, 2006, **13**, 120-130.
158. M. M. Woolfson, *An Introduction to X-ray Crystallography*, Cambridge University Press, Cambridge, 2nd edn., 1997.
159. M. Mahon, *CH40131/CH40155: Advanced Structural Methods/Semester 1/University of Bath*, 2015.
160. P. Main and L. Palatinus, presented in part at the The 14th BCA/CCG Intensive Teaching School in X-ray Structure Analysis, Trevelyan College, Durham, U. K., April 2013.
161. R. I. Cooper and D. Watkin, presented in part at the The 14th BCA/CCG Intensive Teaching School in X-ray Structure Analysis, Trevelyan College, Durham, U. K., April 2013.
162. D. W. Bennett, *Understanding Single-Crystal X-ray Crystallography*, Wiley-VCH, Weinheim, 2010.
163. P. V. Afonine, R. W. Grosse-Kunstleve, A. Urzhumtsev and P. D. Adams, *J. Appl. Crystallogr.*, 2009, **42**, 607-615.
164. V. Schomaker and K. N. Trueblood, *Acta Crystallogr. Sect. B*, 1968, **24**, 63-76.
165. M. G. Rossmann and D. M. Blow, *Acta Crystallogr.*, 1962, **15**, 24-31.
166. J. D. Dunitz, *X-ray Analysis and the Structure of Organic Molecules*, Cornell University Press, Basel, 1979.
167. G. W. Stinton and J. S. O. Evans, *J. Appl. Crystallogr.*, 2007, **40**, 87-95.
168. A. A. Coelho, *Topas-Academic V5.0*, 2013, Bruker AXS Inc.

169. A. F. Mabied, M. Müller, R. E. Dinnebier, S. Nozawa, M. Hoshino, A. Tomita, T. Sato and S.-i. Adachi, *Acta Crystallogr. Sect. B*, 2012, **68**, 424-430.
170. I. Halasz, R. E. Dinnebier and R. Angel, *J. Appl. Crystallogr.*, 2010, **43**, 504-510.
171. G. Agostini, C. Lamberti, L. Palin, M. Milanesio, N. Danilina, B. Xu, M. Janousch and J. A. van Bokhoven, *J. Am. Chem. Soc.*, 2010, **132**, 667-678.
172. V. P. Ting, P. F. Henry, M. Schmidtmann, C. C. Wilson and M. T. Weller, *Phys. Chem. Chem. Phys.*, 2012, **14**, 6914-6921.
173. H. Winick, *SciAm*, 1987, 88-99.
174. P. K. Duke, *Synchrotron Radiation: Production and Properties*, Oxford University Press, Oxford, 2000.
175. A. L. Thompson, presented in part at the The 14th BCA/CCG Intensive Teaching School in X-ray Structure Analysis, Trevelyan College, Durham, UK, April 2013.
176. *Soleil*, http://www.synchrotron-soleil.fr/, Accessed 16/06/16.
177. *Instrumentation II: Synchrotron Sources and Methods*, http://pd.chem.ucl.ac.uk/pdnn/inst2/synindex.htm, Accessed 09/07/2016.
178. J. R. Helliwell, *X-ray Diffraction at Synchrotron Light Sources. In: Encyclopedia of Life Sciences (ELS)*, John Wiley & Sons Ltd., Chichester, 2010.
179. *Australian Synchrotron*, http://www.synchrotron.org.au/synchrotron-science/how-is-synchrotron-light-created, Accessed 20/06/2016.
180. *NSRRC What is Synchtron Radiation?*, http://www.nsrrc.org.tw/english/lightsource.aspx, Accessed 09/07/2016.
181. P. Coppens, *Synchrotron Radiation Crystallography*, Academic Press Ltd., London, 1992.
182. A. Maity, R. Dutta, B. Penkala, M. Ceretti, A. Letrouit-Lebranchu, D. Chernyshov, A. Perichon, A. Piovano, A. Bossak, M. Meven and W. Paulus, *J. Phys. D: Appl. Phys.*, 2015, **48**, 504004.
183. J. M. Cole, P. R. Raithby, M. Wulff, F. Schotte, A. Plech, S. J. Teat and G. Bushnell-Wye, *Faraday Discuss.*, 2003, **122**, 119-129.
184. P. R. Mallinson, G. Barr, S. J. Coles, T. N. Guru Row, D. D. MacNicol, S. J. Teat and K. Woźniak, *J. Synchrotron Rad.*, 2000, **7**, 160-166.
185. M. R. V. Jorgensen, V. R. Hathwar, N. Bindzus, N. Wahlberg, Y.-S. Chen, J. Overgaard and B. B. Iversen, *IUCrJ*, 2014, **1**, 267-280.
186. K. D. M. Harris and E. Y. Cheung, *Chem. Soc. Rev.*, 2004, **33**, 526-538.
187. M. J. Jones, I. J. Shannon and K. D. M. Harris, *J. Chem. Soc., Faraday Trans.*, 1996, **92**, 273-279.
188. V. Pecharsky and P. Zavalij, *Fundamentals of Powder Diffraction and Structural Characterization of Materials*, Springer, New York, 2nd edn., 2009.

189. P. Atkins and J. de Paula, *Elements of Physical Chemistry*, Oxford University Press, Oxford, 4th edn., 2007.
190. K. Lukas and P. K. LeMaire, *Resonance*, 2009, **14**, 807-817.
191. W. W. Wendlandt and P. K. Gallagher, in *Thermal characterisation of Polymeric Materials*, ed. E. A. Turi, Academic Press, Inc., New York, 1981.
192. T. R. Crompton, *Thermal Methods of Polymer Analysis*, ISmithers Rapra Publishing, Shrewsbury, 2013.
193. P. Parlouër, in *Calorimetry and Thermal Methods in Catalysis*, ed. A. Auroux, Springer Berlin, 2013.
194. P. Gill, T. T. Moghadam and B. Ranjbar, *J. Biomol. Tech.*, 2010, **21**, 167-193.
195. H.-H. Tung, E. L. Paul, M. Midler and J. A. McCauley, *Crystallisation of Organic Components: An Industrial Perspective*, John Wiley & Sons Ltd., New Jersey, 2009.
196. M. R. Caira, in *Design of Organic Solids*, ed. E. E. Weber, Springer, Berlin, 1998.
197. A. Jacobs, L. R. Nassimbeni, H. Su and B. Taljaard, *Org Biomol Chem*, 2005, **3**, 1319-1322.
198. J.-L. Dirion, C. Reverte and M. Cabassud, *Chem. Eng. Res. Des.*, 2008, **86**, 618-625.
199. T. Kimura, Y. Kasai, T. Tsujimoto, E. Kawamura, T. Kamiyama and H. Aki, *J. Mass Spectrom. Soc. Jpn.*, 2003, **51**, 242-246.
200. *Thermogravimetric Analysis: A Beginner's Guide*, http://www.perkinelmer.co.uk/CMSResources/Images/44-74556GDE_TGABeginnersGuide.pdf, Accessed 09/07/2016.
201. Y. Koito, K. Yamada and S. Ando, *J Incl. Phenom Macrocycl. Chem.*, 2012, **76**, 143-150.
202. P. G. Jones, *Chem. Br.*, 1981, **17**, 222-225.
203. C. B. Aakeröy, S. Forbes and J. Desper, *J. Am. Chem. Soc.*, 2009, **131**, 17048-17049.
204. K. Wittering, J. King, L. H. Thomas and C. C. Wilson, *Crystals*, 2014, **4**, 123.
205. W. Beckmann, *Crystallization: Basic Concepts and Industrial Applications*, Wiley-VCH, Weinheim, 2013.
206. T. Irisawa, in *Crystal Growth Technology*, eds. T. Ohachi, W. Michaeli, H. Warlimont and E. Weber, William Andrew Inc., Norwich, 2003.
207. R. D. Burbank and K. Knox, *Rev. Sci. Instrum.*, 1962, **33**, 218-222.
208. *Rigaku Corporation*, http://www.rigaku.com/en/smc, Accessed 10/06/2016.
209. *CrystalClear 2.0*, Rigaku Corporation, Tokyo, Japan.
210. *Rigaku Oxford Diffraction*, http://www.rigaku.com/en/smc, Accessed 06/06/2016.
211. *CrysAlis Pro*, Rigaku Oxford Diffraction, Kent, U.K.
212. *DIALS*, Diamond Light Source, Harwell, U.K.
213. G. Winter, *J. Appl. Crystallogr.*, 2010, **43**, 186-190.
214. *Bruker AXS Inc.*, https://www.bruker.com/, Accessed 10/06/16.

215. *Apex2*, Bruker AXS Inc., Madison, Wisconsin, U.S.A.
216. *SADABS*, Bruker AXS Inc., Madison, Wisconsin, USA.
217. *XPREP*, Bruker AXS Inc., Madison, Wisconsin, USA.
218. G. Sheldrick, *Acta Crystallogr. Sect. A*, 2008, **64**, 112-122.
219. G. Sheldrick, *Acta Crystallogr. Sect. C*, 2015, **71**, 3-8.
220. A. Spek, *Acta Crystallogr. Sect. B*, 2009, **65**, 148-155.
221. L. Farrugia, *J. Appl. Crystallogr.*, 2012, **45**, 849-854.
222. C. F. Macrae, P. R. Edgington, P. McCabe, E. Pidcock, G. P. Shields, R. Taylor, M. Towler and J. van de Streek, *J. Appl. Crystallogr.*, 2006, **39**, 453-457.
223. V. Petricek, M. Dusek and L. Palatinus, *Z. Kristallogr.*, 2014, 345-352.
224. M. Ladd and R. Palmer, *Structure Determination by X-ray Crystallography*, Springer, New York, 5th edn., 2003.
225. *JEdit4.3*, Jedit, www.jedit.org.
226. K. D. M. Harris and M. Tremayne, *Chem. Mater.*, 1996, **8**, 2554-2570.
227. C. Grygiel, H. Lebius, S. Bouffard, A. Quentin, J. M. Ramillon, T. Madi, S. Guillous, T. Been, P. Guinement, D. Lelièvre and I. Monnet, *Rev. Sci. Instrum.*, 2012, **83**, 013902.
228. *Agilent Technologies Ltd.*, http://www.agilent.co.uk/home, Accessed 10/06/16.
229. *Oxford Cryosystems Ltd.*, http://www.oxcryo.com/, Accessed 06/06/2016.
230. *Oxford Instruments*, http://www.oxford-instruments.com/, Accessed 12/07/2016.
231. H. Nowell, S. A. Barnett, K. E. Christensen, S. J. Teat and D. R. Allan, *J. Synchrotron Rad.*, 2012, **19**, 435-441.
232. *Crystal Logic*, http://www.xtallogic.com/, Accessed 10/06/2016.
233. *Fluid Film Devices*, http://www.fluidfilmdevices.co.uk/, Accessed 13/06/2016.
234. *DECTRIS*, https://www.dectris.com/, Accessed 10/06/16.
235. *Generic Data Acquisition Software*, Diamond Light Source, Harwell, U.K.
236. *Newport*, https://www.newport.com/, Accessed 13/06/2016.
237. *Beamline 11.3.1 Chemical Crystallography*, https://sites.google.com/a/lbl.gov/bl-11-3-1-chemical-crystallography/home, Accessed 06/06/2016.
238. P. Allé, E. Wenger, S. Dahaoui, D. Schaniel and C. Lecomte, *Phys. Scr.*, 2016, **91**.
239. T. Skarzynski, *Acta Crystallogr. Sect. B*, 2013, **69**, 1283-1288.
240. P. Kraft, A. Bergamaschi, C. Broennimann, R. Dinapoli, E. F. Eikenberry, B. Henrich, I. Johnson, A. Mozzanica, C. M. Schleputz, P. R. Willmott and B. Schmitt, *J. Synchrotron Rad.*, 2009, **16**, 368-375.
241. A. Boultif and D. Louer, *J. Appl. Crystallogr.*, 2004, **37**, 724-731.
242. T. Williams and C. Kelley, *Gnuplot*, http://www.gnuplot.info/.
243. N. Stieger, M. Aucamp, S. Zhang and M. M. de Villiers, *Am. Pharmaceut. Rev.*, 2012.
244. *Mettler Toledo*, http://uk.mt.com/gb/en/home.html, Accessed 13/06/2016.

245. *Leica Microsystems*, http://www.leica-microsystems.com/home/, Accessed 07/07/2016.
246. *Lumenera*, http://www.lumenera.com/, Accessed 22/06/2016.
247. *Studio86Designs*, http://www.studio86designs.co.uk/index.html, Accessed 13/06/2016.
248. *TA Instruments*, http://www.tainstruments.com/, Accessed 13/06/2016.
249. *TA Universal Analysis 2000*, TA Instruments, Hertfordshire, UK.
250. *Thermal Advantage for Q Series*, TA Instruments, Hertfordshire, U.K.
251. *Setaram Instrumentation KEP Technologies*, http://www.setaram.com/, Accessed 12/07/2016.
252. *AKTS*, http://www.akts.com/, Accessed 09/07/2016.
253. *Calisto*, AKTS, Siders, Switzerland.
254. *Pfeiffer Vacuum*, https://www.pfeiffer-vacuum.com/en/, Accessed 13/06/2016.
255. *Quadera*, Pfeiffer Vacuum, Asslar, Germany.
256. H. Hosomi, S. Ohba and Y. Ito, *Acta Crystallogr. Sect. C*, 2000, **56**, e144-e146.
257. D. Lynch, G. Smith, K. Byriel and C. Kennard, *Aust. J. Chem.*, 1991, **44**, 809-819.
258. X. Ding, S. Wang, W. He and W. Huang, *Acta Crystallogr. Sect. E*, 2011, **67**, o2833.
259. A. Ranganathan and V. R. Pedireddi, *Tetrahedron Lett.*, 1998, **39**, 1803-1806.
260. R. H. Blessing and D. A. Langs, *J. Appl. Crystallogr.*, 1987, **20**, 427-428.
261. Z. Dauter, *Acta Crystallogr. Sect. B*, 1999, **55**, 1703-1717.
262. C. V. K. Sharma, K. Panneerselvam, T. Pilati and G. R. Desiraju, *J. Chem. Soc. Perkin Trans. 2*, 1993, 2209-2216.
263. G. Smith, U. D. Wermuth, D. J. Young and J. M. White, *Acta Crystallogr. Sect. C*, 2009, **65**, o543-o548.
264. C. L. Jones, C. C. Wilson and L. H. Thomas, *CrystEngComm*, 2014, **16**, 5849-5858.
265. V. R. Pedireddi, W. Jones, A. P. Chorlton and R. Docherty, *Chem. Commun.*, 1996, 987-988.
266. M. Ratajczak-Sitarz and A. Katrusiak, *J. Mol. Struct.*, 2011, **995**, 29-34.
267. P. Grobelny, A. Mukherjee and G. R. Desiraju, *CrystEngComm*, 2011, **13**, 4358-4364.
268. M. Schmidtmann, L. J. Farrugia, D. S. Middlemiss, M. J. Gutmann, G. J. McIntyre and C. C. Wilson, *J. Phys. Chem. A*, 2009, **113**, 13985-13997.
269. L. C. Remer and J. H. Jensen, *J. Phys. Chem. A*, 2000, **104**, 9266-9275.
270. *ACD/I-Lab, National Chemical Database Service*, http://cds.rsc.org/, Accessed 10/07/2016.
271. D. D. Perrin, *Dissociation Constants of Organic Bases in Aqueous Solution*, Butterworths, London, 1965.
272. E. Marfo-Owusu and A. L. Thompson, *X-Ray Struct. Anal. Online*, 2014, **30**, 45-46.
273. N. Shan, A. D. Bond and W. Jones, *Cryst. Eng.*, 2002, **5**, 9-24.
274. H. Ishida and S. Kashino, *Z. Naturforsch.*, 2002, **A** 829–836.

275. M. B. Zaman, M. Tomura and Y. Yamashita, *Org. Lett.*, 2000, **2**, 273-275.
276. H. Ishida and S. Kashino, *Acta Crystallogr. Sect. C*, 1999, **55**, 1149-1152.
277. D.-J. Yang and S.-H. Qu, *Acta Crystallogr. Sect. E*, 2006, **62**, o4720-o4722.
278. D. Braga, F. Grepioni and A. G. Orpen, *Crystal Engineering: From Molecules and Crystals to Materials*, Springer Science+Business Media, B.V., Dordrecht, 1999.
279. P. Vishweshwar, A. Nangia and V. M. Lynch, *J. Org. Chem.*, 2002, **67**, 556-565.
280. S. Tothadi and G. R. Desiraju, *Philos. Trans. A Math. Phys. Eng. Sci.*, 2012, **370**, 2900-2915.
281. Y.-B. Wang, W.-J. Zhuang, L.-P. Jin and S.-Z. Lu, *J. Mol. Struct.*, 2005, **737**, 165-172.
282. S. K. Callear, M. B. Hursthouse and T. L. Threlfall, *CrystEngComm*, 2010, **12**, 898-908.
283. X.-G. Meng, Z.-D. Lin and A.-M. Li, *Acta Crystallogr. Sect. C*, 2008, **64**, o322-o325.
284. L. Wei, Z. Wang and X. Meng, *Acta Crystallogr. Sect. C*, 2009, **65**, o453-o456.
285. Z.-L. Wang and L.-H. Wei, *Acta Crystallogr. Sect. E*, 2007, **63**, o2574-o2575.
286. E. Marfo-Owusu and A. Thompson, *X-Ray Struct. Anal. Online*, 2014, **30**, 47-48.
287. V. Murugesan, G. Vadivelan, M. Saravanabhavan and M. Sekar, *CSD Communication*, 2014.
288. A. Sikorski and D. Trzybiński, *J. Mol. Struct.*, 2013, **1049**, 90-98.
289. H. Ishida, *Acta Crystallogr. Sect. E*, 2004, **60**, o2005-o2006.
290. M. A. Abbasi, K. Nazir, M. Akkurt, Aziz-ur-Rehman, I. U. Khan and G. Mustafa, *Acta Crystallogr. Sect. E*, 2011, **67**, o2375.
291. C. Foces-Foces, A. L. Llamas-Saiz, P. Lorente, N. S. Golubev and H.-H. Limbach, *Acta Crystallogr. Sect. C*, 1999, **55**, 377-381.
292. Z. M. Jin, Y. J. Pan, D. J. Xu and Y. Z. Xu, *J. Chem. Crystallogr.*, **30**, 119-122.
293. S. Harkema, J. H. M. ter Brake and R. B. Helmholdt, *Acta Crystallogr. Sect. C*, 1984, **40**, 1733-1734.
294. G. J. van Hummel and R. B. Helmholdt, *Acta Crystallogr. Sect. C*, 1991, **47**, 213-215.
295. R. Stewart and M. R. Granger, *Can. J. Chem.*, 1961, **39**, 2508-2515.
296. S. J. Ford, G. J. McIntyre, M. R. Johnson and I. R. Evans, *CrystEngComm*, 2013, **15**, 7576-7582.
297. C. C. Seaton, *CrystEngComm*, 2014, **16**, 5878-5886.
298. C. B. Aakeröy, A. M. Beatty, B. A. Helfrich and M. Nieuwenhuyzen, *Cryst. Growth Des.*, 2003, **3**, 159-165.
299. F. Fontaine-Vive, M. R. Johnson, G. J. Kearley, J. A. K. Howard and S. F. Parker, *J. Am. Chem. Soc.*, 2006, **128**, 2963-2969.
300. C. A. Morrison, M. M. Siddick, P. J. Camp and C. C. Wilson, *J. Am. Chem. Soc.*, 2005, **127**, 4042-4048.
301. C. R. L. Martin, PhD Thesis, University of Glasgow, 2011.

302. J. S. O. Evans, *Substitute*, University of Durham, U.K.
303. P. K. Bakshi, T. S. Cameron and O. Knop, *Can. J. Chem.*, 1996, **74**, 201-220.
304. S. C. Zimmerman, *Science*, 1997, **276**, 543-544.
305. C.-K. Lam and T. C. W. Mak, *Cryst. Eng.*, 2000, **3**, 33-40.
306. Q. Li and T. C. W. Mak, *Acta Crystallogr. Sect. B*, 1996, **52**, 989-998.
307. M. J. Horner, S. Grabowski, K. Sandstrom, K. T. Holman, M. Bader and M. C. Ward, *ACA Trans.*, 2004, **39**, 1-10.
308. M. J. Horner, K. T. Holman and M. D. Ward, *J. Am. Chem. Soc.*, 2007, **129**, 14640-14660.
309. M. Etter, D. Parker, S. Ruberu, T. Panunto and D. Britton, *J. Inclusion Phenom. Mol. Recognit. Chem.*, 1990, **8**, 395-407.
310. S. Bhattacharya and B. K. Saha, *Cryst. Growth Des.*, 2011, **11**, 2194-2204.
311. A. F. Lashua, T. M. Smith, H. Hu, L. Wei, D. G. Allis, M. B. Sponsler and B. S. Hudson, *Cryst. Growth Des.*, 2013, **13**, 3852-3855.
312. P. Brunet, M. Simard and J. D. Wuest, *J. Am. Chem. Soc.*, 1997, **119**, 2737-2738.
313. L. K. Saunders, H. Nowell, P. R. Raithby and C. C. Wilson, *CrystEngComm*, 2016, **18**, 5916-5929.
314. R. C. Bott, G. Smith, U. D. Wermuth and N. C. Dwyer, *Aust. J. Chem.*, 2000, **53**, 767-777.
315. M. Colapietro, A. Domenicano, C. Marciante and G. Portalone, *Acta Crystallogr. Sect. A*, 1984, **40**, C98-C99.
316. S. V. Kolotuchin, E. E. Fenlon, S. R. Wilson, C. J. Loweth and S. C. Zimmerman, *Angew. Chem., Int. Ed.*, 1996, **34**, 2654-2657.
317. H. I. Süss and J. Hulliger, *Microporous Mesoporous Mater.*, 2005, **78**, 23-27.
318. E. Haldoupis, S. Nair and D. S. Sholl, *Phys. Chem. Chem. Phys.*, 2011, **13**, 5053-5060.
319. A. Spek, *Acta Crystallogr. Sect. C*, 2015, **71**, 9-18.
320. K. Endo, T. Sawaki, M. Koyanagi, K. Kobayashi, H. Masuda and Y. Aoyama, *J. Am. Chem. Soc.*, 1995, **117**, 8341-8352.
321. J. Wack, R. Siegel, T. Ahnfeldt, N. Stock, L. Mafra and J. Senker, *J. Phys. Chem. C*, 2013, **117**, 19991-20001.
322. K. Beketov, E. Weber, B. T. Ibragimov, J. Seidel and K. Köhnke, *Adv. Mater.*, 2000, **12**, 664-667.
323. M. Brustolon, A. L. Maniero and U. Segre, *J. Chem. Soc. Perkin Trans. 2*, 1997, 2519-2524.
324. K. Beketov, E. Weber, J. Seidel, K. Kohnke and B. Ibragimov, *Cryst. Eng.*, 2000, **3**, 101.
325. E. Zass, D. A. Plattner, A. K. Beck and M. Neuburger, *Helv. Chim. Acta*, 2002, **85**, 4012-4045.
326. V. A. Logvinenko and D. V. Soldatov, *J. Struct. Chem.*, 1998, **39**, 619-621.

327. T. Hosokawa, S. Datta, A. R. Sheth and D. J. W. Grant, *CrystEngComm*, 2004, **6**, 243-249.
328. L. H. Thomas, E. Cheung, A. O. F. Jones, A. A. Kallay, M.-H. Lemée-Cailleau, G. J. McIntyre and C. C. Wilson, *Cryst. Growth Des.*, 2012, **12**, 1746-1751.
329. E. Weber, *Inclusion Compounds*, Oxford University Press, Oxford, 1991.
330. E. R. T. Tiekink, *The Rigaku Journal*, 2002, **19**.

Appendix A6 (Chapter 6)

A6.1 Molecular complex preparation

Substituted urea organic acid molecular complexes

***N,N*-dimethylurea and 2-nitrobenzoic acid 1:1 (DMU2-NBA)**

Colourless plate crystals of the 1:1 complex of *N,N*-dimethylurea and 2-nitrobenzoic acid were grown from slow evaporation of a 1:1 stoichiometric ratio of the two components in ethanol solvent at room temperature.

***N,N*-dimethylurea and 3-nitrobenzoic acid 1:1 (DMU3-NBA)**

Colourless plate crystals of the 1:1 complex of *N,N*-dimethylurea and 3-nitrobenzoic acid were grown from slow evaporation of a 1:1 stoichiometric ratio of the two components in acetone solvent at room temperature.

***N,N*-dimethylurea and 3-cyanobenzoic acid 2:2 (DMU3-CBA)**

Colourless needle crystals of the 2:2 complex of *N,N*-dimethylurea and 3-cyanobenzoic acid were grown from slow evaporation of a 1:1 stoichiometric ratio of the two components in acetonitrile solvent at room temperature.

***N,N*-dimethylurea and 4-cyanobenzoic acid 1:1 (DMU4-CBA)**

Colourless block crystals of the 1:1 complex of *N,N*-dimethylurea and 4-cyanobenzoic acid were grown from slow evaporation of a 1:1 stoichiometric ratio of the two components in methanol solvent at room temperature.

***N,N*-dimethylurea and 2,4-dinitrobenzoic acid 1:1 (DMU2,4-DNBA)**

Colourless block crystals of the 1:1 complex of *N,N*-dimethylurea and 2,4-dinitrobenzoic acid were grown from slow evaporation of a 2:1 stoichiometric ratio of the two components in methanol solvent at 40 °C.

***N,N*-dimethylurea and 3,5-dinitrobenzoic acid 1:1 (DMU3,5-DNBA)**

Colourless plate crystals of the 1:1 complex of *N,N*-dimethylurea and 3,5-dinitrobenzoic acid were grown from slow evaporation of 2:1 stoichiometric ratio of the two components in ethanol solvent at room temperature.

Urea and isophthalic acid 1:1 (UIP)

Colourless needle crystals of the 1:1 complex of urea and isophthalic acid were grown from slow evaporation of a 2:1 stoichiometric ratio of the two components in ethanol solvent at room temperature.

Urea and 5-aminoisophthalic acid 1:1 (U5-AIP)

Pale pink plate crystals of the 1:1 complex of urea and 5-aminoisophthalic acid were grown from slow evaporation of a 2:1 stoichiometric ratio of the two components in methanol solvent at room temperature.

Urea and 5-nitroisophthalic acid 4:1 (U5-NIP)

Colourless plate crystals of the 4:1 complex of urea and 5-nitroisophthalic acid were grown from slow evaporation of a 2:1 stoichiometric ratio of the two components in ethanol solvent at room temperature.

***N*-methylurea and phthalic acid 1:1 (MUP)**

Colourless plate crystals of the 1:1 complex of *N*-methylurea and phthalic acid were grown from slow evaporation of 2:1 stoichiometric ratio of the two components in ethanol solvent at 30 °C.

***N*-methylurea and isophthalic acid 1:1 (MUIP)**

Colourless plate crystals of the 1:1 complex of *N*-methylurea and isophthalic acid were grown from slow evaporation of a 2:1 stoichiometric ratio of the two components in methanol solvent at 4 °C.

***N*-methylurea and 5-nitroisophthalic acid 2:1 (MU5-NIP)**

Colourless plate crystals of the 2:1 complex of *N*-methylurea and 5-nitroisophthalic acid were grown from slow evaporation of a 2:1 stoichiometric ratio of the two components in acetone solvent at 40 °C.

***N*-methylurea and 5-aminoisophthalic acid 1:1 (MU5-AIP)**

Colourless plate crystals of the 1:1 complex of *N*-methylurea and 5-aminoisophthalic acid were grown from slow evaporation of a 2:1 stoichiometric ratio of the two components in acetone solvent at 40 °C.

***N,N*-dimethylurea and phthalic acid 2:1 (DMUP)**

Colourless plate crystals of the 2:1 complex of *N,N*-dimethylurea and phthalic acid were grown from slow evaporation of a 2:1 stoichiometric ratio of the two components in ethanol solvent at room temperature.

***N,N*-dimethylurea and isophthalic acid 2:1 (DMUIP)**

Colourless plate crystals of the 2:1 complex of *N,N*-dimethylurea and isophthalic acid were grown from slow evaporation of a 2:1 stoichiometric ratio of the two components in ethanol solvent at 4 °C.

***N,N*-dimethylurea and 5-aminoisophthalic acid 2:1 (DMU5-AIP)**

Colourless plate crystals of the 2:1 complex of *N,N*-dimethylurea and 5-aminoisophthalic acid were grown from slow evaporation of a 2:1 stoichiometric ratio of the two components in methanol solvent at 40 and 50 °C.

***N,N*-dimethylurea and 3-nitrophthalic acid 1:1 (DMU3-NP)**

Colourless plate crystals of the 1:1 complex of *N,N*-dimethylurea and 3-nitrophthalic acid were grown from slow evaporation of a 2:1 stoichiometric ratio of the two components in methanol solvent at 4 °C.

***N,N*-dimethylurea and 5-nitroisophthalic acid 2:1 (DMU5-NIP)**

Colourless plate crystals of the 2:1 complex of *N,N*-dimethylurea and 5-nitroisophthalic acid were grown from slow evaporation of a 2:1 stoichiometric ratio of the two components in methanol solvent at room temperature.

***N*-phenylurea and 2,4-dinitrobenzoic acid 1:1 (PhU2,4-DNBA)**

Yellow block crystals of the 1:1 complex of *N*-phenylurea and 2,4-dintirobenzoic acid were grown from slow evaporation of a 1:1 stoichiometric ratio of the two components in methanol solvent at room temperature.

***N*-phenylurea and 3-nitrophthalic acid 1:1 (PhU3-NP)**

Yellow block crystals of the 1:1 complex of *N*-phenylurea and 3-nitrophthalic acid were grown from slow evaporation of a 2:1 stoichiometric ratio of the two components in methanol solvent at 40 °C.

***N*-phenylurea and 5-nitroisophthalic acid 2:1 (PhU5-NIP I)**

Pale yellow hexagonal crystals of the 2:1 complex of *N*-phenylurea and 5-nitroisophthalic acid were grown from slow evaporation of a 2:1 stoichiometric ratio of the two components in water solvent at room temperature.

***N*-phenylurea and 5-nitroisophthalic acid 1:1 (PhU5-NIP II)**

Yellow block crystals of the 1:1 complex of *N*-phenylurea and 5-nitroisophthalic acid were grown from slow evaporation of a 2:1 stoichiometric ratio of the two components in diethylether solvent at room temperature.

***N,N'*-dimethylurea and 5-aminoisophthalic acid 1:1 (DM'U5-AIP)**

Yellow block crystals of the 1:1 complex of *N,N'*-dimethylurea and 5-aminoisophthalic acid were grown from slow evaporation of a 2:1 stoichiometric ratio of the two components in ethanol solvent at 30 °C.

3-deazauracil organic acid molecular complexes

3-deazauracil and 3-nitrophthalic acid 2:1 (3-DAZA3-NP)

Yellow block crystals of the 2:1 complex of 3-deazauracil and 3-nitrophthalic acid were grown from slow evaporation of a 2:1 stoichiometric ratio of the two components in ethanol solvent at 40 °C.

3-deazauracil and 2,4-dinitrobenzoic acid 1:1 (3-DAZA2,4-DNBA)

Yellow block crystals of the 1:1 complex of 3-deazauracil and 2,4-dinitrobenzoic acid were grown from slow evaporation of a 2:1 stoichiometric ratio of the two components in isopropanol solvent at 40 °C.

3-deazauracil and chloranilic acid 1:1 (3-DAZAClA)

Purple plate crystals of the 1:1 complex of 3-deazauracil and chloranilic acid were grown from slow evaporation of a 1:2 stoichiometric ratio of the two components in isopropanol solvent at room temperature.

3-deazauracil, bromanilic acid and water 2:1:2 (3-DAZABrA hydrate)

Purple plate crystals of the 2:1:2 complex of 3-deazauracil, bromanilic acid and water were grown from slow evaporation of a 1:1 stoichiometric ratio of the two components in ethanol solvent at 4 °C.

N-heterocycle organic acid molecular complexes

isonicotinamide phthalic acid 2:1 (INP)

Colourless plank crystals of the 2:1 complex of isonicotinamide and phthalic acid were grown from slow evaporation of a 2:1 stoichiometric ratio of the two components in methanol solvent at 30 °C.

isonicotinamide 2,4-dinitrobenzoic acid 1:1 (IN2,4-DNBA I)

Colourless block crystals of the 1:1 complex of isonicotinamide and 2,4-dinitrobenzoic acid were grown from slow evaporation of a 1:1 stoichiometric ratio of the two components in methanol solvent at 30 °C.

isonicotinamide 2,4-dinitrobenzoic acid 2:2 (IN2,4-DNBA) II

Colourless block crystals of the 2:2 complex of isonicotinamide and 2,4-dinitrobenzoic acid were grown from slow evaporation of a 1:1 stoichiometric ratio of the two components in methanol solvent at room temperature.

isonicotinamide 2,4-dinitrobenzoic acid methanol solvate 1:2:1 (IN2,4-DNBA III)

Colourless block crystals of the 1:2:1 complex of isonicotinamide and 2,4-dinitrobenzoic acid were grown from slow evaporation of a 1:1 stoichiometric ratio of the two components in methanol solvent at 4 °C.

isoniazid 2,4-dinitrobenzoic acid 1:1 (INZ2,4-DNBA)

Colourless block crystals of the 1:1 complex of isoniazid and 2,4-dinitrobenzoic acid were grown from slow evaporation of a 1:1 stoichiometric ratio of the two components in methanol solvent at 4 °C.

isoniazid phthalic acid 1:1 (INZP)

Yellow plate crystals of the 1:1 complex of isoniazid and phthalic acid were grown from slow evaporation of a 2:1 stoichiometric ratio of the two components in methanol solvent at room temperature.

isoniazid 5-nitroisophthalic acid 1:1 (INZ5-NIP)

Yellow plate crystals of the 1:1 complex of isoniazid and 5-nitroisophthalic acid were grown from slow evaporation of a 2:1 stoichiometric ratio of the two components in methanol solvent at 30 °C.

N-heterocycle anilic acid molecular complexes

pyrazole bromanilic acid 1:1 (PYBrA)

Red block crystals of the 1:1 complex of pyrazole and bromanilic acid were grown from slow evaporation of a 2:1 stoichiometric ratio of the two components in isopropanol solvent at room temperature.

pyrazole chloranilic acid hydrate 1:1:1 (PYClA hydrate)

Red block crystals of the 1:1:1 complex of pyrazole, chloranilic acid and water were grown from slow evaporation of a 2:1 stoichiometric ratio of the two components in isopropanol solvent at room temperature.

4(5)-methylimidazole bromanilic acid 1:1 (4(5)-MIBrA)

Purple plank crystals of the 1:1 complex of 4(5)-methylimidazole and bromanilic acid were grown from slow evaporation of a 1:1 stoichiometric ratio of the two components in acetone solvent at room temperature.

4(5)-methylimidazole chloranilic acid hydrate 2:1:1:2 (4(5)-MIClA hydrate)

Purple needle crystals of the 2:1:1:2 complex of 4(5)-methylimidazole, chloranilic acid and water were grown from slow evaporation of a 1:1 stoichiometric ratio of the two components in ethanol solvent at room temperature.

4-acetylpyridine bromanilic acid 1:1 (4-APBrA)

Purple plank crystals of the 1:1 complex of 4-acetylpyridine and bromanilic acid were grown from slow evaporation of a 1:1 stoichiometric ratio of the two components in acetone solvent at room temperature.

4-acetylpyridine chloranilic acid 1:1 (4-APClA)

Purple plank crystals of the 1:1 complex of 4-acetylpyridine and chloranilic acid were grown from slow evaporation of a 1:1 stoichiometric ratio of the two components in acetone solvent at room temperature.

1,2,4-*1H*-triazole chloranilic acid hydrate 2:1:1 (1,2,4-TZClA hydrate)

Red needle crystals of the 2:1:1 complex of 1,2,4-*1H*-triazole, chloranilic acid and water were grown from slow evaporation of a 2:1 stoichiometric ratio of the two components in water solvent at room temperature.

3,5-dimethylpyrazole bromanilic acid hydrate 2:1:2 (3,5-DMPYBrA hydrate)

Red hexagonal block crystals of the 2:1:2 complex of 3,5-dimethylpyrazole, bromanilic acid and water were grown from slow evaporation of a 1:1 stoichiometric ratio of the two components in acetone solvent at room temperature.

3,5-dimethylpyrazole chloranilic acid hydrate 2:1:2 (3,5-DMPYClA hydrate)

Red hexagonal block crystals of the 2:1:2 complex of 3,5-dimethylpyrazole, chloranilic acid and water were grown from slow evaporation of a 1:2 stoichiometric ratio of the two components in isopropanol solvent at room temperature.

3,5-dimethylpyrazole chloranilic acid 1:1 (3,5-DMPYClA)

Red hexagonal block crystals of the 1:1 complex of 3,5-dimethylpyrazole and chloranilic acid were grown from slow evaporation of a 1:1 stoichiometric ratio of the two components in acetone solvent at room temperature.

A6.2 Crystallographic analysis

For 4-APBrA (100 K), INZP (150, 300, 350 K) single crystal X-ray diffraction data were collected using Cu-K_α radiation on a Rigaku Oxford Diffraction [210] SuperNova four-circle κ geometry diffractometer equipped with a Agilent [228] EoS2 CCD detector.

For DMU2-NBA (150, 300 K), DMU3-NBA (150, 300 K), DMU3-CBA (150, 300 K), PhU2,4-DNBA (150, 300 K), DMU5-NIP (150, 300 K), PhU5-NIP II (150 K), DMU3-NP (150, 300 K), MU5-NIP (150 K), PhU3-NIP (150, 300 K), U5-NIP (150 K), 3-DAZA3-NP (150, 300 K), 3-DAZA2,4-DNBA (150, 300 K), INZ5-NIP (150 K), INZ2,4-DNBA (150, 300 K), 1,2,4-TZClA hydrate (150 K) single crystal X-ray diffraction data were collected using Cu-K_α radiation on a Rigaku Oxford Diffraction [210] SuperNova four-circle κ geometry diffractometer equipped with a Agilent [228] Atlas CCD detector.

For PhU5-NIP I (150 K), IN2,4-DNBA I (150, 300 K), IN2,4-DNBA III (150, 300 K) single crystal X-ray diffraction data were collected using Mo-K_α radiation on a Rigaku Oxford Diffraction [210] Xcalibur four-circle κ geometry diffractometer equipped with a Agilent [228] Atlas CCD detector.

For DMU4-CBA (150, 300 K), MUIP (150, 298 K) single crystal X-ray diffraction data were collected using Mo-K_α radiation on a Rigaku Oxford Diffraction [210] Gemini A-Ultra four-circle κ geometry diffractometer equipped with a Agilent [228] Atlas CCD detector.

For DMU5-AIP (100, 300 K), DMUIP (100, 300 K), MU5-AIP (300 K), U-5AIP (300 K), UIP (100, 300 K), MUP (100, 300 K), DM'U5-AIP (100, 300 K) single crystal X-ray diffraction data were collected on beamline 11.3.1 at the Advanced Light Source, U.S.A [2] using Si (111) monochromated radiation at $\lambda = 0.7749$ Å on a Bruker AXS [214] D8 three-circle diffractometer equipped with a Bruker AXS [214] Photon 100 CMOS detector. The data were collected and processed using Bruker AXS [214] software APEX2 [215] and SADABS-2014/2. [216]

For 3-DAZAClA (100 K), 3,5-DMPYClA hydrate (100 K), 3,5-DMPYClA hydrate (100K), 3,5-DMPYClA (100 K), 4(5)-MIBrA (100 K), 4(5)-MIClA hydrate (100 K), PYBrA (100 K), PYClA hydrate (100 K) single crystal X-ray diffraction data were collected using Mo-K_α radiation on a Rigaku [208] R-Axis Rapid X-ray source equipped with a Rigaku [208] Image plate detector. Data collection and processing were performed using Rigaku [208] CrystalClear™. [209]

The sample temperature was controlled using an Oxford Cryosystems [229] Cryostream Plus on the Rigaku Oxford Diffraction [210] Xcalibur, an Oxford Cryosystems [229] Cryostream 700 on the Rigaku Oxford Diffraction [210] SuperNova and using an Oxford Instruments [230] CryojetXL on the Rigaku [208] R-Axis Rapid.

Data collection and processing were performed for DMU4-CBA, DMU5-NIP, PhU5-NIP II, MUIP, 3-DAZA2,4-DNBA using Rigaku Oxford Diffraction [210] CrysAlisPro [211] version 1.171.37.31.

Data collection and processing were performed for DMU2-NBA, DMU3-NBA, PhU5-NIP I, DMU3-NP, MU5-NIP, PhU3-NP, U5-NIP, 3-DAZA3-NP, 4-APBrA, INZ5-NIP, INZ2,4-DNBA, INZP using Rigaku Oxford Diffraction [210] CrysAlisPro [211] version 1.171.37.33.

Data collection and processing were performed for DMU3-CBA, PhU2,4-DNBA using Rigaku Oxford Diffraction [210] CrysAlisPro [211] version 1.171.37.35.

Data collection and processing were performed for IN2,4-DNBA I, IN2,4-DNBA III using Rigaku Oxford Diffraction [210] CrysAlisPro [211] version 1.171.38.41.

Data collection and processing were performed for 4-APClA using Rigaku Oxford Diffraction [210] CrysAlisPro [211] version 1.171.36.32.

Data collection and processing were performed for 1,2,4-TZClA hydrate using Rigaku Oxford Diffraction [210] CrysAlisPro [211] version 1.171.36.28.

All structures in §A6.2 were solved using SHELXS-2013 [218] and refined using SHELXL-2013 [219] within the WinGX package. [221] Crystallographic data are given in Table A6.1 to Table A6.9.

Table A6.1 Crystallographic data for *N*,*N*-dimethylurea 2-nitrobenzoic acid (DMU2-NBA) (1:1), *N*,*N*-dimethylurea 3-nitrobenzoic acid (DMU3-NBA) (1:1) and *N*,*N*-dimethylurea 3-cyanobenzoic acid (DMU3-CBA) (1:1).

Compound	DMU2-NBA	DMU2-NBA	DMU3-NBA	DMU3-NBA	DMU3-CBA	DMU3-CBA
Diffractometer	SuperNova	SuperNova	SuperNova	SuperNova	SuperNova	SuperNova
Radiation (K/a)	Cu	Cu	Cu	Cu	Cu	Cu
Formula	$C_{10}H_{13}N_3O_5$	$C_{10}H_{13}N_3O_5$	$C_{10}H_{13}N_3O_5$	$C_{10}H_{13}N_3O_5$	$C_{11}H_{13}N_3O_3$	$C_{11}H_{13}N_3O_3$
Mol. W ($gmol^{-1}$)	255.23	255.23	255.23	255.23	235.24	235.24
T (K)	150	300	150	300	150	300
Space group	I_2/a	I_2/a	P-1	P-1	P-1	P-1
a (Å)	13.5517(3)	13.8402(3)	7.0519(12)	7.1237(8)	7.4609(4)	7.5803(4)
b (Å)	11.6443(2)	11.7055(2)	7.9987(9)	8.0294(8)	12.1017(6)	12.1334(7)
c (Å)	14.9057(3)	15.0091(3)	11.5203(15)	11.5818(15)	14.1800(7)	14.2002(8)
α (°)	90	90	86.881(9)	86.362(10)	82.828(4)	87.909(4)
β (°)	94.854(2)	94.143(2)	85.116(12)	85.865(11)	74.749(5)	76.739(5)
γ (°)	90	90	64.373(14)	65.558(10)	72.115(5)	72.359(5)
Volume ($Å^3$)	2343.68(8)	2425.22(8)	583.65(15)	601.12(13)	1174.17(11)	1210.69(12)
Z	8	8	2	2	4	4
ρ_{calc} ($g\ cm^{-3}$)	1.447	1.398	1.452	1.410	1.331	1.291
μ (mm^{-1})	1.006	0.972	1.010	0.980	0.827	0.802
Θ range (°)	4.4826-66.490	4.796-66.560	3.052-66.583	3.829-66.594	3.234-67.072	4.901-67.062
Reflections collected	7183	7418	3529	3582	7323	7451
Independent	2066	2151	2066	2128	4176	4298
Observed I>2σ	1790	1909	1509	1538	3569	3511
R_{int}	0.0247	0.0175	0.0305	0.0194	0.0233	0.0184
Completeness (%)	96.9	97.7	97.2	97.7	98.3	97.9
Parameters	215	204	215	193	367	367
GooF	1.055	1.047	0.842	1.013	1.115	1.076
R_1 (observed)	0.032	0.0418	0.0372	0.0376	0.0456	0.0471
R_1 (all)	0.039	0.0465	0.0563	0.055	0.0526	0.0561
wR_2 (all)	0.0878	0.1206	0.094	0.116	0.119	0.1318
Δρ (max, min) ($e\ Å^{-3}$)	0.181, -0.201	0.204, -0.225	0.175, -0.205	0.183, -0.151	0.220, -0.224	0.191, -184

Table A6.2 Crystallographic data for *N*,*N*-dimethylurea 4-cyanobenzoic acid (DMU4-CBA) (1:1), urea isophthalic acid (UIP) (1:1) and urea 5-aminoisophthalic acid (U5-AIP) (1:1).

Compound	DMU4-CBA	DMU4-CBA	UIP	UIP	U5-AIP
Diffractometer	Xcaliber	Xcaliber	Bruker AXS D8	Bruker AXS D8	Bruker AXS D8
Radiation (K/a) /wavelength (λ)	Mo	Mo	0.7749	0.7749	0.7749
Formula	$C_{11}H_{13}N_3O_3$	$C_{11}H_{13}N_3O_3$	$C_9H_{\cdot 0}N_1O_5$	$C_9H_{\cdot 0}N_1O_5$	$C_9H_{11}N_3O_5$
Mol. W ($gmol^{-1}$)	235.24	235.24	226.19	226.19	241.21
T (K)	150	300	100	300	300
Space group	$P2_{1/n}$	$P2_{1/n}$	P-1	P-1	C2/c
a (Å)	9.9927(5)	10.1184(11)	3.6373(2)	3.7120(10)	26.498(3)
b (Å)	5.3155(3)	5.3380(6)	11.4983(6)	11.678(3)	3.7245(4)
c (Å)	22.0390(10)	22.3884(19)	22.6150(12)	22.606(5)	21.216(2)
α (°)	90	90	88.908(3)	91.288(16)	90
β (°)	90.448(4)	91.037(8)	86.073(3)	94.172(16)	92.510(7)
γ (°)	90	90	89.542(3)	91.408(18)	90
Volume ($Å^3$)	1170.59(10)	1209.0(2)	943.41(9)	976.7(4)	2091.9(4)
Z	4	4	4	4	8
ρ_{calc} ($g\ cm^{-3}$)	1.335	1.292	1.593	1.538	1.532
μ (mm^{-1})	0.099	0.096	0.118	0.114	0.113
Θ range (°)	3.429-29.670	3.363-29.667	2.152-33.606	2.212-33.607	2.626-30.209
Reflections collected	8315	9230	13879	14033	13785
Independent	2894	2906	5750	5864	2379
Observed I>2σ	1744	1270	4234	3253	1523
R_{int}	0.0441	0.0473	0.0398	0.0492	0.069
Completeness (%)	99.9	99.9	99.6	98.8	99.2
Parameters	206	184	369	369	190
GooF	1.012	0.964	1.082	0.998	1.071
R_1 (observed)	0.0526	0.0519	0.0634	0.0586	0.0878
R_1 (all)	0.1055	0.1439	0.0911	0.1229	0.1272
wR_2 (all)	0.1228	0.1534	0.1577	0.1514	0.2577
Δρ (max, min) ($e\ Å^{-3}$)	0.184, -0.214	0.155, -0.151	0.478, -0.376	0.290, -0.289	0.454,-0.405

Table A6.3 Crystallographic data for urea 5-nitroisophthalic acid (U5NIP), *N*-methylurea phthalic acid (MUP) (1:1), *N*-methylurea isophthalic acid (MUIP) (1:1), *N*-methylurea 5-nitrosiophthalic acid (MU5-NIP) (2:1) and *N*-methylurea 5-aminosiophthalic acid (MU5-AIP) (1:1).

Compound	U5-NIP	MUP	MUP	MUIP	MUIP	MU5-NIP	MU5-AIP
Diffractometer	SuperNova	Bruker AXS D8	Bruker AXS D8	Xcaliber	Xcalibur	Bruker AXS D8	Bruker AXS D8
Radiation (K/a) /wavelength (λ)	Cu	0.7749	0.7749	Mo	Mo	0.7749	0.7749
Formula	$C_{12}H_{21}N_9O_{10}$	$C_{10}H_{12}N_2O_5$	$C_{10}H_{12}N_2O_5$	$C_{10}H_{12}N_2O_5$	$C_{10}H_{12}N_2O_5$	$C_{12}H_{17}N_5O_8$	$C_{10}H_{13}N_3O_5$
Mol. W ($gmol^{-1}$)	451.38	240.22	240.22	240.22	240.22	359.30	255.23
T (K)	150	100	300	150	298	100	300
Space group	P-1	P-1	P-1	$P2_1/n$	$P2_1/n$	$P2_1/n$	Pn
a (Å)	7.0389(4)	7.1602(5)	7.3118(9)	16.4881(14)	16.5556(15)	12.5875(5)	3.79080(10)
b (Å)	11.2635(8)	12.0603(9)	12.1797(14)	3.8412(3)	3.9093(6)	7.7532(3)	20.8929(7)
c (Å)	12.5990(8)	12.6113(9)	12.6607(14)	16.9194(16)	16.9689(17)	17.4016(5)	14.4602(5)
α (°)	91.858(5)	90.413(4)	90.730(7)	90	90	90	90
β (°)	97.316(5)	92.522(4)	91.871(7)	99.313(9)	99.467(10)	101.690(3)	91.372(2)
γ (°)	99.784(5)	94.101(4)	96.105(7)	90	90	90	90
Volume ($Å^3$)	974.85(11)	1085.14(14)	1120.4(2)	1057.45(16)	1083.3(2)	1663.06(11)	1144.93(6)
Z	2	4	4	4	4	4	4
ρ_{calc} ($g\ cm^{-3}$)	1.538	1.470	1.424	1.509	1.473	1.435	1.481
μ (mm^{-1})	1.167	0.106	0.103	0.123	0.120	1.055	0.146
Θ range (°)	3.542-74.517	2.539-30.208	2.518-30.210	3.201-30.115	3.186-29.537	3.977-67.039	2.623-30.200
Reflections collected	6601	15186	16394	5977	8086	15186	16394
Independent	3829	4983	5151	2746	2659	4983	5151
Observed I>2σ	3210	4133	3447	1875	1464	4133	3447
R_{int}	0.0233	0.034	0.0391	0.0331	0.0478	0.034	0.0391
Completeness (%)	99.7	99.8	99.8	99.7	99.8	98.8	99.8
Parameters	364	403	379	202	190	294	417
GooF	1.036	1.036	1.038	1.078	1.068	1.044	1.026
R_1 (observed)	0.0354	0.0418	0.0493	0.0504	0.0605	0.0298	0.0311
R_1 (all)	0.0442	0.0531	0.0792	0.0879	0.1292	0.0354	0.0335
wR_2 (all)	0.0934	0.1142	0.1419	0.1234	0.1495	0.0819	0.0823
Δρ (max, min) ($e\ Å^{-3}$)	0.286, -0.242	0.348, -0.270	0.192, -0.194	0.249, -0.309	0.247, -0.242	0.183, -0.170	0.154, -0.213

Table A6.4 Crystallographic data for *N*,*N*-dimethylurea isophthalic acid (DMUIP) (2:1), *N*,*N*-dimethylurea 5-aminoisophthalic acid (DMU5-AIP) (2:1), *N*,*N*-dimethylurea 3-nitrophthalic acid (DMU3-NP) (1:1) and *N*,*N*-dimethylurea 5-nitroisophthalic acid (DMU5-NIP) (2:1).

Compound	DMUIP	DMUIP	DMU5-AIP	DMU5-AIP	DMU3-NP	DMU3-NP	DMU5-NIP
Diffractometer	Bruker AXS D8	Bruker AXS D8	Bruker AXS D8	Bruker AXS D8	SuperNova	SuperNova	SuperNova
Radiation (K/a) /wavelength (λ)	0.7749	0.7749	0.7749	0.7749	Cu	Cu	Cu
Formula	$C_{14}H_{22}N_4O_6$	$C_{14}H_{22}N_4O_6$	$C_{14}H_{23}N_5O_6$	$C_{14}H_{23}N_5O_6$	$C_{11}H_{13}N_3O_7$	$C_{11}H_{13}N_3O_7$	$C_{14}H_{21}N_5O_8$
Mol. W ($gmol^{-1}$)	342.35	342.35	357.37	357.37	299.24	299.24	387.36
T (K)	100	300	100	300	150	300	150
Space group	Pnna	Pnna	$P2_1/n$	$P2_1/n$	$P2_1/n$	$P2_1/n$	P-1
a (Å)	11.9844(6)	12.0542(5)	11.0486(6)	11.2015(5)	14.1487(6)	14.1455(7)	8.2131(4)
b (Å)	12.8190(7)	12.8657(6)	12.5054(6)	12.6557(6)	6.7587(2)	6.9209(3)	11.5573(5)
c (Å)	10.6386(6)	10.9715(6)	12.4189(6)	12.5876(5)	15.2680(7)	15.2930(7)	19.6303(10)
α (°)	90	90	90	90	90	90	77.236(4)
β (°)	90	90	90.261(2)	91.417(3)	114.857(5)	114.832(6)	80.328(4)
γ (°)	90	90	90	90	90	90	78.389(4)
Volume ($Å^3$)	1634.39(15)	1701.52(14)	1715.87(15)	1783.91(14)	1324.77(10)	1358.75(12)	1765.15(15)
Z	4	4	4	4	4	4	4
ρ_{calc} ($g\ cm^{-3}$)	1.391	1.336	1.383	1.331	1.500	1.463	1.458
μ (mm^{-1})	0.132	0.127	0.108	0.104	1.100	1.073	1.035
Θ range (°)	2.713-30.194	2.660-30.208	2.520-30.209	2.489-30.210	3.577-66.588	3.576-66.589	3.980-66.595
Reflections collected	22221	23123	23444	24384	7760	8202	11480
Independent	1883	1957	3921	4089	2330	2397	6217
Observed I>2σ	1581	1350	3240	2618	2096	2071	5599
R_{int}	0.0432	0.0545	0.0548	0.0602	0.0179	0.0175	0.0148
Completeness (%)	100.0	100.0	100.0	100.0	97.5	97.5	97.3
Parameters	154	130	318	270	230	218	618
GooF	1.049	1.027	1.053	1.038	1.055	1.038	1.062
R_1 (observed)	0.0332	0.0536	0.0349	0.0536	0.0343	0.0387	0.043
R_1 (all)	0.0423	0.0779	0.0464	0.085	0.0384	0.0445	0.0467
wR_2 (all)	0.0916	0.1746	0.0946	0.1705	0.1	0.1148	0.1288
Δρ (max, min) ($e\ Å^{-3}$)	0.335, -0.266	0.299, -0.236	0.334, -0.270	0.255, -0.219	0.335, -0.305	0.213, -0.167	0.526, -0.372

Table A6.5 Crystallographic data for *N,N*-dimethylurea 5-nitroisophthalic acid (DMU5-NIP) (2:1), *N*-phenylurea 2,4-dinitrobenzoic acid (PhU2,4-DNBA) (1:1), *N*-phenylurea 3-nitroisophthalic acid (PhU3-NP) (1:1), *N*-phenylurea 5-nitroisophthalic acid form I (PhU5-NIP I) (2:1) and *N*-phenylurea 5-nitroisophthalic acid form II (PhU5-NIP II) (1:1).

Compound	DMU5-NIP	PhU2,4-DNBA	PhU2,4-DNBA	PhU3-NP	PhU3-NP	PhU5-NIP I	PhU5-NIP II
Diffractometer	SuperNova	SuperNova	SuperNova	SuperNova	SuperNova	Xcalibur	SuperNova
Radiation (K/a) /wavelength (λ)	Cu	Cu	Cu	Cu	Cu	Mo	Cu
Formula	$C_{14}H_{21}N_5O_8$	$C_{14}H_{12}N_4O_7$	$C_{14}H_{12}N_4O_7$	$C_{15}H_{13}N_3O_{14}$	$C_{15}H_{13}N_3O_7$	$C_{22}H_{21}N_5O_8$	$C_{15}H_{13}N_3O_7$
Mol. W ($gmol^{-1}$)	387.36	348.28	348.28	347.28	347.28	483.44	347.28
T (K)	300	150	300	150	300	150	150
Space group	P-1	P-1	P-1	P-1	P-1	P-1	$P2_1/c$
a (Å)	8.2632(4)	8.1596(6)	8.2414(9)	7.3527(3)	7.4914(3)	8.9131(7)	15.1254(3)
b (Å)	11.6595(4)	9.0985(8)	9.1494(14)	12.9796(7)	13.0439(7)	9.7105(8)	12.7462(2)
c (Å)	20.0925(10)	11.2089(8)	11.1958(15)	16.7922(10)	16.7646(10)	13.3778(11)	16.2905(4)
α (°)	77.535(3)	102.686(7)	101.836(12)	73.189(5)	73.666(5)	71.440(7)	90
β (°)	78.689(4)	93.385(6)	93.173(10)	88.392(4)	88.461(4)	78.479(7)	107.286(3)
γ (°)	78.470(4)	110.566(7)	109.316(12)	87.567(4)	88.117(4)	83.019(7)	90
Volume ($Å^3$)	1828.20(15)	751.60(11)	772.78(19)	1532.49(14)	1570.96(15)	1073.43(16)	2998.81(12)
Z	4	2	2	4	4	2	4
ρ_{calc} ($g\ cm^{-3}$)	1.407	1.539	1.497	1.505	1.468	1.496	1.538
μ (mm^{-1})	1.000	1.087	1.058	1.045	1.020	0.116	1.068
Θ range (°)	3.936-66.582	4.088-67.032	4.071-73.941	3.560-74.308	3.532-74.408	3.321-29.343	4.485-74.591
Reflections collected	11621	4605	5000	10522	10591	8876	20298
Independent	6441	2668	3023	6012	6184	4920	6023
Observed I>2σ	5674	2249	2196	4819	5021	3277	4827
R_{int}	0.0139	0.0178	0.0245	0.0254	0.0199	0.026	0.031
Completeness (%)	97.5	98.3	99.6	99.9	99.7	99.7	99.8
Parameters	576	274	274	555	555	400	555
GooF	1.02	1.049	1.051	1.022	1.024	1.023	1.123
R_1 (observed)	0.0487	0.0356	0.0469	0.0355	0.0386	0.052	0.0526
R_1 (all)	0.0536	0.0436	0.0652	0.0474	0.0483	0.093	0.0659
wR_2 (all)	0.1465	0.0997	0.1405	0.0985	0.1103	0.1101	0.1426
Δρ (max, min) ($e\ Å^{-3}$)	0.374, -0.256	0.228, -0.218	0.306, -0.275	0.237, -0.260	0.182, -0.205	0.240, -0.300	0.279, -0.230

Table A6.6 Crystallographic data for *N.N'*-dimethylurea 5-aminoisophthalic acid (DM'U-5-AIP) (1:1), 3-deazauracil 3-nitrophthalic acid (3-DAZA3-NP) (2:1), 3-deazauracil 2,4-dinitrobenzoic acid (3-DAZA2,4-DNBA) (1:1) and 3-deazauracil chloranilic acid (3-DAZAClA) (1:1).

Compound	DM'U5-AIP	DM'U5-AIP	3-DAZA3-NP	3-DAZA3-NP	3-DAZA2,4-DNBA	3-DAZA2,4-DNBA	3-DAZAClA
Diffractometer	Bruker AXS D8	Bruker AXS D8	SuperNova	SuperNova	SuperNova	SuperNova	R-axis Rapid
Radiation (K/a) /wavelength (λ)	0.7749	0.7749	Cu	Cu	Cu	Cu	Mo
Formula	$C_{14}H_{23}N_5O_6$	$C_{14}H_{23}N_5O_6$	$C_{18}H_{15}N_3O_{10}$	$C_{18}H_{15}N_3O_{10}$	$C_{12}H_9N_3O_8$	$C_{12}H_9N_3O_8$	$C_{11}H_7Cl_2N_1O_6$
Mol. W ($gmol^{-1}$)	357.37	357.37	433.33	433.33	323.22	323.22	320.08
T (K)	100	300	150	300	150	300	100
Space group	$Cmc2_1$	$Cmc2_1$	P-1	P-1	$P2_1/c$	$P2_1/c$	$P2_1/c$
a (Å)	12.7517(5)	13.0778(7)	7.6574(5)	7.6840(6)	7.3224(2)	7.3599(3)	9.1967(5)
b (Å)	8.8495(3)	8.8486(4)	10.9148(8)	11.1084(11)	13.8271(3)	13.8429(4)	6.9054(5)
c (Å)	15.1665(6)	15.1663(7)	11.7875(10)	11.8166(13)	13.4352(3)	13.6114(5)	17.9888(13)
α (°)	90	90	72.045(7)	71.726(9)	90	90	90
β (°)	90	90	75.586(6)	75.373(8)	99.350(2)	98.678(4)	96.850(7)
γ (°)	90	90	87.644(6)	87.114(7)	90	90	90
Volume ($Å^3$)	1711.48(11)	1755.05(15)	907.03(12)	926.26(16)	1342.21(6)	1370.89(8)	1134.26(13)
Z	4	4	2	2	4	4	4
ρ_{calc} ($g\ cm^{-3}$)	1.387	1.353	1.587	1.554	1.600	1.566	1.874
μ (mm^{-1})	0.094	0.097	1.144	1.120	1.203	1.178	0.600
Θ range (°)	2.929-30.206	2.929-30.169	4.070-74.180	4.069-74.229	4.621-74.193	4.583-67.077	2.994-27.484
Reflections collected	11679	12065	6021	6249	8854	8432	24403
Independent	2032	2100	3558	3635	2685	2446	2589
Observed I>2σ	1967	1857	2996	3027	2359	1963	2328
R_{int}	0.032	0.0369	0.019	0.0164	0.022	0.0241	0.0303
Completeness (%)	99.8	100.0	99.7	99.7	100.0	98.6	99.9
Parameters	162	172	340	340	244	244	209
GooF	1.055	1.084	1.035	1.027	1.065	1.054	1.068
R_1 (observed)	0.0358	0.0270	0.0343	0.0364	0.0308	0.038	0.025
R_1 (all)	0.0424	0.0287	0.0425	0.0443	0.0359	0.0484	0.029
wR_2 (all)	0.0922	0.0690	0.099	0.1093	0.0827	0.1112	0.0652
Δρ (max, min) ($e\ Å^{-3}$)	0.202, -0.181	0.201, -0.215	0.252, -0.210	0.225, -0.185	0.210, -0.192	0.204, -0.169	0.450, -0.252

Table A6.7 Crystallographic data for isoniazid phthalic acid (INZP) (1:1), isoniazid 2,4-dinitrobenzoic acid (INZ2,4-DNBA) (1:1), isoniazid 5-nitroisophthalic acid (INZ5-NIP) (1:1) and isonicotinamide 2,4-dinitrobenzoic acid I (IN2,4-DNBA I) (1:1).

Compound	INZP	INZP	INZP	INZ2,4-DNBA	INZ2,4-DNBA	INZ5-NIP	IN2,4-DNBA I
Diffractometer	SuperNova	SuperNova	SuperNova	SuperNova	SuperNova	SuperNova	Xcalibur
Radiation (K/a) /wavelength (λ)	Cu	Cu	Cu	Cu	Cu	Cu	Mo
Formula	$C_{14}H_{13}N_3O_5$	$C_{14}H_{13}N_3O_5$	$C_{14}H_{13}N_3O_5$	$C_{13}H_{11}N_5O_7$	$C_{13}H_{11}N_5O_7$	$C_{14}H_{12}N_4O_7$	$C_{13}H_{10}N_4O_7$
Mol. W ($gmol^{-1}$)	303.27	303.27	303.27	349.27	349.27	348.28	334.25
T (K)	150	300	350	150	300	150	150
Space group	P-1	P-1	P-1	Pbca	Pbca	$P2_12_12_1$	$P2_1/c$
a (Å)	6.8968(4)	6.9506(5)	6.9808(3)	6.98060(10)	7.10480(10)	12.9127(3)	11.0596(6)
b (Å)	9.2467(5)	9.2637(7)	9.2668(4)	15.1050(3)	15.1289(2)	14.6654(2)	11.5003(6)
c (Å)	10.8598(8)	11.0244(7)	11.0943(5)	27.6899(5)	27.6510(4)	15.4334(2)	11.8531(7)
α (°)	96.929(5)	97.707(6)	98.080(4)	90	90	90	90
β (°)	98.849(5)	99.942(6)	100.257(4)	90	90	90	107.925(7)
γ (°)	100.988(5)	100.061(6)	99.798(4)	90	90	90	90
Volume ($Å^3$)	663.69(7)	678.49(8)	685.03(6)	2919.68(9)	2972.15(7)	2922.62(9)	1434.40(15)
Z	2	2	2	8	8	8	4
ρ_{calc} ($g\ cm^{-3}$)	1.518	1.484	1.470	1.589	1.561	1.583	1.548
μ (mm^{-1})	0.996	0.975	0.965	1.142	1.122	1.119	0.129
Θ range (°)	4.931-71.890	4.131-71.829	4.114-71.831	3.192-67.052	3.196-67.071	4.158-67.068	3.508-29.304
Reflections collected	4003	4043	4180	17932	18195	20007	11193
Independent	2536	2574	2606	2605	2655	5221	3455
Observed I>2σ	2330	2260	2337	2364	2410	4762	2670
R_{int}	0.0151	0.0205	0.0161	0.0278	0.0242	0.0243	0.0353
Completeness (%)	99.7	99.1	99.4	98.6	98.8	98.7	99.8
Parameters	251	251	251	270	270	547	257
GooF	1.046	1.034	1.024	1.044	1.073	1.02	1.029
R_1 (observed)	0.0355	0.0398	0.0441	0.0316	0.0361	0.0347	0.0476
R_1 (all)	0.0375	0.0442	0.0475	0.0352	0.0392	0.0385	0.0685
wR_2 (all)	0.1019	0.118	0.131	0.0849	0.0953	0.0982	0.112
Δρ (max, min) ($e\ Å^{-3}$)	0.278, -0.231	0.180,-0.208	0.185, -0.202	0.202,-0.223	0.264, -0.233	0.232, -0.202	0.408, --0.283

Table A6.8 Crystallographic data for isonicotinamide 2,4-dinitrobenzoic acid I (IN2,4-DNBA I) (1:1), isonicotinamide 2,4-dinitrobenzoic acid III (IN2,4-DNBA III) (1:1), pyrazole bromanilic acid (PYBrA) (1:1), pyrazole chloranilic acid hydrate (PYClA hydrate) (1:1:1), 4(5)-methylimidazole bromanilic acid (4(5)-MIBrA) (1:1) and 4(5)-methylimidazole chloranilic acid hydrate (4(5)-MIClA hydrate) (2:1:1:2).

Compound	IN2,4-DNBA I	IN2,4-DNBA III	IN2,4-DNBA III	PYBrA	PYClA hydrate	4(5)-MIBrA	4(5)-MIClA hydrate
Diffractometer	Xcalibur	Xcaliber	Xcaliber	R-axis Rapid	R-axis Rapid	R-axis Rapid	R-axis Rapid
Radiation (K/a) /wavelength (λ)	Mo	Mo	Mo	Mo	Mo	Mo	Mo
Formula	$C_{13}H_{10}N_4O_7$	$C_{21}H_{18}N_6O_{14}$	$C_{21}H_{18}N_6O_{14}$	$C_9H_6Br_2N_2O_4$	$C_9H_7C_{l2}N_2O_{4.50}$	$C_{10}H_8Br_2N_2O_4$	$C_{20}H_{20}C_{24}N_4O_{10}$
Mol. W ($gmol^{-1}$)	334.25	578.41	578.41	365.98	286.07	380	618.20
T (K)	300	150	300	100	100	100	100
Space group	$P2_1/c$	P-1	P-1	$P2_1/c$	I2/a	$P2_1/n$	P-1
a (Å)	11.1978(7)	8.0453(5)	8.1444(6)	11.777(2)	22.309(4)	9.212(2)	3.8091(2)
b (Å)	11.6481(6)	12.2951(8)	12.3304(6)	5.3648(7)	3.7412(5)	7.5553(14)	9.2628(7)
c (Å)	11.9431(9)	12.9535(7)	13.1190(8)	17.526(3)	25.871(5)	17.468(4)	17.4820(12)
α (°)	90	106.245(5)	106.616(4)	90	90	90	84.294(6)
β (°)	108.852(7)	91.418(5)	90.623(5)	92.286(7)	99.513(13)	101.069(7)	87.216(6)
γ (°)	90	95.070(5)	95.514(5)	90	90	90	78.479(5)
Volume ($Å^3$)	1474.21(17)	1223.72(13)	1255.59(14)	1106.4(3)	2129.6(6)	1193.2(4)	601.13(7)
Z	4	2	2	4	4	4	1
ρ_{calc} ($g\ cm^{-3}$)	1.506	1.570	1.530	2.197	1.784	2.115	1.708
μ (mm^{-1})	0.125	0.135	0.131	7.331	0.620	6.802	0.559
Θ range (°)	3.495-29.349	3.248-29.334	3.378-29.330	3.463-27.483	3.194-27.482	3.514-27.483	3.099-27.484
Reflections collected	11809	10638	10683	13847	12078	15280	13173
Independent	3525	5618	5778	2506	2430	2727	2710
Observed I>2σ	2266	4249	3750	2058	2082	2384	2141
R_{int}	0.0377	0.0226	0.0213	0.0535	0.0369	0.0493	0.0425
Completeness (%)	99.8	99.8	99.7	99.5	99.7	99.8	99.7
Parameters	257	442	431	178	187	195	212
GooF	1.034	1.015	1.027	1.1	1.049	1.081	1.134
R_1 (observed)	0.0569	0.0463	0.0565	0.0233	0.0325	0.0285	0.0361
R_1 (all)	0.0994	0.0669	0.0947	0.0344	0.0393	0.035	0.0501
wR_2 (all)	0.1314	0.1074	0.1371	0.0496	0.0793	0.068	0.0851
Δρ (max, min) (e $Å^{-3}$)	0.228, -0.208	0.293, -0.241	0.296, -0.260	0.603, -0.462	0.417, -0.241	0.511, -0.715	0.434, -0.425

Table A6.9 Crystallographic data for 4-acetylpyridine bromanilic acid (4-APBrA) (1:1), 4-acetylpyridine chloranilic acid (4-APClA) (1:1) and 1,2,4-*1H*-triazole chloranilic acid hydrate (1,2,4-TZClA hydrate) (2:1:1), 3,5-dimethylpyrazole bromanilic acid hydrate (3,5-DMPYBrA hydrate) (2:1:2), 3,5-dimethylpyrazole chloranilic acid hydrate (3,5-DMPYClA hydrate) (2:1:2) and 3,5-dimethylpyrazole chloranilic acid (3,5-DMPYClA) (1:1).

Compound	4-APBrA	4-APClA	1,2,4-TZClA hydrate	3,5-DMPYBrA hydrate	3,5-DMPYClA hydrate	3,5-DMPYClA
Diffractometer	Xcalibur	SuperNova	SuperNova	R-axis Rapid	R-axis Rapid	R-axis Rapid
Radiation (K/a) /wavelength (λ)	Mo	Cu	Cu	Mo	Mo	Mo
Formula	$C_{13}H_9Br_2N_1O_5$	$C_{13}H_9C_{l2}N_1O_5$	$C_{10}H_{10}Cl_2N_6O_5$	$C_{16}H_{22}Br_2N_4O_6$	$C_{16}H_{22}Cl_2N_4O_6$	$C_{11}H_{10}Cl_2N_2O_4$
Mol. W ($gmol^{-1}$)	419.03	330.11	365.14	263.1	305.11	305.11
T (K)	150	150	150	100	100	100
Space group	$P2_12_12_1$	$P2_12_12_1$	Pccn	P-1	P-1	$P2_1/c$
a (Å)	5.4204(2)	5.38520(10)	20.035(5)	7.200(5)	7.097(3)	10.6282(7)
b (Å)	13.5342(5)	13.5329(2)	10.318(5)	9.005(7)	8.944(4)	9.3800(6)
c (Å)	18.3781(6)	17.6805(3)	6.370(5)	9.165(7)	8.949(3)	13.5946(10)
α (°)	90	90	90.000(5)	119.306(12)	119.410(9)	90
β (°)	90	90	90.000(5)	101.255(13)	99.235(10)	108.287(8)
γ (°)	90	90	90.000(5)	93.558(12)	93.797(10)	90
Volume ($Å^3$)	1348.23(8)	1288.51(4)	1316.8(13)	526.19	437.27	1286.83(16)
Z	4	4	4	1	1	4
ρ_{calc} ($g\ cm^{-3}$)	2.064	1.702	1.842	1.749	1.508	1.575
μ (mm^{-1})	6.034	4.764	4.843	4.098	0.380	0.515
Θ range (°)	3.651-26.015	4.114-76.841	4.414-76.362	3.401-27.482	3.518-27.484	3.047-27.481
Reflections collected	9532	14856	4502	11610	9785	16057
Independent	2656	2698	1368	2281	2182	2950
Observed I>2σ	2493	2564	1207	2143	2018	2593
R_{int}	0.0383	0.0502	0.0226	0.0383	0.0238	0.0288
Completeness (%)	99.7	100	99.7	99.8	99.5	99.7
Parameters	218	226	126	132	171	212
GooF	1.019	1.037	1.084	1.063	1.089	1.057
R_1 (observed)	0.0229	0.0274	0.0277	0.0234	0.0286	0.0284
R_1 (all)	0.0267	0.0297	0.0314	0.0257	0.0306	0.0327
wR_2 (all)	0.0435	0.0681	0.0822	0.0574	0.0749	0.0757
Δρ (max, min) ($e\ Å^{-3}$)	0.368, -0.272	0.260, -0.193	0.364, -0.376	0.502, -0.368	0.374, -0.239	0.394, -0.184

A6.3 pK_a

Table A6.10 The ΔpKa values of each literature molecular complex in Figure 6.19 calculated using the ACD-I Lab (ACD pKa). [270]

CSD Refcode of molecular complex	Basic component in molecular complex	pK_a [270]	Acidic component in molecular complex	pK_a [270]	ΔpK_a of molecular complex
HOLNIG01 [282]	(4)5-methylimidazole	7.68	succinic	4.24	3.44
LOCJUJ [283]	(4)5-methylimidazole	7.68	terephthalic acid	3.49	4.19
YUCQOD [284]	(4)5-methylimidazole	7.68	2-((2-carboxyphenyl)disulfanyl)benzoic acid	3.02	4.66
XIBWAH [285]	benzimidazole	5.26	2-nitrobenzoic acid	2.19	3.07
NEQWEM01 [286]	benzimidazole	5.26	chloranilic acid	1.38	3.88
XEYQUO01 [287]	benzimidazole	5.26	picric acid	0.62	4.64
AFORIY [288]	9-aminoacridine	9.66	2,4-dinitrobenzoic acid	1.43	8.23
VURVIO [138]	3-methylpyridine	5.52	chloranilic acid	1.38	4.14
ACEWIP [289]	bis(trimethylpyridine)	7.33	chloranilic acid	1.38	5.95
AYUSIX [290]	bis(trimethylpyridine)	7.33	4-nitrobenzoic acid	3.42	3.91
GODNAO [291]	bis(trimethylpyridine)	7.33	benzoic acid	4.2	3.13
GODNES [291]	bis(trimethylpyridine)	7.33	2-nitrobenzoic acid	2.19	5.14
GODNIW [291]	bis(trimethylpyridine)	7.33	3,5-dinitrobenzoic acid	2.77	4.56
GUHREG [292]	bis(trimethylpyridine)	7.33	phthalic acid	2.95	4.38

Appendix A7 (Chapter 7)

A7.1 Molecular complex preparation

benzimidazole 4-hydroxybenzoic acid 4:2 (BZN4-OHBA)

Small colourless plate crystals of the 4:2 complex of benzimidazole and 4-hydroxybenzoic acid were grown from slow evaporation of a 2:1 stoichiometric ratio of the two components in ethanol solvent at room temperature.

A7.2 Identifying temperature dependent proton migration across SSHBs using synchrotron and X-ray diffraction

Table A7.1 The O1—H1···O5 SSHB hydrogen bond parameters in DMU2,4-DNBA over the 100 to 350 K temperature range for refinement model 2.

T (K)	dO1—H1 (Å)	dH1···O5 (Å)	dO1···O5 (Å)	<O1H5O1 (°)
100	1.09(3)	1.36(3)	2.444(1)	168(2)
150	1.07(3)	1.40(3)	2.447(1)	167(3)
200	1.09(3)	1.39(3)	2.448(1)	163(3)
250	1.11(2)	1.35(2)	2.448(1)	169(2)
300	1.16(3)	1.31(3)	2.448(1)	166(3)
350	1.18(3)	1.28(3)	2.448(1)	166(3)

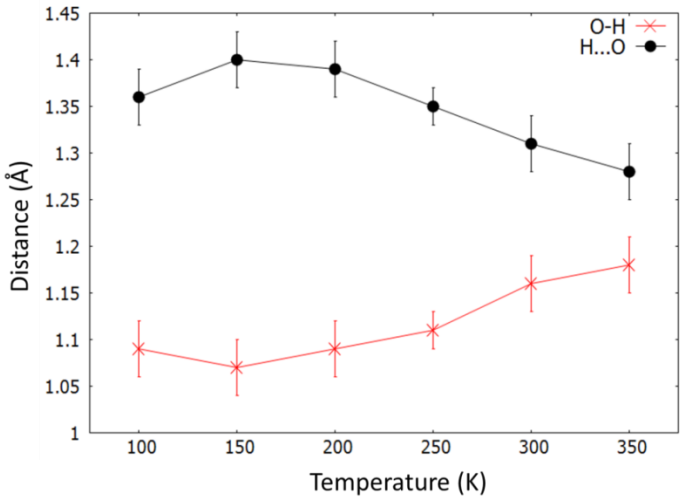

Figure A7.1 The change in the O—H and H···O distances in DMU2,4-DNBA over the 100 to 350 K temperature range for refinement model 2.

Table A7.2 The N^+—H···O^- SSHB hydrogen bond parameters in INP over the 100 to 350 K temperature range for refinement model 2.

T (K)	dN3···O3 (Å)	dN3—H2 (Å)	dH2···O3 (Å)	<N3H2O3 (°)
100	2.551(1)	1.10(3)	1.45(3)	176(2)
150	2.549(1)	1.11(3)	1.44(3)	177(3)
200	2.549(1)	1.12(3)	1.43(3)	176(3)
250	2.549(1)	1.15(3)	1.40(3)	174(3)
300	2.551(1)	1.16(3)	1.39(3)	174(3)
350	2.555(1)	1.19(3)	1.37(3)	174(3)

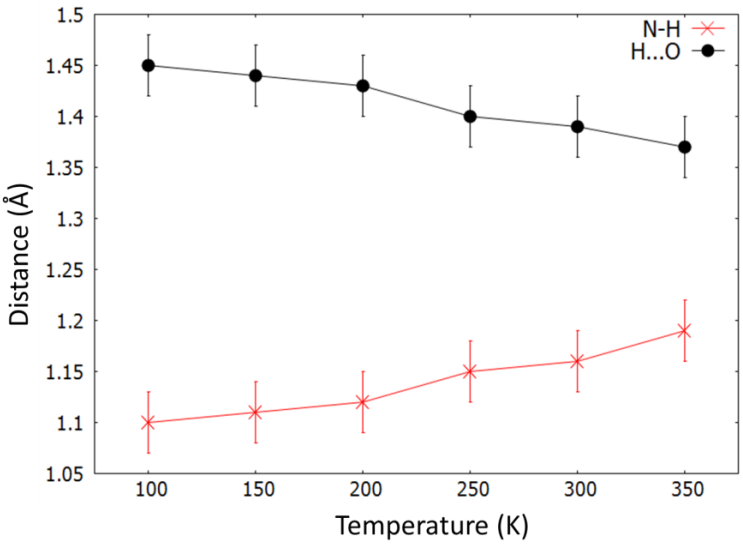

Figure A7.2 The change in the N^+—H and H···O distances between in INP over the 100 to 350 K temperature range for refinement model 2.

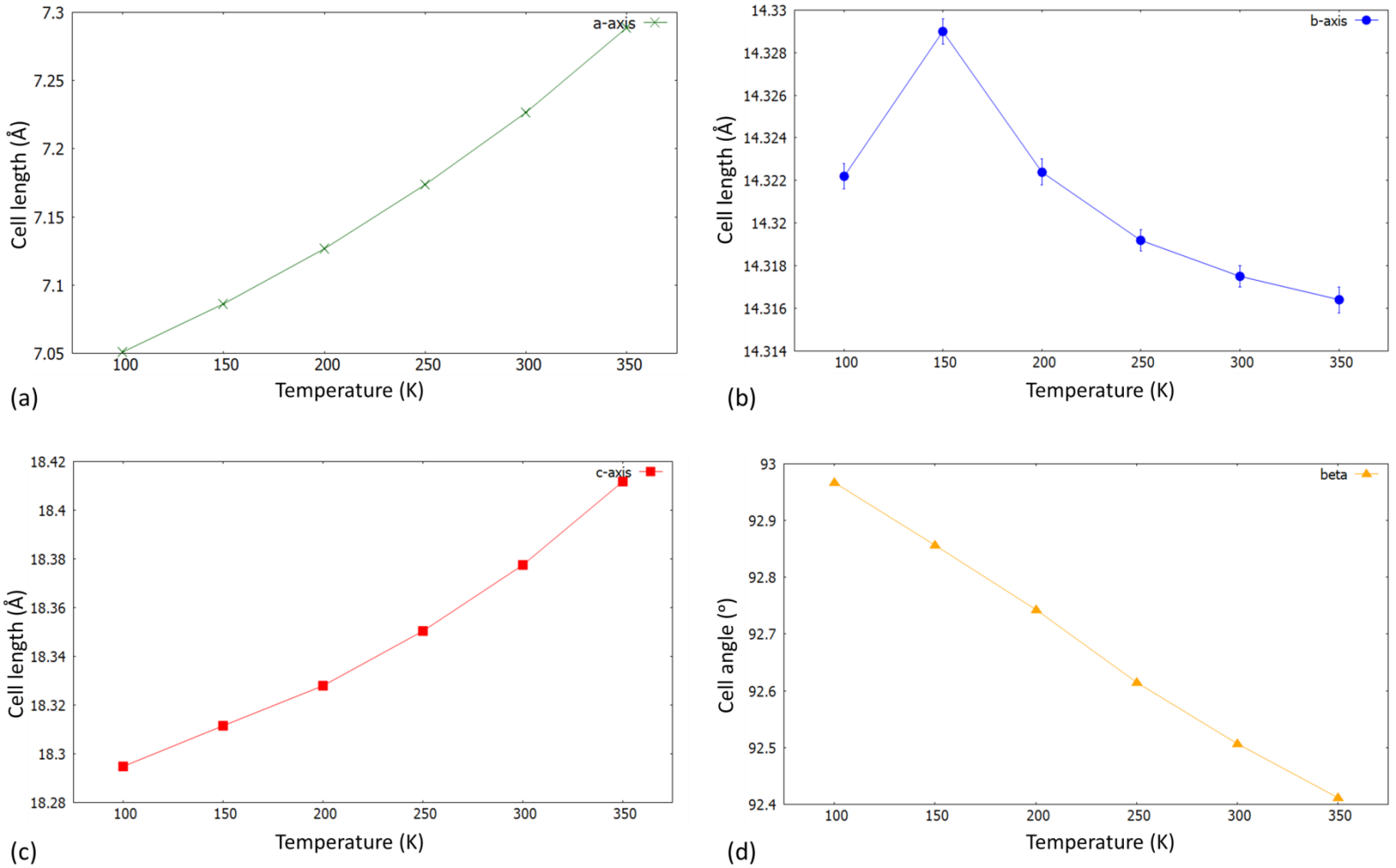

Figure A7.3 Unit cell parameters of INP over the 100 to 350 K temperature range: (a) a-axis, (b) b-axis, (c) c-axis and (d) β-angle.

A7.3 Parametric structural refinement in Topas-Academic V5.0

Table A7.3 Refinement details from the structural refinement of each molecular complex in Jana2006 [223] employing the normal and TLS refinement of the anisotropic thermal parameters.

T (K)	DMU2,4-DNBA		BZN4-OHBA STEP		BZN4-OHBA CONT.	
	300		300		287	
ADP refinement	normal	TLS	normal	TLS	normal	TLS
R(obs)	5.00	12.82	5.86	9.20	5.56	8.48
wR(obs)	6.89	17.82	6.25	9.78	5.48	8.48
R(all)	6.98	16.10	12.27	16.03	13.57	16.78
wR(all)	7.04	17.88	7.09	10.47	6.77	9.55

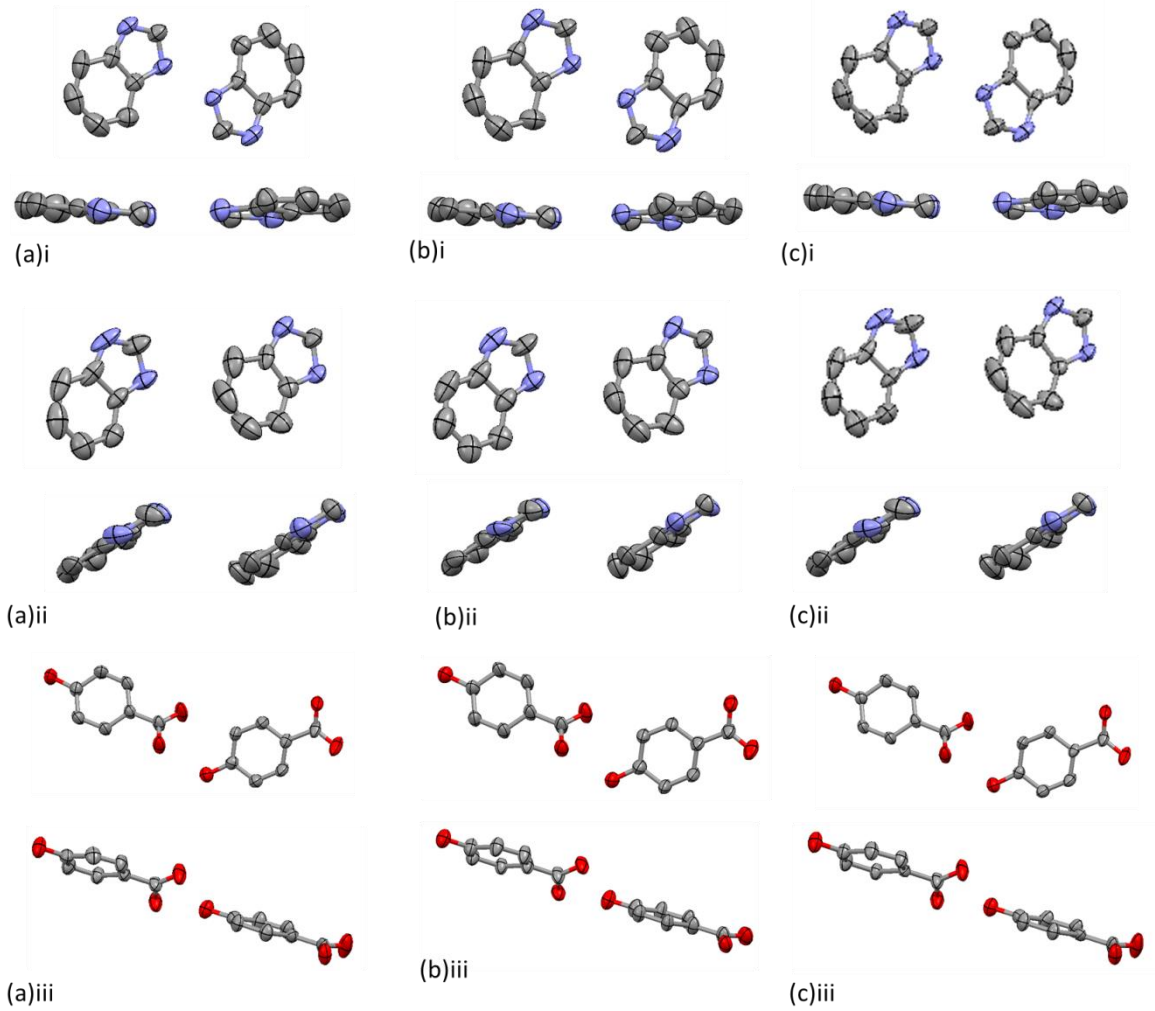

Figure A7.4 A comparison of the heavy atom thermal parameters modelled using a (a) normal and (b) TLS refinement in Topas-Academic V5.0 [168] and (c) TLS refinement in Jana2006 [223] for each molecular pair in BZN4-OHBA stepwise collection structure at 300 K.

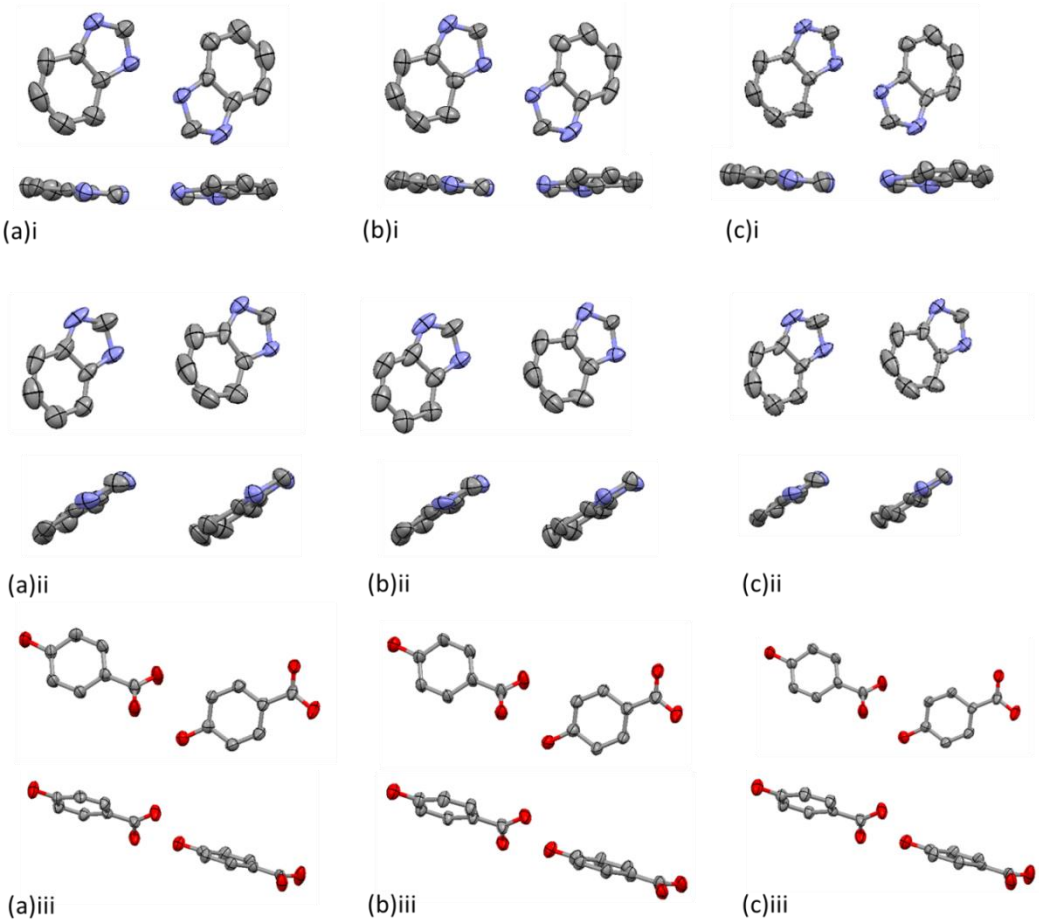

Figure A7.5 A comparison of heavy atom thermal parameters modelled using (a) normal and (b) TLS refinement in Topas-Academic V5.0 [168] and (c) TLS refinement in Jana2006 [223] for each molecular pair in BZN4OHBA continuous collection structure at 287 K.

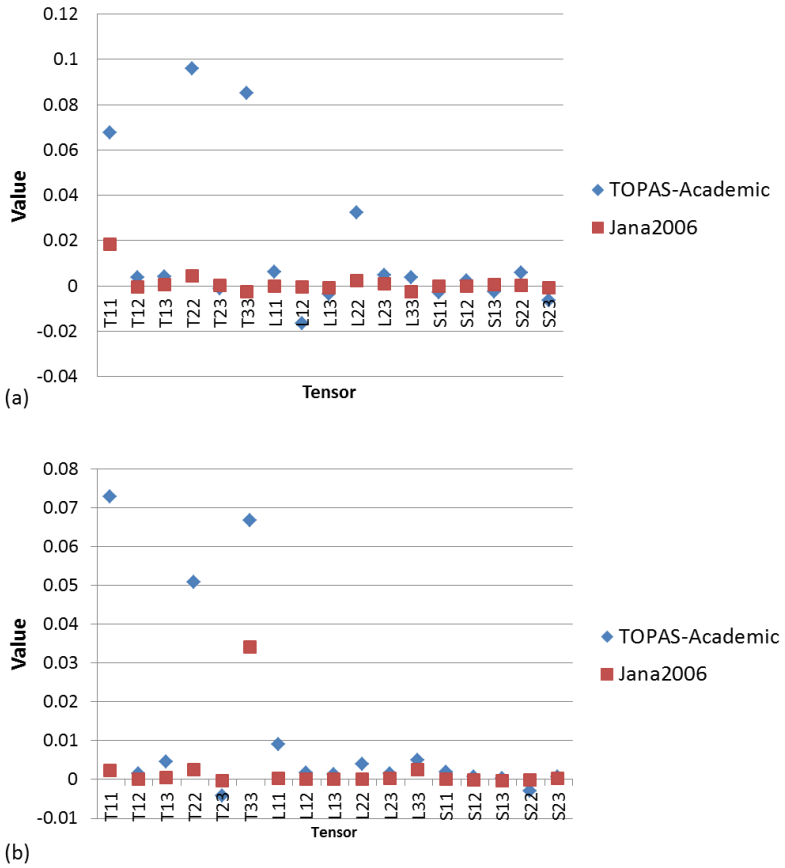

Figure A7.6 A comparison of TLS tensors from TLS refinement model of heavy atom thermal parameters in Topas-Academic V5.0 [168] and in Jana2006 [223] in molecules (a) 2,4-DNBA and (b) DMU in the molecular complex DMU2,4-DNBA at 300 K.

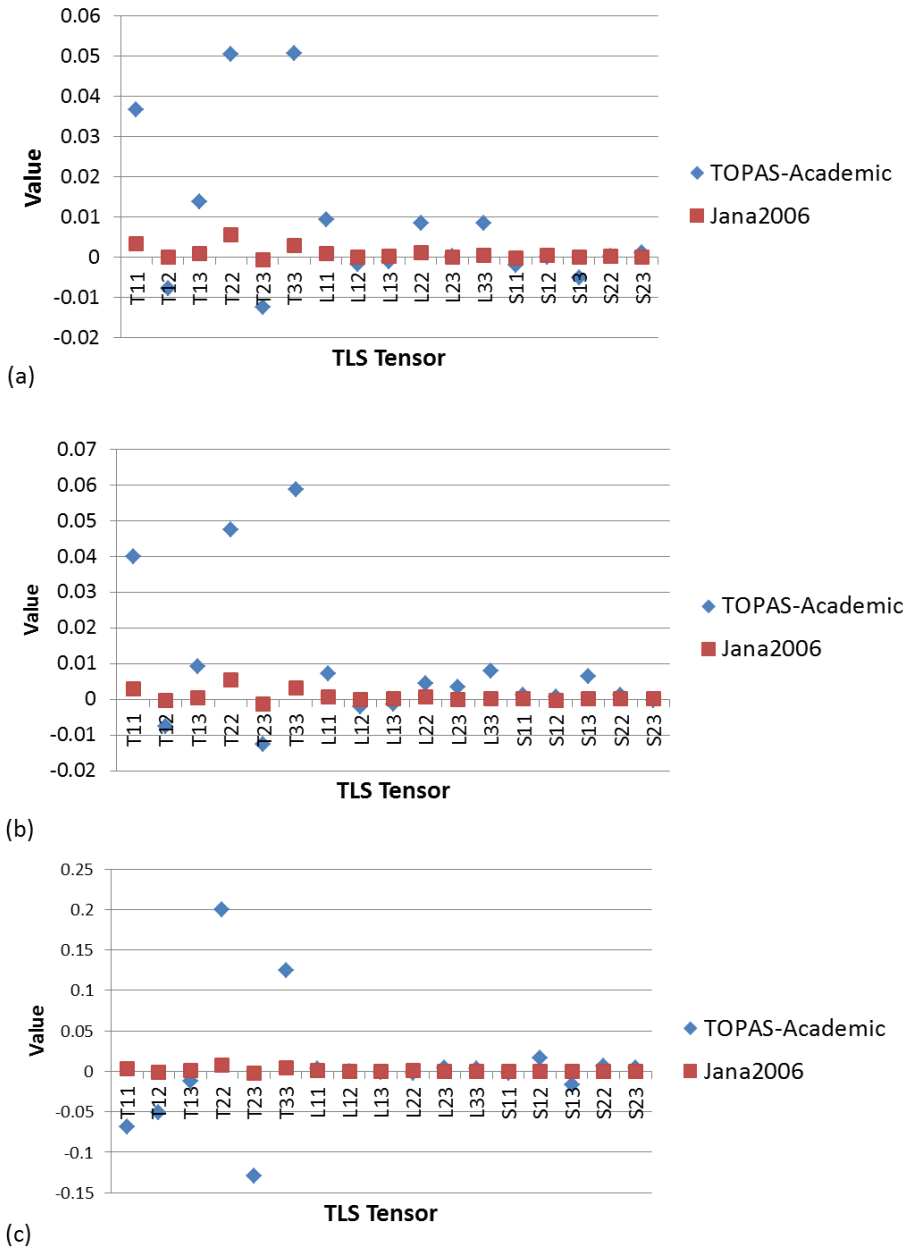

Figure A7.7 A comparison of TLS tensors from TLS refinement model of heavy atom thermal parameters in Topas-Academic V5.0 [168] and in Jana2006 [223] in molecules (a) benzimidazole1 and (b) benzimidazole2 and (c) benzimidazole3 in the molecular complex BZN4-OHBA STEP at 300 K.

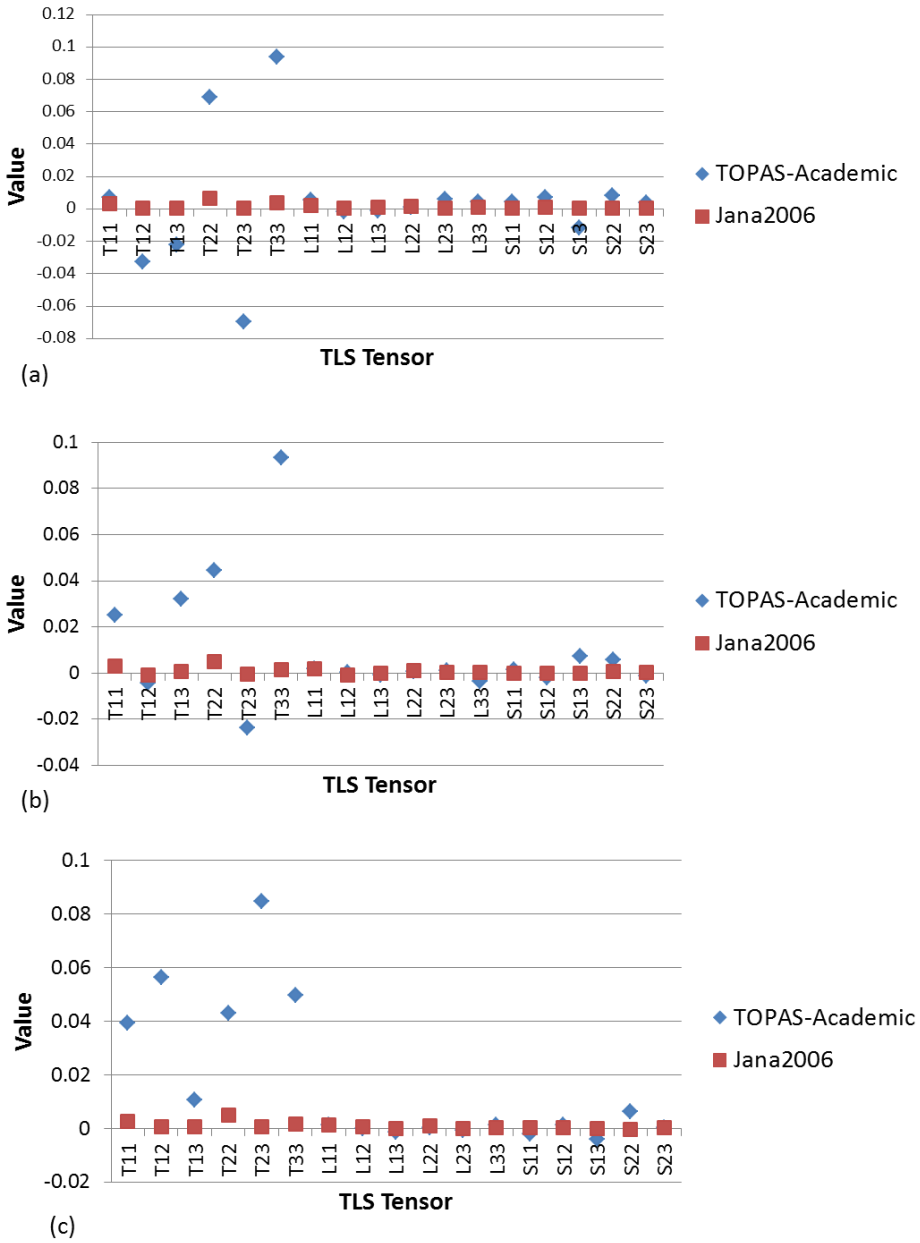

Figure A7.8 A comparison of TLS tensors from TLS refinement model of heavy atom thermal parameters in Topas-Academic V5.0 [168] and in Jana2006 [223] in molecules (a) benzimidazole4 and (b) 4-hydroxybenzoic acid1 and (c) 4-hydroxybenzoic acid2 in the molecular complex BZN4-OHBA STEP at 300 K.

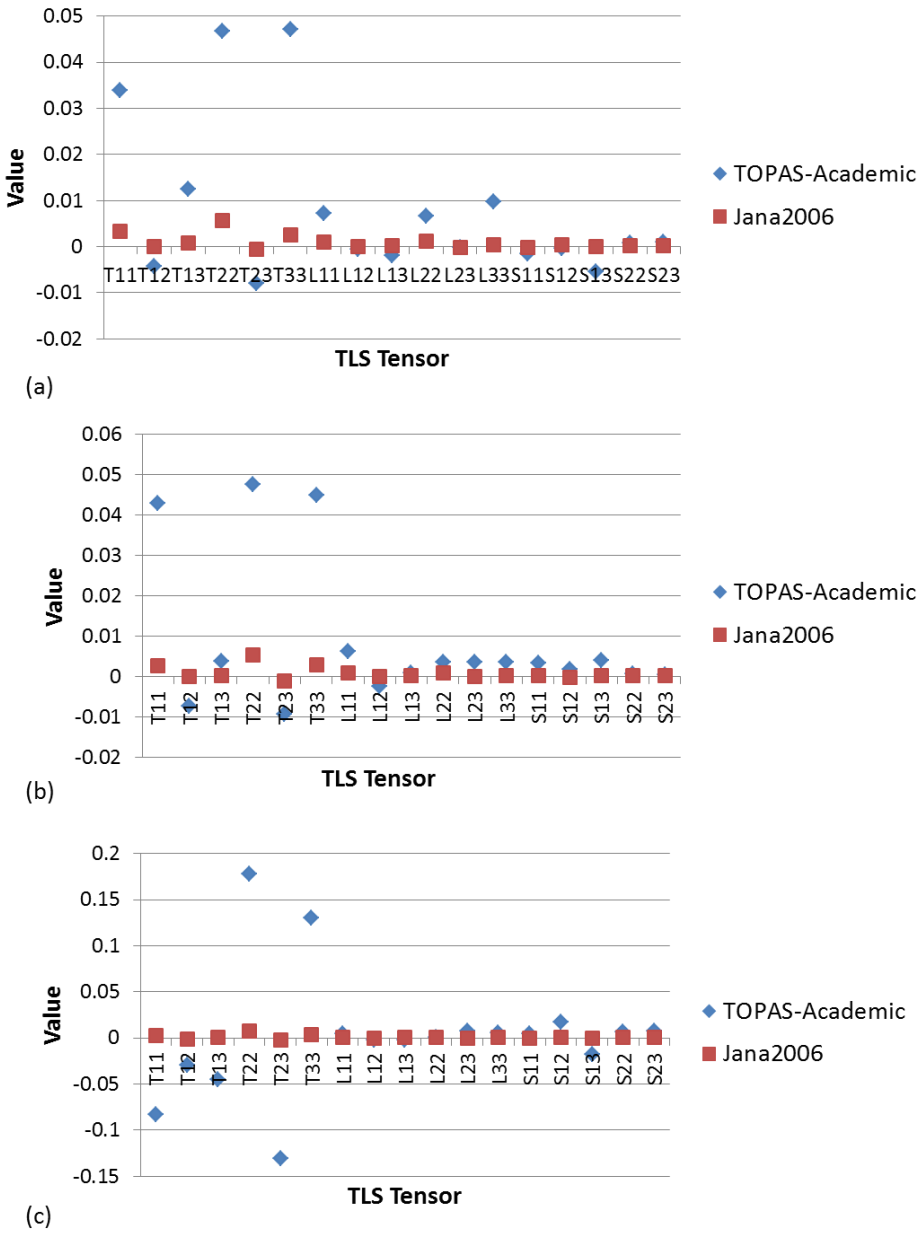

Figure A7.9 A comparison of TLS tensors from TLS refinement model of heavy atom thermal parameters in Topas-Academic V5.0 [168] and in Jana2006 [223] in molecules (a) benzimidazole1 and (b) benzimidazole2 and (c) benzimidazole3 in the molecular complex BZN4-OHBA CONT. at 300 K.

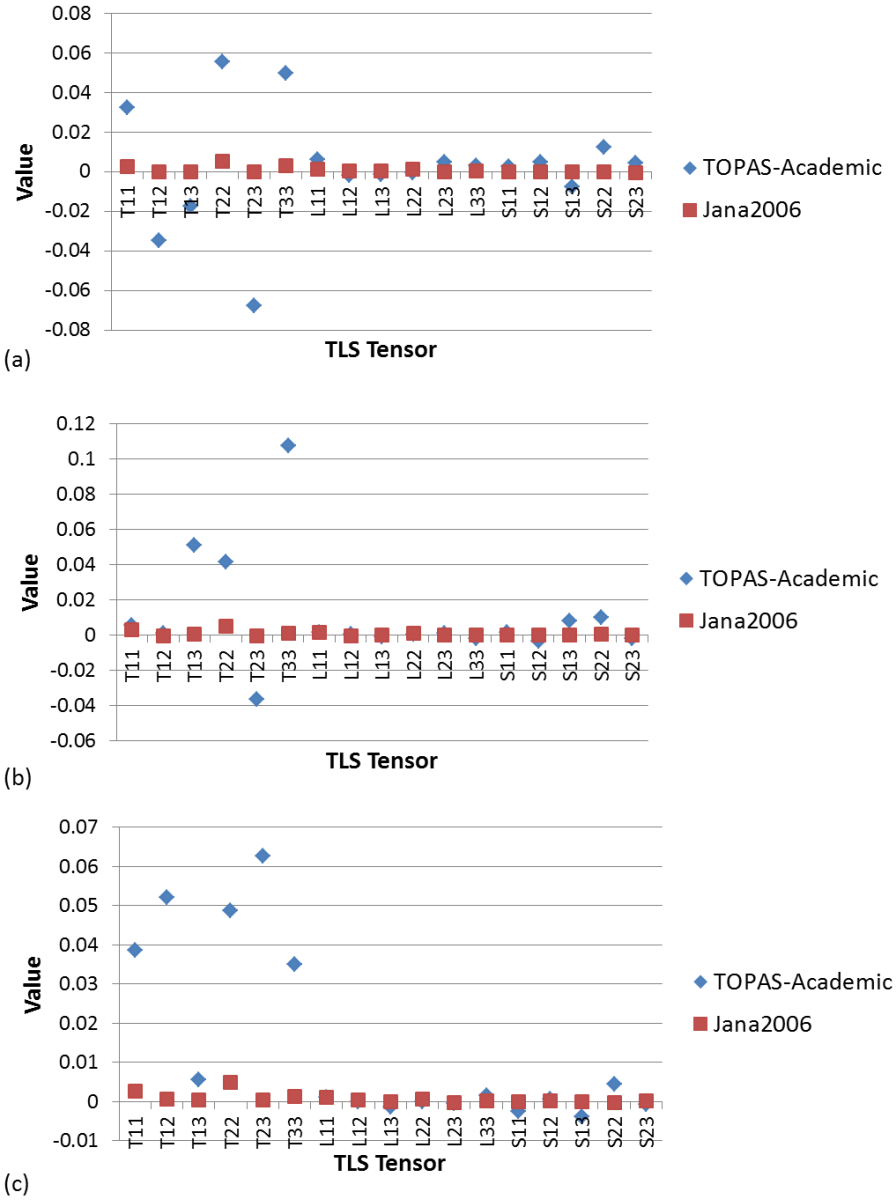

Figure A7.10 A comparison of TLS tensors from TLS refinement model of heavy atom thermal parameters in Topas-Academic V5.0 [168] and in Jana2006 [223] in molecules (a) benzimidazole4 and (b) 4-hydroxybenzoic acid1 and (c) 4-hydroxybenzoic acid2 in the molecular complex BZN4-OHBA CONT. at 300 K.

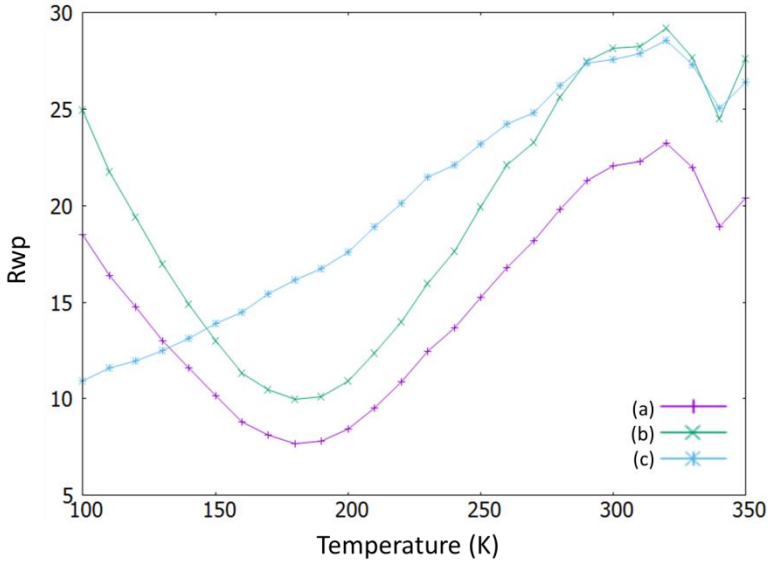

Figure A7.11 R_{wp} as a function of temperature for a surface refinement, employing model H_{para} and (a) normal ADPs 100 K rigid only, (b) normal ADPs all rigid and (c) TLS ADPs 100 K rigid only for DMU2,4-DNBA.

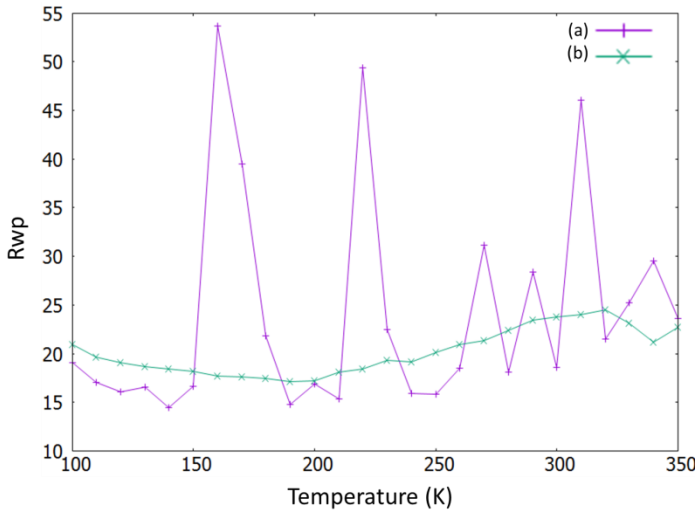

Figure A7.12 R_{wp} as a function of temperature for (a) independent and (b) surface refinements employing a H_{free} model with TLS refined ADPs and 100 K rigid only for DMU2,4-DNBA.

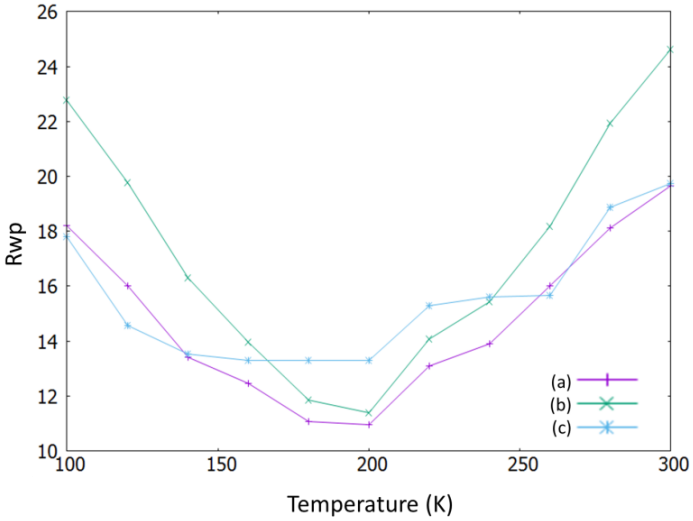

Figure A7.13 R_{wp} as a function of temperature for a surface refinement employing model H_{free} and (a) normal ADPs with 100 K rigid only, (b) normal ADPs with all rigid and (c) TLS ADPs with 100 K rigid only for BZN4-OHBA STEP.

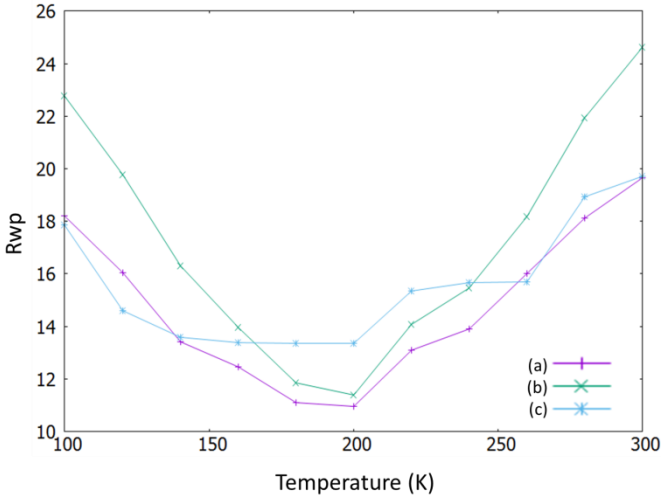

Figure A7.14 R_{wp} as a function of temperature for a surface refinement employing model H_{para} and (a) normal ADPs with 100 K rigid only, (b) normal ADPs with all rigid and (c) TLS ADPs with 100 K rigid only for BZN4-OHBA STEP.

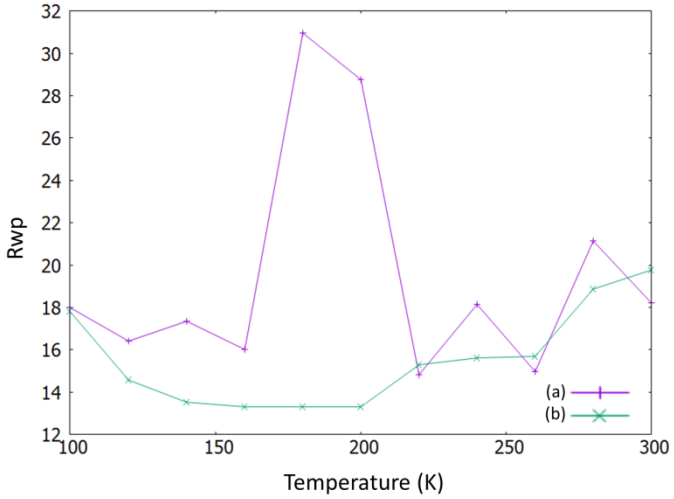

Figure A7.15 R_{wp} as a function of temperature for (a) independent and (b) surface refinements employing a H_{free} model with TLS refined ADPs and 100 K rigid only for BZN4-OHBA STEP.

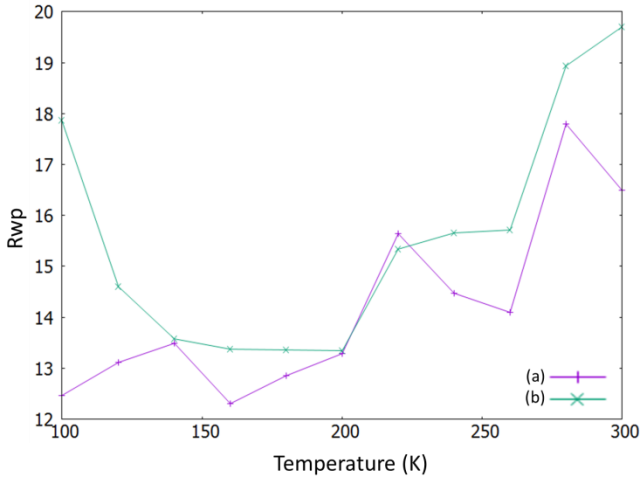

Figure A7.16 R_{wp} as a function of temperature for (a) independent and (b) surface refinements employing a H_{para} model with TLS refined ADPs and 100 K rigid only for BZN4-OHBA STEP.

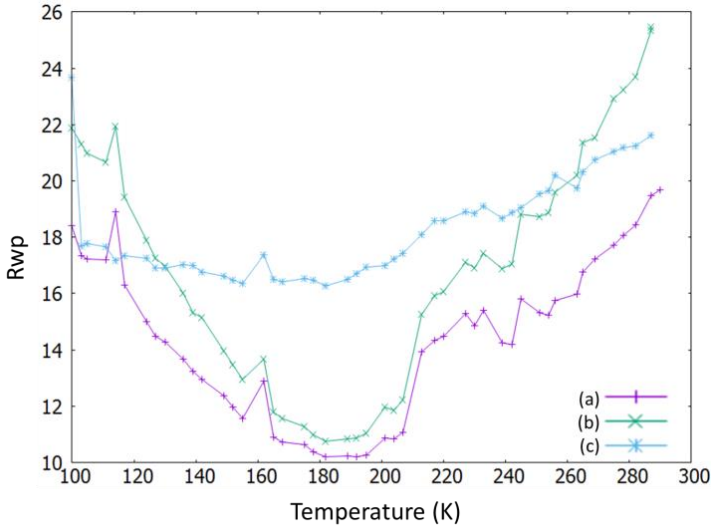

Figure A7.17 R_{wp} as a function of temperature for a surface refinement employing model H_{free} and (a) normal ADPs with 100 K rigid only, (b) normal ADPs with all rigid and (c) TLS ADPs with 100 K rigid only for BZN4-OHBA CONT.

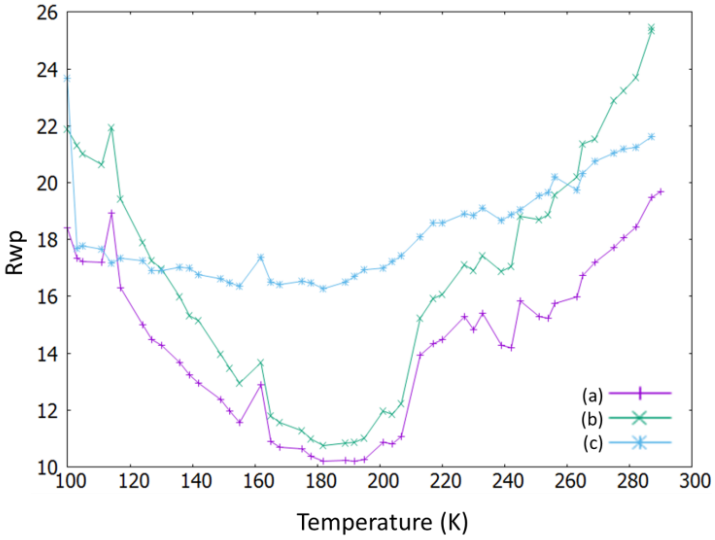

Figure A7.18 R_{wp} as a function of temperature for a surface refinement employing model H_{para} and (a) normal ADPs with 100 K rigid only, (b) normal ADPs with all rigid and (c) TLS ADPs with 100 K rigid only for BZN4-OHBA CONT.

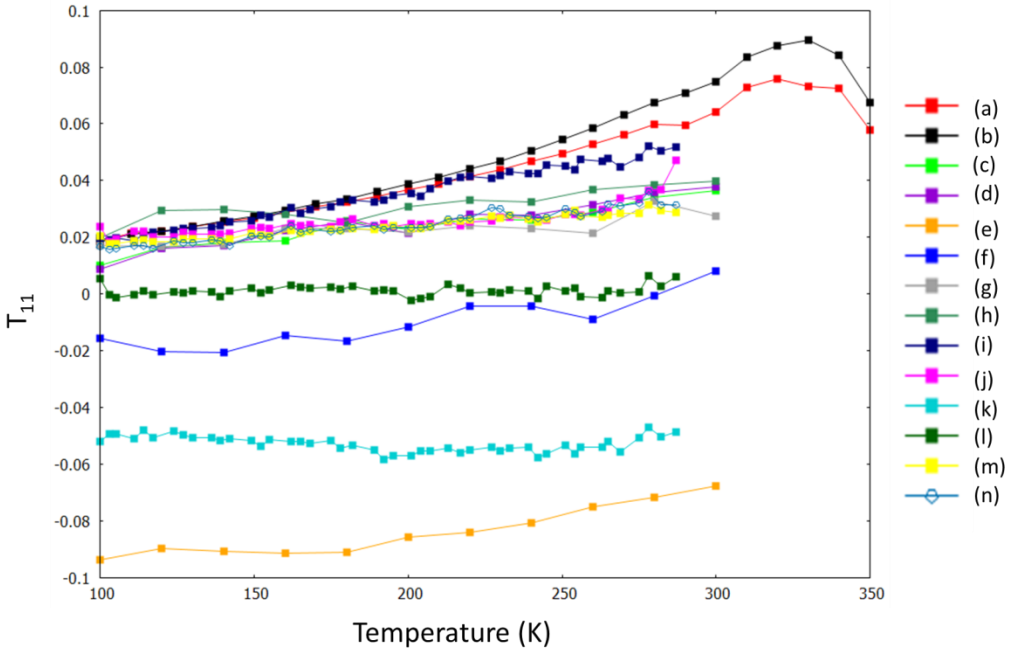

Figure A7.19 Tensor T_{11} as a function of temperature for molecules in DMU2,4-DNBA: (a) DMU and (b) 2,4-DNBA, in BZN4-OHBA STEP: (c) BZN1, (d) BZN2, (e) BZN3, (f) BZN4, (g) 4-OHBA1 and (h) 4-OHBA2 and in BZN4-OHBA CONT: (i) BZN1, (j) BZN2, (k) BZN3, (l) BZN4, (m) 4-OHBA1 and (n) 4-OHBA2.

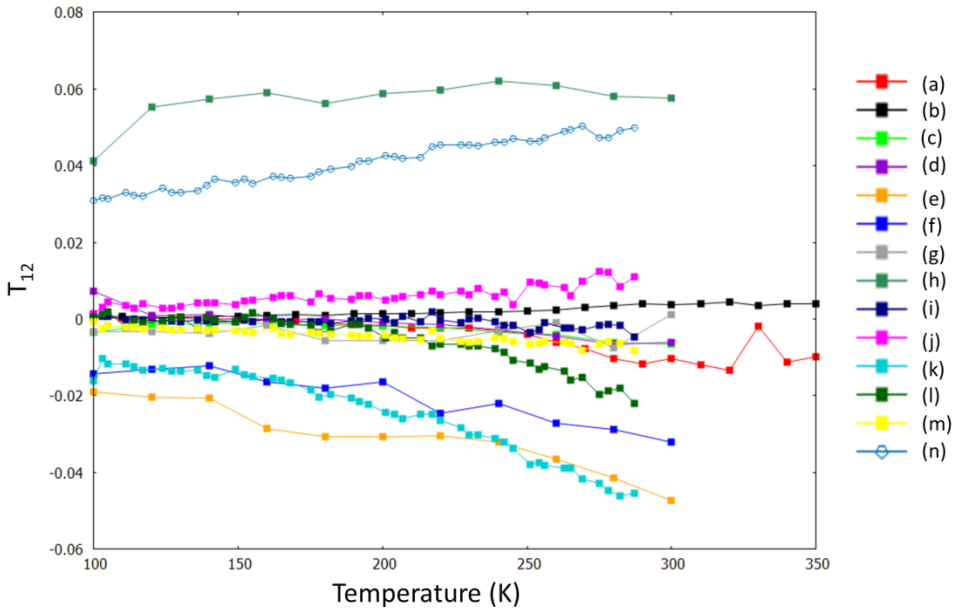

Figure A7.20 Tensor T_{12} as a function of temperature for molecules in DMU2,4-DNBA: (a) DMU and (b) 2,4-DNBA, in BZN4-OHBA STEP: (c) BZN1, (d) BZN2, (e) BZN3, (f) BZN4, (g) 4-OHBA1 and (h) 4-OHBA2 and in BZN4-OHBA CONT. (i) BZN1, (j) BZN2, (k) BZN3, (l) BZN4, (m) 4-OHBA1 and (n) 4-OHBA2.

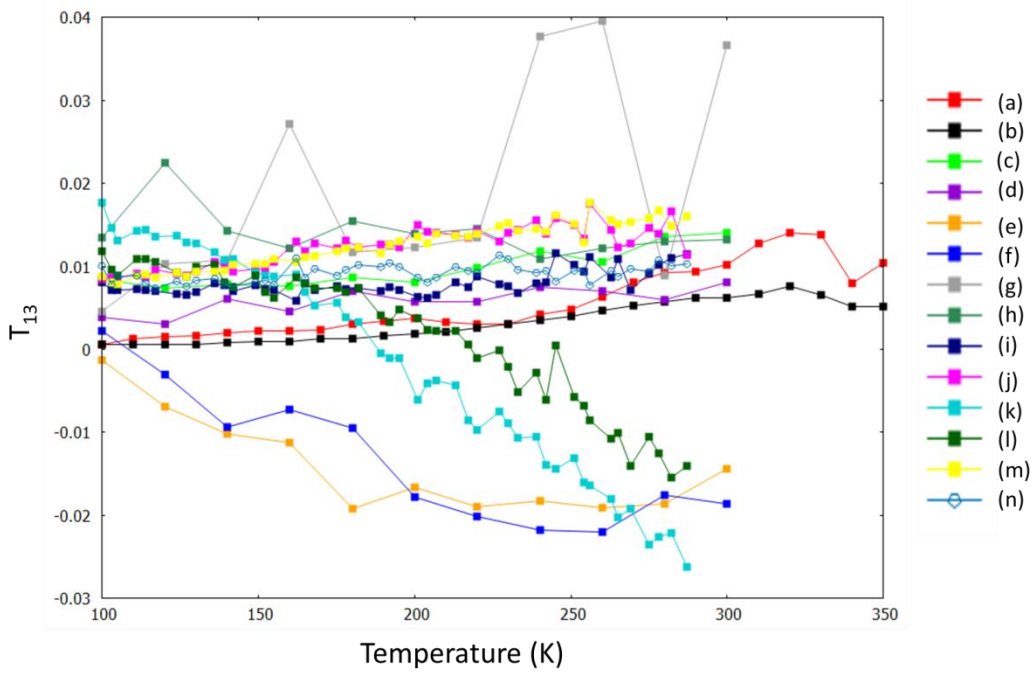

Figure A7.21 Tensor T_{13} as a function of temperature for molecules in DMU2,4-DNBA: (a) DMU and (b) 2,4-DNBA, in BZN4-OHBA STEP (c) BZN1, (d) BZN2, (e) BZN3, (f) BZN4, (g) 4-OHBA1 and (h) 4-OHBA2 and in BZN4-OHBA CONT. (i) BZN1, (j) BZN2, (k) BZN3, (l) BZN4, (m) 4-OHBA1 and (n) 4-OHBA2.

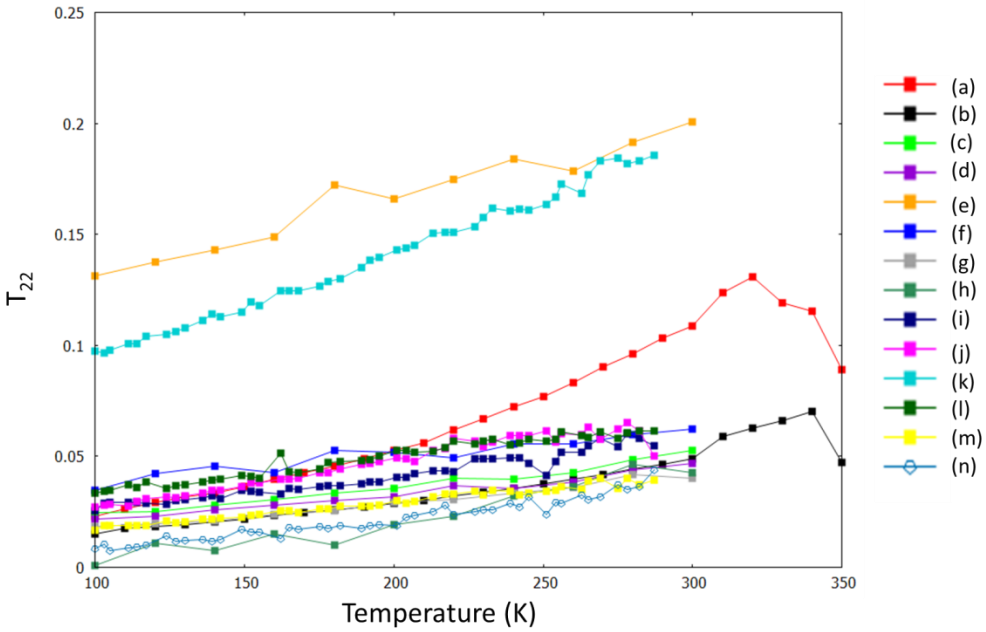

Figure A7.22 Tensor T_{22} as a function of temperature for molecules in DMU2,4-DNBA: (a) DMU and (b) 2,4-DNBA, in BZN4-OHBA STEP: (c) BZN1, (d) BZN2, (e) BZN3, (f) BZN4, (g) 4-OHBA1 and (h) 4-OHBA2 and in BZN4-OHBA CONT. (i) BZN1, (j) BZN2, (k) BZN3, (l) BZN4, (m) 4-OHBA1 and (n) 4-OHBA2.

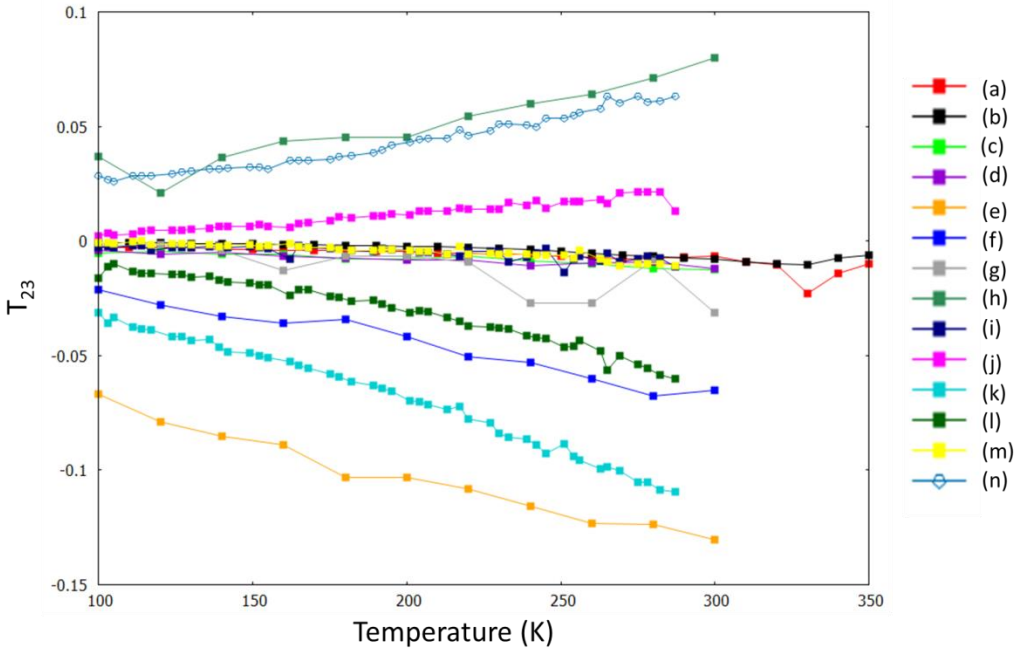

Figure A7.23 Tensor T_{23} as a function of temperature for molecules in DMU2,4-DNBA: (a) DMU and (b) 2,4-DNBA, in BZN4-OHBA STEP: (c) BZN1, (d) BZN2, (e) BZN3, (f) BZN4, (g) 4-OHBA1 and (h) 4-OHBA2 and in BZN4-OHBA CONT: (i) BZN1, (j) BZN2, (k) BZN3, (l) BZN4, (m) 4-OHBA1 and (n) 4-OHBA2.

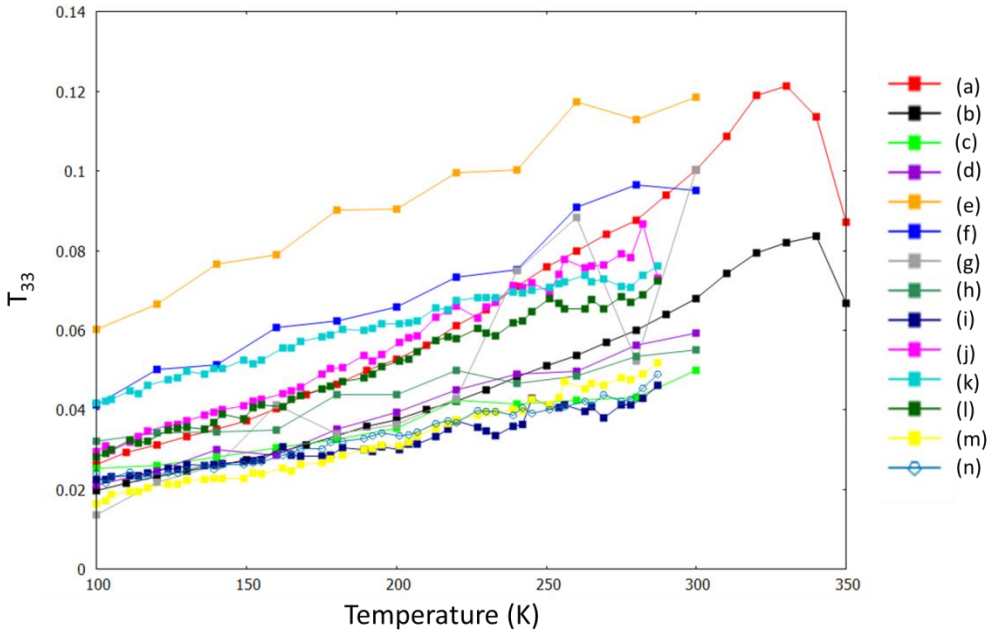

Figure A7.24 Tensor T_{33} as a function of temperature for molecules in DMU2,4-DNBA: (a) DMU and (b) 2,4-DNBA, in BZN4-OHBA STEP: (c) BZN1, (d) BZN2, (e) BZN3, (f) BZN4, (g) 4-OHBA1 and (h) 4-OHBA2 and in BZN4-OHBA CONT. (i) BZN1, (j) BZN2, (k) BZN3, (l) BZN4, (m) 4-OHBA1 and (n) 4-OHBA2.

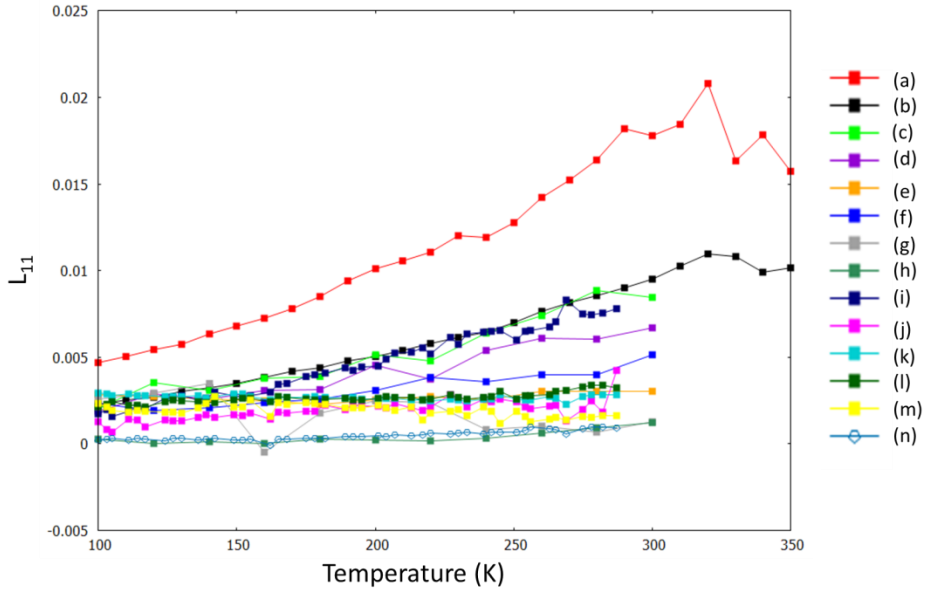

Figure A7.25 Tensor L_{11} as a function of temperature for molecules in DMU2,4-DNBA: (a) DMU and (b) 2,4-DNBA, in BZN4-OHBA STEP: (c) BZN1, (d) BZN2, (e) BZN3, (f) BZN4, (g) 4-OHBA1 and (h) 4-OHBA2 and in BZN4-OHBA CONT: (i) BZN1, (j) BZN2, (k) BZN3, (l) BZN4, (m) 4-OHBA1 and (n) 4-OHBA2.

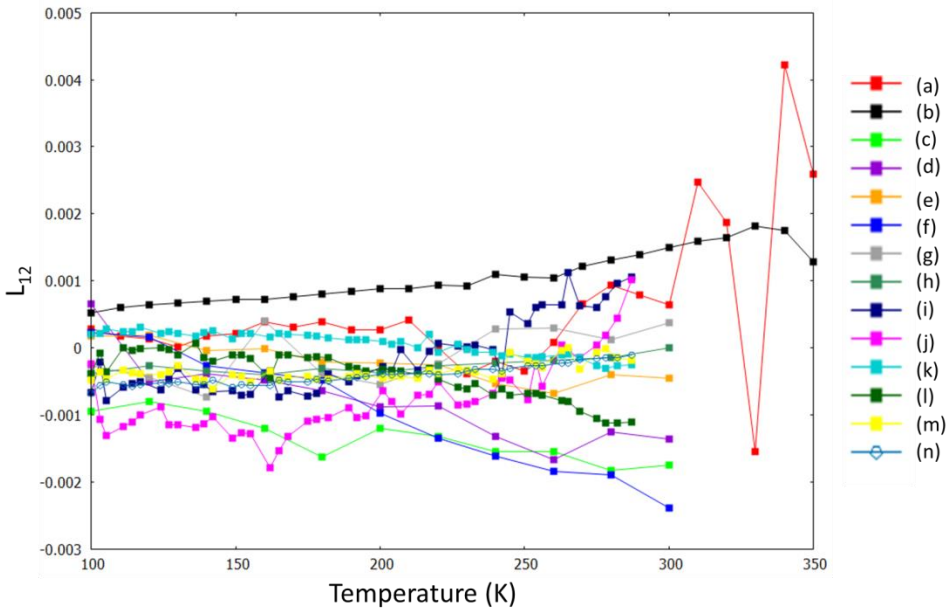

Figure A7.26 Tensor L_{12} as a function of temperature for molecules in DMU2,4-DNBA: (a) DMU and (b) 2,4-DNBA, in BZN4-OHBA STEP: (c) BZN1, (d) BZN2, (e) BZN3, (f) BZN4, (g) 4-OHBA1 and (h) 4-OHBA2 and in BZN4-OHBA CONT. (i) BZN1, (j) BZN2, (k) BZN3, (l) BZN4, (m) 4-OHBA1 and (n) 4-OHBA2.

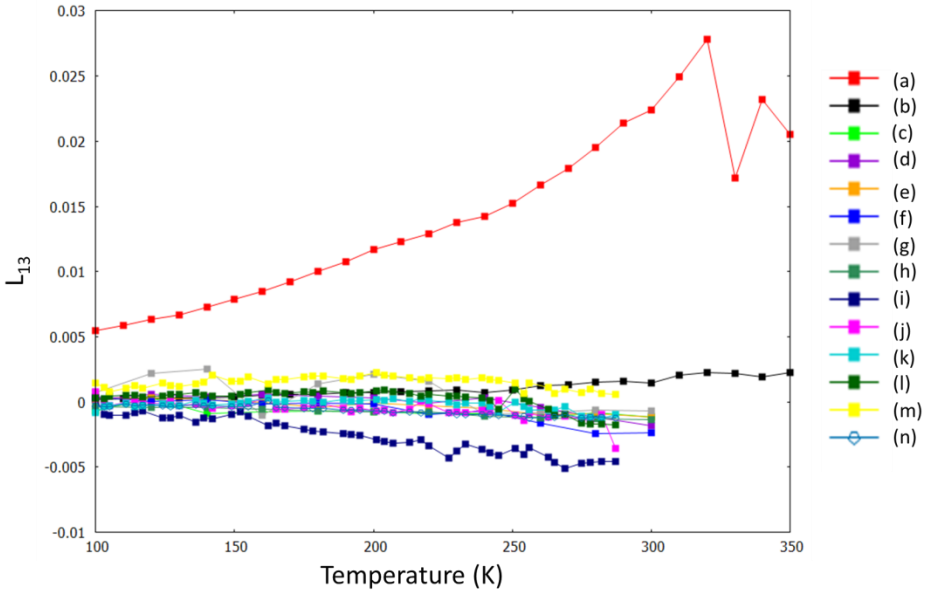

Figure A7.27 Tensor L_{13} as a function of temperature for molecules in DMU2,4-DNBA: (a) DMU and (b) 2,4-DNBA, in BZN4-OHBA STEP: (c) BZN1, (d) BZN2, (e) BZN3, (f) BZN4, (g) 4-OHBA1 and (h) 4-OHBA2 and in BZN4-OHBA CONT.: (i) BZN1, (j) BZN2, (k) BZN3, (l) BZN4, (m) 4-OHBA1 and (n) 4-OHBA2.

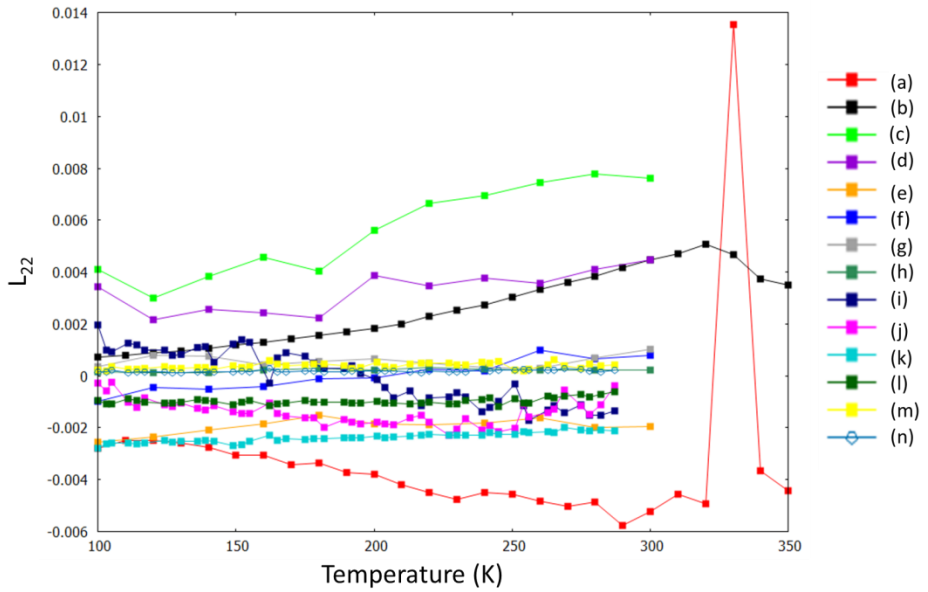

Figure A7.28 Tensor L_{22} as a function of temperature for molecules in DMU2,4-DNBA: (a) DMU and (b) 2,4-DNBA, in BZN4-OHBA STEP: (c) BZN1, (d) BZN2, (e) BZN3, (f) BZN4, (g) 4-OHBA1 and (h) 4-OHBA2 and in BZN4-OHBA CONT.: (i) BZN1, (j) BZN2, (k) BZN3, (l) BZN4, (m) 4-OHBA1 and (n) 4-OHBA2.

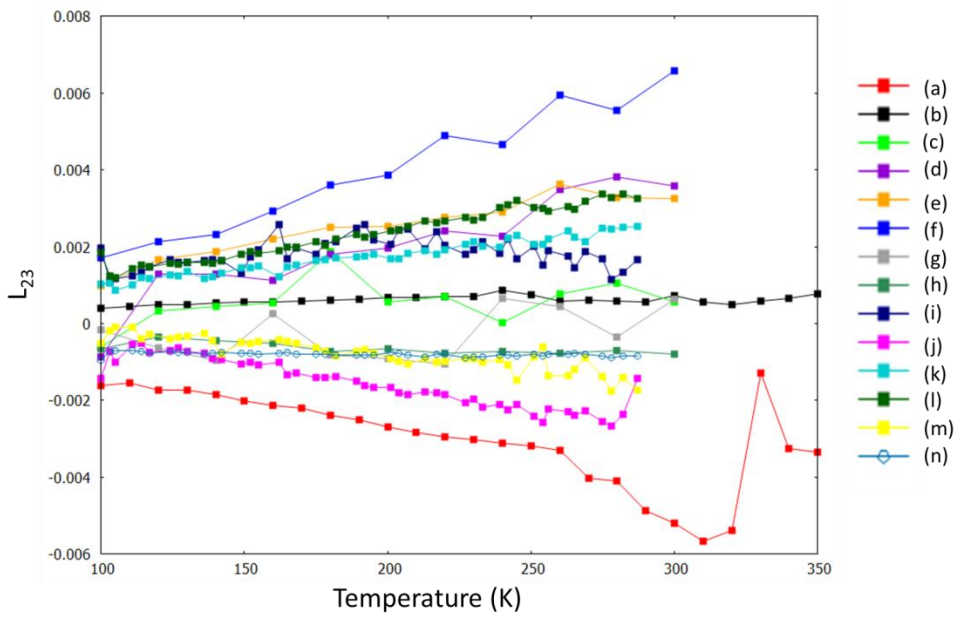

Figure A7.29 Tensor L_{23} as a function of temperature for molecules in DMU2,4-DNBA: (a) DMU and (b) 2,4-DNBA, in BZN4-OHBA STEP: (c) BZN1, (d) BZN2, (e) BZN3, (f) BZN4, (g) 4-OHBA1 and (h) 4-OHBA2 and in BZN4-OHBA CONT.: (i) BZN1, (j) BZN2, (k) BZN3, (l) BZN4, (m) 4-OHBA1 and (n) 4-OHBA2.

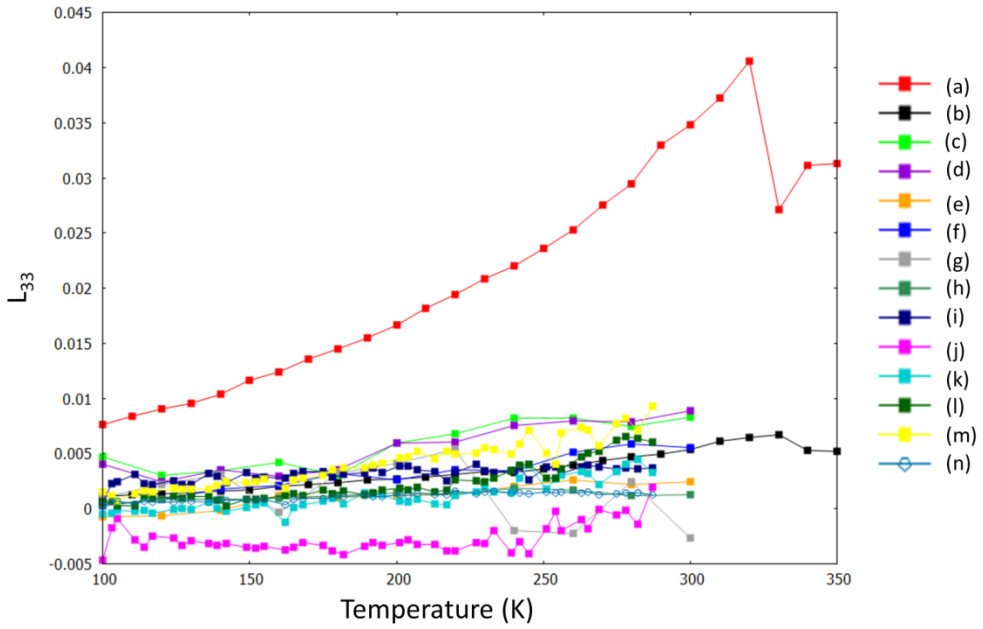

Figure A7.30 Tensor L_{33} as a function of temperature for molecules in DMU2,4-DNBA (a) DMU and (b) 2,4-DNBA, in BZN4-OHBA STEP: (c) BZN1, (d) BZN2, (e) BZN3, (f) BZN4, (g) 4-OHBA1 and (h) 4-OHBA2 and in BZN4-OHBA CONT: (i) BZN1, (j) BZN2, (k) BZN3, (l) BZN4, (m) 4-OHBA1 and (n) 4-OHBA2.

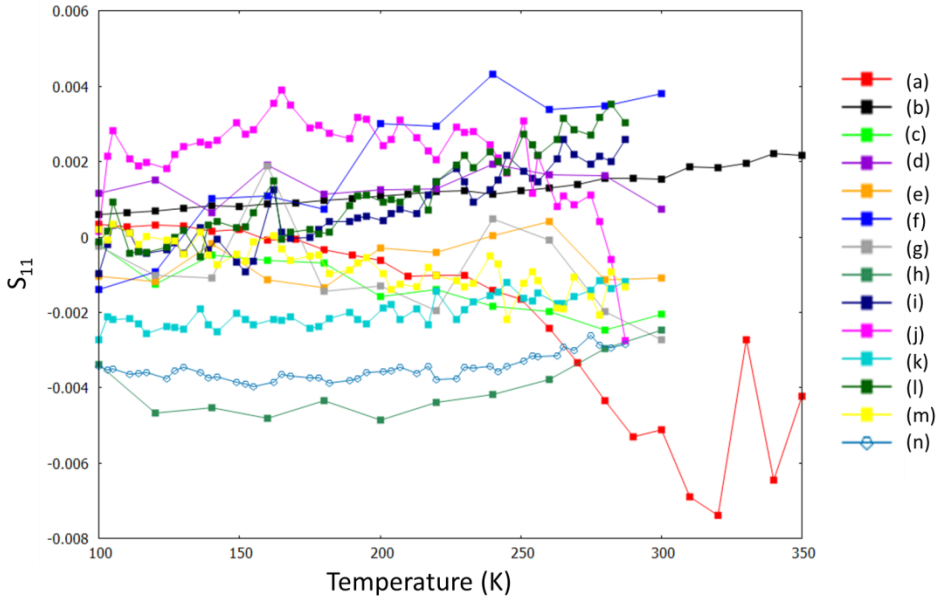

Figure A7.31 Tensor S_{11} as a function of temperature for molecules in DMU2,4-DNBA: (a) DMU and (b) 2,4-DNBA, in BZN4-OHBA STEP: (c) BZN1, (d) BZN2, (e) BZN3, (f) BZN4, (g) 4-OHBA1 and (h) 4-OHBA2 and in BZN4-OHBA CONT: (i) BZN1, (j) BZN2, (k) BZN3, (l) BZN4, (m) 4-OHBA1 and (n) 4-OHBA2.

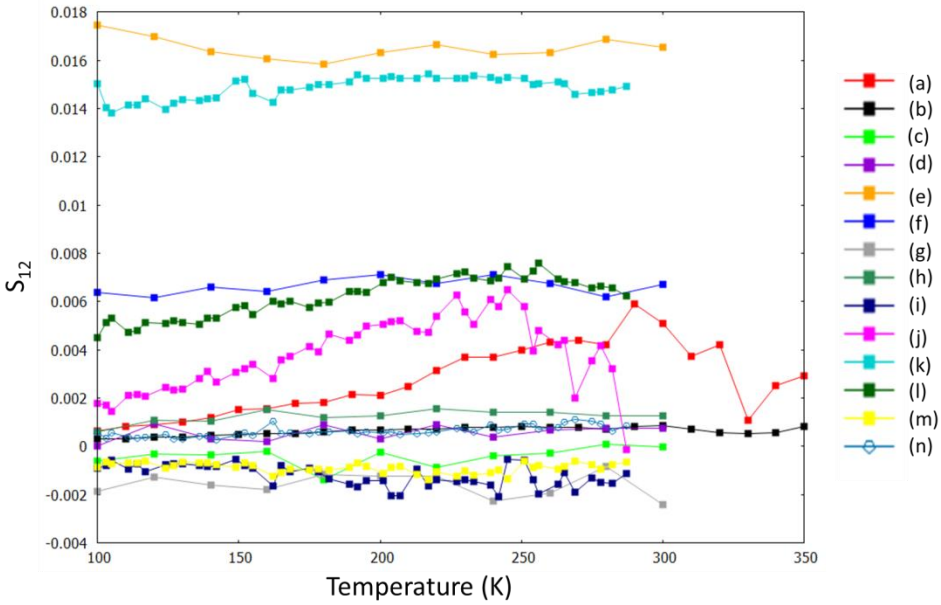

Figure A7.32 Tensor S_{12} as a function of temperature for molecules in DMU2,4-DNBA: (a) DMU and (b) 2,4-DNBA, in BZN4-OHBA STEP: (c) BZN1, (d) BZN2, (e) BZN3, (f) BZN4, (g) 4-OHBA1 and (h) 4-OHBA2 and in BZN4-OHBA CONT. (i) BZN1, (j) BZN2, (k) BZN3, (l) BZN4, (m) 4-OHBA1 and (n) 4-OHBA2.

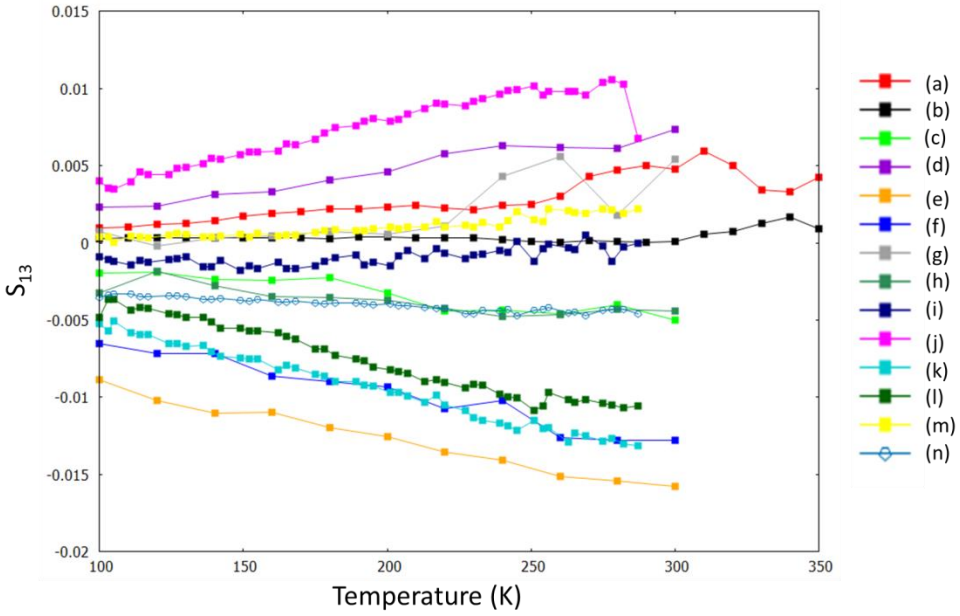

Figure A7.33 Tensor S_{13} as a function of temperature for molecules in DMU2,4-DNBA: (a) DMU and (b) 2,4-DNBA, in BZN4-OHBA STEP: (c) BZN1, (d) BZN2, (e) BZN3, (f) BZN4, (g) 4-OHBA1 and (h) 4-OHBA2 and in BZN4-OHBA CONT. (i) BZN1, (j) BZN2, (k) BZN3, (l) BZN4, (m) 4-OHBA1 and (n) 4-OHBA2.

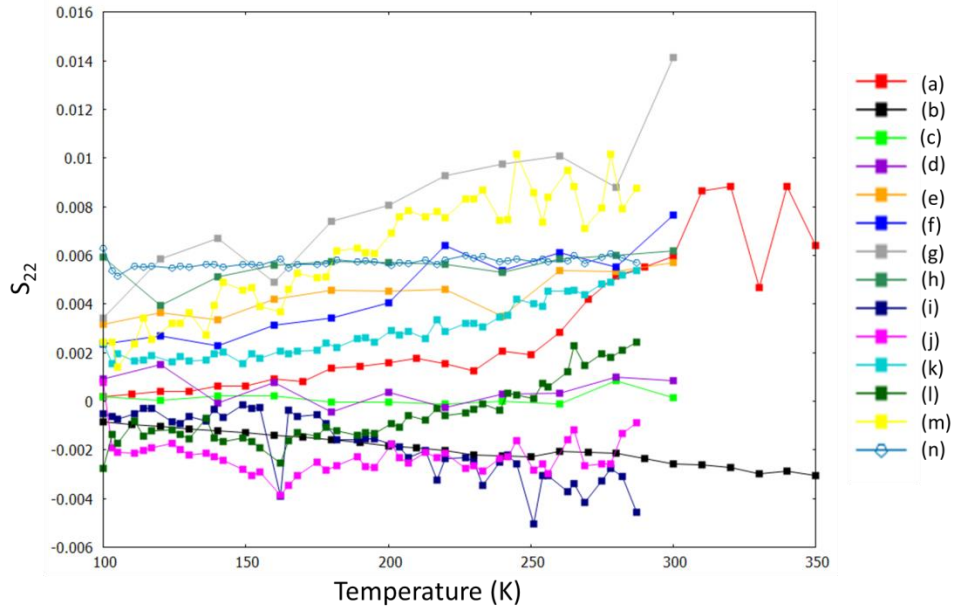

Figure A7.34 Tensor S_{22} as a function of temperature for molecules in DMU2,4-DNBA: (a) DMU and (b) 2,4-DNBA and in BZN4-OHBA STEP: (c) BZN1, (d) BZN2, (e) BZN3, (f) BZN4, (g) 4-OHBA1 and (h) 4-OHBA2 and in BZN4-OHBA CONT: (i) BZN1, (j) BZN2, (k) BZN3, (l) BZN4, (m) 4-OHBA1 and (n) 4-OHBA2.

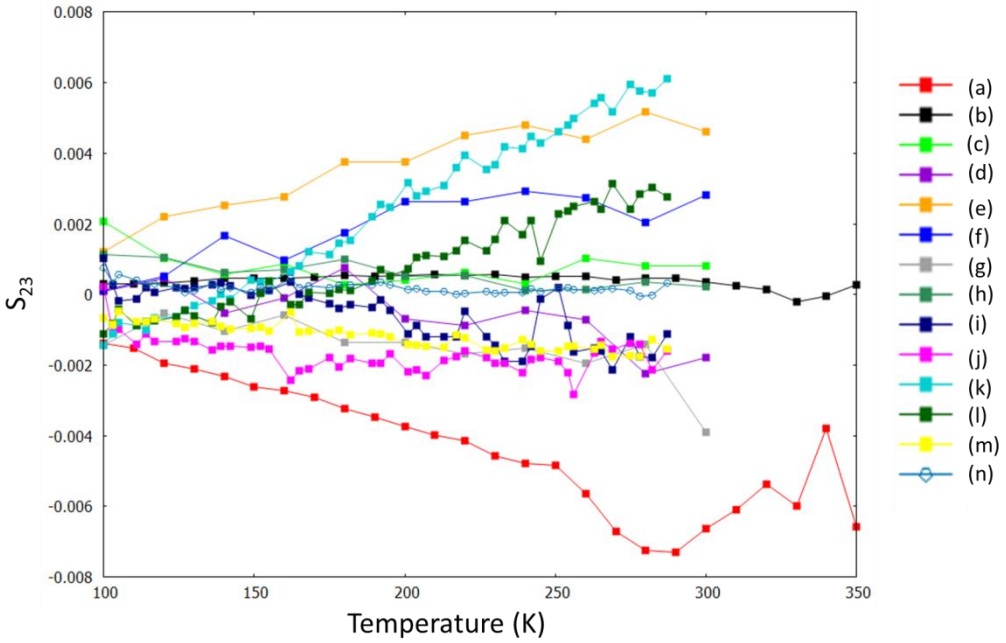

Figure A7.35 Tensor S_{23} as a function of temperature for molecules in DMU2,4-DNBA: (a) DMU and (b) 2,4-DNBA, in BZN4-OHBA STEP: (c) BZN1, (d) BZN2, (e) BZN3, (f) BZN4, (g) 4-OHBA1 and (h) 4-OHBA2 and in BZN4-OHBA CONT: (i) BZN1, (j) BZN2, (k) BZN3, (l) BZN4, (m) 4-OHBA1 and (n) 4-OHBA2.

Appendix A9 (Chapter 9)

A9.1 Competition experiments

1:1 methanol ethanol solvent mix: **NS1** (Figure A9.1).

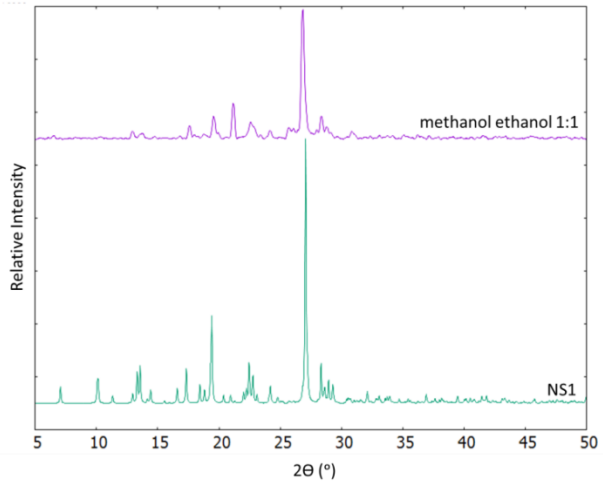

Figure A9.1 PXRD patterns of the 1:1 methanol:ethanol solvent mix crystallisation product and the simulated powder pattern of **NS1** (150 K structure).

1:1 methanol acetonitrile solvent mix: single crystal unit cells of **IM1** and **IM3**.

1:1 methanol acetone solvent mix: single crystal unit cell of **IM1**.

1:1 methanol ethyl acetate solvent mix: single crystal unit cell of **IM1**.

1:1 methanol water solvent mix: PXRD pattern matches that of **NS1** (Figure A9.2).

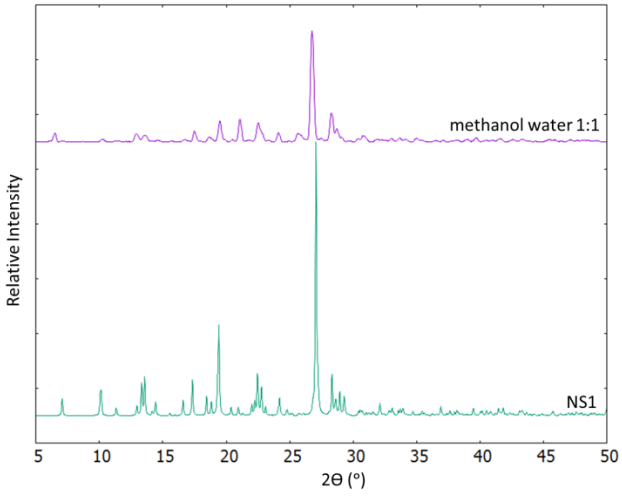

Figure A9.2 PXRD patterns of the 1:1 methanol:water solvent mix crystallisation product and the simulated powder pattern of **NS1** (150 K structure).

1:1 methanol diethyl ether solvent mix: single crystal unit cell of **IM1**.

1:1 ethanol acetonitrile solvent mix: single crystal unit cell of **IM2**.

1:1 ethanol acetone solvent mix: PXRD pattern matches that of **NS1** (Figure A9.3).

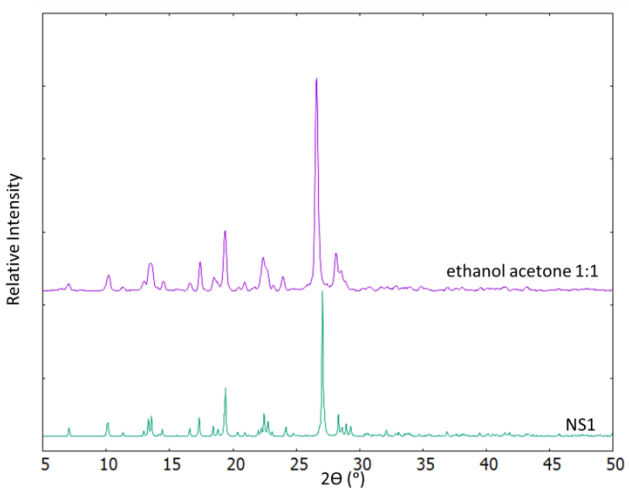

Figure A9.3 PXRD patterns of the 1:1 ethanol:acetone solvent mix crystallisation product and the simulated powder pattern of **NS1** (150 K structure).

1:1 ethanol ethyl acetate solvent mix: single crystal unit cell of **IM2**.

1:1 ethanol water solvent mix: single crystal unit cell of **NS1**.

1:1 ethanol diethyl ether solvent mix: single crystal unit cell of **IM2**.

1:1 acetonitrile acetone solvent mix: single crystal unit cell **IM3**.

1:1 acetonitrile THF solvent mix: PXRD pattern is most similar to that of **IM2** (Figure A9.4).

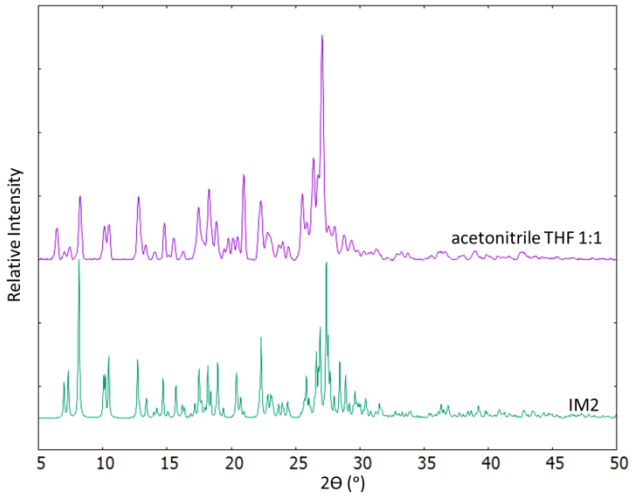

Figure A9.4 PXRD patterns of the 1:1 acetonitrile THF solvent mix crystallisation product and the simulated powder pattern of **IM2** (100 K structure).

1:1 acetonitrile ethyl acetate solvent mix: single crystal unit cell of **IM3**.

1:1 acetonitrile water solvent mix: single crystal unit cell of **NS1**.

1:1 acetonitrile diethyl ether solvent mix: single crystal unit cell of **IM3**.

1:1 acetone THF solvent mix: single crystal unit cell of **IM5**.

1:1 acetone ethyl acetate solvent mix: single crystal cell of **IM6**.

1:1 acetone water solvent mix: PXRD pattern is most similar to that of **IM2** (Figure A9.5).

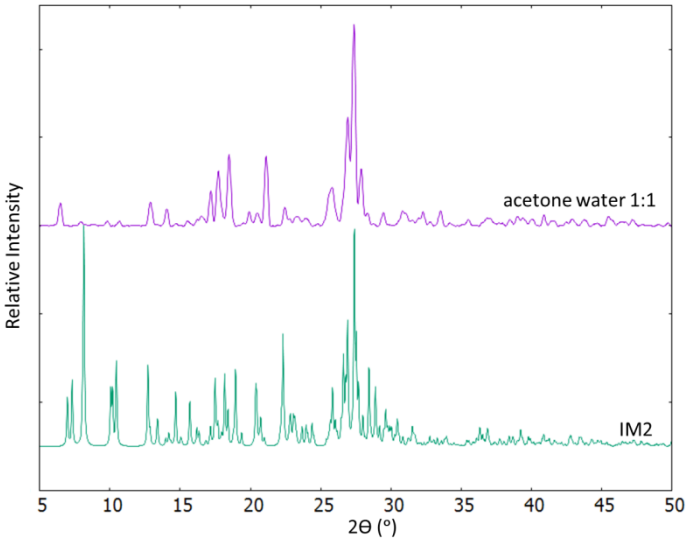

Figure A9.5 PXRD patterns of the 1:1 acetone water solvent mix crystallisation product and the simulated powder pattern for **IM2** (100 K structure).

1:1 acetone diethyl ether solvent mix: PXRD pattern is most similar to that of **IM2** (Figure A9.6).

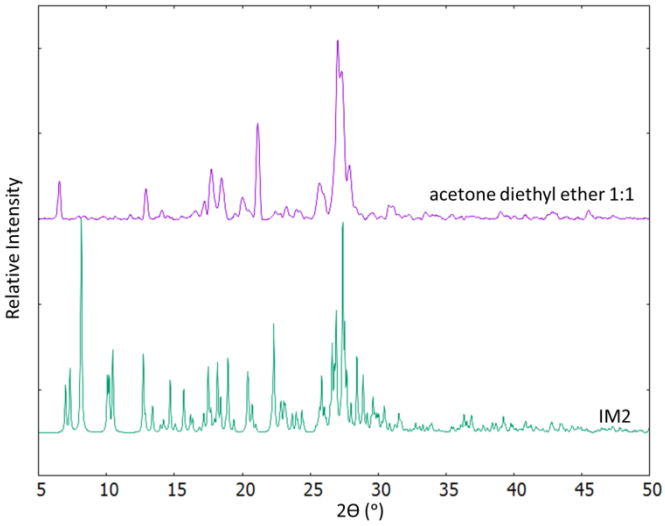

Figure A9.6 PXRD patterns of the 1:1 acetone diethyl ether solvent mix crystallisation product and the simulated powder pattern for **IM2** (100 K structure).

1:1 THF ethyl acetate solvent mix: PXRD pattern is most similar to that of **NS1** (Figure A9.7).

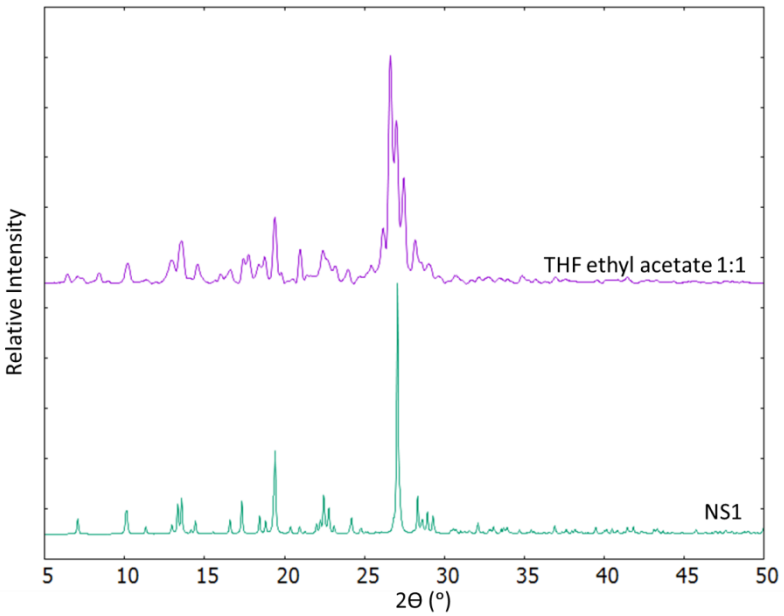

Figure A9.7 PXRD patterns of the 1:1 THF ethyl acetate solvent mix crystallisation product and the simulated powder pattern for **NS1** (150 K structure).

1:1 THF water solvent mix: single crystal unit cell **NS1**.

1:1 THF diethyl ether solvent mix: single crystal unit cell of **IM5**.

1:1 ethyl acetate water solvent mix: Single crystal unit cell of **NS1**.

1:1 ethyl acetate diethyl ether solvent mix: Single crystal unit cell of **IM6**.

A9.2 Thermal behaviour

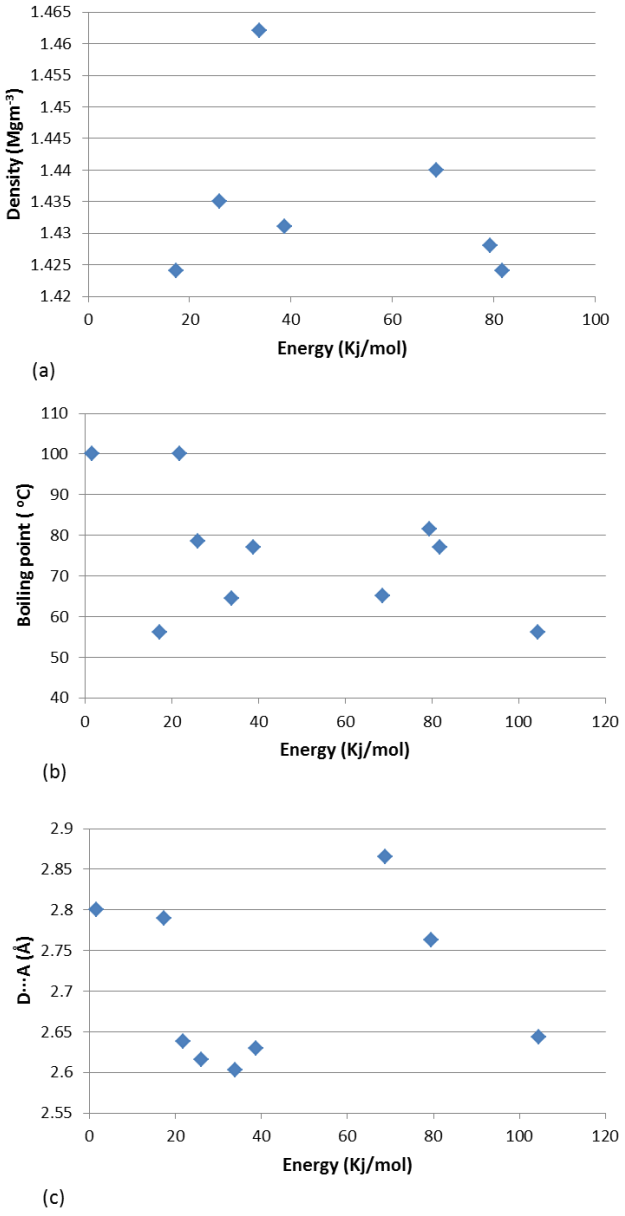

Figure A9.8 Thermal energy of desolvation versus (a) crystal density, (b) solvent boiling point and (c) host-guest interaction length.